



UNIVERSITÀ  
DEGLI STUDI  
DI PADOVA

Sede Amministrativa: Università degli Studi di Padova

Dipartimento di Scienze Chimiche

CORSO DI DOTTORATO DI RICERCA IN SCIENZE MOLECOLARI

CURRICOLO SCIENZE CHIMICHE

XXIX CICLO

Novel antitubercular Ru(III)-, Cu(II)- and Au(III)-based coordination compounds: from rational design, synthesis and physico-chemical characterization to nanoformulation, targeted delivery and *in vitro* evaluation.

**Coordinatore:** Prof. Antonino Polimeno

**Supervisore:** Prof. Dolores Fregona

**Valutatori:** Prof. Stefano Antoniutti (Università Ca' Foscari di Venezia)  
Prof. Luciano Marchiò (Università di Parma)

**Dottorando:** Brustolin Leonardo



## INDEX

ABSTRACT .....	1
ABSTRACT (Italian version) .....	3
1. INTRODUCTION .....	5
1.1 Biological and Medicinal Inorganic Chemistry .....	5
1.2 Cancer as a global burden .....	7
1.2.1 Cancer: brief description of an evolving disease .....	8
1.2.2 Cancer: reprogramming cell division and metabolism .....	11
1.3 Cancer treatments: from chemotherapy and radiotherapy to targeted therapies .....	14
1.3.1 Cisplatin: virtues and faults of the milestone drug in anticancer chemotherapy and medicinal inorganic chemistry .....	16
1.3.2 Targeted treatments based on the cancer hallmarks: “-ib” and “-mab” therapies .....	21
1.4 Discovering and developing new anticancer drugs: the role of academia and the problem of translational science .....	24
2. AIM OF THE WORK .....	29
3. MATERIALS AND INSTRUMENTAL .....	31
3.1 Chemicals for the synthesis of the dithiocarbamate ligands and the Ru(III), Cu(II) and Au(I)/(III) related complexes .....	31
3.2 Chemicals for the modifications of Pluronic® F127 .....	31
3.3 Chemicals for the <i>in vitro</i> biological studies .....	32
3.4 Instrumental information .....	32
4. THE DITHIOCARBAMATES AS CHEMOPROTECTANT LIGANDS .....	37
4.1 Chemical and biological overview of dithiocarbamates .....	37
4.2 Focus on the coordination chemistry of cyclic <i>N,N</i> -disubstituted dithiocarbamates .....	40
4.3 Synthesis of the selected cyclic <i>N,N</i> -disubstituted dithiocarbamate ligands .....	43
4.3.1 Synthesis of dithiocarbamate ligands derived from piperidine (K PipeDTC) and morpholine (K MorphDTC) .....	43
4.3.2 Synthesis of dithiocarbamate ligands derived from indoline (K IndolineDTC) .....	44
4.3.3 Synthesis of dithiocarbamate ligands of L-proline derivatives (Na ProOMeDTC and Na ProOtBuDTC) .....	45
4.3.4 Synthesis of dithiocarbamate ligand of aromatic <i>N</i> -heterocycles (Na CDT, Na IndDTC, and Na PyrDTC) .....	46
4.4 Discussion .....	47
4.4.1 Considerations about the synthetic routes .....	47
4.4.2 <sup>1</sup> H-NMR characterization .....	48
4.4.3 FT-IR characterization .....	49
5. RUTHENIUM DITHIOCARBAMATES .....	53

5.1 Ruthenium as a key player for new metallodrugs.....	53
5.2 Ruthenium dithiocarbamates and their application in the oncological field.....	56
5.3 Synthesis of the Ru(III) derivatives of the selected cyclic <i>N,N</i> -disubstituted dithiocarbamato ligands .	59
5.3.1 Synthesis of Ru(III) dithiocarbamato complexes of PDT, PipeDTC, MorphDTC and IndolineDTC..	59
5.3.2 Synthesis of Ru(III) dithiocarbamato complexes of L-proline ester derivatives (ProOMeDTC and ProOtBuDTC).....	63
5.3.3 Synthesis of Ru(III) dithiocarbamato complexes of CDT .....	64
5.4 Discussion .....	66
5.4.1 Considerations on the synthetic routes .....	66
5.4.2 ESI-MS analysis .....	67
5.4.3 <sup>1</sup> H-NMR characterization.....	68
5.4.4 FT-IR characterization.....	72
5.4.5 UV-Vis characterization .....	75
6. COPPER DITHIOCARBAMATES .....	79
6.1 Copper: an essential element for live beings .....	79
6.1.1 Copper and cancer: the role of the metal in angiogenesis and possible therapies .....	82
6.2 Copper(II) dithiocarbamates as anticancer agents.....	84
6.3 Synthesis of the Cu(II) derivatives with selected cyclic <i>N,N</i> -disubstituted dithiocarbamato ligands ...	85
6.3.1 Synthesis of Cu(II) dithiocarbamato complexes of PDT, PipeDTC, MorphDTC and IndolineDTC...	86
6.3.2 Synthesis of Cu(II) dithiocarbamato complexes of L-proline ester derivatives (ProOMeDTC and ProOtBuDTC).....	87
6.3.3 Synthesis of Cu(II) dithiocarbamato complexes of aromatic <i>N</i> -heterocycles CDT, IndDTC, and PyrrDTC.....	88
6.4 Discussion .....	89
6.4.1 Considerations on the synthetic route and X-ray structural characterization .....	89
6.4.2 ESI-MS analysis .....	91
6.4.3 <sup>1</sup> H-NMR characterization.....	92
6.4.4 FT-IR characterization.....	93
6.4.5 UV-Vis characterization .....	96
7. GOLD DITHIOCARBAMATES.....	99
7.1 Gold: an exogenous metal towards striking opportunities in medicinal inorganic chemistry.....	99
7.1.1 The chemistry of Gold .....	99
7.1.2 Gold in medicine and its potential therapeutic application as anticancer agent.....	100
7.2 Gold(III) dithiocarbamates as anticancer agents.....	104
7.3 Synthesis of the Au(I)/(III) derivatives with the selected cyclic <i>N,N</i> -disubstituted dithiocarbamato ligands.....	107

7.3.1 Synthesis of Au(I) complexes with the selected cyclic <i>N,N</i> -disubstituted dithiocarbamato ligands, [Au <sub>2</sub> (DTC) <sub>2</sub> ] .....	107
7.3.2 Synthesis of Au(III) dithiocarbamato dichloro complexes, [Au <sup>III</sup> Cl <sub>2</sub> (DTC)] .....	111
7.3.3 Synthesis of Au(III) dithiocarbamato dibromo complexes, [Au <sup>III</sup> Br <sub>2</sub> (DTC)] .....	116
7.3.4 Synthesis of ionic Au(III) bis(piperidine dithiocarbamato)complexes, [Au <sup>III</sup> (PipeDTC) <sub>2</sub> ]X (X= Cl, Br) .....	120
7.3.5 Synthesis of the ionic Au(III) bis(piperidine dithiocarbamato)complex [Au <sup>III</sup> (PipeDTC) <sub>2</sub> ][AuBr <sub>2</sub> ] .....	121
7.3.6 Synthesis of the ionic Au(III) bis(piperidine dithiocarbamato) complex [Au <sup>III</sup> (PipeDTC) <sub>2</sub> ][AuCl <sub>4</sub> ] .....	122
7.4 Discussion .....	122
7.4.1 Considerations on the synthetic routes and X-ray structural characterization .....	122
7.4.2 ESI-MS analysis .....	127
7.4.3 <sup>1</sup> H-NMR characterization .....	127
7.4.4 FT-IR characterization .....	129
7.4.5 UV-Vis characterization .....	133
7.4.5.1 Effect of DMSO on [AuX <sub>2</sub> (DTC)] complexes: a UV-Vis study .....	136
8. PLURONIC® F127 MICELLES FOR THE CANCER-DELIVERY OF SELECTED METAL-DTC COMPOUNDS .....	139
8.1 Nanocarrier platforms for anticancer therapy .....	139
8.1.1 Passive vs active targeting and mechanism of nanoparticle cell uptake .....	140
8.2 Metal complexes and their delivery using nanoformulations .....	143
8.3 Chemical and biological overview of Pluronic® F127 .....	144
8.4 Active cancer-targeting by micelle bio-conjugation with carbohydrates .....	146
8.5 Synthesis of the carbohydrate-targeted Pluronic® F127 .....	148
8.5.1 Synthesis of Pluronic® F127 conjugated with 2,3,4,6-penta-O-acetyl-β-D-glucopyranoside (acetyl-protected glucose), PF127-GluOAc .....	148
8.5.2 Synthesis of Pluronic® F127 conjugated with β-D-glucopyranoside (deprotected glucose), PF127-GluOH .....	149
8.5.3 Modification of terminal hydroxyl groups of PF127 into aldehydes, PF127-CHO .....	150
8.5.4 Synthesis of Pluronic® F127 conjugated with 1,3,4,6-penta-O-acetyl-2-amino-2-deoxy-β-D-glucopyranoside (acetyl-protected glucosamine), PF127-GlnOAc .....	151
8.5.5 Synthesis of Pluronic® F127 conjugated with 2-amino-2-deoxy-D-glucose (deprotected glucosamine), PF127-GlnOH .....	152
8.5.6 Synthesis of tosylated Pluronic® F127, PF127-OTs .....	153
8.5.7 Synthesis of phthalimido Pluronic® F127, PF127-Phtha .....	154
8.5.8 Synthesis of amino Pluronic® F127, PF127-NH <sub>2</sub> .....	155
8.5.9 Synthesis of Pluronic® F127 conjugated with fluoresceine via thioureido bond, PF127-FITC .....	156
8.5.10 Pluronic® F127 conjugations achieved in collaboration with the University of Milano-Bicocca .....	157
8.5.10.1 Synthesis of the β-D-aminoxy glucose and maltose .....	157
8.5.10.2 Conversion of the terminal hydroxyl groups of Pluronic® F127 to ketones, PF127-Levu ...	158

8.5.10.3 PF127 bio-conjugation by oxime formation between the ketones of PF127-Levu and the aminoxy moiety of the carbohydrates .....	158
8.6 Discussion about the synthesized carbohydrate-functionalized Pluronic® F127 .....	159
8.6.1 Considerations on the synthetic routes .....	159
8.6.2 <sup>1</sup> H-NMR characterization.....	164
8.6.3 FT-IR characterization.....	166
8.7 Encapsulation of selected metal-dithiocarbamate derivatives in Pluronic® F127 and carbohydrate-labeled Pluronic® F127 micelles .....	166
8.7.1 Preparation of the nanoformulations of the selected metal-DTC complexes .....	168
8.8 Characterization of the prepared nanoformulations .....	169
8.8.1 Loading measurements .....	169
8.8.2 DLS analysis.....	169
8.8.3 TEM analysis .....	171
8.8.4 Solution stability studies.....	171
9. IN VITRO SCREENING OF SYNTHETIZED METAL-DITHIOCARBAMATO COMPLEXES AND PF127 NANOFORMULATIONS AGAINST HUMAN CANCER CELL LINES .....	175
9.1 Cell cultures .....	175
9.1.1 HeLa cancer cell line and culture preparation for in vitro studies .....	175
9.1.2 HepG2 and HepG2/SB3 cancer cell lines, and cultures preparation for in vitro studies.....	176
9.2 Stability in aqueous media of the metal-dithiocarbamate complexes and sample preparation for in vitro studies .....	177
9.3 Results of in vitro cytotoxicity studies on metal-dithiocarbamate samples .....	180
9.4 Selection of the Lead Compounds using the Lipophilic Efficiency (LipE) evaluation .....	183
9.4.1 LogP measurements .....	184
9.4.2 Lipophilic Efficiency (LIPE) evaluation on most active compounds.....	186
9.5 Results of in vitro cytotoxicity studies on Lead Compounds encapsulated in PF127 micelles .....	188
9.6 Confocal microscopy analysis on the HepG2/CTR and HepG2/SB3 cells treated with PF127-FITC micelles.....	193
9.7 xCELLigence measurements for real-time monitoring of HepG2/CTR and HepG2/SB3 cells viability after treatment with the selected Lead Compounds.....	195
10. FINAL REMARKS.....	201
11. COLLABORATIONS .....	205
REFERENCES.....	207
SUPPORTING INFORMATION A - <sup>1</sup> H-NMR spectra of the synthesized dithiocarbamate ligands .....	231
SUPPORTING INFORMATION B - <sup>1</sup> H-NMR spectra of the synthesized Ru(III) dithiocarbamate complexes .....	235
SUPPORTING INFORMATION C - <sup>1</sup> H-NMR spectra of the synthesized Cu(II) dithiocarbamate complexes.....	243
SUPPORTING INFORMATION D - <sup>1</sup> H-NMR spectra of the synthesized Au(I)/(III) dithiocarbamate complexes .....	247

SUPPORTING INFORMATION E - $^1\text{H}$ -NMR and $^{13}\text{C}$ -NMR spectra of the synthesized Pluronic <sup>®</sup> F127 derivatives .....	263
SUPPORTING INFORMATION F - FT-IR spectra of the synthesized dithiocarbamate ligands.....	273
SUPPORTING INFORMATION G - FT-IR spectra of the synthesized Ru(III) dithiocarbamate complexes .....	277
SUPPORTING INFORMATION H - FT-IR spectra of the synthesized Cu(II) dithiocarbamate complexes.....	287
SUPPORTING INFORMATION I - FT-IR spectra of the synthesized Au(I)/(III) dithiocarbamate complexes...	295
SUPPORTING INFORMATION J - FT-IR spectra of the synthesized Pluronic <sup>®</sup> F127 derivatives.....	317
CONGRESS PARTICIPATIONS, COMMUNICATIONS AND PUBLICATIONS DURING THE PhD STUDIES .....	321
Congress participations .....	321
Conference proceedings.....	321
Peer-reviewed papers .....	322
Patents.....	322





## ABSTRACT

There is an essential contribution of inorganic medicinal chemistry in the pharmacopeia. In particular, platinum-based drugs revolutionized the anticancer chemotherapy, and nowadays they find wide application in the treatment of several solid tumors. Nevertheless, their effectiveness is paralleled with severe side-toxicity and the onset of drug resistance. In order to obtain compounds with a better chemotherapeutic index and increased bioavailability, several metal-based compounds have been designed and investigated in the last decades. On these grounds, we present here the synthesis and characterization of a library of coordination compounds containing a biologically-active metal center, namely Ru(III), Cu(II), and Au(III), and one or more dithiocarbamate (DTC) ligands, derived from cyclic amines (aliphatic or aromatic). Several techniques have been used to characterize the compounds, such as elemental analysis, X-ray crystallography, ESI-MS,  $^1\text{H-NMR}$  spectroscopy, FT-IR and UV-Vis spectrophotometries, highlighting different electronic behaviors generated by the DTC substituents. Moreover, the synthesized compounds were tested for their antiproliferative activity against two tumor models. This screening pointed out the druglikeness of some derivatives, which have been successively encapsulated in micellar nanocarriers, being also carbohydrate-functionalized on their hydrophilic surface for a cancer-selective delivery exploiting the Warburg effect. In particular, the nonionic surfactant block copolymer Pluronic<sup>®</sup> F127 (PF127) has been chemically modified with sugars and the derivatives characterized by means of NMR and FT-IR. Then, the two Lead Compounds have been loaded into the hydrophobic core of PF127 non- and cancer-targeting micelles. These nanoformulations have been studied for their dimensions (DLS, TEM) and stability, and tested for their cytotoxicity. The promising results obtained with these nanosystems, accompanied by preliminary *in vitro* mechanistic studies, open intriguing perspectives for the use of this solubility-increasing and neoplasia-targeting strategy for our anticancer metal-DTC complexes.

In conclusion, this work is the basis for optimizing the investigated nanoformulations, followed by future pre-clinical *in vivo* studies on animal models to evaluate i) their carrier capabilities, ii) the cancer-selective release of the cytotoxic cargo, iii) the stability and PK, iv) the anticancer activity and v) the acute/chronic toxicity.



## ABSTRACT

Nella farmacopea odierna vi è un contributo essenziale della chimica farmaceutica inorganica. In particolare, la chemioterapia oncologica è stata rivoluzionata dai farmaci a base di platino, i quali al giorno d'oggi trovano ampio utilizzo nella terapia di molte neoplasie solide. Tuttavia, tale efficacia è controbilanciata dalla tossicità di tali composti, così come dall'insorgenza di resistenza al trattamento. Per questo motivo, negli ultimi decenni sono stati progettati e studiati diversi composti a base di metalli, al fine di migliorare l'indice chemioterapico e la biodisponibilità. Con queste premesse, in questo lavoro di dottorato viene presentata la sintesi e la caratterizzazione di una libreria di composti di coordinazione contenenti un centro metallico attivo biologicamente, ovvero Ru(III), Cu(II) e Au(III), e uno o più leganti ditiocarbammici derivanti da ammine cicliche (alifatiche o aromatiche). Le diverse tecniche spettroscopiche utilizzate per la caratterizzazione di questi complessi, quali l'analisi elementare, la cristallografia a raggi X, ESI-MS, spettroscopia  $^1\text{H-NMR}$ , spettrofotometrie FT-IR e UV-Vis, hanno evidenziato comportamenti elettronici diversi generati dai sostituenti del legante ditiocarbammico. Inoltre, la citotossicità dei composti sintetizzati è stata analizzata su due modelli tumorali umani. I risultati ottenuti hanno dimostrato le ottime proprietà farmacologiche di alcuni complessi, candidandoli ad un ulteriore sviluppo. Di conseguenza, essi sono stati incapsulati in micelle polimeriche funzionalizzate convenientemente con carboidrati, al fine di veicolare selettivamente l'intero sistema supramolecolare verso le cellule tumorali, sfruttando l'effetto Warburg. Al fine di eseguire questi studi, il Pluronic® F127 (PF127), un tensioattivo non ionico co-polimerico, è stato modificato chimicamente per legare degli zuccheri e successivamente caratterizzato mediante NMR e FT-IR. Quindi i due composti *Lead* sono stati caricati sia in micelle di PF127 sia in micelle di PF127 funzionalizzate con carboidrati; le risultanti formulazioni sono state studiate per la loro dimensione (DLS, TEM) e stabilità e successivamente testate *in vitro* per la loro attività citotossica. I risultati promettenti ottenuti con questi nanosistemi, accompagnati da studi meccanicistici preliminari *in vitro*, aprono prospettive interessanti per l'utilizzo di questa strategia capace di aumentare la solubilità dei complessi ditiocarbammici nonché di guidarli selettivamente verso le cellule tumorali.

In conclusione, questo lavoro rappresenta il punto di partenza per l'ottimizzazione delle nanoformulazioni precedentemente analizzate. Esso sarà seguito in futuro da studi pre-clinici *in vivo* su modelli animali, al fine di verificare i) la capacità di trasporto delle micelle, ii) la loro capacità di rilascio del complesso citotossico contenuto in prossimità dell'ambiente tumorale, iii) la stabilità e la farmacocinetica degli aggregati, iv) l'attività tumorale e v) le tossicità cronica e acuta.



## 1. INTRODUCTION

### 1.1 Biological and Medicinal Inorganic Chemistry

Medicinal Inorganic Chemistry is a cross-cutting field that embraces scientific advances in inorganic chemistry, medicinal chemistry, biochemistry, advanced spectroscopy, biophysics, nuclear medicine, physiology clinical medicine and other disciplines in order to bring improvements to human health [1]. Considering the human body, it contains at least 60 detectable elements, although only about 25 of them are supposed to be essential, with an active participation in body healthy [2]. These comprise not only the most common *organic* elements hydrogen, carbon, nitrogen, oxygen and sulfur as prevailing constituents. Indeed, there is a reasonable amount (0.3 %) of metal cations of the *s* group, such as sodium, potassium, magnesium and calcium, and the non-metals (0.25 %) phosphorous, selenium, silicon and halogens (*i.e.*, chlorine, fluorine and iodine). Finally, *d*-block metals (with the exception of the *p*-block element tin) are present as well, for instance cobalt, chrome, copper, iron, manganese, molybdenum, nickel, vanadium and zinc [2-4]. Concerning the latter category, there is a great diversity of metal active sites [5]. As an example, in an estimated 10% of all human proteins, zinc has a catalytic or structural function and remains bound during the protein lifetime, although it is redox-inert maintaining always the oxidation state +2 [6]. On the other hand, manganese has an active redox role in the manganese-dependent superoxide dismutase (MnSOD), an enzyme located in the mitochondria able to transform the toxic superoxide radical ( $O_2^-$ ) into hydrogen peroxide ( $H_2O_2$ ) and oxygen ( $O_2$ ). Furthermore, other SOD-type proteins contain also nickel (NiSOD), iron (FeSOD), or copper and zinc (CuZnSOD) [7].

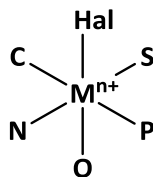
The discovery of important roles in biological processes of metals paved the way to the application of inorganic chemistry to the therapy or diagnosis of different diseases. Nowadays, a significant number of clinical trials or clinically-established molecular entities involve compounds derived from both essential and non-essential metal elements [8].

The medical exploration of derivatives containing metal ions is due to their peculiar properties, such as preferred oxidation states and coordination geometries, although the overall reactivity of a metal-based compound depends on the type and number of ligands and on the biological environment (*e.g.*, pH, oxidizing/reducing conditions, presence of coordinating biomolecules) [9]. In other words, inorganic elements provide for an incredible number of reactions, involving the reduction or oxidation of the metal center and/or the ligands, ligand substitution (see **Figure 1.1**).

## Metal-based drug design

### Metals

- coordination number (range 2-10)
- oxidation state (redox properties)
- coordination geometry (wide range, different biological target)
- metal (10 essential transition metal ions)



### Ligands

- type of ligands (wide range, chelating)
- outer-sphere interactions (H-bond, hydrophobic interaction, targeting moiety)
- ligand-exchange rates (fast/slow)

**Figure 1.1** A coordination compound and some of the features that can be considered in the design of metal-based drugs (or diagnostic agents) [9].

Although the ancient Chinese and Indian practitioners used the gold powder to treat a variety of ailments [10], probably the first metallodrug was *salvarsan* (arsphenamine, a mixture of cyclo-As<sub>3</sub> and cyclo-As<sub>5</sub>, **Figure 1.2 a**), an arsenic-based antimicrobial agent developed by Paul Ehrlich in 1912 and used to fight infectious diseases such as syphilis [11]. Successively, gold(I) thiolates and thiosulfates (*e.g.*, sodium 2-(auriosulfanyl)-3-carboxypropanoate, known as sodium aurothiomalate or Myocrisin, **Figure 1.2 b**) were introduced in the 1930s as injectable formulations against the rheumatoid arthritis, later followed by the oral drug *auranofin* (2,3,4,6-tetra-O-acetyl-1-thio- $\beta$ -L-glucopyranosato- $\kappa$ S<sup>1</sup> triethylphosphoranyliden gold(I), **Figure 1.2 c**) [10]. However, the turning point in the field of Medicinal Inorganic Chemistry was the serendipitous discover of the antitumor action of *cisplatin* (CisDDP, cis-diamminedichloroplatinum(II), **Figure 1.2 d**) by Van Camp and Rosenberg in late 1960s [12]. For its importance in the design and development of new metal-based drugs and its current use against different solid malignances, cisplatin and other platinum derivatives are discussed in detail in **Section 1.3.1**.

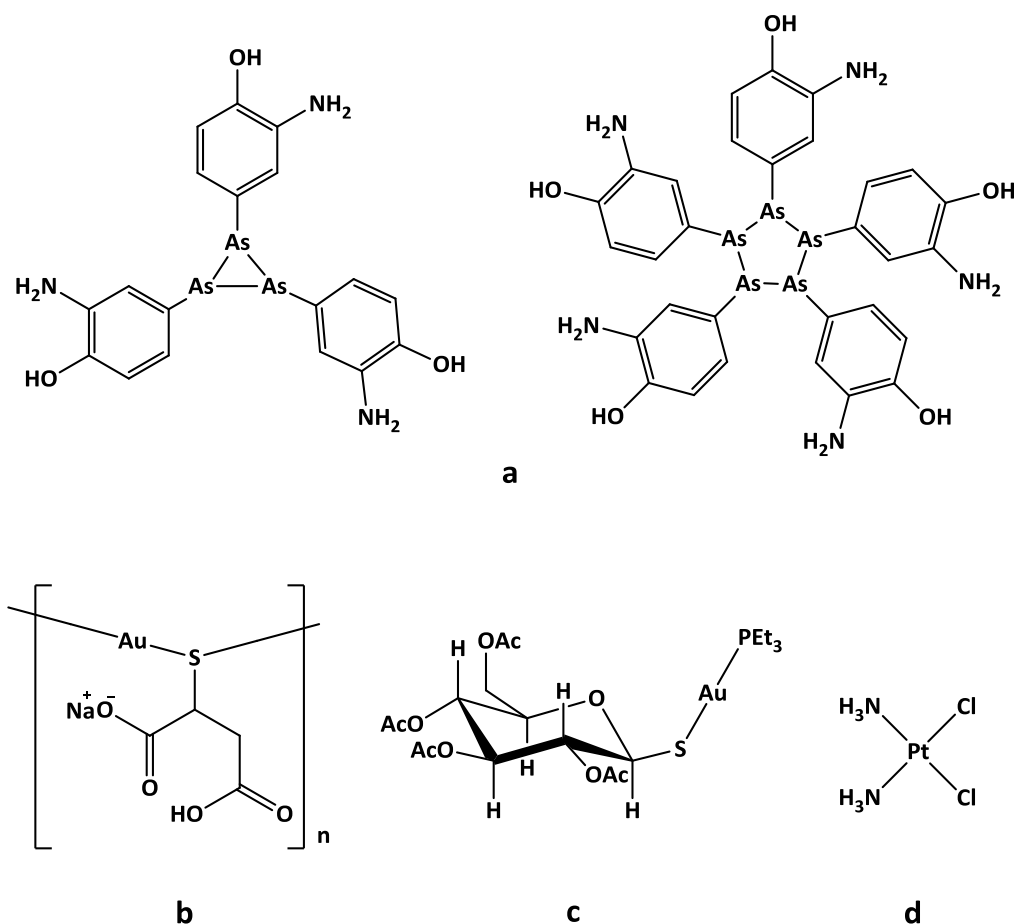


**Figure 1.2** Chemical structures of some inorganic derivatives which have influenced the development of the Medicinal Inorganic Chemistry: *salvarsan* (mixture of 3-amino-4-hydroxyphenyl-arsenic(III) compounds) **a**; *aurothiomalate* (sodium 2-(auriosulfanyl)-3-carboxypropanoate) **b**; *auranofin* (2,3,4,6-tetra-*O*-acetyl-1-thio- $\beta$ -L-glucopyranosato- $\kappa$ S<sup>1</sup> triethylphosphoranyliden gold(I)) **c**; *cisplatin* (CisDDP, cis-diamminedichloroplatinum(II)) **d**.

In conclusion, to date promising novel metal-based drugs are in clinical trials, exploiting the large potential of the inorganic elements, especially transition metals [4]. The applications are in different medical fields, from imaging to the therapy of inflammatory diseases and some infections (*e.g.*, antimalarial, antibacterial and treatment of ophthalmic herpes). However, most researchers are addressing their attention to possible new treatments of cancer as this plague is the first cause of death worldwide according to the recent WHO data [13].

In light of these considerations and taking into account the success of cisplatin as an inhibitor of DNA replication, there is a deep research of an inorganic anticancer therapy, able to overcome the hurdles of the current drugs, including toxicity, onset of resistance and other pharmacological deficiencies.

## 1.2 Cancer as a global burden

In spite of scientific advances in the last decades in oncology, cancer is still the leading cause of death worldwide. The most recent statistics of the World Health Organization (2014) states that the cancer incidence has increased from 12.7 million in 2008 to 14.1 million in 2012, and this trend is projected to

continue, with the number of new cases expected to rise of a further 75%. This will bring the number of cancer cases close to 25 million over the next two decades [14]. If considering females, breast cancer is reported as the most frequent, with 1.6 million of cases in 2012 (25.2 % of all female tumors, **Figure 1.3 a**), whereas lung and prostate cancer are the most common in males, with 1.2 and 1.1 million of cases in 2012, respectively (being 16.7 % and 15 % of all male malignances, **Figure 1.3 b**) [15].

In the last 50 years the amount of scientific publications (today about 2.3 million) and patents (more than 94 thousands) which deal with the word “cancer” are exponentially growing [16]. On the other hand, from the pharmaceutical point of view, over the 2014–2021 forecast period, the breast cancer market (taken as an example) in the eight major markets is expected to increase in value from \$10.4 billion to over \$17.2 billion [17]. Overall, these data demonstrate that the social burden of cancer is associated with an enormous interest from both the scientific community and the Pharma/Biotech industries, thus pushing researchers to find new ways to understand and cure this life-threatening disease.

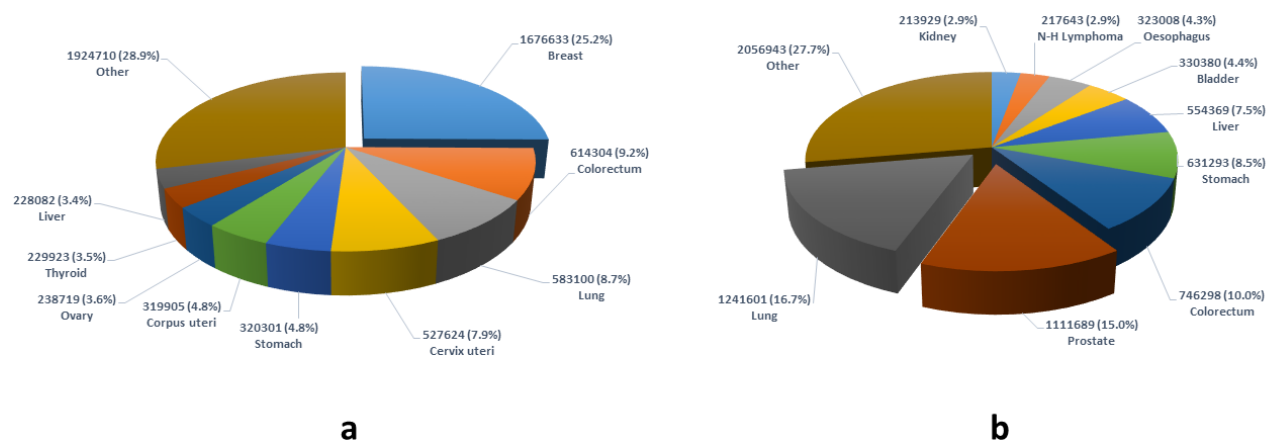


**Figure 1.3** Estimated new cancer cases by sex (female **a**; male **b**) and cancer site worldwide in 2012, with focus on the most common breast cancer (in women) and prostate and lung cancer (in men) [15].

### 1.2.1 Cancer: brief description of an evolving disease

A tumor is an abnormal proliferation of cells leading to an uncontrolled growth of the whole mass, which may be either benign or malignant. A *benign tumor* remains confined to its original location, neither invading the surrounding normal tissue nor spreading to distant body sites. A *malignant tumor* is instead capable of both invading the surrounding normal tissue and spreading throughout the body *via* the circulatory or lymphatic systems (metastasis). Only malignant tumors are referred to as cancers, and it is their ability to invade and metastasize that makes cancer so treacherous. Contrary to benign tumors which are usually removed surgically, the spread of malignant tumors to distant body sites frequently makes them resistant to localized treatments (see **Section 1.3**)[18].

To date, the scientific community has become able to classify the cancer types according to patterns of epidemiology and pathology. Moreover, some malignances are recognized to usually occur at a particular



age, with different frequencies on both sex and, most important, with a particular morphology which usually resembles the originating tissue [19]. The advances in imaging techniques, also thanks to astonishing developments in inorganic nuclear chemistry [20] and its magnetic applications (*e.g.*, shift reagents) [21], enable oncologists to distinguish cancer diagnoses at different stages and, hence, to better predict prognoses and to define different therapies.

However, cancer comprehension is still at the tip of the iceberg. In fact, the definitive cure for this plague is far to be found and, in most cases, the malignance is only medically controlled with an unfortunate prognosis of few months or years.

The main reason of cancer-treatment failure is that tumors are not just masses of malignant cells, but heterogeneous tissues made up of many distinct cell types involved in heterotypic mutual interactions to create the *tumor microenvironment* (TME). The TME has a dynamic and often tumor-promoting function in the multi-step process of cancer progression [22]. It is a complex milieu for tumor growth and survival characterized by acidic pH, low nutrient levels, elevated interstitial fluid pressure (IFP) and fluctuating levels of oxygenation that relate to the abnormal vascular network that exists in tumors. Apart from malignant cells, the TME contains cells of the immune system, the tumor vasculature and lymphatics, as well as fibroblasts, pericytes and sometimes adipocytes. All these “neighbors” act as mediators of the communication among malignant cells and between them and healthy ones and are crucial in the development and spread of the cancerous mass [23]. Going in detail, neoplasms are microcosms of evolution where nature selects cells to produce therapeutically-resistant clones which cooperate each other by means of *ecological interactions* (**Figure 1.4**), just as it is observed in an habitat shared by diverse species [24]. To explain this behavior, Nowell postulated the *clonal evolutionary hypothesis of cancer* in 1976, which states that the tumor initiation occurs in a single, previously normal, cell *via* an induced change, which makes it “neoplastic” and provides it with a selective growth advantage over adjacent normal cells. Because of genetic instability in the expanding tumor population, new mutant cells are produced but some of these variants are eliminated, because of metabolic disadvantage or immunologic destruction. However, occasionally one cell has an additional selective advantage with respect to the original tumor, and it becomes the precursor of a new predominant subpopulation (**Figure 1.4 a**) [25]. In addition, pathological epigenetic changes (non-DNA sequence-based alterations that are inherited through cell division) are increasingly being considered as alternatives to mutations and chromosomal alterations in disrupting gene function [26]. Thus, in the more recent *epigenetic progenitor model of cancer*, which may account for general alterations, such as hypo- and hyper-methylation of DNA, a *stem/progenitor cell* is epigenetically altered and, after different mutations, it drives the development of tumors (**Figure 1.4 b**) [27].

The evidences of these two models highlight the inherently *Darwinian character of cancer* (also referred to as *negative interaction*), paving the way to the primary reason for the therapeutic failure. Patient treatment

can indeed destroy some cancer clones, but it can also provide a potent selective pressure for the expansion of resistant clones (**Figure 1.4 a, b**) [28].

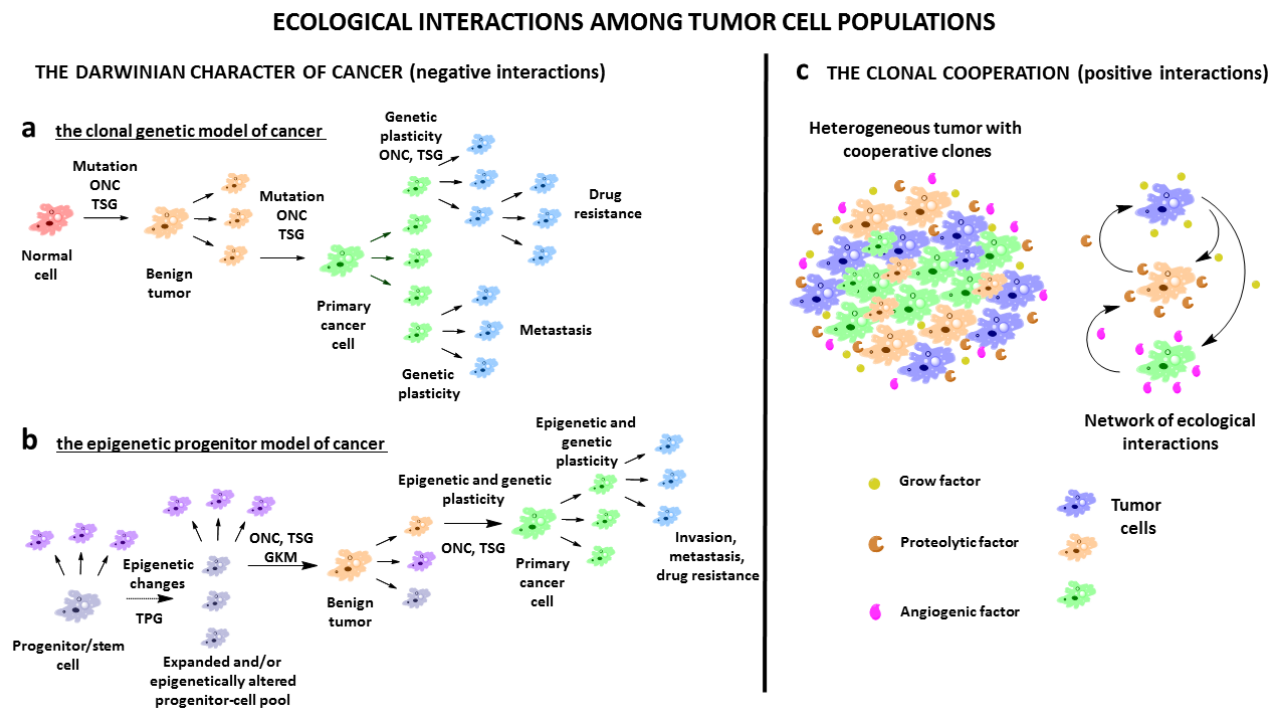


**Figure 1.4** Schematization of the ecological interactions occurring among tumor cell populations, which make tumor microenvironment (TME) a sophisticated tissue, made up of many distinct cell types, able to adapt themselves, to invade normal tissues and to spread to other distant organs. In particular, on the *left side* the negative interactions, associated with a Darwinian competition in order to select the more fit sub-clonal population. Among this kind of interactions it is possible to distinguish the *clonal genetic model of cancer a*, first postulated by Nowell in 1976, which is a classical view of cancer as a consequence of a series of mutations. These are related to dominantly-acting *oncogenes* (ONC, mutated genes that control cell proliferation, survival and motility) and recessively-acting *tumor-suppressor genes* (TSG, with the role of inhibiting cell proliferation/survival). Each mutation leads to the selective overgrowth of a monoclonal population of tumor cells, and each significant tumor property is accounted for by such mutation. In this model, epigenetic changes are only a surrogate alteration for mutations, whereas in the *epigenetic model of cancer b* they start the modification of the progenitor (or stem) cell by an aberrant regulation of the *tumor-progenitor genes* (TPG). The following step is a *gatekeeper mutation* (GKM), the mutation of a gene leading to irregular growth and differentiation. Finally, genetic and epigenetic instability leads to increased cancer evolution. Many properties of advanced tumors (represented in blue), are intrinsic of the progenitor cells that give rise to the primary tumor and they do not require other mutations (and this reflects the epigenetic factors in tumor progression [27].

On the *right side* the positive interactions c, namely a heterogenic driving force of the tumor, where different sub-populations cooperate each other to grow and spread the neoplasia. The network of exchanges and communication (biologically identified as synergism, mutualism and commensalism) between these cell families allows the different sub-populations to take advantage of the tumor-developing mediators (*e.g.*, grow factors, proteolytic factors and angiogenic factors) produced in majority by others in the same TME [29].

Taking together, the negative and positive interactions drive tumor to its evolution, to adapt to different conditions, and eventually to reorganize itself upon medicinal treatment.

Remarkably, if the Darwinian view of clonal selection may diminish the tumor heterogeneity by screening the most resistant sub-clones, the clonal cooperation (also referred to as *positive interaction*) is probably the main driver of persistent intratumor heterogeneity (**Figure 1.4 c**). The latter reflects the experimental evidences on mouse mammary tumors of variation in growth rate, immunogenicity, drug response and ability

to metastasize of cellular subpopulations taken from different sections of the same cancer sample [29]. This is a sort of synergistic or mutualistic tendency, where the most resistant sub-clones modulate the TME in certain ways that enable cancer to grow larger and larger and to metastasize. To better explain this concept, it can be assumed that one sub-clone could secrete angiogenic factors so to form blood vessels in order to bring in nutrients and oxygen, whereas another sub-clone could produce proteinases that degrade the surrounding extracellular matrix to allow invasion and dissemination [30]. One experimental demonstration of clonal cooperation was carried out by Polyak and coworkers in 2014, deriving approximately 20 different sub-clones from the triple negative breast cancer line MDA-MB-468 and comparing their growth (monoclonal tumor) *versus* the growth in the tumors in which all clones are present in equal proportions (polyclonal tumor). *In vivo* evidences showed that the polyclonal tumor was much more aggressive (larger and more metastasizing) than the monoclonal one [31].

### 1.2.2 Cancer: reprogramming cell division and metabolism

All the described interactions (Section 1.3) are the driving force of cancer, namely the ways by which genetically-unstable cells or progenitors evolve to generate selected clones able to cooperate. The result of the mutations is a complex system, the TME, in which Hanahan and Weinberg recognized in 2000 [32], and updated in 2011 [33], eight fundamental hallmarks, which are nowadays at the basis of the anticancer research [34]. In fact, when normal cells evolve to a neoplastic condition, they progressively acquire a series of new features, such as growth factor independence (or self-sufficiency), insensitivity to anti-growth signals, avoidance of programmed cell death (apoptosis), immortalization by inhibition of telomerase, reprogrammed energy metabolism, ability to evade immune destruction and to recruit a dedicated blood supply, activating invasion and metastasis [33]. From a general point of view, these traits summarize the evolution of the malignant cells to overcome the natural ageing and the peculiar controlled growth of healthy tissues. In particular, the self-sufficiency refers to the ability of tumor cells to keep proliferating even in the absence of stimulatory signals. This situation is managed by the oncogenes, mutated genes that promote the synthesis of oncoproteins, proteins stimulating cell division and proliferation [35]. At the same time, tumor suppressor genes act as negative regulators of the cell proliferation. Contrary to the oncogenes, which become hyperactive in cancerous cells, the tumor suppressor genes lose their function in human cancers. This leads to the resistance to the normal “apoptotic trigger”, a natural barrier to tumor development in healthy tissues. In this regard, apoptosis is a mechanism of controlled cell death whereby the organism maintains cell homeostasis in normal tissues and removes damaged cells [36]. However, despite the accumulation of DNA damages in tumors, the natural apoptosis suffers from alteration *via* different mechanisms. A common way to evade this process is the inactivation of the *TP53* gene (observed in over 50 % of human tumors), which encodes for the “DNA guardian” p53 protein [37]. Another way used by the tumor cells to avoid the programmed cell death is the suppression of “senescence”, the mechanism that stops cell

replication once going through a certain number of divisions. This process is governed by telomeres, small hexa-nucleotide sequences protecting the ends of chromosomes, which gradually become shorter after every division, leading to cell cycle arrest or death. Malignant cells possess more extended telomeres to avoid senescence or apoptosis, usually by up-regulating the expression of telomerase (a particular type of DNA polymerase that adds telomere units to the ends of telomeric DNA). Thus, the newly produced telomerase is able to stabilize the mutant genome, conferring an unlimited replication capacity [38].

The availability of oxygen and nutrients supplied by the novel vasculature is crucial for the accelerated progression of malignant cells and the evolution of the TME. The introduction of the concept of angiogenesis (*i.e.*, formation of new blood vessels) in tumors goes back to the 18<sup>th</sup> century, although the details of relationship with neoplastic cells is still debated [39]. Pre-clinical studies showed that tumors induce the sprouting of new vessels from the surrounding vasculature (sprouting angiogenesis), and this process is vital for the growth of tumors beyond 2-3 mm in size. The key driver of this process is the vascular endothelial growth factor (VEGF), which is overexpressed in most solid cancers [40]. Furthermore, multiple molecular mechanisms converge to alter the core cellular metabolism and to provide support for the basic needs of the dividing cells: rapid ATP generation to maintain the energy status, increased biosynthesis of macromolecules, and tightened maintenance of an appropriate redox cellular state. To meet these needs, malignant cells acquire alterations to the metabolism of all the four major classes of macromolecules: carbohydrates, proteins, lipids and nucleic acids [41]. The best-characterized metabolic phenotype observed in tumor cells is the Warburg effect, which is a shift from ATP generation through the glycolysis followed by oxidative phosphorylation to ATP generation through only glycolysis, even under normal oxygen concentrations (**Figure 1.5**). Indeed, despite the lower yield in ATP *per* mole of glucose, this mechanism is preferred because i) muted cells have defects in the mitochondrial function; ii) the glycolytic metabolism arises as an adaptation to hypoxic conditions during the early avascular phase of tumor development; iii) it generates ATP at a higher rate than the whole process (glycolysis plus oxidative phosphorylation); iv) a high flux of substrate through glycolysis allows for effective recycling in terms of biosynthetic carbon [42].

Moreover, the adaptation to the acidic microenvironment caused by the excess of lactate, the final by-product of anaerobic glycolysis, further drives the evolution to the advanced glycolytic phenotype. Indeed, this condition facilitates tumor invasion, since a large number of protons can diffuse from the tumor into peritumoral normal tissue, forcing nontransformed adjacent cells to an extracellular pH significantly lower than normal (pH= 6.5 – 6.9 in malignant tumors vs pH= 7.2 – 7.4 in normal tissues). This leads to the degradation of the interstitial matrix, loss of intracellular gap junctions, enhanced angiogenesis, and inhibition of the host immune response to tumor antigens, allowing cancer cells to remain proliferative and migrate beyond the peritumoral normal tissue [43].

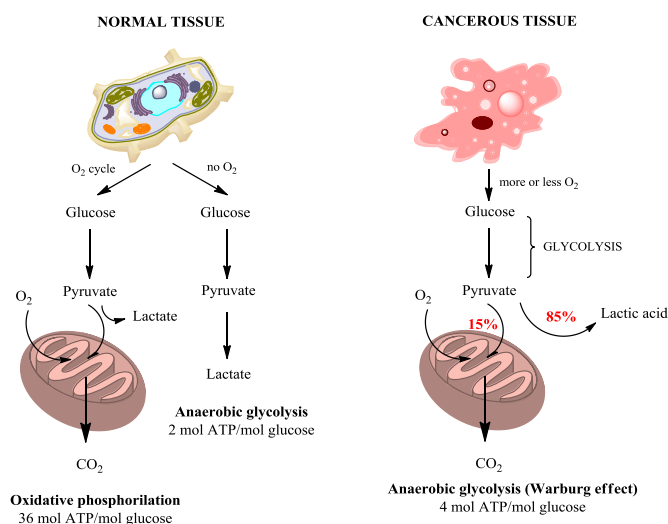


**Figure 1.5** Comparison of glucose metabolism between normal tissues (left) and malignant cells (right). The oxidative phosphorylation is an oxygen-dependent process coupling the oxidation of macromolecules and the electron transport chain with ATP synthesis in mitochondria. In eukaryotic cells it is a source of reactive oxygen species (ROS). On the other hand, glycolysis is an oxygen-independent metabolism of carbohydrates, being degraded into pyruvate to produce energy in the form of ATP and other metabolites [41].

The direct consequence of this mutated ATP production is a need of higher levels of glucose, which determines an increase of the expression of glucose transporters (GLUT) on the tumor cell surface, by means of the hypoxia-inducible factor 1 (HIF1) transcriptional program [44, 45].

On the other hand, the metabolic adaption in tumors extends beyond the Warburg effect. Another key molecule produced from the altered cancer metabolism is reduced nicotinamide adenine dinucleotide phosphate (NADPH), as “reducing power” in many enzymatic reactions and antioxidant defense against the large amount of ROS species produced during rapid proliferation. At the same time, other antioxidants found in high concentrations in malignant cells include glutathione (GSH) and thioredoxin (Trx) [46].

The ultimate process related to the hallmarks of cancer postulated by Hannah is the metastatization. Metastases are the result of a multistage process that includes local invasion by the primary tumor cells, intravasation into the blood or lymphatic system, survival in circulation, extravasation at a distant organ, survival in a new environment, and metastatic colonization to yield a secondary tumor. Each of these steps relies on specific phenotype features of the tumor cell, as well as interactions with the host microenvironment and escaping from the immune system [47]. However, the fact that the oncological patients might develop metastasis after years or even decades from the diagnosis of their primary tumor, makes metastasis even a more complex phenomenon, although different models have been elaborated to examine this process [48]. On the other hand, it should be remembered that metastases, similarly to primary tumor cells, often use strategies that promote the evasion from the immune recognition, including the adoption of low immunogenicity profile *via* a reduced expression of the major histocompatibility complex (MHC), and the promotion of cell error recognition by natural killer cells (NK) [34]. In addition, the tumor microenvironment can prevent the expansion of tumor antigen-specific helper and cytotoxic T cells, and

instead it can promote the production of pro-inflammatory cytokines and other factors. The infiltration of tumors by inflammatory immune cells can result in a state of chronic inflammation that maintains and supports cancer progression and suppresses the innate anticancer immune response [49].

So far, the hallmarks of cancer have been described as acquired functional capabilities that allow the neoplastic cell to survive, proliferate and disseminate. The emerging concept is the adaptability of the neoplasia to ever-evolving conditions. However, thanks to the knowledge of several pathophysiological and molecular traits that distinguish tumor cells from normal ones, in the last 30 years cancer has transformed from a largely fatal disease to one in which many patients receive treatments that result in long-term disease-free survivorship [50]. Conversely, much progress still needs to be made in the field of some lethal cancers that lack of effective treatments or suffer from aggressive surgical treatment as the best possible outcome.

### 1.3 Cancer treatments: from chemotherapy and radiotherapy to targeted therapies

The word *cancer* comes from the Greek term *karkinos*, used by Hippocrates (460 - 370 B.C.) to describe carcinomas. Historically, according to ancient Egyptian inscriptions (1500 B.C.), surface tumors were surgically removed in a similar manner as they are removed today [51]. On the other hand, the first milestone to treat cancer was the advent of general anesthesia in 1846 thanks to William T. G. Morton, opening the doors for the modern cancer surgery. With the Marie Curie's discovery of radium, culminated with the Nobel Prize in 1903, the radiation became widely used to treat many different cancers and, nowadays, the brachytherapy (*i.e.*, implantation of small pieces of radioactive material inside tumors) along with the use of external radiation sources, remains an essential part of cancer diagnosis and treatment (Figure 1.6) [52].

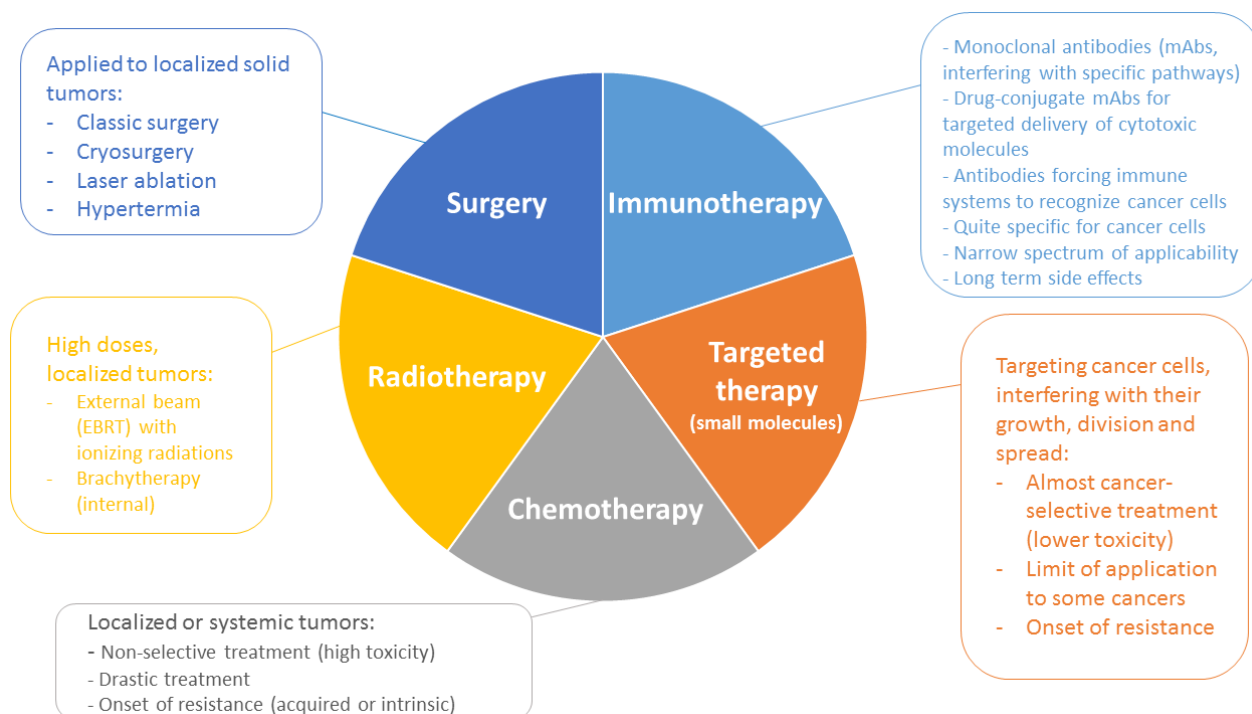


**Figure 1.6** Nowadays cancer treatment usually involves one or more between surgery, radiotherapy and systemic therapy. In the early stage of the disease, low-risk patients are often cured with the sole surgery to remove localized tumors and some neighboring tissue. This method is integrated with chemo- and radiotherapy treatments, to avoid further development of residual cancer cells. Systemic therapy comprises the classic unselective chemotherapeutics, but also targeted treatments based on small molecules and monoclonal antibodies.

The World Wars, which teared the Europe in the first middle of the twentieth century, paved the way to the discovery of the potential of nitrogen mustards (*e.g.*, cyclophosphamide, still used), the first chemotherapy approach approved by the Food and Drug Administration (FDA) in 1949 for the treatment of Hodking lymphoma. In particular, the cyclophosphamide kills cancer cells alkylating their DNA, thus creating a mismatch in the repair process that leads to apoptosis [53]. The progress in chemotherapy was successful in the 1950s, with the development of some compounds which are still used in the treatment of some malignances, for instance the methotrexate (acting as a folate antagonist), 6-mercaptopurine (immunosuppressor in the treatment of leukemia), and 5-fluorouracil (antimetabolite s able to alter RNA) (**Figure 1.7 a-c**) [54]. However, the turning point in the anticancer treatments was the discovery in the early 1960s and the subsequent FDA approval in 1978 of cisplatin (**Figure 1.2 d**) [12]. To date, the cisplatin-based therapy can be considered part of a standard treatment regimen against many forms of neoplasia, including the malignant mesothelioma, squamous cell carcinoma of the head and neck, testicular, bladder, cervical, ovarian, and non-small-cell lung cancers [55]. This discovery opened the way for two new Pt(II) derivatives, namely carboplatin (Paraplatin®) and oxaliplatin (Eloxatin®) (FDA approved in 1989 and 2002 respectively, **Figure 1.7 d, e**), which possess a broad spectrum of antitumor activity and lower nephrotoxicity compared to cisplatin.

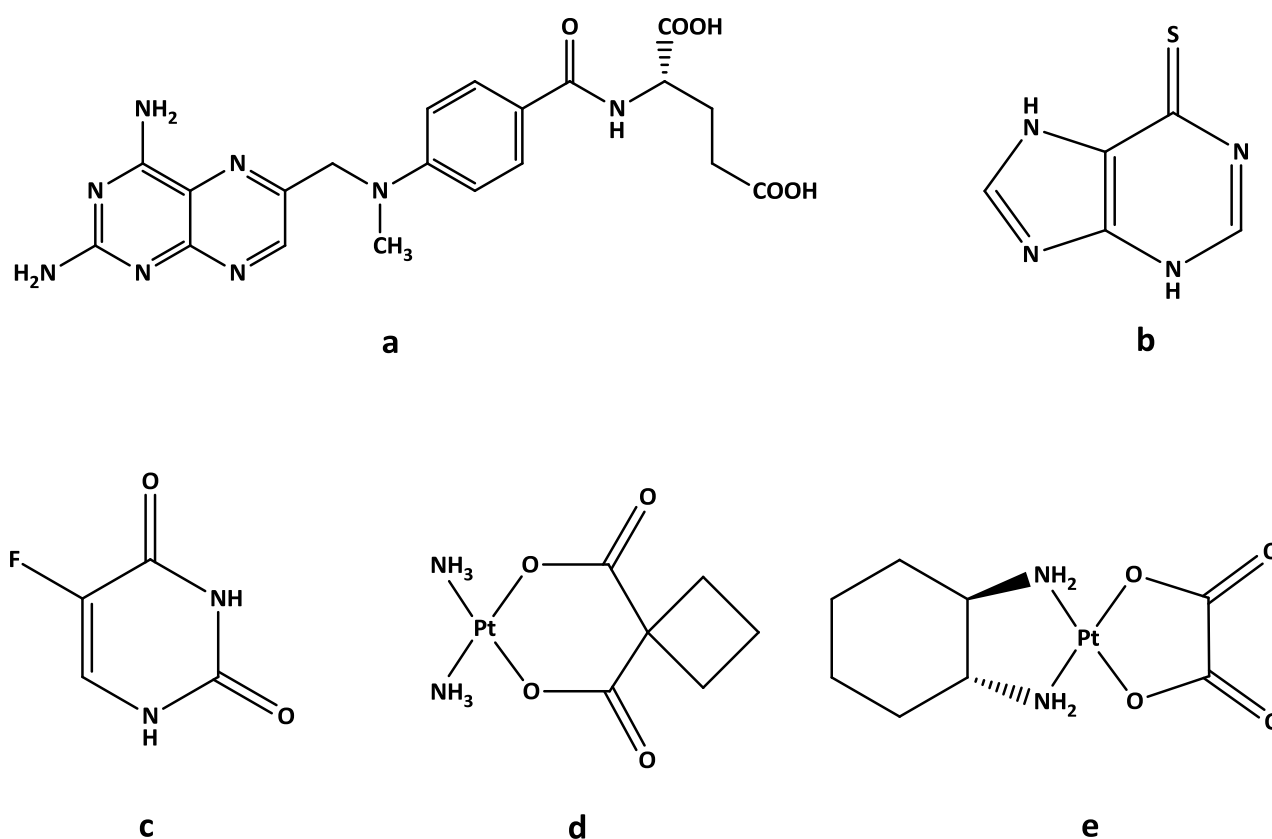


**Figure 1.7** Some examples of non-tumor-specific chemotherapeutics developed in the twentieth century: the folate antagonist methotrexate ((2*S*)-2-[[4-[[[(2,4-diaminopteridin-6-yl)methyl](methyl)amino]benzoyl]amino]pentanedioic acid **a**; the immunosuppressor 6-mercaptopurine (6-MP, 3,7-dihydropurine-6-thione) **b**; the inhibitor of thymidylate synthase 5-fluorouracil (5-FU, 5-fluoro-1*H*,3*H*-pyrimidine-2,4-dione) **c**; the alkylating agent carboplatin (Paraplatin<sup>®</sup>) (*cis*-diammine(cyclobutane-1,1-dicarboxylate-*O,O'*)platinum(II)) **d**; the platinum-based antineoplastic agent oxaliplatin (Eloxatin<sup>®</sup>) ([[1*R*,2*R*]-cyclohexane-1,2-diamine](ethanedioato-*O,O'*)platinum(II)) **e**.

### 1.3.1 Cisplatin: virtues and faults of the milestone drug in anticancer chemotherapy and medicinal inorganic chemistry

The discovery of the anticancer activity of cisplatin (**Figure 1.2 d**) is an historic achievement that has had a worldwide impact on the lives of millions of cancer patients afflicted with solid cancers. Moreover, it has had an enormous impact not only on the current anticancer pharmacopeia, but it has also promoted the exponential growth of the field of medicinal inorganic chemistry [56].

The first one to chemically study cisplatin was the Italian chemist Michele Peyrone in 1845. The drug was biologically discovered by the researchers Bennett Rosenberg and Loretta Van Camp at the Michigan State University in 1965, during their studies on the effects of an electric field on the growth of *E. coli* bacteria. In particular, platinum electrodes used in the experiment reacted by electrolysis with the bacterial growth medium containing NH<sub>4</sub>Cl to produce Pt(II) and Pt(IV) compounds, including [Pt(NH<sub>3</sub>)<sub>2</sub>Cl<sub>2</sub>] [12]. The accurate observations made up by the two scientists, revealed the ability of cisplatin to inhibit cell division, thus causing the bacteria to become long and filamentous. This generated an enormous interest in metal-based drugs in academia, governments, and commercial entities and overcame the stigma that all metal-based compounds are “heavy metal” poisons and devoid of biological activity [56].



Investigating the cisplatin mechanism of action when administered by intravenous injection, the neutral form of the drug can easily diffuse to cytoplasm. In particular, the drug enters the cell membrane by both passive diffusion and active transport, mediated by the copper transporter Ctr1 [57]. The relatively high (~150 mM) serum level of the chloride ion inhibits the extracellular conversion into the hydrolyzed *cis*-[Pt(NH<sub>3</sub>)<sub>2</sub>(H<sub>2</sub>O)<sub>2</sub>]<sup>2+</sup> form. The much lower intracellular concentration of the anion (~4 mM) leads instead to the formation of first the mono- and then the *cis*-diaquadiamineplatinum(II) complex (**Figure 1.8**) [58]. These activated species can then react with a variety of intracellular macromolecules including DNA, RNA and proteins. Among these, DNA is acknowledged as the main target of cisplatin, forming bifunctional adducts by either intrastrand or interstrand cross-links (**Figure 1.8**). In fact, binding of cisplatin to DNA causes a significant distortion of the helical structure and results in inhibition of DNA replication and transcription. This suggests that it might kill cancer cells by blocking their ability to synthesize new DNA required for subsequent cell division. The main adducts are 1,2-intrastrand cross-links involving adjacent bases (47-50 % *cis*-GG and 23-28 % *cis*-AG). This evidence accounts for the inactivity of the *trans* isomer, unable to form this type of adducts. In addition, 8-10 % of the products are associated with 1,3-intrastrand cross-links between non adjacent guanines and interstrand adducts. In all of these cases, platinum(II) is bound to the N7 atom of purine bases [59, 60].

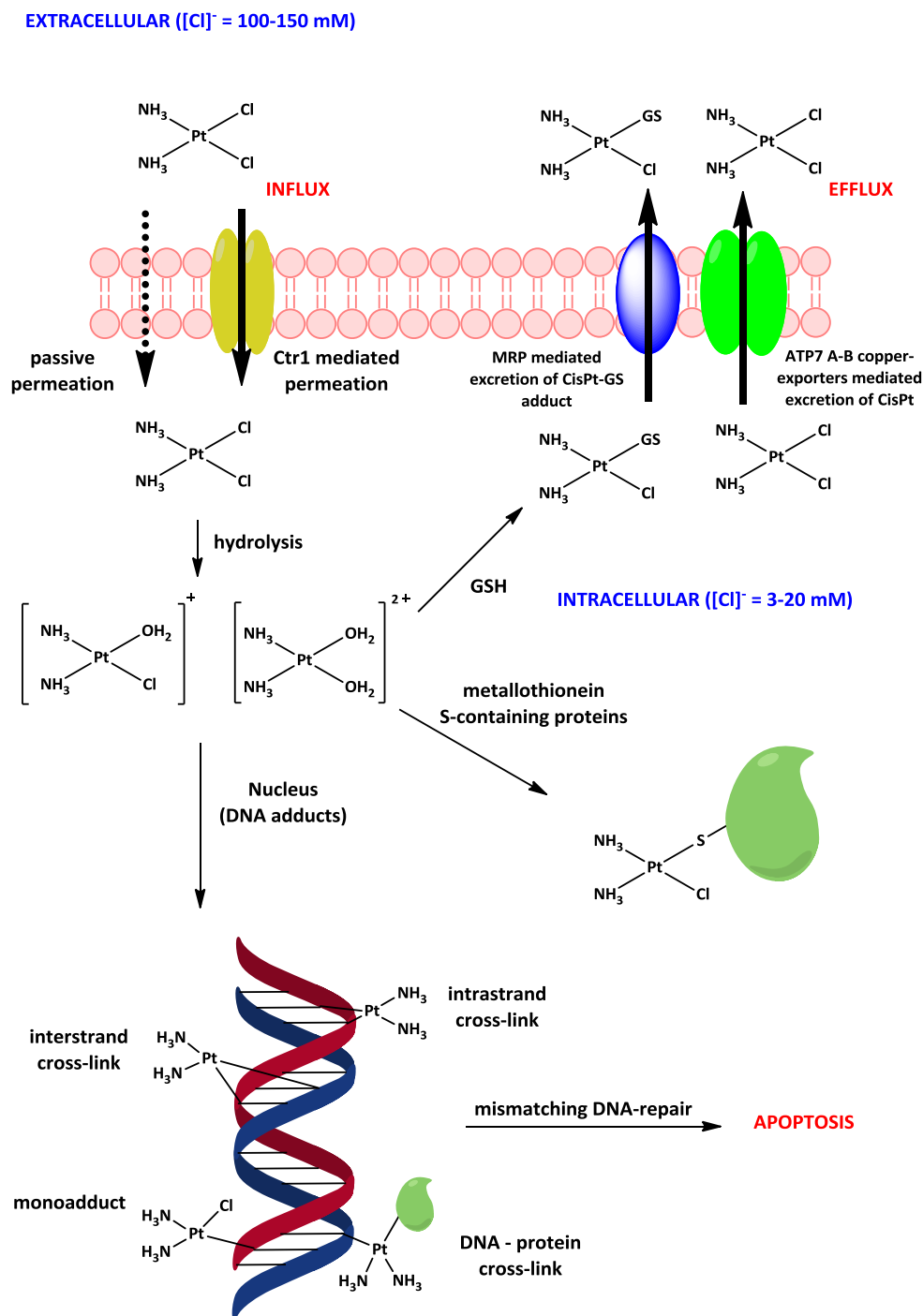


**Figure 1.8** The accumulation of cisplatin in the cytoplasm occurs by passive diffusion across the phospholipid barrier or through the copper transporter Ctr1; once within the cell the low chloride concentration causes the loss of one or both chloride ligands, converting the complex to the positively charged mono- and di-aquo derivatives, respectively. Successively, the hydrolyzed Pt(II) complex forms DNA-adducts that lead to a mismatch in the DNA-repair mechanism, followed by the apoptosis induction. On the other hand, in the cytoplasm, the activated aqua species can react with sulfur-containing proteins and molecules, such as glutathione (GS) or metallothioneins. Consequently, the active export of platinum from the cells - by means of the copper exporters (ATP-based) or GS-adducts export pumps MRP - can contribute to platinum-drug resistance.

From the first FDA approval of cisplatin in 1978 for metastatic testicular cancer, its dose-limiting nephrotoxicity was a problem, paralleled with other patient-disabling side effects, such as nausea, alopecia,

ototoxicity and neurotoxicity [61]. The main reason for organ-related toxicity is ascribable to the accumulation of the drug into the functional cells of the tissues, as in the case of the parenchymal cells of the kidney, due to a high expression of the Ctr1 transporter. In addition, also the organic cation transporter OCT2 seems to participate in the nephrotoxicity and cisplatin uptake. At this point, the Pt(II) drug is transformed into a more toxic derivative by sulfur-containing biomolecules, such as glutathione (GSH), yielding for instance Pt(II)-GSH complexes which accumulate in proximal tubule cells. The overall result is the accumulation of these Pt(II) adducts, with subsequent cytotoxic effects through the previously explained interactions with DNA. Moreover, there is a growing recognition of the importance of inflammation associated with cisplatin toxicity (*e.g.*, an increase in renal expression of cytokines, neutrophils, macrophages and T cells after chemotherapeutic treatment) [62]. Different strategies have been used to limit nephrotoxicity, such as patient pre-hydration with 0.9 % saline solution and the use of amifostine (2-(3-aminopropylamino)ethylsulfanyl phosphonic acid) as a chemoprotector containing a thiol group [63]. Moreover, the studies of less toxic Pt(II) derivatives produced carboplatin (**Figure 1.7 d**), based on the hypothesis that a more stable leaving group than chloride might lower the toxicity without affecting antitumor efficacy. Compared with cisplatin, carboplatin is essentially devoid of nephrotoxicity and is less neurotoxic; by contrast, myelosuppression, principally thrombocytopenia, is dose-limiting for carboplatin [64].

A second drawback of platinum-based therapies emerged soon after the initial promising clinical trial data with cisplatin, and later with carboplatin. Tumor resistance was indeed acquired during the cycles of therapy with these drugs. In other cases, tumors were intrinsically resistant. Further studies have demonstrated that the resistance might be mediated by two mechanisms, i) no sufficient amount of platinum reaching the target DNA and ii) failure to achieve cell death after platinum-DNA adduct formation [61]. Concerning the first one, scientists demonstrated that the exposure to clinical dosage of cisplatin leads to a downregulation of Ctr1 transporters in human ovarian cancer cell lines, by an internalization followed by proteasome-dependent degradation of the copper-designated transporter [65]. Moreover, early studies highlighted the role of efflux proteins, such as MDR1, the multidrug resistance proteins MRP1 and MRP2, and the ATP-mediated copper efflux pumps (ATP7A-B) (**Figure 1.8**) [66]. There is also an extensive body of evidence implicating increased levels of cytoplasmic thiol-containing species with a key role in the resistance to cisplatin or carboplatin. These species, such as the tripeptide glutathione (GSH) and metallothioneins, are rich in the sulphur-containing aminoacids cysteine and methionine, and lead to cell detoxification because a soft ion as Pt(II) has a great affinity towards a soft donor as sulfur (in the Pearson's *HSAB* concept, which states that atoms that are strongly polarizable - soft - interact very well due to an optimal orbital overlap [67]). These reactions make the compound more readily exported out from cells by the ATP-dependent glutathione S-conjugate export (GS-X) pump (*i.e.*, MRP1 or MRP2) (**Figure 1.8**) [68]. In addition, cisplatin can target other sulfur-based proteins, promoting cytotoxic effects in cancer cells, but at the same time unbalancing fundamental

processes in healthy counterparts (*e.g.*, redox mechanisms), associated with side effects such as ototoxicity [69, 70]. On the other hand, after DNA binding the resistance can occur either by DNA repair (*i.e.*, removal of the adducts) or by tolerance mechanisms. The tolerance might occur with platinum-based drugs (and other oncological drugs) through a decreased expression or loss of the apoptotic signaling pathways (either the mitochondrial or death-receptor pathways), being mediated by various proteins, such as the anti-apoptotic and pro-apoptotic members of the BCL2 family [71]. Despite our knowledge on resistance to cisplatin or carboplatin has largely arisen from studies that have been carried out in cell lines *in vitro*, four major DNA-repair mechanisms have been elucidated, *i.e.*, the nucleotide-excision repair (NER), the base-excision repair (BER), the mismatch repair (MMR), and the double-strand-break repair.

Similarly to carboplatin, thought to be less toxic than cisplatin, oxaliplatin (**Figure 1.7 e**), described at the end of 1970s, showed a different pattern of sensitivity in some cell lines (*e.g.*, the NCI-60 tumor cell lines panel) compared to cisplatin, and its cell uptake seems to be less dependent on the Ctr1 transporter. Better results have been also obtained in terms of DNA-repair mediated resistance, where the oxaliplatin-DNA adducts are not affected by the MMR pathway [72].

To date, about 23 platinum-based drugs have entered clinical trials, and besides the three cases previously discussed, other three compounds obtained marketing approval in individual countries (*i.e.*, nedaplatin in Japan, heptaplatin in Korea and lobaplatin in China) (**Figure 1.9 a-c**). Among the platinum derivatives in clinical trials, satraplatin (at present under consideration for approval by the FDA), and picoplatin might further broaden the current activity spectrum to other tumors, such as prostate cancer and small-cell lung cancer, respectively (**Figure 1.9 d, e**) [73].

Undoubtedly, the Rosenberg's discovery has revolutionized the treatment of many types of cancer, especially testicular. In the last years, cisplatin has been attached to carbon nanotubes, gold nanoparticles and polymers, showing an ever-green research on potential new drugs based on this metal center [61]. In other words, the evidence that a metal center could be crucial in the fight against cancer, paved the way to the exploration of the periodic table, so to exploit the different peculiarities of the elements, especially those of the *d*-group [8].

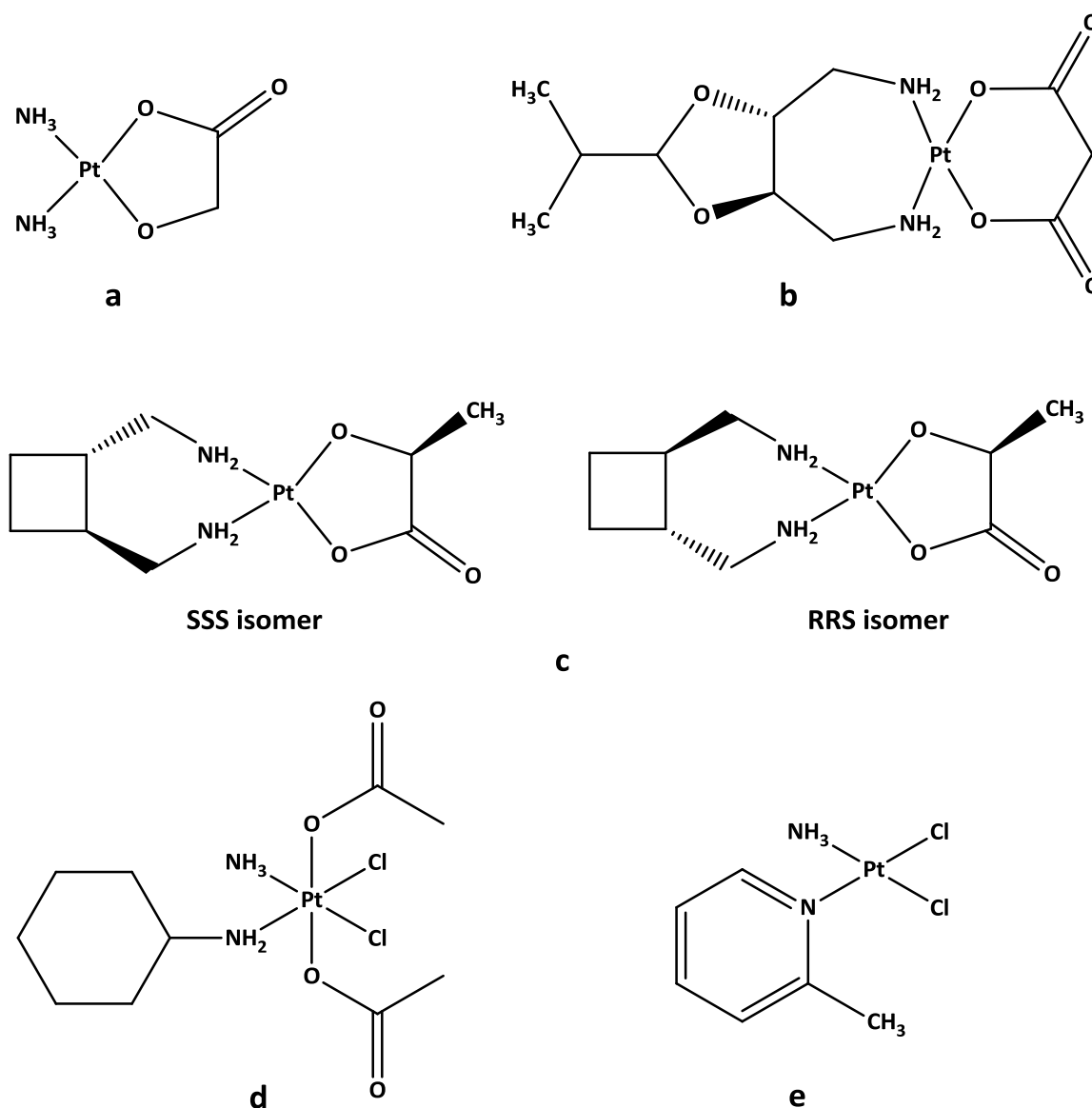


**Figure 1.9** Cisplatin derivatives approved in single countries or still under clinical trials: nedaplatin (Aqupla®) (*cis*-diamine(glycolato-*O,O'*)platinum(II)) **a**; heptaplatin (Sunpla®) (*cis*-(4*R*,5*R*)-4,5-bis(aminomethyl)-2-isopropyl-1,3-dioxolane[(3-acetoxy-cycobutane-1,1'-dicarboxylato)platinum(II)]) **b**; lobaplatin (1,2-diamino-methyl-cyclobutaneplatinum(II)-lactate isomer SSS + RRS) **c**; satraplatin (bis-(acetato)-ammine dichloro(cyclohexylamine)platinum(IV)) **d**; picoplatin (azane(2-methylpyridine)dichloroplatinum(II)) **e**.

### 1.3.2 Targeted treatments based on the cancer hallmarks: “-ib” and “-mab” therapies

Throughout the clinical development of anticancer drugs, researchers repeatedly encountered significant problems because of the acute and long-term toxicities of chemotherapies, which affected virtually every organ of the body (*e.g.*, the cisplatin case) [74]. Fortunately, the discovery of the oncogenes and tumor suppressor genes in the 1970s helped to define the biological hallmarks of cancer, opening a new era based on the use of “targeted small-molecule therapeutics”. Targeted therapies are rationally-designed low-molecular weight compounds (generally identified with the *-ib* suffix), blocking essential biochemical pathways or mutant proteins that are required for the tumor cell growth and survival. Indeed, these drugs can arrest tumor progression and can induce a striking regression in molecularly-defined subsets of patients.

Although this approach is relatively recent, the concept of targeted therapy was conceived by Paul Ehrlich in 1908, who observed that certain substances are capable of selectively staining either tissues or microorganisms [75]. The forefather of this class of anticancer agents is imatinib mesylate (Gleevec<sup>®</sup>, **Figure 1.10 a**), identified in the late 1980s at Ciba Geigy (Novartis) during studies on inhibitors of protein kinase. This molecule, the first small-molecule-targeted agent, has completely transformed the cure for chronic myeloid leukemia (CML), whose malignant cells present the enzyme tyrosine kinase in its active form, encoded by the mutated gene BCR-Abl. Imatinib blocks the phosphorylation process, leading only tumor cells to death [76]. Successively, the awareness of cancer as a multi-factorial disease paved the way for the development of multi-target inhibitors, such as sunitinib (Sutent<sup>®</sup>, **Figure 1.10 b**), a selective inhibitor of the receptor of tyrosine kinases, including the vascular endothelial growth factor receptors (VEGFRs) [77]. Another example of targeted therapy is the first proteasome inhibitor bortezomib (Velcade<sup>®</sup>, **Figure 1.10 c**), FDA approved in 2003 for the treatment of multiple myeloma. Proteasome is an enzymatic complex responsible for the degradation of over 80% cell proteins. Bortezomib binds to the core of this crucial protein blocking the degradation. This molecule is an excellent example of “inorganic medicine” since its boron atom is involved as a Lewis acid in the binding with the catalytic site of the 26S proteasome, and the consequent stop of degradation process leads to cell death by apoptosis [78]. Curiously, the bortezomib development is one of the first examples of translational research between academia and industry. In particular, Alfred Goldberg from the Harvard Medical School decided to exploit his growing basic knowledge of the proteasome by founding a biotech company (named ProScript) in 1992, being focused on the design of proteasome inhibitors. After that, the Goldberg’s fruitful collaborations with academic researchers and the National Cancer Institute (NCI) allowed the company to discover bortezomib and to obtain a sound preclinical proof-of-concept. After a successful phase I trial, the drug was sold to LeukoSite for \$2.7 million in 1999 [79].

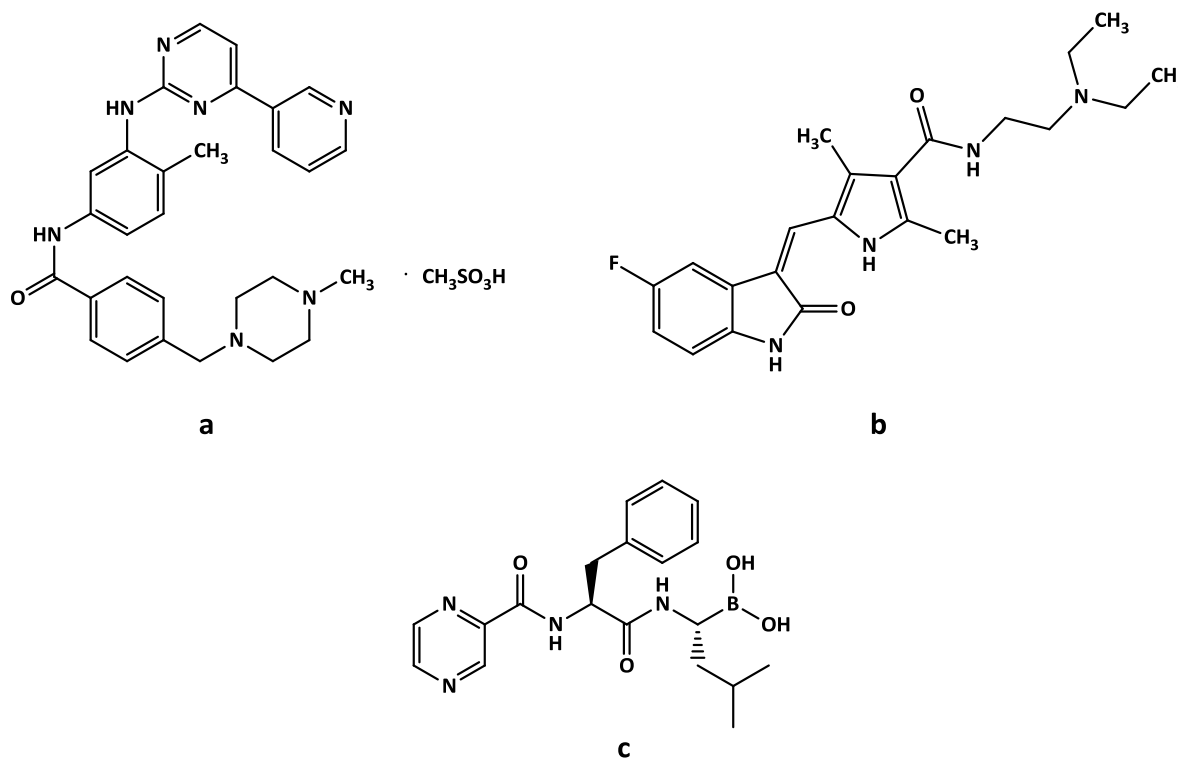


**Figure 1.10** Some examples of cancer-targeting molecules, designed on the basis of the tumor hallmarks: the tyrosine kinase inhibitor imatinib (Gleevec<sup>®</sup>) (4-[4-methylpiperazin-1-yl)methyl]-*N*-(4-methyl-3-[[4-(pyridine-3-yl)pyrimidin-2-yl]amino]phenyl)benzamide mesylate salt **a**; the multi-target tyrosine kinase receptor inhibitor sunitinib (Sutent<sup>®</sup>) (*N*-(2-diethylaminoethyl)-5-[(*Z*)-(5-fluoro-2-oxo-1*H*-indol-3-ylidene)methyl]-2,4-dimethyl-1*H*-pyrrole-3-carboxamide) **b**; the proteasome inhibitor bortezomib (Valcade<sup>®</sup>) ([[(1*R*)-3-methyl-1-((2*S*)-3-phenyl-2-[(pyrazine-2-ylcarbonyl)amino]propanoyl)amino]butyl]boronic acid) **c**.

Although the targeted therapies can generate impressive tumor response in specific subtypes of patients, relapse is very common due to the onset of drug-resistant variants. The major reasons are connected to i) resistance (irreversible lack of response due to secondary mutations associated with the target or feedback changes), and/or ii) persistence (*i.e.*, cell turning into a reversible state usually without requiring any new genetic modification; *e.g.*, quiescence) [29, 80].

Taking into account the well-known hallmarks of cancer, parallel strategies and different from small-molecules, involve monoclonal antibodies to block selected antigens overexpressed in malignant cells, or to manipulate the immune system to give a response against tumors. The fundamental concepts of antibody-based therapy date back to the 1960s with the original observation of antigen expression by tumor cells through serological techniques [81]. The monoclonal antibodies (mAbs, identified by the *-mab* suffix) are made by identical immune cells, being all clones of a unique parent cell and endowed with monovalent affinity, since they bind to the same antigenic epitope [82]. Rituximab (Mabthera<sup>®</sup>) was the first-in-class to be FDA approved in 1997 for the treatment of non-Hodking lymphoma of B cells, and to date 23 mAbs are currently used for the treatment of both solid and liquid cancers [83, 84].

Several antigens have been successfully targeted so far, for instance the epidermal growth factor receptor EGFR, the vascular endothelial growth factor VEGF, the cytotoxic T lymphocyte-associated antigen 4 CTLA4,

and the B-lymphocyte antigen CD20. The efficacy can result from a direct action on the target, an immune-mediated cell-killing mechanism, or a payload delivery of a cytotoxic agent for the antibody-drug conjugates [82].

Latest advances in the field of immunotherapy relate to the mechanism used by tumor cells to evade immune recognition through the down-regulation of foreign antigens. For instance, the transmembrane protein programmed death-ligand 1 (PD-L1) is present on the surface of cancer cells, and binds its receptor PD1 present on the surface of activated T and B cells, thus generating an immunosuppressive effect which allows the tumor to evade immune destruction.

The recent development of agents that inhibit the interaction between PD-L1 and PD-1 have produced innovative mAbs, and among them nivolumab (Opdivo®) was FDA approved in 2014 for the treatment of metastatic melanoma [85]. However, although most antibodies that have been approved have different and often milder toxicities compared with conventional chemotherapeutic drugs, they often cause severe side-immune response, namely immunogenicity (*i.e.*, humoral and/or cell-mediated immune response) or hypersensitivity (*i.e.*, allergies or autoimmunity) [86]. Moreover, their use is limited to subjects that histologically present the specific antigens. Unfortunately, the narrow spectrum of applicability of this most recent anticancer strategy (immunotherapy), highlights those cancers which still nowadays suffer from the lack of an effective cure, such as the triple negative breast cancer (TNBC). Indeed, this particular subtype of breast cancer is negative for estrogen receptors (ER), progesterone receptors (PR) and human epidermal growth factor receptor 2 (HER2), making useless any hormonal therapy or the mAbs therapies targeting HER2 (generally performed with trastuzumab, marketed as Herceptin®). The common treatment-protocol for TNBC is called AC-T, from the names of the used drugs, namely a cocktail of doxorubicin (Adriamycin®), cyclophosphamide (Cytosan®) and docetaxel (Taxotere®). All of them are non-cancer-specific, toxic and old chemotherapeutics, thus demonstrating the incessant need of innovative therapies [87].

#### 1.4 Discovering and developing new anticancer drugs: the role of academia and the problem of translational science

Over the last decades, many therapeutic targets have been identified for cancer treatment, and the day-by-day progress in genomic techniques for the individuation of new cancer-related mutations pushes continuous optimization in the methodology of drug discovery and development (**Figure 1.11**) [88]. Whilst large Pharma companies continue to be the major source of new drugs, they also need research support from other Institutions due to the increasing difficulty to find out new drugs. In this regard, there is a compelling need that academia is more directly involved in translation of fundamental science into therapeutics, thus becoming key players in early stage drug discovery. Indeed, academic research groups are updated and possess new ideas and a broad range of expertise and can enable multidisciplinary collaborations to develop



new approaches in different areas, such as compound design, synthetic methodologies, data mining, informatics, computational chemistry, compound library selection, *in silico* predictions and *in vitro* and *in vivo* models for efficacy and toxicity [89].

On average today, companies spend an estimated \$ 1.2 – 1.3 billion in R&D for each approved drug (accounting also for the cost of failures along the way), almost double compared to the costs of ten years ago [90]. Consequently, pharmaceutical companies have become increasingly risk-averse, less ready to pursue truly innovative new products. In fact, only 113 new drugs approved by the FDA from 1999 to 2013 could be considered “first-in-class” (*i.e.*, drugs that modulate a new drug target or biological pathway) [91]. In this context, the “innovation gap” between basic discoveries related to human diseases and the marketing of new therapeutic options remains stubbornly persistent. Going into detail, there are three stages of medicinal research: i) basic research or discovery (in most cases it is performed in academia), ii) translational research, and iii) clinical research (Figure 1.11).

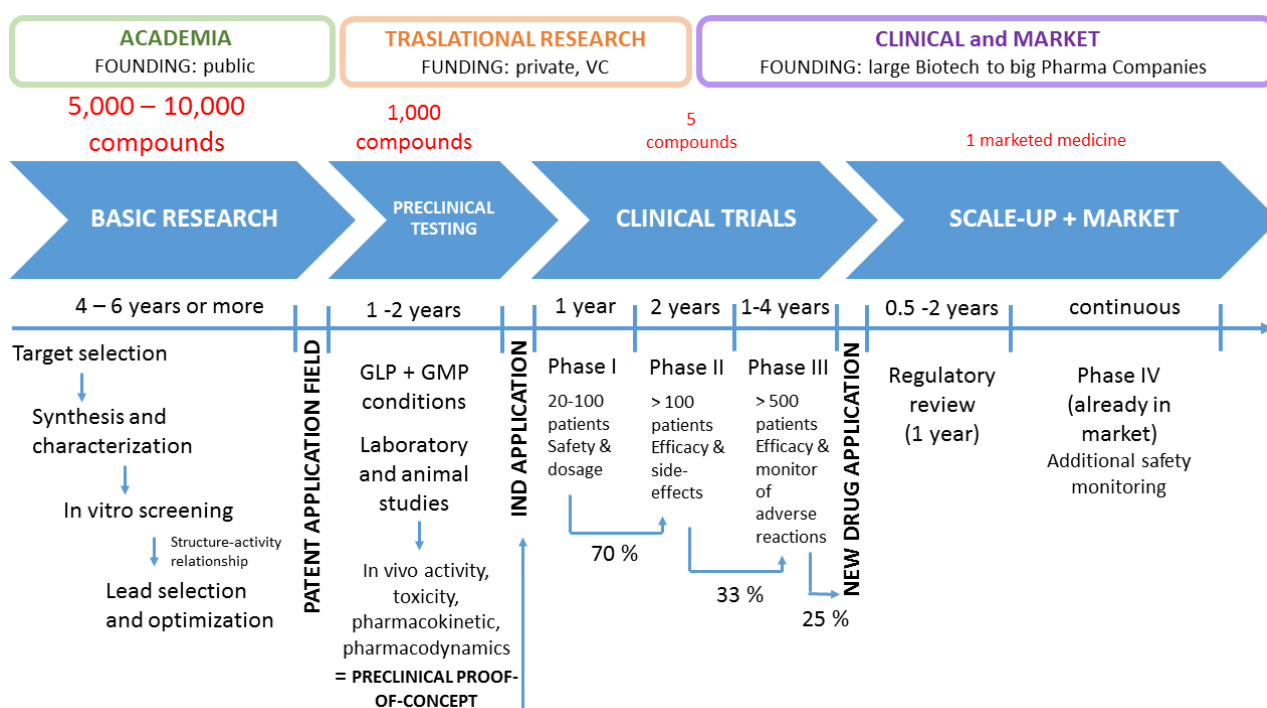


**Figure 1.11** Drug discovery and development proceeds through a series of steps, from basic research to clinical research, passing through the so-called “Valley of death” (*i.e.*, translational research), where researchers encounter difficulties to acquire funding to carry out “killer” experiments. All the process takes about 10–15 years for an experimental drug, going from laboratory to market, with a success rate around 0.01 % (1 marketed drug every 10,000 synthesized in laboratory).

*Basic research* uses a critical and free approach, leading to many advances in our understanding of human disease biology, but it is not sufficient to develop a therapy for a patient due to lack of preclinical and clinical expertise as well as of funding. Nowadays, the enormous progresses in cancer genome sequencing facilitate the identification of new targets, as well as the overexpression of proteins or biomarkers in particular cancer

cells to be exploited for a possible targeted therapy [92]. From the drug chemistry point of view, the general procedure envisages i) the design and the synthesis of a library of similar molecules, thought to inhibit or affect the activity of the chosen hallmark, and ii) the selection of the Lead compound(s) on the basis of its optimal features (both chemical and biological) [93]. Most of the targeted-small-molecules approved by FDA have been selected on the basis of the *structure-activity relationship* concept (SAR), evaluating the potential of a compound with respect to an analogue [94]. In particular, a range of similar molecules (libraries) with quantifiable parameters (*e.g.*, charge distribution and electronic, steric and hydrophobic effects), are related to their biological activity, as a standard tool for the development of cancer therapeutics. SAR generally involves three steps: i) to collect or, if possible, to design a training set of chemicals; ii) to choose a descriptor that can properly relate the chemical structure to the biological activity; iii) to apply statistical methods that correlate changes in structure with changes in biological activity [95]. At this point, the Lead molecule is identified taking into account its activity (mainly *in vitro* screening), and its chemical features (*e.g.*, hydrophobicity, water solubility, stability in physiological media), and it is ready for a patent application. The following step is the optimization of the Lead compound and the collection of preclinical proof-of-concept data to apply for an Investigational New Drug (IND) at the FDA, a permission to ship an experimental drug across human clinical investigation. This stage is the *translational research*, often defined as the “Valley of death”, namely the place where many good ideas in the drug development pipeline drop off.

Translating a basic discovery into a compound or another entity (*e.g.*, antibody) that is ready for clinical testing is not a simple matter [96, 97]. There are a number of complicated and time-consuming steps in between, and the academic scientists who make the discoveries are rarely prepared to translate them to the next step, also because they do not speak the proper language to better interface with investors. First of all, the transformation of a Lead molecule into a drug requires the knowledge of the compound’s absorption, distribution, metabolism and excretion (ADME) profile to optimize its ‘drugability’ (Lead compound optimization) [95]. Then, the compound has to be tested in a rodent species and a non-rodent species (in general, it is dog for anticancer compounds) to assess the activity, lack of toxicity, the pharmacodynamics and pharmacokinetic profiles. All these experiments are very expensive, since they have to be performed under Good Laboratory Practice (GLP) conditions in specialized centers to obtain a certified documentation to submit along with the IND application. Besides, the manufacturing of the tested drug has to be carried out under Good Manufacturing Practice (GMP) [98]. Consequently, although the basic research continues to provide numerous promising ideas and knowledge for all diseases, structural, intellectual, and above all funding barriers have made it difficult to translate basic research into clinical applications.

The final consideration about the so-called “death valley” regards the investors, who to date are often private or venture capitalists (VC) since Pharma companies are highly risk-averse. The reason is that among 5,000-10,000 compounds that enter the drug discovery pipeline, only 250 will progress to pre-clinical development and only five will move forward to Phase I studies, and only one will survive to be an approved drug [90].

The final step is the *clinical research*, which refers to studies or trials carried out in people. It is sub-divided in three phases, i) the Phase I with the purpose to assess safety and dosage of the tested drug, ii) the Phase II to verify the efficacy and side-effects and iii) the Phase III to monitor adverse reactions and again to check the efficacy during a longer period. In general, the percentage of drugs that move from the Phase I to II is 70%, reducing to 33% from Phase II to III, and being 25-30 % after Phase III (**Figure 1.11**) [99]. During the development process of a drug, the phase III stage is the most expensive one, but large Biotech or Big Pharma that previously signed a contract with the drug developers, commonly sponsor it. Moreover, in the case of anticancer drug candidates, some phases can be fused (*e.g.*, phase I/II trial to study safety, side effects and the best dose of a new treatment), in order to allow researchers to have results more quickly or with fewer patients. Another facilitation in oncology is the “breakthrough therapy designation”, established in 2012 by the US Congress to expedite the development of drugs that show promising early clinical evidence of benefit compared to available therapies [100].

Overall, the traditional route of drug development presented is curvy and subject to high-risk of failure. Considering the percentage of drugs that gain success, from laboratory to market, is around 0.01 %, most of researchers and investors are discouraged to undertake such an adventure. On the other hand, the progresses in cancer genome sequencing and the every-day discovery of cancer targets and biomarkers, open a new challenge in terms of designing and developing innovative molecules and therapies that combine the targeting action with the cytotoxic properties in a more effective manner [101, 102].

*The discussion in this chapter has been drafted sailing in the wake of current medicinal approaches, being mainly related to small organic molecules, antibodies, peptides and proteins, considering for instance their, the success percentage, the concept of libraries, etc. Conversely, this PhD thesis places in a new branch of biomedicine, whose forerunner is cisplatin, and with the hope to widen the examples of metallo-drugs in advanced pre-clinical testing, involving metal centers other than platinum.*



## 2. AIM OF THE WORK

To date, platinum-based drugs are among the most widely used anticancer chemotherapeutics. Nevertheless, their effectiveness is counterbalanced by severe adverse effects and the development of drug resistance. Since these drawbacks, in particular renal insufficiency, were shown to be sensibly reduced upon administration of sulfur nucleophiles (*e.g.*, diethyldithiocarbamate), Prof. Fregona's research group has combined - in a single compound - the chemoprotecting action of the latter with the anticancer properties of a metal center. In this regard, a number of metal-dithiocarbamate complexes (*i.e.*, involving Pt(II), Pd(II), Au(III), Ru(III), Zn(II), Cu(II) centers) showed outstanding antitumor activity (both *in vitro* and *in vivo*) together with negligible or even no nephrotoxicity in animal models. In general, the most promising results were obtained with the Au(III), Ru(III) and Cu(II) dithiocarbamates, which proved much more potent than the chemotherapeutic drug cisplatin even at nanomolar concentrations against a wide panel of human tumor cell lines.

The biological *in vitro* screening of the abovementioned metal-dithiocarbamate complexes put in evidence that the antiproliferative activity is triggered by the metal center, but the structure of the ligand also affects the effectiveness of the final antitumor agent. Moreover, it has been observed that the pyrrolidine dithiocarbamate derivatives of Ru(III), Cu(II) and Au(III) are associated with very promising antiproliferative effects. Therefore, in order to gain further insights into structure/activity relationships for this class of compounds, the first goal of this work has been the synthesis of *N,N*-disubstituted dithiocarbamate salts derived from both aliphatic and aromatic cyclic amines (*i.e.*, pyrrolidine, piperidine, morpholine, indoline, L-proline methyl and *tert*-butyl ester, carbazole, indole and pyrrole, **Chapter 4**). Afterwards, these chelating agents have been combined with ruthenium, copper, gold centers to form a number of new coordination compounds, which have been investigated for their physico-chemical features by means of different techniques, such as elemental and ESI-MS analysis, <sup>1</sup>H-NMR spectroscopy, FT-IR and UV-Vis spectrophotometries (**Chapters 5-7**). This deep analysis has been carried out for 9 dithiocarbamate ligands and total 54 metal-DTC complexes. The second goal has been indeed to investigate how the electronic properties of the DTC ligand (affected by the type of substituents) as well as the oxidation state and the coordination geometry of the metal center, influence the strength of the metal-ligand bonds.

The third goal of this PhD work has been the rationalization of the *in vitro* antiproliferative activity data collected for all the synthesized coordination compounds (using DMSO as a vehicle) against three different human tumor cell lines (HeLa, HepG2 and HepG2/SB3) (**Chapter 9**). HeLa cells derive from ovarian carcinoma and represent a starting point for preliminary testing in the light of their widespread use in the last sixty-five years. On the other hand, HepG2 cells come from liver carcinoma, which nowadays is the 2<sup>nd</sup> most common cause of death from cancer worldwide and represents a disease with a high unmet medical need.

This biological evaluation has been aimed at comparing the observed chemical features of the synthesized coordination compounds with their anticancer activity. In addition, in the perspective of developing new drug candidates for preclinical studies, the most promising metal-DTC derivatives have been studied for their lipophilicity, a fundamental criterion to determine the “druglikeness” of a new chemical entity. In this context, a correlation between the biological activity of the compounds and their partition coefficient *n*-octanol/water is useful to generate a LipE (lipophilic efficiency) profile which allowed us to select the two final Lead Compounds for subsequent testing.

The attention has been then addressed to the investigation of bio-compatible nanosystems for the cancer-selective delivery of the Lead Compounds. In fact, in order to increase both the poor water solubility and the stability (in other words, the overall bioavailability) of the Lead Compounds, we exploited the micelle formation of the nonionic surfactant co-polymer Pluronic® F127 (PF127). The choice of this surfactant was not accidental. In fact, PF127 is already in Phase I clinical trial in doxorubicin-based formulations, reporting high maximum tolerated doses.

Notably, based on the blood capillary-leaking of tumor tissues, macromolecular carriers can accumulate in tumor vasculature much more than in the normal one (*passive cancer-targeting*), thus leading to the delivery and retention of antiproliferative cargos in the tumor microenvironment (this phenomenon is referred to as the enhanced permeability and retention -EPR- effect). On the other hand, the *active cancer-targeting* approach is growing in importance and exploits biomolecules with high affinity for their cell-surface targets to selectively deliver drugs to cancerous cells, in order to minimize the damage to healthy ones. In line with these considerations, the fourth aim of this PhD project has been the chemical modification of terminal hydroxyl groups of the PF127 co-polymer for its convenient functionalization with carbohydrates (*i.e.*,  $\beta$ -D-glucopyranose, glucosamine and  $\beta$ -maltose). The new macromolecules have been characterized by means of  $^1\text{H}$ - and  $^{13}\text{C}$ -NMR spectroscopy and FT-IR spectrophotometry. The following purpose has been the encapsulation of the selected Lead Compounds in micelles of these modified PF127 polymers. Their structure and stability have been studied *via* DLS and TEM analyses, and UV-Vis evaluation in human serum and cell culture medium (**Chapter 8**), followed by the screening for their cytotoxic activity towards the HeLa, HepG2/CTR and HepG2/SB3 cell lines. Finally, the ultimate goal has been the preliminary investigation of the mechanism of action of the two Lead Compounds (**Chapter 9**), in terms of time-dependent cellular response profiles (RTCA), confocal microscopy analysis on the fluorescein-labeled nanosystems, and *in vitro* competition with the antagonist 4,6-*O*-ethylidene-D-glucose, a glucose transporter (GLUT1) inhibitor. For clarity reasons, the NMR and FT-IR spectra of all the synthesized complexes and polymers have been collected in a distinct Chapter (**Supporting Information, A-J**) at the end of the work.

### 3. MATERIALS AND INSTRUMENTAL

#### 3.1 Chemicals for the synthesis of the dithiocarbamate ligands and the Ru(III), Cu(II) and Au(I)/(III) related complexes

The following chemicals were purchased and used as provided by suppliers: sodium pyrrolidinedithiocarbamate (NaPDT, 80%), piperidine (99%), morpholine ( $\geq 99\%$ ), indoline (99%), carbazole ( $\geq 95\%$ ), indole ( $\geq 99\%$ ), pyrrole (98%), carbon disulfide ( $\text{CS}_2$ , anhydrous  $\geq 99\%$ ), sodium *tert*-butoxide ( $\text{NaOtBu}$ , 97%), sodium hydride ( $\text{NaH}$ , 60% suspension in mineral oil), ruthenium(III) chloride trihydrate ( $\text{RuCl}_3 \cdot 3\text{H}_2\text{O}$ ), copper chloride dihydrate ( $\text{CuCl}_2 \cdot 2\text{H}_2\text{O}$ ,  $\geq 99\%$ ), sodium chloride ( $\text{NaCl}$ , 99%), sodium sulfite ( $\text{Na}_2\text{SO}_3$ ,  $\geq 98\%$ ), pyridine (anhydrous 99.8%), manganese(IV) oxide ( $\text{MnO}_2$ , 99%), hydrochloric acid ( $\text{HCl}$ , 37%) (Sigma Aldrich). L-Proline methyl ester hydrochloride ( $\text{L-ProOMe} \cdot \text{HCl}$ , 98%), L-Proline *tert*-butyl ester hydrochloride ( $\text{L-ProOtBu} \cdot \text{HCl}$ , 98%), sodium tetrachloroaurate(III) dihydrate ( $\text{NaAuCl}_4 \cdot 2\text{H}_2\text{O}$ , 99%), potassium tetrabromoaurate(III) hydrate ( $\text{KAuBr}_4 \cdot x\text{H}_2\text{O}$ , 99.9%) (Alfa Aesar). Potassium hydroxide ( $\text{KOH}$ ), bromine ( $\text{Br}_2$ , 99%), phosphorous pentoxide ( $\text{P}_2\text{O}_5$ ) (VWR). Silica gel 60 (0.063-0.200 mm, 70-230 mesh) (Merck).

Solvents: ethanol ( $\text{EtOH}$ ), methanol ( $\text{MeOH}$ ), diethyl ether ( $\text{Et}_2\text{O}$ ), tetrahydrofuran (THF), dichloromethane ( $\text{CH}_2\text{Cl}_2$ ), chloroform ( $\text{CHCl}_3$ ), n-hexane, n-pentane, acetone, acetonitrile, dimethyl sulfoxide (DMSO) (Sigma-Aldrich). When used anhydrous, the solvents were purchased from Sigma-Aldrich, with a purity of  $\geq 99.9\%$ , or alternatively dried using standard distillation procedures.

The  $^1\text{H-NMR}$  chemical shifts ( $\delta$ ) of the signals are given in ppm and referenced to residual protons in the deuterated solvents: chloroform-*d* ( $\text{CDCl}_3$ , 7.26 ppm), dichloromethane-*d*<sub>2</sub> ( $\text{CD}_2\text{Cl}_2$ , 5.32 ppm), methanol-*d*<sub>4</sub> ( $\text{CD}_3\text{OD}$ , 3.31 ppm), dimethylsulfoxide-*d*<sub>6</sub> ( $\text{DMSO-d}_6$ , 2.50 ppm) (VWR).

All the aqueous reactions were conducted in distilled water, purified by means of ionic exchange membrane filters.

#### 3.2 Chemicals for the modifications of Pluronic® F127

The following chemicals were purchased and used as provided by suppliers: Pluronic® F127 (BioReagent, for cell cultures), *p*-toluenesulfonyl chloride ( $\text{TsCl}$ ,  $\geq 98\%$ ), triethylamine (TEA,  $\geq 98\%$ ), 4-(dimethylamino)pyridine (DMAP,  $\geq 99\%$ ), hydrazine hydrate solution (24-26%), sulfur trioxide pyridine complex ( $\text{Py} \cdot \text{SO}_3$ , 98%), 1,2,3,4,6-penta-*O*-acetyl- $\beta$ -D-glucopyranose (98%), 1,3,4,6-acetyl-2-amino-2-deoxy- $\beta$ -D-glucopyranose hydrochloride ( $\geq 98\%$ ), boron trifluoride diethyl etherate ( $\text{BF}_3 \cdot \text{Et}_2\text{O}$ ), sodium cyanoborohydride ( $\text{NaBH}_3\text{CN}$ , 95%), sodium methoxide (95%), Amberlite® IR120 hydrogen form (strongly acid), fluorescein isothiocyanate (FITC,  $\geq 90\%$ ), levulinic acid (98%), acetobromo- $\alpha$ -D-glucose (95%), acetobromo- $\alpha$ -maltose (90%), *N*-hydroxyphthalimide (97%), tetrabutylammonium bisulfate (TBAHS, 99%), methylhydrazine (98%), citric acid - sodium citrate buffer solution, ammonium hydroxide solution (28-30%), sodium sulfate anhydrous ( $\text{Na}_2\text{SO}_4$ )

(Sigma-Aldrich). Phthalimide potassium salt (99%), dicyclohexylcarbodiimide (DCC, 98%) Silica gel 60 (0.063-0.200 mm, 70-230 mesh) (Merck).

Solvents: ethanol (EtOH), methanol (MeOH), isopropyl alcohol (iPrOH), diethyl ether (Et<sub>2</sub>O), tetrahydrofuran (THF), dichloromethane (CH<sub>2</sub>Cl<sub>2</sub>), chloroform (CHCl<sub>3</sub>), n-hexane, n-pentane, acetone, acetonitrile, dimethyl sulfoxide (DMSO) (Sigma-Aldrich). When used anhydrous, the solvents were purchased from Sigma-Aldrich, with a purity of ≥99.9%, or alternatively dried using standard distillation procedures.

The <sup>1</sup>H-NMR chemical shifts (δ) of the signals are given in ppm and referenced to residual protons in the deuterated solvents: dichloromethane-*d*<sub>2</sub> (CD<sub>2</sub>Cl<sub>2</sub>, 5.32 ppm), methanol-*d*<sub>4</sub> (CD<sub>3</sub>OD, 3.31 ppm), deuterium oxide (D<sub>2</sub>O, 4.79 ppm) (VWR).

### 3.3 Chemicals for the *in vitro* biological studies

The following chemicals were purchased and used as provided by suppliers: HeLa cells (American Type Culture Collection, ATCC). HepG2 cells (Provitro). Dulbecco Modified Eagle's Medium (D-MEM), L-glutamine, penicillin, streptomycin, fetal bovine serum (FBS), trypsin (0.05%, EDTA 0.02% in PBS) (Euro Clone). Lipofectamin<sup>®</sup> reagent, PLUS reagent, Opti-MEM, (Invitrogen). RPMI-medium 1640, MEM-non essential aminoacids (100x), Minimum Essential Medium (MEM), DMSO (>99.9%, for biological treatments), *in vitro* toxicology assay kit (resazurin based), Thiazolyl Blue Tetrazolium Bromide (MTT), MTT Detergent Reagent, paraformaldehyde, Elvanol<sup>™</sup> (polyvinyl alcohol) (Aldrich).

### 3.4 Instrumental information

#### *Silica gel and thin layer chromatography*

Analytical TLC were performed on Kieselgel F254. UV light (λ = 254 nm). Gravity column chromatography was performed on Silica gel 60 (0.063-0.200 mm, 70-230 mesh) (Merck); the elution of the loaded compound was obtained by using the proper eluent mixture.

#### *Elemental analysis*

Elemental analyses were carried out at Microanalysis Laboratory of the Department of Chemical Sciences, University of Padova by using a microanalyzer Fisons EA-1108 CHNS-O and a microanalyzer Carlo Erba 1108 CHNS-O.

#### *FTIR spectroscopy*

Near-FTIR spectra (4000-400 cm<sup>-1</sup>) were registered at room temperature (32 scans, resolution 2 cm<sup>-1</sup>) by Nicolet Nexus 5SXC spectrophotometer. KBr pellets of samples were prepared according to standard procedures.



Far-FTIR spectra (600-50  $\text{cm}^{-1}$ ) were registered at room temperature with a Nicolet Nexus 870 spectrophotometer. For the analysis, films of sample dispersed in nujol were loaded on polyethylene discs (250 scans, resolution 4  $\text{cm}^{-1}$ ). Spectra were processed with OMNIC 5.2 (Nicolet Instrument Corporation).

#### *NMR spectroscopy*

$^1\text{H}$ -NMR spectra of metal-DTC complexes were recorded at 298 K on a Bruker Avance DRX300 spectrometer equipped with a BBI [1H, X] probe-head, Bruker. Typical acquisition parameters for 1D  $^1\text{H}$ -NMR spectra (1H: 300.13 MHz): 64 transients, spectral width 15 ppm (80 ppm in case of  $[\text{Ru}(\text{DTC})_3]$  compounds), using delay time of 1.0-4.0 seconds. The data sets were processed with the standard Bruker processing software package Topspin 1.3. Chemical shifts were referenced to solvent signal. Peak assignment and integral calculations were carried out by means of MestReNova version 6.2.0 (Mestrelab Research S.L.).

$^1\text{H}$ - and  $^{13}\text{C}$ -NMR spectra of Pluronic® F127 derivatives were recorded at 298 K on a Bruker Avance DMX600 spectrometer equipped with a Triple Resonance Probe TXI [1H, 13C, 15N], 5 mm, 3 axes gradient, Bruker. Typical acquisition parameters for 1D  $^1\text{H}$ -NMR spectra (1H: 599.90 MHz): 64 transients, spectral width 12 KHz, using delay time of 1.0 seconds. Typical acquisition parameters for 1D  $^{13}\text{C}$ -NMR spectra (13C: 150.84 MHz): 2048 transients repeated 32 times, spectral width 210 ppm, using delay time of 2.0 seconds,  $^1\text{H}$ -decoupled  $^{13}\text{C}$  spectrum without NOE (*zgig* experiment). The data sets were processed with the standard Bruker processing software package Topspin 1.3. Chemical shifts were referenced to solvent signal. Peak assignment and integral calculations were carried out by means of MestReNova version 6.2.0 (Mestrelab Research S.L.).

#### *UV-vis analysis*

Absorption spectra of freshly prepared solutions of samples were acquired at 25 °C and 37 °C in the range 200-800 nm, taking into account the solvent cutoff, with an Agilent Cary 100 UV-Vis double beam spectrophotometer. Samples were dissolved in the appropriate solvents and the resulting solutions were placed in QS quartz cuvette (path length 1 cm).

#### *ESI-MS analysis*

ESI-MS spectra were recorded with a positive mode on a Mariner Perspective Biosystem instrument, setting a 5kV ionization potential and a 20  $\mu\text{L}/\text{min}$  flow rate. A mixture of coumarin and 6-methyl-tryptophan was used as a standard. Samples were dissolved in methanol, water or acetonitrile, whereas methanol with 1% formic acid was used as eluent. ESI-MS spectra have been processed by the software Data Explorer.

#### *X-ray structural analysis*

Single crystal data were collected with a Bruker Smart APEXII diffractometer (Mo  $\text{K}\alpha$  radiation,  $\lambda = 0,71073 \text{ \AA}$ ). The unit cell parameters were obtained using 60  $\omega$ -frames of 0.5° width and scanned from three different zone of reciprocal lattice. The intensity data were integrated from several series of exposure frames (0.3°

width) covering the sphere of reciprocal space. Absorption corrections were applied using the program SADABS. The structures were solved by direct methods (SIR2004) and refined  $F^2$  with full matrix least squares (SHELXL-97), using the WinGX software package. Grafical material was prepared with Mercury 3.5 for Windows.

#### *Dynamics Light Scattering (DLS) analysis*

Mean diameter was measured using a ZetasizerNano-S (Malvern Instruments) at 37°C using disposable sizing cuvettes. DLS samples were prepared in deionized water and filtered with a 20  $\mu$ M micro-filter. For each batch, hydrodynamic radius and size distribution were the mean of ten measurements and final values were calculated as the mean of three different batches.

#### *Transmission electron microscopy (TEM) analysis*

Experiments were performed at the Electronic Spectroscopy Laboratory of the Department of Biology, University of Padova with a Tecnai G<sup>2</sup> (FEI) transmission electron microscope operating at 100 kV. Images were captured with a Veleta (Olympus Soft Imaging System) digital camera. To prepare the samples, a drop of investigated micellar solution has been deposited on 400 mesh copper grids type “holy film”, and subsequently contrasted with a 1% uranyl acetate solution for about 2 minutes. The sample was then analyzed without further manipulations.

#### *Incubator*

Cell cultures have been incubated at 37 °C in a 5% carbon dioxide controlled atmosphere of a Hera Cell 150i CO<sub>2</sub> incubator (Termo Scientific).

#### *Optical plate reader*

Cellular vitality was determined by absorbance measurements at 595 nm (resazurin test) and 550 nm (MTT assay), using a plate reader ELISA Microplate Reader Model 550 (Bio-Rad). Data were obtained and processed by Microplate Manager 4.0 and Origin 8.0 software.

#### *Confocal Microscopy*

For confocal microscopy analysis of cell samples treated with fluorescein-labelled PF127 micelles, a Zeiss Axiovert 200M fluorescence/live cell imaging microscope was used (Carl Zeiss MicroImaging GmbH). The optical sectioning of the samples was achieved with structured illumination with Apotome.2, a system that increases the resolution of conventional fluorescence analysis, calculating the optical section from three images with different grid positions without time lag.

#### *xCELLigence experiment*

Impedance for quantification of cell proliferation was monitored with a xCELLigence RTCA DP device (Roche Diagnostics, GmbH) placed in the in the incubator (37 °C in a 5% CO<sub>2</sub>) and controlled via a cable connected to the external control unit using RTCA 2.0 software for real-time interfacingThe three cradles of the DP

instrument enable three separate electronic 16-well plates (E-plate, Roche Diagnostics GmbH) to be controlled and monitored in parallel or independently of one other. The impedance value of each well was automatically monitored by the xCELLigence system and expressed as a Cell Index value (CI).



## 4. THE DITHIOCARBAMATES AS CHEMOPROTECTANT LIGANDS

### 4.1 Chemical and biological overview of dithiocarbamates

*N*-substituted dithiocarbamates (DTC,  $R_2NCS_2^-$ , **Figure 4.1**) form a class of compounds with an extensive use in chemical practice [103]. Indeed, they are used in the industry of polymers [104] or as fungicides [105], pesticides [106] and antioxidants [107]. Moreover, DTC are a versatile class of anionic sulfur-donor ligands of the type LX, widely used in coordination chemistry, with applications in qualitative inorganic analysis [108] and bioinorganic medicine [109].

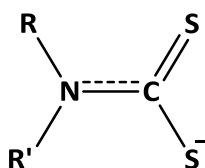


**Figure 4.1** General structure of *N*-substituted dithiocarbamates, where R, R' = H, alkyl group, aryl group. The C-N bond has the character of an almost double bond as the nitrogen atom makes its lone pair available to the carbon atom, and the extent of this phenomenon relies on the type of the R (and R') groups.

DTCs are obtained by the exothermic reaction between carbon disulfide ( $CS_2$ ) and a primary or secondary amine in the presence of a base. The base may be an alkali, such as sodium hydroxide, or an excess of the amine itself. In the last case, the ammonium salt of the ligand ( $[R_2NH_2]^+[R_2NCS_2]^-$ ) is formed. According to Miller and Latimer, the reaction of DTC formation occurs *via* nucleophilic attack of the amine to the electron-poor C atom of carbon disulfide, the crucial step being the hydrogen-transfer from nitrogen to sulfur atoms, followed by acid/base reaction giving rise to the corresponding dithiocarbamate salt [110] (**Figure 4.2 a**). *N*-(mono)substituted dithiocarbamates were found to be more stable in acid solutions, since the *N*-disubstituted ones suffer from the steric influence of the second alkyl group causing a higher strain on the C-N bond [111-113] (**Figure 4.2 b**). On the other hand, dithiocarbamate derivatives of secondary amines are usually stable in alkaline solution, whereas the mono-substituted counterparts can undergo a reaction with hydroxide ions, yielding isothiocyanates ( $R-N=C=S$ ) and elemental sulfur [114] (**Figure 4.2 c**). Finally, dialkyldithiocarbamates form thiuram disulfides upon oxidation with iodine, bromine, hydrogen peroxide, and other common oxidants [115] (**Figure 4.2 d**).

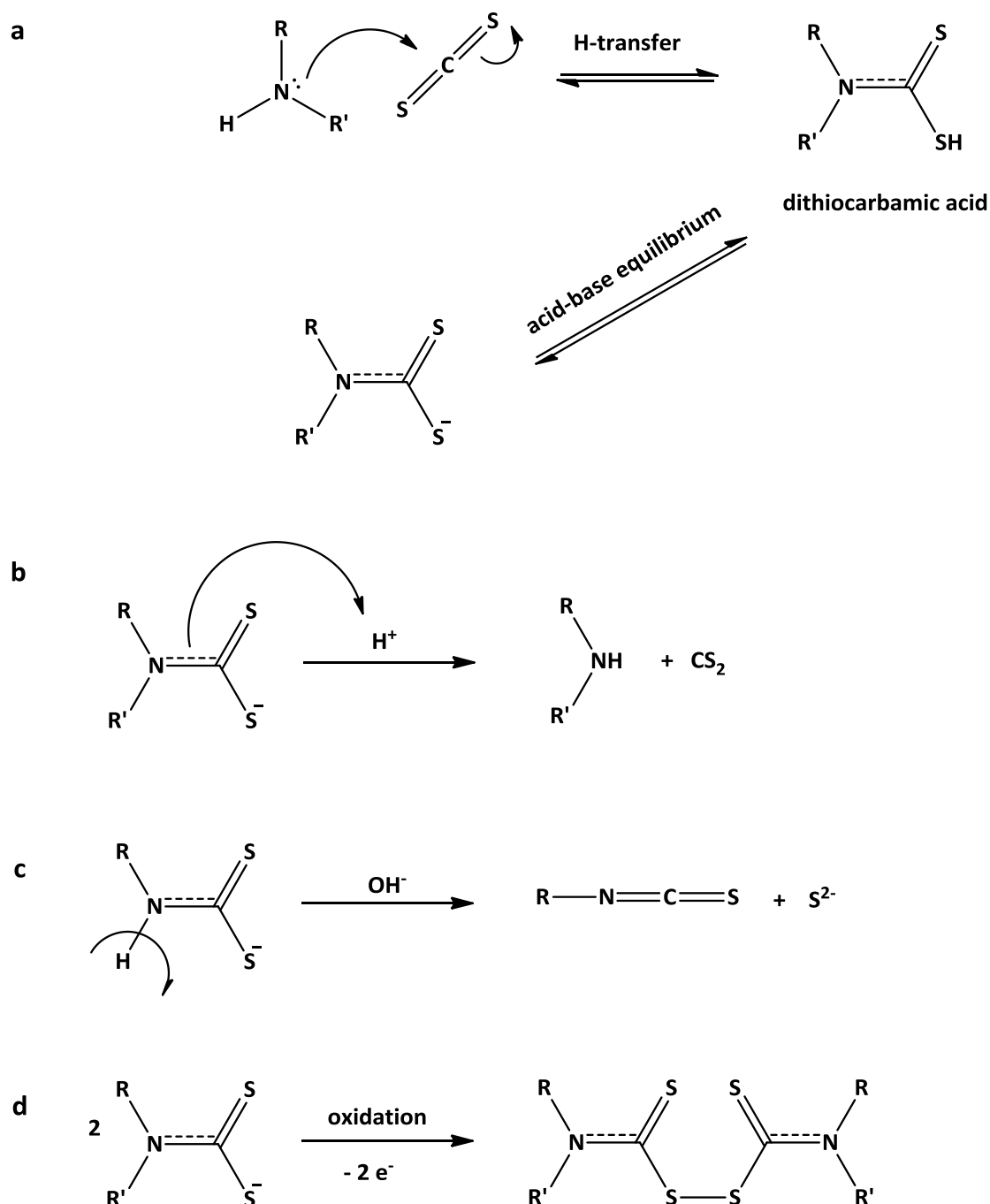


**Figure 4.2** The process of synthesis of a dithiocarbamate salt from a primary or secondary amine by reaction with carbon disulfide in the presence of a base **a**. A dithiocarbamate can undergo acid decomposition in the case of *N*-(di)substituted dithiocarbamates **b**, basic degradation to isothiocyanates for mono-substituted DTC **c**, oxidation to thiuram disulphides in the presence of an oxidant **d**.

Concerning the chelating coordination, according to the ionic model for the electron counting, the DTC ligand can be considered as a four-electron donor (LX) but the two sulfur atoms can coordinate the metal center likewise (**Figure 4.3. a**). In other words, two sulfur atoms in a  $\pi$ -system can coordinate the metal center by a binding mode described by  $\eta^2$  hapticity (also labelled as  $\kappa^2$  since we are dealing with non-carbon donor ligands, **Figure 4.3 a**) [116]. Moreover, in a number of cases the dithiocarbamate may act as a monodentate ligand (**Figure 4.3 b**). This often results from the presence of other sterically hindered coordinated ligands or

it is a consequence of the coordination geometry preferentially adopted by the metal center [117]. Finally, this type of sulfur-based ligands can bridge two metal atoms in a number of other ways (Figure 4.3 c-i). In fact, a significant group of complexes involving the  $\eta^1, \eta^1$ -coordination mode (where each S atom binds to a single metal center) have been characterized by X-ray crystallography [118].

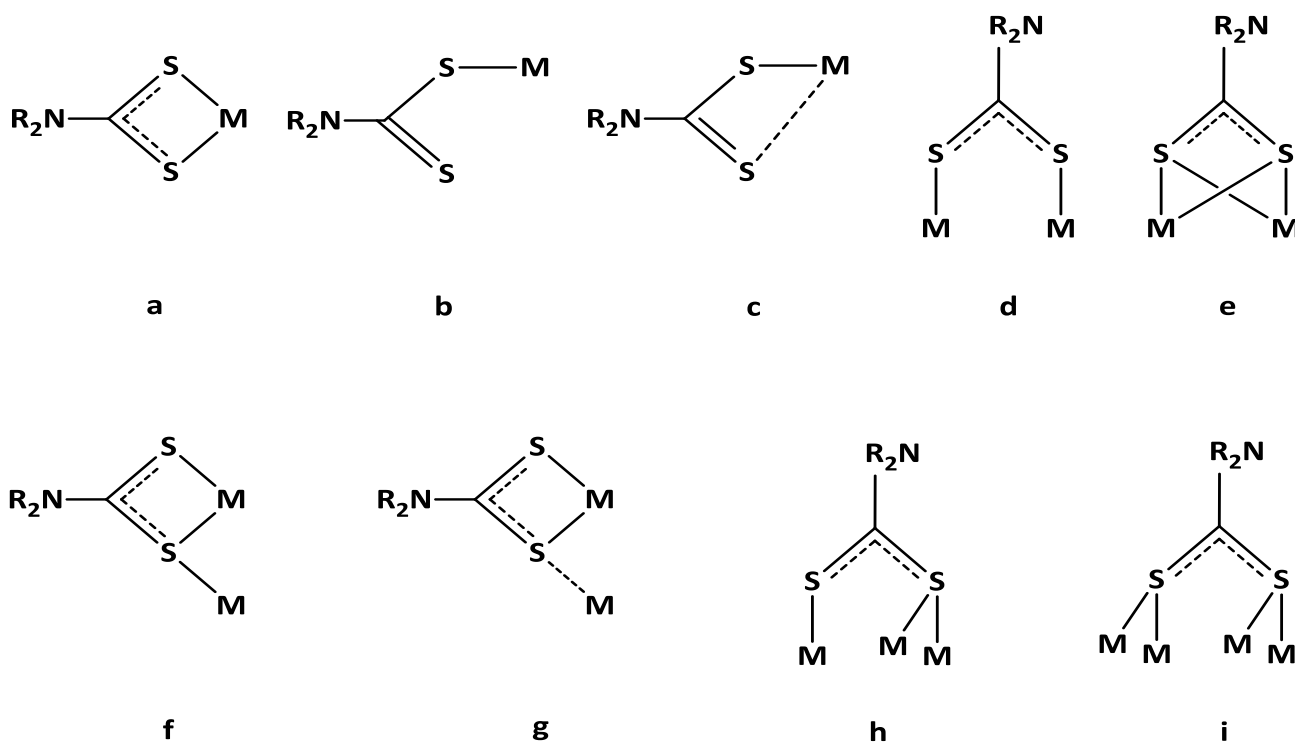


**Figure 4.3.** Possible coordination modes of dithiocarbamates.

The biological profile of dithiocarbamates was extensively explored from 1930s onwards, when they were introduced as pesticides in agriculture. The first DTC derivative to achieve prominence as a fungicide was the tetramethylthiuram disulfide (TMDTS), commonly known as Thiram<sup>®</sup> (Figure 4.4 a) [119]. In 1948 Jacobsen and co-workers discovered the ethanol-sensitizing action of tetraethylthiuram disulfide, sold under the trade names of Antabuse<sup>®</sup> or Antabus<sup>®</sup>, as a support to the treatment of chronic alcoholism (Figure 4.4 b) [120]. On the other hand, the DTC anions, in the form of salts ( $R_2NCSS^-M^+$ ,  $M = \text{alkali or } NH_4^+$ ), proved highly reactive towards other molecules containing -SH groups *in vitro* [121]. Moreover, they were investigated as chelating agents for heavy-metal intoxications *in vivo*, even if they can also bind to endogenous metals, thus triggering toxic effects in the organism [122].

In the oncological field, these sulfur-based ligands appeared for the first time in 1979 in the studies of Borch and coworkers about the chemoprotective effect of diethyldithiocarbamate sodium salt (NaDEDTC) (Figure 4.4 c) during cisplatin-based chemotherapeutic treatment [123]. In fact, this ligand has got the ability to selectively remove platinum centers from the thiol groups of different proteins but not from nucleotides

involved in Pt-DNA adducts. The administration of NaDEDT to patients 3 hours after the drug showed an improvement of the anticancer activity. In this time span, the drug is indeed on its way towards the acknowledged target DNA and NaDEDT can act as a chemoprotectant by removing Pt(II) from several S-donor biomolecules. DEDT reacts indeed with platinum resulting in the formation of DTC-Pt species, thus decreasing the nephrotoxicity and, at the same time, enhancing the bioavailability of the metal for triggering additional antitumor activity as a new anticancer complex (between platinum and the DEDT ligand) [124].

Moreover, diethyldithiocarbamate showed a protective effect against cisplatin-induced ototoxicity, associated with a recovery of the antioxidant system in the cochlea [125]. Nevertheless, the overall benefits of NaDEDT are somewhat limited by its acute toxicity. Metabolic studies have shown that this molecular entity undergoes detoxification through S-glucuronidation or biodegradation to different metabolites such as carbon disulfide, thiourea and alkylamine. CS<sub>2</sub> is a neuropathic and teratogen agent while thiourea interferes with iodine uptake by thyroid and can cause carcinogenic effects. In addition, the sulfur atoms of free dithiocarbamates can react with different enzymes, by creating S-S bonds (e.g., with cysteine or methionine) or chelating biologically active metals, thus inhibiting essential pathways [122, 126].

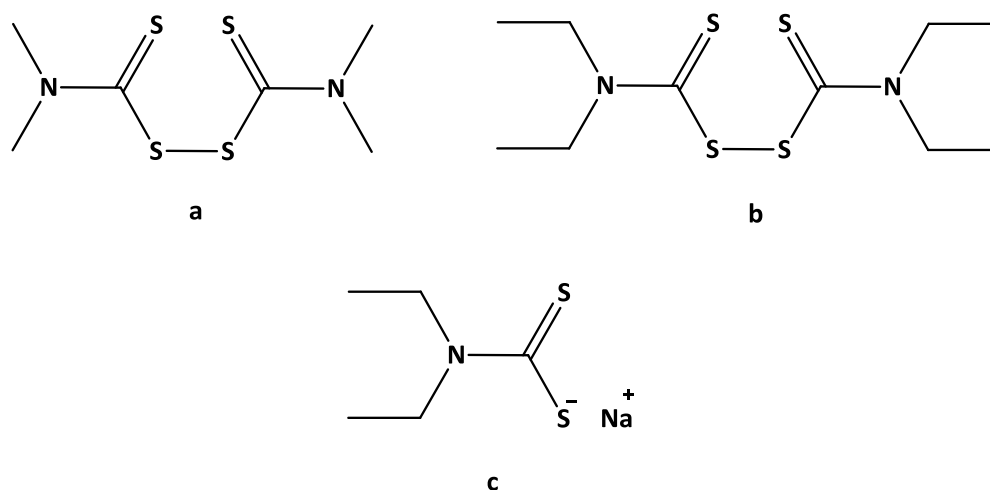


**Figure 4.4** Chemical structure of tetramethylthiuram disulfide (TMDTS, Thiram®) **a**; tetraethylthiuram disulfide (Antabuse® or Antabus®) **b**; diethyldithiocarbamate sodium salt (NaDEDT) **c**.

#### 4.2 Focus on the coordination chemistry of cyclic *N,N*-disubstituted dithiocarbamates

The first studies of electronic features generated by different substituents of the dithiocarbamic nitrogen appeared in the first 1950s, when Klöpping and van der Kerk explored the relationship between chemical composition of nitrogen substituents and antifungal activity of organic sulfur-based fungicides [127, 128]. In this context, considering the dithiocarbamate ion, the canonical structures I-III can be distinguished (**Figure 4.5**).



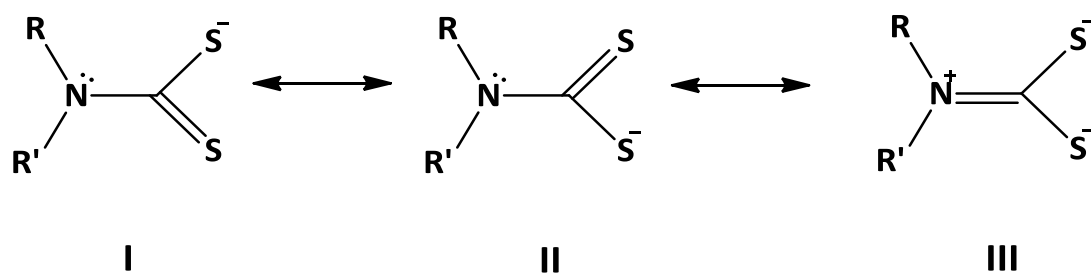


**Figure 4.5** Canonical structures of dithiocarbamate ligands: the dithiocarbamate forms I and II, and the thioureidic form III.

Structures I and II are equivalent regardless of the nature of the *N*-substituents while the structure III can occur only if the nitrogen atom is capable of electron-donating towards the -CSS group. The investigation about this capability is carried out taking into account the *inductive* and *mesomeric* (or *resonance*) effects of different R groups on the electronic charge distribution in the -NCSS moiety [129]. The inductive effect (I) is due to the alteration of the potential field in the -NCSS moiety because of the presence of the substituents, and the main consequence of this is an increase (- I) in the electronegativity of the nitrogen atom (or decrease (+ I) if the electronegativity of the *N*-linked R groups is lower (*vice versa* higher) than that of nitrogen). On the other hand, mesomeric effect (+ or - M) is associated with the addition of two or more  $\pi$ -electrons to the system (resonance), and this is proportional to the corresponding difference in electronegativity between the nitrogen atom and the R substituent. The smaller the latter is, the easier the penetration of the electrons of the *N*-linked group into the -NCSS moiety [129]. In this context, the presence of an electron-donating group attached to the *N* atom enhances the electron density around the nitrogen itself, and hence on the CSS moiety (*i.e.*, + I and + M); *vice versa*, electron-withdrawing groups have the opposite effects (*i.e.*, -I and - M). In the light of the previous considerations, with respect to coordination chemistry, it is evident that dithiocarbamate salts possess the ability to be, at the same time, strong- and weak-field ligands. As an example, in DTC of aromatic amines the nitrogen lone pair is involved in the aromaticity of the ring (the aromatic ring acts as - M on the nitrogen atom), thus endowing the N-CSS bond with a single-bond character (form I and II in **Figure 4.5**). In this case, the dithiocarbamate is a  $\pi$ -acceptor ligand, involving  $\pi^*$  orbitals arising from the low-energy *d*-orbitals of the sulfur atoms (**Figure 4.6 a**), which are characterized by lower electron density if compared with the aliphatic derivatives [130, 131] (form III in **Figure 4.5** and **Figure 4.6 b**). On the other hand, in aliphatic-DTC analogues the lone pair on the nitrogen atom is mostly shifted towards the -CSS moiety, resulting in an increase of the electron density on the sulfur atoms. Therefore, the abovementioned *d*-orbitals of S atoms are partially filled, making the ligand a potential  $\pi$ -donor species [132, 133] (**Figure 4.6 b**). Finally, it is evident that besides the inductive and mesomeric effects of the *N*-substituents, also the type of the metal ion, its oxidation state, the stereochemistry of the complex, and the presence of other different groups in the coordination sphere affect to a great extent the behavior of the dithiocarbamate ligand [133, 134].

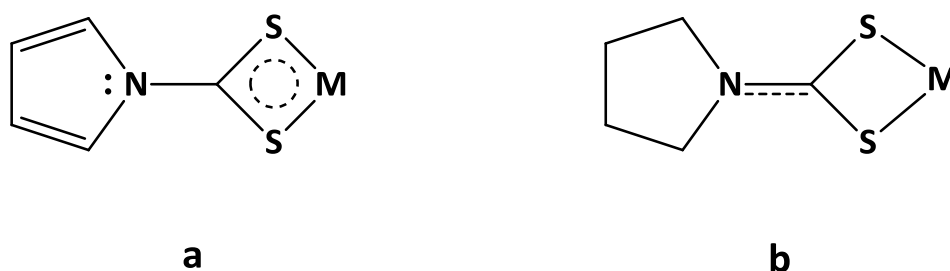


**Figure 4.6** The two limit forms of coordination of a metal center by a DTC ligand are presented, involving as an example the DTC derivatives of pyrrole (**a**) and pyrrolidine (**b**). Aromatic *N*-heterocycles are good examples of DTC which decrease the electron-donating capacity of the *N* atom since the nitrogen lone pair is involved in the aromaticity of the system. Consequently,  $\pi^*$  orbitals located on sulfur atoms are poor in electron density, making possible a metal back-donation. On the contrary, dithiocarbamate derivatives of aliphatic amines are associated with coordination structures of the type **b**, wherein the R substituents donate electron density to the *N* atom, which in turn shift its lone pair onto the -CSS moiety and ultimately onto the metal ion, thus hampering metal back-donation.

As stated in **Chapter 2**, the first purpose of this work was to compare the structural features of some metal dithiocarbamates derived from cyclic amines. Indeed, based on the previous discussion, the nature the *N*-heterocycle influences the behavior of the corresponding dithiocarbamate. In particular, *N*-substituents influence the electron-donating ability of nitrogen towards the -CSS moiety and this is higher in cyclic amines than that of the acyclic counterpart, because of a smaller distance between substituent group and nitrogen (inductive effect), and the presence of conjugate system involving nitrogen lone pair (mesomeric effect) [135, 136]. Moreover, also the steric hindrance may affect the electronic density on the nitrogen atom, and ultimately on the sulfur atoms [137].

The choice of investigating cyclic dithiocarbamates was laid down by recent *in vitro* studies. First, Au(III) derivatives involving a cyclic dithiocarbamate (*i.e.*, pyrrolidine dithiocarbamate, PDT) showed greater anticancer activity than the related acyclic complexes with sarcosine dithiocarbamate as ligand [138]. Similarly, PDT derivatives of Ru(III) and Au(III) proved generally more active than the diethyl dithiocarbamate counterpart as antiproliferative compounds tested on human cancer cell lines [139, 140].

The ligands considered for this project are pyrrolidine dithiocarbamate (PDT, Na salt, commercially available) for comparison purposes, piperidine dithiocarbamate (PipeDTC, K salt), morpholine dithiocarbamate (MorphDTC, K salt), indoline dithiocarbamate (IndolineDTC, K salt), L-proline methyl ester dithiocarbamate (ProOMeDTC, Na salt), L-proline *tert*-butyl ester dithiocarbamate (ProOtBuDTC, Na salt), carbazole dithiocarbamate (CDT, Na salt), indole dithiocarbamate (IndDTC, Na salt) and pyrrole dithiocarbamate (PyrrDTC, Na salt) (**Figure 4.7 a-i**).

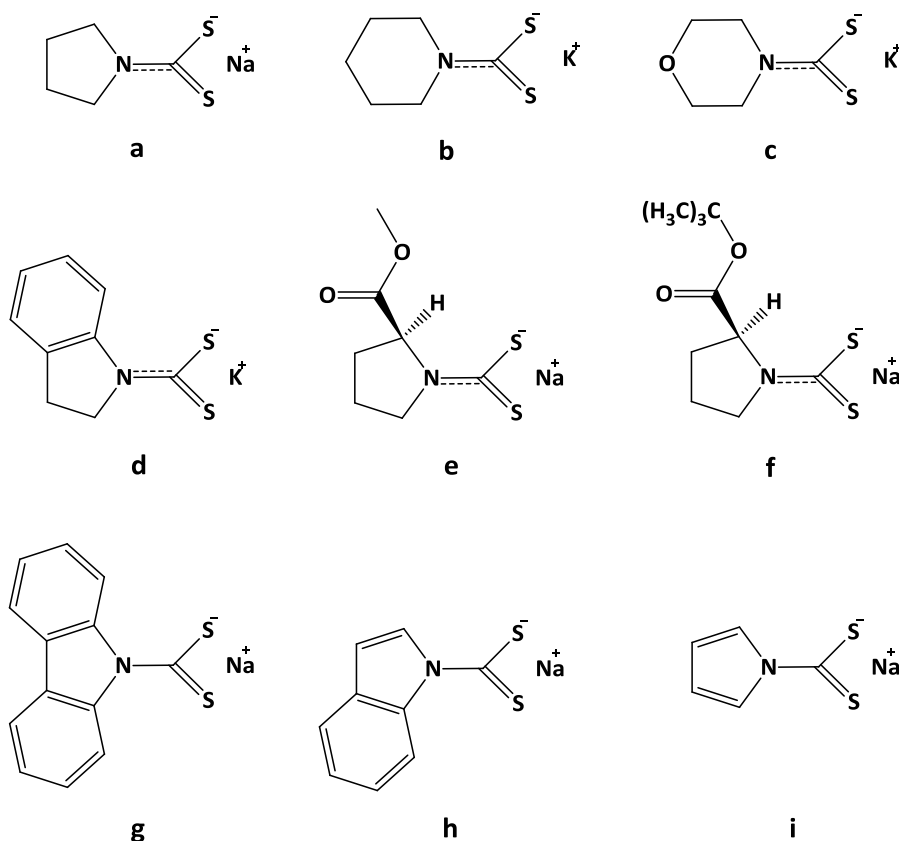


**Figure 4.7.** Chemical structure of the dithiocarbamate salts of pyrrolidine (Na PDT) **a**, piperidine (K PipeDTC) **b**, morpholine (K MorphDTC) **c**, indoline (K IndolineDTC) **d**, L-proline methyl ester (Na ProOMeDTC) **e**, L-proline *tert*-butyl ester (Na ProOtBuDTC) **f**, carbazole (Na CDT) **g**, indole (Na IndDTC) **h**, pyrrole (Na PyrrDTC) **i**.

### 4.3 Synthesis of the selected cyclic *N,N*-disubstituted dithiocarbamate ligands

Taking into account that pyrrolidine dithiocarbamate sodium salt (PDT Na) is commercially available, the remaining eight dithiocarbamate salts have been synthesized as described below.

#### 4.3.1 Synthesis of dithiocarbamate ligands derived from piperidine (K PipeDTC) and morpholine (K MorphDTC)

The syntheses of potassium salts of piperidine dithiocarbamate (K PipeDTC) and morpholine dithiocarbamate (K MorphDTC) are as follows.

10 mmol of KOH were dissolved in 100 mL of ethanol; then 10 mmol of the selected amine (piperidine or morpholine) were added and the solution mixture was set at 0°C. Successively, an excess of carbon disulfide (CS<sub>2</sub>) was added, leading to a deeply yellow mixture which was kept under vigorous stirring for 1 hour. Afterwards, the solvent volume was reduced and the product precipitated by adding cold diethyl ether, filtered and washed with cold ethanol, before being dried *in vacuo* in the presence of P<sub>2</sub>O<sub>5</sub>.

##### *Piperidine dithiocarbamate potassium salt (K PipeDTC)*

Aspect: white solid

Yield: 95 %

Anal. Calc. for  $C_6H_{10}KNS_2$  (MW = 199.38 g·mol<sup>-1</sup>): C 36.14; H 5.06; N 7.03; S 32.16. Found: C 35.84; H 5.02; N 7.05; S 32.22.

<sup>1</sup>H-NMR (DMSO-d<sub>6</sub>, 300.13 MHz): δ (ppm) = 1.39 (m, 4H, H<sub>(3)</sub> + H<sub>(5)</sub>), 1.54 (m, 2H, H<sub>(4)</sub>), 4.27 (t, 4H, H<sub>(2)</sub> + H<sub>(6)</sub>).

Medium FT-IR (KBr):  $\tilde{\nu}$  (cm<sup>-1</sup>) = 2923.75, 2851.10 (ν<sub>a</sub>, C-H); 1417.12 (ν<sub>a</sub>, N-CSS); 965.00 (ν<sub>a</sub>, CSS); 516.25 (ν<sub>s</sub>, CSS).

ESI-MS *m/z*, [DTC<sup>-</sup>] found (calc.): 160.03 (160.02).

#### *Morpholine dithiocarbamate potassium salt (K MorphDTC)*

Aspect: white solid

Yield: 85 %

Anal. Calc. for  $C_5H_8KNOS_2$  (MW = 200.97 g·mol<sup>-1</sup>): C 29.83; H 4.00; N 6.96; S 31.85. Found: C 29.88; H 4.03; N 6.91; S 31.91.

<sup>1</sup>H-NMR (DMSO-d<sub>6</sub>, 300.13 MHz): δ (ppm) = 3.47 (m, 4H, H<sub>(2)</sub> + H<sub>(6)</sub>), 4.30 (t, 4H, H<sub>(3)</sub> + H<sub>(5)</sub>)

Medium FT-IR (KBr):  $\tilde{\nu}$  (cm<sup>-1</sup>) = 2982.44, 2921.73, 2867.68 (ν<sub>a</sub>, C-H); 1410.44 (ν<sub>a</sub>, N-CSS); 1109.77 (ν<sub>a</sub>, C-O); 989.60 (ν<sub>a</sub>, CSS); 546.56 (ν<sub>s</sub>, CSS).

ESI-MS *m/z*, [DTC<sup>-</sup>] found (calc.): 162.01 (162.00).

#### 4.3.2 Synthesis of dithiocarbamate ligands derived from indoline (K IndolineDTC)

An excess of potassium hydroxide (KOH) was suspended in 100 mL of tetrahydrofuran (THF); then 5.5 mmol of indoline were added and the solution mixture was set at 0°C. Successively, 10 mmol of carbon disulfide were added, resulting in a bright yellow mixture which was kept under vigorous stirring for 1 hour. Then, the residual KOH was filtered and the solution evaporated, leading to a solid product, which was dried *in vacuo* over P<sub>2</sub>O<sub>5</sub>.

#### *Indoline dithiocarbamate potassium salt (K IndolineDTC)*

Aspect: bright yellow solid

Yield: 88 %

Anal. Calc. for  $C_9H_8KNS_2$  (MW = 233.39 g·mol<sup>-1</sup>): C 46.31; H 3.45; N 6.00; S 27.48. Found: C 46.19; H 3.44; N 6.09; S 27.40.

<sup>1</sup>H-NMR (DMSO-d<sub>6</sub>, 300.13 MHz): δ (ppm) = 2.87 (t, 2H, H<sub>(3)</sub>), 4.45 (t, 2H, H<sub>(2)</sub>), 6.80 (t, 1H, H<sub>(5)</sub>), 7.00 (t, 1H, H<sub>(6)</sub>), 7.10-7.12 (d, 1H, H<sub>(4)</sub>), 9.52-9.55 (d, 1H, H<sub>(7)</sub>).

Medium FT-IR (KBr):  $\tilde{\nu}$  (cm<sup>-1</sup>) = 2931.52 (ν<sub>a</sub>, C-H); 1452.26 (ν, C=C ring); 1371.36 (ν<sub>a</sub>, N-CSS); 931.11 (ν<sub>a</sub>, CSS); 743.21 (δ, C-H); 507.81 (ν<sub>s</sub>, CSS).

ESI-MS *m/z*, [DTC<sup>-</sup>] found (calc.): 194.02 (194.01).

### 4.3.3 Synthesis of dithiocarbamate ligands of L-proline derivatives (Na ProOMeDTC and Na ProOtBuDTC)

The sodium salts of L-proline methyl ester dithiocarbamate (Na ProOMeDTC) and L-proline *tert*-butyl ester dithiocarbamate (Na ProOtBuDTC) were synthesized in a Schlenk-line apparatus under a N<sub>2</sub> atmosphere. 10 mmol of sodium *tert*-butoxide were dissolved in 20 mL of anhydrous methanol. Afterwards, 5 mmol of the chosen amine hydrochloride, previously dissolved in 10 mL of anhydrous methanol, were added and the solution mixture was set at 0°C. Successively, 10 mmol of carbon disulfide were added, leading to a light yellow mixture which was kept under vigorous stirring for 1 hour. Then, the solvent was evaporated under reduced pressure and the product was taken up in dichloromethane in order to remove NaCl as a byproduct. Finally, the solvent was removed, yielding a hygroscopic solid which was dried in pump over P<sub>2</sub>O<sub>5</sub>. Both products are stored under inert atmosphere, being highly hygroscopic.

#### *L*-proline methyl ester dithiocarbamate sodium salt (Na ProOMeDTC)

Aspect: white hygroscopic solid

Yield: 78 %

Anal. Calc. for C<sub>7</sub>H<sub>10</sub>NNaO<sub>2</sub>S<sub>2</sub> (MW = 227.28 g·mol<sup>-1</sup>): C 36.99; H 4.43; N 6.16; S 28.22. Found: C 36.82; H 4.51; N 6.10; S 28.28.

<sup>1</sup>H-NMR (CD<sub>3</sub>OD, 300.13 MHz): δ (ppm) = 2.03-2.33 (m, 4H, H<sub>(3)</sub> + H<sub>(4)</sub>), 3.69 (s, 3H, O-CH<sub>3</sub>), 3.95 (m, 2H, H<sub>(5)</sub>), 5.07-5.11 (dd, 1H, H<sub>(2)</sub>).

Medium FT-IR (KBr):  $\tilde{\nu}$  (cm<sup>-1</sup>) = 2953.03 (ν<sub>a</sub>, C-H); 1733.20 (ν, C=O); 1392.38 (ν<sub>a</sub>, N-CSS); 1177.76 (ν<sub>a</sub>, C-OMe); 944.78 (ν<sub>a</sub>, CSS); 504.45 (ν<sub>s</sub>, CSS).

ESI-MS *m/z*, [DTC<sup>-</sup>] found (calc.): 204.03 (204.02).

#### *L*-proline *tert*-butyl ester dithiocarbamate sodium salt (Na ProOtBuDTC)

Aspect: beige hygroscopic solid

Yield: 77 %

Anal. Calc. for C<sub>10</sub>H<sub>16</sub>NNaO<sub>2</sub>S<sub>2</sub> (MW = 269.36 g·mol<sup>-1</sup>): C 44.59; H 5.99; N 5.20; S 23.81. Found: C 44.41; H 6.02; N 5.19; S 23.76.

<sup>1</sup>H-NMR (CD<sub>3</sub>OD, 300.13 MHz): δ (ppm) = 1.47 (s, 9H, O-C(CH<sub>3</sub>)<sub>3</sub>), 2.01-2.30 (m, 4H, H<sub>(3)</sub> + H<sub>(4)</sub>), 3.94 (m, 2H, H<sub>(5)</sub>), 4.97-4.99 (dd, 1H, H<sub>(2)</sub>).

Medium FT-IR (KBr):  $\tilde{\nu}$  (cm<sup>-1</sup>) = 2974.63 (ν<sub>a</sub>, C-H); 1722.65 (ν, C=O); 1388.27 (ν<sub>a</sub>, N-CSS); 1151.18 (ν<sub>a</sub>, C-OtBu); 932.89 (ν<sub>a</sub>, CSS); 502.02 (ν<sub>s</sub>, CSS).

ESI-MS *m/z*, [DTC<sup>-</sup>] found (calc.): 246.07 (246.06).

#### 4.3.4 Synthesis of dithiocarbamate ligand of aromatic *N*-heterocycles (Na CDT, Na IndDTC, and Na PyrDTC)

The sodium salts of carbazole dithiocarbamate (Na CDT), indole dithiocarbamate (Na IndDTC), and pyrrole dithiocarbamate (Na PyrDTC) were synthesized in a Schlenk-line apparatus in a N<sub>2</sub> atmosphere. Pyrrole was purified by distillation immediately before use. To 1.44 mmol of aromatic amine previously dissolved in THF (freshly distilled), 2.88 mmol of NaH 60% suspension were added at 0 °C. The mixture was kept under vigorous stirring for 10 minutes, followed by filtration in inert atmosphere of nitrogen to remove NaH residues. Successively, 2.88 mmol of carbon disulfide were added to the resulting solution under stirring at 0 °C. After 2 h the solvent was removed under reduced pressure and the solid was taken up in a minimum amount of anhydrous THF and precipitated with hexane. The resulting solid was filtered and dried under vacuum in the presence of P<sub>2</sub>O<sub>5</sub>.

All products were stored under inert atmosphere, as they resulted highly hygroscopic and air sensitive.

##### *Carbazole dithiocarbamate sodium salt (Na CDT)*

Aspect: orange hygroscopic solid

Yield: 88 %

Anal. Calc. for C<sub>13</sub>H<sub>8</sub>NNaS<sub>2</sub> (MW = 265.33 g·mol<sup>-1</sup>): C 58.85; H 3.04; N 5.28; S 24.17. Found: C 58.69; H 3.15; N 5.31; S 24.11.

<sup>1</sup>H-NMR (DMSO-d<sub>6</sub>, 300.13 MHz): δ (ppm) = 7.17 (t, 2H, H<sub>(3)</sub> + H<sub>(6)</sub>), 7.33 (t, 2H, H<sub>(2)</sub> + H<sub>(7)</sub>), 8.05-8.08 (d, 2H, H<sub>(4)</sub> + H<sub>(5)</sub>), 8.45-8.47 (d, 2H, H<sub>(1)</sub> + H<sub>(8)</sub>).

Medium FT-IR (KBr):  $\tilde{\nu}$  (cm<sup>-1</sup>) = 1435.84 (v, C=C ring); 1281.47 (v<sub>a</sub>, N-CSS); 1040.03 (v<sub>a</sub>, CSS); 832.62 (ω, C-H); 742.53 (δ, C-H); 569.77 (v<sub>s</sub>, CSS).

ESI-MS *m/z*, [DTC<sup>-</sup>] found (calc.): 242.01 (242.01).

##### *Indole dithiocarbamate sodium salt (Na IndDTC)*

Aspect: yellow-orange hygroscopic solid

Yield: 71 %

Anal. Calc. for C<sub>9</sub>H<sub>6</sub>NNaS<sub>2</sub> (MW = 215.27 g·mol<sup>-1</sup>): C 50.21; H 2.81; N 6.51; S 29.79. Found: C 50.11; H 2.99; N 6.40; S 29.89.

<sup>1</sup>H-NMR (DMSO-d<sub>6</sub>, 300.13 MHz): δ (ppm) = 6.36-6.37 (d, 1H, H<sub>(3)</sub>), 7.03-7.11 (m, 2H, H<sub>(5)</sub> + H<sub>(6)</sub>), 7.45-7.48 (d, 1H, H<sub>(4)</sub>), 8.66-8.68 (d, 1H, H<sub>(2)</sub>), 9.31-9.34 (d, 1H, H<sub>(7)</sub>).

Medium FT-IR (KBr):  $\tilde{\nu}$  (cm<sup>-1</sup>) = 2923.17 (v<sub>a</sub>, C-H); 1439.44 (v, C=C ring); 1289.94 (v<sub>a</sub>, N-CSS); 997.91 (v<sub>a</sub>, CSS); 824.65 (ω, C-H); 752.33 (δ, C-H); 550.32 (v<sub>s</sub>, CSS).

ESI-MS *m/z*, [DTC<sup>-</sup>] found (calc.): 192.00 (191.99).

*Pyrrole dithiocarbamate sodium salt (Na PyrrDTC)*

Aspect: dark yellow hygroscopic solid

Yield: 66 %

Anal. Calc. for  $C_5H_4NNaS_2$  (MW = 165.21  $g \cdot mol^{-1}$ ): C 36.35; H 2.44; N 8.48; S 38.22. Found: C 36.22; H 2.57; N 8.69; S 38.31.

$^1H$ -NMR (DMSO- $d_6$ , 300.13 MHz):  $\delta$  (ppm) = 5.99 (s, 2H,  $H_{(3)} + H_{(4)}$ ), 8.03 (s, 2H,  $H_{(2)} + H_{(5)}$ ).

Medium FT-IR (KBr):  $\tilde{\nu}$  ( $cm^{-1}$ ) = 2923.10 ( $\nu_a$ , C-H); 1457.21 ( $\nu$ , C=C ring); 1259.12 ( $\nu_a$ , N-CSS); 1012.45 ( $\nu_a$ , CSS); 815.10 ( $\omega$ , C-H); 746.04 ( $\delta$ , C-H); 548.16 ( $\nu_s$ , CSS).

ESI-MS  $m/z$ , [DTC] found (calc.): 141.98 (141.98).

## 4.4 Discussion

### 4.4.1 Considerations about the synthetic routes

The syntheses of the dithiocarbamate salts derived from aliphatic amines follow the general route presented in **Figure 4.2 a**, where the acid-base equilibrium is shifted to products by the addition of an equivalent of base (KOH for piperidine, morpholine and indoline or sodium *tert*-butoxide for L-proline esters). In addition, to avoid the hydrolysis of the -OR group (R= Me, *t*Bu) of the L-proline esters, the syntheses of the corresponding DTC salts were performed under anhydrous conditions ( $N_2$  atmosphere, dry methanol) and using a sterically hindered base. On the other hand, the formation of the dithiocarbamate salts of aromatic *N*-heterocycles (*i.e.*, carbazole, indole and pyrrole) was carried out in dry THF under inert atmosphere and using NaH to remove the hydrogen at the N-H position, thus yielding the easy-to-remove by-product  $H_2$ . Then, the anionic species acts as a nucleophile attacking the electrophilic carbon of  $CS_2$ , generating the correspondent dithiocarbamate. The syntheses here discussed for the aromatic amines are a modification of those described by Bereman and Nalewajek, who used metallic Na instead of NaH. The same authors stated that these aromatic dithiocarbamates were extremely air sensitive, "decomposing into a black tar in few minutes" [141]. On the contrary, we found that the products are very hygroscopic, but we did not observe any decomposition over time (*e.g.*, 8 hours of air or water exposition), confirmed by  $^1H$ -NMR (**Figure 4.8**). Finally, all the dithiocarbamate salts obtained were analyzed for their purity by means of elemental analysis and negative ESI-MS (mixture MeOH/ $H_2O$  50:50 % v/v), confirming their stoichiometry and ionic nature.

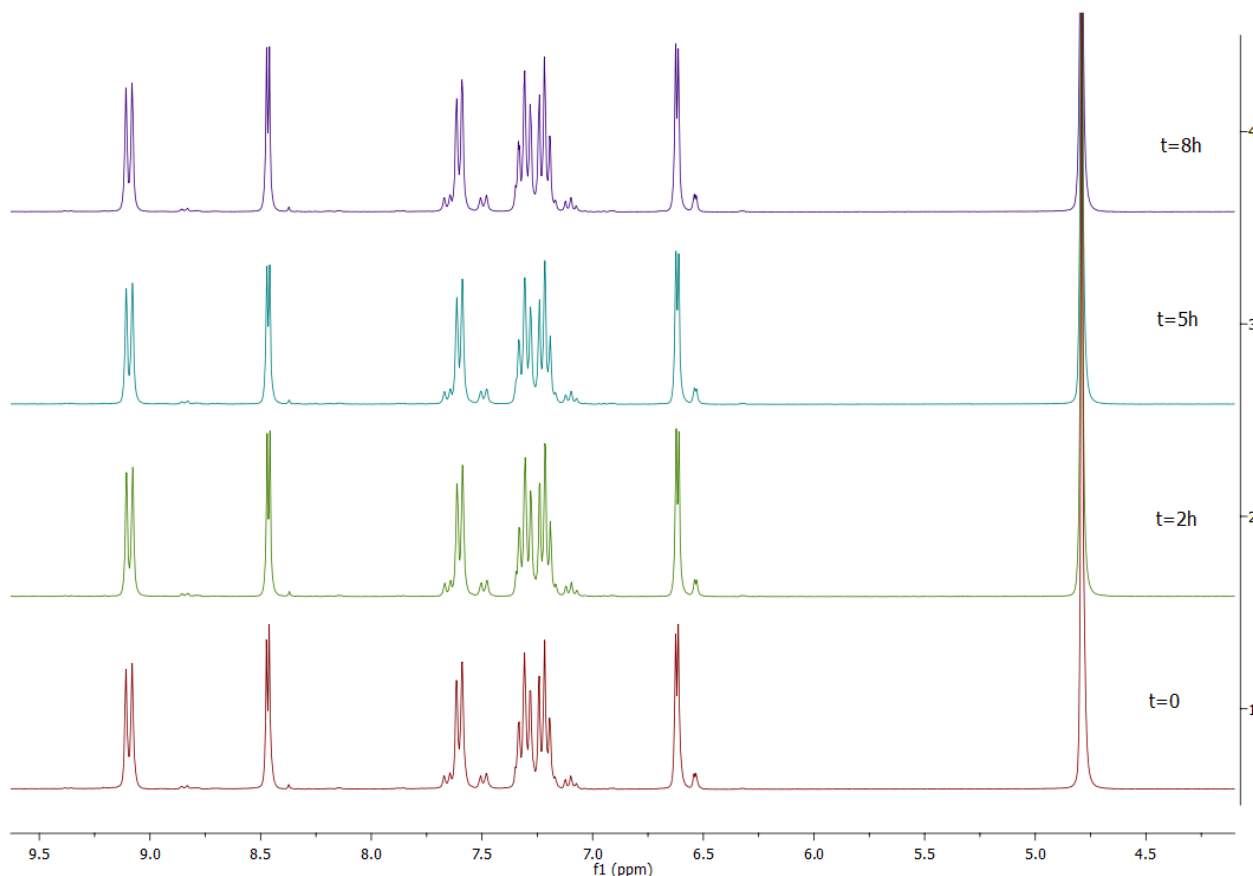


**Figure 4.8:**  $^1\text{H-NMR}$  ( $\text{D}_2\text{O}$ , 300.13 MHz) of indole dithiocarbamate sodium salt over 8 h. The compound is stable in water, as well as air stable, except for its hygroscopicity.

#### 4.4.2 $^1\text{H-NMR}$ characterization

All the selected dithiocarbamate salts have been analyzed by  $^1\text{H-NMR}$  spectroscopy (**Supporting Information A**), and compared to the parent amines. The results are reported in **Table 4.1**.

The  $^1\text{H-NMR}$  analysis has been useful to assess the completeness of the formation reaction of dithiocarbamate salts. In fact, the signal ascribed to the *N-H* proton disappeared in all cases. Interestingly, on passing from the free amine to the corresponding DTC ligand, the *C-H* signals closest to the nitrogen atom overall shift to lower fields of about 1 – 2 ppm, thus highlighting the electron-withdrawing properties of the  $-\text{NCSS}$  moiety. This feature is observed for both the aliphatic and aromatic derivatives but occurs to a lesser extent for the *L*-proline dithiocarbamates, as their ester groups compete as electron-withdrawing moieties with the  $-\text{NCSS}$  one, affecting mainly the chemical shift of the proton in position 5.



	$H_{(1)}$	$H_{(2)}$	$H_{(3)}$	$H_{(4)}$	$H_{(5)}$	$H_{(6)}$	$H_{(7)}$	$H_{(8)}$	$H_{(8)}$	OMe	OtBu
Na PDT	<i>n.d.</i> (2.24)	<b>3.67</b> <b>(2.67)</b>	1.84 (1.55)	1.84 (1.55)	<b>3.67</b> <b>(2.67)</b>	-	-	-	-	-	-
K PipeDTC	<i>n.d.</i> (2.21)	<b>4.27</b> <b>(2.68)</b>	1.39 (1.40)	1.54 (1.40)	1.39 (1.40)	<b>4.27</b> <b>(2.68)</b>	-	-	-	-	-
K MorphDTC	-	3.47 (3.53)	<b>4.30</b> (2.77)	<i>n.d.</i> (2.42)	<b>4.30</b> (2.77)	3.47 (3.53)	-	-	-	-	-
K IndolineDTC	<i>n.d.</i> (3.51)	<b>4.45</b> <b>(3.40)</b>	2.87 (2.91)	7.11 (7.08)	6.80 (6.69)	7.00 (6.97)	<b>9.53</b> <b>(7.12)</b>	-	-	-	-
Na ProOMeDTC	<i>n.d.</i> (3.57)	<b>5.09</b> <b>(4.72)</b>	2.03- 2.33 (1.80- 2.10)	2.03- 2.33 (1.80- 2.10)	<b>3.95</b> <b>(2.84- 3.06)</b>	-	-	-	-	3.69 (3.67)	-
Na ProOtBuDTC	<i>n.d.</i> (3.59)	<b>4.98</b> <b>(4.71)</b>	2.01- 2.30 (1.79- 2.11)	2.01- 2.30 (1.79- 2.11)	<b>3.94</b> <b>(2.85- 3.05)</b>	-	-	-	-	-	1.47 (1.50)
Na CDT	<b>8.46</b> <b>(7.42)</b>	7.33 (7.42)	7.17 (7.24)	8.07 (8.09)	8.07 (8.09)	7.17 (7.24)	7.33 (7.42)	<b>8.46</b> <b>(7.42)</b>	<i>n.d.</i> (11.22)	-	-
Na IndDTC	<i>n.d.</i> (11.04)	<b>8.67</b> <b>(7.05)</b>	6.36 (6.42)	7.46 (7.57)	7.07 (7.33)	7.07 (7.33)	<b>9.33</b> <b>(7.29)</b>	-	-	-	-
Na PyrDTC	<i>n.d.</i> (10.75)	<b>8.03</b> <b>(6.73)</b>	5.99 (6.01)	5.99 (6.01)	<b>8.03</b> <b>(6.73)</b>	-	-	-	-	-	-

**Table 4.1** Comparison between proton chemical shifts (ppm) of the dithiocarbamate salts and the parent amine (reported in brackets). The  $H$ -signals proximal to the dithiocarbamic moiety are highlighted by bold fonts; *n.d.* stands for “not detected”. Attribution was made following *IUPAC* nomenclature for *N*-heterocyclic compounds. All the spectra were recorded in DMSO- $d_6$  except for those of L-proline esters, obtained in CD $_3$ OD, with a 300.13 MHz NMR spectrometer.

#### 4.4.3 FT-IR characterization

As described in **Section 4.2**, the dithiocarbamate can be considered as a strong-field ligand when the resonance form endowed with the negative charge delocalized between the two sulfur atoms is dominating (form I and II, **Figure 4.5**). On the other hand, a significant contribution of the thioureide resonance hybrid (form III, **Figure 4.5**) suggests a weak-field ligand behavior. The preference for one or the other depend on the nature of the parent amine, which determines whether or not the nitrogen lone pair shifts towards the -CSS moiety [130-133]. The medium-infrared spectra (4000-500  $\text{cm}^{-1}$ ) of the selected dithiocarbamate salts (**Supporting Information F**) are likely the foremost tool to detect the molecular signatures for the two forms mentioned above.

The diagnostic absorptions have been identified by comparison of the IR spectra of the free amines with those of the related DTC ligands and the fundamental vibrations are summarized in **Table 4.2**.

	$\nu(C=O)$	$\nu(C=C)$	$\nu(N-CSS)$	$\nu_a(C-O)$	$\nu_a(CSS)$	$\omega(C-H)$	$\delta(C-H)$	$\nu_s(CSS)$
Na PDT	-	-	1422 $cm^{-1}$	-	942 $cm^{-1}$	-	-	542 $cm^{-1}$
K PipeDTC	-	-	1417 $cm^{-1}$	-	965 $cm^{-1}$	-	-	516 $cm^{-1}$
K MorphDTC	-	-	1410 $cm^{-1}$	1109 $cm^{-1}$	990 $cm^{-1}$	-	-	547 $cm^{-1}$
K IndolineDTC	-	1452 $cm^{-1}$	1371 $cm^{-1}$	-	931 $cm^{-1}$	-	743 $cm^{-1}$	508 $cm^{-1}$
Na ProOMeDTC	1733 $cm^{-1}$	-	1392 $cm^{-1}$	1178 $cm^{-1}$	945 $cm^{-1}$	-	-	504 $cm^{-1}$
Na ProOtBuDTC	1723 $cm^{-1}$	-	1388 $cm^{-1}$	1151 $cm^{-1}$	933 $cm^{-1}$	-	-	502 $cm^{-1}$
Na CDT	-	1436 $cm^{-1}$	1281 $cm^{-1}$	-	1040 $cm^{-1}$	832 $cm^{-1}$	742 $cm^{-1}$	570 $cm^{-1}$
Na IndDTC	-	1439 $cm^{-1}$	1290 $cm^{-1}$	-	998 $cm^{-1}$	825 $cm^{-1}$	752 $cm^{-1}$	550 $cm^{-1}$
Na PyrrDTC	-	1457 $cm^{-1}$	1259 $cm^{-1}$	-	1012 $cm^{-1}$	815 $cm^{-1}$	746 $cm^{-1}$	548 $cm^{-1}$

**Table 4.2** Collection of diagnostic IR-vibrations (4000-500  $cm^{-1}$ ) of the synthesized dithiocarbamate salts.

Three main IR-regions must be taken into account when characterizing dithiocarbamate derivatives, both salts and metal-DTC complexes. First, the spectral region 1100-1550  $cm^{-1}$  wherein the  $\nu(N-CSS)$  band can be found and its position depends on the form adopted by the dithiocarbamate ligand (**Figure 4.5**) [132]. In the case of a single-bond-form (resonance form III), the band is located at 1250÷1350  $cm^{-1}$ , whereas it is found at higher wavenumbers (1640-1690  $cm^{-1}$ ) if the DTC ligand contains a basically double C=N bond. It is worth noting that the **Figure 4.5** collects limiting forms and that the real situation is intermediate between them and shifted toward form I (and II) or III based on the extent of electron lone pair sharing in the -NCSS moiety. At this point, observing the  $\nu(N-CSS)$  values presented in **Table 4.2**, it is clear that substituents with a significant +I effect, such as those of pyrrolidine and piperidine, confer to the corresponding dithiocarbamate a preference for form I/II, while aromatic DTC of carbazole, indole and pyrrole are associated with the preferred form III. Indeed, in the latter case, the nitrogen lone pair is engaged in the aromaticity of the ring (this is a -M effect), thus making the electron shift to the -NCSS group impossible. Halfway between these two situations there are DTC salts of morpholine, indoline, and L-proline ester derivatives, which contain either electron-withdrawing groups (*i.e.*, ester moiety for the two prolines or an oxygen atom in the case of morpholine, acting as -I units), or resonance groups with a -M effect (*i.e.*, the aromatic ring of indoline) [142]. However, these dithiocarbamates possess also a +I effect, mediated by the piperidine-like ring for morpholine and from the pyrrolidine ring for the prolines and indoline, thus accounting again for an intermediate situation between the forms I/II and III.

In light of these observations, plotting the N-CSS stretching mode versus the  $pK_a$  of the conjugate acid of the parent amines highlights a linear correlation (**Figure 4.9**). Thus, the weaker the conjugate acid of the parent amine, the stronger is the N-CSS bond, being supported from a larger propensity of the nitrogen atom to share its lone pair. PDT and PipeDTC showed the highest  $\nu(\text{N-CSS})$  wavenumbers (*ca.* 1417  $\text{cm}^{-1}$ ) while the PyrDTC the lowest (1259  $\text{cm}^{-1}$ ). In other words, the inductive and mesomeric effects underlying the base strength of the investigated amines (with respect to their acid-base equilibria, [135, 136]) are the same that contribute to the possibility of shifting the nitrogen lone pair towards the -NCSS moiety. The steric influence of different cyclic substituents may account for small deviations from linearity... with specific effects being difficult to envisage, especially in the case of dithiocarbamate derivatives [137].

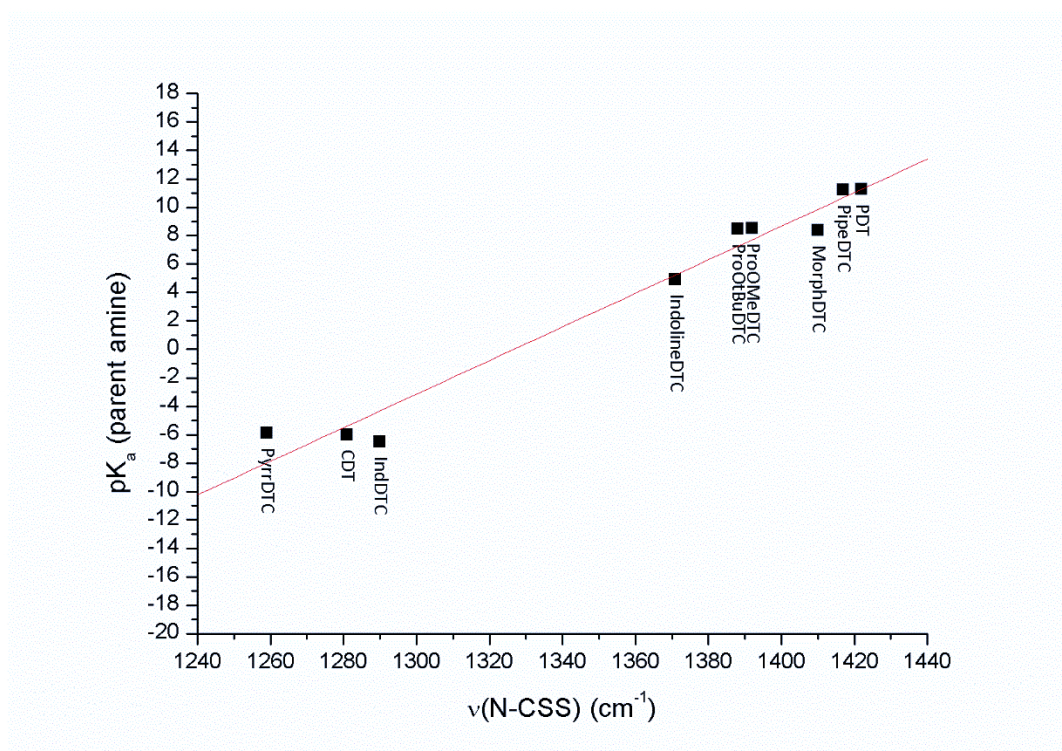


**Figure 4.9** Plot of the  $pK_a$  values of the conjugate acid of the parent amines for the synthesized dithiocarbamate salts against the wavenumbers of the N-CSS stretching mode. The plot follows an almost linear correlation ( $\rho^2 = 0.97$ ). The  $pK_a$  values are: pyrrolidine 11.27 [136]; piperidine 11.22 [136]; morpholine 8.36 [136]; L-proline methyl ester 8.50 [143]; L-proline *tert*-butyl ester 8.47 [143]; indoline 4.90; carbazole -6.00 [144]; indole -6.50 [145]; pyrrole -5.90 [146].

The second diagnostic region spans from 800 to 1100  $\text{cm}^{-1}$ , and it is ascribable to the asymmetric stretching  $\nu_a(\text{CSS})$  (**Table 4.2**). It is also possible to detect the symmetric counterpart  $\nu_s(\text{CSS})$  in the range 410-700  $\text{cm}^{-1}$  [132, 147]. Contrary to the N-CSS stretching mode, the  $\nu(\text{CSS})$  does not show any correlation with the strength of the parent amine. Indeed, this vibration is influenced by steric effects, which are determined by the hindrance of the *N*-substituents. However, the CSS stretching is fundamental in the determination of the coordination mode of the dithiocarbamate ligand. According to the Bonati-Ugo method [148], the presence of only one band in this diagnostic region is assumed to point out a symmetric bidentate ligand, whereas a

double band is associated with either an asymmetrically bidentate or monodentate coordination (**Figure 4.3**). According to these considerations, this vibration will be used in the next chapters (**Chapters 5-7**) to identify the coordination mode of the metal-dithiocarbamate derivatives studied in this work. Metal-sulfur vibrations, found in the Far-IR region at 200-500  $\text{cm}^{-1}$ , [149] are the third diagnostic modes, and will be discussed later.

## 5. RUTHENIUM DITHIOCARBAMATES

### 5.1 Ruthenium as a key player for new metallodrugs

Ruthenium is the 44<sup>th</sup> element of the periodic table and belongs, along with iron and osmium, to the 6<sup>th</sup> group of transition metals. Its electronic configuration is [Kr]4d<sup>7</sup>5s<sup>1</sup>.

The aqueous chemistry of ruthenium is mainly represented by the Ru(II) and Ru(III) ions; in both oxidation states the metal is hexa-coordinated, with a distorted octahedral geometry. Due to the high ligand-field energy of stabilization, Ru(III) complexes have the electronic configuration  $t_{2g}^5$ , with an unpaired electron that confers a paramagnetic character on the ion, generating a ground state of the type  $^2T_{2g}$ . Conversely, Ru(II) complexes are diamagnetic, characterized by low-spin with the electronic configuration  $t_{2g}^6$ , which is reflected in a  $^1A_{1g}$  ground state. All complexes of Ru(II) and Ru(III) are usually kinetically inert [150].

Ruthenium is one of the rarest metals on earth, found uncombined in nature or associated with other metals of the platinum family in the minerals pentlandite and pyroxinite [151]. Concerning the uses, most of this metal is used in the electronics industry for chip resistors and electric contacts or, as oxide, to coat anodes [152]. Moreover, some ruthenium compounds find application in catalysis, for the production of ammonia [153], acetic acid [154], and in the Noyori catalyst BINAP-Ru(II) (BINAP= 2,2'-bis(diphenylphosphino)-1,1'-(binaphthyl)) used in the asymmetric hydrogenation of ketones [155].

Intriguingly, ruthenium has been attracting a considerable interest as the starting material and key player for the development of new compounds in anticancer therapy. This is confirmed by the ever-growing number of review papers about this topic, highlighting the properties of this metal and its coordination compounds, especially *versus* those of platinum derivatives [156]. In 1950s Dwyer first recognized the biological activity of Ru metal center, demonstrating the inhibition of the enzyme cholinesterase by the Ru(II) derivative [Ru(phen)<sub>3</sub>](ClO<sub>4</sub>)<sub>2</sub> (**Figure 5.1 a**) [157]. However, only after the unexpected discovery of cisplatin, the interest in new metal-based drugs led researchers to focus their attention on this element. In fact, in 1980 Clarke and his collaborators hypothesized the cancer-selective action of Ru(III) derivatives in terms of “*activation by reduction*”, proposing that Ru(III) may work as a “pro-drug” by reduction to Ru(II) in tumor tissues ( $E^\circ_{\text{Ru(III)/Ru(II)}} = +0.25 \text{ V vs. SHE at } 298.15 \text{ K}$  [158]). This would allow a faster coordination to biomolecules [159]. In fact, the reduction of Ru(III) to Ru(II) results in completely filled  $d_\pi$  ( $t_{2g}$ ) orbitals, therefore preventing any  $\pi$ -donor ligand from electron donating to the metal ion. This reduces the overall stability of the complex that can lose one or more ligands, hence favoring interactions with biological targets. The low O<sub>2</sub> content (hypoxic conditions) and the decreased pH in tumor cells (due to the well-known Warburg effect, see **Section 1.2**) favor a strongly reducing environment [160]. This evidence was demonstrated with experiments carried out with the Ru(III) complex [*cis*-RuCl<sub>2</sub>(NH<sub>3</sub>)<sub>4</sub>]Cl (**Figure 5.1 b**) ( $E^\circ_{\text{Ru(III)/Ru(II)}} = -0.10 \text{ V vs. SHE at } 298.15 \text{ K}$  [158]), which was able to concentrate in tumor tissues [161]. In this context, it is worth noting that glutathione ( $E^\circ_{\text{S-S/S-H}} = -$

0.26 vs. SHE at pH 7.07, 298.15 K, 0.1 M buffer phosphate) and a large number of redox-active proteins are capable of reducing Ru(III) complexes *in vivo* [161]. On the contrary, if Ru(II) compounds were transported far from the tumor microenvironment, they would turn into Ru(III) counterparts by reaction with molecular oxygen, cytochrome oxidase and other oxidants [162]. Notably, we should bear in mind that the “*activation by reduction*” mechanism of action is only a hypothesis and it cannot account for the cytotoxicity of all Ru(III) complexes. For instance, the widely studied Ru(III) complex NAMI-A ([ImH][*trans*-RuCl<sub>4</sub>(DMSO)(Im)], Im=imidazole, **Figure 5.1 c**), first synthesized by Alessio and co-workers, was the first ruthenium-containing anticancer drug to enter clinical evaluation [163], and has been recently studied in phase I/II in combination with gemcitabine as anti-metastasizing agent [164]. In particular, contrary to its low cytotoxicity *in vitro*, NAMI-A inhibits lung metastasis formation *in vivo*, without affecting primary tumors [165]. Intriguingly, lung metastases lie in a tissue which is considered as the most oxygenated in the body, thus ruling out a reductive environment. Accordingly, the “*activation by reduction*” mechanism is questionable when exploring the anticancer activity of the Ru(III) derivative NAMI-A [166].

In the investigation on the biological peculiarities of ruthenium, another important step was the work of Som and co-workers, who studied the *iron-mimicking properties* of this metal center. In 1983 they labeled transferrin with the radioisotopes <sup>97</sup>Ru and <sup>103</sup>Ru, demonstrating the uptake of these adducts in tumor- and abscess-bearing animals [167]. Ruthenium can indeed mimic iron in binding to serum transferrin (Tf) and albumin (HSA) [168]. Remarkably, the accumulation of ruthenium complexes in tumors might be mediated by the former since neoplastic cells require high levels of iron. In particular, *in vivo* studies have shown that there is a 2- to 12-fold increase in ruthenium concentration inside cancer cells compared to healthy ones [169]. In this context, recent investigations have revealed that the reducing properties of tumor-microenvironment can influence the affinity of the above-mentioned NAMI-A complex, and likely other similar Ru(III)-based compounds, towards albumin and transferrin. These experiments have demonstrated that even small changes in the composition of serum models (*e.g.*, pH) can result in a pronounced effect on binding of ruthenium complexes to proteins [170].

After the hypothesis of “*activation by reduction*” and the description of the *iron-mimicking properties*, in 2002 Brabec showed the ability of ruthenium to bind DNA in a different manner if compared to cisplatin [171]. In this regard, it is worth noting that Pt(II) and both Ru(II) and Ru(III) centers are associated with a slow rate of ligand exchange. Thus, the derived complexes do not undergo ligand dissociation before reaching any of their biological targets [172]. On the other hand, even if the initial DNA binding site of several ruthenium derivatives were the same of cisplatin and its analogues, their DNA-binding mode would be diverse, inducing different conformational distortions [173]. In fact, in both oxidation states +2 and +3 ruthenium is placed in an octahedral environment, contrary to the square planar coordination geometry of Pt(II) species. This behavior may account for important cytotoxic effects of ruthenium derivatives in tumor cell lines, inherently or treatment-induced, resistant to cisplatin [174]. The RM- and RAPTA-complexes (**Figure 5.1 d, e**), developed

by Sadler [175] and Dyson [176] respectively, are ruthenium (II) derivatives with DNA as a major target. These complexes are characterized by the presence of metal-carbon bonds, chloride ligands as leaving groups and diamine or phosphadamantane as non-leaving groups. On passing from the ethylenediamine (RM) complex to phosphadamantane (RAPTA) derivative, the adduct formation profile switches from merely DNA-targeting to binding proteins associated with chromatin [177]. In addition to the previous examples of DNA-interacting ruthenium compounds, it is worth mentioning the Ru(III) drug KP1019 ([IndH][*trans*-RuCl<sub>4</sub>(Ind)<sub>2</sub>], Ind= indazole) and its sodium salt NKP-1339 (Na[*trans*-RuCl<sub>4</sub>(Ind)<sub>2</sub>]) (Figure 5.1 f, g), where the latter is the first-in-class ruthenium-based anticancer drug in clinical development (phase I) against solid malignancies [178]. These two derivatives efficiently untwist DNA and weakly bend it, showing a preference for N7 of the purine bases guanosine and adenosine and inducing lesions with different biochemical outcomes if compared to cisplatin [179].

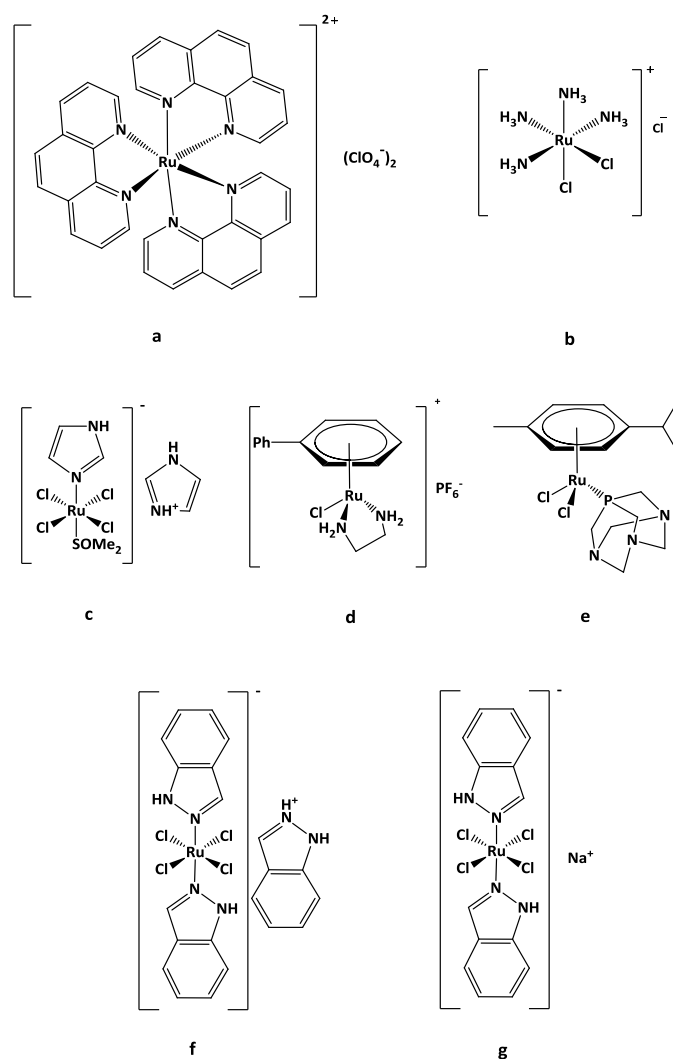


**Figure 5.1** Ruthenium (II)/(III) compounds that showed biologically-relevant properties, [Ru<sup>II</sup>(phen)<sub>3</sub>](ClO<sub>4</sub>)<sub>2</sub> (phen= phenanthroline) **a**, [*cis*-Ru<sup>III</sup>Cl<sub>2</sub>(NH<sub>3</sub>)<sub>4</sub>]Cl **b**, NAMI-A [ImH][*trans*-RuCl<sub>4</sub>(DMSO)(Im)] (Im= imidazole) **c**, the RM-type complex [Ru<sup>II</sup>Cl(η<sup>6</sup>-diphenyl)(en)]PF<sub>6</sub> (en= ethylenediamine) **d**, the RAPTA-type complex RAPTA-C [Ru<sup>II</sup>Cl<sub>2</sub>(η<sup>6</sup>-*p*-cymene)(pta)] (pta= 1,3,5-triaza-7-phosphadamantane) **e**, KP1019 [IndH][*trans*-Ru<sup>III</sup>Cl<sub>4</sub>(Ind)<sub>2</sub>] (Ind= indazole) **f**, and the sodium salt of the latter NKP-1339 Na[*trans*-Ru<sup>III</sup>Cl<sub>4</sub>(Ind)<sub>2</sub>] **g**.

## 5.2 Ruthenium dithiocarbamates and their application in the oncological field

Ruthenium-dithiocarbamates (DTC) were first synthesized by the Italian chemist Lamberto Malatesta in 1938, by mixing the corresponding salt  $\text{NaS}_2\text{CNR}_2$  with  $\text{K}_2[\text{Ru}^{\text{IV}}\text{Cl}_6]$  to obtain Ru(III)-DTC derivatives (with the consequent oxidation of a ligand to disulfide) [180]. However, the in-depth investigation on the chemical properties of this class of complexes dates back to the early 1970s, when Hendrickson and Pignolet reported the synthesis and the chemical/electrochemical interrelations of a number of tris- and pentakis-(dialkyldithiocarbamato) complexes of Ru(III), with the formulae  $[\text{Ru}(\text{DTC})_3]$  and  $[\text{Ru}_2(\text{DTC})_5]\text{Cl}$ , respectively [181-184]. These were obtained from the reaction between  $\text{RuCl}_3$  and the dithiocarbamato salt, followed by purification *via* gravity column chromatography (Figure 5.2). In both the mono- and dinuclear Ru(III) derivatives, the metal centers are characterized by a distorted octahedral coordination attained by six sulfur-donor atoms. Moreover,  $[\text{Ru}(\text{DTC})_3]$  is paramagnetic, whereas the  $[\text{Ru}_2(\text{DTC})_5]\text{Cl}$  is diamagnetic, with the two ruthenium centers antiferromagnetically coupled at a distance of  $\sim 2.7 \text{ \AA}$ . Furthermore, two isomers ( $\alpha$  and  $\beta$ ) of the  $[\text{Ru}_2(\text{DTC})_5]\text{Cl}$  are obtained and the conversion to the thermodynamically favored  $\beta$ - $[\text{Ru}_2(\text{DTC})_5]\text{Cl}$  is carried out in methanol under reflux (Figure 5.2) [181].

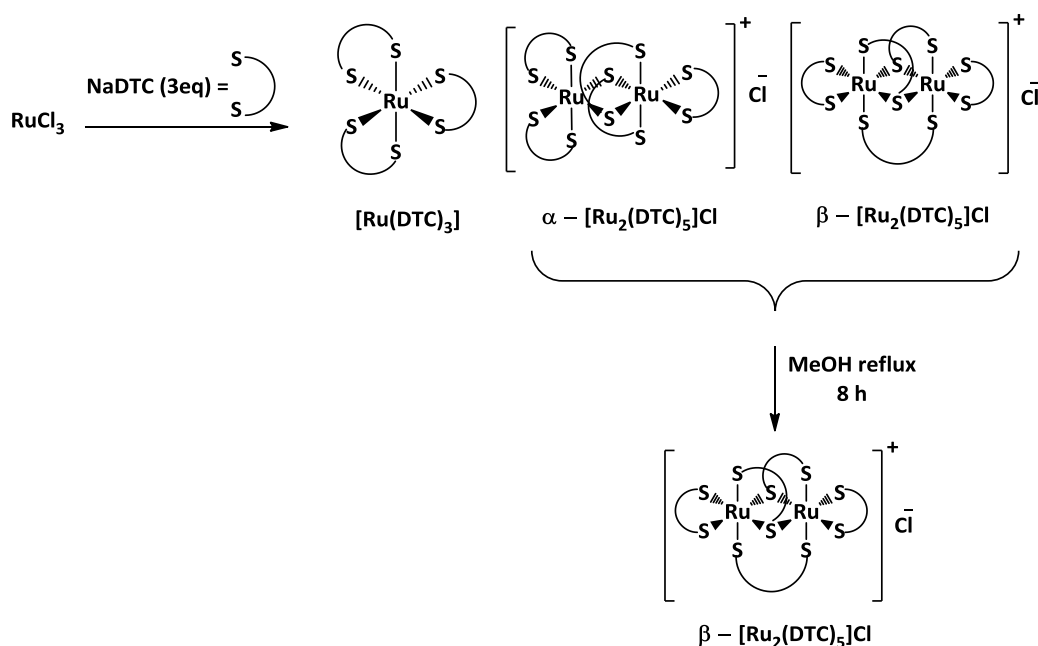


**Figure 5.2** Strategy for the synthesis of homoleptic Ru(III)-DTC derivatives, resulting in a product mixture and consisting of the neutral mononuclear paramagnetic  $[\text{Ru}(\text{DTC})_3]$  and the two ionic dinuclear diamagnetic isomers  $\alpha$ - and  $\beta$ - $[\text{Ru}_2(\text{DTC})_5]\text{Cl}$ . The compounds are generally separated by silica gel chromatography, and the dinuclear derivatives are treated in methanol under reflux to obtain only the thermodynamically stable  $\beta$ - $[\text{Ru}_2(\text{DTC})_5]\text{Cl}$ .

To broaden these studies, in the past years our research group developed novel homoleptic Ru(III) complexes with different dithiocarbamato ligands. In particular, we focused on the dithiocarbamato ligands of dimethylamine (DMDT), diethylamine (DEDT), sarcosine ester (RSDT, where R can be methyl (M), ethyl (E) or *tert*-butyl (T) ester) and, more recently of the pyrrolidine(PDT) [185-187]. Their stability was studied in



dimethyl sulphoxide (used as solubilizing agent for *in vitro* antitumor screening), phosphate buffered saline and cell culture medium DMEM by means of UV-Vis spectrophotometry. All the compounds, both mono- and dinuclear, proved stable without significant spectral changes over 24 hours, thus confirming the chemoprotective and stabilizing action of the DTC ligands [186]. Afterwards, the *in vitro* cytotoxicity assays, performed with 13 human tumor cell lines over 72-h exposure to different concentrations of the Ru(III) complexes, highlighted the significant antiproliferative effects of the ionic dinuclear derivatives  $[\text{Ru}_2(\text{DTC})_5]\text{Cl}$ , with  $\text{IC}_{50}$  values (the concentration of the test agent inducing 50% reduction in cell number compared with control cell cultures), in some cases, up to ten-fold lower than cisplatin, which was used as a reference drug. Moreover, a comparison between the corresponding  $\alpha$ - and  $\beta$  isomers of the dinuclear derivatives  $[\text{Ru}_2(\text{DMDT})_5]\text{Cl}$  and  $[\text{Ru}_2(\text{PDT})_5]\text{Cl}$  pointed out similar cytotoxic effects, hence ruling out that isomerism affects the biological activity of these complexes. On the other hand,  $[\text{Ru}(\text{DTC})_3]$  derivatives are generally less active than the dinuclear counterparts, except against the CEM lines (leukemia cells), thus highlighting the possibility of a selective action of mononuclear complexes against not-solid tumors [140].

The crystal structures of some of these derivatives have been solved and confirmed the observations of Hendrickson and Pignolet (**Figure 5.3**).

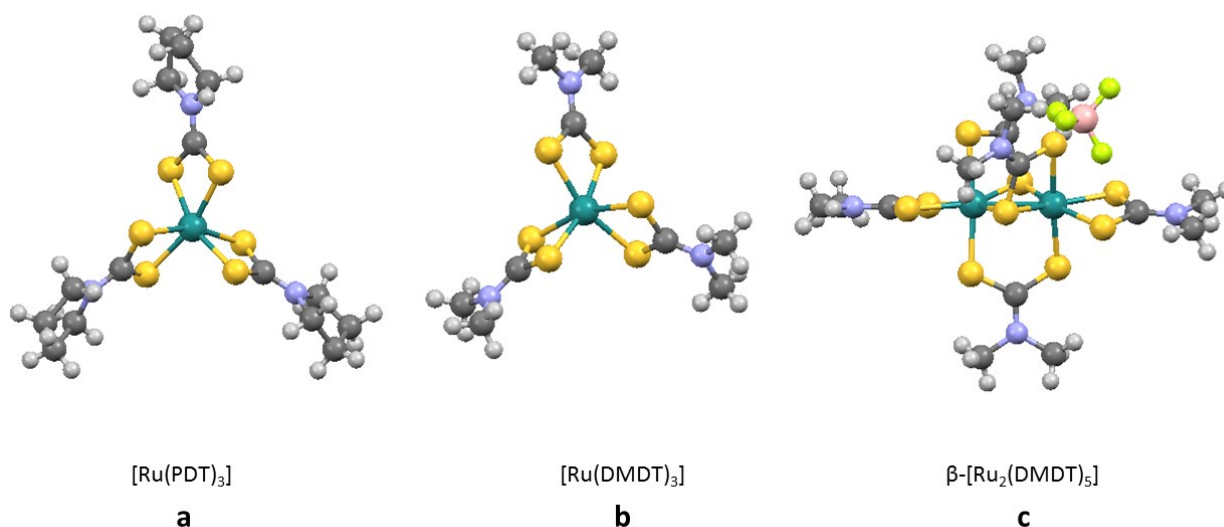


**Figure 5.3** Crystal structures of some Ru(III) dithiocarbamate derivatives which displayed promising *in vitro* antiproliferative activity against a number of human tumor cell lines: tris(pyrrolidinedithiocarbamate)ruthenium(III)  $[\text{Ru}(\text{PDT})_3]$  **a**, tris(dimethyldithiocarbamate)ruthenium(III)  $[\text{Ru}(\text{DMDT})_3]$  **b**, and the dinuclear complex pentakis(dimethyldithiocarbamate)diruthenium(III) tetrafluoroborate  $\beta\text{-}[\text{Ru}_2(\text{DMDT})_5]\text{BF}_4$  **c**.

When considering heteroleptic Ru(III)-DTC complexes, it is worth mentioning the work of Cameron and collaborators, which developed the Ru(III) triazacyclononane dithiocarbamate  $[\text{Ru}^{\text{III}}(\text{tacn})(\eta^2\text{-DTC})(\eta^1\text{-DTC})]\text{PF}_6$  (tacn= 1,4,7-tri-azacyclononane) [188]. In the reported complexes, the dithiocarbamate ligands are both mono- and bidentate, while the tacn ligand coordinates the Ru(III) center with a facial geometry (**Figure 5.4 a**). The researchers demonstrated the nitric oxide (NO) scavenging properties of this class of compounds,

since NO is able to replace the monodentate DTC, forming an extremely strong Ru-NO bond [189]. These findings are important, as there are many diseases in which the overproduction of NO is implicated, including cancer, where the large amount of nitric oxide seems to promote tumor growth by regulating the blood flow or by acting as a mediator in angiogenesis [190]. Concerning our researches, we reported the synthesis of heteroleptic DTC derivatives of both Ru(III) and Ru(II) [187, 191]. In the first case, the dithiocarbamate ligand was methylated to obtain the neutral forms DTCM, with the methylation occurring only at one of the two sulfur atoms. The resulting ligand possesses a less nucleophilic character than the starting DTC salt, so the reaction with the Ru(III) precursor  $\text{Na}[\text{trans-Ru}^{\text{III}}\text{Cl}_4(\text{DMSO})_2]$  in a 1:1 metal-to-ligand stoichiometry yields the neutral paramagnetic complex  $[\text{mer-Ru}^{\text{III}}\text{Cl}_3(\text{DMSO})(\text{DTCM})]$  (DTCM= methylated DMDT and methylated PDT **Figure 5.4 b**) [191]. With respect to the oxidation state +2, although it is overall the most common for dithiocarbamate complexes of ruthenium [116], and Ru(II) derivatives are object of intense studies in the research of new anticancer drugs [192, 193], Ru(II)-DTC complexes of the type  $[\text{Ru}(\text{DTC})_2(\text{DMSO})_2]$  (DTC= DMDT and PDT, **Figure 5.4 c**) described by our research group are the only examples of application in the oncological field [187]. However, both Ru(III) and Ru(II) heteroleptic dithiocarbamate derivatives tested in our laboratories did not afford any result in terms of *in vitro* cytotoxic activity, with  $\text{IC}_{50}$  values being largely higher than those of cisplatin towards the investigated human tumor cell lines [140].

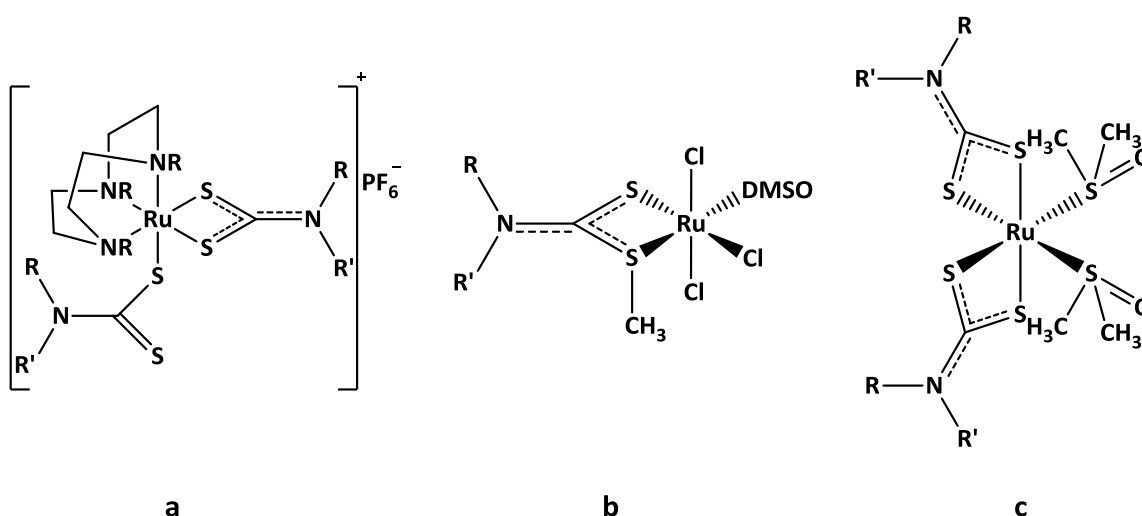


**Figure 5.4** Chemical structures of some heteroleptic ruthenium dithiocarbamate derivatives tested for their potential anticancer activity: the Ru(III) triazacyclononane dithiocarbamate complex  $[\text{fac-Ru}^{\text{III}}(\text{tacn})(\eta^2\text{-DTC})(\eta^1\text{-DTC})]\text{PF}_6$  (tacn= 1,4,7-tri-azacyclononane) **a**, the neutral Ru(III) paramagnetic complex  $[\text{mer-Ru}^{\text{III}}\text{Cl}_3(\text{DMSO})(\text{DTCM})]$  (DTCM= methylated DMDT and methylated PDT) **b**, and the Ru(II) compound of the type  $[\text{Ru}(\text{DTC})_2(\text{DMSO})_2]$  (DTC= DMDT and PDT) **c**.

The previously discussed results, achieved in the last years about the cytotoxic properties of some ruthenium dithiocarbamate complexes, pave the way to some considerations. First of all, the Ru(II)-DTC compounds are not active, hence the abovementioned “activation by reduction” mechanism, already hypothesized for other ruthenium derivatives such as NAMI-A, is not conceivable for Ru-DTC derivatives [140]. Moreover, experimental evidence showed that homoleptic Ru(III) compounds are usually associated with a better

antiproliferative profile than heteroleptic ones. Among them, the ionic dinuclear complexes of the type  $[\text{Ru}_2(\text{DTC})_5]\text{Cl}$  stand out. In this context, it is worth noting that new polynuclear complexes of different metals (*i.e.*, Pt(II), Au(I/III), Os(0)) are also reported in literature and involve novel modes of action [194-196]. They make use of chemical features that are often not accessible with mononuclear complexes, such as improved redox activity by cooperative action of two or more metal centers or steric hindrance associated with rigidity of the polynuclear structure. As an example, some researchers have very recently demonstrated that dinuclear polypyridylruthenium(II) complexes are able to induce cell death *via* a reactive oxygen species (ROS)-mediated pathway, by damaging the cytoplasmic cell membrane [197]. Finally, the *in vitro* biological tests put in evidence that the antiproliferative activity is not only associated with the +3 oxidation state of ruthenium, but it strongly depends on the chemical structure of the dithiocarbamato ligand as well [140]. In this scenario, it appears of particular importance to design and screen for antiproliferative activity, a library of new ruthenium(III)-based agents with varied ligands characterized by different electronic, steric and lipophilic properties, so to evaluate how the ligand affects the cytotoxic potential of the Ru(III) center.

### 5.3 Synthesis of the Ru(III) derivatives of the selected cyclic *N,N*-disubstituted dithiocarbamato ligands

Taking into account the final considerations about ruthenium dithiocarbamates as potential anticancer agents, and considering the different electronic, steric and lipophilic properties of the cyclic dithiocarbamato ligands presented in **Chapter 4**, we designed and obtained a library of Ru(III) mono and dinuclear derivatives. Indeed, the aims of this work were to evaluate how the features of the DTC ligand affect the chemical characteristics of the final complexes, and ultimately the cytotoxic activity of the Ru(III) center. The Ru(III)-PDT complexes have been synthesized and characterized for comparison purposes in light of our previous work.

#### 5.3.1 Synthesis of Ru(III) dithiocarbamato complexes of PDT, PipeDTC, MorphDTC and IndolineDTC

To a solution of  $\text{RuCl}_3 \cdot 3\text{H}_2\text{O}$  (1.5 mmol) in water (4 mL), 10 mL of an aqueous solution of the dithiocarbamato salt (4.5 mmol) were added dropwise. A dark brown solid started to precipitate in few minutes. The mixture was stirred for 1 h at room temperature, afterwards the solid was filtrated and washed with water (3 x 3.0 mL) and diethyl ether (2 x 2.5 mL). The isolated product was dried and re-dissolved in  $\text{CH}_2\text{Cl}_2$  to be purified by silica gel chromatography. A gradient from  $\text{CH}_2\text{Cl}_2$  100% to  $\text{CH}_2\text{Cl}_2/\text{MeOH}$  90%:10% was used to elute first the mononuclear complex and then the dinuclear derivative (as mixture of  $\alpha+\beta$  isomers, **Figure 5.2**). Successively, the mixture of  $\alpha,\beta\text{-}[\text{Ru}_2(\text{PDT})_5]\text{Cl}$  was isomerized to the thermodynamically stable  $\beta\text{-}[\text{Ru}_2(\text{PDT})_5]\text{Cl}$  by reflux in methanol for 8 hours. All the compounds were re-precipitated from  $\text{CH}_2\text{Cl}_2$  - diethyl ether, washed with *n*-pentane, and dried in vacuum pump in the presence of  $\text{P}_2\text{O}_5$ .

*Tris(pyrrolidine dithiocarbamate)ruthenium(III), [Ru(PDT)<sub>3</sub>]*

Aspect: dark green solid

Yield: 31 %

R.f. (on silica gel, CH<sub>2</sub>Cl<sub>2</sub>): 0.85

Anal. Calc. for C<sub>15</sub>H<sub>24</sub>N<sub>3</sub>RuS<sub>6</sub> (MW = 539.83 g·mol<sup>-1</sup>): C 33.37; H 4.48; N 7.78; S 35.64. Found: C 33.50; H 4.49; N 7.72; S 35.51.

<sup>1</sup>H-NMR (CDCl<sub>3</sub>, 300.13 MHz): δ (ppm) = 0.39 (s, 12H, H<sub>(3)</sub> + H<sub>(4)</sub>), 35.83 (s br, 6H, H<sub>(2)</sub> + H<sub>(5)</sub>), 44.29 (s br, 6H, H<sub>(2)</sub> + H<sub>(5)</sub>).

Medium FT-IR (KBr):  $\tilde{\nu}$  (cm<sup>-1</sup>) = 2945.32, 2865.58 (v<sub>a</sub>, C-H); 1487.12, 1469.76, 1444.15 (v<sub>a</sub>, N-CSS); 942.18 (v<sub>a</sub>, CSS).

Far FT-IR (nujol):  $\tilde{\nu}$  (cm<sup>-1</sup>) = 565.37 (v<sub>s</sub>, CSS); 447.75 (v<sub>a</sub>, Ru-S); 318.90 (v<sub>s</sub>, Ru-S).

ESI-MS *m/z*, [M<sup>+</sup>] found (calc.): 539.96 (539.93).

*β-pentakis(pyrrolidine dithiocarbamate)diruthenium(III) chloride, β-[Ru<sub>2</sub>(PDT)<sub>5</sub>]Cl*

Aspect: dark red solid

Yield: 32 %

R.f. (on silica gel, CH<sub>2</sub>Cl<sub>2</sub>/MeOH 92:8): 0.23

Anal. Calc. for C<sub>25</sub>H<sub>40</sub>ClN<sub>5</sub>Ru<sub>2</sub>S<sub>10</sub> (MW = 968.86 g·mol<sup>-1</sup>): C 30.99; H 4.16; N 7.23; S 33.10. Found: C 31.12; H 4.26; N 7.39; S 33.30.

<sup>1</sup>H-NMR (CDCl<sub>3</sub>, 300.13 MHz): δ (ppm) = 1.81-2.19 (m, 20H, H<sub>(3)</sub> + H<sub>(4)</sub>), 3.46-3.94 (m, 20H, H<sub>(2)</sub> + H<sub>(5)</sub>).

Medium FT-IR (KBr):  $\tilde{\nu}$  (cm<sup>-1</sup>) = 2947.10, 2667.69 (v<sub>a</sub>, C-H); 1505.71, 1473.13, 1447.94 (v<sub>a</sub>, N-CSS); 946.59 (v<sub>a</sub>, CSS).

Far FT-IR (nujol):  $\tilde{\nu}$  (cm<sup>-1</sup>) = 563.86 (v<sub>s</sub>, CSS); 445.81 (v<sub>a</sub>, Ru-S); 347.83 (v<sub>s</sub>, Ru-S).

ESI-MS *m/z*, [M-Cl<sup>+</sup>] found (calc.): 932.87 (932.86).

*Tris(piperidine dithiocarbamate)ruthenium(III), [Ru(PipeDTC)<sub>3</sub>]*

Aspect: dark green solid

Yield: 34 %

R.f. (on silica gel, CH<sub>2</sub>Cl<sub>2</sub>): 0.80

Anal. Calc. for C<sub>18</sub>H<sub>30</sub>N<sub>3</sub>RuS<sub>6</sub> (MW = 581.91 g·mol<sup>-1</sup>): C 37.15; H 5.20; N 7.22; S 33.06. Found: C 37.21; H 5.29; N 7.25; S 33.22.

<sup>1</sup>H-NMR (CDCl<sub>3</sub>, 300.13 MHz): δ (ppm) = 0.87 (s, 12H, H<sub>(3)</sub> + H<sub>(5)</sub>), 3.54 (s, 6H, H<sub>(4)</sub>), 24.03 (s br, 12H, H<sub>(2)</sub> + H<sub>(6)</sub>).

Medium FT-IR (KBr):  $\tilde{\nu}$  (cm<sup>-1</sup>) = 2936.08, 2850.82 (v<sub>a</sub>, C-H); 1487.83, 1455.07, 1439.06 (v<sub>a</sub>, N-CSS); 1001.97 (v<sub>a</sub>, CSS).

Far FT-IR (nujol):  $\tilde{\nu}$  (cm<sup>-1</sup>) = 538.14 (v<sub>s</sub>, CSS); 405.74 (v<sub>a</sub>, Ru-S); 330.99 (v<sub>s</sub>, Ru-S).

ESI-MS  $m/z$ , [M<sup>+</sup>] found (calc.): 581.98 (581.98).

*β-pentakis(piperidine dithiocarbamate)diruthenium(III) chloride, β-[Ru<sub>2</sub>(PipeDTC)<sub>5</sub>]Cl*

Aspect: brown solid

Yield: 29 %

R.f. (on silica gel, CH<sub>2</sub>Cl<sub>2</sub>/MeOH 9:1): 0.39

Anal. Calc. for C<sub>30</sub>H<sub>50</sub>ClN<sub>5</sub>Ru<sub>2</sub>S<sub>10</sub> (MW = 1039.00 g·mol<sup>-1</sup>): C 34.68; H 4.85; N 6.74; S 30.86. Found: C 34.58; H 4.80; N 6.81; S 30.88.

<sup>1</sup>H-NMR (CDCl<sub>3</sub>, 300.13 MHz): δ (ppm) = 1.50 (m, 10H, H<sub>(4)</sub>), 1.83 (m, 20H, H<sub>(3)</sub> + H<sub>(5)</sub>), 3.03-4.65 (m, 20H, H<sub>(2)</sub> + H<sub>(6)</sub>).

Medium FT-IR (KBr):  $\tilde{\nu}$  (cm<sup>-1</sup>) = 2933.43 (v<sub>a</sub>, C-H); 1503.23, 1441.03 (v<sub>a</sub>, N-CSS); 1001.63 (v<sub>a</sub>, CSS).

Far FT-IR (nujol):  $\tilde{\nu}$  (cm<sup>-1</sup>) = 544.23 (v<sub>s</sub>, CSS); 406.62 (v<sub>a</sub>, Ru-S); 321.88 (v<sub>s</sub>, Ru-S).

ESI-MS  $m/z$ , [M-Cl<sup>+</sup>] found (calc.): 1003.93 (1003.94).

*Tris(morpholine dithiocarbamate)ruthenium(III), [Ru(MorphDTC)<sub>3</sub>]*

Aspect: dark green solid

Yield: 33 %

R.f. (on silica gel, CH<sub>2</sub>Cl<sub>2</sub>/MeOH 98:2): 0.83

Anal. Calc. for C<sub>15</sub>H<sub>24</sub>N<sub>3</sub>O<sub>3</sub>RuS<sub>6</sub> (MW = 587.83 g·mol<sup>-1</sup>): C 30.65; H 4.12; N 7.15; S 32.73. Found: C 30.62; H 4.15; N 7.19; S 32.56.

<sup>1</sup>H-NMR (CDCl<sub>3</sub>, 300.13 MHz): δ (ppm) = 3.15 (s, 12H, H<sub>(2)</sub> + H<sub>(6)</sub>), 24.90 (s br, 12H, H<sub>(3)</sub> + H<sub>(5)</sub>).

Medium FT-IR (KBr):  $\tilde{\nu}$  (cm<sup>-1</sup>) = 2859.46 (v<sub>a</sub>, C-H); 1486.03, 1430.57 (v<sub>a</sub>, N-CSS); 1111.74 (v<sub>a</sub>, C-O); 994.13 (v<sub>a</sub>, CSS).

Far FT-IR (nujol):  $\tilde{\nu}$  (cm<sup>-1</sup>) = 541.55 (v<sub>s</sub>, CSS); 412.70 (v<sub>a</sub>, Ru-S); 324.59 (v<sub>s</sub>, Ru-S).

ESI-MS  $m/z$ , [M<sup>+</sup>] found (calc.): 587.92 (587.92).

*β-pentakis(morpholine dithiocarbamate)diruthenium(III) chloride, β-[Ru<sub>2</sub>(MorphDTC)<sub>5</sub>]Cl*

Aspect: brick red solid

Yield: 32 %

R.f. (on silica gel, CH<sub>2</sub>Cl<sub>2</sub>/MeOH 9:1): 0.30

Anal. Calc. for  $C_{30}H_{50}ClN_5O_5Ru_2S_{10}$  (MW = 1048.86 g·mol<sup>-1</sup>): C 28.63; H 3.84; N 6.68; S 30.57. Found: C 28.49; H 3.90; N 6.72; S 30.63.

<sup>1</sup>H-NMR (CDCl<sub>3</sub>, 300.13 MHz): δ (ppm) = 3.25-4.65 (m, 40H, H<sub>(2)</sub> + H<sub>(3)</sub> + H<sub>(5)</sub> + H<sub>(6)</sub>).

Medium FT-IR (KBr):  $\tilde{\nu}$  (cm<sup>-1</sup>) = 2846.95 (v<sub>a</sub>, C-H); 1503.25, 1435.18 (v<sub>a</sub>, N-CSS); 1106.81 (v<sub>a</sub>, C-O); 993.99 (v<sub>a</sub>, CSS).

Far FT-IR (nujol):  $\tilde{\nu}$  (cm<sup>-1</sup>) = 546.95 (v<sub>s</sub>, CSS); 413.98 (v<sub>a</sub>, Ru-S); 310.23 (v<sub>s</sub>, Ru-S).

ESI-MS *m/z*, [M-Cl<sup>+</sup>] found (calc.): 1013.86 (1013.83).

*Tris(indoline dithiocarbamate)ruthenium(III), [Ru(IndolineDTC)<sub>3</sub>]*

Aspect: dark green solid

Yield: 27 %

R.f. (on silica gel, CH<sub>2</sub>Cl<sub>2</sub>): 0.92

Anal. Calc. for  $C_{27}H_{24}N_3RuS_6$  (MW = 683.96 g·mol<sup>-1</sup>): C 47.41; H 3.54; N 6.14; S 28.13. Found: C 47.58; H 3.56; N 6.15; S 28.24.

<sup>1</sup>H-NMR (CD<sub>2</sub>Cl<sub>2</sub>, 300.13 MHz): δ (ppm) = 0.16 (m, 6H, H<sub>(3)</sub>), 7.27 (m, 3H, H<sub>(5)</sub>), 8.67 (s, 3H, H<sub>(4)</sub>), 8.95 (s, 3H, H<sub>(6)</sub>), 35.92 (s br, 3H, H<sub>(2)</sub>), 45.63 (s br, 3H, H<sub>(2)</sub>).

Medium FT-IR (KBr):  $\tilde{\nu}$  (cm<sup>-1</sup>) = 2842.06 (v<sub>a</sub>, C-H); 1475.67 (v, C=C ring); 1387.37, 1347.88, 1322.11 (v<sub>a</sub>, N-CSS); 947.54 (v<sub>a</sub>, CSS); 750.41 (δ, C-H).

Far FT-IR (nujol):  $\tilde{\nu}$  (cm<sup>-1</sup>) = 546.68 (v<sub>s</sub>, CSS); 424.20 (v<sub>a</sub>, Ru-S); 333.12 (v<sub>s</sub>, Ru-S).

ESI-MS *m/z*, [M<sup>+</sup>] found (calc.): 683.95 (683.93).

*β-pentakis(indoline dithiocarbamate)diruthenium(III) chloride, β-[Ru<sub>2</sub>(IndolineDTC)<sub>5</sub>]Cl*

Aspect: brown solid

Yield: 25 %

R.f. (on silica gel, CH<sub>2</sub>Cl<sub>2</sub>/MeOH 95:5): 0.40

Anal. Calc. for  $C_{30}H_{50}ClN_5Ru_2S_{10}$  (MW = 1209.08 g·mol<sup>-1</sup>): C 44.70; H 3.33; N 5.79; S 26.52. Found: C 44.74; H 3.38; N 6.01; S 26.47.

<sup>1</sup>H-NMR (CD<sub>2</sub>Cl<sub>2</sub>, 300.13 MHz): δ (ppm) = 3.22-4.88 (m, 20H, H<sub>(2)</sub> + H<sub>(3)</sub>), 7.35-8.87 (m, 20H, H<sub>(4)</sub> + H<sub>(5)</sub> + H<sub>(6)</sub> + H<sub>(7)</sub>).

Medium FT-IR (KBr):  $\tilde{\nu}$  (cm<sup>-1</sup>) = 2850.49 (v<sub>a</sub>, C-H); 1484.25 (v, C=C ring); 1431.19, 1323.61 (v<sub>a</sub>, N-CSS); 952.20 (v<sub>a</sub>, CSS); 750.98 (δ, C-H).

Far FT-IR (nujol):  $\tilde{\nu}$  (cm<sup>-1</sup>) = 558.76 (v<sub>s</sub>, CSS); 421.19 (v<sub>a</sub>, Ru-S); 323.76 (v<sub>s</sub>, Ru-S).

ESI-MS *m/z*, [M-Cl<sup>+</sup>] found (calc.): 1173.88 (1173.86).

### 5.3.2 Synthesis of Ru(III) dithiocarbamate complexes of L-proline ester derivatives (ProOMeDTC and ProOtBuDTC)

To a solution of  $\text{RuCl}_3 \cdot 3\text{H}_2\text{O}$  (1.5 mmol) in water (4 mL), 10 mL of an aqueous solution of the sodium salt of L-proline ester dithiocarbamate (4.5 mmol) were added dropwise. A dark brown solid quickly precipitated but the mixture was stirred for 1 h at room temperature. Then, the solid was filtrated and washed with water (3 x 3 mL) and *n*-hexane (3 x 5 mL). The isolated product was dried and re-dissolved in  $\text{CH}_2\text{Cl}_2$  to be purified by silica gel chromatography (gradient from  $\text{CH}_2\text{Cl}_2$  100% to  $\text{CH}_2\text{Cl}_2/\text{MeOH}$  90%:10%, to elute first the mononuclear complex and then the dinuclear derivative). The dinuclear derivative is obtained as a mixture of  $\alpha+\beta$  isomers, then put at reflux in methanol for 8 hours to isolate the thermodynamically stable  $\beta$ - $[\text{Ru}_2(\text{PDT})_5]\text{Cl}$ . All the compounds were re-precipitated from ethyl acetate-hexane, washed with *n*-pentane, and dried *in vacuo* over  $\text{P}_2\text{O}_5$ .

#### *Tris(L-proline methyl ester dithiocarbamate)ruthenium(III), [Ru(ProOMeDTC)<sub>3</sub>]*

Aspect: dark green solid

Yield: 34 %

R.f. (on silica gel,  $\text{CH}_2\text{Cl}_2$ ): 0.50

Anal. Calc. for  $\text{C}_{21}\text{H}_{30}\text{N}_3\text{O}_3\text{RuS}_6$  (MW = 713.94  $\text{g}\cdot\text{mol}^{-1}$ ): C 35.33; H 4.24; N 5.89; S 26.95. Found: C 35.31; H 4.28; N 5.95; S 26.83.

$^1\text{H-NMR}$  ( $\text{CDCl}_3$ , 300.13 MHz):  $\delta$  (ppm) = 0.47-2.27 (m, 12H,  $\text{H}_{(3)} + \text{H}_{(4)}$ ), 3.07 (m, 9H, O- $\text{CH}_3$ ), 23.55-28.34 (4s br, 3H,  $\text{H}_{(5)}$ ), 31.41-34.64 (3s br, 3H,  $\text{H}_{(5)}$ ), 38.65-46.27 (4s br, 3H,  $\text{H}_{(2)}$ ).

Medium FT-IR (KBr):  $\tilde{\nu}$  ( $\text{cm}^{-1}$ ) = 2949.05 ( $\nu_a$ , C-H); 1742.31 ( $\nu$ , C=O); 1439.74 ( $\nu_a$ , N-CSS); 1169.25 ( $\nu_a$ , C-OMe); 942.14 ( $\nu_a$ , CSS).

Far FT-IR (nujol):  $\tilde{\nu}$  ( $\text{cm}^{-1}$ ) = 546.88 ( $\nu_s$ , CSS); 453.06 ( $\nu_a$ , Ru-S); 323.86 ( $\nu_s$ , Ru-S).

ESI-MS  $m/z$ ,  $[\text{M}^+]$  found (calc.): 713.97 (713.95).

#### $\beta$ -pentakis(L-proline methyl ester dithiocarbamate)diruthenium(III) chloride, $\beta$ - $[\text{Ru}_2(\text{ProOMeDTC})_5]\text{Cl}$

Aspect: dark red solid

Yield: 37 %

R.f. (on silica gel,  $\text{CH}_2\text{Cl}_2/\text{MeOH}$  94:6): 0.40

Anal. Calc. for  $\text{C}_{30}\text{H}_{50}\text{ClN}_5\text{Ru}_2\text{S}_{10}$  (MW = 1259.04  $\text{g}\cdot\text{mol}^{-1}$ ): C 33.39; H 4.00; N 5.56; S 25.47. Found: C 33.46; H 4.04; N 5.59; S 25.40.

$^1\text{H-NMR}$  ( $\text{CDCl}_3$ , 300.13 MHz):  $\delta$  (ppm) = 2.20 (m, 20H,  $\text{H}_{(3)} + \text{H}_{(4)}$ ), 3.28-3.98 (m, 25H,  $\text{H}_{(5)} + \text{O-CH}_3$ ), 5.02-5.38 (m, 5H,  $\text{H}_{(2)}$ ).

Medium FT-IR (KBr):  $\tilde{\nu}$  ( $\text{cm}^{-1}$ ) = 2950.23 ( $\nu_a$ , C-H); 1741.36 ( $\nu$ , C=O); 1480.37, 1447.83 ( $\nu_a$ , N-CSS); 1170.04 ( $\nu_a$ , C-OMe); 944.45 ( $\nu_a$ , CSS).

Far FT-IR (nujol):  $\tilde{\nu}$  ( $\text{cm}^{-1}$ ) = 546.95 ( $\nu_s$ , CSS); 461.98 ( $\nu_a$ , Ru-S); 335.16 ( $\nu_s$ , Ru-S).

ESI-MS  $m/z$ ,  $[M-Cl]^+$  found (calc.): 1223.92 (1223.89).

*Tris(L-proline tert-butyl ester dithiocarbamate)ruthenium(III), [Ru(ProOtBuDTC)<sub>3</sub>]*

Aspect: dark green solid

Yield: 29 %

R.f. (on silica gel, CH<sub>2</sub>Cl<sub>2</sub>): 0.70

Anal. Calc. for C<sub>30</sub>H<sub>48</sub>N<sub>3</sub>O<sub>3</sub>RuS<sub>6</sub> (MW = 840.18 g·mol<sup>-1</sup>): C 42.89; H 5.76; N 5.00; S 22.90. Found: C 42.83; H 5.72; N 5.17; S 22.99.

<sup>1</sup>H-NMR (CDCl<sub>3</sub>, 300.13 MHz): δ (ppm) = 0.50-2.27 (m, 39H, H<sub>(3)</sub> + H<sub>(4)</sub> + O-C(CH<sub>3</sub>)<sub>3</sub>), 23.65-26.70 (4s, 3H, H<sub>(5)</sub>), 30.00-33.38 (4s, 3H, H<sub>(5)</sub>), 40.07-44.47 (4s, 3H, H<sub>(2)</sub>).

Medium FT-IR (KBr):  $\tilde{\nu}$  (cm<sup>-1</sup>) = 2975.22, 2872.34 (ν<sub>a</sub>, C-H); 1736.11 (ν, C=O); 1440.10 (ν<sub>a</sub>, N-CSS); 1148.66 (ν<sub>a</sub>, C-OtBu); 933.50 (ν<sub>a</sub>, CSS).

Far FT-IR (nujol):  $\tilde{\nu}$  (cm<sup>-1</sup>) = 547.60 (ν<sub>s</sub>, CSS); 470.56 (ν<sub>a</sub>, Ru-S); 320.98 (ν<sub>s</sub>, Ru-S).

ESI-MS  $m/z$ ,  $[M]^+$  found (calc.): 840.12 (840.09).

*β-pentakis(L-proline tert-butyl ester dithiocarbamate)diruthenium(III) chloride, β-[Ru<sub>2</sub>(ProOtBuDTC)<sub>5</sub>]Cl*

Aspect: dark red solid

Yield: 32 %

R.f. (on silica gel, CH<sub>2</sub>Cl<sub>2</sub>/MeOH 94:6): 0.52

Anal. Calc. for C<sub>50</sub>H<sub>80</sub>ClN<sub>5</sub>O<sub>10</sub>Ru<sub>2</sub>S<sub>10</sub> (MW = 1469.64 g·mol<sup>-1</sup>): C 40.87; H 5.49; N 4.77; S 21.82. Found: C 40.80; H 5.39; N 4.60; S 21.88.

<sup>1</sup>H-NMR (CDCl<sub>3</sub>, 300.13 MHz): δ (ppm) = 1.41-2.26 (m, 65H, H<sub>(3)</sub> + H<sub>(4)</sub> + O-C(CH<sub>3</sub>)<sub>3</sub>), 3.21-4.02 (m, 10H, H<sub>(5)</sub>), 4.36-5.30 (m, 5H, H<sub>(2)</sub>).

Medium FT-IR (KBr):  $\tilde{\nu}$  (cm<sup>-1</sup>) = 2975.16 (ν<sub>a</sub>, C-H); 1735.39 (ν, C=O); 1481.10, 1450.06 (ν<sub>a</sub>, N-CSS); 1148.87 (ν<sub>a</sub>, C-OtBu); 935.12 (ν<sub>a</sub>, CSS).

Far FT-IR (nujol):  $\tilde{\nu}$  (cm<sup>-1</sup>) = 551.30 (ν<sub>s</sub>, CSS); 471.19 (ν<sub>a</sub>, Ru-S); 325.69 (ν<sub>s</sub>, Ru-S).

ESI-MS  $m/z$ ,  $[M-Cl]^+$  found (calc.): 1434.16 (1434.12).

### 5.3.3 Synthesis of Ru(III) dithiocarbamate complexes of CDT

The synthesis was carried out in a Schlenk-line apparatus under N<sub>2</sub> atmosphere. Briefly, 2.7 mmol of synthesized carbazole dithiocarbamate Na(CDT) and 0.9 mmol of RuCl<sub>3</sub>·3H<sub>2</sub>O were dissolved in 18 mL of anhydrous tetrahydrofuran (THF). The mixture was left under stirring for 15 h at room temperature. The solvent was subsequently removed under reduced pressure leaving a black solid that was washed with cold pentane (5 x 5.0 mL). The dinuclear complex [Ru<sub>2</sub>(CDT)<sub>5</sub>]Cl (as a mixture of α+β isomers) was isolated by several precipitation cycles in THF/pentane mixture (room temperature), and then refluxed in CH<sub>2</sub>Cl<sub>2</sub> for 8



hours to obtain the isomer  $\beta$ -[Ru<sub>2</sub>(CDT)<sub>5</sub>]Cl. On the other hand, the THF/pentane solution was concentrated up to obtain a dark green solid that was dried under vacuum and purified by silica gel chromatography using CH<sub>2</sub>Cl<sub>2</sub>/*n*-hexane 40%:60% to elute the mononuclear complex. All the complexes have been re-precipitated in CH<sub>2</sub>Cl<sub>2</sub>- *n*-hexane, washed with *n*-pentane and dried *in vacuo* over P<sub>2</sub>O<sub>5</sub>.

*Tris(carbazole dithiocarbamate)ruthenium(III), [Ru(CDT)<sub>3</sub>]*

Aspect: dark green solid

Yield: 20 %

R.f. (on silica gel, CH<sub>2</sub>Cl<sub>2</sub>/hexane 1:1): 0.88

Anal. Calc. for C<sub>39</sub>H<sub>24</sub>N<sub>3</sub>RuS<sub>6</sub> (MW = 828.09 g·mol<sup>-1</sup>): C 56.57; H 2.92; N 5.07; S 23.23. Found: C 56.59; H 2.96; N 5.21; S 23.20.

<sup>1</sup>H-NMR (CDCl<sub>3</sub>, 300.13 MHz):  $\delta$  (ppm) = 7.71-7.73 (d, 6H, H<sub>(4)</sub> + H<sub>(5)</sub>), 8.90 (t, 6H, H<sub>(3)</sub> + H<sub>(6)</sub>), 9.01-9.03 (d, 6H, H<sub>(2)</sub> + H<sub>(7)</sub>).

Medium FT-IR (KBr):  $\tilde{\nu}$  (cm<sup>-1</sup>) = 2953.17 (v<sub>a</sub>, C-H); 1484.71, 1435.79 (v, C=C ring); 1363.04, 1324.09, 1294.58 (v<sub>a</sub>, N-CSS); 1035.97 (v<sub>a</sub>, CSS); 847.98 ( $\omega$ , C-H); 745.87 ( $\delta$ , C-H).

Far FT-IR (nujol):  $\tilde{\nu}$  (cm<sup>-1</sup>) = 586.98 (v<sub>s</sub>, CSS); 459.76 (v<sub>a</sub>, Ru-S); 413.25 (v<sub>s</sub>, Ru-S).

ESI-MS *m/z*, [M<sup>+</sup>] found (calc.): 827.97 (827.94).

*$\beta$ -pentakis(carbazole dithiocarbamate)diruthenium(III) chloride,  $\beta$ -[Ru<sub>2</sub>(CDT)<sub>5</sub>]Cl*

Aspect: brown solid

Yield: 22 %

R.f. (on silica gel, CH<sub>2</sub>Cl<sub>2</sub>/hexane 1:1): 0.60

Anal. Calc. for C<sub>65</sub>H<sub>40</sub>ClN<sub>5</sub>Ru<sub>2</sub>S<sub>10</sub> (MW = 1449.29 g·mol<sup>-1</sup>): C 53.87; H 2.78; N 4.83; S 22.12. Found: C 53.94; H 2.91; N 4.92; S 22.18.

<sup>1</sup>H-NMR (CDCl<sub>3</sub>, 300.13 MHz):  $\delta$  (ppm) = 7.46-7.53 (m, 20H, H<sub>(2)</sub> + H<sub>(3)</sub> + H<sub>(6)</sub> + H<sub>(7)</sub>), 7.98-8.00 (d, 10H, H<sub>(4)</sub> + H<sub>(5)</sub>), 9.17-9.19 (d, 10H, H<sub>(1)</sub> + H<sub>(8)</sub>).

Medium FT-IR (KBr):  $\tilde{\nu}$  (cm<sup>-1</sup>) = 3056.37 (v<sub>a</sub>, C-H); 1485.29, 1436.67 (v, C=C ring); 1364.09, 1325.58, 1299.44 (v<sub>a</sub>, N-CSS); 1038.43 (v<sub>a</sub>, CSS); 851.92 ( $\omega$ , C-H); 744.39 ( $\delta$ , C-H).

Far FT-IR (nujol):  $\tilde{\nu}$  (cm<sup>-1</sup>) = 586.98 (v<sub>s</sub>, CSS); 466.20 (v<sub>a</sub>, Ru-S); 415.14 (v<sub>s</sub>, Ru-S).

ESI-MS *m/z*, [M-Cl<sup>+</sup>] found (calc.): 1490.89 (1490.87).

## 5.4 Discussion

### 5.4.1 Considerations on the synthetic routes

To optimize the synthesis of homoleptic Ru(III) dithiocarbamato compounds, several media (*e.g.*, MeOH, EtOH, toluene, water) as well as different Ru(III) precursors (*e.g.*, Na[*trans*-Ru<sup>III</sup>Cl<sub>4</sub>(DMSO)<sub>2</sub>]) or different Ru(III)/DTC molar ratios were investigated but in any case a mixture of mono- and dinuclear derivatives was obtained [140]. Comparing all these synthetic routes, no one leads to pure dinuclear derivatives or an enriched mixture thereof, as these derivatives are the most promising from the biological point of view (see **Section 5.2** and **9.3**). For all the performed syntheses, we observed also the formation of the disulfide byproduct (DTC)<sub>2</sub>, and consequently an accurate purification was necessary (**Figure 5.5 a**).

As reported in **Section 5.3**, in general 3 equivalents of chelating dithiocarbamato ligand totally can replace the chlorido ligands of the starting material RuCl<sub>3</sub>, resulting in a mixture of the neutral mononuclear [Ru(DTC)<sub>3</sub>], and the ionic dinuclear [Ru<sub>2</sub>(PDT)<sub>5</sub>]Cl, both as  $\alpha$  and  $\beta$  isomer.

In light of the previous biological data (**Section 5.2**) [140], we mainly addressed our attention to the dinuclear derivatives. Thus, in order to increase their yields, the RuCl<sub>3</sub> precursor was preferred owing to its polymeric nature, which favors a bridging coordination of the DTC ligand between two metal centers.

Concerning the  $\alpha$ -to- $\beta$  conversion of [Ru<sub>2</sub>(DTC)<sub>5</sub>]Cl isomers, methanol was usually a suitable solvent, but also dichloromethane and chloroform lead to the same results. According to Hendriksen, the thermal conversion to the most thermodynamically stable  $\beta$ -[Ru<sub>2</sub>(DTC)<sub>5</sub>]Cl is achieved by the breaking of the strongest Ru-S bond (bridge), followed by rearrangement [199].

At the best of our knowledge, except for the Ru(III)-PDT derivatives and [Ru(MorphDTC)<sub>3</sub>] whose crystal structure was solved by Raston [200], this is the first library of homoleptic Ru(III) compounds with the selected cyclic dithiocarbamato ligands. Indeed, Preti and coworkers reported in 1979 the synthesis of some ruthenium derivatives of morpholine and piperidine, but they stated to obtain only Ru-DTC complexes with a metal-to-ligand stoichiometry 1:1 and 1:2 [201].

To date, we obtained and well characterized by means of different techniques the mono and dinuclear Ru(III) complexes of PDT, PipeDTC, MorphDTC, IndolineDTC, ProOMeDTC, ProOtBuDTC, and CDT. Conversely, the IndDTC and PyrrDTC derivatives have not been isolated because of the presence of a large amount of by-products, not easily removable. It is possible to hypothesize that these aromatic ligands are not stable in the reaction environment in presence of RuCl<sub>3</sub>, leading to some side-reactions. The crystal structure recently solved for an unexpected species from the mother liquor of the reaction between RuCl<sub>3</sub> and Na IndDTC may account for this (**Figure 5.5 a**).

In addition, the carried out reactions occur in low yields because of the side reaction of Ru(III) ion with *O*-donor ligands (*i.e.* H<sub>2</sub>O), leading to the formation of [Ru(H<sub>2</sub>O)<sub>6</sub>]<sup>3+</sup>, [Ru(H<sub>2</sub>O)<sub>5</sub>Cl]<sup>2+</sup>, [Ru(H<sub>2</sub>O)<sub>5</sub>OH]<sup>2+</sup> and [Ru(H<sub>2</sub>O)<sub>4</sub>(OH)<sub>2</sub>]<sup>+</sup> species. These possess a strong tendency to oligomerize and, successively, to form an inert brown-orange precipitate, thus removing metal ions from the reaction environment [198].

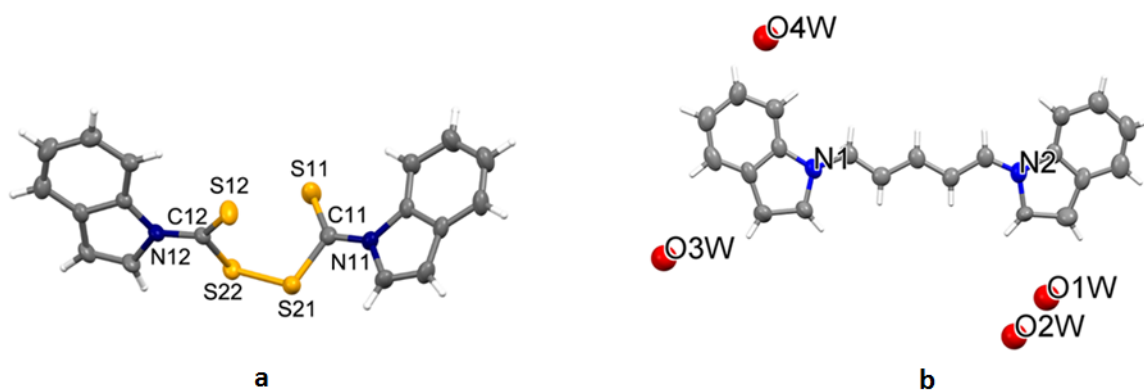


**Figure 5.5** Crystal structures of two by-products from the reaction between  $\text{RuCl}_3 \cdot 3\text{H}_2\text{O}$  and IndDTC sodium salt in THF: the ligand dimer  $(\text{IndDTC})_2$  **a** and an unforeseen species, likely formed *via* a catalytic process promoted by Ru(III) centers **b**.

#### 5.4.2 ESI-MS analysis

As an example, the **Figure 5.6** shows two expanded views of the ESI-MS spectra (positive ion mode) collected for solution samples of the purified compounds  $\text{Ru}(\text{MorphDTC})_3$  (**left**) and  $[\text{Ru}_2(\text{MorphDTC})_5]\text{Cl}$  (**right**) in methanol, and their simulations (below). The spectrum for the mononuclear complex showed a molecular ion  $[\text{M}]^+$  at 587.92  $m/z$  (calc. = 587.92), whereas for the dinuclear one a pattern was detected at 1013.86  $m/z$  and ascribed to the cation of the complex,  $[\text{M}-\text{Cl}]^+$  (calc. = 1013.93). These two examples highlight the general behavior observed in ESI-MS analysis of all the synthesized Ru(III)-DTC derivatives. In fact, for mononuclear complexes, the presence of a  $\text{M}^+$  signal is observed, consistent with the oxidation of the Ru(III) center to Ru(IV), and the pattern of the peaks reflects the wide ruthenium isotopic range. On the other hand, due to their ionic nature the dinuclear compounds generate a MS signal as such. All the attributions have been confirmed by simulations of the spectra, which totally match the experimental data.

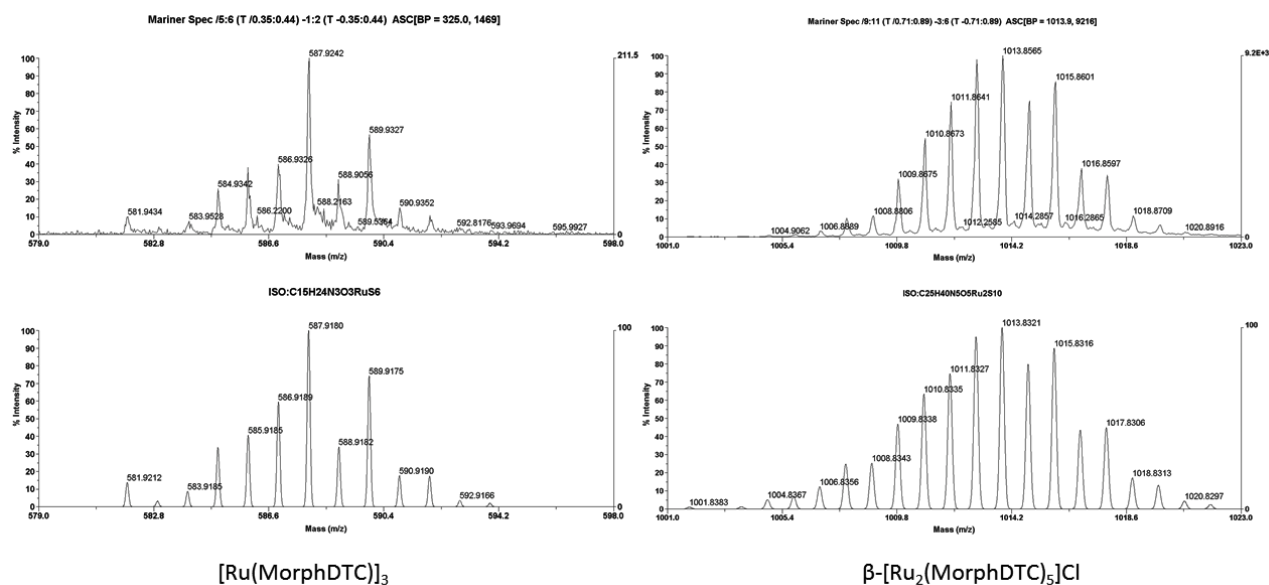


**Figure 5.6** ESI-MS spectra (positive ion mode) of  $[\text{Ru}(\text{MorphDTC})_3]$  (**left**) and  $\beta\text{-}[\text{Ru}_2(\text{MorphDTC})_5]\text{Cl}$  (**right**) in methanol. For the mononuclear complex the experimental spectrum (top) is perfectly simulated by the signals of the species  $[\text{Ru}^{\text{IV}}(\text{MorphDTC})_3]^+$  (down). A similar match was found when simulating the spectrum of the dinuclear ionic complex  $[\text{Ru}_2(\text{MorphDTC})_5]^+$ .

The behavior exhibited by the Ru(III)-MorphDTC compounds was found for all the other ruthenium dithiocarbamate products synthesized in this work.

### 5.4.3 $^1\text{H}$ -NMR characterization

All the synthesized ruthenium-dithiocarbamate derivatives have been characterized by means of  $^1\text{H}$ -NMR spectroscopy (300.13 MHz, 298 K, see **Supporting Information B**). The assignments were carried out by comparing the spectra of the obtained complexes with those of the ligands (see **Section 4.4.2**), taking into account the paramagnetic nature of the Ru(III) metal center, and the summary is reported in **Table 5.1**.

The  $^1\text{H}$ -NMR spectrum of  $[\text{Ru}(\text{DTC})_3]$  complexes confirms the coordination of dithiocarbamate ligands to the Ru(III) ion that significantly broadens and downfield shifts the  $\alpha\text{-CH}$  signals (bold-labeled in **Table 5.1**). The paramagnetic nature of the metal ion drastically reduces the relaxation time and affects the resonance of the proximal protons ( $\alpha$  protons, with respect to the nitrogen atom). Indeed, such an effect is the consequence of the coupling of the magnetic moment of the unpaired electron with that of the observed nuclei. In particular, the observed shift of a nucleus  $I$  can be formalized as:

$$\delta_I = \delta_o + \delta_{FC} + \delta_{PC}$$

where the term  $\delta_o$  is associated with the shielding of diamagnetic contributes,  $\delta_{FC}$  derives from the Fermi contact (which takes into account the coupling between nucleus and electron spins), and  $\delta_{PC}$  (*i.e.*, pseudo-contact component) accounts for the dipolar interaction between the static magnetic moment arising from the unpaired electron spin and the magnetic moment of the nuclear spin. The last term is appreciable only within a few angstrom distance where the unpaired spin density resides, since it is proportional to the anisotropy of the magnetic susceptibility tensor  $\chi$ . Hence, this accounts for the small spatial effect of the Ru(III) center, limited to the case of  $\alpha\text{-CH}$  signals [202].

	$H_{(1)}$	$H_{(2)}$	$H_{(3)}$	$H_{(4)}$	$H_{(5)}$	$H_{(6)}$	$H_{(7)}$	$H_{(8)}$	$H_{(8)}$	OMe	OtBu
[Ru(PDT) <sub>3</sub> ]	<i>n.d.</i>	<b>35.83,</b> <b>44.29</b>	0.39	0.39	<b>35.83,</b> <b>44.29</b>	-	-	-	-	-	-
β[Ru <sub>2</sub> (PDT) <sub>5</sub> ]Cl	<i>n.d.</i>	<b>3.46-</b> <b>3.94</b>	1.81-	1.81-	<b>3.46-</b> <b>3.94</b>	-	-	-	-	-	-
[Ru(PipeDTC) <sub>3</sub> ]	<i>n.d.</i>	<b>24.03</b>	0.87	3.54	0.87	<b>24.03</b>	-	-	-	-	-
β[Ru <sub>2</sub> (PipeDTC) <sub>5</sub> ]Cl	<i>n.d.</i>	<b>3.03-</b> <b>4.65</b>	1.83	1.50	1.83	<b>3.03-</b> <b>4.65</b>	-	-	-	-	-
[Ru(MorphDTC) <sub>3</sub> ]	-	3.15	<b>24.90</b>	<i>n.d.</i>	<b>24.90</b>	3.15	-	-	-	-	-
β[Ru <sub>2</sub> (MorphDTC) <sub>5</sub> ]Cl	-	3.25-	<b>3.25-</b>	<i>n.d.</i>	<b>3.25-</b>	3.25-	-	-	-	-	-
		4.65	<b>4.65</b>		<b>4.65</b>	4.65					
[Ru(IndolineDTC) <sub>3</sub> ]	<i>n.d.</i>	<b>35.92,</b> <b>45.63</b>	0.16	8.67	7.27	8.95	<i>n.d.</i>	-	-	-	-
β[Ru <sub>2</sub> (IndolineDTC) <sub>5</sub> ]Cl	<i>n.d.</i>	<b>3.22-</b> <b>4.88</b>	3.22-	7.35-	7.35-	7.35-	<b>7.35-</b> <b>8.87</b>	-	-	-	-
	<i>n.d.</i>	<b>38.65-</b> <b>46.27</b>	0.47-	0.47-	<b>23.55-</b> <b>28.34,</b> <b>31.41-</b> <b>34.64</b>	-	-	-	-	3.07	-
[Ru(ProOMeDTC) <sub>3</sub> ]			2.27	2.27							
β[Ru <sub>2</sub> (ProOMeDTC) <sub>5</sub> ]Cl	<i>n.d.</i>	<b>5.02-</b> <b>5.38</b>	2.20	2.20	<b>3.28-</b> <b>3.98</b>	-	-	-	-	3.28-	-
										3.98	
	<i>n.d.</i>	<b>40.07-</b> <b>44.47</b>	0.50-	0.50-	<b>23.65-</b> <b>26.70,</b> <b>30.00-</b> <b>33.38</b>	-	-	-	-	-	0.50-
[Ru(ProOtBuDTC) <sub>3</sub> ]			2.27	2.27							2.27
β[Ru <sub>2</sub> (ProOtBuDTC) <sub>5</sub> ]Cl	<i>n.d.</i>	<b>4.36-</b> <b>5.30</b>	1.41-	1.41-	<b>3.21-</b> <b>4.02</b>	-	-	-	-	-	1.41-
			2.26	2.26							2.26
[Ru(CDT) <sub>3</sub> ]	<i>n.d.</i>	9.01-	8.90	7.71-	7.71-	8.90	9.01-	<i>n.d.</i>	<i>n.d.</i>	-	-
		9.03		7.73	7.73		9.03				
β[Ru <sub>2</sub> (CDT) <sub>5</sub> ]Cl	<b>9.17-</b> <b>9.19</b>	7.46-	7.46-	7.98-	7.98-	7.46-	7.46-	<b>9.17-</b> <b>9.19</b>	<i>n.d.</i>	-	-
		7.53	7.53	8.00	8.00	7.53	7.53				

**Table 5.1** List of the proton chemical shifts (ppm) of Ru(III)-DTC derivatives, both mono- and dinuclear, synthesized in this work. The signals of protons close to the dithiocarbamic moiety are highlighted by bold font; *n.d.* stands for “not detected”. Attribution was made based on the IUPAC nomenclature for *N*-heterocyclic compounds. All the spectra were recorded with a 300.13 MHz spectrometer at 298 K in CDCl<sub>3</sub>, except for those of the Ru(III)-IndolineDTC derivatives, obtained in CD<sub>2</sub>Cl<sub>2</sub>,

Taking into account these considerations the resonances related to the aliphatic α-CH protons shift to downfields in the range 20-40 ppm, while the signals of the N-CH protons of aromatic derivatives ( $H_{(7)}$ ) of

indoline and H<sub>(1)</sub>, H<sub>(8)</sub> of carbazole), disappear upon coordination to the Ru(III) center, as they are broadened under the limit of detection (**Table 5.1**).

An additional effect influences the <sup>1</sup>H-NMR spectra of Ru(DTC)<sub>3</sub> derivatives, namely their dynamic stereochemistry [203-206]. In fact, at the NMR timescale, this type of complexes undergo metal-centered inversion between the two optical isomers  $\Lambda$  and  $\Delta$ , thus giving a signal for each species at equilibrium (**Figure 5.7 a**). Such intramolecular inversion may occur according to four different mechanisms but for our Ru(DTC)<sub>3</sub> complexes the trigonal twist (or Bailar's twist) is the most favored (**Figure 5.7 b**) [207]. This mechanism does not involve bond breakage and the inversion takes place by means of a rotation around a C<sub>3</sub> symmetry axis, with a transitional state D<sub>3h</sub> [208].

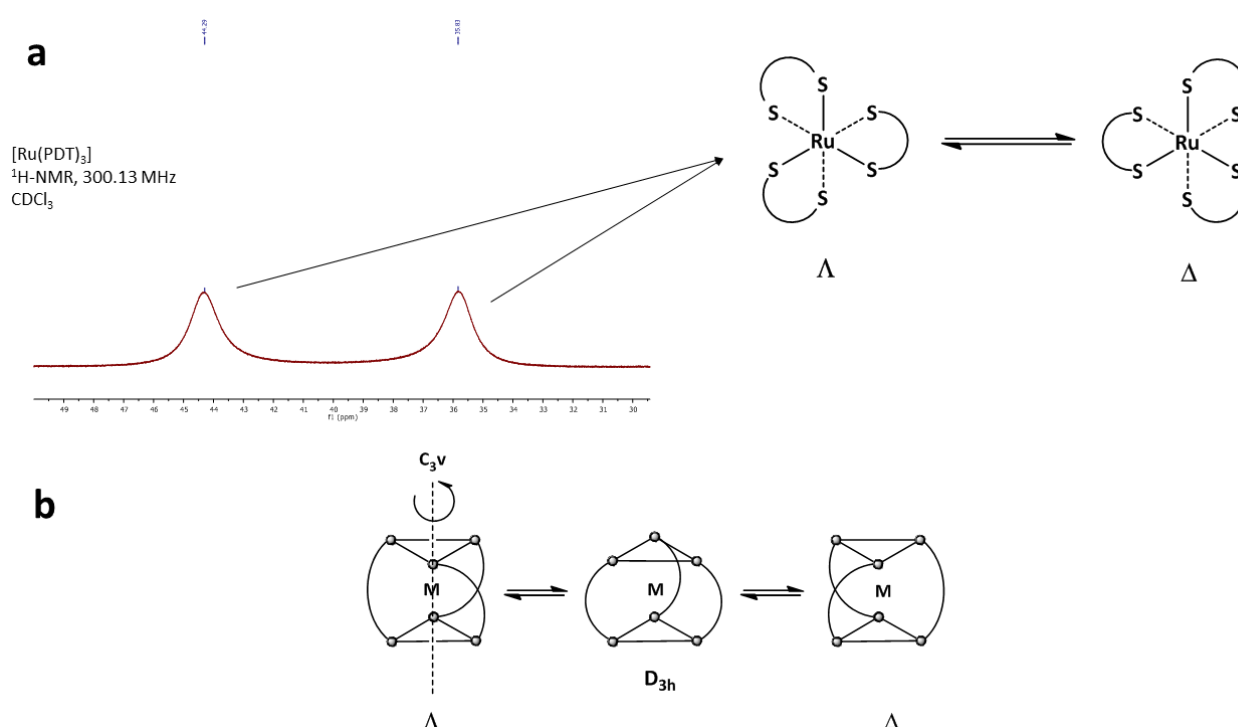


**Figure 5.7** [Ru(DTC)<sub>3</sub>] complexes are examples of tris-chelate complexes, which undergo metal-centered intramolecular inversion between the two optical isomers  $\Lambda$  and  $\Delta$ . Based on the NMR timescale, it is possible to observe this equilibrium, as in the case of Ru(PDT)<sub>3</sub> which exhibits two distinct broad singlets (at downfield compared to the free ligand) and corresponding to the two isomers (300.13 MHz, 298 K, CDCl<sub>3</sub>) **a**. The mechanism proposed for the dynamic conversion is the Bailar's twist, which considers the rotation around one of the C<sub>3</sub> symmetry axes with a D<sub>3h</sub> transitional state, without bond breakage **b**.

To better explain this phenomenon, the spectra of the complexes [Ru(PDT)<sub>3</sub>] and [Ru(ProOtBuDTC)<sub>3</sub>] have been compared as they contain *N*-substituent symmetric and asymmetric ligands, respectively. In the first case, the <sup>1</sup>H-NMR analysis shows the presence of two different broad singlets at 35.83 and 44.29 ppm, related to the  $\alpha$ -CH<sub>2</sub> protons of the  $\Lambda$  and  $\Delta$  isomers whose unambiguous attribution is not possible (**Figure 5.7 a**). The spectrum of the [Ru(ProOtBuDTC)<sub>3</sub>] derivative is more complex as 12 singlets are detected that appear in three four-membered sets.

Considering ProOtBuDTC as an asymmetric ligand, with reference to Figure 5.8, the  $-\text{CH}$  group in position 2 and the two protons in position 5 (diastereotopic) result magnetically different, thus leading to three distinct resonances. Moreover, from the spectrum analysis one can infer that for each of them there is a split likely due to the presence of the  $\Lambda$  and  $\Delta$  isomers and *cis* or *trans* geometric isomers [203]. According to this hypothesis, the resonances could come from the coupling of 3 (protons)  $\times$  2 (optical isomers  $\Lambda$  and  $\Delta$ )  $\times$  2 (geometric isomers *cis* and *trans*) = 12 total signals (Figure 5.8). Such hypothesis will be checked in future studies *via* homo- and heteronuclear NMR analysis at different temperatures in halogenated solvents.

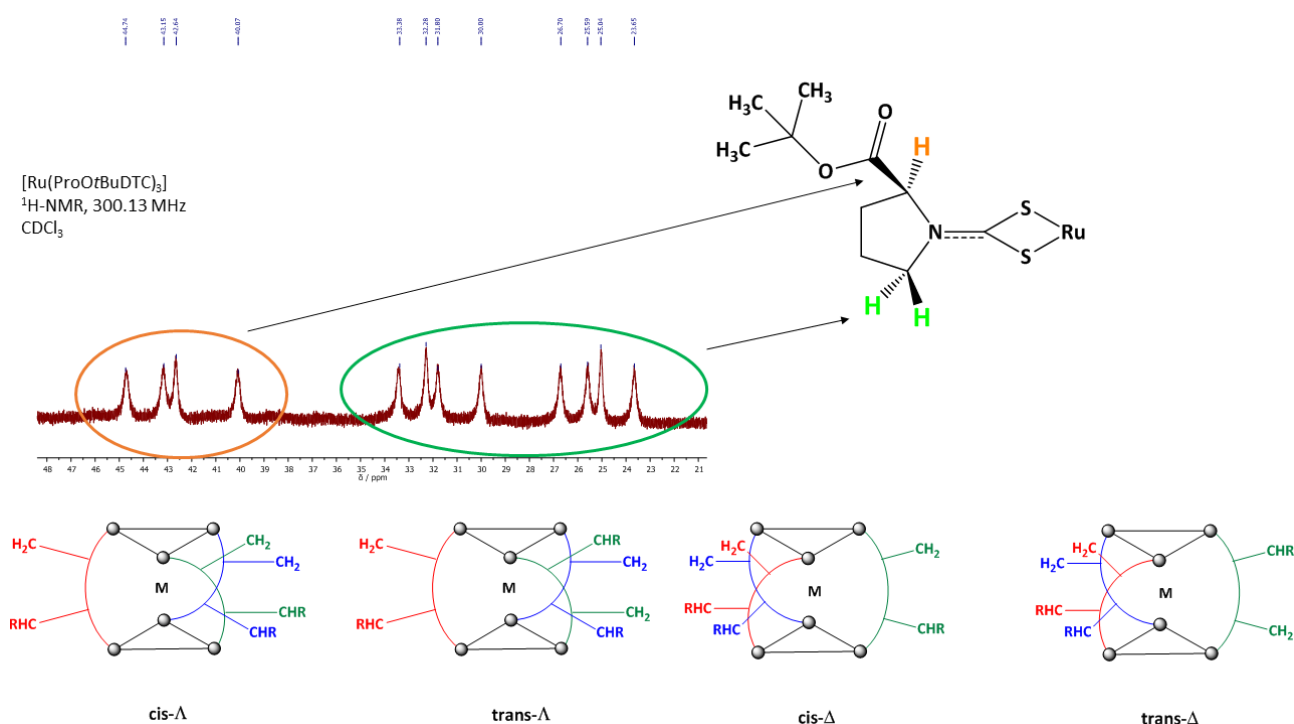


**Figure 5.8** Particular of the  $^1\text{H-NMR}$  spectrum of  $[\text{Ru}(\text{ProOtBuDTC})_3]$  (300.13 MHz, 298 K,  $\text{CDCl}_3$ ), range 50-20 ppm. It is possible to observe 12 different singlets, corresponding to three chemically different  $\alpha$ -protons (position 2 and 5), which are in the limit of NMR timescale-slow *cis-trans* isomerization (by rotation around the C-N bond) and slow optical inversion ( $\Lambda$  and  $\Delta$  isomers).

Concerning the dinuclear species  $[\text{Ru}_2(\text{DTC})_5]\text{Cl}$ , the  $^1\text{H-NMR}$  spectra appear quite complex. The absence of signals out of the 0-12 ppm range points out the diamagnetic nature of these derivatives, which possess two antiferromagnetically-coupled Ru(III) ions. The complexity of the spectra could be ascribed to the different coordination modes adopted by the ligands, which lead the proton signals to be different even if placed in similar chemical environment [187]. However, despite of the high number of multiplets, the  $^1\text{H-NMR}$  analysis of this type of complexes is fundamental to verify the completeness of the isomerization reaction between  $\alpha$  and  $\beta$  isomers. After silica gel purifications of the compounds, a mixture of  $\alpha$  and  $\beta$ - $[\text{Ru}_2(\text{DTC})_5]\text{Cl}$  is indeed obtained (Section 5.3). Refluxing this mixture in methanol for 8 hours results in the complete isomerization of the residual  $\alpha$ - $[\text{Ru}_2(\text{DTC})_5]\text{Cl}$  to the most thermodynamically stable  $\beta$ - $[\text{Ru}_2(\text{DTC})_5]\text{Cl}$  complex. In particular,

taking as an example  $[\text{Ru}_2(\text{PipeDTC})_5]\text{Cl}$ , we observe the disappearance of some multiplets (blue boxes, **Figure 5.9**) and the increase in intensity of others (orange boxes **Figure 5.9**).

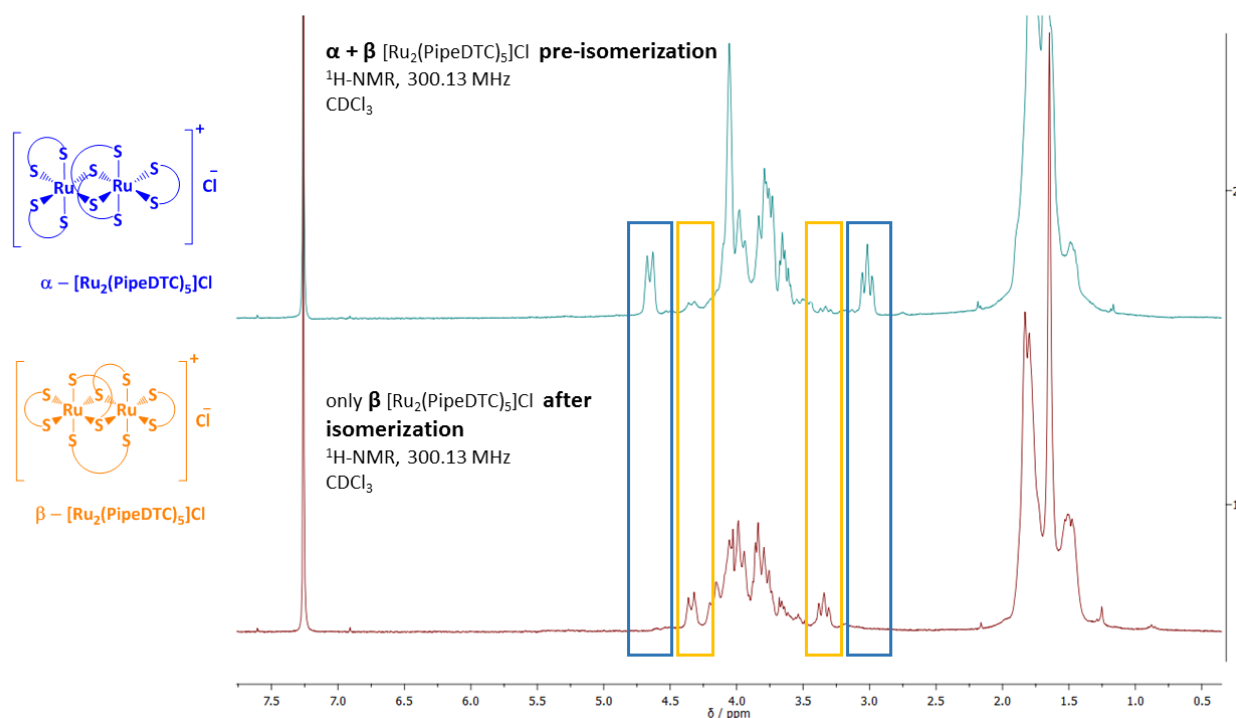


**Figure 5.9**  $^1\text{H-NMR}$  analysis of  $[\text{Ru}_2(\text{PipeDTC})_5]\text{Cl}$  before and after isomerization in methanol at reflux for 8 hours, showing the disappearance of the  $\alpha$ -isomer signals (blue boxes) and progressive increase in intensity of  $\beta$ - $[\text{Ru}_2(\text{PipeDTC})_5]\text{Cl}$  multiplets (orange boxes). It is worth underlining that in the crude dinuclear product (top spectrum), the  $\alpha$ -isomer is prevalent but after reflux the conversion (bottom spectrum) is quantitative.

#### 5.4.4 FT-IR characterization

The FT-IR spectra were recorded for all Ru(III)-DTC derivatives in both medium ( $4000\text{-}600\text{ cm}^{-1}$ ) and far ( $600\text{-}200\text{ cm}^{-1}$ ) wavenumber range (**Supporting Information G**) and the diagnostic absorptions are reported in **Table 5.2**.

The main features of the IR spectra of metal-DTC derivatives have been previously discussed in **Section 4.4.3**. Three fundamental IR-regions must be taken into account to when studying transition metal-dithiocarbamate complexes, of which the following bands corresponding to stretching vibration modes ( $\nu$ ) can be found [209, 210]:

- backbone  $\nu(\text{SSC-N})$  vibration, between  $1200$  and  $1550\text{ cm}^{-1}$ ;
- $\nu_a(\text{C-S})$  vibration between  $950$  and  $1050\text{ cm}^{-1}$  and  $\nu_s(\text{C-S})$  vibration between  $550$  and  $650\text{ cm}^{-1}$ ;
- $\nu(\text{Ru-S})$  vibration between  $300$  and  $470\text{ cm}^{-1}$ .



	$\nu(\text{C=O})$	$\nu(\text{C=C})$	$\nu(\text{N-CSS})$	$\nu_a(\text{C-O})$	$\nu_a(\text{CSS})$	$\omega(\text{C-H})$	$\delta(\text{C-H})$	$\nu_s(\text{CSS})$	$\nu_a(\text{Ru-S})$	$\nu_s(\text{Ru-S})$
[Ru(PDT) <sub>3</sub> ]	-	-	1487, 1470, 1444 cm <sup>-1</sup>	-	942 cm <sup>-1</sup>	-	-	565 cm <sup>-1</sup>	448 cm <sup>-1</sup>	319 cm <sup>-1</sup>
β[Ru <sub>2</sub> (PDT) <sub>5</sub> ]Cl	-	-	1506, 1473, 1448 cm <sup>-1</sup>	-	947 cm <sup>-1</sup>	-	-	564 cm <sup>-1</sup>	446 cm <sup>-1</sup>	348 cm <sup>-1</sup>
[Ru(PipeDTC) <sub>3</sub> ]	-	-	1488, 1455, 1439 cm <sup>-1</sup>	-	1002 cm <sup>-1</sup>	-	-	538 cm <sup>-1</sup>	405 cm <sup>-1</sup>	330 cm <sup>-1</sup>
β[Ru <sub>2</sub> (PipeDTC) <sub>5</sub> ]Cl	-	-	1503, 1441 cm <sup>-1</sup>	-	1002 cm <sup>-1</sup>	-	-	544 cm <sup>-1</sup>	407 cm <sup>-1</sup>	322 cm <sup>-1</sup>
[Ru(MorphDTC) <sub>3</sub> ]	-	-	1486, 1431 cm <sup>-1</sup>	1112 cm <sup>-1</sup>	994 cm <sup>-1</sup>	-	-	542 cm <sup>-1</sup>	413 cm <sup>-1</sup>	325 cm <sup>-1</sup>
β[Ru <sub>2</sub> (MorphDTC) <sub>5</sub> ]Cl	-	-	1503, 1435 cm <sup>-1</sup>	1107 cm <sup>-1</sup>	994 cm <sup>-1</sup>	-	-	547 cm <sup>-1</sup>	414 cm <sup>-1</sup>	310 cm <sup>-1</sup>
[Ru(IndolineDTC) <sub>3</sub> ]	-	1476 cm <sup>-1</sup>	1387, 1348, 1322 cm <sup>-1</sup>	-	948 cm <sup>-1</sup>	-	750 cm <sup>-1</sup>	547 cm <sup>-1</sup>	424 cm <sup>-1</sup>	333 cm <sup>-1</sup>
β[Ru <sub>2</sub> (IndolineDTC) <sub>5</sub> ]Cl	-	1484 cm <sup>-1</sup>	1431, 1324 cm <sup>-1</sup>	-	952 cm <sup>-1</sup>	-	751 cm <sup>-1</sup>	559 cm <sup>-1</sup>	421 cm <sup>-1</sup>	324 cm <sup>-1</sup>
[Ru(ProOMeDTC) <sub>3</sub> ]	1742 cm <sup>-1</sup>	-	1440 cm <sup>-1</sup>	1169 cm <sup>-1</sup>	942 cm <sup>-1</sup>	-	-	547 cm <sup>-1</sup>	453 cm <sup>-1</sup>	324 cm <sup>-1</sup>
β[Ru <sub>2</sub> (ProOMeDTC) <sub>5</sub> ]Cl	1741 cm <sup>-1</sup>	-	1480, 1448 cm <sup>-1</sup>	1170 cm <sup>-1</sup>	944 cm <sup>-1</sup>	-	-	547 cm <sup>-1</sup>	462 cm <sup>-1</sup>	335 cm <sup>-1</sup>
[Ru(ProOtBuDTC) <sub>3</sub> ]	1736 cm <sup>-1</sup>	-	1440 cm <sup>-1</sup>	1149 cm <sup>-1</sup>	934 cm <sup>-1</sup>	-	-	548 cm <sup>-1</sup>	471 cm <sup>-1</sup>	321 cm <sup>-1</sup>
β[Ru <sub>2</sub> (ProOtBuDTC) <sub>5</sub> ]Cl	1735 cm <sup>-1</sup>	-	1481, 1450 cm <sup>-1</sup>	1149 cm <sup>-1</sup>	935 cm <sup>-1</sup>	-	-	551 cm <sup>-1</sup>	471 cm <sup>-1</sup>	326 cm <sup>-1</sup>
[Ru(CDT) <sub>3</sub> ]	-	1485, 1436 cm <sup>-1</sup>	1363, 1324, 1295 cm <sup>-1</sup>	-	1036 cm <sup>-1</sup>	848 cm <sup>-1</sup>	746 cm <sup>-1</sup>	587 cm <sup>-1</sup>	460 cm <sup>-1</sup>	413 cm <sup>-1</sup>
β[Ru <sub>2</sub> (CDT) <sub>5</sub> ]Cl	-	1485, 1437 cm <sup>-1</sup>	1364, 1326, 1299 cm <sup>-1</sup>	-	1038 cm <sup>-1</sup>	852 cm <sup>-1</sup>	744 cm <sup>-1</sup>	587 cm <sup>-1</sup>	466 cm <sup>-1</sup>	415 cm <sup>-1</sup>

**Table 5.2** Collection of the main IR-vibrations (4000-200 cm<sup>-1</sup>) of the analyzed Ru(III)-DTC complexes.

First of all, concerning the  $\nu(\text{SSC-N})$  vibration, the Ru-DTC derivatives, both mono- and dinuclear, show the same trend observed for the correspondent dithiocarbamate ligands. Indeed, moving from PDT and PipeDTC complexes to indoline derivatives, then to the Ru(III)-CDT compounds, a shift to lower energies of the  $\nu(\text{SSC-N})$

N) bands is detected. In general, comparing the energy of the  $\nu(\text{SSC-N})$  vibration, for the analyzed Ru(III) dithiocarbamato complexes the following series is obtained:



As observed for the free ligands, it is possible to state that in the coordinated PDT, PipeDTC and MorphDTC the thioureido form is predominant. On the contrary, moving to DTC ligands which contain electron withdrawing groups (*i.e.*, L-proline ester derivatives) or dithiocarbamates where resonance effects are relevant (*i.e.*, IndolineDTC, and CDT to a greater extent), the dithiocarbamic form is majority.

Another important feature associated with the  $\nu(\text{SSC-N})$  vibration is the number of bands observed in the spectra of Ru(III)-DTC derivatives. In particular, the IR spectra of mononuclear complexes show three bands (or one very broad), due to the distorted octahedral geometry adopted by the complexes, which makes not equivalent the three dithiocarbamato ligands. A similar behavior was previously reported for  $[\text{Fe}(\text{PyrrDTC})_3]$  [211], as well as for our  $[\text{Ru}(\text{DTC})_3]$  derivatives (DTC= PDT, ESDT, DMDT, **Figure 5.3 a, b**) [186]. On the other hand, the different coordination modes of the dithiocarbamato ligands in the dinuclear derivatives may account for the observed splitting in the  $\nu(\text{SSC-N})$  band (**Figure 5.3 c**).

The second diagnostic region, ascribed to the C-S stretching mode, is useful to determine the coordination mode of the dithiocarbamato ligands. Indeed, according to the Bonati-Ugo method, the presence of only a band in the region 950 and 1050  $\text{cm}^{-1}$  (corresponding to the asymmetric C-S stretching) is assumed to point out a symmetric bidentate coordination of the ligand [148]. Moreover, this diagnostic mode, together with the Ru-S vibration modes (occurring in the far IR domain, at 450-300  $\text{cm}^{-1}$  [212]), is a fingerprint of the ligand effect on the Ru-DTC bond-strength. Indeed, the previously reported analysis of the  $\nu(\text{SSC-N})$  vibration highlights how some ligands coordinated to the ruthenium center prefer a thioureidic form, whereas others, affected by inductive or resonance effects, are associated with a dithiocarbamic form (**Figure 5.10**). As observed in **Section 4.2**, a thioureido form reflects the presence of electron density in low energy *d*-orbitals of sulfur atoms, due to the shift of the nitrogen lone pair towards the NCSS moiety. The direct consequence is the reduced tendency of the metal center to back-donate to the sulfur atoms. On the contrary, the dithiocarbamato form provides empty *d*-orbitals at the sulfur atoms, which are able to accept metal  $\pi$ -retrodonation [130-133]. This effect is related to a more covalent character of the Ru-S bond and, consequently, to a higher electron density in the  $\text{Ru} \left\langle \overset{\text{S}}{\text{S}} \right\rangle \text{C}$  ring. To confirm this behavior, the C-S and Ru-S stretching frequencies were compared between the Ru-PDT complexes and Ru-CDT counterparts, taken as examples for the thioureidic form (**Figure 5.10 a**) and dithiocarbamic form (**Figure 5.10 b**). From the data reported in **Table 5.2**, it is evident that Ru-CDT derivatives are associated with higher values, whereas Ru-PDT complexes basically show no or negligible ruthenium-to-sulfur back-donation, being endowed with lower C-S and Ru-S bond orders.

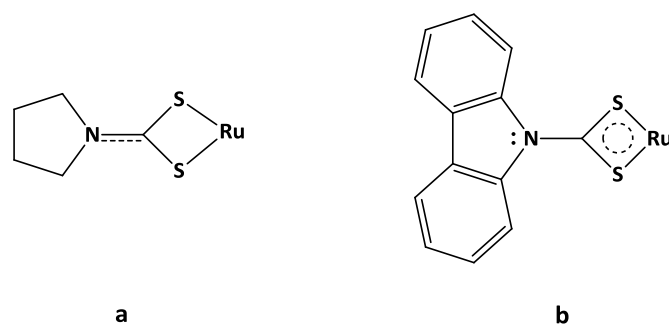


**Figure 5.10** The two limiting forms for dithiocarbamato-chelation of transition metals, representing forbidden (*i.e.*, PDT, **a**) and allowed (*i.e.*, CDT, **b**) metal-to-sulfur retrodonation.

#### 5.4.5 UV-Vis characterization

Electronic absorption studies were carried out for the synthesized ruthenium dithiocarbamate complexes by means of UV-Vis spectrophotometry in  $\text{CH}_2\text{Cl}_2$  (800-240 nm) at 25 °C, and the diagnostic absorptions are summarized in **Table 5.3**.

	$\lambda$ ( $\epsilon$ , $M^{-1} \text{cm}^{-1}$ )					
	<i>band I</i>	<i>band II</i>	<i>band III</i>	<i>band IV</i>	<i>band V</i>	<i>band VI</i>
$[\text{Ru}(\text{PDT})_3]$	241 nm (42450)	255 <sup>sh</sup> nm (39130)	280 <sup>sh</sup> nm (25761)	362 nm (10190)	467 nm (2542)	565 nm (1415)
$\beta[\text{Ru}_2(\text{PDT})_5]\text{Cl}$	247 nm (42097)	268 nm (44151)	288 nm (43678)	333 <sup>sh</sup> nm (21886)	468 <sup>sh</sup> nm (2633)	-
$[\text{Ru}(\text{PipeDTC})_3]$	242 nm (43002)	259 nm (41288)	290 nm (26690)	367 nm (11716)	472 nm (2980)	557 nm (1823)
$\beta[\text{Ru}_2(\text{PipeDTC})_5]\text{Cl}$	246 nm (42333)	267 nm (42667)	287 nm (42351)	332 nm (18040)	464 nm (2033)	-
$[\text{Ru}(\text{MorphDTC})_3]$	241 nm (41989)	258 nm (38726)	286 nm (26096)	368 nm (10078)	470 nm (2236)	566 nm (1020)
$\beta[\text{Ru}_2(\text{MorphDTC})_5]\text{Cl}$	244 nm (39666)	268 nm (41001)	284 nm (39618)	327 nm (19050)	445 nm (3167)	-
$[\text{Ru}(\text{IndolineDTC})_3]$	- <sup>a</sup>	- <sup>a</sup>	280 nm (33333)	345 nm (29740)	449 nm (16206)	612 nm (2073)
$\beta[\text{Ru}_2(\text{IndolineDTC})_5]\text{Cl}$	- <sup>a</sup>	- <sup>a</sup>	286 nm (54229)	330 nm (50490)	410 nm (31116)	-
$[\text{Ru}(\text{ProOMeDTC})_3]$	240 nm (40920)	259 nm (34654)	284 nm (20950)	359 nm (9181)	460 nm (1693)	575 nm (956)
$\beta[\text{Ru}_2(\text{ProOMeDTC})_5]\text{Cl}$	248 nm (39500)	262 nm (39371)	288 nm (38552)	323 nm (14706)	453 nm (2533)	-
$[\text{Ru}(\text{ProOtBuDTC})_3]$	241 nm (41996)	260 nm (35400)	283 nm (23840)	362 nm (9297)	463 nm (2076)	577 nm (1626)
$\beta[\text{Ru}_2(\text{ProOtBuDTC})_5]\text{Cl}$	249 nm (40433)	264 nm (41860)	287 nm (37448)	322 nm (15880)	449 nm (2666)	-
$[\text{Ru}(\text{CDT})_3]$	- <sup>a</sup>	- <sup>a</sup>	279 nm (39870)	341 nm (31920)	445 nm (18440)	626 nm (2760)
$\beta[\text{Ru}_2(\text{CDT})_5]\text{Cl}$	- <sup>a</sup>	- <sup>a</sup>	278 nm (60794)	361 nm (56490)	421 nm (35672)	-

**Table 5.3** UV-Visible spectral data (800-240 nm) of the synthesized Ru(III) dithiocarbamate complexes in  $\text{CH}_2\text{Cl}_2$  at 25 °C; sh= shoulder; <sup>a</sup>= the band is not reported since it is placed below the solvent cut-off (240 nm).

All the analyzed complexes proved stable in CH<sub>2</sub>Cl<sub>2</sub> solution for at least 10 days, as no significant spectral changes were observed. As examples, the recorded spectra of Ru(III)- derivatives of PDT and CDT are reported in **Figure 5.11**.

The *band I* at 240-250 nm for the aliphatic complexes is still subject of debate in the literature, and so far it has been assigned either to an intraligand  $\pi^* \leftarrow \pi$  transition located in the -NCSS moiety or to an intraligand  $p \leftarrow d$  transition between levels originated by sulfur atoms [213].

The *band II* at around 250-260 nm and the *band III* at 280-290 nm have been attributed to the intraligand  $\pi^* \leftarrow \pi$  transition located in the N-C-S and the S-C-S moieties of the dithiocarbamate ligands, respectively [214].

In the 300-800 nm range, the spectra of the mononuclear species consist of three absorption bands, significantly differing from each other in terms of intensity and spectral shape (**Figure 5.11 a, b**). Based on the high values of the molar extinction coefficient ( $\epsilon > 100 \text{ M}^{-1} \text{ cm}^{-1}$ ), the absorption *band IV* at about 330-360 nm can be assigned to a charge-transfer (CT) transition rather than to *d-d* transitions. As the dithiocarbamate ligand is characterized by both filled  $\pi$  (bonding) and empty  $\pi^*$  (antibonding) orbitals localized at the sulfur atoms, it is conceivable an interaction with the metal ion  $t_{2g}$  orbitals. Although both the transitions ligand-to-metal ( $d \leftarrow \pi$ , LMCT) and the metal-to-ligand ( $\pi \leftarrow d$ , MLCT) charge transfer are theoretically allowed, the first one is the most favored in this case, as it can easily occur when the metal is in a high oxidation state [215, 216]. On the other hand, the *band V* at 440-460 nm and the *band VI* at ca. 600 nm may be assigned to *d-d* transitions. According to the Tanabe-Sugano diagrams, the crystal field ground state of low-spin Ru(III) centers is  ${}^2T_{2g}$ , arising from the  $t_{2g}^5 e_g^0$  electronic configuration in a  $O_h$  environment. All *d-d* transitions are spin-allowed and the absorption spectrum should show four bands, as the excited states are  ${}^2T_{1g}$  and  ${}^2A_{2g}$  (degenerate),  ${}^2T_{2g}$ ,  ${}^2E_g$ , and  ${}^2A_{1g}$  [217]. It is known that the *d-d* transitions have small molar extinction coefficients (ca.  $1\text{-}100 \text{ M}^{-1} \text{ cm}^{-1}$ ) since they are Laporte-forbidden. Nevertheless, the X-ray structure of [Ru(PDT)<sub>3</sub>] (**Figure 5.3 a**) displays a slightly distorted octahedral geometry for this class of complexes and, therefore, upon loss of symmetry, more intense *d-d* transitions are foreseen and actually detected in the spectra ( $\epsilon$  ca.  $1000\text{-}2000 \text{ M}^{-1} \text{ cm}^{-1}$ ) [186]. Remarkably, the high molar extinction coefficients observed for the *band V* can be explained by considering also the contribution of charge-transfer transitions. Moreover, in the case of [Ru(DTC)<sub>3</sub>] with IndolineDTC and CDT as ligands, the aromatic nature of the ligand favors this behavior, giving rise to an  $\epsilon$  value of ca.  $9000 \text{ M}^{-1} \text{ cm}^{-1}$  (**Figure 5.11 b, d**). Finally, it is worth noting that the absorption bands observed in the visible region are very broad, supporting the hypothesis that some transitions are overlapped.

The absorption spectra of the  $\beta$ -[Ru<sub>2</sub>(DTC)<sub>5</sub>]Cl derivatives show in the 300-700 nm region an intense *band IV* at 330-360 nm and a broad weak *band V* at 420-470 nm (**Figure 5.11 c, d**). Due to their quite dissimilar structures, any correlation between the spectra acquired for mono- and di-nuclear complexes cannot be assessed. Indeed, dinuclear complexes involve two ruthenium centers anti-ferromagnetically coupled. This,

as previously reported (**Section 5.4.3**), annihilates the paramagnetic effects of the metal centers. Therefore, since a strong metal-metal interaction may take place between the two units, the absorption *band IV* can be ascribed to a metal-metal to ligand charge transfer transition (MMLCT), whereas the very broad *band V* may be due to a metal-to-metal charge transfer (MMCT) as the molar extinction coefficient values are higher than expected for a *d-d* transition [216].

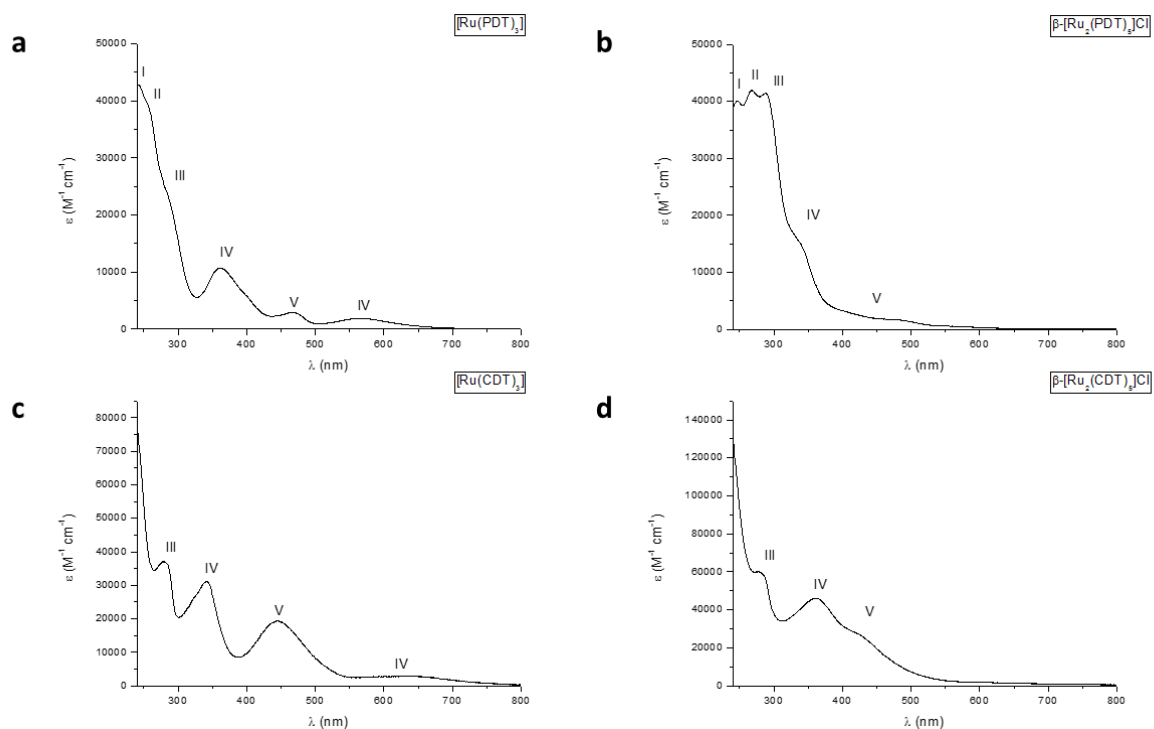


**Figure 5.11** UV-Vis spectra of  $[\text{Ru}(\text{PDT})_3]$  **a**,  $[\text{Ru}(\text{CDT})_3]$  **b**,  $\beta\text{-}[\text{Ru}_2(\text{PDT})_5]\text{Cl}$  **c**, and  $\beta\text{-}[\text{Ru}_2(\text{CDT})_5]\text{Cl}$  **d** in  $\text{CH}_2\text{Cl}_2$  at  $25^\circ\text{C}$ .



## 6. COPPER DITHIOCARBAMATES

### 6.1 Copper: an essential element for live beings

Copper is the 29<sup>th</sup> element of the periodic table with a  $[\text{Ar}]3d^{10}4s^1$  configuration and belongs to the 11<sup>th</sup> group and the 1<sup>st</sup> row of transition metals. Copper presents four oxidation states: Cu(I), Cu(II), Cu(III) and rarely Cu(IV). Although Cu(II) is the most stable oxidation state, copper is the only metal of the first row to show also a quite satisfying stability in the +1 oxidation state [150].

Copper has a wide range of available redox potentials, thus being capable of forming adducts with many classes of ligands bearing different donor atom sets and endowed with distinct properties in terms of electronic and steric effects, and possible chelation. At the same time, both the nature of the possible neighboring ligands and the easy switch between the two main oxidation states +1 and +2 allow remarkable modifications in the geometry of the related complex, with no high energy requirements [218]. For example, a distorted octahedral Cu(II) complex can smoothly turn into a tetrahedral Cu(I) species. It is worth noting that all these features make the Cu(I)/Cu(II) complexes much less predictable from the structural point of view than other first-row transition metal counterparts as well as the Cu(I)/Cu(II) redox pair a catalytic-active moiety widely involved in biological macromolecules [219].

The chemistry of copper is mainly represented by the +2 oxidation state especially in solution. With a  $3d^9$  electronic configuration cupric compounds are paramagnetic and susceptible to Jahn-Teller distortion in an octahedral coordination [220]. Thereby, all Cu(II) compounds should virtually be blue or green despite there are some exceptions generally caused by strong ultraviolet bands (charge-transfer bands) tailing off into the blue-end of the visible spectrum and, hence, they appear red or brown [221]. According to the “hard and soft acids and bases” (HSAB) theory of Pearson, the cupric ion is regarded as a borderline metal, therefore capable of being tightly coordinated by both soft and hard ligands, even if it prefers nitrogen donor atoms [67]. Furthermore, Cu(II) can adopt different coordination numbers, most commonly 4, 5 and 6 and associated with distinct coordination geometries, respectively the i) tetrahedral/ square planar, ii) the trigonal bipyramidal/ the square-based pyramidal and iii) the octahedral [222].

Concerning the role of copper in the homeostasis of living beings (**Figure 6.1**), its involvement in biological pathways started about 1.7 billion years ago with the increase of O<sub>2</sub> concentration to a significant value [223]. In fact, the biologically-essential iron was oxidized to Fe(III), thus leading to the precipitation of hydroxides and making its use more energy-demanding. On the other hand, the insoluble Cu(I) turned into the more soluble and bioavailable Cu(II) ion [224]. Moreover, a larger and larger amount of O<sub>2</sub> was produced by cyanobacteria and other prokaryotic organisms, resulting in an oxidizing environment with the need for a redox-active metal endowed with reduction potentials between 0.0 and 0.6 V [225], being satisfied by the Cu(II)/Cu(I) catalytical pair. Therefore, it is not surprising that copper plays a key role in many enzymes and

proteins involved in reactions with oxygen as a substrate, as well as in the degradation or transformation of its side products (*i.e.*,  $O_2^-$ ,  $NO_2^-$ ,  $NO$  or  $N_2O$ ) [226]. For instance, the Cu(II)/Cu(I) pair can be found in the hemocyanin (oxygen carrier found in the hemolymph of most mollusks and some arthropods), in the superoxide dismutase (catalyst of the dismutation of reactive  $O_2^-$  radical into both  $O_2$  and  $H_2O_2$ ) and in many other oxidoreductase and hydroxylase enzymes (*i.e.*, tyrosinase, ascorbate oxidase, dopamine- $\beta$ -hydroxylase) [227]. Furthermore, copper is also involved as a catalytic center in many electron transfer proteins due to its ability to switch between various oxidation states and to easily twist among different coordination numbers and geometries. Although trivalent copper sites were hypothesized in the literature as possible intermediates in some enzymes [228], further studies ruled out their presence [229] and, at the best of our knowledge, no example of the oxidation state +3 has been observed yet in copper biochemistry [230].

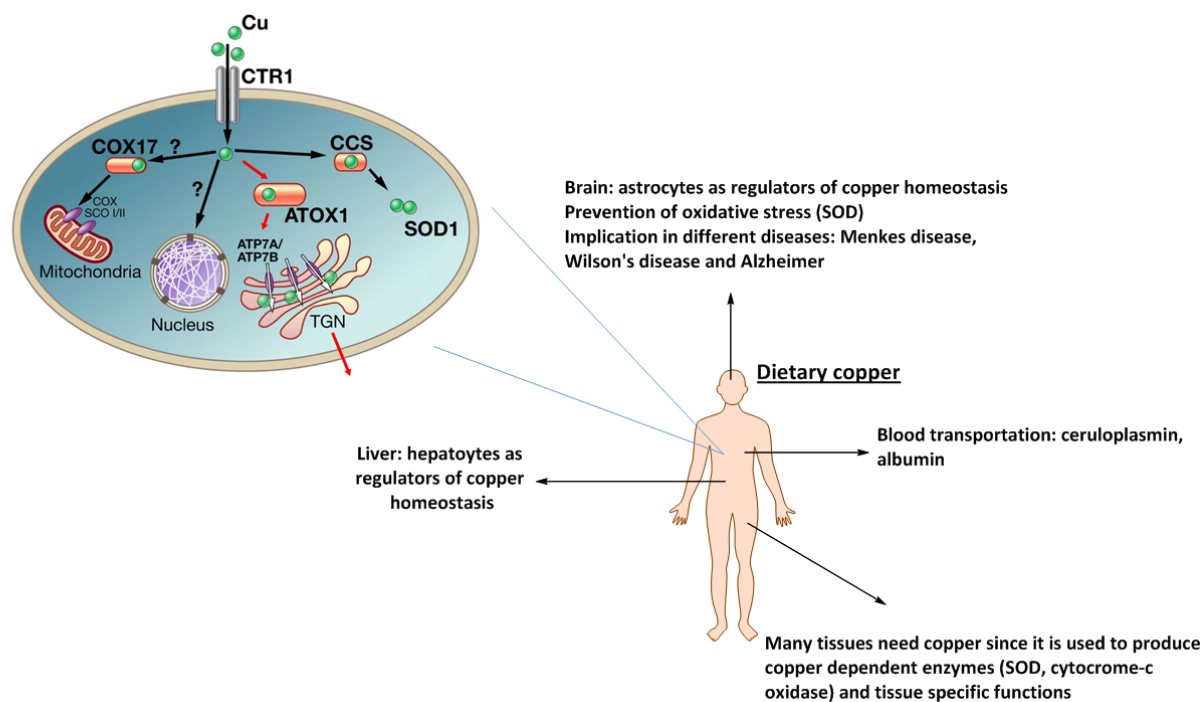


**Figure 6.1** Experiments in rats using orally administered radioactive copper revealed that newly absorbed copper appears in the bloodstream in two waves: an initial peak (after 2 h) corresponds to copper exiting the intestine, and the second peak (after ~6 h) represents copper incorporated into ceruloplasmin, which is secreted by the liver. This element is fundamental in the homeostasis of human beings and its lack or altered distribution is associated with aggressive diseases. If moving towards intracellular details (top, on the left), copper enters the cell through the high-affinity copper transporter Ctr1 and binds to its cytosolic chaperones. Current structural data as well as dependence of copper trafficking proteins on reducing reagents suggest that copper enters the cell, migrates within the cell, and then is exported from the cell in the reduced Cu(I) form. Cox17 may participate in the delivery of copper to the mitochondrion, although this role has recently been questioned, and together with Sco proteins facilitates the incorporation of copper into cytochrome-c oxidase (Cox). CCS transfers copper to cytosolic SOD1. The red arrows indicate the pathway regulated by Cu-ATPases. In this pathway, Cu-ATPases receive copper from ATOX1, transfer copper into the lumen of the secretory pathway, and also export excess copper from the cell [231].



In humans, copper ranks third among the most abundant transition metals and it is considered as an essential element. The body of a healthy 70-kg adult contains less than 110 mg of Cu, mainly found in the liver (10 mg), brain (8.8 mg), blood (6 mg), skeleton (bone marrow includes 46 mg) and skeletal muscles (28 mg) [232]. The Recommended Dietary Allowance (RDA) for adult men and women is 0.9 mg of copper/day and the Tolerable Upper Intake level has been set at 10 mg/day [233], since an excessive uptake results in potentially harmful free ions. Copper is indeed a potent source of free radicals and reactive oxygen species (ROS) [234].

Copper is primarily absorbed in the small intestine and then delivered mainly to the liver wherein it is incorporated into ceruloplasmin and, hence, released into the blood. Ceruloplasmin is the main vector in the serum carrying about 70% of the total copper, followed by albumin with 12-18% [219]. Afterwards, copper is uptaken by the eukaryotic cells as Cu(I) by the hCTR copper transporter proteins (Figure 6.1) [235]. All the members of this family show similar structures consisting of three transmembrane helices, with a hydrophilic *N*-terminus, usually rich in methionine residues towards the extracellular matrix and a number of conserved Cys/His residues at the *C*-terminus in the cytoplasm [236]. The suggested model of action of these proteins envisages firstly the coordination of the cuprous ion by the methionine-rich motifs at the extracellular *N*-terminus and, then, a series of copper-exchange reactions between specific Cu(I) binding sites exploiting well-defined conformational changes [237-239]. Once inside the cytosol, Cu(I) is coordinated and vehicled by different soluble proteins called copper chaperones through a currently unknown mechanism (**Figure 6.1**). First of all, the chaperones for superoxide dismutase (CCS) deliver copper to the antioxidant enzyme Cu,Zn superoxide dismutase (SOD1) [240]. On the other hand, the Cox17 (cytochrome *c* oxidase copper chaperone) is proposed to transport this metal ion to Sco1 (cytochrome *c* oxidase assembly protein) in the inner mitochondrial membrane, which may then transfer copper to the cytochrome *c* oxidase (COX) subunit 2 Cu<sub>A</sub> site [241]. Differently, the human Atox1 (Antioxidant-1) transfers Cu(I) to the mitochondrial membrane-bound metal-transporting P1B-type ATPases, respectively ATP7A and ATP7B, in the trans-Golgi network for the ultimate incorporation into ceruloplasmin [242]. Finally, the intracellular excess of copper is removed by metallothioneins, thus avoiding acute hepatitis owing to the production of ROS [243].

Alterations of this tightly-regulated homeostasis can lead to peculiar disorders, including Alzheimer (AD), PRION diseases (PrPD), amyotrophic lateral sclerosis (ALS), Menkes' disease (MD) and Wilson's disease (WD) [233, 234]. In particular, the latter two are characterized by a mutation in ATP7A and ATP7B genes (encoding for Menkes MNKP and Wilson WNDP proteins) which causes the deficiency (MD) or the accumulation (WD) of copper in the tissues, respectively [244, 245]. *Vice versa*, the metabolism of this redox-active metal center becomes profoundly altered also in cancer cells, with many types of tumors presenting high serum and tissue levels of Cu [246].

### 6.1.1 Copper and cancer: the role of the metal in angiogenesis and possible therapies

The involvement of endogenous metals in cancer metabolism has been studied for several decades [247]. Numerous papers report copper levels being aberrant in cancerous tissues of tumor-bearing mice and in cancer patients [248]. Although the mechanisms implicated in increasing the copper concentration in the serum of cancer patients have not been elucidated yet, it is undoubtedly the importance of copper as a key component of many cellular functions and modulator of cellular signaling, and not surprisingly, it is involved in cancer development and progression processes [249]. Among them, the most crucial process influenced by copper-altered homeostasis is angiogenesis and concerns the migration, proliferation and differentiation of endothelial cells to form new blood vessels as [250]. As introduced in **Section 1.2**, this is a crucial step in cancer growth, as most tumors cannot get larger than 2-3 mm without forming new blood vessels. Since angiogenesis is regulated by the so-called vascular endothelial growth factors (VEGFs), studies performed in mice by Kang and coworkers showed that the supplementation of copper promotes VEGF expression and, hence, the angiogenesis itself [251]. Moreover, copper affects transcriptional activity of hypoxia-inducible transcription factor-1 (HIF-1). It can inhibit the process of HIF-1 degradation, thus favoring its accumulation and activation, which leads to an overproduction of VEGF [252, 253]. Finally, in a recent work, after treating cells with VEGF, authors proved by X-ray fluorescence microscopy that copper moves from the intracellular milieu to the extracellular matrix, so highlighting again the relationship between VEGF and copper [254].

The concept that tumor microenvironment is associated with high levels of copper, due to its involvement in angiogenesis and tumor cell growth, opened intriguing perspectives in the development of antitumor drugs based on metal chelators and Cu-based coordination compounds [255, 256]. Historically, copper chelating agents (*i.e.*, trientine, tetrathiomolybdate “TM”, and D-penicillamine, **Figure 6.2 a-c**) were developed to treat the Wilson’s disease, by eliminating the excess of copper from the body [257]. The same agents were later investigated for their capacity to inhibit angiogenesis and, hence, to impair cancer growth and metastasis [258, 259]. The initial results on animal models showed the ability of these compounds to inhibit the progression of microscopic to macroscopic tumors. Moreover, trientine was able to induce apoptosis through the generation of ROS, ascribable to the *in situ* coordination of the nitrogen-based drug with the redox-active copper of certain enzymes [258]. However, even if a number of clinical trials investigated the anticancer activities of this group of chelating agents, no improvement in patients’ survival was recorded, rather it was associated with a marked reduction of bioavailable copper in serum, thus pointing out that copper chelation alone is insufficient to kill malignant cell [260].

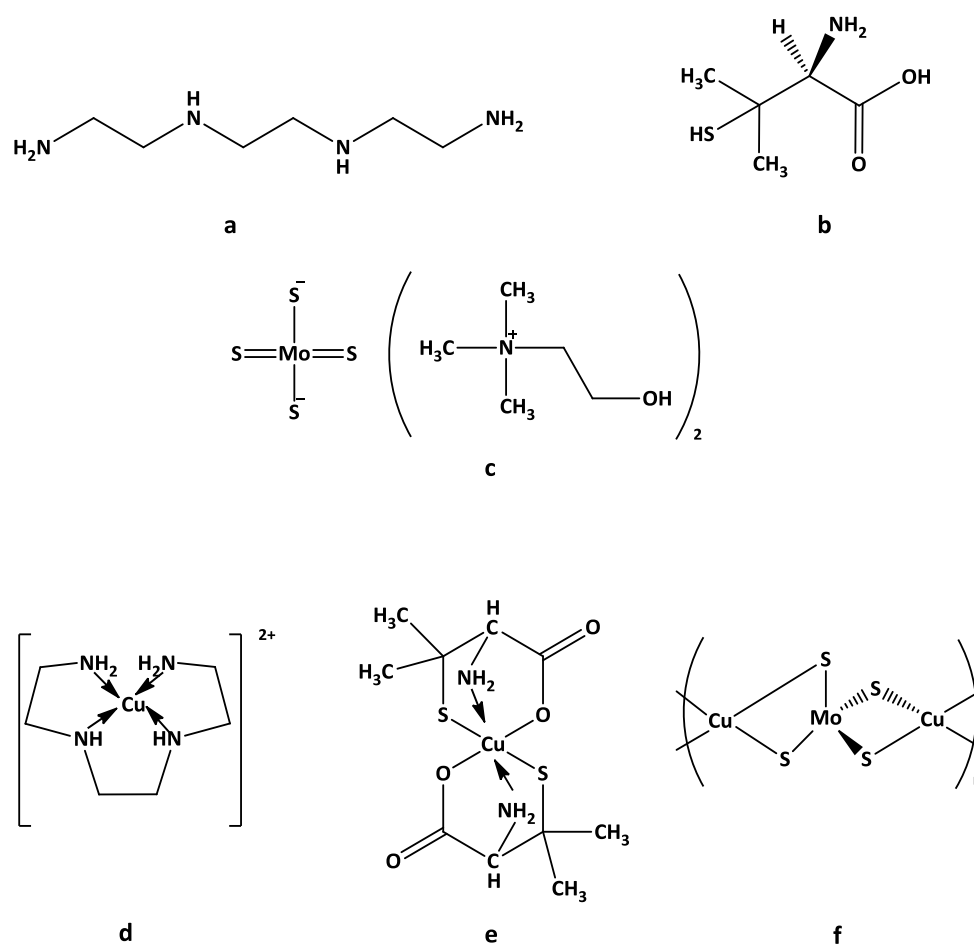


**Figure 6.2** Chemical structure of some investigated copper chelators, clinically established (or in clinical trials) for the therapy of the Wilson disease: trientine (Spyrine®,  $(N,N'$ -bis(2-aminoethyl)ethane-1,2-diamine) **a**, tetrathiomolybdate TM bis-choline salt (Decuprate®) **b**, D-penicillamine (Cuprimine®,  $(2S)$ -2-amino-3-methyl-3-sulfanylbutanoic acid) **c**, and their copper(II) derivatives, **c**, **d**, **e** respectively.

As aforementioned, the great need of copper in growing tissues provided scientists with the rationale for developing Cu-coordination compound [255, 261]. Copper (I/II) complexes are redox active, frequently labile, and atypical in their preference for distorted coordination geometries. In general, Cu(I) prefers ligands having soft donor atoms such as phosphorous, carbon, sulfur and aromatic amines, and the coordination is almost invariably tetrahedral. The few literature reported copper(I) complexes involve phosphine and heterocyclic carbene ligands and showed a micromolar cytotoxic activity *in vitro* when tested against different human cancer cell lines. Concerning the Cu(II) derivatives, the coordination number varies from four with square planar or tetrahedral geometries, to five in square pyramidal and six in octahedral coordination compounds. This reflects in a wide range of selectable ligands and donor atoms (*i.e.*, N, O, S, halides) [261]. As discussed for the +1 oxidation state, also Cu(II)-based compounds proved biologically active, and a possible biological target was identified for some of them. The Cu(II)-TACN complex (TACN= 1,4,7-triazacyclononane, **Figure 6.3 a**) acts as a “molecular scissor”, cleaving supercoiled DNA under both aerobic and anaerobic conditions, producing fragments that cannot be enzymatically re-ligated [262]. Differently,  $\text{CuCl}_2$  was found to inhibit Topo I (topoisomerase I, an enzyme that plays an important role in the DNA replication) [263], whereas

copper derivatives of thiosemicarbazones (TSC) of the type  $[\text{Cu}(\text{TSC})\text{Cl}]$  (**Figure 6.3 b**) were potent antitumor agents able to inhibit Topo II [264]. Finally, recently investigated  $[\text{Cu}(\text{DTC})_2]$  (DTC= PDT, DEDT, **Figure 6.3 c**) synthesized in our research group showed inhibition of the proteasome chymotrypsin-like activity (essential for many fundamental cellular processes, including cell cycle, apoptosis, angiogenesis and differentiation), blocking proliferation of breast cancer cells and inducing apoptosis [265].

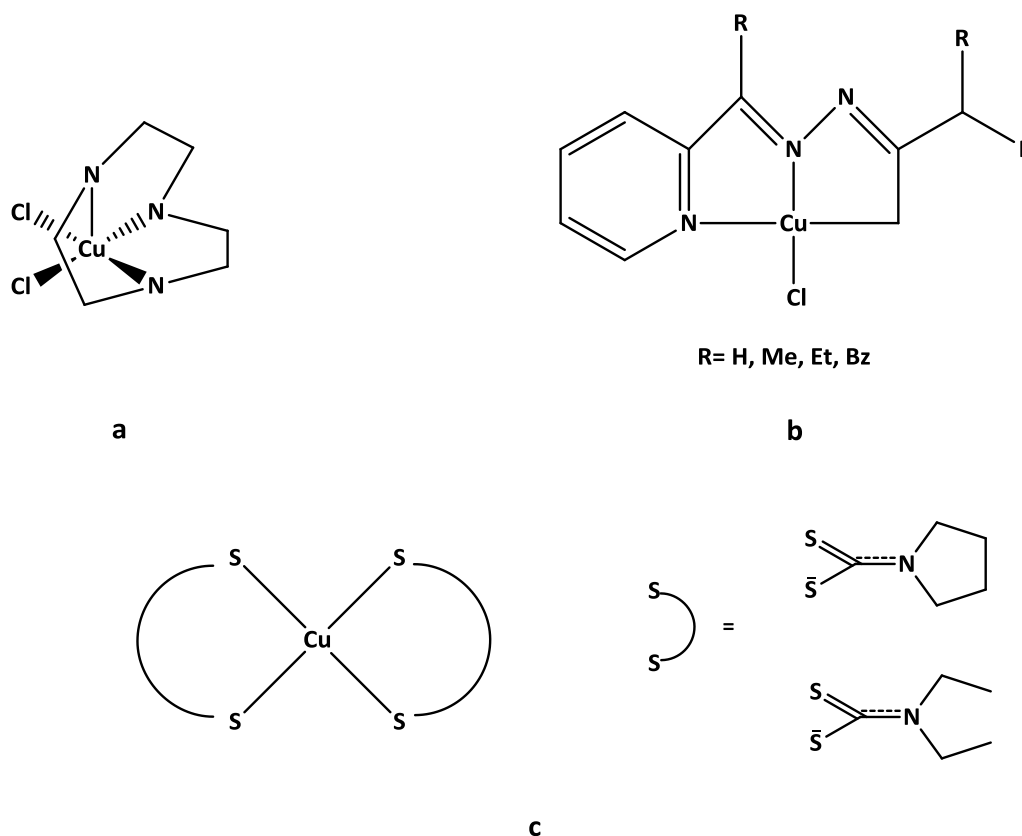


**Figure 6.3** Some Cu(II) derivatives for which a possible target was identified: the “DNA-scissor” Cu(II)-TACN complex  $[\text{CuCl}_2(\text{TACN})]$  (TACN= 1,4,7-triazacyclononane) **a**, the thiosemicarbazone (TSC) derivative  $[\text{Cu}(\text{TSC})\text{Cl}]$  acting as inhibitor of Topo II **b**, and the proteasome inhibitors of the type  $[\text{Cu}(\text{DTC})_2]$  (DTC= PDT, DEDT) **c**.

## 6.2 Copper(II) dithiocarbamates as anticancer agents

Copper dithiocarbamates (DTC) were first explored in the late 1960s, when they were investigated for their electrochemical and structural peculiarities [266, 267]. The easy access to different oxidation states of this transition metal, led to the isolation of different Cu-DTC complexes involving Cu(I), Cu(II) or Cu(III) metal centers [268, 269]. Notwithstanding, only in the 1990s the cytotoxic properties of this class of compounds were disclosed, demonstrating the cytotoxic effect of a Cu-PDT complex formed *in situ* (**Figure 6.3 c**) on thymocytes with *in vitro* experiments [270]. Indeed, during previous studies, researchers observed that the administration of pyrrolidinedithiocarbamate as sodium salt had an antioxidant effect due to the inhibition of the oxidative activation of the transcription factor NF $\kappa$ B (a cellular component with a key role in the activation of immunity system in case of oxidative stress) [271]. Since these observations candidate dithiocarbamates as potent antioxidants in medicine, on the contrary Slater demonstrated that PDT was

associated with a toxic pro-oxidant effect in thymocytes, inducing apoptotic cell shrinkage and chromatin fragmentation prior to cell lysis. This toxicity was demonstrated to be dependent on the ability of administered pyrrolidinedithiocarbamate to chelate *in situ* endogenous copper and transport it into the cells, and thereby generate an intracellular oxidative stress [270].

To date, it is commonly accepted that the administration of PDT increases the cellular copper concentration and the combination of Cu and the DTC ligand exerts cytotoxic effects on cancer cells [272-274]. Other dithiocarbamates (*e.g.*, DEDT) yielded the same experimental biological result [275]. Taken together, these findings have fostered researchers to explore synthetic copper-DTC derivatives as potential anticancer agents. As previously reported in **Section 6.1.1**, the  $[\text{Cu}(\text{PDT})_2]$  complex was found to be a potent proteasome inhibitor and an apoptosis inducer [265]. Moreover, PDT (as sodium salt) spontaneously binds copper, forming derivatives that have proteasome-inhibitory and apoptosis-inducing activities in breast tumor cells but not in normal/not transformed counterparts [276]. These encouraging results prompted our research group to synthesize and biologically study new Cu(II) dithiocarbamate derivatives of sarcosine esters and dimethylamine as potential chemotherapeutic agents (**Figure 6.4**). In all compounds, the metal-to-ligand stoichiometry is 1:2 with symmetrical bidentate (chelate) coordination of the ligands. All the investigated compounds inhibited tumor cell growth *in vitro* in a dose-dependent manner both in wild type and in cisplatin-resistant cells of cervix carcinoma (C13 and A431Pt cell lines), with the complex  $[\text{Cu}(\text{ESDT})_2]$  (**Figure 6.4 a**) resulting the most active one with  $\text{IC}_{50} < 0.5 \mu\text{M}$  in all the tested human tumor cell lines [277].

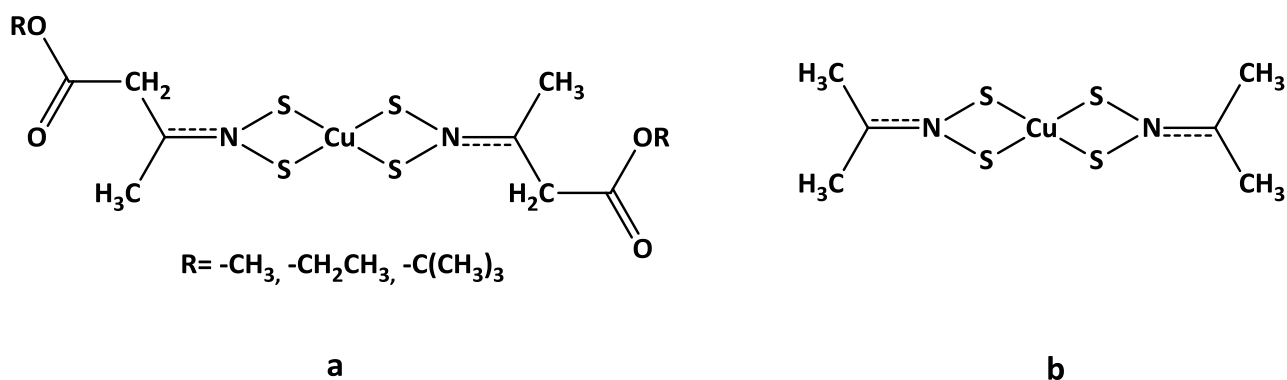


**Figure 6.4** Chemical structure of Cu(II) dithiocarbamate complexes recently investigated in our research group: the sarcosine ester compounds  $[\text{Cu}(\text{RSDT})_2]$  (RSDT= sarcosine ester dithiocarbamate, R= M (methyl), E (ethyl), T (*tert*-butyl) **a**, and dimethylamine derivative  $[\text{Cu}(\text{DMDT})_2]$  **b**.

### 6.3 Synthesis of the Cu(II) derivatives with selected cyclic *N,N*-disubstituted dithiocarbamate ligands

Overall, the evidence in literature, previously discussed, associating copper levels and species with tumor biochemistry suggest that the biological activity of copper complexes, found in the micromolar domain in

different studies, is mainly related to specific proteins, enzymes (*e.g.*, proteasome) or cellular pathways of paramount importance in cancer cell homeostasis. Consequently, in this PhD work, after the synthesis and physico-chemical characterization, we evaluated the *in vitro* cytotoxic activity of 5 DMSO-soluble complexes of copper(II) whose dithiocarbamate ligands involve different cyclic amines. The [Cu(PDT)<sub>2</sub>] complex was synthesized, characterized and biologically tested for comparison purposes.

### 6.3.1 Synthesis of Cu(II) dithiocarbamate complexes of PDT, PipeDTC, MorphDTC and IndolineDTC

The copper(II) complexes of the ligands PDT, PipeDTC, MorphDTC and IndolineDTC were obtained by dropwise addition of 1.7 mmol (2 eq) of the corresponding dithiocarbamate salt dissolved in methanol (5 mL) to a methanol solution containing 0.85 mmol of CuCl<sub>2</sub>·2H<sub>2</sub>O. The green cupric solution rapidly turned into brown with a precipitate immediately formed. The reaction mixture was let stir at room temperature for 30 minutes, then the precipitate was centrifuged, washed with water (2x 5mL), cold methanol (2x3 mL) and cold diethyl ether (2x3 mL). Finally, the obtained dark brown solid was dried *in vacuum* in the presence of P<sub>2</sub>O<sub>5</sub>.

#### *Bis(pyrrolidine dithiocarbamate)copper(II), [Cu(PDT)<sub>2</sub>]*

Aspect: brown solid

Yield: 83 %

R.f. (on silica gel, CH<sub>2</sub>Cl<sub>2</sub>): 0.90

Anal. Calc. for C<sub>10</sub>H<sub>18</sub>CuN<sub>2</sub>S<sub>4</sub> (MW = 356.05 g·mol<sup>-1</sup>): C 33.73; H 4.53; N 7.87; S 36.02. Found: C 33.83; H 4.22; N 7.33; S 35.94.

<sup>1</sup>H-NMR (CDCl<sub>3</sub>, 300.13 MHz): δ (ppm) = 4.47 (s br, 8H, H<sub>(3)</sub> + H<sub>(4)</sub>), 8.76 (s br, 4H, H<sub>(2)</sub> + H<sub>(5)</sub>).

Medium FT-IR (KBr):  $\tilde{\nu}$  (cm<sup>-1</sup>) = 2965.40, 2871.44 (ν<sub>a</sub>, C-H); 1497.92 (ν<sub>a</sub>, N-CSS); 947.33 (ν<sub>a</sub>, CSS).

Far FT-IR (nujol):  $\tilde{\nu}$  (cm<sup>-1</sup>) = 559.05 (ν<sub>s</sub>, CSS); 338.54 (ν<sub>a</sub>, Cu-S); 291.40 (ν<sub>s</sub>, Cu-S).

ESI-MS *m/z*, [M<sup>+</sup>] found (calc.): 354.95 (354.95).

#### *Bis(piperidine dithiocarbamate)copper(II), [Cu(PipeDTC)<sub>2</sub>]*

Aspect: dark brown solid

Yield: 90 %

R.f. (on silica gel, CH<sub>2</sub>Cl<sub>2</sub>): 0.92

Anal. Calc. for C<sub>12</sub>H<sub>20</sub>CuN<sub>2</sub>S<sub>4</sub> (MW = 384.11 g·mol<sup>-1</sup>): C 37.52; H 5.25; N 7.29; S 33.39. Found: C 37.54; H 4.77; N 7.10; S 33.18.

<sup>1</sup>H-NMR (CDCl<sub>3</sub>, 300.13 MHz): δ (ppm) = 0.33 (s, 4H, H<sub>(4)</sub>), 1.17 (s, 4H, H<sub>(3)</sub> + H<sub>(5)</sub>).

Medium FT-IR (KBr):  $\tilde{\nu}$  (cm<sup>-1</sup>) = 2941.17, 2850.28 (ν<sub>a</sub>, C-H); 1501.54 (ν<sub>a</sub>, N-CSS); 947.25 (ν<sub>a</sub>, CSS).

Far FT-IR (nujol):  $\tilde{\nu}$  (cm<sup>-1</sup>) = 563.41 (ν<sub>s</sub>, CSS); 353.57 (ν<sub>a</sub>, Cu-S); 291.76 (ν<sub>s</sub>, Cu-S).

ESI-MS  $m/z$ ,  $[M^+]$  found (calc.): 382.98 (382.98)

*Bis(morpholine dithiocarbamate)copper(II)*,  $[Cu(\text{MorphDTC})_2]$

Aspect: brown solid

Yield: 94 %

R.f. (on silica gel,  $\text{CH}_2\text{Cl}_2$ ): 0.42

Anal. Calc. for  $\text{C}_{10}\text{H}_{16}\text{CuN}_2\text{O}_2\text{S}_4$  (MW = 388.07  $\text{g}\cdot\text{mol}^{-1}$ ): C 30.95; H 4.16; N 7.22; S 33.05. Found: C 31.08; H 4.18; N 7.09; S 32.94.

Medium FT-IR (KBr):  $\tilde{\nu}$  ( $\text{cm}^{-1}$ ) = 2968.97, 2853.40 ( $\nu_a$ , C-H); 1485.33 ( $\nu_a$ , N-CSS); 1110.23 ( $\nu_a$ , C-O); 1010.40 ( $\nu_a$ , CSS).

Far FT-IR (nujol):  $\tilde{\nu}$  ( $\text{cm}^{-1}$ ) = 558.69 ( $\nu_s$ , CSS); 338.25 ( $\nu_a$ , Cu-S); 291.38 ( $\nu_s$ , Cu-S).

ESI-MS  $m/z$ ,  $[M^+]$  found (calc.): 386.94 (386.94).

*Bis(indoline dithiocarbamate)copper(II)*,  $[Cu(\text{IndolineDTC})_2]$

Aspect: dark brown solid

Yield: 94 %

R.f. (on silica gel): *n.a.*

Anal. Calc. for  $\text{C}_{18}\text{H}_{16}\text{CuN}_2\text{S}_4$  (MW = 452.14  $\text{g}\cdot\text{mol}^{-1}$ ): C 47.82; H 3.57; N 6.20; S 28.37. Found: C 47.33; H 3.37; N 5.99; S 28.27.

Medium FT-IR (KBr):  $\tilde{\nu}$  ( $\text{cm}^{-1}$ ) = 2923.89 ( $\nu_a$ , C-H); 1481.41 ( $\nu$ , C=C ring); 1422.33 ( $\nu_a$ , N-CSS); 1038.58 ( $\nu_a$ , CSS); 739.18 ( $\delta$ , C-H).

Far FT-IR (nujol):  $\tilde{\nu}$  ( $\text{cm}^{-1}$ ) = 556.43 ( $\nu_s$ , CSS); 343.83 ( $\nu_a$ , Cu-S); 271.35 ( $\nu_s$ , Cu-S).

ESI-MS  $m/z$ ,  $[M^+]$  found (calc.): 450.96 (450.95).

### 6.3.2 Synthesis of Cu(II) dithiocarbamate complexes of L-proline ester derivatives (ProOMeDTC and ProOtBuDTC)

The copper(II) derivatives of L-proline ester dithiocarbamates were obtained by adding dropwise 1.4 mmol (2 eq) of the dithiocarbamate salt dissolved in ethanol (5 mL) to an ethanol solution containing 0.70 mmol of  $\text{CuCl}_2\cdot 2\text{H}_2\text{O}$ . The cupric green solution turned rapidly into green/brown, and the mixture was let stir at room temperature for 30 minutes. Then, the solvent volume was reduced by half and the solution was placed at -20 °C for 12 hours, allowing the formation of a green/brown precipitate, which was centrifuged, and washed with water (2x 5mL) and *n*-pentane (3x3 mL). Finally, the obtained solid was dried under vacuum in the presence of  $\text{P}_2\text{O}_5$ .

*Bis(L-proline methyl ester dithiocarbamate)copper(II)*,  $[Cu(\text{ProOMeDTC})_2]$

Aspect: dark green solid

Yield: 80 %

R.f. (on silica gel, CH<sub>2</sub>Cl<sub>2</sub>): 0.50

Anal. Calc. for C<sub>14</sub>H<sub>20</sub>CuN<sub>2</sub>O<sub>4</sub>S<sub>4</sub> (MW = 472.13 g·mol<sup>-1</sup>): C 35.62; H 4.27; N 5.93; S 27.17. Found: C 35.83; H 4.13; N 5.81; S 27.47.

<sup>1</sup>H-NMR (CDCl<sub>3</sub>, 300.13 MHz): δ (ppm) = 2.11-2.93 (m, 8H, H<sub>(3)</sub> + H<sub>(4)</sub>), 3.94 (m, 6H, O-CH<sub>3</sub>).

Medium FT-IR (KBr):  $\tilde{\nu}$  (cm<sup>-1</sup>) = 2951.87 (v<sub>a</sub>, C-H); 1750.79 (v, C=O); 1471.56 (v<sub>a</sub>, N-CSS); 1153.76 (v<sub>a</sub>, C-OMe); 939.75 (v<sub>a</sub>, CSS).

Far FT-IR (nujol):  $\tilde{\nu}$  (cm<sup>-1</sup>) = 565.71 (v<sub>s</sub>, CSS); 342.87 (v<sub>a</sub>, Cu-S); 279.96 (v<sub>s</sub>, Cu-S).

ESI-MS *m/z*, [M<sup>+</sup>] found (calc.): 470.97 (470.96).

*Bis(L-proline tert-butyl ester dithiocarbamate)copper(II), [Cu(ProOtBuDTC)<sub>2</sub>]*

Aspect: brown solid

Yield: 74 %

R.f. (on silica gel, CH<sub>2</sub>Cl<sub>2</sub>): 0.72

Anal. Calc. for C<sub>20</sub>H<sub>32</sub>CuN<sub>2</sub>O<sub>4</sub>S<sub>4</sub> (MW = 556.29 g·mol<sup>-1</sup>): C 43.18; H 5.80; N 5.04; S 23.06. Found: C 43.42; H 5.92; N 4.90; S 23.21.

<sup>1</sup>H-NMR (CDCl<sub>3</sub>, 300.13 MHz): δ (ppm) = 1.57 (s, 18H, O-C(CH<sub>3</sub>)<sub>3</sub>), 1.99-2.83 (m, 8H, H<sub>(3)</sub> + H<sub>(4)</sub>).

Medium FT-IR (KBr):  $\tilde{\nu}$  (cm<sup>-1</sup>) = 2974.81 (v<sub>a</sub>, C-H); 1733.37 (v, C=O); 1469.68 (v<sub>a</sub>, N-CSS); 1148.53 (v<sub>a</sub>, C-OtBu); 930.08 (v<sub>a</sub>, CSS).

Far FT-IR (nujol):  $\tilde{\nu}$  (cm<sup>-1</sup>) = 568.57 (v<sub>s</sub>, CSS); 340.11 (v<sub>a</sub>, Cu-S); 276.11 (v<sub>s</sub>, Cu-S).

ESI-MS *m/z*, [M<sup>+</sup>] found (calc.): 555.06 (555.05).

### 6.3.3 Synthesis of Cu(II) dithiocarbamate complexes of aromatic *N*-heterocycles CDT, IndDTC, and PyrrDTC

The copper(II) complexes involving the aromatic ligands CDT, IndDTC and PyrrDTC were obtained by dropwise addition of 1.5 mmol (2 eq) of the dithiocarbamate salt (dissolved in 5 mL of tetrahydrofuran) to a solution containing 0.75 mmol of CuCl<sub>2</sub>·2H<sub>2</sub>O dissolved in THF. The cupric green solution quickly turned into black and a dark solid immediately precipitated. The reaction mixture was let stir at room temperature for 30 minutes, then the precipitate was centrifuged, and washed with water (5x 5mL), diethyl ether (3x3 mL) and *n*-hexane (3x3 mL). Finally, the obtained dark brown solid was dried in vacuum pump in the presence of P<sub>2</sub>O<sub>5</sub>.

*Bis(carbazole dithiocarbamate)copper(II), [Cu(CDT)<sub>2</sub>]*

Aspect: dark brown solid

Yield: 89 %



R.f. (on silica gel): *n.a.*

Anal. Calc. for  $C_{26}H_{16}CuN_2S_4$  (MW = 548.22  $g \cdot mol^{-1}$ ): C 56.96; H 2.94; N 5.11; S 23.40. Found: C 56.40; H 2.45; N 4.94; S 23.20.

Medium FT-IR (KBr):  $\tilde{\nu}$  ( $cm^{-1}$ ) = 3011.02 ( $\nu_a$ , C-H); 1485.75, 1446.99, 1435.70 ( $\nu$ , C=C ring); 1333.30 ( $\nu_a$ , N-CSS); 1038.66 ( $\nu_a$ , CSS); 843.59 ( $\omega$ , C-H); 743.78, 707.83 ( $\delta$ , C-H).

Far FT-IR (nujol):  $\tilde{\nu}$  ( $cm^{-1}$ ) = 595.47 ( $\nu_s$ , CSS); 412.14 ( $\nu_a$ , Cu-S); 346.20 ( $\nu_s$ , Cu-S).

ESI-MS  $m/z$ ,  $[M^+]$  found (calc.): 546.98 (546.95).

*Bis(indole dithiocarbamate)copper(II)*,  $[Cu(IndDTC)_2]$

Aspect: dark brown solid

Yield: 87 %

R.f. (on silica gel): *n.a.*

Anal. Calc. for  $C_{18}H_{12}CuN_2S_4$  (MW = 448.11  $g \cdot mol^{-1}$ ): C 48.25; H 2.70; N 6.25; S 28.62. Found: C 48.07; H 2.31; N 6.14; S 28.85.

Medium FT-IR (KBr):  $\tilde{\nu}$  ( $cm^{-1}$ ) = 3046.82 ( $\nu_a$ , C-H); 1445.35, 1388.04 ( $\nu$ , C=C ring); 1333.98 ( $\nu_a$ , N-CSS); 1017.17 ( $\nu_a$ , CSS); 847.19 ( $\omega$ , C-H); 749.97, 730.36 ( $\delta$ , C-H).

Far FT-IR (nujol):  $\tilde{\nu}$  ( $cm^{-1}$ ) = 591.13 ( $\nu_s$ , CSS); 413.37 ( $\nu_a$ , Cu-S); 340.40 ( $\nu_s$ , Cu-S).

ESI-MS  $m/z$ ,  $[M^+]$  found (calc.): 446.94 (446.92).

*Bis(pyrrole dithiocarbamate)copper(II)*,  $[Cu(PyrroleDTC)_2]$

Aspect: dark brown solid

Yield: 88 %

R.f. (on silica gel,  $CH_2Cl_2$ ): 0.86

Anal. Calc. for  $C_{10}H_8CuN_2S_4$  (MW = 347.99  $g \cdot mol^{-1}$ ): C 34.51; H 2.32; N 8.05; S 36.86. Found: C 34.61; H 2.29; N 8.08; S 36.68.

Medium FT-IR (KBr):  $\tilde{\nu}$  ( $cm^{-1}$ ) = 3131.02 ( $\nu_a$ , C-H); 1472.85, 1409.66 ( $\nu$ , C=C ring); 1333.66 ( $\nu_a$ , N-CSS); 1012.56 ( $\nu_a$ , CSS); 836.97 ( $\omega$ , C-H); 729.40 ( $\delta$ , C-H).

Far FT-IR (nujol):  $\tilde{\nu}$  ( $cm^{-1}$ ) = 591.99 ( $\nu_s$ , CSS); 411.07 ( $\nu_a$ , Cu-S); 338.87 ( $\nu_s$ , Cu-S).

ESI-MS  $m/z$ ,  $[M^+]$  found (calc.): 346.90 (346.89).

## 6.4 Discussion

### 6.4.1 Considerations on the synthetic route and X-ray structural characterization

By reaction of the selected cyclic dithiocarbamate salts and  $CuCl_2$  in a 2:1 ligand-to-metal molar ratio, new  $[Cu(DTC)_2]$  complexes were obtained wherein the dithiocarbamate ligands coordinate the metal center

through both sulfur atoms. Such stoichiometry and the chelating coordination of the DTC ligands were confirmed by elemental analysis and by X-ray crystallography (crystal structures solved for the L-proline esters and piperidine derivatives (**Figure 6.5**)).

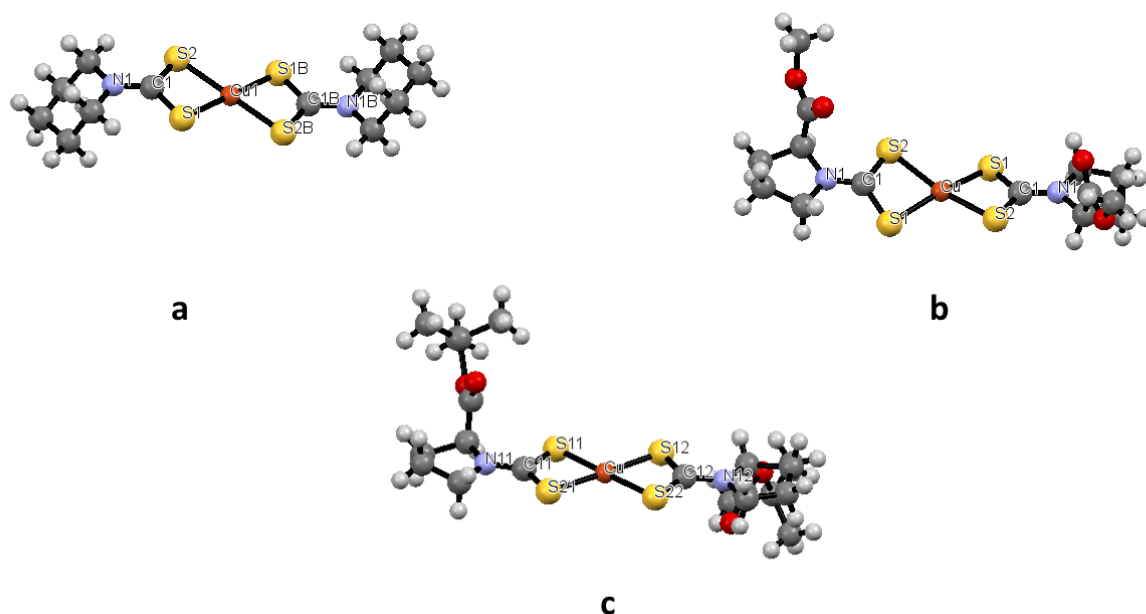


**Figure 6.5** ORTEP drawing of [Cu(PipeDTC)<sub>2</sub>] **a**, [Cu(ProOMeDTC)<sub>2</sub>] **b**, and [Cu(ProOtBuDTC)<sub>2</sub>] **c**. The compounds were crystallized from CH<sub>2</sub>Cl<sub>2</sub>/Et<sub>2</sub>O solutions.

	Cu-S1 (Å)	Cu-S2 (Å)	S1-C1 (Å)	S2-C1 (Å)	C1-N1 (Å)	S1-Cu-S2 (°)	S1-Cu-S1 (°)
[Cu(PipeDTC) <sub>2</sub> ]	2.304	2.284	1.717	1.731	1.338	77.66	102.34
[Cu(ProOMeDTC) <sub>2</sub> ]	2.305	2.285	1.713	1.714	1.303	78.10	103.59
[Cu(ProOMeDTC) <sub>2</sub> ]	2.303	2.309	1.758	1.649	1.328	76.50	103.90
	2.290	2.380	1.732	1.697	1.330	77.26	102.35

**Table 6.1:** Selected bond lengths and angles of the crystallized Cu(II) dithiocarbamate complexes.

[Cu(PipeDTC)<sub>2</sub>] (**a**) crystallizes according to the P 2<sub>1</sub>/c space group, [Cu(ProOMeDTC)<sub>2</sub>] (**b**) adopts the P 2<sub>1</sub> 2<sub>1</sub> 2 group, and finally [Cu(ProOtBuDTC)<sub>2</sub>] (**c**) the C 2 group. The structures presented in **Figure 6.5** show a distorted square planar (SP) geometry for the complexes **a** and **c**, with a planarity not limited to the MS<sub>4</sub> core but also including the C-N bond. On the other hand, the derivative **b** is nearly tetrahedral. The deviation from a perfect SP coordination is due to the small bite angle of the DTC ligand. The collected bond lengths as well as angles are in agreement with data presented in literature [278]. In particular, the S-C bond lengths are

shorter than the single-bond length (generally 1.69 Å, accounting for a partial double bond character). Similarly, this occurs also for the C-N bond, confirming the higher contribution of the thioureidic form (see **Section 4.4.3**) for this type of ligands (piperidine and L-proline ester dithiocarbamates). Finally, in [Cu(PipeDTC)<sub>2</sub>] the central atom lies on an inversion center, while for Cu(II)-proline ester dithiocarbamate compounds the ligands arrange the methyl and *tert*-butyl substituents on the same plane [279].

The Cu(II) derivatives of aliphatic DTC ligands, are soluble in most common organic solvents (*e.g.*, ethanol, chloroform, dichloromethane, dimethyl sulfoxide), whereas the copper(II) complexes involving aromatic *N*-heterocyclic DTC ligands (*i.e.*, CDT, IndDTC and PyrrDTC) and indolineDTC, first synthesized by Bereman in 1970s [141], showed very low solubility in all solvents except pyridine.

#### 6.4.2 ESI-MS analysis

In ESI-MS spectra the presence of copper(II)-dithiocarbamates is confirmed by two different signal patterns, as reported by Cummings and coworkers in the study of [Cu(DEDTC)<sub>2</sub>] [280]. One is ascribed to the *in situ* formation of the species [Cu<sup>I</sup>(DTC) + H<sup>+</sup>], whereas the other is associated with the oxidation of the metal center, thus turning out the [Cu<sup>III</sup>(DTC)<sub>2</sub>]<sup>+</sup> derivative.

Regarding the [Cu(DTC)<sub>2</sub>] complexes synthesized in this work, the ESI-MS spectra of those with cyclic aliphatic dithiocarbamates (the only soluble in methanol or acetonitrile) displayed an intense pattern perfectly matching with the *m/z* of the species [Cu<sup>III</sup>(DTC)<sub>2</sub>]<sup>+</sup> and the copper isotopic abundance (<sup>63</sup>Cu and <sup>65</sup>Cu, 69.17% and 30.83% respectively).

The spectra of [Cu(ProOMeDTC)<sub>2</sub>] and [Cu(ProOtBuDTC)<sub>2</sub>] (**Figure 6.6**) are shown below as an example.

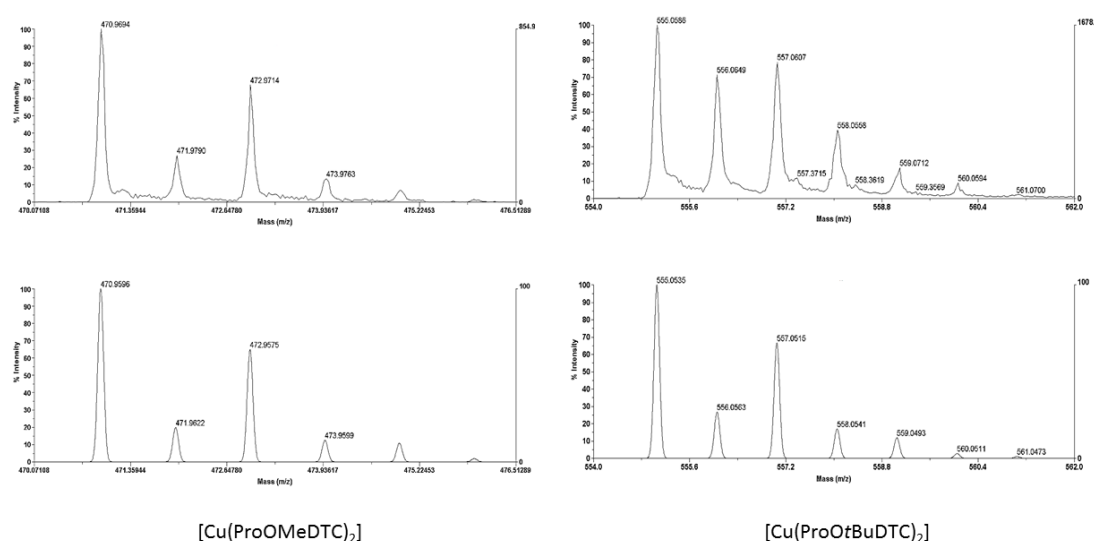


**Figure 6.6** ESI-MS spectra (positive ion mode) of [Cu(ProOMeDTC)<sub>2</sub>] (**left**) and [Cu(ProOtBuDTC)<sub>2</sub>] (**right**) in methanol. In both cases, the experimental data (top) fit perfectly the mass spectrum simulation for species of the type [Cu<sup>III</sup>(DTC)<sub>2</sub>]<sup>+</sup> (down).

6.4.3  $^1\text{H-NMR}$  characterization

The synthesized copper(II) derivatives with PDT, PipeDTC, and L-proline ester DTCs as ligands have been characterized also by means of  $^1\text{H-NMR}$  spectroscopy (300.13 MHz, 298 K, see **Supporting Information C**). It is worth noting that the poor solubility of the aromatic compounds as well as the IndolineDTC and MorphDTC copper(II) complexes in the common deuterated solvents, hampered this instrumental analysis. The assignments of the resonances (**Table 6.2**) were guided by the comparison between the spectra of the obtained complexes with those of the corresponding ligands (see **Section 4.4.2**), also taking into account the paramagnetic nature of the Cu(II).

	$H_{(1)}$	$H_{(2)}$	$H_{(3)}$	$H_{(4)}$	$H_{(5)}$	$H_{(6)}$	OMe	OtBu
[Cu(PDT) $_2$ ]	<i>n.d.</i>	<b>8.76</b>	4.47	4.47	<b>8.76</b>	-	-	-
[Cu(PipeDTC) $_2$ ]	<i>n.d.</i>	<i>n.d.</i>	1.17	0.33	1.17	<i>n.d.</i>	-	-
[Cu(ProOMeDTC) $_2$ ]	<i>n.d.</i>	<i>n.d.</i>	2.11- 2.93	2.11- 2.93	<i>n.d.</i>	-	3.94	-
[Cu(ProOtBuDTC) $_2$ ]	<i>n.d.</i>	<i>n.d.</i>	1.99- 2.83	1.99- 2.83	<i>n.d.</i>	-	-	1.57

**Table 6.2** List of the proton chemical shifts (ppm) of the Cu(II) derivatives of PDT, PipeDTC and L-proline ester DTCs. The  $H$ -signals proximal to the dithiocarbamic moiety are labeled with bold font; *n.d.* stands for “not detected”. Attribution was carried out according to the IUPAC nomenclature for  $N$ -heterocyclic compounds. All the spectra were recorded in  $\text{CDCl}_3$  with a 300.13 MHz spectrometer at 298 K.

The  $^1\text{H-NMR}$  spectrum of each [Cu(DTC) $_2$ ] complex resulted affected by the paramagnetism associated with the  $d^9$  electronic configuration of the metal center. A brief description of this effect was presented in **Section 5.4.3**, and the observable consequences are the hyperfine shifts ( $\delta$ ) to NMR signals and the shortening of both nuclear longitudinal ( $T_1$ ) and transverse ( $T_2$ ) relaxation times [281]. The shift and low intensity observed for methylene protons  $H_{(2)}$  and  $H_{(5)}$  in [Cu(PDT) $_2$ ] ( $\delta = 8.76$  ppm) is the evidence of the first. On the other hand, the signals of the  $\alpha$ -protons of the Cu(II) derivatives involving PipeDTC and L-proline ester DTCs as ligands completely disappear, whereas the resonances of the previously mentioned  $H_{(2)}$  and  $H_{(5)}$  in [Cu(PDT) $_2$ ] result very broad, near the limit of detection. This phenomenon is related to the relaxation times, and in particular, it strictly depends on the electronic relaxation time ( $\tau_s$ ) of the paramagnetic metal center [281]. When the value of  $\tau_s$  is short enough (*e.g.*, Ru(III) possesses a  $\tau_s$  in the domain of  $10^{-11}$  s $^{-1}$ ) the NMR analysis returns information-containing signals which are not too broad, as in the case of Ru(DTC) $_3$  complexes [282]. However, for mononuclear copper(II) complexes ( $S = \frac{1}{2}$ ), the ground state is well isolated from excited states, thus not providing efficient electronic relaxations. This generally leads to long  $\tau_s$  values ( $10^{-8} - 10^{-9}$  s $^{-1}$ ) that broad the  $^1\text{H-NMR}$  resonances, sometimes under the detection limit [283].

In contrast, the Cu(II) paramagnetism affects to a lesser extent the ester protons of both proline derivatives, whose peak is less broadened with respect to the other resonances within the same coordination compound, being the –OR group (R= methyl, *tert*-butyl) spatially more distant from the metal center. The presence of this signal confirms the absence of hydrolysis side-reactions during the synthesis of [Cu(DTC)<sub>2</sub>] complexes.

Concerning the aromatic class of copper derivatives, due to their low solubility in common deuterated solvents, an attempt of <sup>1</sup>H-NMR analysis was carried out using pyridine-d<sub>6</sub> as a deuterated solubilizing agent. However, since the pyridine (py) can form five-coordinated adducts of the type [Cu(py)(DTC)<sub>2</sub>] by apical coordination [284], the synthesized Cu(II)-DTC complexes of aromatic amines were dissolved in a 60:40 mixture of CDCl<sub>3</sub>/pyridine-d<sub>6</sub>. In fact, chloroform was shown to form a hydrogen bond with pyridine, thus avoiding the formation of the penta-coordinated adduct without preventing solubilizing properties of pyridine [285]. Nevertheless, the attribution of the <sup>1</sup>H-NMR signals was hampered by the presence of pyridine intense residual solvent resonances, as well as by the low intensity of the aromatic signals, due to the paramagnetic broadening of Cu(II) and the small amount of solubilized [Cu(DTC)<sub>2</sub>] complex.

#### 6.4.4 FT-IR characterization

The FT-IR spectra of all Cu(II)-DTC derivatives have been collected (**Supporting Information H**) in both the medium (4000-600 cm<sup>-1</sup>) and far (600-200 cm<sup>-1</sup>) wavenumber domain, and the diagnostic absorptions are reported in **Table 6.3**.

	$\nu(\text{C=O})$	$\nu(\text{C=C})$	$\nu(\text{N-CSS})$	$\nu_a(\text{C-O})$	$\nu_a(\text{CSS})$	$\omega(\text{C-H})$	$\delta(\text{C-H})$	$\nu_s(\text{CSS})$	$\nu_a(\text{Cu-S})$	$\nu_s(\text{Cu-S})$
[Cu(PDT) <sub>2</sub> ]	-	-	1498 cm <sup>-1</sup>	-	947 cm <sup>-1</sup>	-	-	559 cm <sup>-1</sup>	339 cm <sup>-1</sup>	291 cm <sup>-1</sup>
[Cu(PipeDTC) <sub>2</sub> ]	-	-	1502 cm <sup>-1</sup>	-	947 cm <sup>-1</sup>	-	-	563 cm <sup>-1</sup>	354 cm <sup>-1</sup>	292 cm <sup>-1</sup>
[Cu(MorphDTC) <sub>2</sub> ]	-	-	1485 cm <sup>-1</sup>	1110 cm <sup>-1</sup>	1010 cm <sup>-1</sup>	-	-	559 cm <sup>-1</sup>	338 cm <sup>-1</sup>	291 cm <sup>-1</sup>
[Cu(IndolineDTC) <sub>2</sub> ]	-	1481 cm <sup>-1</sup>	1422 cm <sup>-1</sup>	-	1039 cm <sup>-1</sup>	-	739 cm <sup>-1</sup>	556 cm <sup>-1</sup>	344 cm <sup>-1</sup>	271 cm <sup>-1</sup>
[Cu(ProOMeDTC) <sub>2</sub> ]	1751 cm <sup>-1</sup>	-	1472 cm <sup>-1</sup>	1154 cm <sup>-1</sup>	940 cm <sup>-1</sup>	-	-	566 cm <sup>-1</sup>	343 cm <sup>-1</sup>	280 cm <sup>-1</sup>
[Cu(ProOtBuDTC) <sub>2</sub> ]	1733 cm <sup>-1</sup>	-	1470 cm <sup>-1</sup>	1149 cm <sup>-1</sup>	930 cm <sup>-1</sup>	-	-	569 cm <sup>-1</sup>	340 cm <sup>-1</sup>	276 cm <sup>-1</sup>
[Cu(CDT) <sub>2</sub> ]	-	1486, 1447, 1436 cm <sup>-1</sup>	1333 cm <sup>-1</sup>	-	1039 cm <sup>-1</sup>	844 cm <sup>-1</sup>	744, 708 cm <sup>-1</sup>	595 cm <sup>-1</sup>	412 cm <sup>-1</sup>	346 cm <sup>-1</sup>
[Cu(IndDTC) <sub>2</sub> ]	-	1445, 1388 cm <sup>-1</sup>	1334 cm <sup>-1</sup>	-	1017 cm <sup>-1</sup>	847 cm <sup>-1</sup>	750, 730 cm <sup>-1</sup>	591 cm <sup>-1</sup>	413 cm <sup>-1</sup>	340 cm <sup>-1</sup>
[Cu(PyrrDTC) <sub>2</sub> ]	-	1473, 1410 cm <sup>-1</sup>	1334 cm <sup>-1</sup>	-	1013 cm <sup>-1</sup>	837 cm <sup>-1</sup>	729 cm <sup>-1</sup>	592 cm <sup>-1</sup>	411 cm <sup>-1</sup>	339 cm <sup>-1</sup>

**Table 6.3** Collection of the fundamental IR-vibrations (4000-200 cm<sup>-1</sup>) of the analyzed Cu(II)-DTC complexes.

Similarly, to the Ru(III)-DTC derivatives (**Section 5.4.4**), the IR spectra of copper(II)-dithiocarbamate derivatives contain three fundamental IR-regions, corresponding to the following stretching vibration modes ( $\nu$ ) [209, 210]:

- backbone  $\nu(\text{SSC-N})$  vibration, between 1200 and 1550  $\text{cm}^{-1}$ ;
- $\nu_a(\text{C-S})$  vibration between 950 and 1050  $\text{cm}^{-1}$  and  $\nu_s(\text{C-S})$  vibration between 550 and 650  $\text{cm}^{-1}$ ;
- $\nu(\text{Cu-S})$  vibration between 270 and 420  $\text{cm}^{-1}$ .

First of all, concerning the  $\nu(\text{SSC-N})$  vibration, the Cu-DTC derivatives display the same trend observed for the corresponding dithiocarbamate ligands and the Ru(III)-DTC compounds. Indeed, moving from PDT and PipeDTC complexes to proline and indoline derivatives, then to the Cu(II) complexes involving aromatic ligands, the  $\nu(\text{SSC-N})$  shifts to lower energies. In particular, for the analyzed Cu(II) dithiocarbamate complexes, comparing the energy of the  $\nu(\text{SSC-N})$  vibration, the following series is obtained:



This trend runs parallel to the ability of the nitrogen atom to shift its lone pair towards the C-N bond. Thus, in the copper-coordinated PDT, PipeDTC, MorphDTC and proline dithiocarbamates, the thioureido form is predominant. This behavior has been confirmed also by X-ray crystallography on single crystals of the Cu-DTC complexes previously presented (**Section 6.4.1**), with the distances C-N close to that of a double bond (**Table 6.1**). On the contrary, taking into account dithiocarbamates where resonance effects are relevant (*i.e.*, IndolineDTC and mainly aromatic DTCs), the dithiocarbamic form is associated with a larger contribution, generating  $\nu(\text{SSC-N})$  frequencies associated with to a single C-N bond.

On passing from the IR spectra of the synthesized Cu(II) complexes to those of their corresponding free ligands, a shift in the  $\nu(\text{N-CSS})$  band towards lower energies could be observed (**Table 6.4**). This behavior can be explained by the electron-withdrawing effect of the transition metal on the dithiocarbamate (effect on  $\sigma$  bonds), along with a further shift of the nitrogen lone pair toward the -CSS moiety ( $\pi$  contribution) occurring for this class of aliphatic compounds, overall resulting in an increased C-N bond order. Such shift toward higher wavenumbers is smaller for aromatic derivatives, including the indolineDTC complex, if compared to the aliphatic ones.

The nature of the effect generated by the DTC substituent on the ability of the nitrogen atom to share its lone pair can account for this evidence. In fact, ligands associated with a higher  $\Delta\nu$  ( $>70 \text{ cm}^{-1}$ ) involve only inductive effects (here PyrrDTC is an exception), whereas dithiocarbamates with lower  $\Delta\nu$  ( $\approx 50 \text{ cm}^{-1}$ ) experience mainly resonance effects. The first can be overtaken by the electron-withdrawing effect of the transition metal, while the latter cannot, due to the ligand aromaticity which prevents the nitrogen lone pair from being shared within SSC-N bond.

	$\nu(\text{SSC-N})$ Cu(II) complex	$\nu(\text{SSC-N})$ free DTC ligand	$\Delta\nu$ ( $\text{cm}^{-1}$ )
[Cu(PDT) <sub>2</sub> ]	1498 $\text{cm}^{-1}$	1422 $\text{cm}^{-1}$	76
[Cu(PipeDTC) <sub>2</sub> ]	1502 $\text{cm}^{-1}$	1417 $\text{cm}^{-1}$	85
[Cu(MorphDTC) <sub>2</sub> ]	1485 $\text{cm}^{-1}$	1410 $\text{cm}^{-1}$	75
[Cu(IndolineDTC) <sub>2</sub> ]	1422 $\text{cm}^{-1}$	1371 $\text{cm}^{-1}$	51
[Cu(ProOMeDTC) <sub>2</sub> ]	1472 $\text{cm}^{-1}$	1392 $\text{cm}^{-1}$	80
[Cu(ProOtBuDTC) <sub>2</sub> ]	1470 $\text{cm}^{-1}$	1388 $\text{cm}^{-1}$	82
[Cu(CDT) <sub>2</sub> ]	1333 $\text{cm}^{-1}$	1281 $\text{cm}^{-1}$	52
[Cu(IndDTC) <sub>2</sub> ]	1334 $\text{cm}^{-1}$	1290 $\text{cm}^{-1}$	44
[Cu(PyrrDTC) <sub>2</sub> ]	1334 $\text{cm}^{-1}$	1259 $\text{cm}^{-1}$	75

**Table 6.4** SSC-N frequencies in the Cu(II)-DTC complexes compared to the corresponding free dithiocarbamate ligands.

A higher  $\nu(\text{SSC-N})$  is generally accompanied by a lower  $\nu_a(\text{CSS})$  mode, based on the influence of the thioureidic or dithiocarbamic form on Cu<math>\langle S \rangle</math>C ring, as stated for the Ru(III) analogs in **Section 5.4.4**. It is worth highlighting that the band assigned to the C-S stretching is not a pure vibration but is generally coupled with bending modes of the -NCS moiety  $\delta(\text{NCS})$  [286]. In general, this trend is respected in the presented Cu(II)-DTC complexes, and as examples it is possible to observe the asymmetric stretching frequencies of [Cu(PDT)<sub>2</sub>] and [Cu(PipeDTC)<sub>2</sub>], being lower (947  $\text{cm}^{-1}$ ), compared to that of [Cu(CDT)<sub>2</sub>] (1039  $\text{cm}^{-1}$ ). For the former, the metal-to-sulfur back-donation is less favored than the latter, because of the presence of electron density on low-energy *d* orbitals of S, in turn originated from nitrogen lone pair shift (canonical thioureidic form of PDT and PipeDTC). Thus, the metal-sulfur bond is stronger in the aromatic compounds than the aliphatic ones, in agreement with the presence of metal-to-ligand retrodonation and, hence, a multiple M-S bond order for the class of aromatic complexes. On the other hand, it is worth noting that the nature of the aliphatic substituents affects to a lesser extent the M-S stretching frequency, as well as the nature of the aromatic N-heterocycle, in agreement with XPS results presented in literature [287]. Indeed, **Table 6.3** shows how the derivatives belonging to the category of aliphatic derivatives are associated with near the same Cu-S stretching frequencies. The same is also for complexes of CDT, IndDTC and PyrrDTC, although they possess higher values (stronger M-S bond).

In conclusion, some intense bands remain to be discussed and are related to the ligand backbone. Firstly, two absorptions are visible in the spectra of the ProOMeDTC and ProOtBuDTC copper derivatives at 1752 and 1734  $\text{cm}^{-1}$ , respectively, and are ascribed to the stretching of the ester moiety. Other characteristic bands of the organic backbone are visible with medium or weak intensity in the ranges 1200-1800  $\text{cm}^{-1}$  (C-C) for aliphatic derivatives, and 1500-1400  $\text{cm}^{-1}$  (C=C) for aromatic ones. Finally, some C-H vibrations, typical of aromatic rings, have been identified between 700 and 850  $\text{cm}^{-1}$ , being related to the C-H wagging ( $\omega$ ) and bending out of the plane of the ring ( $\delta$ ) [288].

## 6.4.5 UV-Vis characterization

Electronic absorption studies were carried out on soluble copper-dithiocarbamate complexes (*i.e.*, [Cu(PDT)<sub>2</sub>], [Cu(PipeDTC)<sub>2</sub>], [Cu(ProOMeDTC)<sub>2</sub>], and [Cu(ProOtBuDT)<sub>2</sub>]) by mean of UV-Vis spectrophotometry in CH<sub>2</sub>Cl<sub>2</sub> (800-240 nm) at 25 °C, and the diagnostic absorptions are summarized in **Table 6.5**.

	$\lambda$ ( $\epsilon$ , $M^{-1} cm^{-1}$ )				
	<i>band I</i>	<i>band II</i>	<i>band III</i>	<i>band IV</i>	<i>band V</i>
[Cu(PDT) <sub>2</sub> ]	269 nm (27004)	287 nm (14432)	453 nm (10760)	512 nm (2199) <sup>sh</sup>	614 nm (771)
[Cu(PipeDTC) <sub>2</sub> ]	272 nm (29246)	285 nm (17565)	436 nm (11314)	495 nm (3760) <sup>sh</sup>	604 nm (872)
[Cu(ProOMeDTC) <sub>2</sub> ]	270 nm (25646)	292 nm (13990)	435 nm (9788)	506 nm (1996) <sup>sh</sup>	617 nm (620)
[Cu(ProOtBuDTC) <sub>2</sub> ]	270 nm (27232)	291 nm (14805)	435 nm (10361)	509 nm (2060) <sup>sh</sup>	627 nm (646)

**Table 6.5** UV-visible spectral data (800-240 nm) of soluble Cu(II) dithiocarbamate complexes in CH<sub>2</sub>Cl<sub>2</sub> at 25 °C; sh= shoulder.

All the analyzed complexes proved stable in CH<sub>2</sub>Cl<sub>2</sub> solution for at least 10 days, as no significant spectral changes were observed. The recorded spectra of Cu(II)-DTC derivatives are reported in **Figure 6.7**.

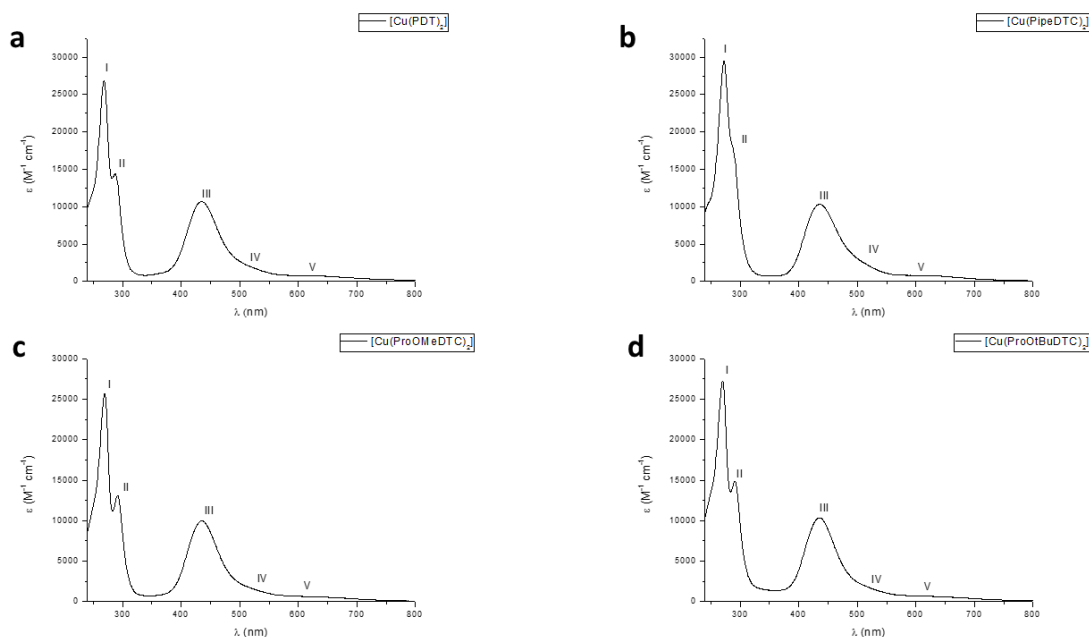


**Figure 6.7** UV-Vis spectra of [Cu(PDT)<sub>2</sub>] **a**, [Cu(PipeDTC)<sub>2</sub>] **b**, [Cu(ProOMeDTC)<sub>2</sub>] **c**, and [Cu(ProOtBuDTC)<sub>2</sub>] **d** in CH<sub>2</sub>Cl<sub>2</sub> at 25 °C.



According to the **Figure 6.7** and **Table 6.5**, the UV-Vis spectra in  $\text{CH}_2\text{Cl}_2$  of the synthesized aliphatic dithiocarbamate complexes show the *band I* at about 260 nm and the *band II* at around 290 nm, ascribed to the  $\pi^* \leftarrow \pi$  absorption in the -NCSS group, and the intraligand  $\pi^* \leftarrow \pi$  transition located in the -CSS moiety, respectively [215, 289]. In particular, analyzing the wavelengths related to the band II in **Table 6.5**, a red shift is observed on passing from PDT and PipeDTC derivatives (*ca.* 285 nm) to ProlineDTC (*ca.* 290 nm) counterparts. This behavior has been associated with a combination of inductive and hyperconjugation effects by ester groups, thus turning out an electron delocalization towards the chromophores [290].

The discussion on the *bands III-IV* needs a brief theoretical introduction on the electronic spectra of Cu(II) complexes. Indeed, as mentioned in **Section 6.1**, Cu(II) is able to form complexes with a large variety of geometries. In particular, the Jahn-Teller effect for this ion ( $d^9$  electronic configuration) rules out regular  $O_h$  and  $T_d$  symmetries in favor of distorted structures, unless rigid and sterically-demanding ligands are present [291]. In the distorted symmetries (*i.e.*,  $D_{4h}$  and  $D_{2d}$ ), three different  $d-d$  absorption bands could be observed in the UV-Vis range whereas octahedral and tetrahedral geometries give rise to only one electronic transition (respectively, the  $E_g \leftarrow T_{2g}$  and the  $T_{2g} \leftarrow E_g$ ) (**Figure 6.8**) [150]. Moreover, its  $d^9$ -electronic configuration allows also the use of the positive hole formalism. In this method, the excitation of the electronic hole, instead of that of electrons, is taken into account, thus simplifying both the prevision and assignment of the UV-Vis bands [150]. As a result, UV-Vis transitions are easily obtained for any geometry simply reversing the energetic order of the  $d$  orbitals.

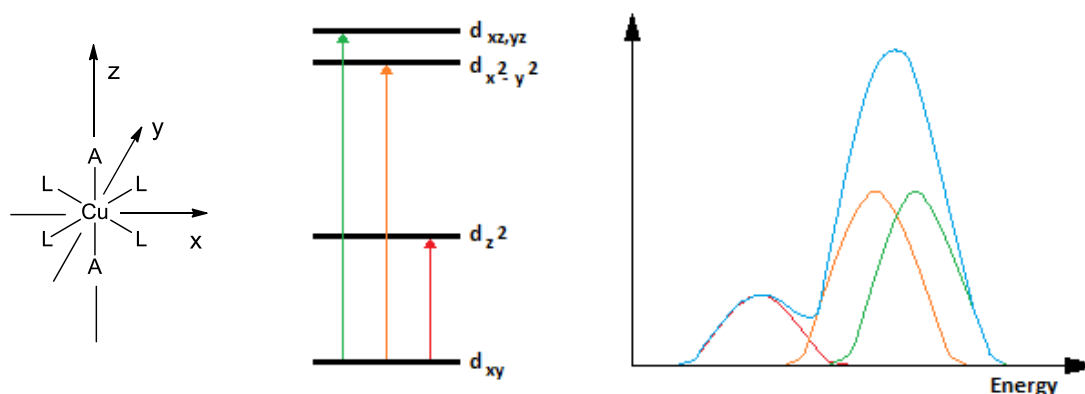


**Figure 6.8** Schematic representation of  $d-d$  transitions for a  $D_{2h}$  symmetry using the positive hole formalism.

Concerning Cu(II)-dithiocarbamates of aliphatic amines, their electronic spectra have been firstly rationalized by Choi using bis(di-isopropyl)dithiocarbamate)copper(II) in DMSO as a model compound. Starting from an ideal  $D_{2h}$  geometry for the metal center (**Figure 6.8**), Choi and co-workers were able to calculate the energy sequence of the  $d$ -orbitals as  $d_{xy} > d_{z^2} > d_{x^2-y^2} > d_{xz,yz}$ . Based on these findings and on the positive hole formalism, the band occurring at lower energies was attributed to a  $d_{z^2} \leftarrow d_{xy}$  absorption, while the  $d_{x^2-y^2}$

$\leftarrow d_{xy}$  and the  $d_{xz,yz} \leftarrow d_{xy}$  transitions are detectable at lower wavelengths and are partly overlapped, resulting in a broad band (**Figure 6.8**) [292].

With respect to the band intensities,  $d-d$  absorptions in a  $D_{2h}$  symmetry should show a low molar extinction coefficient due to their forbidden character as defined by the Laporte rule [293]. Starting from this postulate, the high intensity of the band associated with the  $d_{x^2-y^2} \leftarrow d_{xy}$  and the  $d_{xz,yz} \leftarrow d_{xy}$  transitions led Choi *et al.* to hypothesize that some kind of distortion in the  $D_{2h}$  geometry may occur. On the other hand, the Cu(II) center in a  $C_{2v}$  symmetry, wherein it is lifted out of the plane of the four sulfur atoms, would make the  $d_{xz,yz} \leftarrow d_{xy}$  transition allowed according to the group theory, contrary to the other two transitions, still forbidden [292]. In light of this, in the 350-600 nm region, the *band III* is ascribable to  $d_{xz,yz} \leftarrow d_{xy}$  transition, combined with either a metal-to-ligand charge transfer (MLCT) or a ligand-to-metal charge transfer (LMCT), whereas the *band IV* and *band V* are assigned to the lowest energy  $d-d$  transitions  $d_{x^2-y^2} \leftarrow d_{xy}$  and  $d_{z^2} \leftarrow d_{xy}$ , respectively.

This discussion here reported has been drafted taking into account copper(II)-dithiocarbamate derivatives in non-coordinating solvents (*e.g.*,  $CH_2Cl_2$ ), hence tetra-coordinate in a distorted tetrahedral geometry. Conversely, if considering coordinating media, such as DMSO and water (**Section 8.8.4**), a different coordination sphere and geometry (octahedral) is expected due to the apical coordination of the solvent molecules. In this context, no sensible spectral changes are observed in terms of maximum wavelengths and shape on passing from apolar non-coordinating solvents to polar coordinating ones (**Figure 8.26**). The main change is the intensity decrease of the *band II* in the presence of water and DMSO (1 % v/v), the only transition experiencing the coordination of apical ligands.

## 7. GOLD DITHIOCARBAMATES

### 7.1 Gold: an exogenous metal towards striking opportunities in medicinal inorganic chemistry

Gold is the most noble metal and its properties yield peculiar features at the bio-chemical level which are exploitable in a great number of applications. Nowadays, after silicon, gold is probably the most frequently used element in nanoscale science. Moreover, in recent years, its solution chemistry ranges from catalysis to medicinal inorganic chemistry [294]. In the following section, a brief introduction on the atomic and chemical features of gold will be given, followed by some examples of gold-based complexes studied for their use in medicine.

#### 7.1.1 The chemistry of Gold

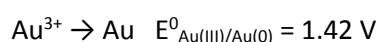
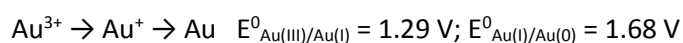
Gold (Au) is the 79<sup>th</sup> element of the periodic table and belongs to the 11<sup>th</sup> group and the 3<sup>rd</sup> row of transition metals, with a [Xe]4f<sup>14</sup>5d<sup>10</sup>6s<sup>1</sup> electronic configuration. Thus, compounds with gold in oxidation state +1 are endowed with a closed-shell configuration 5d<sup>10</sup>. When gold(0) is dissolved in powerful oxidants (*aqua regia*, bromine, and chlorine), Au(III) derivatives are obtained (and also Au(V) with fluorine). Intriguingly, gold is able to form stable compounds in the oxidation state -1 (*auride anion*), as in the case of cesium auride CsAu, thus pointing out that gold has got high electron affinity (2.039 eV) [295]. The chemistry of this element, as well as some bulk properties (*i.e.*, its bright yellow color), can be ascribed to the pronounced presence of *relativistic effects*, resulting in i) *s-orbital contraction*, ii) *spin-orbit splitting* of energetic levels, and iii) *d-orbital expansion* [296, 297]. To explain these phenomena, first of all we have to consider the starting point of the special theory of relativity, stating that it is impossible to accelerate particles to speeds higher than *c* (speed of light in vacuum, *ca.* 3.00 · 10<sup>8</sup> m s<sup>-1</sup>):

$$m = m_0 / \sqrt{1 - (v/c)^2}$$

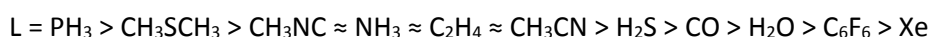
Indeed, for  $v = c$ , the mass  $m$  would become infinite. Since the average radial velocity of the electrons in the  $1s$  shell of an element is proportional to its atomic number, when  $Z > 72$  (post-lanthanoid atoms) electrons move around the atomic core in a highly positive electric field, causing them to have velocities approaching that of the light [298]. The first consequence is a clear contraction of  $s$ -type orbitals (remembering that the radius is inversely proportional to the mass of the electron), with the  $p$ -type ones contracting as well. This points out the high electron affinity of gold, due to the high stabilization of the  $6s$  orbital, associated with the formation of the auride anion. Moreover, in a relativistic treatment, neither the orbital angular momentum  $l$  nor the spin angular momentum  $s$  of an electron are “good” quantum numbers, but only the vector sum  $j$  is ( $\vec{j} = \vec{l} + \vec{s}$ ). Thus, for a  $p$ -type electron ( $l = 1$ ), two values of  $j$  are possible, namely  $j = 1/2$  or  $3/2$ . The energetic splitting between these two  $j$  values is a relativistic effect and may raise up to a few electronvolts for the valence electrons of the heaviest elements [297, 299]. Finally,  $d$ -type orbitals (and in the same manner  $f$ -type

ones) undergo indirect relativistic effects. Indeed, since the *s* and *p* atomic orbitals (AOs) are contracted, they screen the nuclear attraction more efficiently. Consequently, *d* and *f* AOs experience a weaker attraction, expand radially, and are destabilized energetically [297]. On this basis, the yellow color of bulk gold can be ascribed to the small gap between the full 5*d* band (expanded orbitals) and the Fermi level of the half-filled 6*s*-band (contracted orbitals), which would be much larger for the non-relativistic set of orbitals [300].

These relativistic effects influence the chemistry of this element. In particular, the molecular chemistry of gold is dominated by the complexes involving the oxidation states +1 and +3, ruled by the following standard electrochemical potentials ( $E^0$ ), which are the highest among metals [158]:



The gold(I) center ( $5d^{10}$  electronic configuration) is generally found two-coordinated with a linear coordination geometry, although also trigonal planar or tetrahedral complexes are reported. The ligands can be neutral (L) or anionic ( $X^-$ ), thus resulting in species of the type  $[\text{L-Au}^I\text{-X}]$ ,  $[\text{X-Au}^I\text{-X}]^-$ , and  $[\text{L-Au}^I\text{-L}]^+$ . Moreover, taking into account the reaction  $\text{Au(I)} + \text{L} \rightarrow [\text{AuL}]^+$ , the experimental and calculated gold-ligand strength varies according the following series:



It is worth highlighting that the ability of Au(I) to accept two or more ligands (*e.g.*,  $[\text{AuL}_4]^+$ ,  $[\text{AuX}_3]^{2-}$ ) shows the special situation of gold valence orbitals experiencing relativistic effects, and it is a clear variance with respect to the features of Cu(I) and Ag(I) [295, 301].

On the other hand, the Au(III) complexes ( $5d^8$  electron configuration) require a square planar coordination geometry. The ready access to the highest oxidation state of gold can be rationalized on the basis of relativistic effects. Indeed, with expanded 5*d* and contracted 6*s* valence orbitals separated by a small energy gap, and with modified spin-orbit coupling effects, hybrid orbitals are suitable for the construction of strong bonds in square planar configurations [295].

Moreover, it should be mentioned that some gold compounds with the metal center in the +2 oxidation state are described in literature. They were first reported in 1980s and proved stable only at very low temperature (-78 °C) using chelating soft ligands, such as dithiocarbamates. These Au(II)-DTC complexes are generally synthesized by oxidative addition from dinuclear Au(I)-DTCs, treating them at -78 °C with 1 eq of  $\text{Br}_2$  and  $\text{I}_2$  or pseudo-halides such as  $(\text{SCN})_2$  and  $(\text{SeCN})_2$  [302]. In light of this, the Au(II) oxidation state could be considered as an intermediate in the oxidation process of  $[\text{Au}^I_2(\text{DTC})_2]$  complexes to  $[\text{Au}^{III}\text{X}_2(\text{DTC})]$  ( $X = \text{Cl}, \text{Br}$ ), if the reaction previously described is carried out at room temperature or under reflux [303].

### 7.1.2 Gold in medicine and its potential therapeutic application as anticancer agent

The earliest applications of gold in medicine took place in China starting from 2500 B.C., when it was used as colloidal gold or in alloy with other heavy metals to treat furuncles, skin ulcers, and to remove mercury from

skin [304]. With the growing knowledge about the elements and their reactivity, alchemists explored different ways to produce “potable gold”, and in the 17<sup>th</sup> century AuCl<sub>3</sub> (produced by oxidation of bulk gold with *aqua regia*) was usually swallowed, previous dissolution in water, although the resulting solution was corrosive. Then, in 19<sup>th</sup> century scientists discovered that gold(III) chloride dissolved in NaCl solution resulted less caustic and, at the same time, it proved efficient in the treatment of syphilis [305]. In 1890 Robert Koch discovered the *in vitro* bacteriostatic properties of gold, founding that a solution of gold cyanide at a concentration of 0.5 ppm can inhibit the growth of the tubercule bacillus [306]. However, clinicians generally ignored these findings until the success of Ehrlich’s new chemotherapeutic agent Salvarsan (**Figure 1.2 a**). Indeed, this important discovery paved the way to the modern research in the field of inorganic medicinal chemistry, leading to the development of the clinically-established gold(I)-based anti-arthritis drugs (see **Section 1.1**) [75]. In particular, since the 1930s, gold(I) thiolates such as aurothiomalate (Myocrysine, **Figure 1.2 b**) have been widely used for the treatment of rheumatoid arthritis (the so-called *Chrysotherapy*), and in 1979 auranofin (Ridaura, **Figure 1.2 c**) was introduced in the pharmacopoeia with the significant advantage of oral administration. To date, chrysotherapy still represents an effective option for the treatment of severe forms of arthritis, although it is being progressively replaced by the so-called biological drugs [307]. Concerning the mechanism of action of this class of drugs, it is commonly accepted that gold-based drugs are “thiol-reactive species” and act as inhibitors of a number of proteases (mostly cysteine proteases), involved in the progression of rheumatoid arthritis [308, 309]. Moreover, auranofin and some related gold complexes are strong inhibitors of the mammalian thioredoxin reductases (TrxR), both in the cytosol and in the mitochondria [310]. Due to its antioxidant properties, the TrxR system protects cells from oxidative stress, which is a key factor in DNA damage. Moreover, TrxR is overexpressed in several human tumor cell lines, and potent chemotherapeutics, such as cisplatin and carmustine (1,3-bis(2-chloroethyl)-1-nitrosurea), are inhibitors of this enzyme [311]. Overall, since the drug auranofin was identified as a TrxR inhibitor and it is nowadays under clinical trial investigation as antiproliferative agent (*e.g.*, for the treatment of lung cancers, leukemia and ovarian cancer), in recent years researchers have explored the antiproliferative properties of many gold(I)/(III) derivatives [312-314]. Indeed, only in the last five years, 22 patents have been filed to protect gold compounds with promising biomedical therapeutic properties [315]. Concerning anticancer gold(I) complexes, most of the derivatives presented in literature contain a thiolate group (S<sup>-</sup>) and/or a phosphine ligand, designed and developed starting from the structure and activity of auranofin. For these compounds, a strong anticancer activity against lung cancer was observed *in vivo*, especially in the case of aurothioglucose (ATG, **Figure 7.1 a**), an analogue of aurothiomalate [316]. Moreover, it is worth noting that the intramuscular injection of sodium aurothiomalate produces lysosomes (*aurosomes*) characterized by particle and granule-studded electron-dense membranous formations with a rod-like structure [317]. This behavior could be associated with a reduction of the Au(I) ion to Au(0) in the cell, generating inert species responsible for the low toxicity of these drugs [318]. On the other hand, the significant cytotoxic activity of the four coordinated

gold(I)-phosphine product  $[\text{Au}(\text{dppe})_2]\text{Cl}$  (dppe= bis(diphenylphosphino)ethane, **Figure 7.1 b**) was counterbalanced by severe heart toxicity in dogs and rabbits, probably caused by high lipophilicity and reactivity, which led to mitochondrial dysfunction [319]. After exploring different ligands to develop new anticancer gold(I) complexes, the electron-donating NHC ligand (*N*-heterocyclic carbene) was studied to form  $[\text{Au}(\text{NHC})_2]\text{Cl}$  derivatives (**Figure 7.1 c**). NHC forms strong metal-C bonds, and these Au(I) compounds showed micromolar antiangiogenic and antiproliferative activity *in vivo*. In particular, these products inhibited the TrxR system, as well as they induced mitochondrial membrane permeabilization (MMP) [320], a release of proteins from the intermembrane space of mitochondria, defined as the pivotal event in the apoptotic process [321]. Finally, the versatility and the great ability of the gold(I) center to interact with different donor-atoms, led to the development of other Au(I)-alkynyl-phosphino  $[\text{Au}(\text{PR}_3)(\text{alkynyl})]$  and Au(I)-thiourea complexes (**Figure 7.1 d, e** respectively). Both gold(I) derivatives inhibited the TrxR system and demonstrated *in vivo* anticancer activity against human tumors inoculated in mice [322, 323].

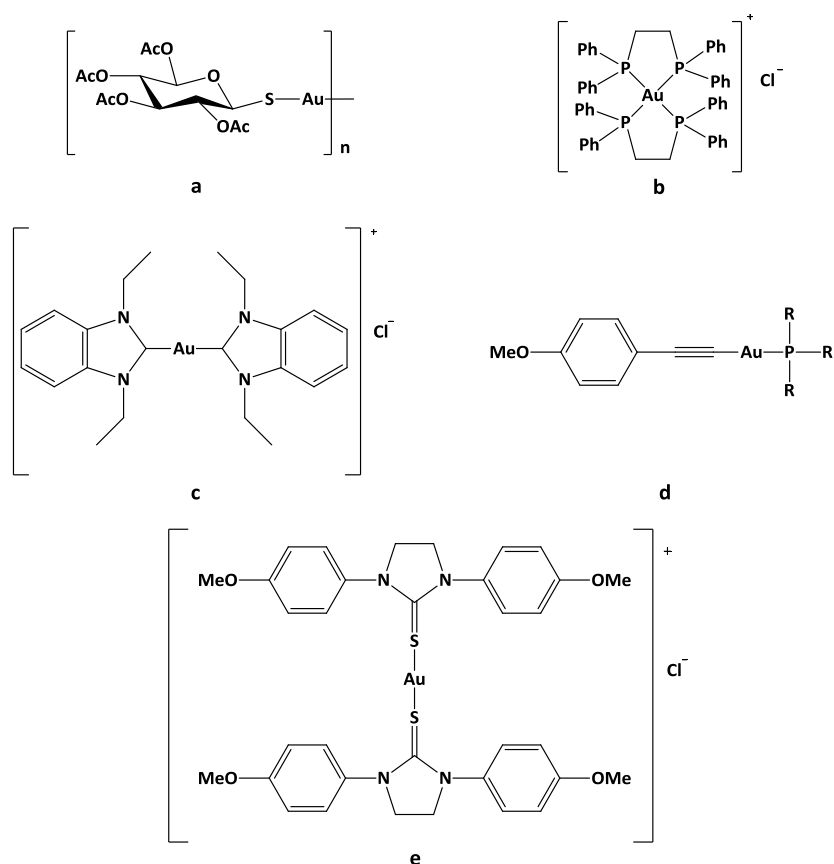


**Figure 7.1** Chemical structure of some gold(I) derivatives with proved anticancer effects against human tumors, both *in vitro* and *in vivo*: aurothioglucose (ATG) **a**, the four coordinated gold(I)-phosphine product  $[\text{Au}(\text{dppe})_2]\text{Cl}$  (dppe= bis(diphenylphosphino)ethane) **b**, the gold(I)-NHC derivatives (*N*-heterocyclic carbene) of the type  $[\text{Au}(\text{NHC})_2]\text{Cl}$  **c**, the alkynyl compounds  $[\text{Au}(\text{PR}_3)(\text{alkynyl})]$  (R= -Ph, -2-fuyl, PTA, -CH<sub>3</sub>, -CH<sub>2</sub>CH<sub>3</sub>) **d**, and the thiourea derivative  $[\text{Au}(\text{thiourea})_2]\text{Cl}$  **e**.

Concerning gold(III)-based complexes, it is worth underlining that they appear natural alternatives to platinum(II)-based drugs, since Au(III) is isoelectronic with Pt(II) ( $d^8$  electronic configuration) and these two ions share the same coordination geometry, square planar (SP) [324]. However, DNA seems not to be the main target of this class of gold compounds [325]. As an example, studies on the bipyridine complex  $[\text{Au}(\text{bipy})(\text{OH})_2][\text{PF}_6]$  (**Figure 7.2 a**) indicated that the interaction of the compound with DNA is weak and reversible [326]. Moreover, some porphyrin derivatives of the type  $[\text{Au}(\text{TPP})]\text{Cl}$  (TPP= tetraphenylporphyrin, **Figure 7.2 b**) showed nanomolar activity against cisplatin-resistant cancer cell lines, being indicative of a molecular mechanism different from cisplatin [327]. In particular, similarly to the case of gold(I) derivatives, for these compounds the inhibition of TrxR system was observed, [314]. On the other hand, the research of a class of ligands able to better stabilize Au(III) in physiological environment compared to porphyrins, led to the development of the two C-deprotonated C<sup>N</sup>C and C<sup>N</sup> coordinating systems derived from 2,6-diphenylpyridine and 2-[(dimethylamino)methyl]-phenyl (damp), respectively (**Figure 7.2 c, d**) [328, 329]. Both the ligands prevented the reduction  $\text{Au(III)} \rightarrow \text{Au(I)}$  under physiological conditions. These complexes displayed promising tumor growth inhibition in animal models, associated with toxicity studies that revealed a lethal dose (LD) in mice between 9.0 and 13.5 mg kg<sup>-1</sup> upon single i.v. administration. The TrxR system resulted again inhibited by both types of complexes, leading to mitochondria dysfunction induced by reactive oxygen species [314]. This intracellular target seems to be involved also in the cytotoxic activity of Au(III)-NHC complexes of the type  $[\text{AuL}(\text{NHC})]\text{OTf}$  (L= 2,6-(bis-imidazol-2-yl)pyridine, (**Figure 7.2 e**). In particular, these compounds undergo physiological reduction with L release (reaction experimentally monitored by fluorescence analysis of L), and generation of the active species Au(I)-NHC [330].

Contrary to the previously described Au(III) complexes, based on C- and N-donor ligands, despite of the “harder” Lewis acid character of Au(III) than Au(I), gold(III)-based derivatives were developed with S-donor atoms, mainly with dithiocarbamates as ligands (see **Section 7.2**), in light of the borderline “hard-soft” nature of this oxidation state [331]. These complexes demonstrated an excellent *in vitro* and *in vivo* antiproliferative activity against cisplatin-resistant tumors, and an excellent toxicological profile [332, 346]. Moreover, the Au(III)-DTC complex  $[\text{AuBr}_2(\text{DMDT})]$  (**Figure 7.2 f**) was demonstrated to inhibit the TrxR activity, due to its irreversible binding to the enzyme catalytic site, as well as the proteasomal chymotrypsin-like activity *in vivo* [333].

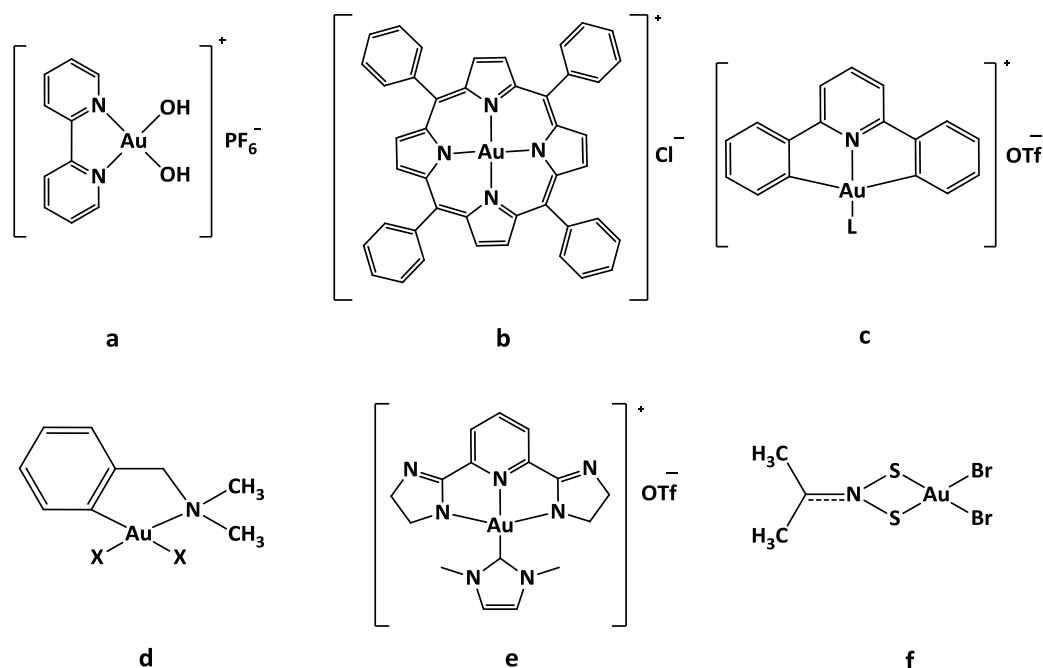


**Figure 7.2** Chemical structure of some gold(III) complexes with cytotoxic potential against human tumor cell lines: the bipyridine complex  $[\text{Au}(\text{bipy})(\text{OH})_2][\text{PF}_6]$  **a**, the porphyrin derivative  $[\text{Au}(\text{TPP})]\text{Cl}$  (TPP= tetraphenylporphyrin) **b**, the gold(III) compound derived from C-deprotonated ligands of the type  $\text{C}^{\wedge}\text{N}^{\wedge}\text{C}$ ,  $[\text{Au}(\text{C}^{\wedge}\text{N}^{\wedge}\text{C})\text{L}]\text{OTf}$ , ( $\text{C}^{\wedge}\text{N}^{\wedge}\text{C}$ = 2,6-diphenylpyridine; L= pyridine,  $\text{PPh}_3$ , methyl-1*H*-imidazole, NHC) **c**, the analogue derived from C-deprotonated ligands of the type  $\text{C}^{\wedge}\text{N}$ ,  $[\text{AuX}_2(\text{damp})]$  (X= Cl, OAc, DTC, malonato; damp= 2-[(dimethylamino)methyl]-phenyl ligand) **d**, the Au(III)-NHC complexes  $[\text{AuL}(\text{NHC})]\text{OTf}$  (L= 2,6-(bis-imidazol-2-yl)pyridine) **e**, and the Au(III)-DTC complex  $[\text{AuBr}_2(\text{DMDT})]$  **f**.

## 7.2 Gold(III) dithiocarbamates as anticancer agents

The first synthesis of gold-dithiocarbamate complexes is undefinable but, in a seminal paper of 1907, Delepine reported the synthesis of a range of aliphatic DTC salts and also their derivatives of some transition metals, including gold [334]. Afterwards, between 1930 and 1949, Gibson and coworkers synthesized many mono- and dialkyl-gold derivatives derived from trivalent gold with coordination number 4 [335]. However, the chemistry of this class of compounds was deeply investigated only in the 1960s by a group of Dutch scientists at the Universities of Nijmegen and Utrecht [336-339], and more recently by Preti and coworkers in 1980s [340]. In particular, the former synthesized both gold(I) and gold(III) dithiocarbamate derivatives, observing that the addition of DTC ligand to an Au(III) precursor according to different stoichiometries, led to different species (**Figure 7.3**). To better understand this behavior, we can consider the simple addition of an equivalent of DTC ligand to an aqueous solution of  $\text{NaAu}^{\text{III}}\text{Cl}_4$ . Immediately a precipitate forms, made up of two different species: the neutral  $[\text{Au}^{\text{III}}\text{X}_2(\text{DTC})]$  and the ionic  $[\text{Au}^{\text{III}}(\text{DTC})_2]^+[\text{Au}^{\text{III}}\text{X}_4]^-$  (**Figure 7.3 a**). Moreover, the dissolution of this mixture in a halogenated solvent (*e.g.*,  $\text{CH}_2\text{Cl}_2$ ) leads to the conversion of the ionic complex to neutral one (**Figure 7.3 b**). Finally, the pure species  $[\text{Au}^{\text{III}}\text{X}_2(\text{DTC})]$  can be synthesized using an adequate precursor or by oxidative addition of halogen ( $\text{Cl}_2$  and  $\text{Br}_2$ ) to the corresponding Au(I)-DTC precursor (**Figure 7.3 c**). To obtain the ionic complex  $[\text{Au}^{\text{III}}(\text{DTC})_2]\text{X}$ , 1 equivalent of DTC ligand should be added to the



$[\text{AuX}_2(\text{DTC})]$  (**Figure 7.3 d**). Both species  $[\text{Au}^{\text{III}}\text{X}_2(\text{DTC})]$  and  $[\text{Au}^{\text{III}}(\text{DTC})_2]^+$  involve a near square-planar geometry with a  $S_4$  coordination core characterized by a small bite angle of the DTC ligand [338].

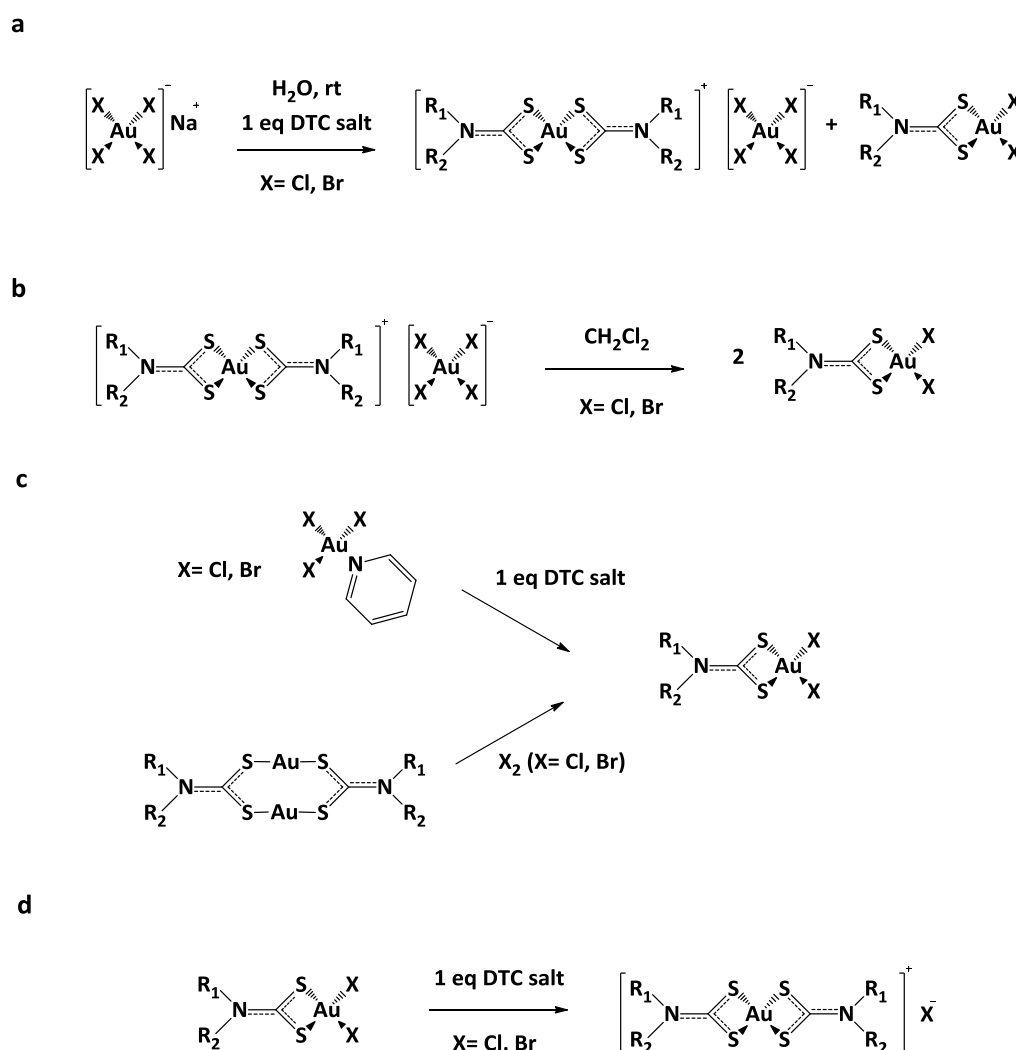


**Figure 7.3** Classes of syntheses involving gold(III) and the DTC ligand: the aqueous synthesis using  $\text{NaAu}^{\text{III}}\text{Cl}_4$  leads to the generation of the neutral  $[\text{Au}^{\text{III}}\text{X}_2(\text{DTC})]$  and the ionic  $[\text{Au}^{\text{III}}(\text{DTC})_2]^+[\text{Au}^{\text{III}}\text{X}_4]^-$  species **a**, and the latter could be converted to the first in halogenated solvents **b**. There is the possibility to obtain pure species: in the case of the neutral complex, one can use  $\text{AuX}_3\text{py}$  ( $\text{X} = \text{Cl}, \text{Br}$ ;  $\text{py} = \text{pyridine}$ ) + 1 equivalent of DTC salt, or a reaction of oxidative addition of  $\text{X}_2$  ( $\text{X} = \text{Cl}, \text{Br}$ ) to the gold(I) complex  $[\text{Au}^{\text{I}}_2(\text{DTC})_2]$  **c**; on the other hand, the ionic complex of the type  $[\text{Au}^{\text{III}}(\text{DTC})_2]\text{X}$  is synthesized by addition of 1 equivalent of DTC ligand to  $[\text{Au}^{\text{III}}\text{X}_2(\text{DTC})]$  **d**.

The interest in these compounds grew in our research group because they combine the anticancer properties of the Au(III) center with the stabilizing properties of the dithiocarbamates [341, 342]. As a proof of this, the standard reduction potential of the couple Au(III)-Au(0) passes from 1.002 V for  $[\text{AuCl}_4]^-$  to -0.22 V for  $[\text{Au}(\text{DMDT})_2]^+$  [343], consistent with a large stabilization of the +3 oxidation state upon coordination with DTC ligands. Our first generation of compounds of the type  $[\text{AuBr}_2(\text{DTC})]$  (DTC= DMDT **Figure 7.2 f**, ESDT, **Figure 7.4 a**) were tested *in vitro* for their antiproliferative activity against numerous human tumor cell lines,

and they proved cytotoxic also against cisplatin-resistant cancers, recording IC<sub>50</sub> values in most cases lower than 10 μM. Moreover, *in vivo* studies with mice bearing androgen-resistant prostate cancer (PC3 cells) demonstrated the efficacy of [AuBr<sub>2</sub>(DMDT)] causing a 85% tumor reduction after every other day s.c. injection of 1 mg kg<sup>-1</sup> of complex for 19 days [344]. In addition, these complexes were well tolerated by animals, as confirmed by toxicological studies in rodents, which displayed no renal toxicity, no histopathological changes in the observed most important organs, with a LD<sub>50</sub>= 30 mg kg<sup>-1</sup> [345].

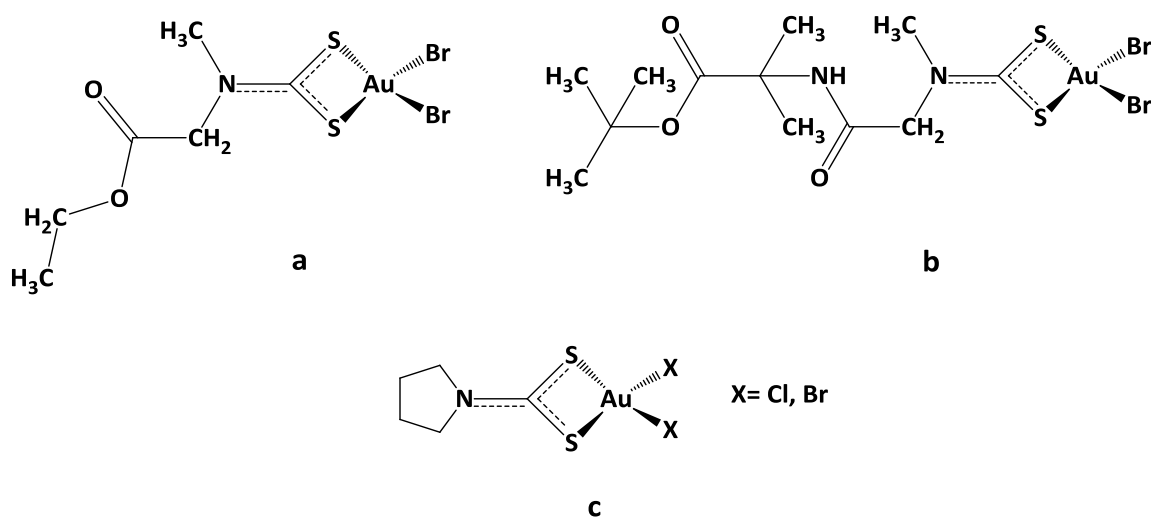


**Figure 7.4** Chemical structures of investigated Au(III) neutral dithiocarbamate complexes: the sarcosine ethyl ester compound of the “first generation” [AuBr<sub>2</sub>(ESDT)] **a**, the representative “second generation” peptidomimetic derivative [AuBr<sub>2</sub>(A<sub>1</sub>A<sub>2</sub>DTC)] where A<sub>1</sub>= sarcosine and A<sub>2</sub>= 2-amino-isobutyric *tert*-butyl ester, a non-natural amino acid **b**, and the [AuX<sub>2</sub>(PDT)] complex (X= Cl, Br) **c**.

Our second generation of gold(III)-DTC derivatives is related to complexes of the type [AuBr<sub>2</sub>(A<sub>1</sub>A<sub>2</sub>DTC)] where A<sub>1</sub>A<sub>2</sub>DTC stands for an esterified peptide dithiocarbamate (A<sub>1</sub>= sarcosine; A<sub>2</sub>= glycine or 2-amino-isobutyric *tert*-butyl ester, **Figure 7.4 b**) [346]. These compounds were indeed designed to achieve cancer-selective drug delivery and improved intracellular transfer, by exploiting the transporters PEPT1 and PEPT2, mammalian membrane proteins responsible for the cellular uptake of di- and tri-peptides and peptide-like drugs, being overexpressed in certain types of tumors [347]. Their anticancer activity was tested *in vitro* towards the human “orphan tumors” triple-negative breast cancer (MDA-MB-231 cell line) and castration resistant prostate cancer (PC3 cell line), with IC<sub>50</sub> values (72-h treatment) in the low micromolar range. Then, *in vivo* experiments in mice showed a 53% of tumor growth inhibition compared to control in the case of the breast cancer (1 mg kg<sup>-1</sup> day<sup>-1</sup> after a 27-day treatment), whereas a 70 % inhibition was recorded against the prostate cancer (2 mg kg<sup>-1</sup> every other day for 19 days). As observed for the first-generation compounds, no toxicity or histologically-observable side effects were observed in the major organs [332, 348].

Concerning the mechanism of action of Au(III)-DTC derivatives, the complexes of both the first and second generation are able to inhibit the activity of 20S and 26S proteasome in highly metastatic MDA-MB-231 cancer cells, *in vitro* and *in vivo*, resulting in the accumulation of ubiquitinated proteins [349]. Moreover, the

investigated complexes are able to reduce the thioredoxin reductase activity and generate free radicals, thus modifying some mitochondrial functions [350]. Finally, in a recent paper, we demonstrated that novel  $[\text{AuX}_2(\text{PDT})]$  complexes ( $\text{X} = \text{Cl}, \text{Br}$ , **Figure 7.4 c**) elicit oxidative stress with effects on the permeability transition pore, whose opening is related to cell death [139].

### 7.3 Synthesis of the Au(I)/(III) derivatives with the selected cyclic *N,N*-disubstituted dithiocarbamate ligands

According to the previously reported observations on  $[\text{AuX}_2(\text{PDT})]$  complexes, in this PhD work we aimed to evaluate the influence of the cyclic ligand structure on the cytotoxic activity of different dithiocarbamate derivatives of gold(III).

The  $[\text{Au}^{\text{III}}\text{X}_2(\text{DTC})]$  complexes with  $\text{X} = \text{Cl}, \text{Br}$  (**Figure 7.5 a**) have been synthesized by oxidative addition of halogen to the corresponding Au(I)-DTC precursor of the type  $[\text{Au}^{\text{I}}_2(\text{DTC})_2]$  (**Figure 7.5 b**). The  $[\text{AuX}_2(\text{PDT})]$  complex has been synthesized, characterized and tested *in vitro* under the same experimental conditions for comparison purposes. Moreover, in the case of PipeDTC, the ionic complexes  $[\text{Au}^{\text{III}}(\text{DTC})_2]\text{X}$  ( $\text{X} = \text{Cl}^-, \text{Br}^-$ ,  $[\text{AuBr}_2]^-$ ,  $[\text{AuCl}_4]^-$ , **Figure 7.5 c**) were also synthesized for gaining further insights in terms of biological activity.

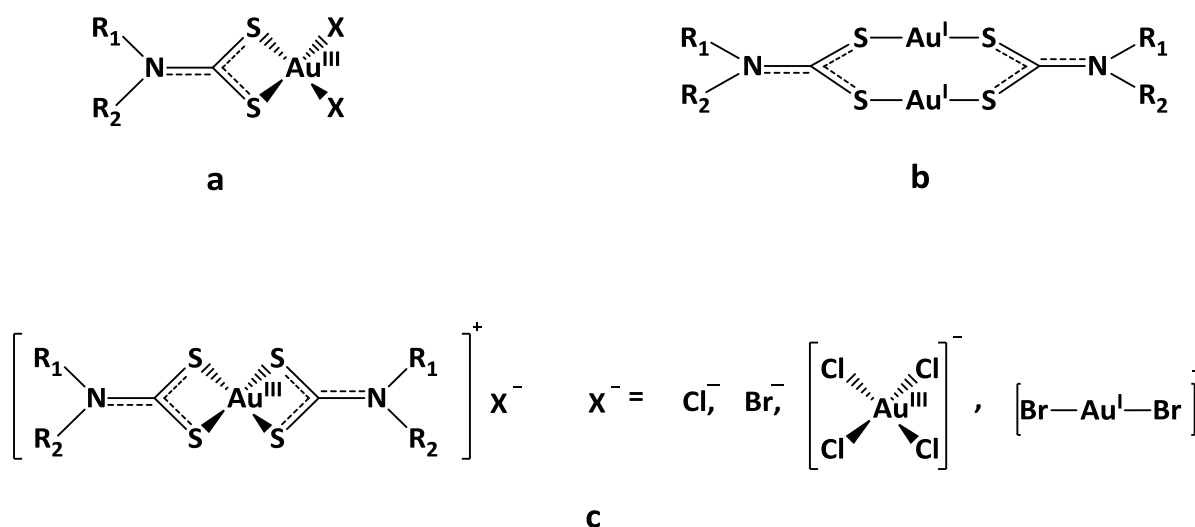


**Figure 7.5** Chemical drawing of the synthesized Au(I)/(III)-DTC complexes,  $[\text{Au}^{\text{III}}\text{X}_2(\text{DTC})]$  complexes with  $\text{X} = \text{Cl}, \text{Br}$  **a**, Au(I)-DTC derivatives of the type  $[\text{Au}^{\text{I}}_2(\text{DTC})_2]$  **b**, and the ionic compound  $[\text{Au}^{\text{III}}(\text{DTC})_2]\text{X}$  ( $\text{X} = \text{Cl}^-, \text{Br}^-$ ,  $[\text{AuBr}_2]^-$ ,  $[\text{AuCl}_4]^-$ ) **c**.

#### 7.3.1 Synthesis of Au(I) complexes with the selected cyclic *N,N*-disubstituted dithiocarbamate ligands, $[\text{Au}^{\text{I}}_2(\text{DTC})_2]$

The gold(I) complexes of the ligands PDT, PipeDTC, MorphDTC, IndolineDTC, ProOMeDTC, ProOtBuDTC, CDT, IndDTC and PyrrDTC were obtained starting from a gold(I) solution, freshly prepared by dissolving 1 mmol of  $\text{NaAuCl}_4 \cdot 2\text{H}_2\text{O}$  in NaCl saturated water (10 mL) followed by reduction  $\text{Au}(\text{III}) \rightarrow \text{Au}(\text{I})$  with 1 mmol of  $\text{Na}_2\text{SO}_3$  at 0 °C under stirring. When the solution turned from orange (Au(III)) into colorless (Au(I)), immediately 1

mmol (1 eq) of the dithiocarbamate salt, dissolved in water (5 mL), was added, leading to the instantaneous formation of an orange solid which for aliphatic derivatives turned into light green or marron (depending on the nature of the ligand) by few minutes. The mixture was left under vigorous stirring for 5 minutes, and then the precipitate was centrifuged, washed three times with 5mL of water and dried *in vacuo* in the presence of P<sub>2</sub>O<sub>5</sub>.

*Bis(pyrrolidine dithiocarbamate)digold(I), [Au<sub>2</sub>(PDT)<sub>2</sub>]*

Aspect: green-yellow solid

Yield: 91 %

R.f. (on silica gel): *n.a.*

Anal. Calc. for C<sub>10</sub>H<sub>16</sub>Au<sub>2</sub>N<sub>2</sub>S<sub>4</sub> (MW = 686.44 g·mol<sup>-1</sup>): C 17.50; H 2.35; N 4.08; S 18.68. Found: C 17.45; H 2.33; N 4.09; S 18.88.

<sup>1</sup>H-NMR (DMSO-d<sub>6</sub>, 300.13 MHz): δ (ppm) = 1.80 (m, 8H, H<sub>(3)</sub> + H<sub>(4)</sub>), 3.48 (m, 8H, H<sub>(2)</sub> + H<sub>(5)</sub>).

Medium FT-IR (KBr):  $\tilde{\nu}$  (cm<sup>-1</sup>) = 2963.93, 2866.22 (ν<sub>a</sub>, C-H); 1428.25 (ν<sub>a</sub>, N-CSS); 953.75 (ν<sub>a</sub>, CSS).

Far FT-IR (nujol):  $\tilde{\nu}$  (cm<sup>-1</sup>) = 558.78 (ν<sub>s</sub>, CSS); 451.04 (ν<sub>a</sub>, Au-S).

*Bis(piperidine dithiocarbamate)digold(I), [Au<sub>2</sub>(PipeDTC)<sub>2</sub>]*

Aspect: green-yellow solid

Yield: 98 %

R.f. (on silica gel): *n.a.*

Anal. Calc. for C<sub>12</sub>H<sub>20</sub>Au<sub>2</sub>N<sub>2</sub>S<sub>4</sub> (MW = 714.49 g·mol<sup>-1</sup>): C 20.17; H 2.82; N 3.92; S 17.95. Found: C 20.20; H 2.82; N 3.99; S 17.89.

<sup>1</sup>H-NMR (DMSO-d<sub>6</sub>, 600 MHz): δ (ppm) = 0.85 (m, 12H, H<sub>(3)</sub> + H<sub>(4)</sub> + H<sub>(5)</sub>), 4.13 (m, 8H, H<sub>(2)</sub> + H<sub>(6)</sub>).

Medium FT-IR (KBr):  $\tilde{\nu}$  (cm<sup>-1</sup>) = 2934.15, 2846.67 (ν<sub>a</sub>, C-H); 1427.69 (ν<sub>a</sub>, N-CSS); 967.97 (ν<sub>a</sub>, CSS).

Far FT-IR (nujol):  $\tilde{\nu}$  (cm<sup>-1</sup>) = 556.72 (ν<sub>s</sub>, CSS); 478.93 (ν<sub>a</sub>, Au-S).

*Bis(morpholine dithiocarbamate)digold(I), [Au<sub>2</sub>(MorphDTC)<sub>2</sub>]*

Aspect: green solid

Yield: 91 %

R.f. (on silica gel): *n.a.*

Anal. Calc. for  $C_{10}H_{16}Au_2N_2O_2S_4$  (MW = 718.44 g·mol<sup>-1</sup>): C 16.72; H 2.24; N 3.90; S 17.85. Found: C 16.62; H 2.45; N 3.99; S 17.66.

<sup>1</sup>H-NMR (DMSO-d<sub>6</sub>, 300.13 MHz): δ (ppm) = 3.72 (t, 8H, H<sub>(2)</sub> + H<sub>(6)</sub>), 4.18 (t, 8H, H<sub>(3)</sub> + H<sub>(5)</sub>).

Medium FT-IR (KBr):  $\tilde{\nu}$  (cm<sup>-1</sup>) = 2964.06, 2852.55 (ν<sub>a</sub>, C-H); 1417.16 (ν<sub>a</sub>, N-CSS); 1107.83 (ν<sub>a</sub>, C-O); 993.02 (ν<sub>a</sub>, CSS).

Far FT-IR (nujol):  $\tilde{\nu}$  (cm<sup>-1</sup>) = 541.35 (ν<sub>s</sub>, CSS); 462.02 (ν<sub>a</sub>, Au-S).

*Bis(indoline dithiocarbamate)digold(I), [Au<sub>2</sub>(IndolineDTC)<sub>2</sub>]*

Aspect: brown-orange solid

Yield: 96 %

R.f. (on silica gel): *n.a.*

Anal. Calc. for  $C_{18}H_{16}Au_2N_2S_4$  (MW = 782.53 g·mol<sup>-1</sup>): C 27.63; H 2.06; N 3.58; S 16.39. Found: C 27.65; H 2.09; N 3.54; S 16.50.

<sup>1</sup>H-NMR (DMSO-d<sub>6</sub>, 300.13 MHz): δ (ppm) = 3.20 (t, 4H, H<sub>(3)</sub>), 4.59 (t, 4H, H<sub>(2)</sub>), 7.28 (m, 4H, H<sub>(5)</sub> + H<sub>(6)</sub>), 7.43 (d, 2H, H<sub>(4)</sub>), 8.63 (d, 2H, H<sub>(7)</sub>).

Medium FT-IR (KBr):  $\tilde{\nu}$  (cm<sup>-1</sup>) = 2991.12 (ν<sub>a</sub>, C-H); 1473.49, 1458.24 (ν, C=C ring); 1375.82 (ν<sub>a</sub>, N-CSS); 1070.09 (ν<sub>a</sub>, CSS); 749.38 (δ, C-H).

Far FT-IR (nujol):  $\tilde{\nu}$  (cm<sup>-1</sup>) = 556.25 (ν<sub>s</sub>, CSS); 467.17 (ν<sub>a</sub>, Au-S).

*Bis(L-proline methyl ester dithiocarbamate)digold(I), [Au<sub>2</sub>(ProOMeDTC)<sub>2</sub>]*

Aspect: beige solid

Yield: 83 %

R.f. (on silica gel): *n.a.*

Anal. Calc. for  $C_{14}H_{20}Au_2N_2O_4S_4$  (MW = 802.51 g·mol<sup>-1</sup>): C 20.95; H 2.51; N 3.49; S 15.98. Found: C 21.12; H 2.64; N 3.38; S 15.92.

<sup>1</sup>H-NMR (DMSO-d<sub>6</sub>, 300.13 MHz): δ (ppm) = 2.06 (m, 8H, H<sub>(3)</sub> + H<sub>(4)</sub>), 3.69 (s, 6H, O-CH<sub>3</sub>), 3.82-3.89 (m, 4H, H<sub>(5)</sub>), 4.94 (s, 2H, H<sub>(2)</sub>).

Medium FT-IR (KBr):  $\tilde{\nu}$  ( $\text{cm}^{-1}$ ) = 2952.82 ( $\nu_a$ , C-H); 1738.78 ( $\nu$ , C=O); 1418.46 ( $\nu_a$ , N-CSS); 1158.52 ( $\nu_a$ , C-OMe); 950.14 ( $\nu_a$ , CSS).

Far FT-IR (nujol):  $\tilde{\nu}$  ( $\text{cm}^{-1}$ ) = 552.59 ( $\nu_s$ , CSS); 452.10 ( $\nu_a$ , Au-S).

*Bis(L-proline tert-butyl ester dithiocarbamate)digold(I), [Au<sub>2</sub>(ProOtBuDTC)<sub>2</sub>]*

Aspect: beige solid

Yield: 81 %

R.f. (on silica gel): *n.a.*

Anal. Calc. for C<sub>20</sub>H<sub>32</sub>Au<sub>2</sub>N<sub>2</sub>O<sub>4</sub>S<sub>4</sub> (MW = 886.67 g·mol<sup>-1</sup>): C 27.09; H 3.64; N 3.16; S 14.17. Found: C 27.28; H 3.72; N 3.11; S 14.32.

<sup>1</sup>H-NMR (DMSO-d<sub>6</sub>, 300.13 MHz):  $\delta$  (ppm) = 1.45 (s, 18H, O-C(CH<sub>3</sub>)<sub>3</sub>), 2.10 (m, 8H, H<sub>(3)</sub> + H<sub>(4)</sub>), 3.84-3.91 (m, 4H, H<sub>(5)</sub>), 4.98 (s, 2H, H<sub>(2)</sub>).

Medium FT-IR (KBr):  $\tilde{\nu}$  ( $\text{cm}^{-1}$ ) = 2973.43 ( $\nu_a$ , C-H); 1733.78 ( $\nu$ , C=O); 1412.10 ( $\nu_a$ , N-CSS); 1156.90 ( $\nu_a$ , C-OtBu); 964.82 ( $\nu_a$ , CSS).

Far FT-IR (nujol):  $\tilde{\nu}$  ( $\text{cm}^{-1}$ ) = 535.91 ( $\nu_s$ , CSS); 444.31 ( $\nu_a$ , Au-S).

*Bis(carbazole dithiocarbamate)digold(I), [Au<sub>2</sub>(CDT)<sub>2</sub>]*

Aspect: dark orange solid

Yield: 97 %

R.f. (on silica gel): *n.a.*

Anal. Calc. for C<sub>26</sub>H<sub>16</sub>Au<sub>2</sub>N<sub>2</sub>S<sub>4</sub> (MW = 878.61 g·mol<sup>-1</sup>): C 35.54; H 1.84; N 3.19; S 14.60. Found: C 35.71; H 1.96; N 3.17; S 14.75.

<sup>1</sup>H-NMR (DMSO-d<sub>6</sub>, 300.13 MHz):  $\delta$  (ppm) = 7.14-7.71 (m, 8H, H<sub>(3)</sub> + H<sub>(4)</sub> + H<sub>(5)</sub> + H<sub>(6)</sub>), 8.12-8.72 (m, 8H, H<sub>(1)</sub> + H<sub>(2)</sub> + H<sub>(7)</sub> + H<sub>(8)</sub>).

Medium FT-IR (KBr):  $\tilde{\nu}$  ( $\text{cm}^{-1}$ ) = 3047.18 ( $\nu_a$ , C-H); 1438.28 ( $\nu$ , C=C ring); 1285.62 ( $\nu_a$ , N-CSS); 1023.11 ( $\nu_a$ , CSS); 831.11 ( $\omega$ , C-H); 739.06, 710.79 ( $\delta$ , C-H).

Far FT-IR (nujol):  $\tilde{\nu}$  ( $\text{cm}^{-1}$ ) = 560.62 ( $\nu_s$ , CSS); 464.05 ( $\nu_a$ , Au-S).

*Bis(indole dithiocarbamate)digold(I), [Au<sub>2</sub>(IndDTC)<sub>2</sub>]*

Aspect: yellow-orange solid

Yield: 95 %

R.f. (on silica gel): *n.a.*

Anal. Calc. for C<sub>18</sub>H<sub>12</sub>Au<sub>2</sub>N<sub>2</sub>S<sub>4</sub> (MW = 778.49 g·mol<sup>-1</sup>): C 27.77; H 1.55; N 3.60; S 16.48. Found: C 27.65; H 1.71; N 3.52; S 16.32.

<sup>1</sup>H-NMR (DMSO-d<sub>6</sub>, 300.13 MHz): δ (ppm) = 6.68-6.69 (d, 2H, H<sub>(3)</sub>), 7.21 (t, 2H, H<sub>(5)</sub>), 7.29 (t, 2H, H<sub>(6)</sub>), 7.59-7.60 (d, 2H, H<sub>(4)</sub>), 8.36 (d, 2H, H<sub>(2)</sub>), 8.96-8.97 (d, 2H, H<sub>(7)</sub>).

Medium FT-IR (KBr):  $\tilde{\nu}$  (cm<sup>-1</sup>) = 3142.99, 3046.85 (ν<sub>a</sub>, C-H); 1444.20 (ν, C=C ring); 1314.02 (ν<sub>a</sub>, N-CSS); 1008.07 (ν<sub>a</sub>, CSS); 828.45 (ω, C-H); 738.23, 722.56 (δ, C-H).

Far FT-IR (nujol):  $\tilde{\nu}$  (cm<sup>-1</sup>) = 567.62 (ν<sub>s</sub>, CSS); 469.95 (ν<sub>a</sub>, Au-S).

*Bis(pyrrole dithiocarbamate)digold(I), [Au<sub>2</sub>(PyrrDTC)<sub>2</sub>]*

Aspect: red-orange solid

Yield: 92 %

R.f. (on silica gel): *n.a.*

Anal. Calc. for C<sub>10</sub>H<sub>8</sub>Au<sub>2</sub>N<sub>2</sub>S<sub>4</sub> (MW = 678.38 g·mol<sup>-1</sup>): C 17.71; H 1.19; N 4.13; S 18.19. Found: C 17.89; H 1.22; N 4.24; S 18.38.

<sup>1</sup>H-NMR (DMSO-d<sub>6</sub>, 300.13 MHz): δ (ppm) = 6.29 (s, 4H, H<sub>(3)</sub> + H<sub>(4)</sub>), 6.88 (s, 4H, H<sub>(2)</sub> + H<sub>(5)</sub>).

Medium FT-IR (KBr):  $\tilde{\nu}$  (cm<sup>-1</sup>) = 3139.71 (ν<sub>a</sub>, C-H); 1456.26 (ν, C=C ring); 1284.38 (ν<sub>a</sub>, N-CSS); 1010.63 (ν<sub>a</sub>, CSS); 819.95 (ω, C-H); 720.12 (δ, C-H).

Far FT-IR (nujol):  $\tilde{\nu}$  (cm<sup>-1</sup>) = 556.75 (ν<sub>s</sub>, CSS); 463.71 (ν<sub>a</sub>, Au-S).

### 7.3.2 Synthesis of Au(III) dithiocarbamate dichloro complexes, [Au<sup>III</sup>Cl<sub>2</sub>(DTC)]

The dichlorodithiocarbamatogold(III) derivatives of the ligands PDT, PipeDTC, MorphDTC, IndolineDTC, ProOMeDTC, ProOtBuDTC, CDT, IndDTC and PyrrDTC were synthesized as follows. 0.5 mmol of gold(I)-DTC complex were suspended in 20 mL of halogenated solvent (chloroform or dichloromethane) and the mixture was refluxed under stirring. After 10 minutes an excess of Cl<sub>2</sub>, generated in a separate flask by mixing 300 mg of MnO<sub>2</sub> with 3 mL of concentrated HCl, was gurgled for 1 hour. It was possible to observe that, after some minutes, the solution turned brown with the dissolution of the Au(I) precursor, and then became yellow.

After an additional hour, the reaction flask was cooled, the mixture filtered and the volume of the solvent half-reduced. Successively, 40 mL of diethyl ether were added, leading to the precipitation of a yellow-orange solid that was filtered, washed with 2x 4 mL of diethyl ether and 2x 5mL of distilled water, and dried in pump in the presence of P<sub>2</sub>O<sub>5</sub>.

*Dichloro(pyrrolidine dithiocarbamate)gold(III), [AuCl<sub>2</sub>(PDT)]*

Aspect: light orange solid

Yield: 88 %

R.f. (on silica gel, CH<sub>2</sub>Cl<sub>2</sub>): 0.79

Anal. Calc. for C<sub>5</sub>H<sub>8</sub>AuCl<sub>2</sub>NS<sub>2</sub> (MW = 414.13 g·mol<sup>-1</sup>): C 14.50; H 1.95; N 3.38; S 15.49. Found: C 14.52; H 1.92; N 3.39; S 15.38.

<sup>1</sup>H-NMR (DMSO-d<sub>6</sub>, 300.13 MHz): δ (ppm) = 2.05 (m, 4H, H<sub>(3)</sub> + H<sub>(4)</sub>), 3.81 (m, 4H, H<sub>(2)</sub> + H<sub>(5)</sub>).

Medium FT-IR (KBr):  $\tilde{\nu}$  (cm<sup>-1</sup>) = 2980.15, 2946.81 (ν<sub>a</sub>, C-H); 1587.97 (ν<sub>a</sub>, N-CSS); 943.77 (ν<sub>a</sub>, CSS).

Far FT-IR (nujol):  $\tilde{\nu}$  (cm<sup>-1</sup>) = 536.73 (ν<sub>s</sub>, CSS); 375.34 (ν<sub>a</sub>, Au-S); 351.75 (ν<sub>a</sub>, Au-Cl); 338.52 (ν<sub>s</sub>, Au-S); 314.83 (ν<sub>s</sub>, Au-Cl).

*Dichloro(piperidine dithiocarbamate)gold(III), [AuCl<sub>2</sub>(PipeDTC)]*

Aspect: dark yellow solid

Yield: 93 %

R.f. (on silica gel, CH<sub>2</sub>Cl<sub>2</sub>): 0.86

Anal. Calc. for C<sub>5</sub>H<sub>8</sub>AuCl<sub>2</sub>NS<sub>2</sub> (MW = 428.15 g·mol<sup>-1</sup>): C 16.83; H 2.35; N 3.27; S 14.98. Found: C 16.86; H 2.37; N 3.21; S 15.02.

<sup>1</sup>H-NMR (DMSO-d<sub>6</sub>, 600 MHz): δ (ppm) = 1.72 (s, 6H, H<sub>(3)</sub> + H<sub>(4)</sub> + H<sub>(5)</sub>), 3.82 (s, 4H, H<sub>(2)</sub> + H<sub>(6)</sub>).

Medium FT-IR (KBr):  $\tilde{\nu}$  (cm<sup>-1</sup>) = 2944.60, 2858.64 (ν<sub>a</sub>, C-H); 1581.42 (ν<sub>a</sub>, N-CSS); 947.36 (ν<sub>a</sub>, CSS).

Far FT-IR (nujol):  $\tilde{\nu}$  (cm<sup>-1</sup>) = 539.66 (ν<sub>s</sub>, CSS); 366.20 (ν<sub>a</sub>, Au-S); 349.71 (ν<sub>a</sub>, Au-Cl); 334.59 (ν<sub>s</sub>, Au-S); 315.67 (ν<sub>s</sub>, Au-Cl).

*Dichloro(morpholine dithiocarbamate)gold(III), [AuCl<sub>2</sub>(MorphDTC)]*

Aspect: pink-orange solid



Yield: 89 %

R.f. (on silica gel, CH<sub>2</sub>Cl<sub>2</sub>): 0.54

Anal. Calc. for C<sub>5</sub>H<sub>8</sub>AuCl<sub>2</sub>NOS<sub>2</sub> (MW = 430.13 g·mol<sup>-1</sup>): C 13.96; H 1.87; N 3.26; S 14.91. Found: C 14.03; H 1.92; N 3.19; S 14.80.

<sup>1</sup>H-NMR (DMSO-d<sub>6</sub>, 300.13 MHz): δ (ppm) = 3.80-3.82 (m, 4H, H<sub>(2)</sub> + H<sub>(6)</sub>), 3.88-3.89 (m, 4H, H<sub>(3)</sub> + H<sub>(5)</sub>).

Medium FT-IR (KBr):  $\tilde{\nu}$  (cm<sup>-1</sup>) = 2983.71, 2929.91, 2870.89 (ν<sub>a</sub>, C-H); 1572.21 (ν<sub>a</sub>, N-CSS); 1109.10 (ν<sub>a</sub>, C-O); 993.32 (ν<sub>a</sub>, CSS).

Far FT-IR (nujol):  $\tilde{\nu}$  (cm<sup>-1</sup>) = 543.46 (ν<sub>s</sub>, CSS); 364.39 (ν<sub>a</sub>, Au-S); 357.21 (ν<sub>a</sub>, Au-Cl); 337.85 (ν<sub>s</sub>, Au-S); 317.83 (ν<sub>s</sub>, Au-Cl).

*Dichloro(indoline dithiocarbamate)gold(III), [AuCl<sub>2</sub>(IndolineDTC)]*

Aspect: pink-orange solid

Yield: 89 %

R.f. (on silica gel, CH<sub>2</sub>Cl<sub>2</sub>): 0.92

Anal. Calc. for C<sub>9</sub>H<sub>8</sub>AuCl<sub>2</sub>NS<sub>2</sub> (MW = 462.17 g·mol<sup>-1</sup>): C 23.39; H 1.74; N 3.03; S 13.88. Found: C 23.47; H 1.75; N 3.07; S 13.74.

<sup>1</sup>H-NMR (DMSO-d<sub>6</sub>, 300.13 MHz): δ (ppm) = 3.38 (t, 2H, H<sub>(3)</sub>), 4.51 (t, 2H, H<sub>(2)</sub>), 7.44 (m, 2H, H<sub>(5)</sub> + H<sub>(6)</sub>), 7.56-7.58 (d, 1H, H<sub>(4)</sub>), 8.05-8.07 (d, 1H, H<sub>(7)</sub>).

Medium FT-IR (KBr):  $\tilde{\nu}$  (cm<sup>-1</sup>) = 2998.65, 2937.52 (ν<sub>a</sub>, C-H); 1540.70 (ν<sub>a</sub>, N-CSS); 1473.66, 1460.19 (ν, C=C ring); 1074.82 (ν<sub>a</sub>, CSS); 751.61 (δ, C-H).

Far FT-IR (nujol):  $\tilde{\nu}$  (cm<sup>-1</sup>) = 553.12 (ν<sub>s</sub>, CSS); 381.82 (ν<sub>a</sub>, Au-S); 367.82 (ν<sub>a</sub>, Au-Cl); 339.07 (ν<sub>s</sub>, Au-S); 318.79 (ν<sub>s</sub>, Au-Cl).

*Dichloro(L-proline methyl ester dithiocarbamate)gold(III), [AuCl<sub>2</sub>(ProOMeDTC)]*

Aspect: orange solid

Yield: 89 %

R.f. (on silica gel, CH<sub>2</sub>Cl<sub>2</sub>): 0.51

Anal. Calc. for C<sub>7</sub>H<sub>10</sub>AuCl<sub>2</sub>NO<sub>2</sub>S<sub>2</sub> (MW = 472.16 g·mol<sup>-1</sup>): C 17.81; H 2.13; N 2.97; S 13.58. Found: C 17.86; H 2.22; N 2.90; S 13.65.

$^1\text{H-NMR}$  (DMSO- $d_6$ , 300.13 MHz):  $\delta$  (ppm) = 2.01-2.40 (4m, 4H,  $\text{H}_{(3)} + \text{H}_{(4)}$ ), 3.76 (s, 3H, O- $\text{CH}_3$ ), 3.92-4.01 (2m, 2H,  $\text{H}_{(5)}$ ), 5.16-5.17 (dd, 1H,  $\text{H}_{(2)}$ ).

Medium FT-IR (KBr):  $\tilde{\nu}$  ( $\text{cm}^{-1}$ ) = 2951.38 ( $\nu_a$ , C-H); 1746.56 ( $\nu$ , C=O); 1559.95 ( $\nu_a$ , N-CSS); 1173.93 ( $\nu_a$ , C-OMe); 979.24 ( $\nu_a$ , CSS).

Far FT-IR (nujol):  $\tilde{\nu}$  ( $\text{cm}^{-1}$ ) = 546.77 ( $\nu_s$ , CSS); 381.91 ( $\nu_a$ , Au-S); 359.01 ( $\nu_a$ , Au-Cl); 339.07 ( $\nu_s$ , Au-S); 318.79 ( $\nu_s$ , Au-Cl).

*Dichloro(L-proline tert-butyl ester dithiocarbamate)gold(III), [AuCl<sub>2</sub>(ProOtBuDTC)]*

Aspect: yellow-orange needles

Yield: 86 %

R.f. (on silica gel,  $\text{CH}_2\text{Cl}_2$ ): 0.64

Anal. Calc. for  $\text{C}_{10}\text{H}_{16}\text{AuCl}_2\text{NO}_2\text{S}_2$  (MW = 514.24  $\text{g}\cdot\text{mol}^{-1}$ ): C 23.36; H 3.14; N 2.72; S 12.47. Found: C 23.50; H 3.05; N 2.60; S 12.65.

$^1\text{H-NMR}$  (DMSO- $d_6$ , 300.13 MHz):  $\delta$  (ppm) = 1.45 (s, 9H, O-C( $\text{CH}_3$ )<sub>3</sub>), 1.97-2.40 (4m, 4H,  $\text{H}_{(3)} + \text{H}_{(4)}$ ), 3.92-3.99 (2m, 2H,  $\text{H}_{(5)}$ ), 5.01-5.02 (dd, 1H,  $\text{H}_{(2)}$ ).

Medium FT-IR (KBr):  $\tilde{\nu}$  ( $\text{cm}^{-1}$ ) = 2975.38 ( $\nu_a$ , C-H); 1737.74 ( $\nu$ , C=O); 1558.38 ( $\nu_a$ , N-CSS); 1146.04 ( $\nu_a$ , C-OtBu); 950.15 ( $\nu_a$ , CSS).

Far FT-IR (nujol):  $\tilde{\nu}$  ( $\text{cm}^{-1}$ ) = 545.20 ( $\nu_s$ , CSS); 380.68 ( $\nu_a$ , Au-S); 358.23 ( $\nu_a$ , Au-Cl); 341.14 ( $\nu_s$ , Au-S); 319.14 ( $\nu_s$ , Au-Cl).

*Dichloro(carbazole dithiocarbamate)gold(III), [AuCl<sub>2</sub>(CDT)]*

Aspect: dark yellow solid

Yield: 89 %

R.f. (on silica gel,  $\text{CH}_2\text{Cl}_2$ ): 0.99

Anal. Calc. for  $\text{C}_{13}\text{H}_8\text{AuCl}_2\text{NS}_2$  (MW = 510.21  $\text{g}\cdot\text{mol}^{-1}$ ): C 30.60; H 1.58; N 2.75; S 12.57. Found: C 30.78; H 1.49; N 2.62; S 12.48.

$^1\text{H-NMR}$  (DMSO- $d_6$ , 300.13 MHz):  $\delta$  (ppm) = 7.15 (t, 2H,  $\text{H}_{(3)} + \text{H}_{(6)}$ ), 7.47 (d, 2H,  $\text{H}_{(4)} + \text{H}_{(5)}$ ), 8.14-8.15 (m, 2H,  $\text{H}_{(2)} + \text{H}_{(7)}$ ), 8.56-8.58 (d, 2H,  $\text{H}_{(1)} + \text{H}_{(8)}$ ).

Medium FT-IR (KBr):  $\tilde{\nu}$  (cm<sup>-1</sup>) = 3059.79 (v<sub>a</sub>, C-H); 1492.04, 1451.11 (v, C=C ring); 1349.67 (v<sub>a</sub>, N-CSS); 1041.89 (v<sub>a</sub>, CSS); 854.82 (ω, C-H); 748.64, 707.54 (δ, C-H).

Far FT-IR (nujol):  $\tilde{\nu}$  (cm<sup>-1</sup>) = 574.41 (v<sub>s</sub>, CSS); 408.47 (v<sub>a</sub>, Au-S); 378.03 (v<sub>s</sub>, Au-S); 357.83 (v<sub>a</sub>, Au-Cl); 321.90 (v<sub>s</sub>, Au-Cl).

*Dichloro(indole dithiocarbamate)gold(III), [AuCl<sub>2</sub>(IndDTC)]*

Aspect: dark yellow solid

Yield: 89 %

R.f. (on silica gel, CH<sub>2</sub>Cl<sub>2</sub>): 0.98

Anal. Calc. for C<sub>9</sub>H<sub>6</sub>AuCl<sub>2</sub>NS<sub>2</sub> (MW = 460.15 g·mol<sup>-1</sup>): C 23.49; H 1.31; N 3.04; S 13.94 Found: C 23.65; H 1.13; N 3.16; S 14.08.

<sup>1</sup>H-NMR (DMSO-d<sub>6</sub>, 300.13 MHz): δ (ppm) = 7.04 (s, 1H, H<sub>(3)</sub>), 7.12 (s, 1H, H<sub>(4)</sub>), 7.33 (s, 2H, H<sub>(5)</sub> + H<sub>(6)</sub>), 8.27 (s, 1H, H<sub>(2)</sub>), 8.85 (s, 1H, H<sub>(7)</sub>).

Medium FT-IR (KBr):  $\tilde{\nu}$  (cm<sup>-1</sup>) = 3102.12 (v<sub>a</sub>, C-H); 1480.68, 1462.24 (v, C=C ring); 1357.82 (v<sub>a</sub>, N-CSS); 1095.44 (v<sub>a</sub>, CSS); 859.26 (ω, C-H); 748.92, 706.63 (δ, C-H).

Far FT-IR (nujol):  $\tilde{\nu}$  (cm<sup>-1</sup>) = 564.06 (v<sub>s</sub>, CSS); 409.33 (v<sub>a</sub>, Au-S); 381.73 (v<sub>s</sub>, Au-S); 347.36 (v<sub>a</sub>, Au-Cl); 324.00 (v<sub>s</sub>, Au-Cl).

*Dichloro(pyrrrole dithiocarbamate)gold(III), [AuCl<sub>2</sub>(PyrrDTC)]*

Aspect: dark yellow solid

Yield: 78 %

R.f. (on silica gel, CH<sub>2</sub>Cl<sub>2</sub>): 0.93

Anal. Calc. for C<sub>5</sub>H<sub>4</sub>AuCl<sub>2</sub>NS<sub>2</sub> (MW = 410.09 g·mol<sup>-1</sup>): C 14.64; H 0.98; N 3.42; S 15.64. Found: C 14.81; H 1.11; N 3.45; S 15.88.

<sup>1</sup>H-NMR (DMSO-d<sub>6</sub>, 300.13 MHz): δ (ppm) = 6.15-6.16 (d, 2H, H<sub>(3)</sub> + H<sub>(4)</sub>), 6.57-6.58 (d, 2H, H<sub>(2)</sub> + H<sub>(5)</sub>).

Medium FT-IR (KBr):  $\tilde{\nu}$  (cm<sup>-1</sup>) = 3090.23, 2958.37 (v<sub>a</sub>, C-H); 1479.58 (v, C=C ring); 1345.15 (v<sub>a</sub>, N-CSS); 1022.79 (v<sub>a</sub>, CSS); 842.63 (ω, C-H); 762.79 (δ, C-H).

Far FT-IR (nujol):  $\tilde{\nu}$  (cm<sup>-1</sup>) = 567.43 (v<sub>s</sub>, CSS); 413.46 (v<sub>a</sub>, Au-S); 380.98 (v<sub>s</sub>, Au-S); 347.42 (v<sub>a</sub>, Au-Cl); 320.83 (v<sub>s</sub>, Au-Cl).

### 7.3.3 Synthesis of Au(III) dithiocarbamate dibromo complexes, [Au<sup>III</sup>Br<sub>2</sub>(DTC)]

The dibromodithiocarbamatogold(III) derivatives of the ligands PDT, PipeDTC, MorphDTC, IndolineDTC, ProOMeDTC, ProOtBuDTC, CDT, IndDTC and PyrrDTC were synthesized with the same strategy of the dichloro counterparts, as presented in **Section 7.3.2**. An excess of bromine was directly added to the Au(I)-DTC suspension (100 equivalents of liquid Br<sub>2</sub> previously dissolved in dichloromethane), and the solution turned immediately deep red, and then orange. After an additional hour, the reaction flask was cooled, the mixture filtered and the volume of the solvent half-reduced. Successively, 40 mL of diethyl ether were added, leading to the precipitation of an orange solid that was filtered, washed with 2x 4 mL of diethyl ether and 2x 5 mL of distilled water, and dried in pump in the presence of P<sub>2</sub>O<sub>5</sub>.

#### *Dibromo(pyrrolidine dithiocarbamate)gold(III), [AuBr<sub>2</sub>(PDT)]*

Aspect: orange solid

Yield: 94 %

R.f. (on silica gel, CH<sub>2</sub>Cl<sub>2</sub>): 0.75

Anal. Calc. for C<sub>5</sub>H<sub>8</sub>AuBr<sub>2</sub>NS<sub>2</sub> (MW = 503.03 g·mol<sup>-1</sup>): C 11.94; H 1.60; N 2.78; S 12.75. Found: C 12.01; H 1.65; N 2.90; S 12.79.

<sup>1</sup>H-NMR (DMSO-d<sub>6</sub>, 300.13 MHz): δ (ppm) = 2.04 (m, 4H, H<sub>(3)</sub> + H<sub>(4)</sub>), 3.79 (m, 4H, H<sub>(2)</sub> + H<sub>(5)</sub>).

Medium FT-IR (KBr):  $\tilde{\nu}$  (cm<sup>-1</sup>) = 2974.48, 2951.88 (ν<sub>a</sub>, C-H); 1585.73 (ν<sub>a</sub>, N-CSS); 943.07 (ν<sub>a</sub>, CSS).

Far FT-IR (nujol):  $\tilde{\nu}$  (cm<sup>-1</sup>) = 538.94 (ν<sub>s</sub>, CSS); 372.67 (ν<sub>a</sub>, Au-S); 337.91 (ν<sub>s</sub>, Au-S); 239.82 (ν<sub>a</sub>, Au-Br); 218.33 (ν<sub>s</sub>, Au-Br).

#### *Dibromo(piperidine dithiocarbamate)gold(III), [AuBr<sub>2</sub>(PipeDTC)]*

Aspect: orange needles

Yield: 96 %

R.f. (on silica gel, CH<sub>2</sub>Cl<sub>2</sub>): 0.83

Anal. Calc. for C<sub>6</sub>H<sub>10</sub>AuBr<sub>2</sub>NS<sub>2</sub> (MW = 517.05 g·mol<sup>-1</sup>): C 13.94; H 1.95; N 2.71; S 12.40. Found: C 13.99; H 1.98; N 2.73; S 12.42.

<sup>1</sup>H-NMR (DMSO-d<sub>6</sub>, 600 MHz): δ (ppm) = 1.72 (s, 6H, H<sub>(3)</sub> + H<sub>(4)</sub> + H<sub>(5)</sub>), 3.79 (s, 4H, H<sub>(2)</sub> + H<sub>(6)</sub>).

Medium FT-IR (KBr):  $\tilde{\nu}$  (cm<sup>-1</sup>) = 2941.65 (ν<sub>a</sub>, C-H); 1573.91 (ν<sub>a</sub>, N-CSS); 941.52 (ν<sub>a</sub>, CSS).

Far FT-IR (nujol):  $\tilde{\nu}$  (cm<sup>-1</sup>) = 538.90 (v<sub>s</sub>, CSS); 369.79 (v<sub>a</sub>, Au-S); 350.61 (v<sub>s</sub>, Au-S); 239.11 (v<sub>a</sub>, Au-Br); 223.85 (v<sub>s</sub>, Au-Br).

*Dibromo(morpholine dithiocarbamate)gold(III), [AuBr<sub>2</sub>(MorphDTC)]*

Aspect: light orange solid

Yield: 95 %

R.f. (on silica gel, CH<sub>2</sub>Cl<sub>2</sub>): 0.55

Anal. Calc. for C<sub>5</sub>H<sub>8</sub>AuBr<sub>2</sub>NOS<sub>2</sub> (MW = 519.03 g·mol<sup>-1</sup>): C 11.57; H 1.55; N 2.70; S 12.36. Found: C 11.68; H 1.64; N 2.72; S 12.41.

<sup>1</sup>H-NMR (DMSO-d<sub>6</sub>, 300.13 MHz):  $\delta$  (ppm) = 3.80-3.81 (m, 4H, H<sub>(2)</sub> + H<sub>(6)</sub>), 3.85-3.87 (m, 4H, H<sub>(3)</sub> + H<sub>(5)</sub>).

Medium FT-IR (KBr):  $\tilde{\nu}$  (cm<sup>-1</sup>) = 2983.60, 2927.54, 2869.24 (v<sub>a</sub>, C-H); 1561.66 (v<sub>a</sub>, N-CSS); 1108.57 (v<sub>a</sub>, C-O); 993.49 (v<sub>a</sub>, CSS).

Far FT-IR (nujol):  $\tilde{\nu}$  (cm<sup>-1</sup>) = 541.58 (v<sub>s</sub>, CSS); 357.80 (v<sub>a</sub>, Au-S); 347.90 (v<sub>s</sub>, Au-S); 237.51 (v<sub>a</sub>, Au-Br); 220.11 (v<sub>s</sub>, Au-Br).

*Dibromo(indoline dithiocarbamate)gold(III), [AuBr<sub>2</sub>(IndolineDTC)]*

Aspect: light orange solid

Yield: 93 %

R.f. (on silica gel, CH<sub>2</sub>Cl<sub>2</sub>): 0.90

Anal. Calc. for C<sub>9</sub>H<sub>8</sub>AuBr<sub>2</sub>NS<sub>2</sub> (MW = 551.07 g·mol<sup>-1</sup>): C 19.62; H 1.46; N 2.54; S 11.64. Found: C 19.71; H 1.48; N 2.60; S 11.78.

<sup>1</sup>H-NMR (DMSO-d<sub>6</sub>, 300.13 MHz):  $\delta$  (ppm) = 4.49 (t, 2H, H<sub>(2)</sub>), 7.43 (m, 2H, H<sub>(5)</sub> + H<sub>(6)</sub>), 7.55-7.57 (d, 1H, H<sub>(4)</sub>), 8.04-8.07 (d, 1H, H<sub>(7)</sub>).

Medium FT-IR (KBr):  $\tilde{\nu}$  (cm<sup>-1</sup>) = 3001.11 (v<sub>a</sub>, C-H); 1535.90 (v<sub>a</sub>, N-CSS); 1472.58, 1460.29 (v, C=C ring); 1074.79 (v<sub>a</sub>, CSS); 747.78 ( $\delta$ , C-H).

Far FT-IR (nujol):  $\tilde{\nu}$  (cm<sup>-1</sup>) = 551.69 (v<sub>s</sub>, CSS); 376.44 (v<sub>a</sub>, Au-S); 358.67 (v<sub>s</sub>, Au-S); 236.51 (v<sub>a</sub>, Au-Br); 220.68 (v<sub>s</sub>, Au-Br).

*Dibromo(L-proline methyl ester dithiocarbamate)gold(III), [AuBr<sub>2</sub>(ProOMeDTC)]*

Aspect: orange needles

Yield: 91 %

R.f. (on silica gel, CH<sub>2</sub>Cl<sub>2</sub>): 0.53

Anal. Calc. for C<sub>7</sub>H<sub>10</sub>AuCl<sub>2</sub>NO<sub>2</sub>S<sub>2</sub> (MW = 561.06 g·mol<sup>-1</sup>): C 14.98; H 1.80; N 2.50; S 11.43. Found: C 15.12; H 1.79; N 2.36; S 11.56.

<sup>1</sup>H-NMR (DMSO-d<sub>6</sub>, 300.13 MHz): δ (ppm) = 2.00-2.41 (4m, 4H, H<sub>(3)</sub> + H<sub>(4)</sub>), 3.76 (s, 3H, O-CH<sub>3</sub>), 3.91-3.99 (2m, 2H, H<sub>(5)</sub>), 5.13-5.15 (dd, 1H, H<sub>(2)</sub>).

Medium FT-IR (KBr):  $\tilde{\nu}$  (cm<sup>-1</sup>) = 2949.35 (v<sub>a</sub>, C-H); 1746.46 (v, C=O); 1550.36 (v<sub>a</sub>, N-CSS); 1173.25 (v<sub>a</sub>, C-OMe); 985.14 (v<sub>a</sub>, CSS).

Far FT-IR (nujol):  $\tilde{\nu}$  (cm<sup>-1</sup>) = 544.59 (v<sub>s</sub>, CSS); 378.26 (v<sub>a</sub>, Au-S); 349.40 (v<sub>s</sub>, Au-S); 237.49 (v<sub>a</sub>, Au-Br); 219.92 (v<sub>s</sub>, Au-Br).

*Dibromo(L-proline tert-butyl ester dithiocarbamate)gold(III), [AuBr<sub>2</sub>(ProOtBuDTC)]*

Aspect: orange needles

Yield: 90 %

R.f. (on silica gel, CH<sub>2</sub>Cl<sub>2</sub>): 0.66

Anal. Calc. for C<sub>10</sub>H<sub>16</sub>AuCl<sub>2</sub>NO<sub>2</sub>S<sub>2</sub> (MW = 603.14 g·mol<sup>-1</sup>): C 19.91; H 2.67; N 2.32; S 10.63. Found: C 20.02; H 2.70; N 2.29; S 10.71.

<sup>1</sup>H-NMR (DMSO-d<sub>6</sub>, 300.13 MHz): δ (ppm) = 1.45 (s, 9H, O-C(CH<sub>3</sub>)<sub>3</sub>), 1.98-2.38 (4m, 4H, H<sub>(3)</sub> + H<sub>(4)</sub>), 3.89-3.97 (2m, 2H, H<sub>(5)</sub>), 4.98-5.00 (dd, 1H, H<sub>(2)</sub>).

Medium FT-IR (KBr):  $\tilde{\nu}$  (cm<sup>-1</sup>) = 2977.36 (v<sub>a</sub>, C-H); 1736.46 (v, C=O); 1559.96 (v<sub>a</sub>, N-CSS); 1146.69 (v<sub>a</sub>, C-OtBu); 952.67 (v<sub>a</sub>, CSS).

Far FT-IR (nujol):  $\tilde{\nu}$  (cm<sup>-1</sup>) = 540.70 (v<sub>s</sub>, CSS); 379.35 (v<sub>a</sub>, Au-S); 344.53 (v<sub>s</sub>, Au-S); 238.34 (v<sub>a</sub>, Au-Br); 219.02 (v<sub>s</sub>, Au-Br).

*Dibromo(carbazole dithiocarbamate)gold(III), [AuBr<sub>2</sub>(CDT)]*

Aspect: orange solid

Yield: 94 %

---

R.f. (on silica gel, CH<sub>2</sub>Cl<sub>2</sub>): 0.99

Anal. Calc. for C<sub>13</sub>H<sub>8</sub>AuBr<sub>2</sub>NS<sub>2</sub> (MW = 599.11 g·mol<sup>-1</sup>): C 26.06; H 1.35; N 2.34; S 10.70. Found: C 26.19; H 1.37; N 2.51; S 10.88.

<sup>1</sup>H-NMR (DMSO-d<sub>6</sub>, 300.13 MHz): δ (ppm) = 7.14 (t, 2H, H<sub>(3)</sub> + H<sub>(6)</sub>), 7.45 (d, 2H, H<sub>(4)</sub> + H<sub>(5)</sub>), 8.13-8.14 (m, 2H, H<sub>(2)</sub> + H<sub>(7)</sub>), 8.55-8.56 (d, 2H, H<sub>(1)</sub> + H<sub>(8)</sub>).

Medium FT-IR (KBr):  $\tilde{\nu}$  (cm<sup>-1</sup>) = 3060.11 (ν<sub>a</sub>, C-H); 1491.19, 1450.39 (ν, C=C ring); 1349.25 (ν<sub>a</sub>, N-CSS); 1041.10 (ν<sub>a</sub>, CSS); 852.83 (ω, C-H); 749.22, 707.51 (δ, C-H).

Far FT-IR (nujol):  $\tilde{\nu}$  (cm<sup>-1</sup>) = 569.95 (ν<sub>s</sub>, CSS); 407.96 (ν<sub>a</sub>, Au-S); 376.46 (ν<sub>s</sub>, Au-S); 248.53 (ν<sub>a</sub>, Au-Br); 222.82 (ν<sub>s</sub>, Au-Br).

*Dibromo(indole dithiocarbamate)gold(III), [AuBr<sub>2</sub>(IndDTC)]*

Aspect: orange solid

Yield: 89 %

R.f. (on silica gel, CH<sub>2</sub>Cl<sub>2</sub>): 0.96

Anal. Calc. for C<sub>9</sub>H<sub>6</sub>AuBr<sub>2</sub>NS<sub>2</sub> (MW = 549.06 g·mol<sup>-1</sup>): C 19.69; H 1.10; N 2.55; S 11.68. Found: C 19.75; H 0.98; N 2.33; S 11.86.

<sup>1</sup>H-NMR (DMSO-d<sub>6</sub>, 300.13 MHz): δ (ppm) = 7.03 (s, 1H, H<sub>(3)</sub>), 7.11 (s, 1H, H<sub>(4)</sub>), 7.31 (s, 2H, H<sub>(5)</sub> + H<sub>(6)</sub>), 8.25 (s, 1H, H<sub>(2)</sub>), 8.82 (s, 1H, H<sub>(7)</sub>).

Medium FT-IR (KBr):  $\tilde{\nu}$  (cm<sup>-1</sup>) = 3101.70 (ν<sub>a</sub>, C-H); 1484.04, 1448.33 (ν, C=C ring); 1356.94 (ν<sub>a</sub>, N-CSS); 1076.69 (ν<sub>a</sub>, CSS); 858.17 (ω, C-H); 750.34, 705.58 (δ, C-H).

Far FT-IR (nujol):  $\tilde{\nu}$  (cm<sup>-1</sup>) = 574.49 (ν<sub>s</sub>, CSS); 408.70 (ν<sub>a</sub>, Au-S); 378.25 (ν<sub>s</sub>, Au-S); 252.27 (ν<sub>a</sub>, Au-Br); 226.85 (ν<sub>s</sub>, Au-Br).

*Dibromo(pyrrole dithiocarbamate)gold(III), [AuBr<sub>2</sub>(PyrrDTC)]*

Aspect: orange solid

Yield: 85 %

R.f. (on silica gel, CH<sub>2</sub>Cl<sub>2</sub>): 0.91

Anal. Calc. for C<sub>5</sub>H<sub>4</sub>AuCl<sub>2</sub>NS<sub>2</sub> (MW = 499.00 g·mol<sup>-1</sup>): C 12.03; H 0.81; N 2.81; S 12.85. Found: C 12.14; H 0.91; N 3.00; S 12.69.

$^1\text{H-NMR}$  (DMSO- $d_6$ , 300.13 MHz):  $\delta$  (ppm) = 6.14-6.15 (d, 2H,  $\text{H}_{(3)}$  +  $\text{H}_{(4)}$ ), 6.56-6.57 (d, 2H,  $\text{H}_{(2)}$  +  $\text{H}_{(5)}$ ).

Medium FT-IR (KBr):  $\tilde{\nu}$  ( $\text{cm}^{-1}$ ) = 3099.21, 2958.58 ( $\nu_a$ , C-H); 1478.77 ( $\nu$ , C=C ring); 1345.40 ( $\nu_a$ , N-CSS); 1022.33 ( $\nu_a$ , CSS); 762.58 ( $\delta$ , C-H).

Far FT-IR (nujol):  $\tilde{\nu}$  ( $\text{cm}^{-1}$ ) = 577.58 ( $\nu_s$ , CSS); 412.78 ( $\nu_a$ , Au-S); 377.37 ( $\nu_s$ , Au-S); 232.85 ( $\nu_a$ , Au-Br); 214.74 ( $\nu_s$ , Au-Br).

#### 7.3.4 Synthesis of ionic Au(III) bis(piperidine dithiocarbamato)complexes, $[\text{Au}^{\text{III}}(\text{PipeDTC})_2]\text{X}$ (X= Cl, Br)

The ionic bis(dithiocarbamato)gold(III) complexes  $[\text{Au}^{\text{III}}(\text{PipeDTC})_2]^+$  with X (X= Cl<sup>-</sup>, Br<sup>-</sup>) as a counterion were obtained by adding dropwise 1 mmol of the dithiocarbamato salt NaPipeDTC dissolved in methanol (2 mL) to a solution containing 1 mmol of  $[\text{AuX}_2(\text{PipeDTC})]$  dissolved in 3 mL of dichloromethane. The deep orange solution of the neutral Au(III)-DTC complex became immediately yellow-orange. The completion of the reaction was detected by TLC analysis. Then, the solvent was removed under reduced pressure, the residual solid taken up with 1 mL of anhydrous dichloromethane and the NaX (X= Cl or Br) was removed by filtration. At this point, the product was collected by precipitation with 10 mL of *n*-hexane, and dried *in vacuo*. These ionic products resulted water-soluble.

##### *Bis(piperidine dithiocarbamate)gold(III) chloride, $[\text{Au}(\text{PipeDTC})_2]\text{Cl}$*

Aspect: yellow-orange solid

Yield: 82 %

R.f. (on silica gel,  $\text{CH}_2\text{Cl}_2/\text{MeOH}$  9:1): 0.12

Anal. Calc. for  $\text{C}_{12}\text{H}_{20}\text{AuClN}_2\text{S}_4$  (MW = 552.98  $\text{g}\cdot\text{mol}^{-1}$ ): C 26.02; H 3.65; N 5.07; S 23.19. Found: C 26.07; H 3.71; N 5.19; S 23.11.

$^1\text{H-NMR}$  (DMSO- $d_6$ , 600 MHz):  $\delta$  (ppm) = 1.74 (m, 12H,  $\text{H}_{(3)}$  +  $\text{H}_{(4)}$  +  $\text{H}_{(5)}$ ), 3.83 (m, 8H,  $\text{H}_{(2)}$  +  $\text{H}_{(6)}$ ).

Medium FT-IR (KBr):  $\tilde{\nu}$  ( $\text{cm}^{-1}$ ) = 2936.83, 2861.75 ( $\nu_a$ , C-H); 1560.51 ( $\nu_a$ , N-CSS); 951.13 ( $\nu_a$ , CSS).

Far FT-IR (nujol):  $\tilde{\nu}$  ( $\text{cm}^{-1}$ ) = 511.54 ( $\nu_s$ , CSS); 414.36 ( $\nu_a$ , Au-S); 370.15 ( $\nu_s$ , Au-S).

ESI-MS  $m/z$ ,  $[\text{M-Cl}^+]$  found (calc.): 517.03 (517.02)

##### *Bis(piperidine dithiocarbamate)gold(III) bromide, $[\text{Au}(\text{PipeDTC})_2]\text{Br}$*

Aspect: yellow-orange solid

Yield: 85 %



R.f. (on silica gel, CH<sub>2</sub>Cl<sub>2</sub>/MeOH 9:1): 0.12

Anal. Calc. for C<sub>12</sub>H<sub>20</sub>AuBrN<sub>2</sub>S<sub>4</sub> (MW = 597.43 g·mol<sup>-1</sup>): C 24.12; H 3.37; N 4.69; S 21.47. Found: C 24.23; H 3.52; N 4.78; S 21.60.

<sup>1</sup>H-NMR (DMSO-d<sub>6</sub>, 600 MHz): δ (ppm) = 1.74 (m, 12H, H<sub>(3)</sub> + H<sub>(4)</sub> + H<sub>(5)</sub>), 3.83 (m, 8H, H<sub>(2)</sub> + H<sub>(6)</sub>).

Medium FT-IR (KBr):  $\tilde{\nu}$  (cm<sup>-1</sup>) = 2935.18, 2864.80 (ν<sub>a</sub>, C-H); 1558.23 (ν<sub>a</sub>, N-CSS); 950.98 (ν<sub>a</sub>, CSS).

Far FT-IR (nujol):  $\tilde{\nu}$  (cm<sup>-1</sup>) = 514.51 (ν<sub>s</sub>, CSS); 423.38, 410.84 (ν<sub>a</sub>, Au-S); 378.55, 367.76 (ν<sub>s</sub>, Au-S).

ESI-MS *m/z*, [M-Br<sup>+</sup>] found (calc.): 517.03 (517.02)

### 7.3.5 Synthesis of the ionic Au(III) bis(piperidine dithiocarbamato)complex [Au<sup>III</sup>(PipeDTC)<sub>2</sub>][AuBr<sub>2</sub>]

The ionic bis(dithiocarbamato)gold(III) coordination compound [Au<sup>III</sup>(PipeDTC)<sub>2</sub>]<sup>+</sup>[AuBr<sub>2</sub>]<sup>-</sup> was obtained starting from the gold(III) precursor [AuBr<sub>3</sub>py] (py= pyridine; 1 mmol), previously synthesized as reported in literature [351] and then dissolved in 25 mL of dichloromethane. This solution was put at reflux under stirring. After 10 minutes, 1.5 mmol (1.5 eq) of Na PipeDTC dissolved in 2 mL of methanol were added to the Au(III) solution, which in few minutes turned from red to orange. The reaction was left under stirring at reflux for 2 hours, then the solution was cooled, filtered and reduced to half its initial volume. After the addition of 5 mL of diethyl ether, the flask was left at - 10 ° C for two days, leading to the formation of orange needles. This product did not result water-soluble.

#### *Bis(piperidine dithiocarbamate)gold(III) dibromogold(I), [Au(PipeDTC)<sub>2</sub>][AuBr<sub>2</sub>]*

Aspect: light orange needles

Yield: 83 %

R.f. (on silica gel, CH<sub>2</sub>Cl<sub>2</sub>/MeOH 9:1): 0.14

Anal. Calc. for C<sub>12</sub>H<sub>20</sub>Au<sub>2</sub>Br<sub>2</sub>N<sub>2</sub>S<sub>4</sub> (MW = 874.30 g·mol<sup>-1</sup>): C 16.48; H 2.31; N 3.20; S 14.67. Found: C 16.42; H 2.38; N 3.25; S 14.69.

<sup>1</sup>H-NMR (DMSO-d<sub>6</sub>, 600 MHz): δ (ppm) = 1.72 (s, 12H, H<sub>(3)</sub> + H<sub>(4)</sub> + H<sub>(5)</sub>), 3.83 (s, 8H, H<sub>(2)</sub> + H<sub>(6)</sub>).

Medium FT-IR (KBr):  $\tilde{\nu}$  (cm<sup>-1</sup>) = 2954.64 (ν<sub>a</sub>, C-H); 1556.93 (ν<sub>a</sub>, N-CSS); 962.11 (ν<sub>a</sub>, CSS).

Far FT-IR (nujol):  $\tilde{\nu}$  (cm<sup>-1</sup>) = 512.63 (ν<sub>s</sub>, CSS); 410.06 (ν<sub>a</sub>, Au-S); 370.54 (ν<sub>s</sub>, Au-S); 228.52 (ν<sub>a</sub>, Au-Br).

ESI-MS *m/z*, [M-AuBr<sub>2</sub><sup>+</sup>] found (calc.): 517.03 (517.02)

### 7.3.6 Synthesis of the ionic Au(III) bis(piperidine dithiocarbamate) complex $[\text{Au}^{\text{III}}(\text{PipeDTC})_2][\text{AuCl}_4]$

The synthetic procedure used to obtain the complex  $[\text{Au}^{\text{III}}(\text{PipeDTC})_2]^+[\text{AuCl}_4]^-$  was the same reported for the previous compound in **Section 7.3.5**. However, the literature-known  $[\text{AuCl}_3\text{py}]$  precursor was used (py=pyridine) [352], and the ligand PipeDTC was added according to a ligand-to-metal stoichiometry 0.5:1. Also in this case orange needles were obtained, and the product did not result water-soluble.

*Bis(piperidine dithiocarbamate)gold(III) tetrachlorogold(III),  $[\text{Au}(\text{PipeDTC})_2][\text{AuCl}_4]$*

Aspect: light orange needles

Yield: 79 %

R.f. (on silica gel): *n.a.*

Anal. Calc. for  $\text{C}_{12}\text{H}_{20}\text{Au}_2\text{Cl}_4\text{N}_2\text{S}_4$  (MW = 856.31 g·mol<sup>-1</sup>): C 16.83; H 2.35; N 3.27; S 14.98. Found: C 16.81; H 2.36; N 3.30; S 14.90.

<sup>1</sup>H-NMR (DMSO-d<sub>6</sub>, 600 MHz): δ (ppm) = 1.73 (s, 12H, H<sub>(3)</sub> + H<sub>(4)</sub> + H<sub>(5)</sub>), 3.83 (m, 8H, H<sub>(2)</sub> + H<sub>(6)</sub>).

Medium FT-IR (KBr):  $\tilde{\nu}$  (cm<sup>-1</sup>) = 2936.89 (ν<sub>a</sub>, C-H); 1558.74 (ν<sub>a</sub>, N-CSS); 961.10 (ν<sub>a</sub>, CSS).

Far FT-IR (nujol):  $\tilde{\nu}$  (cm<sup>-1</sup>) = 509.85 (ν<sub>s</sub>, CSS); 411.98 (ν<sub>a</sub>, Au-S); 361.10 (ν<sub>s</sub>, Au-S); 334.29 (ν<sub>a</sub>, Au-Cl).

ESI-MS *m/z*,  $[\text{M}-\text{AuCl}_4]^+$  found (calc.): 517.03 (517.02)

## 7.4 Discussion

### 7.4.1 Considerations on the synthetic routes and X-ray structural characterization

During this PhD work, different strategies have been explored (**Figure 7.6**) to obtain the planned Au(I)/(III)-DTC complexes, both neutral and ionic, with the highest yields. In particular, the final routes adopted to isolate the complexes  $[\text{Au}^{\text{III}}\text{X}_2(\text{DTC})]$  (X= Cl, Br),  $[\text{Au}^{\text{III}}(\text{PipeDTC})_2]\text{X}$  (X= Cl, Br) and  $[\text{Au}^{\text{III}}(\text{PipeDTC})_2]\text{Y}$  (Y=  $[\text{Au}^{\text{III}}\text{Cl}_4]$ ,  $[\text{Au}^{\text{I}}\text{Br}_2]$ ) are red-, green- and blue-highlighted, respectively.

The different routes (**Figure 7.6, ROUTE 1-8**) used in this work to obtain the planned Au(III)-DTC derivatives are the result of a deep literature research, combined with the experience in this type of syntheses matured by our research group in the last years.

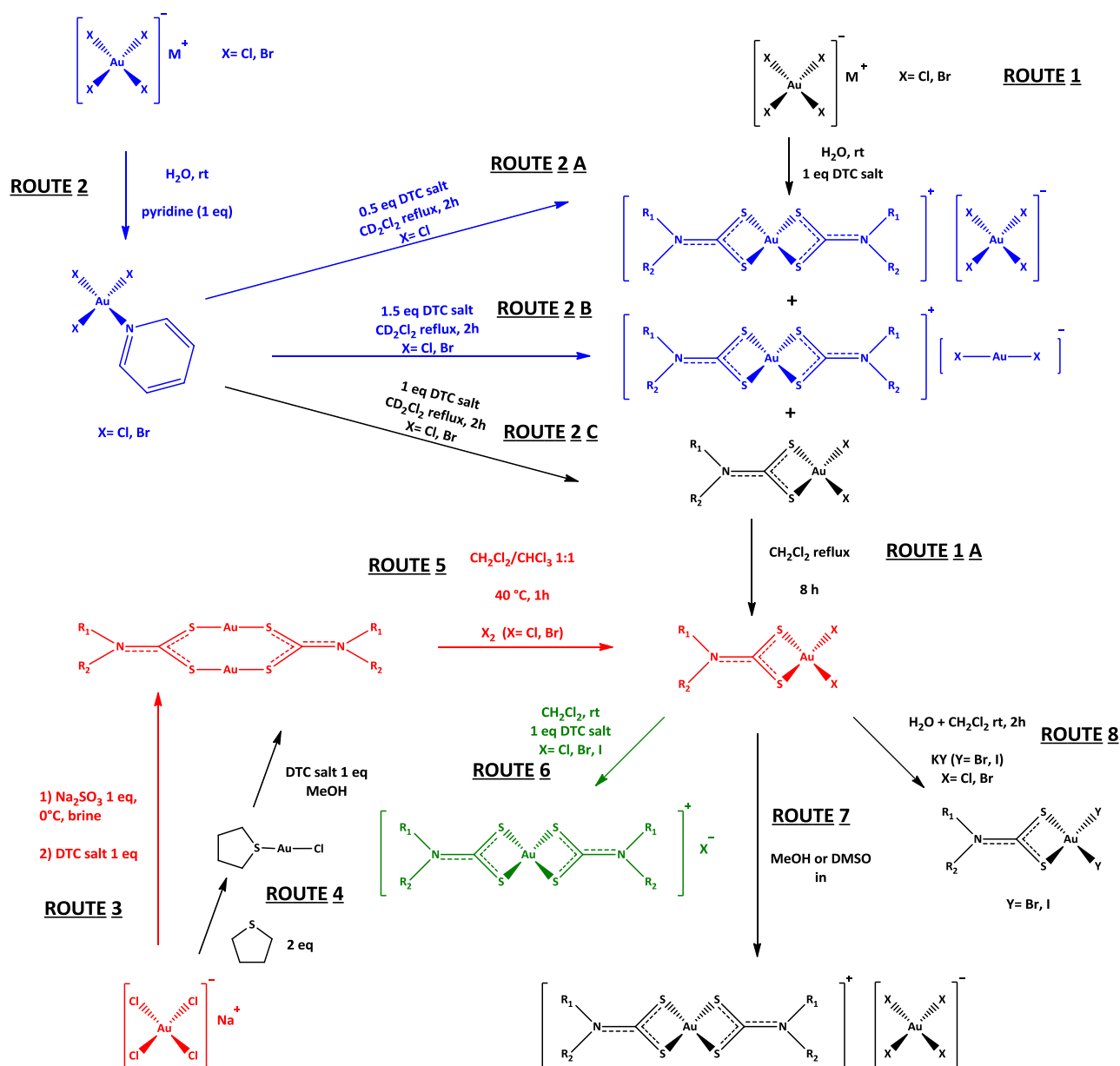


**Figure 7.6** Different strategies adopted for the syntheses of new Au(III)-DTC derivatives. The approaches generating better yields for the compounds  $\text{Au}^{\text{III}}\text{X}_2(\text{DTC})$  ( $\text{X} = \text{Cl}, \text{Br}$ ),  $[\text{Au}^{\text{III}}(\text{PipeDTC})_2]\text{X}$  ( $\text{X} = \text{Cl}, \text{Br}$ ) and  $[\text{Au}^{\text{III}}(\text{PipeDTC})_2]\text{Y}$  ( $\text{Y} = [\text{Au}^{\text{III}}\text{Cl}_4], [\text{Au}^{\text{I}}\text{Br}_2]$ ) are colored in red, green and blue, respectively.

In general, to obtain the neutral species  $[\text{Au}^{\text{III}}\text{X}_2(\text{DTC})]$  the **ROUTE 1** was preferred, followed by chromatographic purification by silica gel gravity column. Remarkably, the recent identification of the precipitation products after addition of 1 eq of DTC ligand to the Au(III) salt (*i.e.*,  $[\text{Au}^{\text{III}}\text{X}_2(\text{DTC})]$ ,  $[\text{Au}^{\text{III}}(\text{DTC})_2][\text{Au}^{\text{I}}\text{X}_2]$  and  $[\text{Au}^{\text{III}}(\text{DTC})_2][\text{AuX}_4]$ ), led us to exploit the **ROUTE 1A** to convert ionic species to neutral ones in halogenated solvents, as reported by Beurskens and co-workers (**Figure 7.3 b**) [339]. In particular, it is possible to suppose that this process occurs *via* a series of substitution reactions involving the coordination spheres of two interacting Au(III) ions bearing opposite charges (*i.e.* that of  $[\text{Au}(\text{DTC})_2]^+$  and that of  $[\text{AuX}_4]^-$ ), based on the substitution scheme identified by Basolo [353]. It is worth noting that the addition of a small

amount of  $\text{NaAuX}_4$  salt is required to achieve the quantitative conversion of ionic species, as the counter ion  $[\text{AuX}_2]^-$  cannot undergo such conversion. On the other hand, this type of reaction does not take place when the substrate shows poor solubility in halogenated solvents, as happens for complexes involving from cyclic aromatic dithiocarbamates. Accordingly, the synthetic **ROUTE 3 (red)** was adopted for these derivatives, involving the formation of the Au(I)-DTC precursor, followed by oxidative addition of chlorine or bromine to generate the  $[\text{Au}^{\text{III}}\text{X}_2(\text{DTC})]$  complex. Moreover, starting from the  $[\text{AuCl}_2(\text{DTC})]$ , it is possible to substitute the halogen with bromine and iodine, as reported in **ROUTE 8 [354]**. Concerning the Au(I)-DTC derivative, although the gold(I) precursor  $[\text{Au}^{\text{I}}\text{Cl}(\text{THT})]$  (THT= tetrahydrothiophene) is a useful starting material to obtain dinuclear Au(I)-dithiocarbamato complexes (**ROUTE 4**), the faster process based on the *in situ* reduction with  $\text{Na}_2\text{SO}_3$  was preferred (**ROUTE 3**) [355].

Moving to ionic derivatives, the water soluble Au(III)-PipeDTC complexes  $[\text{Au}^{\text{III}}(\text{DTC})_2]\text{X}$  (X= Cl, Br) have been obtained following the **ROUTE 6 (green)** by addition of 1 eq of the PipeDTC ligand to the neutral complex. The corresponding  $[\text{Au}^{\text{III}}(\text{DTC})_2]\text{Y}$ , where Y=  $[\text{Au}^{\text{III}}\text{Cl}_4]$  or  $[\text{Au}^{\text{III}}\text{Br}_2]$ , have been obtained as crystals after addition of 0.5 and 1.5 eq of PipeDTC ligand respectively, to a  $\text{CH}_2\text{Cl}_2$  refluxing solution of  $[\text{AuX}_3\text{py}]$  precursor (**ROUTES 2A, 2B blue**). These examples demonstrate how the metal-to-ligand ratio influences the type of obtained product for this family of coordination compounds. Moreover, recently the neutral complex was found to convert to the ionic derivative  $[\text{Au}^{\text{III}}(\text{DTC})_2][\text{Au}^{\text{III}}\text{X}_4]$  in coordinating solvents (*e.g.*, DMSO, ethanol) and in the presence of light (**ROUTE 7**) [356]. Although this process needs further investigations, a brief description is presented in **Section 7.4.5.1**.

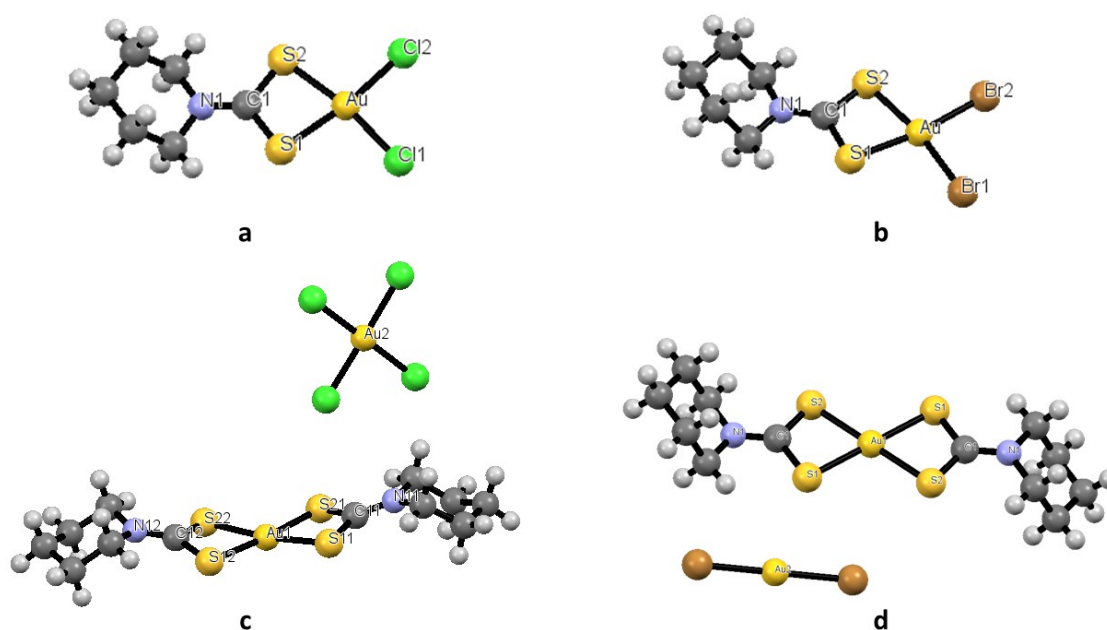


**Figure 7.7** ORTEP drawing of  $[\text{AuCl}_2(\text{PipeDTC})]$  **a**,  $[\text{AuBr}_2(\text{PipeDTC})]$  **b**,  $[\text{Au}(\text{PipeDTC})_2][\text{AuCl}_4]$  **c**, and  $[\text{Au}(\text{PipeDTC})_2][\text{AuBr}_2]$  **d**. The compounds were crystallized from  $\text{CH}_2\text{Cl}_2/\text{Et}_2\text{O}$  solutions at  $-10^\circ\text{C}$ .

	<i>Au-S1</i> (Å)	<i>Au-S2</i> (Å)	<i>Au-X1</i> (Å)	<i>Au-X2</i> (Å)	<i>C1-N1</i> (Å)	<i>Au-Au</i> (Å)	<i>S1-Au-</i> <i>S2</i> (°)	<i>X1-Au-</i> <i>X2</i> (°)	<i>S-Au-X</i> (°)	<i>S-Au-S</i> (°)
[AuCl <sub>2</sub> (PipeDTC)]	2.289(2)	2.299(2)	2.323(2)	2.307(2)	1.289(8)	-	75.67(7)	94.55(9)	94.43(8)	-
[AuBr <sub>2</sub> (PipeDTC)]	2.320(5)	2.314(5)	2.460(4)	2.463(5)	1.300(1)	-	75.60(1)	95.32(6)	94.09(8)	-
[Au(PipeDTC) <sub>2</sub> ][AuCl <sub>4</sub> ]	2.337(3)	2.328(3)	-	-	1.300(1)	7.2942(8)	75.4(1)	-	-	106.7(1)
	2.343(3)	2.315(3)					75.3(1)			102.23(9)
[Au(PipeDTC) <sub>2</sub> ][AuBr <sub>2</sub> ]	2.338(0)	2.335(0)	-	-	1.323(9)	5.521(0)	75.52(0)	-	-	104.48(0)

**Table 7.1:** Selected bond lengths and angles of the crystallized Au(III)-PipeDTC complexes (X= Cl, Br). Halogen-gold data reported in the table are related to the dithiocarbamato complex and not to the counter ion.

The crystal structures of the Au(III)-PipeDTC derivatives, both neutral and ionic, have been obtained and are presented in **Figure 7.7**. [AuX<sub>2</sub>(PipeDTC)] (X= Cl, Br, **a** and **b** respectively) crystallize in the P 2<sub>1</sub> 2<sub>1</sub> 2<sub>1</sub> space group, [Au(PipeDTC)<sub>2</sub>][AuCl<sub>4</sub>] (**c**) adopts the Pna 2<sub>1</sub> group, and finally [Au(PipeDTC)<sub>2</sub>][AuBr<sub>2</sub>] (**d**) the P  $\bar{1}$  group. In all complexes it is possible to observe the chelating coordination of the dithiocarbamato ligands. All structures show a distorted square-planar (SP) geometry with a planarity including also the C-N bonds. The deviation from a perfect SP coordination is due to the small bite angle of the DTC ligand (*ca.* 75 °, as reported in literature for analogous Au(III)-DTC complexes [337]). Focusing on selected bond lengths in **Table 7.1**, for the neutral [AuX<sub>2</sub>(PipeDTC)] complexes the Au-S distances are shorter in the case of dichloro-derivative with respect to the dibromo one. This is due to the effect of the halogen on the gold(III) center, caused by the higher electronegativity of Cl compared to those of Br. Moreover, the length of the C-N bond in all complexes (*ca.* 1.3 Å) results closer to values known for the C=N bond (1.32 Å [158]) than the C-N bond (1.47 Å [158]), thus highlighting the prevalence of the thioureidic form for the PipeDTC ligand (see **Sections 4.2** and **4.4.3**), as observed for [Cu(PipeDTC)<sub>2</sub>] (**Section 6.4.1**) [357]. Concerning the ionic derivatives (**c**, **d**), the crystal structure analysis confirmed the compound composition to include the cation [Au(PipeDTC)<sub>2</sub>]<sup>+</sup> and the anion [AuCl<sub>4</sub>]<sup>-</sup> or [AuBr<sub>2</sub>]<sup>-</sup>. The measured Au(III)-Au(III) (**c**) and Au(III)-Au(I) (**d**) distances are 7.3 and 5.5 Å, respectively, thus pointing out the absence of aurophilic interactions, generally observed in the range 3-3.4 Å [358]. Finally, the cation [Au(PipeDTC)<sub>2</sub>]<sup>+</sup> does not maintain the same arrangement in the two ionic complexes, since in **d** the central Au(III) ion lies on an inversion center, while in **c** the ligands arrange the piperidine chair-configuration on the same plane.

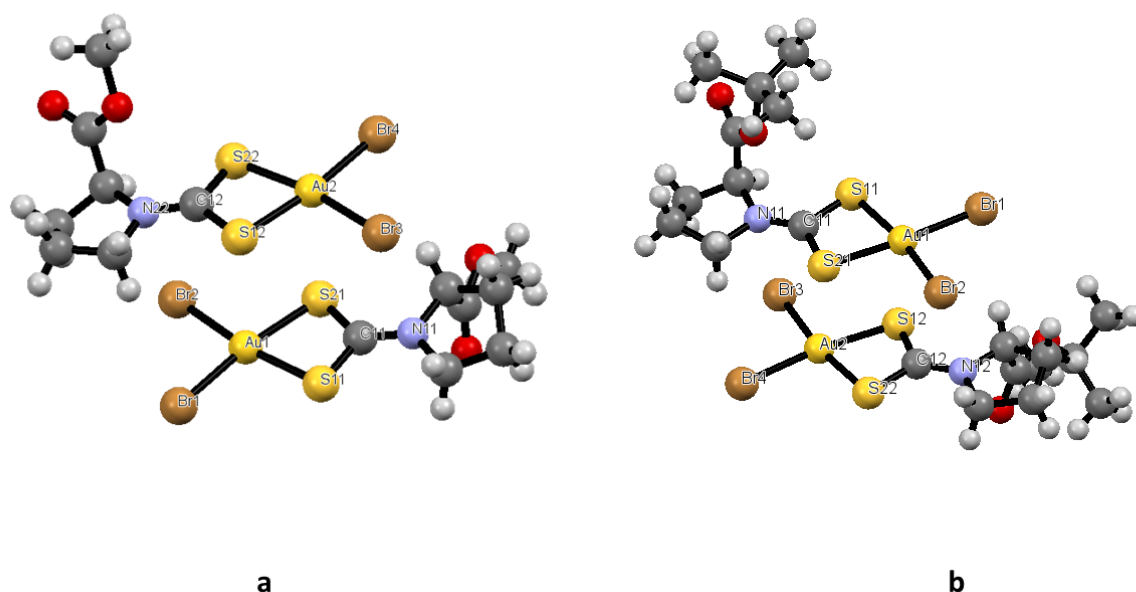


**Figure 7.8** ORTEP drawing of  $[\text{AuBr}_2(\text{ProOMeDTC})]$  **a**, and  $[\text{AuBr}_2(\text{ProOtBuDTC})]$  **b**. The compounds were crystallized from  $\text{CH}_2\text{Cl}_2/\text{Et}_2\text{O}$  solutions at  $-10^\circ\text{C}$ . It is possible to observe that, in both cases, the asymmetric unit comprises 2 molecules.

	<i>Au-S1</i> (Å)	<i>Au-S2</i> (Å)	<i>Au-X1</i> (Å)	<i>Au-X2</i> (Å)	<i>C1-N1</i> (Å)	<i>Au-Au</i> (Å)	<i>S1-Au-S1</i> (°)	<i>X1-Au-X2</i> (°)	<i>S1-Au-X1</i> (°)
$[\text{AuBr}_2(\text{ProOMeDTC})]$	2.316(3)	2.315(3)	2.436(1)	2.435(2)	1.29(1)	4.3850(9)	75.7(1)	94.71(5)	94.67(8) 94.93(8)
$[\text{AuBr}_2(\text{ProOtBuDTC})]$	2.315(4)	2.315(3)	2.435(2)	2.428(2)	1.31(2)	4.416(1)	75.4(1)	93.58(6)	95.2(1) 95.8(1)

**Table 7.2:** Selected bond lengths and angles of the crystallized Au(III)-dibromo(L-proline ester dithiocarbamate) complexes.

Moreover, the crystal structures of dibromo(L-proline ester dithiocarbamate)gold(III) derivatives have been solved and are presented in **Figure 7.8**. Also in this case it is possible to observe the chelating coordination of the DTC ligands, with  $[\text{AuBr}_2(\text{ProOMeDTC})]$  (**a**) crystallizing in the  $P 2_1 2_1 2_1$  space group and  $[\text{AuBr}_2(\text{ProOtBuDTC})_2]$  (**b**) adopting the  $P 2_1$  group. In both cases, the asymmetric unit comprises 2 molecules. The structures show a distorted square-planar (SP) geometry because of the small bite angle of the DTC ligand (*ca.*  $75^\circ$ ). Bond distances as well as angles (**Table 7.2**) are in agreement with data previously discussed for the  $[\text{AuBr}_2(\text{PipeDTC})]$ . Again, the C-N bond length is in agreement with the thioureidic structure above described (see **Sections 4.2** and **4.4.3**). The distance between the two Au(III) centers in the asymmetric unit results *ca.*  $4.4 \text{ \AA}$ . This value is too high to hypothesize aurophilic interactions but is smaller than those observed for the ionic complexes  $[\text{Au}(\text{PipeDTC})_2][\text{AuCl}_4]$  and  $[\text{Au}(\text{PipeDTC})_2][\text{AuBr}_2]$ .

### 7.4.2 ESI-MS analysis

The positive ESI-MS analysis is useful to identify the presence of the cationic Au(III) species. Indeed, the analysis carried out after dissolution of the  $[\text{Au}(\text{PipeDTC})_2]\text{X}$  ( $\text{X} = \text{Cl}, \text{Br}, [\text{AuCl}_4]$  and  $[\text{AuBr}_2]$ ) in methanol points out the presence of a single peak at  $m/z = 517.03$ , undoubtedly assigned to the  $[\text{Au}(\text{PipeDTC})_2]^+$  ion. On the other hand, methanol solutions of the neutral complexes  $[\text{AuX}_2(\text{DTC})]$  ( $\text{X} = \text{Cl}, \text{Br}$ ) generate a signal corresponding to the  $[\text{Au}(\text{DTC})_2]^+$  species. In previous studies, the latter was thought to be originated under the ESI-MS analysis conditions due to the high electrospray ionization potential [359]. Notwithstanding, in the light of **ROUTE 7**, previously presented in **Figure 5**, it is possible to state that the signal detected for the neutral complexes is the consequence of the neutral-to-ionic complex conversion, taking place in coordinating solvents on exposure to light (**Section 7.4.5.1**).

### 7.4.3 $^1\text{H}$ -NMR characterization

The synthesized gold(I)/(III)-dithiocarbamate derivatives have been studied by means of  $^1\text{H}$ -NMR spectroscopy (300.13 MHz, 298 K, see **Supporting Information D**). All spectra were recorded in  $\text{DMSO}-d_6$ . In this regard, although it has been previously reported that  $[\text{AuX}_2(\text{DTC})]$  complexes result unstable in coordinating solvents (*e.g.*, DMSO, MeOH, EtOH), converting to their ionic counterpart  $[\text{Au}(\text{DTC})_2]\text{X}$  this behavior is not observed in deuterated solvent. A possible explanation is some isotopic effect, which influences the interconversion-mechanism, stabilizing the neutral complex in deuterated solvent, as it will be discussed in more detail in **Section 7.4.5.1**.

The assignments have been done by comparing the spectra of the obtained complexes to those of the ligands (see **Section 4.4.2**), and the summary is reported in **Table 7.3**.

	$H_{(1)}$	$H_{(2)}$	$H_{(3)}$	$H_{(4)}$	$H_{(5)}$	$H_{(6)}$	$H_{(7)}$	$H_{(8)}$	$H_{(8)}$	OMe	OtBu
$[\text{Au}_2(\text{PDT})_2]$	<i>n.d.</i>	<b>3.48</b>	1.80	1.80	<b>3.48</b>	-	-	-	-	-	-
$[\text{AuCl}_2(\text{PDT})]$	<i>n.d.</i>	<b>3.81</b>	2.05	2.05	<b>3.81</b>	-	-	-	-	-	-
$[\text{AuBr}_2(\text{PDT})]$	<i>n.d.</i>	<b>3.79</b>	2.04	2.04	<b>3.79</b>	-	-	-	-	-	-
$[\text{Au}_2(\text{PipeDTC})_2]$	<i>n.d.</i>	<b>4.13</b>	0.85	0.85	0.85	<b>4.13</b>	-	-	-	-	-
$[\text{AuCl}_2(\text{PipeDTC})]$	<i>n.d.</i>	<b>3.82</b>	1.72	1.72	1.72	<b>3.82</b>	-	-	-	-	-
$[\text{AuBr}_2(\text{PipeDTC})]$	<i>n.d.</i>	<b>3.79</b>	1.72	1.72	1.72	<b>3.79</b>	-	-	-	-	-
$[\text{Au}(\text{PipeDTC})_2]\text{Cl}$	<i>n.d.</i>	<b>3.83</b>	1.74	1.74	1.74	<b>3.83</b>	-	-	-	-	-
$[\text{Au}(\text{PipeDTC})_2]\text{Br}$	<i>n.d.</i>	<b>3.83</b>	1.74	1.74	1.74	<b>3.83</b>	-	-	-	-	-
$[\text{Au}(\text{PipeDTC})_2][\text{AuCl}_4]$	<i>n.d.</i>	<b>3.83</b>	1.73	1.73	1.73	<b>3.83</b>	-	-	-	-	-
$[\text{Au}(\text{PipeDTC})_2][\text{AuBr}_2]$	<i>n.d.</i>	<b>3.83</b>	1.72	1.72	1.72	<b>3.83</b>	-	-	-	-	-
$[\text{Au}_2(\text{MorphDTC})_2]$	-	3.72	<b>4.18</b>	<i>n.d.</i>	<b>4.18</b>	3.72	-	-	-	-	-
$[\text{AuCl}_2(\text{MorphDTC})]$	-	3.80-	<b>3.88-</b>	<i>n.d.</i>	3.80-	<b>3.88-</b>	-	-	-	-	-
		3.82	<b>3.89</b>		3.82	<b>3.89</b>					

Gold Dithiocarbamates

[AuBr <sub>2</sub> (MorphDTC)]	-	3.80- 3.81	<b>3.85-</b> <b>3.87</b>	<i>n.d.</i>	3.80- 3.81	<b>3.85-</b> <b>3.87</b>	-	-	-	-	-
[Au <sub>2</sub> (IndolineDTC) <sub>2</sub> ]	<i>n.d.</i>	<b>4.59</b>	3.20	7.43	7.28	7.28	<b>8.63</b>	-	-	-	-
[AuCl <sub>2</sub> (IndolineDTC)]	<i>n.d.</i>	<b>4.51</b>	3.38	7.56- 7.58	7.44	7.44	<b>8.05-</b> <b>8.07</b>	-	-	-	-
[AuBr <sub>2</sub> (IndolineDTC)]	<i>n.d.</i>	<b>4.49</b>	<i>n.d.</i>	7.55- 7.57	7.43	7.43	<b>8.04-</b> <b>8.07</b>	-	-	-	-
[Au <sub>2</sub> (ProOMeDTC) <sub>2</sub> ]	<i>n.d.</i>	<b>4.94</b>	2.06	2.06	<b>3.82-</b> <b>3.89</b>	-	-	-	-	3.69	-
[AuCl <sub>2</sub> (ProOMeDTC)]	<i>n.d.</i>	<b>5.16-</b> <b>5.17</b>	2.01- 2.40	2.01- 2.40	<b>3.92-</b> <b>4.01</b>	-	-	-	-	3.76	-
[AuBr <sub>2</sub> (ProOMeDTC)]	<i>n.d.</i>	<b>5.13-</b> <b>5.15</b>	2.00- 2.41	2.00- 2.41	<b>3.91-</b> <b>3.99</b>	-	-	-	-	3.76	-
[Au <sub>2</sub> (ProOtBuDTC) <sub>2</sub> ]	<i>n.d.</i>	<b>4.98</b>	2.10	2.10	<b>3.84-</b> <b>3.91</b>	-	-	-	-	-	1.45
[AuCl <sub>2</sub> (ProOtBuDTC)]	<i>n.d.</i>	<b>5.01-</b> <b>5.02</b>	1.97- 2.40	1.97- 2.40	<b>3.92-</b> <b>3.99</b>	-	-	-	-	-	1.45
[AuBr <sub>2</sub> (ProOtBuDTC)]	<i>n.d.</i>	<b>4.98-</b> <b>5.00</b>	1.98- 2.38	1.98- 2.38	<b>3.89-</b> <b>3.97</b>	-	-	-	-	-	1.45
[Au <sub>2</sub> (CDT) <sub>2</sub> ]	<b>8.12-</b> <b>8.72</b>	8.12- 8.72	7.14- 7.71	7.14- 7.71	7.14- 7.71	7.14- 7.71	8.12- 8.72	<b>8.12-</b> <b>8.72</b>	<i>n.d.</i>	-	-
[AuCl <sub>2</sub> (CDT)]	<b>8.56-</b> <b>8.58</b>	8.14- 8.15	7.15	7.47	7.47	7.15	8.14- 8.15	<b>8.56-</b> <b>8.58</b>	<i>n.d.</i>	-	-
[AuBr <sub>2</sub> (CDT)]	<b>8.55-</b> <b>8.56</b>	8.13- 8.14	7.14	7.45	7.45	7.14	8.13- 8.14	<b>8.55-</b> <b>8.56</b>	<i>n.d.</i>	-	-
[Au <sub>2</sub> (IndDTC) <sub>2</sub> ]	<i>n.d.</i>	<b>8.36</b>	6.68- 6.69	7.59- 7.60	7.21	7.29	<b>8.96-</b> <b>8.97</b>	-	-	-	-
[AuCl <sub>2</sub> (IndDTC)]	<i>n.d.</i>	<b>8.27</b>	7.04	7.12	7.33	7.33	<b>8.85</b>	-	-	-	-
[AuBr <sub>2</sub> (IndDTC)]	<i>n.d.</i>	<b>8.25</b>	7.03	7.11	7.31	7.31	<b>8.82</b>	-	-	-	-
[Au <sub>2</sub> (PyrrDTC) <sub>2</sub> ]	<i>n.d.</i>	<b>6.88</b>	6.29	6.29	<b>6.88</b>	-	-	-	-	-	-
[AuCl <sub>2</sub> (PyrrDTC)]	<i>n.d.</i>	<b>6.57-</b> <b>6.58</b>	6.15- 6.16	6.15- 6.16	<b>6.57-</b> <b>6.58</b>	-	-	-	-	-	-
[AuBr <sub>2</sub> (PyrrDTC)]	<i>n.d.</i>	<b>6.56-</b> <b>6.57</b>	6.14- 6.15	6.14- 6.15	<b>6.56-</b> <b>6.57</b>	-	-	-	-	-	-

**Table 7.3** List of the proton chemical shifts (ppm) of the Au(I)/(III)-DTC derivatives. The *H*-signals proximal to the dithiocarbamic moiety are highlighted with bold font; *n.d.* stands for “not detected”. Attribution was carried out according to the *IUPAC* nomenclature for *N*-heterocyclic compounds. All the spectra were recorded in DMSO-*d*<sub>6</sub>, with a 300.13 MHz spectrometer at 298 K.



First of all, it is worth reminding that both Au(I) ( $d^{10}$  electronic configuration) and Au(III) ( $d^8$ , in a singlet ground state due to the square-planar geometry) centers are diamagnetic, and generate complexes whose NMR signals are located within the common spectral window 0-12 ppm.

The  $^1\text{H-NMR}$  spectra of the gold(I) precursors of the type  $[\text{Au}^{\text{I}}_2(\text{DTC})_2]$  have a low signal-to-noise ratio due to the poor solubility of this kind of complexes in all deuterated solvents. However, the  $^1\text{H-NMR}$  spectroscopy allowed us to assess their purity, as well as to check the course of the oxidation reaction by comparison of Au(I)/Au(III) spectra.

Comparing the chemical shifts of all complexes reported in **Table 7.3** with those of free dithiocarbamate ligands (**Section 4.4.2**), a lower-field shift of the signals related to the  $\alpha$ -protons with respect to the dithiocarbamic nitrogen atom is detected upon coordination, except for aromatic gold(I) derivatives. For this, a possible explanation is the metal-to-ligand back-donation, allowed by the presence of low-energy empty  $d$ -orbitals of sulfur atoms (dithiocarbamic form of the ligand, see **Section 4.2**), which makes the DTC-protons more shielded. A similar effect was reported for phosphinogold(I)-dithiocarbamate complexes [360].

Concerning the neutral Au(III)-DTC coordination compounds  $[\text{Au}^{\text{III}}\text{X}_2(\text{DCT})]$ , the  $H(\alpha)$ -signals of the chloro-derivatives are found at slightly lower fields with respect to the bromo-counterparts, due to the higher electronegativity of the former. However, the presence of the halogen as well as the +3 oxidation state of the metal center does not affect, or affects to a small extent, the resonance of ligand protons if compared to those of Au(I) derivatives. Finally, on passing from the neutral to the ionic Au(III)-PipeDTC complexes, the  $\alpha$ -proton signals are slightly shifted to lower fields. At the same time, the nature of the counter-ion in  $[\text{Au}^{\text{III}}(\text{PipeDTC})_2]\text{X}$  compounds seems not to affect the resonance of any proton.

#### 7.4.4 FT-IR characterization

The FT-IR spectra have been collected for all the Au(I)/(III)-DTC derivatives both in the medium (4000-600  $\text{cm}^{-1}$ ) and far (600-200  $\text{cm}^{-1}$ ) wavenumber domain (**Supporting Information I**), and the diagnostic absorptions are reported in **Table 7.4**.

This spectrophotometric technique is the most useful tool to detect the different chemical features generated by the different oxidation states of the gold metal centers, as well as by the substituents of the DTC ligands.

Gold Dithiocarbamates

	$\nu(C=O)$	$\nu(C=C)$	$\nu(N-CSS)$	$\nu_a(C-O)$	$\nu_a(CSS)$	$\delta(C-H)$	$\nu_s(CSS)$	$\nu_a(Au-S)$	$\nu_s(Au-S)$	$\nu_a(Au-X)$	$\nu_s(Au-X)$
[Au <sub>2</sub> (PDT) <sub>2</sub> ]	-	-	1428 cm <sup>-1</sup>	-	954 cm <sup>-1</sup>	-	559 cm <sup>-1</sup>	451 cm <sup>-1</sup>	-	-	-
[AuCl <sub>2</sub> (PDT)]	-	-	1588 cm <sup>-1</sup>	-	944 cm <sup>-1</sup>	-	537 cm <sup>-1</sup>	375 cm <sup>-1</sup>	339 cm <sup>-1</sup>	352 cm <sup>-1</sup>	315 cm <sup>-1</sup>
[AuBr <sub>2</sub> (PDT)]	-	-	1586 cm <sup>-1</sup>	-	943 cm <sup>-1</sup>	-	539 cm <sup>-1</sup>	373 cm <sup>-1</sup>	338 cm <sup>-1</sup>	240 cm <sup>-1</sup>	218 cm <sup>-1</sup>
[Au <sub>2</sub> (PipeDTC) <sub>2</sub> ]	-	-	1428 cm <sup>-1</sup>	-	968 cm <sup>-1</sup>	-	557 cm <sup>-1</sup>	479 cm <sup>-1</sup>	-	-	-
[AuCl <sub>2</sub> (PipeDTC)]	-	-	1581 cm <sup>-1</sup>	-	947 cm <sup>-1</sup>	-	540 cm <sup>-1</sup>	366 cm <sup>-1</sup>	335 cm <sup>-1</sup>	350 cm <sup>-1</sup>	316 cm <sup>-1</sup>
[AuBr <sub>2</sub> (PipeDTC)]	-	-	1574 cm <sup>-1</sup>	-	942 cm <sup>-1</sup>	-	539 cm <sup>-1</sup>	370 cm <sup>-1</sup>	351 cm <sup>-1</sup>	239 cm <sup>-1</sup>	224 cm <sup>-1</sup>
[Au(PipeDTC) <sub>2</sub> ]Cl	-	-	1561 cm <sup>-1</sup>	-	951 cm <sup>-1</sup>	-	512 cm <sup>-1</sup>	414 cm <sup>-1</sup>	370 cm <sup>-1</sup>	-	-
[Au(PipeDTC) <sub>2</sub> ]Br	-	-	1558 cm <sup>-1</sup>	-	951 cm <sup>-1</sup>	-	515 cm <sup>-1</sup>	423, 410 cm <sup>-1</sup>	379, 368 cm <sup>-1</sup>	-	-
[Au(PipeDTC) <sub>2</sub> ][AuCl <sub>4</sub> ]	-	-	1559 cm <sup>-1</sup>	-	961 cm <sup>-1</sup>	-	510 cm <sup>-1</sup>	412 cm <sup>-1</sup>	361 cm <sup>-1</sup>	334 cm <sup>-1</sup>	-
[Au(PipeDTC) <sub>2</sub> ][AuBr <sub>2</sub> ]	-	-	1557 cm <sup>-1</sup>	-	962 cm <sup>-1</sup>	-	513 cm <sup>-1</sup>	410 cm <sup>-1</sup>	371 cm <sup>-1</sup>	229 cm <sup>-1</sup>	-
[Au <sub>2</sub> (MorphDTC) <sub>2</sub> ]	-	-	1417 cm <sup>-1</sup>	1108 cm <sup>-1</sup>	993 cm <sup>-1</sup>	-	541 cm <sup>-1</sup>	462 cm <sup>-1</sup>	-	-	-
[AuCl <sub>2</sub> (MorphDTC)]	-	-	1572 cm <sup>-1</sup>	1109 cm <sup>-1</sup>	993 cm <sup>-1</sup>	-	543 cm <sup>-1</sup>	364 cm <sup>-1</sup>	338 cm <sup>-1</sup>	357 cm <sup>-1</sup>	318 cm <sup>-1</sup>
[AuBr <sub>2</sub> (MorphDTC)]	-	-	1562 cm <sup>-1</sup>	1109 cm <sup>-1</sup>	993 cm <sup>-1</sup>	-	542 cm <sup>-1</sup>	358 cm <sup>-1</sup>	348 cm <sup>-1</sup>	238 cm <sup>-1</sup>	220 cm <sup>-1</sup>
[Au <sub>2</sub> (IndolineDTC) <sub>2</sub> ]	-	1473, 1458 cm <sup>-1</sup>	1376 cm <sup>-1</sup>	-	1070 cm <sup>-1</sup>	749 cm <sup>-1</sup>	556 cm <sup>-1</sup>	467 cm <sup>-1</sup>	-	-	-
[AuCl <sub>2</sub> (IndolineDTC)]	-	1474, 1460 cm <sup>-1</sup>	1541 cm <sup>-1</sup>	-	1075 cm <sup>-1</sup>	752 cm <sup>-1</sup>	553 cm <sup>-1</sup>	383 cm <sup>-1</sup>	339 cm <sup>-1</sup>	368 cm <sup>-1</sup>	319 cm <sup>-1</sup>
[AuBr <sub>2</sub> (IndolineDTC)]	-	1473, 1460 cm <sup>-1</sup>	1536 cm <sup>-1</sup>	-	1075 cm <sup>-1</sup>	748 cm <sup>-1</sup>	552 cm <sup>-1</sup>	376 cm <sup>-1</sup>	359 cm <sup>-1</sup>	237 cm <sup>-1</sup>	221 cm <sup>-1</sup>
[Au <sub>2</sub> (ProOMeDTC) <sub>2</sub> ]	1739 cm <sup>-1</sup>	-	1418 cm <sup>-1</sup>	1158 cm <sup>-1</sup>	950 cm <sup>-1</sup>	-	553 cm <sup>-1</sup>	452 cm <sup>-1</sup>	-	-	-
[AuCl <sub>2</sub> (ProOMeDTC)]	1747 cm <sup>-1</sup>	-	1560 cm <sup>-1</sup>	1174 cm <sup>-1</sup>	979 cm <sup>-1</sup>	-	547 cm <sup>-1</sup>	382 cm <sup>-1</sup>	339 cm <sup>-1</sup>	359 cm <sup>-1</sup>	319 cm <sup>-1</sup>
[AuBr <sub>2</sub> (ProOMeDTC)]	1746 cm <sup>-1</sup>	-	1550 cm <sup>-1</sup>	1173 cm <sup>-1</sup>	985 cm <sup>-1</sup>	-	546 cm <sup>-1</sup>	378 cm <sup>-1</sup>	349 cm <sup>-1</sup>	237 cm <sup>-1</sup>	219 cm <sup>-1</sup>
[Au <sub>2</sub> (ProOtBuDTC) <sub>2</sub> ]	1734 cm <sup>-1</sup>	-	1412 cm <sup>-1</sup>	1157 cm <sup>-1</sup>	965 cm <sup>-1</sup>	-	536 cm <sup>-1</sup>	444 cm <sup>-1</sup>	-	-	-
[AuCl <sub>2</sub> (ProOtBuDTC)]	1738 cm <sup>-1</sup>	-	1558 cm <sup>-1</sup>	1146 cm <sup>-1</sup>	950 cm <sup>-1</sup>	-	545 cm <sup>-1</sup>	381 cm <sup>-1</sup>	341 cm <sup>-1</sup>	358 cm <sup>-1</sup>	319 cm <sup>-1</sup>
[AuBr <sub>2</sub> (ProOtBuDTC)]	1736 cm <sup>-1</sup>	-	1560 cm <sup>-1</sup>	1147 cm <sup>-1</sup>	953 cm <sup>-1</sup>	-	541 cm <sup>-1</sup>	379 cm <sup>-1</sup>	345 cm <sup>-1</sup>	238 cm <sup>-1</sup>	219 cm <sup>-1</sup>
[Au <sub>2</sub> (CDT) <sub>2</sub> ]	-	1438 cm <sup>-1</sup>	1286 cm <sup>-1</sup>	-	1023 cm <sup>-1</sup>	739, 710 cm <sup>-1</sup>	561 cm <sup>-1</sup>	464 cm <sup>-1</sup>	-	-	-

[AuCl <sub>2</sub> (CDT)]	-	1492, 1451 cm <sup>-1</sup>	1350 cm <sup>-1</sup>	-	1042 cm <sup>-1</sup>	749, 708, cm <sup>-1</sup>	574 cm <sup>-1</sup>	408 cm <sup>-1</sup>	378 cm <sup>-1</sup>	358 cm <sup>-1</sup>	322 cm <sup>-1</sup>
[AuBr <sub>2</sub> (CDT)]	-	1491, 1450 cm <sup>-1</sup>	1349 cm <sup>-1</sup>	-	1041 cm <sup>-1</sup>	749, 708 cm <sup>-1</sup>	570 cm <sup>-1</sup>	408 cm <sup>-1</sup>	376 cm <sup>-1</sup>	249 cm <sup>-1</sup>	223 cm <sup>-1</sup>
[Au <sub>2</sub> (IndDTC) <sub>2</sub> ]	-	1444 cm <sup>-1</sup>	1314 cm <sup>-1</sup>	-	1008 cm <sup>-1</sup>	738, 723 cm <sup>-1</sup>	568 cm <sup>-1</sup>	470 cm <sup>-1</sup>	-	-	-
[AuCl <sub>2</sub> (IndDTC)]	-	1481, 1462 cm <sup>-1</sup>	1358 cm <sup>-1</sup>	-	1095 cm <sup>-1</sup>	749, 707 cm <sup>-1</sup>	564 cm <sup>-1</sup>	409 cm <sup>-1</sup>	382 cm <sup>-1</sup>	347 cm <sup>-1</sup>	324 cm <sup>-1</sup>
[AuBr <sub>2</sub> (IndDTC)]	-	1484, 1448 cm <sup>-1</sup>	1357 cm <sup>-1</sup>	-	1077 cm <sup>-1</sup>	750, 706 cm <sup>-1</sup>	574 cm <sup>-1</sup>	409 cm <sup>-1</sup>	378 cm <sup>-1</sup>	252 cm <sup>-1</sup>	227 cm <sup>-1</sup>
[Au <sub>2</sub> (PyrrDTC) <sub>2</sub> ]	-	1456 cm <sup>-1</sup>	1284 cm <sup>-1</sup>	-	1011 cm <sup>-1</sup>	720 cm <sup>-1</sup>	557 cm <sup>-1</sup>	464 cm <sup>-1</sup>	-	-	-
[AuCl <sub>2</sub> (PyrrDTC)]	-	1480 cm <sup>-1</sup>	1345 cm <sup>-1</sup>	-	1023 cm <sup>-1</sup>	763 cm <sup>-1</sup>	567 cm <sup>-1</sup>	413 cm <sup>-1</sup>	381 cm <sup>-1</sup>	347 cm <sup>-1</sup>	321 cm <sup>-1</sup>
[AuBr <sub>2</sub> (PyrrDTC)]	-	1479 cm <sup>-1</sup>	1345 cm <sup>-1</sup>	-	1022 cm <sup>-1</sup>	763 cm <sup>-1</sup>	578 cm <sup>-1</sup>	413 cm <sup>-1</sup>	377 cm <sup>-1</sup>	233 cm <sup>-1</sup>	215 cm <sup>-1</sup>

**Table 7.4** Collection of the fundamental IR-vibrations (4000-200 cm<sup>-1</sup>) of the synthesized Au(I)/(III)-DTC complexes.

Concerning the gold(I)-DTC complexes, Hesse and Jennische resolved the crystal structure of [Au<sub>2</sub>(propylamineDTC)<sub>2</sub>], demonstrating the dimeric nature of these compounds with each Au(I) ion coordinated by two sulfur atoms coming from different ligands. Moreover, they observed that the structure is highly symmetric, and the distance between the two gold centers (2.76 Å) evidences an aurophilic interaction [361]. Moreover, according to the data presented in Table 7.4, it is worth noting that the SSC-N stretching frequencies are located in the range 1410-1430 cm<sup>-1</sup> and 1280-1315 cm<sup>-1</sup> for aliphatic and aromatic dithiocarbamate derivatives, respectively. Intriguingly, the Au(I)-IndolineDTC presents the ν(SSC-N) vibration at 1376 cm<sup>-1</sup>, being intermediate between the values found for aliphatic and aromatic compounds. Conversely, for the Au(III)-DTC compounds the coordination is bidentate surrounding a single metal center, and the SSC-N stretching frequencies are up-shifted of *ca.* 150 cm<sup>-1</sup> in all aliphatic compounds (comprised indoline derivatives) if compared to the gold(I) counterparts, while this increment is of about 40-60 cm<sup>-1</sup> for aromatic complexes. As observed by Calabro and co-workers in their work on Au(II)-DTC derivatives, there is a small increase in the ν(SSC-N) frequency of the DTC ligand as the oxidation state of gold increases [302], and, in line with these observations, taking PipeDTC complexes as an example, the following trend is achieved:

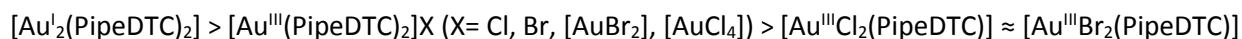


This sequence considers also electronegativity effects deriving from the two halide ligands in the neutral Au(III) complexes, further promoting the shift of the nitrogen atom lone pair to the -CSS moiety, resulting in a higher positive charge on the nitrogen atom. In general, for aliphatic DTC complexes, the thioureidic form

(see **Section 4.2**) of the ligand is preferred, whereas the aromatic ones mainly involve the dithiocarbamic form with a single C-N bond (frequencies in the range 1250-1350 cm<sup>-1</sup>). Remarkably, the presence of a single band associated with this vibration mode, clearly indicates that the dithiocarbamate groups are linked to the metal ion in a single way, *i.e.*, bi-dentate chelate for the Au(III) complexes, and mono-dentate bridge for gold(I) compounds, with each sulfur atom bound to a different Au(I) center.

Concerning the C-S stretching, it has been previously reported for copper(II)-DTCs (Section 6.4.4) that the higher the  $\nu(\text{SSC-N})$  frequency and the lower the  $\nu(\text{CSS})$  one, based on the main influence of the thioureidic or dithiocarbamic form. In general, the presented Au(I)/(III)-DTC complexes comply with this trend, when considering both the asymmetric (900-1000 cm<sup>-1</sup>) and symmetric (500-600 cm<sup>-1</sup>) component of this vibration mode, although the latter involves more contributions, namely  $\nu(\text{CSS}) + \delta(\text{CSS}) + \text{Au} \langle \overset{\text{S}}{\underset{\text{S}}{\text{C}}} \rangle \text{C}$  ring deformations [362]. To sum up, focusing on gold(III) molecules, the ligand dithiocarbamic form adopted by the aromatic derivatives, and by indolineDTC complexes to a lesser extent, is associated with a major electron density in the ring  $\text{Au} \langle \overset{\text{S}}{\underset{\text{S}}{\text{C}}} \rangle \text{C}$ , and hence stronger bonds between the metal center and the chelating ligand, compared to aliphatic derivatives.

Overall, the most striking differences among the synthesized derivatives occur in the far-IR domain, where the stretching vibrational modes metal-sulfur (330-470 cm<sup>-1</sup>), and Au-halide (315-360 cm<sup>-1</sup> and 220-250 cm<sup>-1</sup> for chlorine and bromine, respectively) are found. In particular, focusing on the PipeDTC complexes, the Au-S stretching frequency results in the order:



The Au-S bond is hence stronger in gold(I) derivatives and the gold(III) ones with 1:2 metal-to-DTC ligand stoichiometry. The Au-S frequency increases as the oxidation number of the metal center decreases, and this is probably related to a reduced possibility of the gold(III) ion to back-donate  $\pi$  electron density to the DTC ligand.

Concerning metal-halide bonds, the collected frequencies are in agreement with previously reported results for analogous compounds [336-340]. The absence of Au-X bands in the spectra of Au(I)-DTC derivatives confirms the Jennische's structural findings about the dimeric structure  $[\text{Au}^{\text{I}}_2(\text{DTC})_2]$  of these complexes [361]. Likewise, in the spectra of the  $[\text{Au}^{\text{III}}(\text{PipeDTC})_2]\text{X}$  coordination compounds, the Au-X vibration is not found when the counter ion is Cl or Br, thus confirming the ionic nature of the complexes, identified by the previous analyses. On the other hand, in the case  $\text{X} = [\text{AuBr}_2]$  or  $[\text{AuCl}_4]$  the values presented in **Table 7.4** resemble those found in literature for similar ionic Au(III)-DTC derivatives [337, 339], as well as other inorganic complexes with these counter ions [363, 364].

Finally, similarly to the Ru(III) and Cu(II) derivatives (**Section 5.4.4** and **6.4.4** respectively), the diagnostic features of the ester group of proline ligands (1740 cm<sup>-1</sup>), as well as the aromatic ring vibrations (*ca.* 1470 cm<sup>-1</sup> and 750 cm<sup>-1</sup>, referred to the C=C stretching and C-H bending vibration, respectively) have been identified for the synthesized Au(I)/(III) complexes.

## 7.4.5 UV-Vis characterization

Electronic spectra were acquired in CH<sub>2</sub>Cl<sub>2</sub> (800-240 nm) at 25 °C for all the synthesized gold(III)-DTC derivatives, and in DMSO (800-270 nm) at 25 °C for the Au(I) counterparts, and the diagnostic absorptions are summarized in **Table 7.5** and **7.6**, respectively.

	$\lambda$ ( $\epsilon$ , $M^{-1} cm^{-1}$ )				
	<i>band I</i>	<i>band II</i>	<i>band III</i>	<i>band IV</i>	<i>band V</i>
[AuCl <sub>2</sub> (PDT)]	<i>n.d.</i>	<i>n.d.</i>	265 nm (28650)	327 nm (2330)	428 nm (212)
[AuBr <sub>2</sub> (PDT)]	255 nm (25567)	265 <sup>sh</sup> nm (26311)	285 nm (29543)	385 nm (2431)	435 nm (1965)
[AuCl <sub>2</sub> (PipeDTC)]	<i>n.d.</i>	<i>n.d.</i>	264 nm (28212)	326 nm (2488)	428 nm (249)
[AuBr <sub>2</sub> (PipeDTC)]	254 nm (25839)	267 nm (26054)	286 nm (29082)	383 nm (2598)	434 nm (1861)
[Au(PipeDTC) <sub>2</sub> ]Cl	269 <sup>sh</sup> nm (27470)	276 nm (30145)	318 nm (27650)	<i>n.d.</i>	387 nm (1346)
[Au(PipeDTC) <sub>2</sub> ]Br	269 <sup>sh</sup> nm (27616)	276 nm (29671)	318 nm (27421)	<i>n.d.</i>	387 nm (1308)
[Au(PipeDTC) <sub>2</sub> ][AuBr <sub>2</sub> ]	269 <sup>sh</sup> nm (27538)	276 nm (29290)	318 nm (27513)	<i>n.d.</i>	387 nm (1291)
[AuCl <sub>2</sub> (MorphDTC)]	<i>n.d.</i>	<i>n.d.</i>	267 nm (30141)	324 nm (2753)	433 nm (320)
[AuBr <sub>2</sub> (MorphDTC)]	254 nm (27753)	271 <sup>sh</sup> nm (28004)	282 nm (31758)	387 nm (2719)	442 nm (1868)
[AuCl <sub>2</sub> (IndolineDTC)]	<i>n.d.</i>	<i>n.d.</i>	272 nm (37090)	324 nm (3765)	<i>n.d.</i>
[AuBr <sub>2</sub> (IndolineDTC)]	<i>n.d.</i>	288 <sup>sh</sup> nm (36544)	314 nm (39715)	390 nm (4010)	427 <sup>sh</sup> nm (2590)
[AuCl <sub>2</sub> (ProOMeDTC)]	<i>n.d.</i>	<i>n.d.</i>	265 nm (27564)	330 nm (2771)	431 nm (319)
[AuBr <sub>2</sub> (ProOMeDTC)]	255 <sup>sh</sup> nm (25321)	272 <sup>sh</sup> nm (26001)	284 nm (28861)	387 nm (2698)	439 nm (1874)
[AuCl <sub>2</sub> (ProOtBuDTC)]	<i>n.d.</i>	<i>n.d.</i>	266 nm (29801)	330 nm (2787)	431 nm (286)
[AuBr <sub>2</sub> (ProOtBuDTC)]	255 <sup>sh</sup> nm (25615)	271 <sup>sh</sup> nm (27564)	285 nm (29729)	388 nm (2764)	438 nm (1634)
[AuCl <sub>2</sub> (CDT)]	<i>n.d.</i>	<i>n.d.</i>	278 nm (38318)	350 nm (4216)	<i>n.d.</i>
[AuBr <sub>2</sub> (CDT)]	252 nm (42539)	280 <sup>sh</sup> nm (41071)	290 nm (38415)	354 nm (4349)	<i>n.d.</i>
[AuCl <sub>2</sub> (IndDTC)]	<i>n.d.</i>	<i>n.d.</i>	275 nm (38888)	349 nm (4379)	<i>n.d.</i>
[AuBr <sub>2</sub> (IndDTC)]	250 nm (42566)	280 nm (41985)	289 nm (39192)	345 nm (4280)	<i>n.d.</i>
[AuCl <sub>2</sub> (PyrrDTC)]	<i>n.d.</i>	<i>n.d.</i>	276 nm (38583)	344 nm (3916)	<i>n.d.</i>
[AuBr <sub>2</sub> (PyrrDTC)]	250 nm (41998)	281 <sup>sh</sup> nm (40713)	290 nm (39125)	340 nm (4006)	<i>n.d.</i>

**Table 7.5** UV-Vis spectral data (800-240 nm) of Au(III)-dithiocarbamate complexes of the type [Au<sup>III</sup>X<sub>2</sub>(DTC)] and [Au<sup>III</sup>(PipeDTC)<sub>2</sub>]X with X= Cl, Br, and [AuBr<sub>2</sub>], recorded in CH<sub>2</sub>Cl<sub>2</sub> at 25 °C. *n.d.* stands for “not detected”.

Concerning the Au(III)-DTC derivatives, it is worth reminding that both neutral and ionic derivatives are square planar (SP) complexes. Consequently, the five degenerate  $d$ -orbitals of the free Au(III)  $d^8$  ion split into four different levels. In particular, Gray and Ballhausen described the molecular orbital theory for SP complexes, discussing two distinct cases [365]. The first is related to SP compounds in which the ligands themselves have a  $\pi$ -orbital system, whereas the second is associated with SP complexes with no intra-ligand  $\pi$ -orbital system. For both cases, there are three spin-allowed  $d-d$  transitions, corresponding to the one-electron transitions  $^1A_{1g} \rightarrow ^1A_{2g}$ ,  $^1A_{1g} \rightarrow ^1B_{1g}$  and  $^1A_{1g} \rightarrow ^1E_g$ . Moreover, considering DTC ligands as moieties containing a  $\pi$ -orbital system three charge-transfer (CT) transitions are foreseen, namely  $^1A_{1g} \rightarrow ^1E_u$ ,  $^1A_{1g} \rightarrow ^1A_{2u}$ , and  $^1A_{1g} \rightarrow ^1B_{1u}$ . However, only the first and second are allowed, with the  $^1A_{1g} \rightarrow ^1E_u$  transition expected to have considerably greater intensity. On the other hand, halido ligands belong to the second case presented, and in general generate two allowed CT transitions of the type  $^1A_{1g} \rightarrow ^1E_u$  (more intense) and  $^1A_{1g} \rightarrow ^1A_{2u}$  [365-367]. Observing the examples shown in **Figure 7.9**, the *bands I, II* and *III* have not been undoubtedly ascribed in literature to a particular electronic transition, since they could be assigned to either an intra-ligand  $\pi^* \leftarrow \pi$  transition located in the -NCSS moiety or an intraligand  $p \leftarrow d$  transition between levels originated by sulfur atoms [368]. Moreover, data presented in **Table 7.5** highlight a blue-shift of the *band I* combined with a slight red-shift of the *band II* on passing from aliphatic neutral Au(III)-DTC derivatives to compounds containing aromatic moieties, thus pointing out both a stabilization and a destabilization respectively of some energetic levels in hyperconjugated systems. On the other hand, an overall red-shift is also observed in ionic PipeDTC complexes of the type  $[Au(\text{PipeDTC})_2]X$  when compared with neutral counterparts.

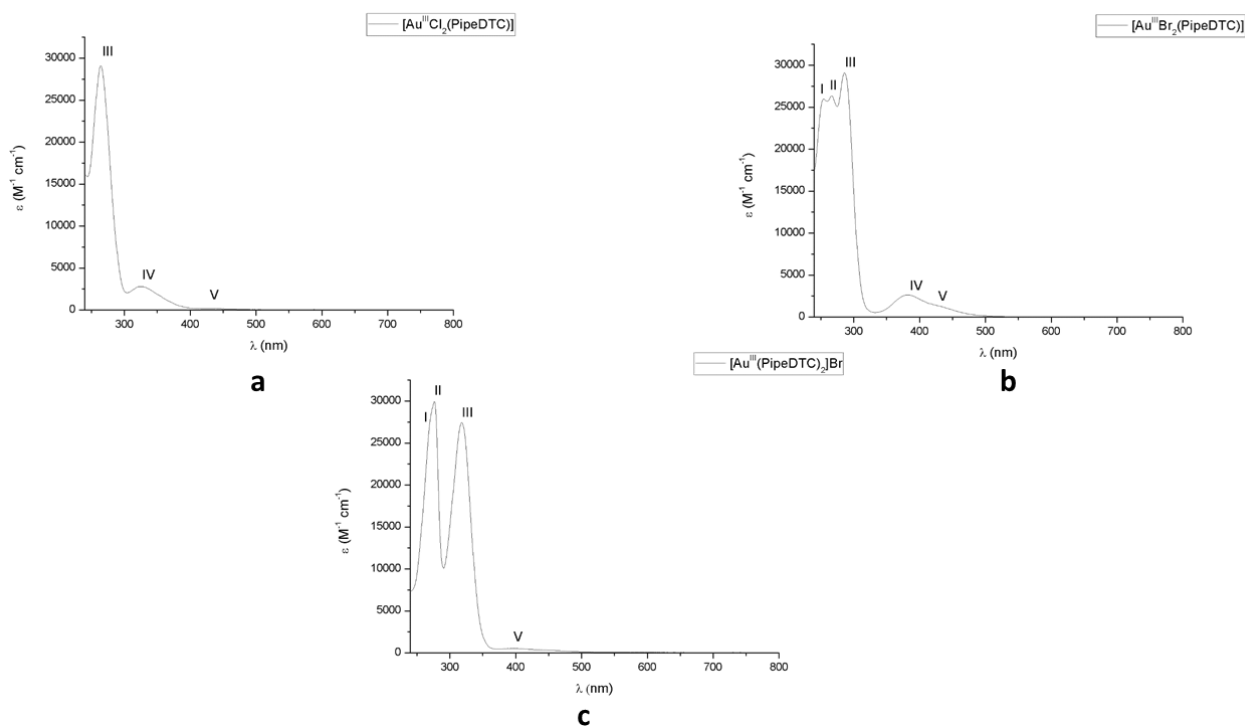


**Figure 7.9** UV-Vis spectra of  $[Au^{III}Cl_2(\text{PipeDTC})]$  **a**,  $[Au^{III}Br_2(\text{PipeDTC})]$  **b**, and  $[Au^{III}(\text{PipeDTC})_2]Br$  **c** recorded in  $CH_2Cl_2$  at 25 °C.

Another significant difference between neutral and ionic Au(III)-DTC systems is the lack in the latter of the band IV, which is generally attributed to either an intramolecular L←M charge transfer, involving the M *nd* orbitals and the dithiocarbamato π\*-system (case 1 abovementioned), or an electron transfer of the type u←g from a 4*p* orbital of the halide ligands to the lowest unfilled 5*d* orbital (case 2) [369]. In light of this, the values collected for this absorption band in neutral [AuX<sub>2</sub>(DTC)] (Table 7.5) point out that the electron transfer halogen-gold(III) is the most conceivable for Au(III)-aliphatic dithiocarbamato compounds, with dichlorido complexes presenting an absorption at *ca.* 325 nm and the dibromido at about 390 nm. However, when the ligand acts as a π acceptor (dithiocarbamic form of the aromatic ligands CDT, IndDTC and PyrrDTC (Section 4.2), a L←M charge transfer (metal back-donation, case 1) takes place more likely, generating a strong absorption at 340-350 nm with an ε value of about 4,000 M<sup>-1</sup> cm<sup>-1</sup>. Again, as already observed during the interpretation of IR spectra, the [AuX<sub>2</sub>(IndolineDTC)] complexes assume a behavior closer to the thioureidic form, where the DTC ligand is a weak π-acceptor. It turns out that, although indoline is an aromatic amine, the aliphatic *N*-substituent is predominant in affecting the final properties of the corresponding DTC ligand.

Finally, the *band V* is a weak absorption and it is easily detected in dibromido derivatives since it appears as a shoulder of the CT transition. It is attributable to the three allowed *d-d* transitions <sup>1</sup>A<sub>1g</sub>→<sup>1</sup>A<sub>2g</sub>, <sup>1</sup>A<sub>1g</sub>→<sup>1</sup>B<sub>1g</sub> and <sup>1</sup>A<sub>1g</sub>→<sup>1</sup>E<sub>g</sub> [340, 367]. Intriguingly, these have not been detected for the aromatic dithiocarbamato complexes, likely owing to their too low intensity in comparison with the CT and intra-ligand transitions, which could also benefit in terms of intensity from the hyperconjugated aromatic system.

	λ	
	<i>band II</i>	<i>band III</i>
[Au <sub>2</sub> (PDT) <sub>2</sub> ]	283 nm	316 <sup>sh</sup> nm
[Au <sub>2</sub> (PipeDTC) <sub>2</sub> ]	279 nm	317 nm
[Au <sub>2</sub> (MorphDTC) <sub>2</sub> ]	288 nm	314 <sup>sh</sup> nm
[Au <sub>2</sub> (IndolineDTC) <sub>2</sub> ]	296 nm	334 nm
[Au <sub>2</sub> (ProOMeDTC) <sub>2</sub> ]	286 nm	317 <sup>sh</sup> nm
[Au <sub>2</sub> (ProOtBuDTC) <sub>2</sub> ]	284 nm	319 <sup>sh</sup> nm
[Au <sub>2</sub> (CDT) <sub>2</sub> ]	294 nm	338 nm
[Au <sub>2</sub> (IndDTC) <sub>2</sub> ]	298 nm	340 nm
[Au <sub>2</sub> (PyrrDTC) <sub>2</sub> ]	302 nm	346 nm

**Table 7.6** UV-Vis spectral data (800-240 nm) of Au(I)-dithiocarbamato complexes of the type [Au<sup>I</sup><sub>2</sub>(DTC)<sub>2</sub>], acquired in DMSO at 25 °C. Due to the low solubility of these complexes in all common organic solvents, the real concentration of the samples was not evaluated, and ε (M<sup>-1</sup> cm<sup>-1</sup>) neither.

**Table 7.6** summarizes the absorption values for the synthesized gold(I)-DTC precursors. The spectra present two main absorptions that sometimes are accompanied by not well-defined shoulders. The low solubility of

these complexes in common organic solvents limited the pieces of information obtainable from the UV-Vis analysis, for instance the molar absorptivity was not determined. The first band observed, labeled as *band II* according to the numbering used for the previously discussed Au(III) complexes, could be related to intraligand electronic transfers of the type  $\pi^* \leftarrow \pi$ . This type of transition was confirmed also for analogous dimeric Au(I) complexes containing dithiolato ligands [370]. Intriguingly, as previously observed for the Au(III)-DTC compounds, this absorption is red-shifted on passing from aliphatic to aromatic compounds. Concerning the second major absorption, it could be ascribed to an intraligand  $p \leftarrow d$  transition between levels originated by sulfur atoms, although some works associate this band with a ligand-to-metal CT (LMCT) [370]. Indeed, even if for mononuclear gold(I)-phosphine complexes this type of transition occurs in general at  $40,000 \text{ cm}^{-1}$  (250 nm), in gold(I) dinuclear complexes involving an Au(I)-Au(I) interaction, metal-centered transitions are foreseen at lower energy (range 300-350 nm), due to the destabilization of the highest occupied *d* orbitals (which becomes antibonding) [371]. Moreover, the large red-shift observed for this band in gold(I)-aromatic DTC compounds (*ca.* 20 nm) could be related to a metal-to-ligand CT [372], which is preferred in the case of these  $\pi$ -acceptor ligands.

#### 7.4.5.1 Effect of DMSO on $[\text{AuX}_2(\text{DTC})]$ complexes: a UV-Vis study

In one of his papers, Isab and coworkers highlighted the possibility that the complexes of the type  $[\text{Au}^{\text{III}}\text{X}_2(\text{DTC})]$ , if dissolved in DMSO, convert to the ionic species  $[\text{Au}(\text{PipeDTC})_2]^+$  [356]. To verify this behavior, an UV-Vis analysis was carried in DMSO for the  $[\text{Au}^{\text{III}}\text{Cl}_2(\text{PipeDTC})]$ , chosen as a model compound, over 72 hours. The **Figure 7.10** shows that the neutral compound undergoes a transformation over time, with the final spectrum resembling the features of the ionic  $[\text{Au}^{\text{III}}(\text{PipeDTC})][\text{AuCl}_4]$ .

Remarkably, in our laboratories it has been observed that a sample containing a DMSO solution of  $[\text{Au}^{\text{III}}\text{Cl}_2(\text{PipeDTC})]$  protected from light does not undergo any transformation over more than 72 hours. Therefore, UV-Vis radiation (with a still undefined wavelength) is required to achieve the formation of the ionic species. These are preliminary results and further investigations will be performed soon to better understand the conversion mechanism. Conversely, the same over-time experiment carried out using deuterated dimethyl sulfoxide (DMSO- $d_6$ ) highlighted the stability of the  $[\text{Au}^{\text{III}}\text{Cl}_2(\text{PipeDTC})]$  complex. This phenomenon points out the crucial role of the solvent in the neutral  $\rightarrow$  ionic conversion, and that a deuterated solvent can stabilize a transition state, thus hampering the reaction course.



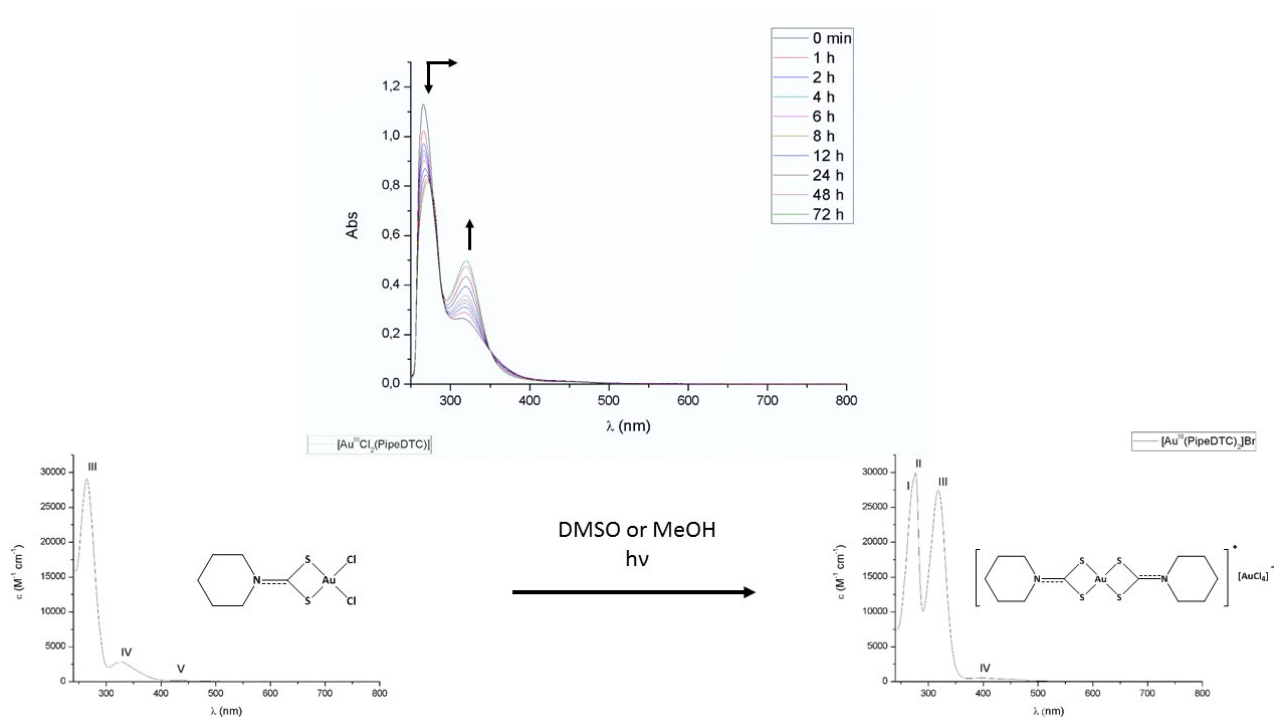


**Figure 7.10** The UV-Vis analysis over 72 hours of  $[\text{Au}^{\text{III}}\text{Cl}_2(\text{PipeDTC})]$  dissolved in DMSO (top) shows its transformation to the ionic  $[\text{Au}^{\text{III}}(\text{PipeDTC})][\text{AuCl}_4]$ . In particular, this behavior is clearer comparing the spectra of the purified species (bottom) in  $\text{CH}_2\text{Cl}_2$ . The conversion mechanism needs of the presence of an undefined UV-Vis radiation  $h\nu$ .



## 8. PLURONIC® F127 MICELLES FOR THE CANCER-DELIVERY OF SELECTED METAL-DTC COMPOUNDS

### 8.1 Nanocarrier platforms for anticancer therapy

Although the use of polymeric carriers for medicinal purposes is known since 1950s [373], only in the past two decades nanoparticle-based therapeutics (size range: 1 to 1,000 nm) have been successfully introduced in clinics for the treatment of cancer diseases [374, 375]. Indeed, several advantages have been associated with the use of these systems when compared to over the corresponding free drugs as they i) prevent drug from degradation or interaction with blood components, ii) enhance drug absorption in a selected tissue (e.g., solid tumor), iii) control the pharmacokinetic and distribution profile, and iv) improve intracellular penetration [376]. To date, many different carriers have been explored to achieve an improvement in terms of drug-delivery using synthetic transporters [377] and to date 12 nanoformulations are clinically approved for treating some types of cancers [378]. Among them, liposomes and polymeric nanoparticles (including micelles) are the main approved platforms [378]. Concerning *liposomes*, they are spherical vesicles with a hydrophilic (polar) cavity surrounded by a bi-layer of amphiphilic phospholipids, whose hydrophobic-lipid and hydrophilic-phosphate tails drive their self-assembly in water [379]. Their cellmembrane-mimicking characteristics confer unique properties on liposomes, including biocompatibility, biodegradability, low toxicity and, above all, lack of immune system activation [380]. The first liposome-based therapeutic, liposome-encapsulated doxorubicine (Doxil®), was approved by the FDA in 1995 for the treatment of the Kaposi's sarcoma, and then for ovarian carcinoma and multiple myeloma [381]. This "nano-goal" opened the way to new liposomal formulations, and nowadays different liposome-encapsulated cytotoxic agents (e.g., cytarabine and vincristine sulfate) have reached the clinic [382, 383], while others are under trial evaluation [384]. On the other hand, *polymeric nanoparticles* have attracted the attention since they can carry the drug buried within their core or conjugated to their surface. Polyethylene glycol (PEG), which can reduce immunogenicity of proteins and enhance their solubility and plasma stability, has been the most widely studied polymer for this application so far [385]. In 1994, PEG-L-asparaginase (Oncospar®) became the first nanoparticle therapeutic to receive FDA approval for the treatment of acute lymphocytic leukaemia [386]. Remarkably, PEG has become important also to cover the surface of particles or liposomes by grafting (PEGylation). This approach increases the hydrodynamic size of the nanoparticle (thus avoiding renal clearance), raises its body circulation half-life and masks the agent from the host's immune system, giving rise to the so-called "stealth effect". [387, 388]. Such polymers have been also modified to develop block copolymers containing both hydrophobic and hydrophilic chains, able to self-assembly in micelles for the drug delivery of drugs suffering from poor water solubility [389, 390]. These systems have solid-like cores and remain intact above their critical micellar concentration (CMC), acting as carriers able to circumvent the host defense, with bioaccumulation in solid tumors [391]. Different micellar systems are under clinical trial

evaluation for the enhanced delivery of doxorubicin, oxaliplatin and cisplatin [378], whereas a poly(ethylene glycol)-poly(D,L-lactide) copolymer micelle nanoformulation entrapping paclitaxel (Genexol®) has been already approved for the Asiatic market for treating breast cancer [392].

### 8.1.1 Passive vs active targeting and mechanism of nanoparticle cell uptake

One of the pillars of the nanomedicine applied to oncology is the ability of the drug-delivery systems to take advantage of some peculiarities of the tumor microenvironment, in particular the structural changes in vascular pathophysiology (**Figure 8.1**) [393]. The fast angiogenic process, which occurs in the early stages of cancer development, as well as the high concentration of proteolytic enzymes in solid tumors, give rise to irregular-shaped dilated and tortuous blood vessels [394, 395]. Consequently, endothelium presents open fenestration, with pore sizes varying from 10 to 1000 nm [396], hence particles, such as liposomes and micelles with size in the range 20-200 nm, can extravasate and accumulate inside the interstitial space. Moreover, the general lack of lymphatic vessels in tumors, contributes to the inefficient drainage of the accumulated delivery systems. This *passive cancer-targeting* phenomenon is referred to as the “Enhanced Permeability and Retention” (EPR) effect (**Figure 8.1 b**) [397]. According to these observations, the EPR effect results optimal for those nanocarriers that can evade immune surveillance and, above all, are able to circulate in the blood stream without drug-releasing for a long period. Thus, very high local concentrations of drug-loaded nanocarriers can be achieved at the tumor site, for instance 10- to 50-fold higher than in normal tissues within 1-2 days [398].

It is worth underlining that the particle size has a fundamental role to exploit the lability of tumor blood vessels. It has been demonstrated that particles with hydrodynamic diameters less than 5 nm are too rapidly cleared from the circulation through renal clearance or extravasation to healthy and cancerous tissues [399], whereas particulate matter larger than 1.5 µm is removed from the blood circulation by mechanical filtration in capillaries and can be lethal depending on the dosage [400].

Tumor tissues are characterized by large osmotic pressure due to lack of drainage, generating high tumor interstitial fluid pressure (IFP), which acts as a barrier for efficient anti-cancer drug delivery [401]. Therefore, nanosystems with size higher than 10 nm (to avoid easily diffusion by IFP) but smaller than 100 nm (to avoid capture by liver) are more retained in the tumor microenvironment, with a recently-demonstrated ideal size near 50 nm [402].

Other physicochemical parameters that influence both systemic circulation times and intratumor processes are the charge and shape of the particles [403]. Concerning the first, in general neutral systems are more convenient since *ex vivo* studies carried out on extracellular matrix isolated from mice sarcoma showed that the charge, when present, had deleterious effects on the movement of nanoparticles through the matrix [404]. In particular, it is hypothesized that positive charges limit the deeper diffusion intra the tumor tissues due to a higher reactivity of the nanomaterial surface with the endothelial lumen [405, 406]. On the other

hand, regarding the shape, spherical nanoparticles have been traditionally used and in general yield good results in terms of stability and biodistribution both in blood and tumor tissues, although many recent findings suggest that non-spherical nanoparticles (*e.g.*, rods, discs, hemispheres, ellipsoids) may target tumors more effectively [407].

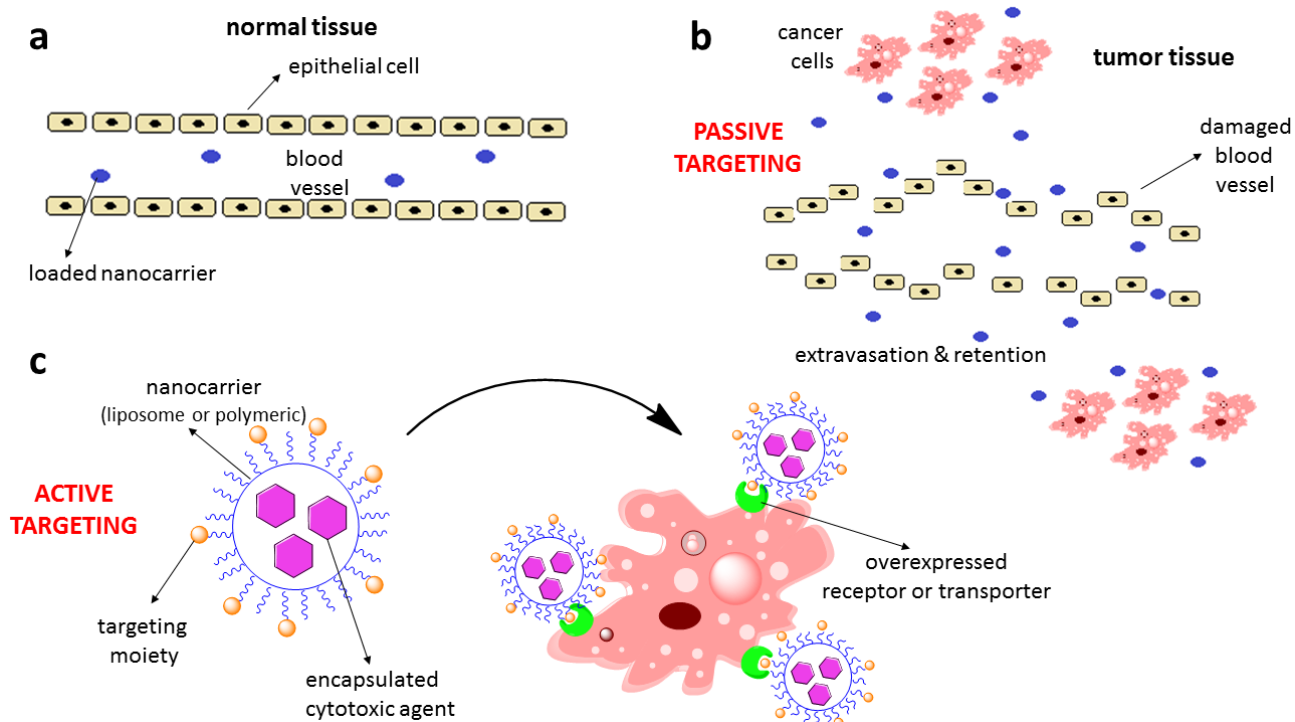


**Figure 8.1** Passive vs active cancer-targeting. In normal tissues, the assembly of epithelial cells results in the development of blood vessels with no extravasation of nanocarriers, and a well-developed lymphatic system is associated with a correct drainage of various substances, thus hampering any drug accumulation **a**. On the contrary, tumor tissue is characterized by a fast growth of the epithelial barrier, generating tortuous and dilated blood vessels. The extravasation of the drug carrier is facilitated, as well as its retention due to the lack of lymphatic drainage (EPR effect), thus achieving the so-called passive cancer targeting, with the cell uptake of the particle occurring by endocytosis (based on clathrin or caveolin proteins) **b**. The structure of the drug-delivery system involves an external shell (liposome or polymeric protection, such as in a micelle) and a hydrophobic or hydrophilic core, encapsulating the cytotoxic agent. It is possible to conjugate the surface of this nanocarrier with a cancer-targeting biomolecule to take advantage of the up-regulation of specific receptors and transporters after malignant transformation, achieving an active cancer targeting. In this manner, an increased uptake of the anticancer payload is mediated by these cell membrane proteins, or alternatively the biomolecule acts as an anchor to facilitate cancer-cell localization **c**. In this second case, uptake of the cargo is mediated by endocytosis.

Until now, the EPR phenomenon together with nanoparticle physicochemical features were demonstrated to affect the final distribution of the drug/carrier within the tumor microenvironment, without necessarily increasing the ability of the drug to reach its pharmacological target. In the light of this, researchers have developed bio-conjugated systems with cancer-targeting biomolecules (ligands) bound on the surface of the nanocarrier, in order to achieve an *active cancer targeting* (**Figure 8.1 c**) [408]. In particular, these ligands are selected to bind transporters or receptors overexpressed in cells or subcellular domains within diseased tissues or organs [409, 410]. It is worth mentioning that also the actively-targeted systems can exploit the

previously described passive targeting, allowing their accumulation in the proximity of their correspondent target, followed by an additional phenomenon of *active* recognition, at the extra-/intracellular level. Such a phenomenon beyond the active targeting is the selective binding of the ligand to its cellular or molecular target. In the first case, the recognition event is usually followed by cellular internalization. The ability of the nanocarrier to be internalized thus depends also on the selection of proper targeting ligands. Indeed, Chang and Pirolo questioned how the targeting ligand influences the nanoparticle tumor localization and uptake [411]. In most cases, the ligand-receptor interactions result in an efficient uptake of the complex into the tumor cell by receptor-mediated endocytosis (such as in the case of the RGD peptides, epidermal growth factor (EGF), folate, transferrin (Tf) or antibodies fragments) [412-416]. On the other hand, the dimension, shape and the charge of the particle, as well as the receptor characteristics could result in unfavorable interactions, thus hampering the receptor-mediated intracellular transportation of the cargo [417]. In this case, the targeting moiety does play a significant role in tumor localization but not in the cell uptake, acting as an anchor for the nanosystem at the cell surface, to be successively endocytosed by cell-membrane large-particles transporters [418].

In this context, when a nanoparticle is placed in the external milieu of a cell, the endocytotic process may occur and involves multiple stages. First, the nanocarrier is engulfed in membrane invaginations that are pinched off to form membrane-bound vesicles, referred to as endosomes. Cells contain heterogeneous populations of endosomes equipped with distinct types of endocytic machinery, present at different sites of the cell membrane. Second, the endosomes deliver the cargo to various specialized vesicular structures, which enable cargo sorting towards different destinations. Finally, the cargo can be delivered to various intracellular compartments, expelled to the extracellular milieu or delivered across cells [419].

In general, endocytosis is mainly regulated by two proteins, clathrin (giving rise to the clathrin-mediated endocytosis, CME) and caveolae [420]. CME is the “classical route” of cellular entry, inherently active in all mammalian cells. It is responsible for uptake of essential nutrients, such as cholesterol, carried into cells by the low-density lipoprotein (LDL) *via* the LDL receptor, and iron(III), carried by transferrin *via* the Tf receptor. Within cells, the clathrin shell is lost and the transported particles are fused to the so called early endosomes where they are sorted to late endosomes/lysosomes, to the trans-Golgi network or to the recycling endosomes to be transported back to the plasma membrane [421]. On the other hand, caveolin proteins are abundant in muscle, endothelial cells, fibroblasts and adipocytes and absent in neurons and leukocytes. Their mechanism of action is similar to that of clathrin but its pathway, with the ability to bypass lysosomes, has attracted remarkable attention in nanomedicine. Furthermore, the caveolae-mediated endocytosis is the most prominent trans-endothelial pathway and thus this route may be exploited for trans-vascular delivery of nanomaterials [422].

In conclusion, in the last 20 years drug delivery systems have proved excellent tools to preserve the integrity of the loaded drug up to the final destination of the tumor microenvironment. This is favored by abnormal

characteristics of the cancerous endothelium (EPR effect) but also by the structural and physico-chemical features of the nanoparticles. Moreover, the hydrophilic surface of the carriers can be modified to achieve active cancer-targeting, exploiting the high affinity of a selected ligand for the corresponding up-regulated tumor-cell receptor. This interaction can either drive itself the uptake of the cytotoxic cargo, or determine a localization-effect by anchoring the nanoparticle to the cell surface, thus favoring endocytosis processes mediated in general by designated proteins, such as clatrin and caveolin.

## 8.2 Metal complexes and their delivery using nanoformulations

In order to exploit the previously presented drug delivery benefits generated by the use of nanosystems, some clinically-established Pt(II) compounds, *i.e.* cisplatin and oxaliplatin, have been considered to design and obtain other platinum complexes functionalized with hydrophilic polymers (**Fig. 8.2 a, b**, respectively). The latter can arrange in water to form water-soluble micelles whose core is formed by the Pt(II) complex (**Fig. 8.2 c**) [423, 424], thus prolonging platinum half-time circulation in the blood stream. These systems are under clinical trials for the treatment of different malignances, such as advanced solid tumors, non-small-cell lung cancer, and pancreatic cancer [425, 426]. Moreover, two liposomal formulations of oxaliplatin, namely Lipoxal and MBP-426, the latter being based on transferrin-conjugated liposomes, have completed phase II and I respectively for the treatment of colorectal cancer [427, 428].

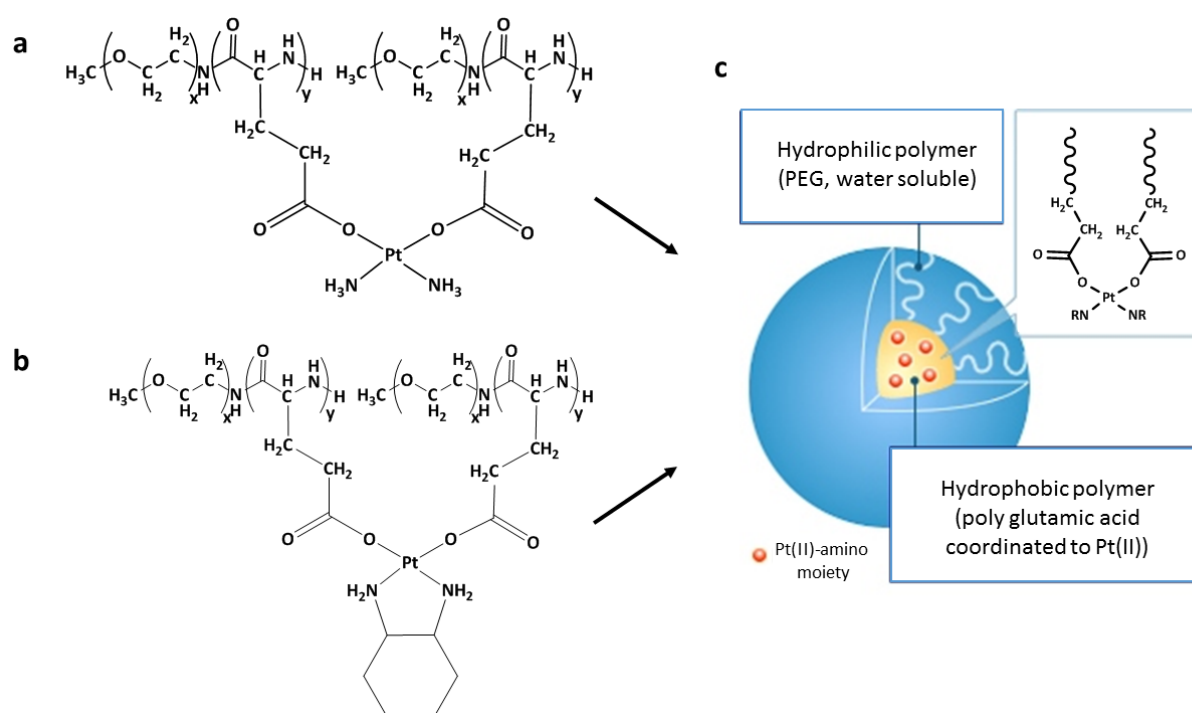


**Figure 8.2** Pt(II)-compounds derived from the complexation of cisplatin (NC 6004) **a** and oxaliplatin (NC 4016) **b** with the polyethylene glycol-poly (glutamic acid) block copolymer, PEG-P(Glu). In aqueous media these complexes self-assemble to generate micelles with a Pt(II)-amino core and a PEG hydrophilic corona **c**, which confers a prolonged half-time circulation in the blood stream on the cytotoxic drug, to achieve accumulation in tumor tissue.

Conversely, these delivery techniques have been recently explored also with other non-platinum metal-based derivatives, to increase their water solubility and bioavailability. Indeed, those metal compounds tested for their biological activity and characterized by poor water solubility are first dissolved in an organic solvent such as DMSO or EtOH, so to facilitate the subsequent dissolution in aqueous solutions, such as saline solution, phosphate buffered saline and cell culture medium. These organic solvents are generally well tolerated in biological systems (*e.g.*, cells) if added at low concentrations (typically < 2 v/v).

The investigation of delivery systems for cytotoxic metal complexes is an ever growing research field, since the resulting formulations benefit not only from the increased solubility and stability of the loaded complex, but also from the passive and, where performed, active cancer-targeting coming from the carrier properties [429]. Based on these considerations, the Ru(III) complex KP1019 (see **Section 5.1**) has been encapsulated in poly(lactic acid) nanoparticles to increase its water stability [430], whereas some Ru(III)-phosphocoline conjugates have been loaded into liposomes, achieving nanoaggregates stable for months with encouraging anticancer activity *in vitro* [431].

In recent years, our research group has developed an expertise in loading metal-based agents into delivery systems. The gold(III) complex dibromo(sarcosine ethyl ester [AuBr<sub>2</sub>(ESDT)]) (see **Section 7.2**) and the Ru(III)-PDT derivatives (both mono- and dinuclear, see **Section 5.2**), have been successfully loaded into the lipophilic core of the triblock copolymer Pluronic® F127-based micelles. Stability studies and *in vitro* experiments carried out with a panel of human tumor cell lines showed an enhanced water solubility together with increased antiproliferative activity of all tested complexes with respect to the same compounds in DMSO vehicle [432,433]. Overall, the loading of cytotoxic metal-based compounds into Pluronic® micelles seems a winning solubility-increasing strategy, and the versatility of the polymer to undergo *ad hoc* chemical modifications opens intriguingly perspectives in designing new approaches to treat cancer, being one of the goals of this PhD work.

### 8.3 Chemical and biological overview of Pluronic® F127

Pluronic® F127 (PF127) is the BASF-registered name of the Polaxamer 407, a non-ionic surfactant of the more general class of copolymers known as polaxamers, synthetic derivatives introduced in the late 1950s for diverse pharmaceutical applications [434]. In particular, PF127 is a triblock copolymer composed of both hydrophilic poly(ethylene oxide) (PEO) and hydrophobic poly(propylene oxide) (PPO), arranged in A-B-A structure (PEO<sub>x</sub>-PPO<sub>y</sub>-PEO<sub>x</sub>, **Figure 8.3**). Its molecular weight is about 12,600 Da (9,840-14,600), and x and y are equal to 95÷105 and 65÷75, respectively [435].



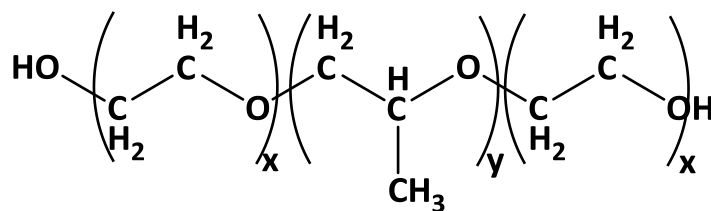


**Figure 8.3** Chemical drawing of the polaxamers' structure, in particular for Pluronic® F127  $x$  and  $y$  are equal to  $95 \div 105$  and  $65 \div 75$ , respectively.

These systems are characterized by their critical micelle concentration (CMC) – the concentration at which free and disordered surfactant molecules (unimers) aggregate into micelles, with a dynamic equilibrium establishing between micelles and unimers – and by their hydrophile-lipophile balance (HLB) – a number indicating the proportion of hydrophilic-to-lipophilic portions of the amphipathic molecule. Regarding the latter, HLB is usually measured on a scale of 0 to 20, and since the value for PF127 is out-of-range, being equal to 22, it is indicative of high water solubility [436, 437]. The CMC value is a function of temperature, since micelle formation is the result of the dehydration of PO and EO units upon increase in temperature. Typically, Pluronic® copolymers at the body temperature (37 °C) have a CMC ranging from  $1 \cdot 10^{-6}$  M to  $1 \cdot 10^{-3}$  M, and in particular  $\text{CMC}_{\text{PF127}}(37\text{ °C}) = 2.8 \cdot 10^{-6}$  M ( $\approx 3.5 \cdot 10^{-2}$  mg mL<sup>-1</sup>) [438].

Concerning the biological overview of PF127, the FDA guide considers this polaxamer as an “inactive” ingredient for different types of preparations (*e.g.*, inhalation, oral solutions and suspensions, ophthalmic or topical formulations) [439]. Moreover, in a Phase I clinical trial report about the doxorubicin-PF127-PL61 formulation (PL61= Pluronic® L61, a polaxamer-member copolymer where  $x = 2 \div 30$  and  $y = 15 \div 67$ ), the maximum tolerated dose (MTD) accounts for a PF127 dosage of 700 mg m<sup>-2</sup> (in general 1 m<sup>2</sup> = 31 kg of body weight), thus demonstrating that this polymer is well tolerated by man even at very high concentrations [440].

With respect to the micellar properties of this class of copolymers, Pluronic® micelles do not act only as inert nanocarriers able to exploit the EPR effect, but they act also as biological response modifiers at the cell level [441]. This is associated with their ability to incorporate into cell membranes [442], followed by translocation into cytoplasm with effects on various cellular functions, such as mitochondrial respiration [443], ATP synthesis [444], activity of drug efflux transporters [445], apoptotic signal transduction and gene expression [446]. As a result, Pluronics cause drastic sensitization of multi-drug-resistant (MDR) tumors to chemotherapy, enhancing drug transport across different types of biological membranes [447].

Intriguingly, the effect of this class of copolymers towards normal and cancer cells is quite different. In fact, after incubation with low concentrations of Pluronic® L61 the microviscosity of tumor cells membrane decreases whereas that of normal cells increases [448]. Finally, regarding the cellular uptake of amphiphilic triblock copolymers, PF127 utilizes multiple routes depending on its aggregation state (*e.g.*, regular micelles, disordered tangle-shaped architectures, gel consistency) [449]. In particular, the unimers internalize

predominantly through the calveolae-mediated endocytosis [450]. On the contrary, micelles internalize prevalently through CME, while calveolae-mediated endocytosis is still debated if occurs to a lesser extent, likely being inhibited by these nanosystems [450, 451].

#### 8.4 Active cancer-targeting by micelle bio-conjugation with carbohydrates

Targeting the altered tumor metabolism is one of the strategies to selectively deliver cytotoxic agents to cancer cells [452]. As presented in **Section 1.2** and **Figure 1.5**, many cancer cells metabolize glucose by anaerobic glycolysis. This phenomenon, known as Warburg effect, is characterized by fast glycolysis and larger lactate production, overall being fueled by increased glucose (**Figure 8.4 a**) uptake, with respect to normal tissues [41]. Exploiting this behavior, many tumors (and metastases) are usually diagnosed using  $^{18}\text{F}$ -2-deoxyglucose positron emission tomography (FDG-PET) (**Figure 8.4 b**). FDG is a glucose-analogue metabolized similarly to glucose since it is transported across the cell membrane by glucose transporters proteins, and then enzymatically phosphorylated. However, in contrast with glucose-6-phosphate, once phosphorylation takes place, FDG-6-phosphate is metabolically trapped, thus leading to a direct visualization of metabolism-mutated cancer cells thanks to their higher uptake of this carbohydrate (**Figure 8.4 c**) [453]. In particular,  $^{18}\text{F}$  ( $t_{1/2} = 110$  minutes) decays by a  $\beta^+$  transition (positron emission) and electron capture directly to the ground state of the stable  $^{18}\text{O}$ , which forms normal phosphorylated glucose, readily metabolized by the cell. At the same time, the produced positron annihilates with an electron to yield gamma rays, detected by the  $\gamma$  camera of the PET instrument [454].

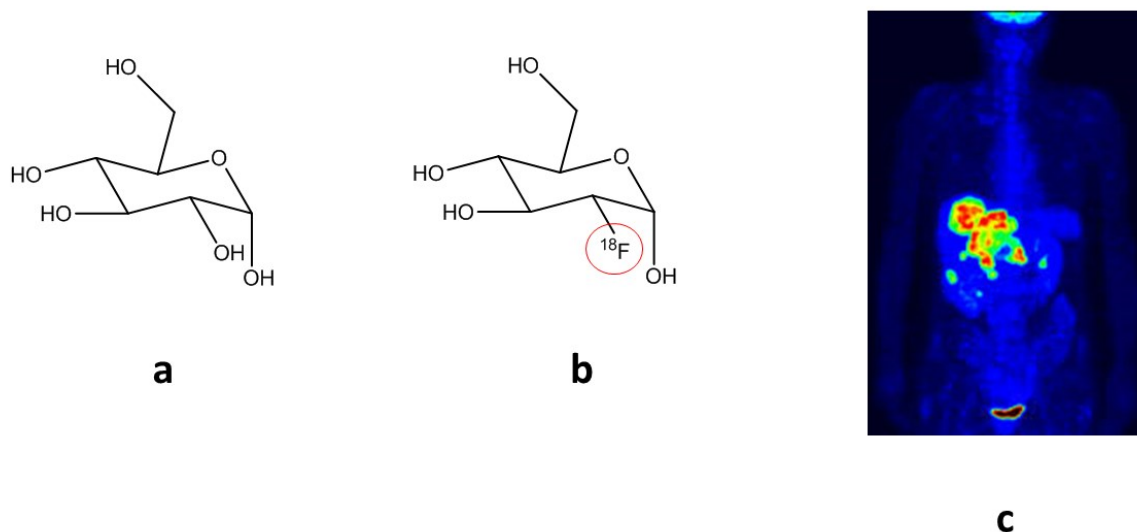


**Figure 8.4** Chemical drawing of glucose **a** and  $^{18}\text{F}$ -2-deoxyglucose (FDG) **b**. The 6-phosphorylation of the first leads to a readily-metabolized substrate, whereas 6-phosphorylated FDG undergoes no metabolic pathway until  $^{18}\text{F}$  decays to  $^{18}\text{O}$ . In particular, due to the Warburg effect, FDG accumulates in cancerous tissues, giving the PET imagine of tumor localization **c** (primary colorectal tumor and liver metastases).

The FDG uptake mechanism has been extensively studied *in vitro* and *in vivo*, nowadays acknowledged to be mediated by the glucose transporters proteins (GLUTs) [455]. To date, thirteen members of the GLUT family have been identified, as well as six Na<sup>+</sup>-dependent glucose transporters (SGLT family) [456], but the most up-regulated protein found in tumor cells remains GLUT1 [457], whose high levels in human cancers have been associated with a general poor survival [458]. GLUT1 is a passive, bidirectional glucose uniporter consisting of 12 transmembrane helical domains, 8 of which are circle-shaped from an exofacial view [459]. Since this transporter could be a useful cell target in cancer treatment, the ability of different analogues to be substrates for GLUT1 has been recently investigated, pointing out some guidelines reported in **Table 8.1** [460].

C1	<ul style="list-style-type: none"> <li>• Substitution generally tolerated, as long as H-bond acceptors remain bonded to C1</li> <li>• GLUT1 recognizes preferentially equatorial (<math>\beta</math> form of the pyranoside)</li> </ul>
C2	<ul style="list-style-type: none"> <li>• Not involved in H bond <math>\rightarrow</math> loss of H bond acceptor tolerated</li> <li>• Bulky substituents seem tolerated (but transporter affinity may decline)</li> </ul>
C3	<ul style="list-style-type: none"> <li>• Further study are required</li> <li>• No anticancer glycol-conjugates reported linked to C3</li> </ul>
C4	<ul style="list-style-type: none"> <li>• Not involved in H bond <math>\rightarrow</math> loss of H bond acceptor tolerated</li> <li>• No anticancer glycol-conjugates reported linked to C4</li> </ul>
C6	<ul style="list-style-type: none"> <li>• Not involved in H bond <math>\rightarrow</math> loss of H bond acceptor tolerated</li> <li>• Bulky substituents seem tolerated (but transporter affinity may decline)</li> </ul>

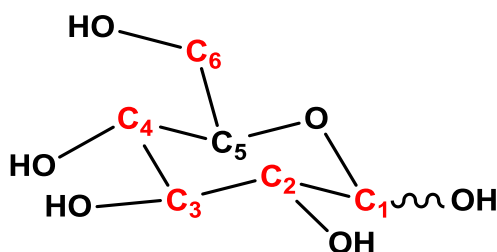


**Table 8.1** Structure-activity relationship of D-glucose as a substrate for the GLUT-1 transporter. This table is re-adapted from the reference [460].

The first sugar-conjugate to be designed and evaluated as a cancer-targeting cytotoxic compound was glufosfamide (**Figure 8.5**), developed to increase the selectivity of the DNA-alkylating agent ifosfamide mustard [461]. This drug has successfully passed Phase I and II of clinical trials in the treatment of pancreatic cancer, non-small lung cancer and glioblastoma, and currently is in a Phase III clinical trial [462].

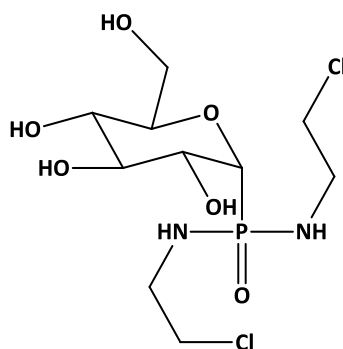


**Figure 8.5** Chemical drawing of the sugar-conjugate drug glufosfamide.

Moving to targeted nanosystems, Venturelli and coworkers have recently demonstrated that glucose-coated magnetic  $\text{CoFe}_2\text{O}_4$  nanoparticles (mean size: 27 nm) target the MDA-MB-231 breast cancer cells to a greater extent compared to the MCF7 counterpart, due to a higher expression of the GLUT1 protein in the cell membrane of the former. Moreover, the selective inhibition of GLUT1 by gene silencing determined a decreased uptake of the functionalized nanosystem in both cancer cell lines [463]. On the other hand, the encapsulation of doxorubicine in mixed Pluronic® P105 micelles, previously bio-conjugated with D-glucose (by modification of the C6 position) and folic acid, generated nanosystems able to induce glioma cell death, with increased transport across the blood brain barrier (both *in vitro* and *in vivo*) [464].

## 8.5 Synthesis of the carbohydrate-targeted Pluronic® F127

As previously discussed, the bio-conjugation of cytotoxic payloads (both small molecules and drug delivery systems) have proved a useful tool to achieve an active cancer-targeting, exploiting the increased glucose uptake of cancer cells, due to the overexpression of the GLUT transporters in comparison with healthy cells. In light of these findings, in this PhD work the conjugation of PF127 with glucose (C1 position) and glucosamine has been achieved in order to generate neoplasia-targeting and drug solubility-increasing carriers, loaded with two selected cytotoxic metal-dithiocarbamate derivatives. Moreover, a fluorescein-linked PF127 substrate has been obtained, in order to perform confocal microscopy studies using fluorescein-labelled micelles. For clarity reasons, the reader can refer to **Figures 8.18** and **8.20** for the synthetic routes.

### 8.5.1 Synthesis of Pluronic® F127 conjugated with 2,3,4,6-penta-O-acetyl- $\beta$ -D-glucopyranoside (acetyl-protected glucose), PF127-GluOAc

The conjugation of the acetyl-glucose at C1 position to terminal hydroxyl groups of PF127 was achieved as follows. To a mixture of PF127 (1 mmol) and 1,2,3,4,6-penta-O-acetyl- $\beta$ -D-glucopyranoside (3 eq) in 20 mL dry  $\text{CH}_2\text{Cl}_2$  at  $0^\circ\text{C}$ , 3 equivalents of  $\text{BF}_3 \cdot \text{Et}_2\text{O}$  were added and the reaction was kept under stirring for 48 h. Afterwards, the solution was concentrated under vacuum and precipitated with  $\text{Et}_2\text{O}$ , yielding a white solid dried under vacuum. The solid was precipitated again using  $\text{CH}_2\text{Cl}_2/\text{Et}_2\text{O}$ , until the TLC analysis ruled out the presence of unreacted acetyl-glucose.

The degree of functionalization was 15%, evaluated by  $^1\text{H-NMR}$  ( $\text{CD}_2\text{Cl}_2$ ) and by comparison of the signals of the methyl protons of acetate (red colored) and the methyl protons of the PPO central moiety of PF127 (blue colored) (**Figure 8.6**).

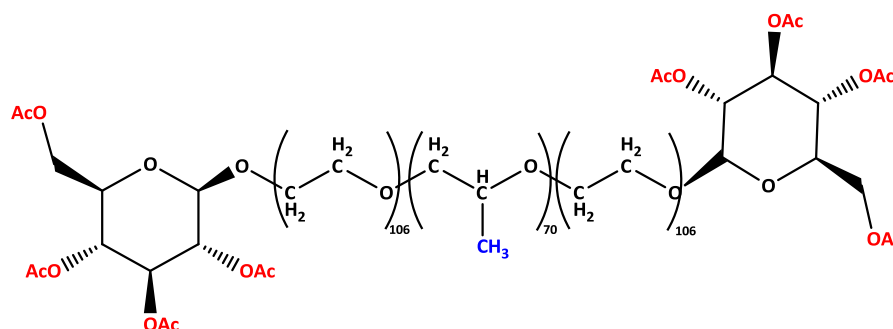


**Figure 8.6** Chemical drawing of Pluronic® F127 conjugated with 2,3,4,6-penta-O-acetyl- $\beta$ -D-glucopyranoside (acetyl-protected glucose), PF127-GluOAc

$^1\text{H-NMR}$  (599.90 MHz,  $\text{CD}_2\text{Cl}_2$ ):  $\delta$  (ppm) = 1.09 (t, 688H,  $\text{CH}_3$  PF127), 1.95 (s, 3H,  $\text{COCH}_3$ ), 1.98 (s, 3H,  $\text{COCH}_3$ ), 2.00 (s, 3H,  $\text{COCH}_3$ ), 2.04 (s, 3H,  $\text{COCH}_3$ ), 2.33 (s br, OH PF127), 3.37 (m, 225H,  $\text{OCHHCH}(\text{CH}_3)\text{O}$  PF127), 3.47-3.52 (m, 414H,  $\text{OCHHCH}(\text{CH}_3)\text{O}$  PF127), 3.55 (m, 62H,  $\text{CH}_2\text{-CH}_2\text{-OH}$  PF127), 3.58 (m, 3106H,  $(\text{CH}_2\text{-CH}_2\text{-O})_n$  PF127 + H-5 glucopyranoside), 3.70 (m, 22H,  $\text{CH}_2\text{-CH}_2\text{-O}$ -glucopyranoside +  $\text{CH}_2\text{-CH}_2\text{-OH}$  PF127), 4.08-4.10 (dd, 1H, H-6 glucopyranoside), 4.22-4.24 (dd, 1H, H-6 glucopyranoside), 4.59-4.60 (d, 1H, H-1 glucopyranoside), 4.91 (dd, 1H, H-2 glucopyranoside), 5.03 (dd, 1H, H-4 glucopyranoside), 5.17 (dd, 1H, H-3 glucopyranoside).

$^{13}\text{C-NMR}$  (151.2 MHz,  $\text{CD}_2\text{Cl}_2$ ):  $\delta$  (ppm) = 17.58, 17.66 (2s,  $\text{OCHHCH}(\text{CH}_3)\text{O}$  PF127), 20.91, 20.96, 21.00 (3s,  $\text{COCH}_3$ ), 62.09 (s,  $\text{CH}_2\text{-OH}$  PF127), 62.39 (s, C-6 glucopyranoside), 65.49 (s,  $\text{CH}_2\text{-O}$ -glucopyranoside PF127), 68.90 (s, C-4 glucopyranoside), 68.95 (s,  $\text{CH}_2\text{-CH}_2\text{-O}$ -glucopyranoside PF127), 70.82, 71.02 (2s,  $(\text{CH}_2\text{-CH}_2\text{-O})_n$  PF127 + C-2 glucopyranoside), 71.38 (s, C-5 glucopyranoside), 73.04 (s, C-3 glucopyranoside), 73.24, 73.32, 73.66 (3s,  $\text{OCHHCH}(\text{CH}_3)\text{O}$  PF127), 75.62, 75.78, 75.92 (3s,  $\text{OCHHCH}(\text{CH}_3)\text{O}$  PF127), 101.36 (s, C-1 glucopyranoside), 169.77, 169.83, 170.42, 170.88 (4s, 4  $\text{COCH}_3$ ).

Medium FT-IR (KBr):  $\tilde{\nu}$  ( $\text{cm}^{-1}$ ) = 2887, 1759, 1467, 1344, 1111, 1060, 842.

### 8.5.2 Synthesis of Pluronic® F127 conjugated with $\beta$ -D-glucopyranoside (deprotected glucose), PF127-GluOH

The deprotection of conjugated acetyl-glucose was performed in this manner: to 5 g of PF127-GluOAc (15% of functionalization) dissolved in 10 mL dry methanol at room temperature, 0.3 equivalents (with respect to the moles of conjugated sugar) of MeONa were added, and the mixture was left under stirring for 15 hours. Successively, the necessary amount of Amberlite® IR120  $\text{H}^+$  form was added, until pH was neutral. At this point, the resin was filtered and the conjugated polymer precipitated with the addition of 30 mL of diethyl

ether. The obtained solid was washed with 3x 5 mL of the Et<sub>2</sub>O, yielding a white solid, then dried under vacuum.

The degree of functionalization remained 15%, evaluated by <sup>1</sup>H-NMR (CD<sub>3</sub>OD) and by comparison of the signals of H-1 protons of glucose (red colored) and the methyl protons of the PPO central moiety of PF127 (blue colored) (Figure 8.7).

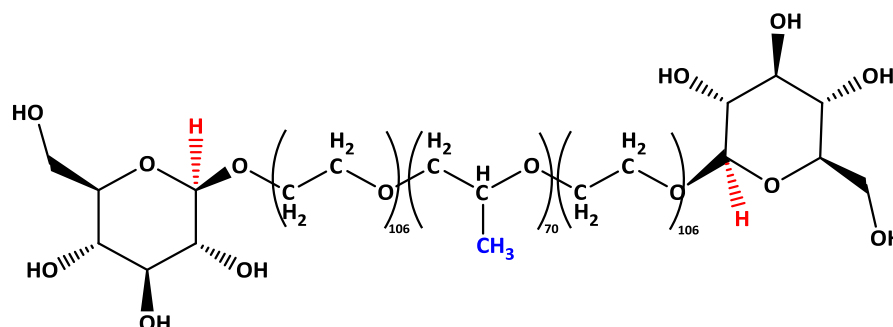


**Figure 8.7** Chemical drawing of Pluronic® F127 conjugated with β-D-glucopyranoside (deprotected glucose), PF127-GluOH.

<sup>1</sup>H-NMR (599.90 MHz, CD<sub>3</sub>OD): δ (ppm) = 1.14 (t, 519H, CH<sub>3</sub> PF127), 3.19 (t, 1H, H-2 glucopyranoside), 3.27-3.28 (d, 1H, H-3 glucopyranoside), 3.46-3.52 (m, 356H, OCHHCH(CH<sub>3</sub>)O PF127 + H-4 and H-5 glucopyranoside), 3.59 (m, 153, CH<sub>2</sub>-CH<sub>2</sub>-OH PF127), 3.64 (m, 2342H, (CH<sub>2</sub>-CH<sub>2</sub>-O)<sub>n</sub> PF127), 3.75 (m, 18H, CH<sub>2</sub>-CH<sub>2</sub>-O-glucopyranoside + CH<sub>2</sub>-CH<sub>2</sub>-OH PF127), 3.86 (dd, 1H, H-6 glucopyranoside), 4.01 (dd, 1H, H-6 glucopyranoside), 4.30 (d, 1H, H-1 glucopyranoside).

<sup>13</sup>C-NMR (151.2 MHz, CD<sub>3</sub>OD): δ (ppm) = 17.72 (s, OCHHCH(CH<sub>3</sub>)O PF127), 62.23 (s, CH<sub>2</sub>-OH PF127), 66.04 (s, C-6 glucopyranoside), 68.82 (s, CH<sub>2</sub>-O-glucopyranoside PF127), 69.66 (s, CH<sub>2</sub>-CH<sub>2</sub>-O-glucopyranoside PF127), 71.57 (s, (CH<sub>2</sub>-CH<sub>2</sub>-O)<sub>n</sub> PF127), 73.68 (s, C-5 glucopyranoside), 74.32 (s, C-2 glucopyranoside), 74.04, 74.12, 74.39, 74.43 (4s, OCHHCH(CH<sub>3</sub>)O PF127), 76.34 (s, C-3 glucopyranoside), 76.54, 76.68, 76.82 (3s, OCHHCH(CH<sub>3</sub>)O PF127), 77.98 (s, C-4 glucopyranoside), 104.46 (s, C-1 glucopyranoside).

Medium FT-IR (KBr):  $\tilde{\nu}$  (cm<sup>-1</sup>) = 3453, 2886, 1759, 1467, 1344, 1112, 1060, 842.

### 8.5.3 Modification of terminal hydroxyl groups of PF127 into aldehydes, PF127-CHO

The oxidation of each terminal hydroxyl group of PF127 to aldehyde was achieved by the *Parikh-Doering oxidation* [465]. Briefly, a DMSO solution of PF127 (1 eq) was mixed with a solution containing 3 equivalents of sulfur trioxide/pyridine complex (Py·SO<sub>3</sub>) in DMSO and Et<sub>3</sub>N (6 eq) at 20°C. After 24 hours the mixture was diluted in CH<sub>2</sub>Cl<sub>2</sub> and washed with brine. The organic phase was then dried with Na<sub>2</sub>SO<sub>4</sub>, concentrated and treated with Et<sub>2</sub>O, thus precipitating a white solid.

The degree of oxidation to aldehyde of the terminal hydroxyl group was found to be 74% by  $^1\text{H-NMR}$  spectroscopy ( $\text{CD}_2\text{Cl}_2$ ), considering the integration value related to the aldehyde proton (red colored) and the methylic protons of the PPO central moiety of PF127 (blue colored) (**Figure 8.8**).

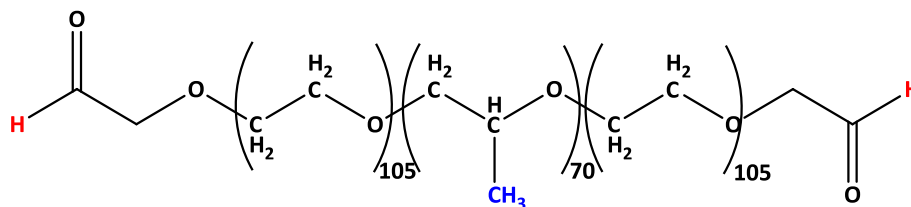


**Figure 8.8** Chemical drawing of Pluronic® F127 where the terminal hydroxyl groups of the polymer have been oxidized to aldehydes, PF127-CHO.

$^1\text{H-NMR}$  (599.90 MHz,  $\text{CD}_2\text{Cl}_2$ ):  $\delta$  (ppm) = 1.10 (t, 145H,  $\text{CH}_3$  PF127), 1.70 (s br, OH PF127), 3.38 (m, 54H,  $\text{OCHHCH}(\text{CH}_3)\text{O}$  PF127), 3.47-3.50 (m, 74H,  $\text{OCHHCH}(\text{CH}_3)\text{O}$  PF127), 3.54 (m, 18H,  $\text{CH}_2\text{-CH}_2\text{-OH}$  PF127), 3.60 (m, 646H,  $(\text{CH}_2\text{-CH}_2\text{-O})_n$  PF127), 3.83 (m, 4H,  $\text{CH}_2\text{-CH}_2\text{-OH}$  PF127), 9.68 (s, 1H, CHO).

$^{13}\text{C-NMR}$  (151.2 MHz,  $\text{CD}_2\text{Cl}_2$ ):  $\delta$  (ppm) = 17.62, 17.71 (2s,  $\text{OCHHCH}(\text{CH}_3)\text{O}$  PF127), 62.18 (s,  $\text{CH}_2\text{-OH}$  PF127), 65.51 (s,  $\text{CH}_2\text{-CH}_2\text{-CHO}$ ), 71.08 (s,  $(\text{CH}_2\text{-CH}_2\text{-O})_n$  PF127), 73.29, 73.36, 73.72 (3s,  $\text{OCHHCH}(\text{CH}_3)\text{O}$  PF127), 75.68, 75.85, 76.00 (3s,  $\text{OCHHCH}(\text{CH}_3)\text{O}$  PF127), 201.24 (s, CHO).

Medium FT-IR (KBr):  $\tilde{\nu}$  ( $\text{cm}^{-1}$ ) = 2884, 1630, 1467, 1344, 1115, 1061, 842.

#### 8.5.4 Synthesis of Pluronic® F127 conjugated with 1,3,4,6-penta-*O*-acetyl-2-amino-2-deoxy- $\beta$ -D-glucopyranoside (acetyl-protected glucosamine), PF127-GlnOAc

The conjugation of the acetyl-protected glucosamine to PF127 was achieved by reductive amination starting from PF127-CHO. Briefly, 0.5 mmol of PF127-CHO (74%) and 0.5 mmol of 1,3,4,6-penta-*O*-acetyl-2-amino-2-deoxy- $\beta$ -D-glucopyranoside were mixed at room temperature in 30 mL of acetonitrile for 2 hours. Successively, 3 equivalents of  $\text{NaCNBH}_3$  were added, and the solution was left under stirring for 30 minutes. After that, the solvent was removed and the residual matter taken up with 50 mL of  $\text{CH}_2\text{Cl}_2$  and washed with 3x 50 mL of brine. The organic solution was then treated with  $\text{Na}_2\text{SO}_4$ , and the addition of 50 mL of  $\text{Et}_2\text{O}$  led to the precipitation of a white solid, which was then dried under vacuum.

The degree of amination with acetyl-glucosamine was found to be 44% by  $^1\text{H-NMR}$  spectroscopy ( $\text{CD}_2\text{Cl}_2$ ), considering the integration value related to acetyl protons of protected glucosamine (red colored) and methylic protons of the PPO central moiety of PF127 (blue colored) (**Figure 8.9**).

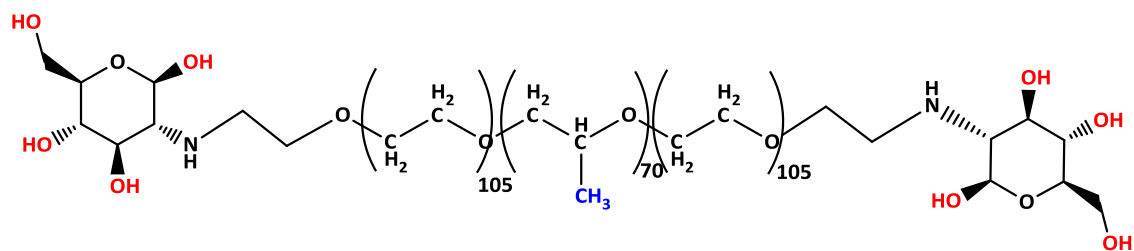


**Figure 8.9** Chemical drawing of Pluronic® F127 conjugated with 1,3,4,6-penta-*O*-acetyl-2-amino-2-deoxy-β-D-glucopyranoside (aceto-protected glucosamine), PF127-GlnOAc.

$^1\text{H-NMR}$  (599.90 MHz,  $\text{CD}_2\text{Cl}_2$ ):  $\delta$  (ppm) = 1.10 (t, 241H,  $\text{CH}_3$  PF127), 1.99 (s, 3H,  $\text{COCH}_3$ ), 2.03 (s, 3H,  $\text{COCH}_3$ ), 2.03 (s, 3H,  $\text{COCH}_3$ ), 2.12 (s, 3H,  $\text{COCH}_3$ ), 2.14 (s br, OH PF127), 2.76-2.82 (m, 4H,  $\text{CH}_2\text{-NH-glucopyranoside} + \text{H-2 glucopyranoside}$ ), 3.37 (m, 81H,  $\text{OCHHCH}(\text{CH}_3)\text{O}$  PF127), 3.47-3.52 (m, 159H,  $\text{OCHHCH}(\text{CH}_3)\text{O}$  PF127), 3.55 (m, 24H,  $\text{CH}_2\text{-CH}_2\text{-OH}$  PF127), 3.59 (m, 1116H,  $(\text{CH}_2\text{-CH}_2\text{-O})_n$  PF127), 3.70 (m, 8H,  $\text{CH}_2\text{-CH}_2\text{-O-glucopyranoside} + \text{CH}_2\text{-CH}_2\text{-OH}$  PF127), 3.76-3.77 (m, 1H, H-5 glucopyranoside), 4.04-4.02 (dd, 1H, H-6 glucopyranoside), 4.21-4.23 (d, 1H, H-6 glucopyranoside), 4.99-5.04 (m, 2H, H-2 + H-4 glucopyranoside), 5.52-5.53 (d, 1H, H-1 glucopyranoside).

$^{13}\text{C-NMR}$  (151.2 MHz,  $\text{CD}_2\text{Cl}_2$ ):  $\delta$  (ppm) = 17.58, 17.66 (2s,  $\text{OCHHCH}(\text{CH}_3)\text{O}$  PF127), 20.98, 21.00, 21.08, 21.36 (4s,  $\text{COCH}_3$ ), 48.01 (s,  $\text{CH}_2\text{-NH-glucopyranoside}$  PF127), 61.42 (s, C-6 glucopyranoside), 62.10 (s,  $\text{CH}_2\text{-OH}$  PF127), 62.40 (s, C-2 glucopyranoside), 65.50 (s,  $\text{CH}_2\text{-CH}_2\text{-NH-glucopyranoside}$  PF127), 68.91 (s, C-4 glucopyranoside), 71.03 (s,  $(\text{CH}_2\text{-CH}_2\text{-O})_n$  PF127), , 71.39 (s, C-5 glucopyranoside), 73.07 (s, C-3 glucopyranoside), 73.25, 73.33, 73.67 (3s,  $\text{OCHHCH}(\text{CH}_3)\text{O}$  PF127), 75.64, 75.80, 75.94 (3s,  $\text{OCHHCH}(\text{CH}_3)\text{O}$  PF127), 95.24 (s, C-1 glucopyranoside), 169.54, 170.03, 170.85, 171.06 (4s, 4  $\text{COCH}_3$ ).

Medium FT-IR (KBr):  $\tilde{\nu}$  ( $\text{cm}^{-1}$ ) = 2883, 1757, 1467, 1344, 1114, 1060, 842.

#### 8.5.5 Synthesis of Pluronic® F127 conjugated with 2-amino-2-deoxy-D-glucose (deprotected glucosamine), PF127-GlnOH

The deprotection of acetyl protecting groups of glucosamine was performed as reported for the glucose derivative in **Section 8.5.2**.

The degree of functionalization remained 44%, evaluated by  $^1\text{H-NMR}$  ( $\text{CD}_3\text{OD}$ ) and by comparison of the signals of H-1 protons of the conjugated glucosamine (red colored) and the methyl protons of the PPO central moiety of PF127 (blue colored) (**Figure 8.10**).



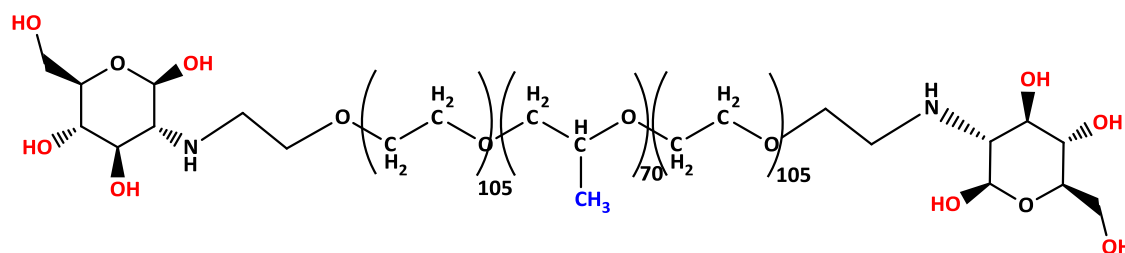


**Figure 8.10** Chemical drawing of Pluronic® F127 conjugated with 2-amino-2-deoxy-D-glucose (deprotected glucosamine), PF127-GlnOH.

$^1\text{H-NMR}$  (599.90 MHz,  $\text{CD}_3\text{OD}$ ):  $\delta$  (ppm) = 1.14 (t, 653H,  $\text{CH}_3$  PF127), 2.51-2.53 (dd, 1H, 4.53-4.54 H-2 $\beta$  glucopyranoside), 2.85-2.90 (m, 2H,  $\text{CH}_2\text{-NH}$ -glucopyranoside), 2.96 (m, 1H, H-2 $\alpha$  glucopyranoside), 3.11-3.12 (dd, 1H, H-3 $\beta$  glucopyranoside), 3.46-3.52 (m, 448H,  $\text{OCHHCH}(\text{CH}_3)\text{O}$  PF127 + H-4 and H-5 glucopyranoside), 3.59 (m, 199,  $\text{CH}_2\text{-CH}_2\text{-OH}$  PF127), 3.64 (m, 2831H,  $(\text{CH}_2\text{-CH}_2\text{-O})_n$  PF127), 3.75 (m, 22H,  $\text{CH}_2\text{-CH}_2\text{-O}$ -glucopyranoside +  $\text{CH}_2\text{-CH}_2\text{-OH}$  PF127), 3.84-3.86 (dd, 1H, H-3 $\alpha$  glucopyranoside), 4.19 (m, 2H, H-6 glucopyranoside), 4.36 (m, 2H, H-6 glucopyranoside) 4.52-4.53 (d, 1H, H-1 $\beta$  glucopyranoside), 5.24 (d, 1H, H-1 $\alpha$  glucopyranoside).

$^{13}\text{C-NMR}$  (151.2 MHz,  $\text{CD}_3\text{OD}$ ):  $\delta$  (ppm) = 17.72 (s,  $\text{OCHHCH}(\text{CH}_3)\text{O}$  PF127), 62.23 (s,  $\text{CH}_2\text{-OH}$  PF127), 66.04 (s,  $\text{CH}_2\text{-CH}_2\text{-NH}$ -glucopyranoside PF127), 68.81 (s, C-6 glucopyranoside), 69.66 (s, C-2 glucopyranoside), (s, C-2 glucopyranoside), 71.57 (s,  $(\text{CH}_2\text{-CH}_2\text{-O})_n$  PF127), 71.90 (s, C-4 glucopyranoside), 72.51 (s, C-3 glucopyranoside), 73.67 (s, C-5 glucopyranoside), 74.04, 74.13, 74.39, 74.43 (4s,  $\text{OCHHCH}(\text{CH}_3)\text{O}$  PF127), 76.54, 76.69, 76.82 (3s,  $\text{OCHHCH}(\text{CH}_3)\text{O}$  PF127), 93.64 (s, C-1 $\beta$  glucopyranoside), 96.29 (s, C-1 $\alpha$  glucopyranoside).

Medium FT-IR (KBr):  $\tilde{\nu}$  ( $\text{cm}^{-1}$ ) = 3432, 2885, 1467, 1344, 1112, 1060, 842.

### 8.5.6 Synthesis of tosylated Pluronic® F127, PF127-OTs

Each terminal hydroxyl group of PF127 was made more reactive by its conversion to a tosyl (Ts) group as follows. To a solution of 1 mmol of PF127 in 20 mL  $\text{CH}_2\text{Cl}_2$  dry, 0.5 eq of 4-dimethylaminopyridine (DMAP) and 10 eq of triethylamine ( $\text{Et}_3\text{N}$ ) were added together at  $0^\circ\text{C}$ . Then, 10 eq of p-toluensulfonyl chloride (TsCl) were added, and the reaction was kept under stirring for 24 h. The subsequent washing with 2x5 mL of HCl 0.1 M and 10 mL of brine, followed by precipitation with  $\text{Et}_2\text{O}$ , led to the isolation of a white product, endowed with a 100% functionalization degree. Such percentage was evaluated by  $^1\text{H-NMR}$  in  $\text{CD}_2\text{Cl}_2$  considering the integration values of the NMR signals related to aromatic protons of tosylate (red colored) and methylic protons of the PPO central moiety of PF127 (blue colored) (**Figure 8.11**).

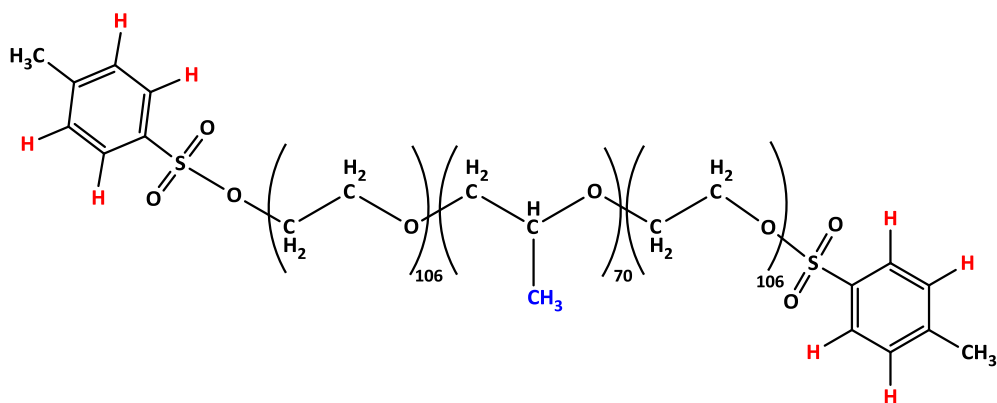


**Figure 8.11** Chemical drawing of Pluronic® F127 where terminal hydroxyl groups of the polymer have been activated with the good leaving group tosylate, PF127-OTs.

$^1\text{H-NMR}$  (599.90 MHz,  $\text{CD}_2\text{Cl}_2$ ):  $\delta$  (ppm) = 1.10 (t, 99H,  $\text{CH}_3$  PF127), 2.31 (s br, OH PF127), 2.44 (s,  $\text{CH}_3$  tosylate), 3.37 (m, 33H,  $\text{OCHHCH}(\text{CH}_3)\text{O}$  PF127), 3.48-3.52 (m, 69H,  $\text{OCHHCH}(\text{CH}_3)\text{O}$  PF127), 3.56 (m, 12H,  $\text{CH}_2\text{-CH}_2\text{-OH}$  PF127), 3.59 (m, 463H,  $(\text{CH}_2\text{-CH}_2\text{-O})_n$  PF127), 3.70 (m, 3H,  $\text{CH}_2\text{-CH}_2\text{-OH}$  PF127), 3.70 (t, 4H,  $\text{CH}_2\text{-Tosylate}$  PF127), 7.36-7.37 (d, 2H,  $H^*_{\text{meta}}$  tosylate), 7.76-7.78 (d, 2H,  $H^*_{\text{orto}}$  tosylate).

$^{13}\text{C-NMR}$  (151.2 MHz,  $\text{CD}_2\text{Cl}_2$ ):  $\delta$  (ppm) = 17.60, 17.68 (2s,  $\text{OCHHCH}(\text{CH}_3)\text{O}$  PF127), 21.91 (s,  $\text{CH}_3$  tosylate), 62.13 (s,  $\text{CH}_2\text{-OH}$  PF127), 65.52 (s,  $\text{CH}_2\text{-CH}_2\text{-OH}$ ), 68.93, 69.11 (2s,  $\text{CH}_2\text{-Tosylate}$  PF127), 70.03 (s,  $\text{CH}_2\text{-CH}_2\text{-Tosylate}$ ), 71.04 (s,  $(\text{CH}_2\text{-CH}_2\text{-O})_n$  PF127), 73.26, 73.34, 73.69 (3s,  $\text{OCHHCH}(\text{CH}_3)\text{O}$  PF127), 75.64, 75.81, 75.95 (3s,  $\text{OCHHCH}(\text{CH}_3)\text{O}$  PF127), 128.40 (s,  $\text{C}^*_{\text{orto}}$  tosylate), 130.40 (s,  $\text{C}^*_{\text{meta}}$  tosylate), 133.51 (s,  $\text{C}^*_{\text{para}}$  tosylate), 145.55 (s,  $\text{C}^*_{\text{ipso}}$  tosylate).

\* in agreement with data reported in reference [478]

Medium FT-IR (KBr):  $\tilde{\nu}$  ( $\text{cm}^{-1}$ ) = 2885, 1467, 1344, 1113, 1060, 842, 664.

### 8.5.7 Synthesis of phthalimido Pluronic® F127, PF127-Phtha

To a solution of 0.5 mmol of PF127-Ts in 10 mL of DMF dry at reflux, 10 mmol of phthalimide potassium salt (Phtha K) were added and the reaction was kept under stirring for 5 hours. After filtration of the by-products and precipitation with  $\text{Et}_2\text{O}$ , a light-yellow solid was obtained. The functionalization degree was identified as 97% by  $^1\text{H-NMR}$  ( $\text{CD}_2\text{Cl}_2$ ), comparing the integration values related to aromatic protons of phthalimide (red colored) and methylic protons of the PPO central moiety of PF127 (blue colored) (**Figure 8.12**).

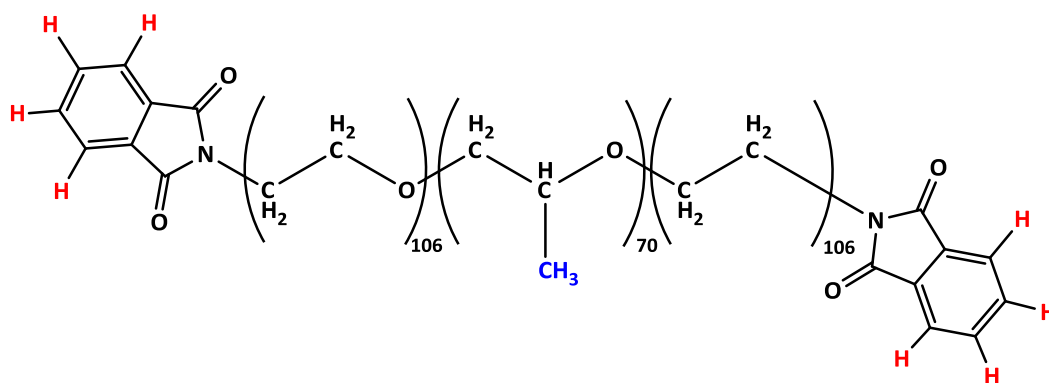


**Figure 8.12** Chemical drawing of Pluronic® F127 where terminal tosylate has been substituted with a phthalimido group, PF127-Phtha.

$^1\text{H-NMR}$  (599.90 MHz,  $\text{CD}_2\text{Cl}_2$ ):  $\delta$  (ppm) = 1.11 (t, 108H,  $\text{CH}_3$  PF127), 1.94 (s br, OH PF127), 2.33 (t, 2H,  $\text{CH}_2$ -phthalimide), 3.38 (m, 37H,  $\text{OCHHCH}(\text{CH}_3)\text{O}$  PF127), 3.48-3.52 (m, 78H,  $\text{OCHHCH}(\text{CH}_3)\text{O}$  PF127), 3.56 (m, 13H,  $\text{CH}_2\text{-CH}_2\text{-OH}$  PF127), 3.60 (m, 501H,  $(\text{CH}_2\text{-CH}_2\text{-O})_n$  PF127), 3.70 (m, 6H,  $\text{CH}_2\text{-CH}_2\text{-OH}$  PF127), 3.85 (t, 2H,  $\text{CH}_2\text{-CH}_2\text{-phthalimide}$  PF127), 7.74 (m, 2H, H-4 phthalimide), 7.82 (m, 2H, H-3 phthalimide).

$^{13}\text{C-NMR}$  (151.2 MHz,  $\text{CD}_2\text{Cl}_2$ ):  $\delta$  (ppm) = 17.61, 17.70 (2s,  $\text{OCHHCH}(\text{CH}_3)\text{O}$  PF127), 37.97 (s,  $\text{CH}_2\text{-phthalimide}$  PF127), 68.39 (s,  $\text{CH}_2\text{-CH}_2\text{-phthalimide}$ ), 71.04 (s,  $(\text{CH}_2\text{-CH}_2\text{-O})_n$  PF127), 73.28, 73.35, 73.72 (3s,  $\text{OCHHCH}(\text{CH}_3)\text{O}$  PF127), 75.67, 75.84, 75.99 (3s,  $\text{OCHHCH}(\text{CH}_3)\text{O}$  PF127), 123.99 (s, C-2 phthalimide), 132.75 (s, C-3 phthalimide), 134.48 (s, C-4, phthalimide), 168.99 (s, C-1 ( $\text{C}=\text{O}$ ) phthalimide).

Medium FT-IR (KBr):  $\tilde{\nu}$  ( $\text{cm}^{-1}$ ) = 2885, 1716, 1467, 1344, 1114, 1060, 842, 724, 690.

### 8.5.8 Synthesis of amino Pluronic® F127, PF127-NH<sub>2</sub>

A *Gabriel-like synthesis* was run according to a modified literature procedure [466]. To a solution of 0.3 mmol of PF127-Phtha (97%) in 20 mL of EtOH at reflux, 50 eq of hydrazine ( $\text{NH}_2\text{NH}_2$ ) were added. After 16 h at reflux, the product was precipitated with  $\text{Et}_2\text{O}$ , obtaining a white solid with a functionalization degree ( $-\text{NH}_2$  terminal group) of 45%. This was determined by  $^1\text{H-NMR}$  ( $\text{CD}_2\text{Cl}_2$ ) comparing the integration areas of the methylenic protons nearest to the amine ( $\text{CH}_2\text{-NH}_2$ , red colored) and the methylic protons of the PPO central moiety of PF127 (blue colored) (**Figure 8.13**).

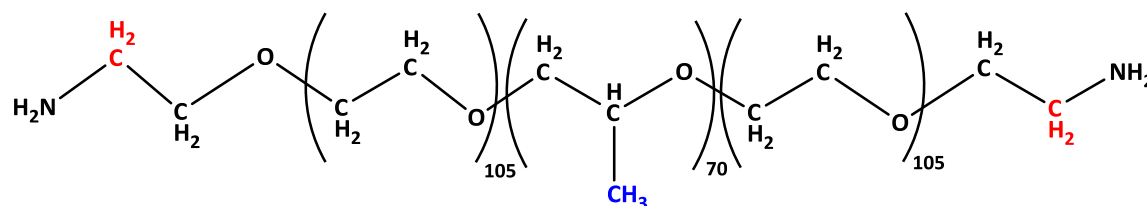


**Figure 8.13** Chemical drawing of Pluronic® F127 where terminal phthalimido groups have been converted to two amine groups *via* a Gabriel-like reaction, PF127-NH<sub>2</sub>.

$^1\text{H-NMR}$  (599.90 MHz,  $\text{CD}_2\text{Cl}_2$ ):  $\delta$  (ppm) = 1.11 (t, 235H,  $\text{CH}_3$  PF127), 2.05 (s br, OH PF127), 2.84 (t, 2H,  $\text{CH}_2\text{-NH}_2$ ), 3.38 (m, 80H,  $\text{OCHHCH}(\text{CH}_3)\text{O}$  PF127), 3.47-3.52 (m, 144H,  $\text{OCHHCH}(\text{CH}_3)\text{O}$  PF127), 3.55 (m, 12H,  $\text{CH}_2\text{-CH}_2\text{-OH}$  PF127), 3.60 (m, 1143H,  $(\text{CH}_2\text{-CH}_2\text{-O})_n$  PF127), 3.71 (m, 7H,  $\text{CH}_2\text{-CH}_2\text{-OH}$  PF127).

$^{13}\text{C-NMR}$  (151.2 MHz,  $\text{CD}_2\text{Cl}_2$ ):  $\delta$  (ppm) = 17.62, 17.70 (2s,  $\text{OCHHCH}(\text{CH}_3)\text{O}$  PF127), 42.17 (s,  $\text{CH}_2\text{-NH}_2$  PF127), 62.16 (s,  $\text{CH}_2\text{-OH}$  PF127), 65.54 (s,  $\text{CH}_2\text{-CH}_2\text{-NH}_2$ ), 71.07 (s,  $(\text{CH}_2\text{-CH}_2\text{-O})_n$  PF127), 73.28, 73.36, 73.72 (3s,  $\text{OCHHCH}(\text{CH}_3)\text{O}$  PF127), 75.67, 75.84, 75.99 (3s,  $\text{OCHHCH}(\text{CH}_3)\text{O}$  PF127).

Medium FT-IR (KBr):  $\tilde{\nu}$  ( $\text{cm}^{-1}$ ) = 2884, 1467, 1344, 1113, 1060, 842.

### 8.5.9 Synthesis of Pluronic® F127 conjugated with fluorescein via thioureido bond, PF127-FITC

The conjugation of fluorescein to the terminal amino groups of PF127 resulted in the formation of a thioureido bond, exploiting the well-known reactivity of an isothiocyanato group towards amines [467].

Briefly, 0.2 mmol of PF127-NH<sub>2</sub> (45%) were dissolved in 15 mL of dry THF and then 0.2 mmol of fluorescein isothiocyanate (FITC) and 0.5 mmol of diisopropylethylamine (DIPEA) were added. The solution was kept under stirring at 25 °C, protected from light, for 15 hours. Then, the solvent was removed, and the raw product was purified by silica gel chromatography using  $\text{CH}_2\text{Cl}_2/\text{MeOH}$  9:1 as an eluent. A yellow solid was obtained, and the degree of functionalization was determined to be 45% by  $^1\text{H-NMR}$  ( $\text{CD}_2\text{Cl}_2$ ) comparing the integration areas of the thioureidic -NH- protons (red colored) and the methyl protons of the PPO central moiety of PF127 (blue colored). For NMR attributions, the positions of carbons and related protons have been assigned as drawn in **Figure 8.14**.

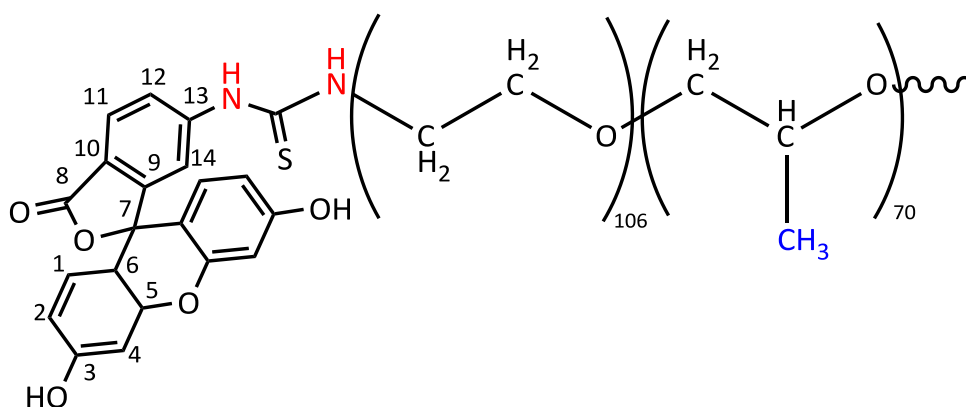


**Figure 8.14** Chemical drawing of the fluorescein moiety conjugated to PF127 via a thioureido group. Proton labelling is based on reference [467].

$^1\text{H-NMR}$  (599.90 MHz,  $\text{CD}_2\text{Cl}_2$ ):  $\delta$  (ppm) = 1.11 (t, 221H,  $\text{CH}_3$  PF127), 2.10 (s br, OH PF127), 3.38 (m, 73H,  $\text{OCHHCH}(\text{CH}_3)\text{O}$  PF127), 3.48-3.52 (m, 143H,  $\text{OCHHCH}(\text{CH}_3)\text{O}$  PF127), 3.57 (m, 11H,  $\text{CH}_2\text{-CH}_2\text{-OH}$  PF127), 3.60 (m, 905H,  $(\text{CH}_2\text{-CH}_2\text{-O})_n$  PF127), 3.71 (m, 11H,  $\text{CH}_2\text{-CH}_2\text{-OH}$  PF127), 6.98 (s br, 2H, H-1), 7.12-7.14 (d, 2H, H-2),

7.31 (m, 2H, H-3), 7.48 (m, 1H, H-11), 7.86 (s br, 1H, PF127-NH-CS-NH-fluorescein), 8.15 (m, 1H, H-12), 8.50 (s, 1H, H-14), 9.67 (s br, 1H, PF127-NH-CS-NH-fluorescein).

$^{13}\text{C}$ -NMR (151.2 MHz,  $\text{CD}_2\text{Cl}_2$ ):  $\delta$  (ppm) = 17.62, 17.71 (2s,  $\text{OCHHCH}(\text{CH}_3)\text{O}$  PF127), 68.95 (s,  $\text{CH}_2\text{-NH-S-NH}$  PF127), 69.00 (s,  $\text{CH}_2\text{-CH}_2\text{-NH-CS-NH}$  PF127), 71.07 (s,  $(\text{CH}_2\text{-CH}_2\text{-O})_n$  PF127), 73.29, 73.36, 73.73 (3s,  $\text{OCHHCH}(\text{CH}_3)\text{O}$  PF127), 75.68, 75.85, 76.00 (3s,  $\text{OCHHCH}(\text{CH}_3)\text{O}$  PF127), 103.50 (s, C-3), 106.14 (s, C-2), 189.87 (s, N(C-S)N). Other C signals are too weak to be seen.

Medium FT-IR (KBr):  $\tilde{\nu}$  ( $\text{cm}^{-1}$ ) = 3441, 2884, 1759, 1619, 1467, 1344, 1114, 1060, 842.

**8.5.10 Pluronic® F127 conjugations achieved in collaboration with the University of Milano-Bicocca**  
In collaboration with the Prof. L. Cipolla's research group of the University of Milano-Bicocca, two additional conjugations were performed, exploiting the formation of an oxime functional group and yielding a PF127 linked to a  $\beta$ -D-glucopyranoside (PF127- $\beta$ -D-glucopyranoside) or to the disaccharide  $\beta$ -D-maltose (PF127- $\beta$ -maltose).

#### 8.5.10.1 Synthesis of the $\beta$ -D-aminoxy glucose and maltose

Acetobromo- $\alpha$ -D-carbohydrate (carbohydrate= glucose and maltose) was mixed with 2 eq of *N*-hydroxy phtalimide in  $\text{CH}_2\text{Cl}_2$  in the presence of tetra(*n*-butyl)ammonium hydrogenosulfate (TBAHS) for 4 hours at room temperature. Then, the product was precipitated with  $\text{Et}_2\text{O}$  as *O*-acetyl- $\beta$ -D-phtalimido-sugar. The latter was then treated with methyl hydrazine ( $\text{NH}_2\text{NHMe}$ ) in MeOH at reflux, to both remove acetyl protective groups and to form the aminoxy moiety, obtaining  $\beta$ -D-aminoxy-sugar (**Figure 8.15 a, b**) as a white solid by precipitation with  $\text{Et}_2\text{O}$ .

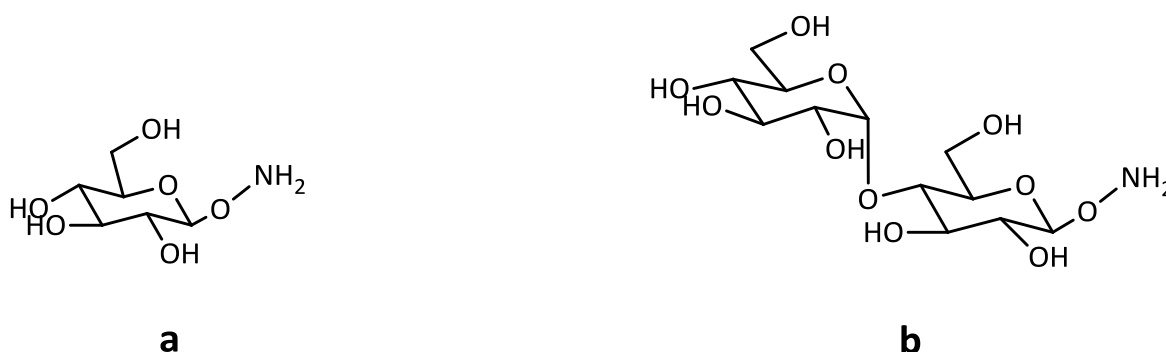


**Figure 8.15** Chemical drawing of the obtained  $\beta$ -D-aminoxy-sugars:  $\beta$ -D-aminoxy-glucopyranoside **a**, and  $\beta$ -D-aminoxy-maltose **b**.

### 8.5.10.2 Conversion of the terminal hydroxyl groups of Pluronic® F127 to ketones, PF127-Levu

This reaction was carried out to replace each hydroxyl group with a ketone as a terminal functional group of PF127, able to react with an aminoxy moiety to form an oxime. Briefly, PF127 was allowed to react with 10 eq of levulinic acid (activated by 10 eq of dicyclohexylcarbodiimide) for 24 hours in CH<sub>2</sub>Cl<sub>2</sub>. Then, the solution was reduced under vacuum and the product was precipitated with Et<sub>2</sub>O, yielding a white solid. The functionalization degree was identified as 100% by <sup>1</sup>H-NMR (CD<sub>2</sub>Cl<sub>2</sub>), comparing the integration area related to the methyl protons nearest the carbonyl group (blue colored) and methyl protons the PPO central moiety of PF127 (orange colored) (**Figure 8.16**).

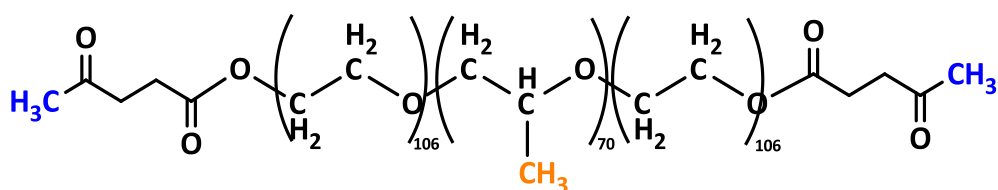


**Figure 8.16** Chemical drawing of the modified Pluronic® F127 by conjugation with levulinic acid to obtain a terminal ketone moiety, PF127-Levu.

### 8.5.10.3 PF127 bio-conjugation by oxime formation between the ketones of PF127-Levu and the aminoxy moiety of the carbohydrates

The oxime formation was achieved by mixing PF127-Levu and β-D-aminoxy-sugar in a 1:2 molar ratio in aqueous solution (buffered at pH 3.5 using citric acid/sodium citrate). Then, the solution was lyophilized and the resulting solid purified by silica gel chromatography using a mixture of isopropanol/ammonia 9:1 to remove unreacted sugar.

The functionalization degree was 51% in the case of glucose and 60% for maltose, evaluated by <sup>1</sup>H-NMR spectroscopy, focusing on the integration values of the peaks of the terminal methyl protons of the final oxime (green colored, **Figure 8.17**) and the same protons of the unreacted PF127-Levulinic acid (blue colored, **Figure 8.16**).

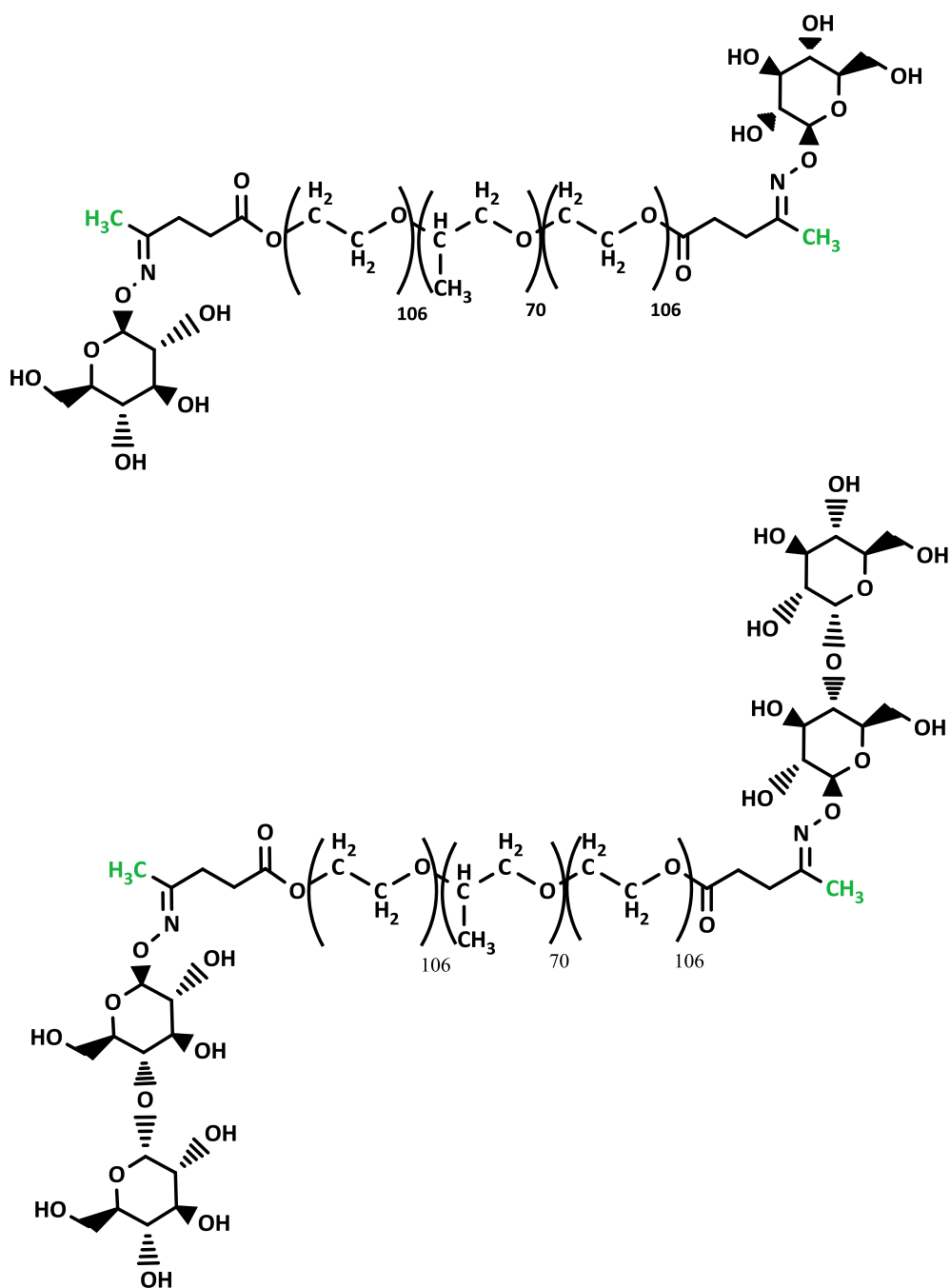


**Figure 8.17** Chemical drawing of the modified Pluronic® F127 by conjugation of  $\beta$ -D-aminoxy-sugar to PF127-Levu to form an oxime group, PF127-  $\beta$ -D-glucopyranoside (up) and PF127- $\beta$ -maltose (down).

## 8.6 Discussion about the synthesized carbohydrate-functionalized Pluronic® F127

### 8.6.1 Considerations on the synthetic routes

With reference to the **Section 8.5.1-8.5.9**, a scheme of the reactions performed in our laboratories to achieve the functionalization of PF127 with glucose, glucosamine and fluorescein, is reported in **Figure 8.18**.

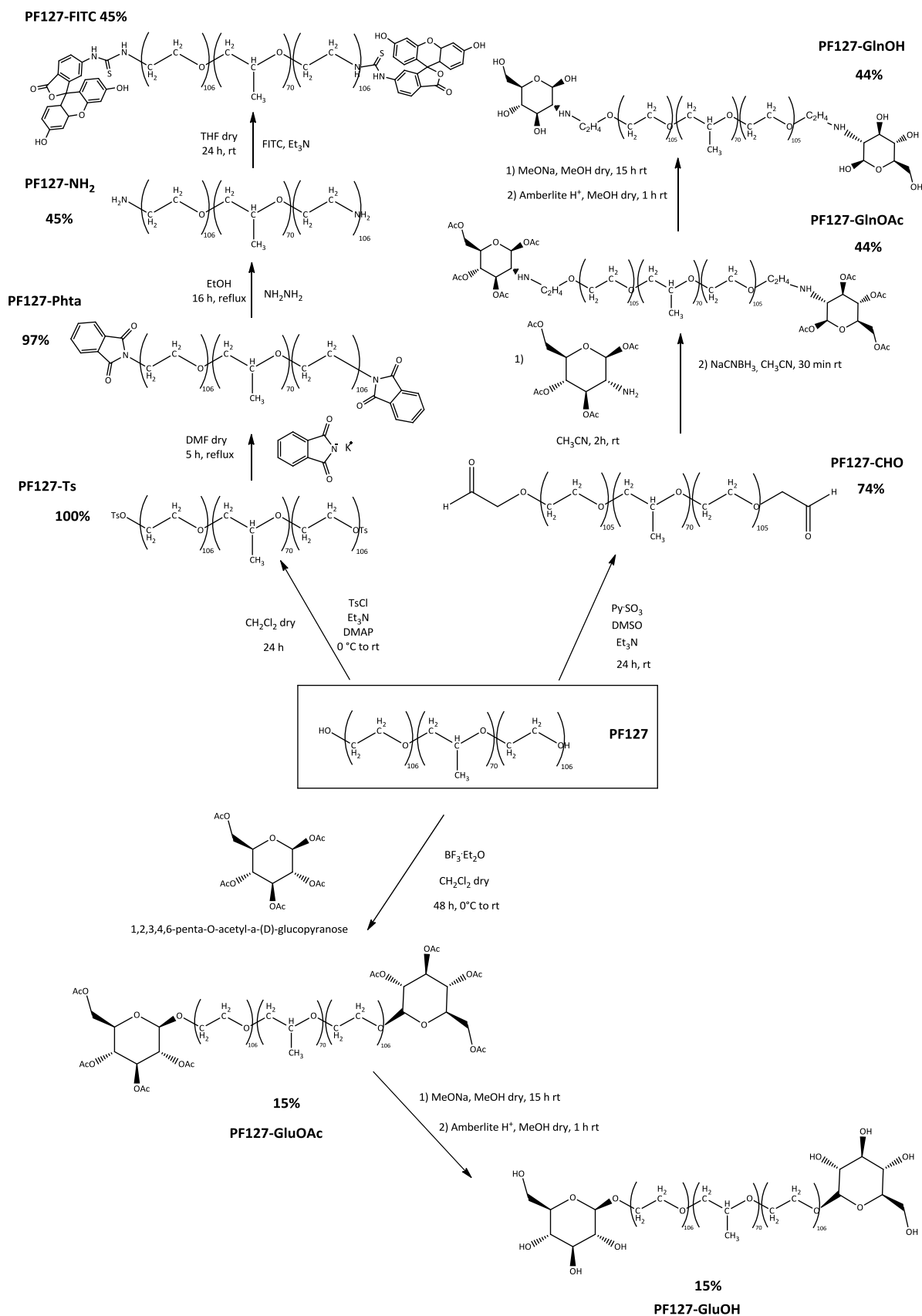


**Figure 8.18** Scheme of the reactions carried out during this PhD work in our laboratories, for the modification of the terminal hydroxyl groups of PF127 in order to conjugate the cancer-targeting moieties glucose ( $\beta$ -form) and glucosamine, and to link the fluorescent probe fluorescein.



The approach used in these syntheses is either the direct conjugation of the sugar (*e.g.*, glucose) to the hydroxyl terminal groups of PF127 or the modification of the latter to generate active substrates toward glucosamine and fluorescein. The choice to work with acetyl-protected carbohydrates is due to the low or none solubility of the corresponding deprotected sugars in organic solvents, which limits their reactivity, along with to hamper the occurrence of side reactions [468]. In all cases, the acetyl groups have been removed by basic ester cleavage using MeONa in methanol (namely *Zemplén deacetylation*), followed by neutralization with the strong cationic ( $H^+$ ) Amberlite IR120 resin [469].

The direct conjugation of acetylated glucose to hydroxyl groups of PF127 was performed by a *O*-glycosylation reaction, starting from per-*O*-acetylated-glucopyranoside in the presence of a Lewis acid ( $BF_3$ ) (Figure 8.19) [470]. The latter acts as an activator, promoting the exit of the C1 acetyl group (LG) with the subsequent formation of an oxocarbenium ion. At this point, the acetyl group at the position 2 allows the formation of the acetoxium ion intermediate that forces the nucleophile (the terminal hydroxyl moiety of PF127) to attack the positively charged C1 to mostly form a  $\beta$ -glycoside [471, 472]. It is worth mentioning that, since glycosylation is performed at the anomeric position 1, the ring cannot undergo the epimeric equilibrium  $\alpha \leftrightarrow \beta$ , and hence the product remains in its  $\beta$ -form, which is the epimer recognized by the GLUT1 protein [473].

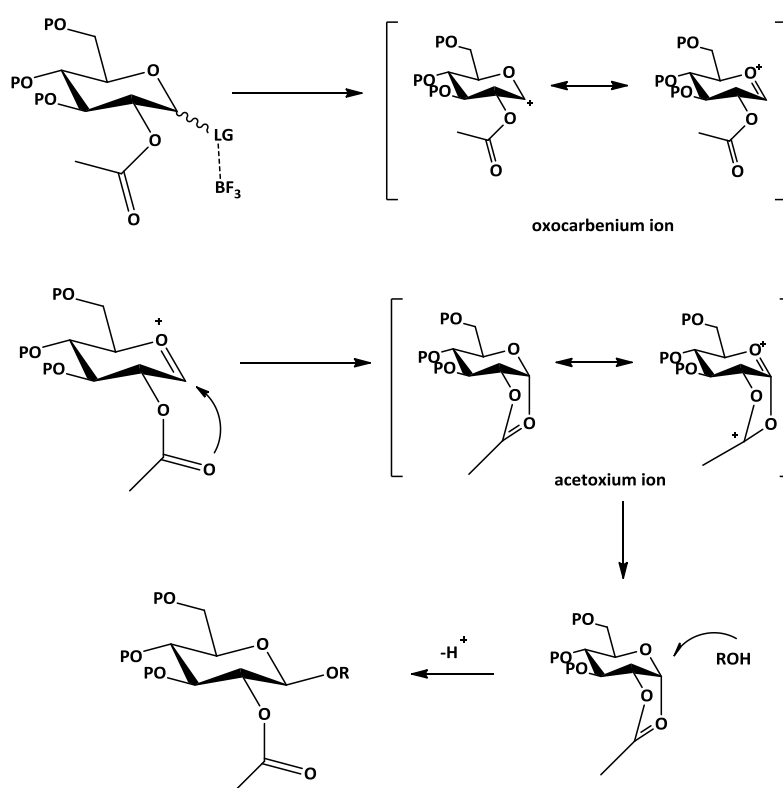


**Figure 8.19** Glycosylation mechanism carried out for the per-*O*-acetylated-glucopyranoside in the presence of a nucleophile (ROH; in this work PF127, whereas LG= OAc) and  $BF_3$ .

On the other hand, the conjugation of *O*-acetylated-2-amino-2-deoxy-D-glucopyranoside (acetylated glucosamine) was performed using the *reductive amination reaction*, thus forming an *N*-glycoside in position 2. Accordingly, once deprotected, the sugar undergoes the epimeric equilibrium  $\alpha \leftrightarrow \beta$ . To carry out this reaction, the two terminal hydroxyl groups of PF127 have been first converted into two aldehyde groups *via* a Parikh-Doering oxidation, so to have the imine formation in the presence of the glucosamine amino group, being successively reduced to a secondary amine by addition of NaCNBH<sub>3</sub>. It is worth mentioning that Harris and coworkers reported a reductive amination for poly(ethylene glycol) aldehyde using deprotected glucosamine [474]. However, as observed in our laboratories, this strategy leads to the reduction of the aldehyde group of the sugar in the open-chain form, forming 2-amino-2-deoxy-glucitol [475]. Thus, the reaction was performed using *O*-acetyl-protected glucosamine.

Finally, a 3-step procedure was planned to convert the terminal hydroxyl group of PF127 into an amine, suitable for the subsequent conjugation with fluorescein isothiocyanate, forming a thioureido group [467]. First of all, both -OH groups were converted to the good leaving group -OTs (OTs= tosyl) using *p*-toluensulfonyl chloride [476], then a phthalimido group was introduced to generate the primary amine using hydrazine, taking advantage of the well-known Gabriel's synthesis of amines [466].

Concerning the Pluronic® F127 modifications carried out in collaboration with the University of Milano-Bicocca, under the supervision of Professor Laura Cipolla, the aim was to functionalize the block polymer with either a mono-saccharide as  $\beta$ -epimer ( $\beta$ -D-glucose) or with a di-saccharide endowed with a terminal glycoside in the  $\alpha$ -form of the epimer ( $\alpha$ -D-glucose). In this regard, maltose was chosen since it is a di-saccharide consisting of two units of D-glucose joined by a  $\alpha$ -(1 $\rightarrow$ 4) bond. A scheme of the reactions performed within this collaboration, described in **Section 8.5.10**, is reported in **Figure 8.20**. This type of PF127 derivatives contains a carbohydrate bonded *via* an oxime linker. The choice was not accidental, since the oxime as a linking group is stable under physiological conditions (oxime cleavage occurs only in strong acid conditions under reflux) [477].

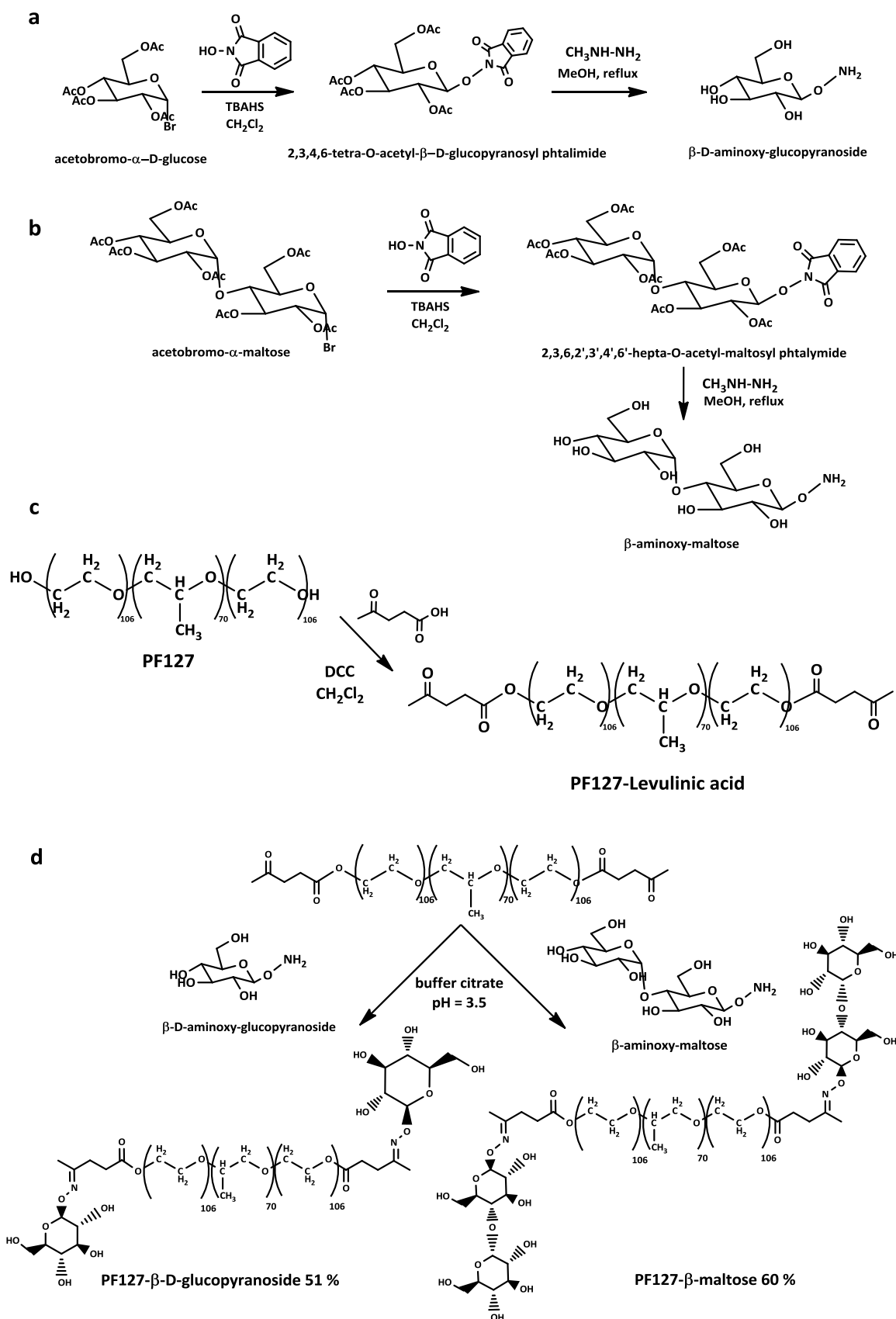


**Figure 8.20** Conjugation procedure of  $\beta$ -D-glucopyranoside and  $\beta$ -maltose to PF127. Synthesis of  $\beta$ -D-aminoxy-glucopyranoside (a) and  $\beta$ -aminoxy-maltose (b) via Gabriel reaction a; synthesis of PF127-Levulinic acid c; oxime coupling to obtain PF127- $\beta$ -D-glucopyranoside (left) and PF127- $\beta$ -maltose (right) d.

8.6.2 <sup>1</sup>H-NMR characterization

All the modifications performed on the terminal group of PF127 copolymer were analyzed by <sup>1</sup>H- and <sup>13</sup>C-NMR (**Supporting Information E**), and compared with the unmodified Pluronic® F127. In particular, <sup>1</sup>H-NMR spectroscopic technique is useful to assess the degree of functionalization of the modified polymers, taking into account the mean number of PPO repeating units, for PF127 being about 70 [435]. Indeed, despite the molecular mass of the copolymer is near 12,600 Da and its <sup>1</sup>H-NMR signals result very intense with respect to those of the conjugated substituents, the selection of those resonances at quite distant chemical shifts from those of the bulk of the polymer, allows the comparison between their areas with that of the signal ascribed to the methyl protons of the PPO chain. The ratio between this value and the theoretical value, which accounts for a 100% functionalization (considering n°(PPO)= 70), generates the degree of functionalization of PF127 conjugates synthesized in our laboratories. As an example the <sup>1</sup>H-NMR spectrum of PF127-GluOAc is taken here into account (**Supporting Information E, Figure E15**). The acetyl protecting groups of 2,3,4,6-tetra-*O*-acetyl-β-D-glucopyranoside generate four different singlets, each of them having an integral value of 3. On the other hand, the -CH<sub>3</sub> moiety of the PPO chain gives back a “triplet” at 1.09 ppm, accounting for 688 protons. On the other hand, supposing a quantitative functionalization, the integral for one acetyl should be 6 (*i.e.*, 3 protons x 2 terminal PF127 conjugations), whereas the PPO methyl protons are 210 (3 protons x 70 PPO repetitive units). The following formula gives the degree of functionalization:

$$\text{degree of functionalization (\%)} = \frac{\left(\frac{3}{688}\right)_{\text{experimental measurement}}}{\left(\frac{6}{210}\right)_{\text{theoric ratio}}} \times 100 = 15.3 \%$$

Concerning the use of NMR spectroscopy for the characterization of the PF127 derivatives, first of all it is possible to detect the intense signals related to the PEO and PPO backbones of Pluronic®, being identified by a multiplet in the range 3.60-3.75 ppm and a “triplet” at *ca.* 1.10 ppm, respectively. In the <sup>13</sup>C-NMR spectra, these moieties generate different signals at 72-75 ppm and 17 ppm, respectively [478]. It has to be underlined that the <sup>13</sup>C-NMR experiments have been performed with the C-H decoupling in order to obtain well defined signals, mainly for the terminal substituents (*e.g.*, glucosamine). Overall, it is possible to state that the PEO and PPO backbone resonances seem not to be affected by the terminal modifications. On the other hand, the variation of the PEO -CH<sub>2</sub> resonances proximal to the different substituents, as well as the signals of the linked groups (*e. g.*, glucose) have been useful in evaluating the success of labeling reactions, although some peaks in <sup>1</sup>H-NMR were lost due to the intensity of the backbone peaks.

Concerning the PF127-carbohydrate conjugates, both the <sup>1</sup>H- and <sup>13</sup>C-NMR analysis have been fundamental in the assessment of acetyl deprotection. Indeed, in the spectra of PF127-GluOH and PF127-Gln-OH (**Supporting Information E, Figure E17 and E13**, respectively) the absence of acetyl groups is clear, whereas four distinct proton signals are located at 1.90-2.10 ppm and four well-identified carbon peaks have been found at *ca.* 170 ppm for protected derivatives (**Supporting Information E, Figure E15 and E11**, respectively).

Finally, the presence of only a doublet at 4.29-4.31 ppm in the  $^1\text{H}$ -NMR spectrum of the conjugate PF127-GluOH points out the presence of the pure  $\beta$ -epimer [479]. On the contrary, the glucosamine derivative PF127-Gln presents two sets of anomeric signals, due to the epimeric equilibrium  $\alpha \leftrightarrow \beta$  which takes place in solution after deprotection [475].

Moving to the PF127 derivatives obtained in collaboration with the University of Milano-Bicocca, the degree of functionalization of PF127 oxime-conjugates of  $\beta$ -D-glucopyranoside and  $\beta$ -maltose, was calculated by the formula:

$$\text{degree of functionalization (\%)} = \frac{\int \text{CH}_3 \text{oxime terminal}}{\int \text{CH}_3 \text{keton terminal} + \int \text{CH}_3 \text{oxime terminal}} \cdot 100$$

In particular, the areas of the signals of the terminal methyl group of unreacted PF127-levu (blue colored, **Figure 8.16**) and the final PF127-oxime (green colored, **Figure 8.17**) were compared. As an example, the  $^1\text{H}$ -NMR spectrum ( $\text{D}_2\text{O}$ ) of oxime-linked PF127- $\beta$ -D-glucopyranoside is reported in **Figure 8.21**. Concerning the characterization of these derivatives, the  $^1\text{H}$ - and  $^{13}\text{C}$ -NMR spectral features were the same of the previously discussed PF127 conjugates obtained in our laboratories.

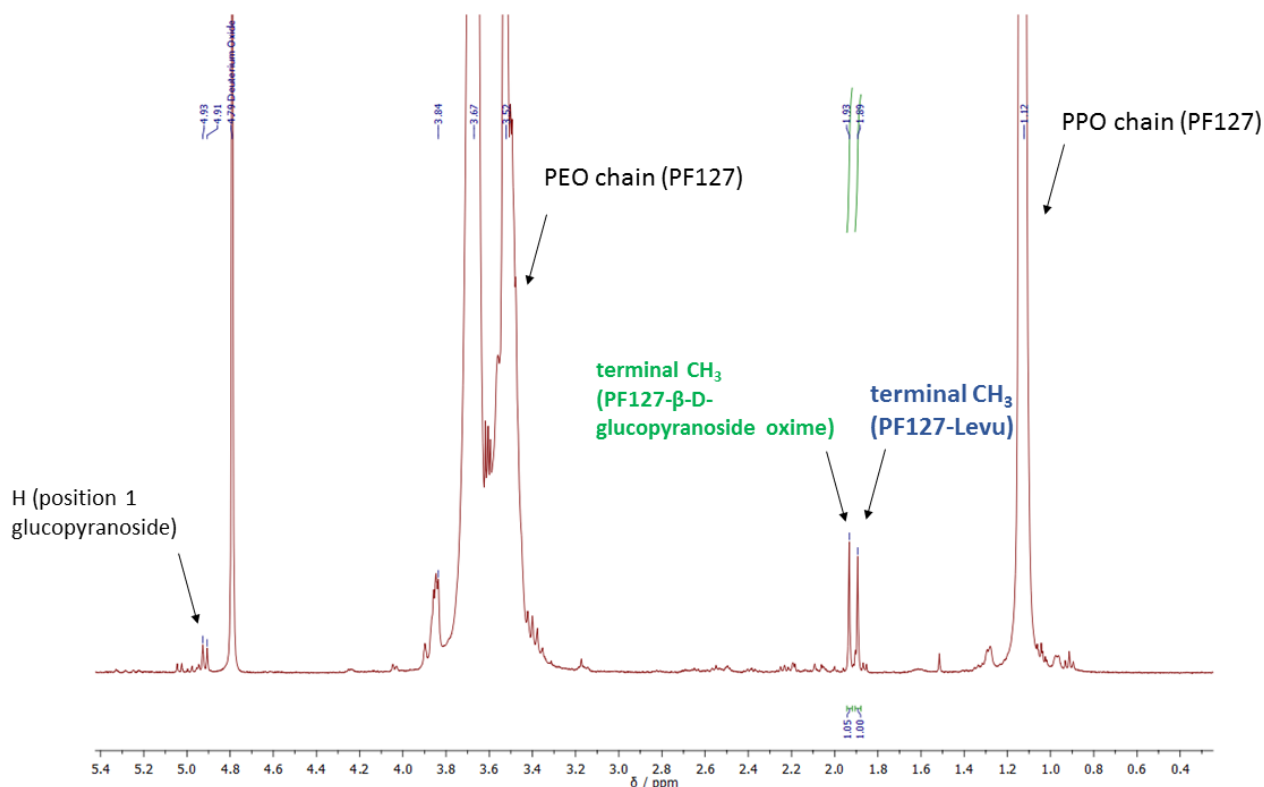


**Figure 8.21**  $^1\text{H}$ -NMR spectrum ( $\text{D}_2\text{O}$ , 599.90 MHz, 298 K) of oxime-linked PF127- $\beta$ -D-glucopyranoside. It is possible to determine the degree of functionalization comparing the integration value related to the terminal  $\text{CH}_3$  signal of oxime (green-colored) with that of the unfunctionalized ketone (blue highlighted). In particular, according to the previously presented formula, the degree of functionalization =  $[1.05/(1.00+1.05)] \cdot 100 = 51.2\%$ .

### 8.6.3 FT-IR characterization

The diagnostic absorptions of the conjugated carbohydrates and fluorescein, as well as of the modified terminal hydroxyl groups of PF127 have been identified by comparison of the FT-IR spectra of the synthesized derivatives (**Supporting Information L**) with that of commercial Pluronic® F127. All spectra, recorded in the range 4000-500  $\text{cm}^{-1}$ , show the common fingerprint of the PEO-PPO-PEO triblock copolymers, with a medium absorption at *ca.* 2885  $\text{cm}^{-1}$  attributed to the C-H stretching  $\nu(\text{C-H})$  and different bands in the region 1500-900  $\text{cm}^{-1}$ . These have been deeply discussed in literature [480-482], and the attributions are presented in **Table 8.2**.

<b><i>CH<sub>3</sub> symmetry deformation</i></b>	<b><i>CH<sub>2</sub> wag + C-C stretching</i></b>	<b><i>CH<sub>2</sub> wag</i></b>	<b><i>CH<sub>2</sub> wag</i></b>	<b><i>C-O-C stretching + C-C stretching</i></b>
1467 $\text{cm}^{-1}$	1360 $\text{cm}^{-1}$	1343 $\text{cm}^{-1}$	1280, 1242 $\text{cm}^{-1}$	1149 $\text{cm}^{-1}$
<b><i>C-O-C</i></b>	<b><i>C-O-C + CH<sub>2</sub> rocking</i></b>	<b><i>CH<sub>2</sub> rocking</i></b>	<b><i>C-O-C + CH<sub>2</sub> rocking</i></b>	
1114 $\text{cm}^{-1}$	1060 $\text{cm}^{-1}$	964 $\text{cm}^{-1}$	945 $\text{cm}^{-1}$	

**Table 8.2** Assignment of the detected FT-IR bands for our PF127 derivatives in the Pluronic® fingerprint range 1500-900  $\text{cm}^{-1}$ .

The infrared analysis has allowed also the detection of the characteristic signals of PF127-conjugates. For instance, the spectra of PF127-GlnOAc and PF127-GluOAc (**Appendix L, Figure L6 and L8**, respectively) show the presence of a weak absorption at 1756-1759  $\text{cm}^{-1}$ , ascribed to the C=O stretching vibration of the acetyl protecting groups. This band disappears indeed after basic cleavage of the esters, as observed in **Figure L7** (PF127-GlnOH) **and L9** (PF127-GluOH). Conversely, the carbonyl vibration is observed at 1759  $\text{cm}^{-1}$  only in the spectrum of fluorescein-conjugate PF127-FITC, and at 1630  $\text{cm}^{-1}$  in that of aldehyde derivative PF127-CHO (**Figure L5**). Concerning the latter, the C=O absorption occurs at lower wavenumbers due to the presence of the long-chain PF127 group, directly bound to the aldehydic function [483].

Finally, in the FT-IR spectra of the aromatic function-containing PF127 derivatives, it is possible to observe some ring-deformations in the spectral region 750-650  $\text{cm}^{-1}$  [484].

## 8.7 Encapsulation of selected metal-dithiocarbamate derivatives in Pluronic® F127 and carbohydrate-labeled Pluronic® F127 micelles

As reported in **Section 8.2**, the encapsulation of cytotoxic agents in nanosystems could improve their bioavailability and delivery. In this regard, if the passive cancer-targeting is a common denominator of all

nanocarriers with specific dimensions, that active can be achieved only with the functionalization of the external surface of the particles with cancer-selective moieties. In light of this, the sugar-conjugated PF127 polymers synthesized during this PhD work can be an optimal tool to favor a tumor localization of the corresponding micelles. The latter, acting as *Trojan horses*, drive the uptake of the cargo by cancer cells which overexpress GLUT1 transporters (see **Chapter 1**)

The metal derivatives of cyclic dithiocarbamates, whose synthesis and characterization have been described and discussed in the **Chapters 5-7**, result soluble in common organic solvents, but none of them are water soluble, except for the ionic  $[\text{Au}(\text{PipeDTC})_2]\text{X}$ , X= Cl, Br. On the basis of these considerations, they require pre-dissolution in dimethyl sulfoxide prior to carrying out *in vitro* experiments (presented in **Chapter 9**).

In this work, PF127 micelles have been designed, prepared and tested to solubilize our metal-DTC complexes, and to increase their stability in cell culture media and physiological milieu. Thus, two synthesized compounds, namely  $\beta$ - $[\text{Ru}_2(\text{PDT})_5]\text{Cl}$  and  $[\text{Cu}(\text{ProOMeDTC})_2]$ , have been selected for their cytotoxic and lipophilic properties (according to methodology presented in **Chapter 9**), to be encapsulated in Pluronic® F127 and Pluronic® F127-sugar conjugated micellar systems. In total, 10 different formulations have been prepared, 5 for each metal derivative, and they are reported in **Table 8.3**.

<i>Formulation name</i>	<i>Micelle Composition (w/w)</i>	<i>Encapsulated metal-complex</i>
<b>RuA</b>	PF127 100%	$\beta$ - $[\text{Ru}_2(\text{PDT})_5]\text{Cl}$
<b>RuC</b>	PF127 90% + PF127-GluOH 10%	$\beta$ - $[\text{Ru}_2(\text{PDT})_5]\text{Cl}$
<b>RuE</b>	PF127 90% + PF127- $\beta$ -D-glucopyranoside 10%	$\beta$ - $[\text{Ru}_2(\text{PDT})_5]\text{Cl}$
<b>RuG</b>	PF127 90% + PF127-GlnOH 10%	$\beta$ - $[\text{Ru}_2(\text{PDT})_5]\text{Cl}$
<b>RuI</b>	PF127 90% + PF127- $\beta$ -maltose	$\beta$ - $[\text{Ru}_2(\text{PDT})_5]\text{Cl}$
<b>CuA</b>	PF127 100%	$[\text{Cu}(\text{ProOMeDTC})_2]$
<b>CuC</b>	PF127 90% + PF127-GluOH 10%	$[\text{Cu}(\text{ProOMeDTC})_2]$
<b>CuE</b>	PF127 90% + PF127- $\beta$ -D-glucopyranoside 10%	$[\text{Cu}(\text{ProOMeDTC})_2]$
<b>CuG</b>	PF127 90% + PF127-GlnOH 10%	$[\text{Cu}(\text{ProOMeDTC})_2]$
<b>CuI</b>	PF127 90% + PF127- $\beta$ -maltose	$[\text{Cu}(\text{ProOMeDTC})_2]$

**Table 8.3** List of the prepared formulations with their name, composition in terms of Pluronic® copolymer, and metal complex encapsulated.

For targeted micelles, the percentage in composition of the sugar-modified PF127 has been chosen to be the 10% in weight. Indeed, different studies have recently discussed the ideal number of ligands on the surface of a nanoparticle to achieve the optimal cancer-targeting [485, 486]. In this context, most researchers concord that a greater ligand density does not necessarily lead to a higher intracellular concentration, since they can decrease the “stealth” surface characteristics, and consequently generate an accelerated clearance

[487]. In our opinion, higher the ligand density (> 40%), lower the cell uptake due to steric hindrance in the target-ligand recognition event.

### 8.7.1 Preparation of the nanoformulations of the selected metal-DTC complexes

The encapsulation of the selected complexes, namely  $\beta$ -[Ru<sub>2</sub>(PDT)<sub>5</sub>]Cl and [Cu(ProOMeDTC)<sub>2</sub>] in PF127 and PF127-sugar mixed micelles was performed by the thin film hydration method, using deionized water [433, 488]. Briefly,  $1 \cdot 10^{-6}$  moles of metal-DTC compound and 500 mg of PF127 polymer have been dissolved in 5 mL of acetonitrile. When cancer-targeting micelles have been prepared, the polymer was PF127 at 90% w/w and PF127-sugar at 10% w/w (taking into account the specific degree of functionalization of each conjugate, according to **Section 8.5**). The acetonitrile solution was mixed for 5 minutes and then the solvent evaporated to produce a homogeneous thin film of the complex and the polymer. To ensure the complete evaporation of acetonitrile, the resulted layer was dried *in vacuum* for 24 hours. After that, the addition of 5 mL of deionized water, followed by sonication for 10 minutes, led to the formation of a brown or a yellow-green transparent solution in the case of  $\beta$ -[Ru<sub>2</sub>(PDT)<sub>5</sub>]Cl and [Cu(ProOMeDTC)<sub>2</sub>] formulations, respectively. These have been filtered (cut-off: 20  $\mu$ m) to eliminate unloaded complex, followed by lyophilization to yield a pale brown powder for the Ru(III) formulation, or a pale green product when the Cu(II) complex is encapsulated (**Figure 8.22**).

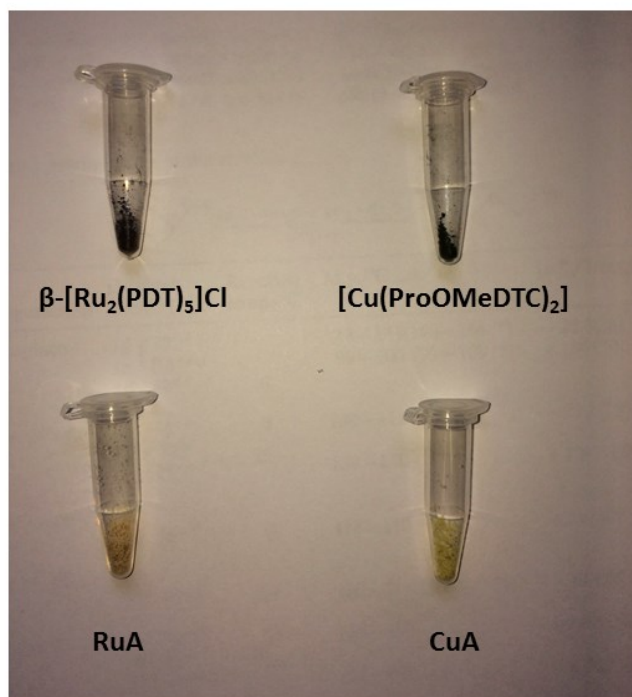


**Figure 8.22:** Top: the free metal-DTC complexes  $\beta$ -[Ru<sub>2</sub>(PDT)<sub>5</sub>]Cl (**left**) and [Cu(ProOMeDTC)<sub>2</sub>] (**right**), bottom: a picture of the corresponding lyophilized PF127 formulations RuA and CuA.



## 8.8 Characterization of the prepared nanoformulations

The formulations previously described have been characterized for i) complex loading , ii) shape and dimension, and iii) stability in cell culture medium (Dulbecco's Modified Eagle Medium, DMEM) and in human serum, for future *in vivo* studies.

### 8.8.1 Loading measurements

After filtration and lyophilization of the aqueous solution (presented in **Section 8.7.1**), the evaluation of *compound loading* and the *encapsulation efficiency* was accomplished for each complex in the different formulations using UV-Vis spectrophotometry (**Table 8.4**). Briefly, the molar extinction coefficient ( $\epsilon$ ) was determined for some absorption bands of all complexes in acetonitrile or dichloromethane. Then, a defined amount of lyophilized formulation (polymer + metal-DTC compound) was dissolved in CH<sub>3</sub>CN or CH<sub>2</sub>Cl<sub>2</sub> and, after UV-Visible analysis, the concentration of the complex was evaluated using the Lambert Beer's law [489].

<i>Formulation</i>	<i>Drug loading</i>	<i>Encapsulation efficiency</i>
<b>RuA</b>	$1.74 \cdot 10^{-9} \text{ mol mg}^{-1}$	87.0 %
<b>RuC</b>	$1.81 \cdot 10^{-9} \text{ mol mg}^{-1}$	90.5 %
<b>RuE</b>	$1.99 \cdot 10^{-9} \text{ mol mg}^{-1}$	99.5 %
<b>RuG</b>	$1.39 \cdot 10^{-9} \text{ mol mg}^{-1}$	69.5 %
<b>RuI</b>	$2.00 \cdot 10^{-9} \text{ mol mg}^{-1}$	100 %
<b>CuA</b>	$1.28 \cdot 10^{-9} \text{ mol mg}^{-1}$	64.0 %
<b>CuC</b>	$1.60 \cdot 10^{-9} \text{ mol mg}^{-1}$	80.0 %
<b>CuE</b>	$1.32 \cdot 10^{-9} \text{ mol mg}^{-1}$	66.0 %
<b>CuG</b>	$1.81 \cdot 10^{-9} \text{ mol mg}^{-1}$	90.5 %
<b>CuI</b>	$1.98 \cdot 10^{-9} \text{ mol mg}^{-1}$	99.0 %

**Table 8.4** Drug loading (expressed as moles of complex *per* mg of formulation) and encapsulation efficiency (expressed as moles of loaded complex/ moles of weighted complex, %) for the two selected metal-DTC compounds, formulated with PF127 or sugar-conjugated PF127.

### 8.8.2 DLS analysis

The Dynamic Light Scattering analysis (DLS) is a technique for measuring the size distribution profile of particles in solution typically in the sub-micron region [490]. In particular, DLS measures the speed at which the nanosystems are diffusing due to random movement (Brownian motion). This is done by measuring the rate at which the intensity of the scattered light fluctuates when detected using a suitable optical arrangement. Then, these fluctuations are transformed into a correlation function, which is further elaborated by an algorithm to give the mean size (Z-average diameter) of the studied particles, and an estimate of the distribution width (polydispersity index) [491]. Each formulation was dissolved in deionized

water at a concentration of 10 mg mL<sup>-1</sup> and the hydrodynamic diameter and distribution size were the mean of ten measurements at 37 °C. Values of Z-average diameter (expressed in nm) and polydispersity index (PDI) are reported in **Table 8.5**.

<i>Formulation</i>	<i>Z-average diameter ( nm)</i>	<i>Polydispersity index</i>
<b>RuA</b>	26.04	0.048
<b>RuC</b>	23.41	0.062
<b>RuE</b>	23.72	0.053
<b>RuG</b>	23.16	0.040
<b>RuI</b>	24.01	0.027
<b>CuA</b>	23.41	0.081
<b>CuC</b>	24.33	0.058
<b>CuE</b>	23.88	0.035
<b>CuG</b>	23.97	0.067
<b>CuI</b>	23.49	0.059

**Table 8.5** Structural parameters (mean hydrodynamic diameters, and polydispersity indexes) from dynamic light scattering measurements for the studied systems.

In agreement with literature data, the mean size of the prepared nanoparticles, both in the case of PF127 micelles and mixed supramolecular aggregates, ranges from 23 to 26 nm at 37°C [492]. Intriguingly, the hydrodynamic diameter of empty PF127 micelles was measured to be 21.91 nm at 37 °C, thus indicating that there is no significant effect on size when loading a cytotoxic cargo. Finally, concerning the polydispersity index, the found values are related to monodisperse samples with narrow size distributions (an example is reported in **Figure 8.23**), in agreement with similar nanosystem solutions at 37 °C presented in literature [492, 493].

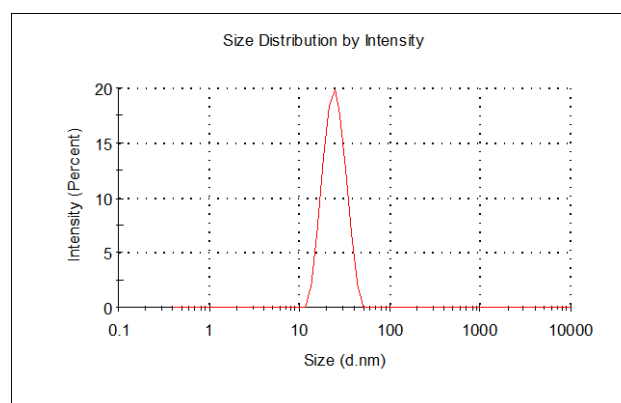


**Figure 8.23** The size distribution profile of the RuC formulation, taken as an example, gives an average diameter of 23.41 nm and a PDI of 0.062.

### 8.8.3 TEM analysis

The morphological characteristics of our Pluronic F127-based nanosystems were evaluated by transmission electron microscopy (TEM), and some representative images are collected in **Figure 8.24**.

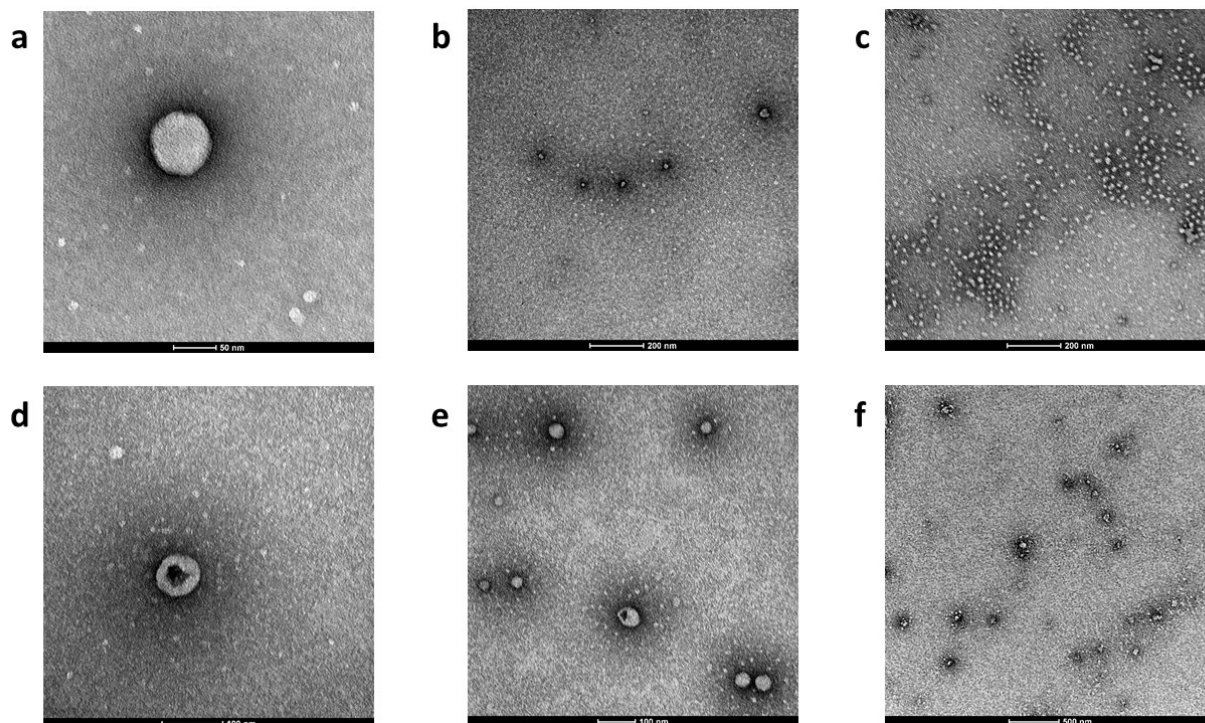


**Figure 8.24** TEM images of the investigated micelles, dissolved in aqueous solution at a concentration of  $2 \text{ mg mL}^{-1}$  and visualized with a negative stain of  $[\text{UO}_2(\text{CH}_3\text{COO})_2]$ . Pictures **a** and **b** are related to the RuA formulation, **c** represents RuG nanoparticles. On the bottom figure, **d** and **e** represents CuC, and finally **f** is related to CuE micelles.

The prepared nanosystems are spherical, well dispersed and separated from each other. The dimensions are generally in the range 40-60 nm. It has to be underlined that the TEM analysis gives a direct measure of the micelle diameter, whereas the previously reported DLS dimensions are related to the hydrodynamic diameter.

In some cases (**Figure 8.24 d**), the micelles show a core-shell structure, pointing out a dark and denser core, due to TEM-electron absorption by the metals in the investigated formulations (*ie.*, copper and ruthenium). Since this phenomenon is mainly observed for the Cu-containing systems, further studies are planned to investigate the composition and the architecture of the core of the studied micelles.

### 8.8.4 Solution stability studies

The prepared nanosystems have been studied for their stability in cell culture medium (DMEM diluted to 10% v/v in phosphate buffered saline) and human serum, diluted to 5% v/v in phosphate buffered saline), by means of UV-Vis spectrophotometry at  $37^\circ\text{C}$ .

Taking the dissolution of the formulation as time zero and the electronic spectra in DCM of the encapsulated complexes as a reference (see **Chapter 5.4.5**, and **6.4.5**), the behavior was monitored over time.

Remarkably, none of the formulations showed some modification in the UV-Vis spectra, thus highlighting a general stability of the loaded complexes in both cell culture medium and human serum. In addition, the collected curves, reported in **Figure 8.25** point out that our goal of achieving water soluble therapeutics has been reached.

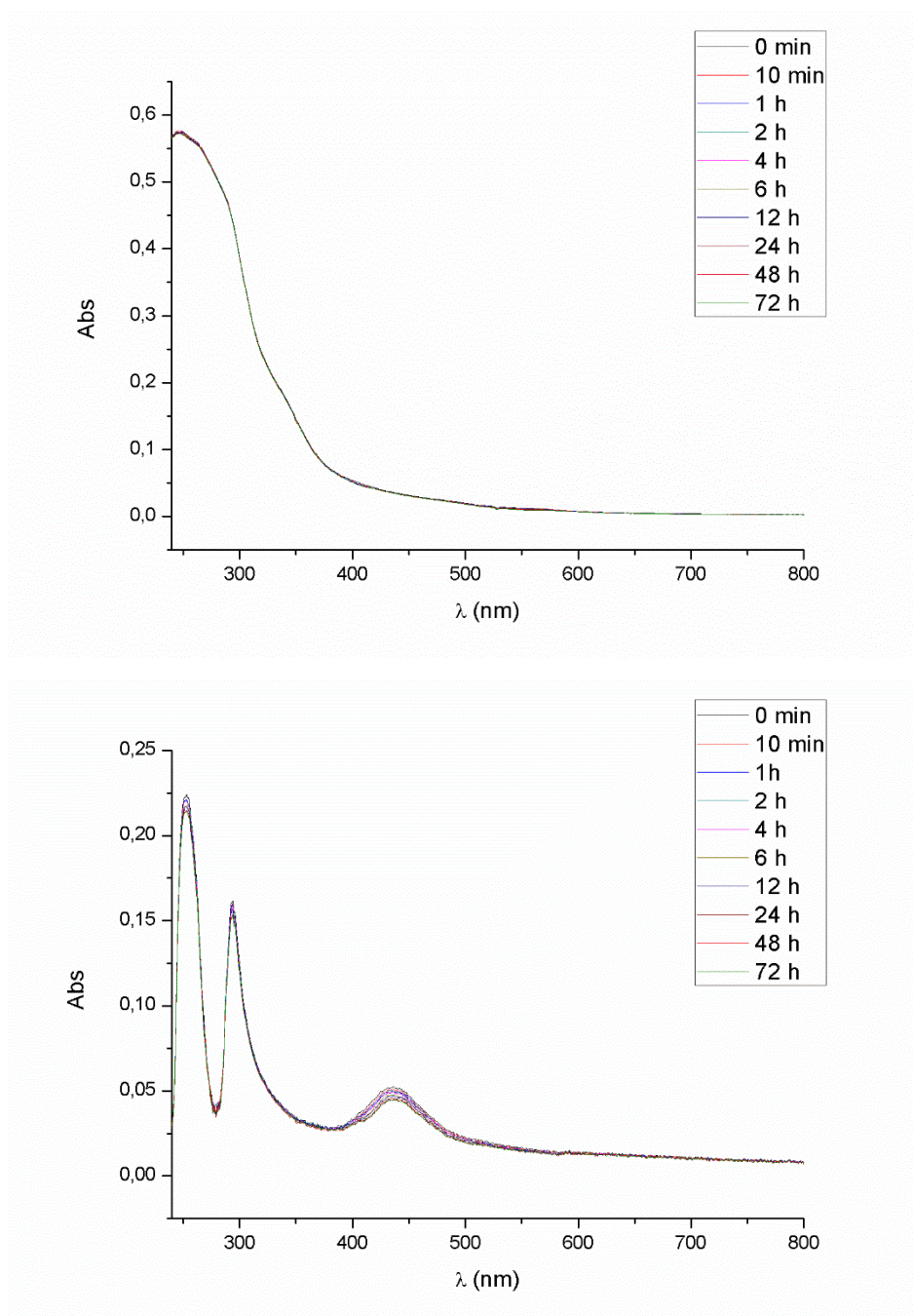


**Figure 8.25** Two examples of over- time UV-Vis analysis of Ru(III) and Cu(II) dithiocarbamate complexes loaded in PF127 micelles, tested for their stability in cell culture medium DMEM and human serum.

**Top:** Formulation RuA ( $5 \text{ mg mL}^{-1}$ ) in DMEM-PBS 10-90 % v/v at  $37^\circ\text{C}$  over 72 hours; **bottom:** CuA ( $5 \text{ mg mL}^{-1}$ ) in human serum, diluted at 5% in PBS at  $37^\circ\text{C}$  over 72 hours. These profiles are stable and similar for all the prepared formulations.

In fact, by comparing the spectra of these formulations with those of the metal-DTC complexes in the same environments (*i.e.*, DMEM and human serum), but previously dissolved in dimethyl sulfoxide (**Figure 8.26**), the solubilizing and stabilizing properties of Pluronic® micelles are clear. As previously reported, both  $\beta$ -[Ru<sub>2</sub>(PDT)<sub>5</sub>]Cl and [Cu(ProOMeDTC)<sub>2</sub>] are not soluble in aqueous solutions, and they tend to precipitate over time (see **Chapter 5** and **6**, respectively). On the other hand, their encapsulation in PF127 micelles (also cancer-targeting micelles) boosts their water solubility, as shown by the stable UV-Vis intensity, being almost constant in the 72 hours of analysis.

On the basis of these promising findings, some *in vitro* studies have been carried out (**Chapter 9**), to test both the maintenance of anticancer activity upon loading and, hence, the cargo release.

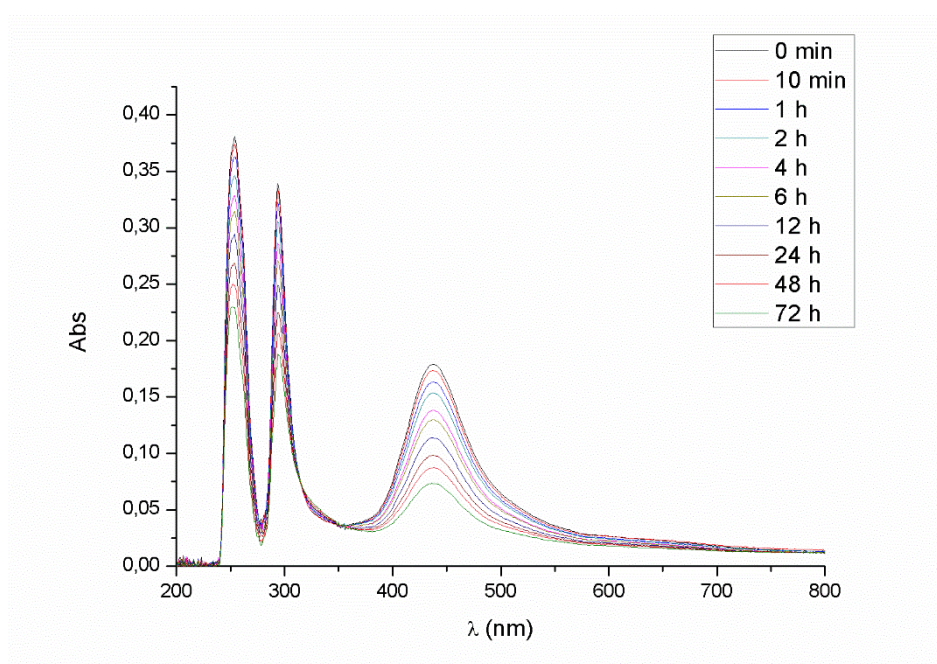


**Figure 8.26** UV-Vis spectrum of [Cu(ProOMeDTC)<sub>2</sub>] at a concentration of  $2.5 \cdot 10^{-5}$  M in human serum (5% v/v in PBS), previously dissolved in dimethyl sulfoxide (1% v/v with respect to the total volume). In comparison with the spectrum presented in **Figure 8.25** (bottom panel), this example shows an intensity decrease of the bands related to the Cu(II)-DTC complex, due to precipitation. Overall, the studied PF127 micelles confer stability and solubility to the encapsulated compounds.



## 9. IN VITRO SCREENING OF SYNTHETIZED METAL-DITHIOCARBAMATO COMPLEXES AND PF127 NANOFORMULATIONS AGAINST HUMAN CANCER CELL LINES

### 9.1 Cell cultures

In the preclinical development of potential new drugs, the first step is the use of cell models to assess the biological activity and cancer cell lines have been widely used for research purposes [494, 495]. In particular, the aim of this PhD work is the selection of one or more Lead Compounds from a library of new metal-dithiocarbamate complexes, in order to generate proof-of-concept data for future preclinical studies. In light of this, all the synthesized complexes presented in the **Chapter 5-7** have been tested for their cytotoxic activity against two different human tumor cell lines. The first, HeLa (epithelial cells of human cervix adenocarcinoma), has been selected since it is the most commonly used human cancer cell line, and it allows a comparison with other anticancer agents previously synthesized by our research group, but also from the scientific community [496]. The synthesized compounds have been also screened against the HepG2 cell line (epithelial cells of human liver hepatocellular carcinoma) and its more aggressive counterpart HepG2/SB3 (upregulating the anti-apoptotic protein SerpinB3). Remarkably, the hepatocellular carcinoma is to date the sixth most prevalent cancer and the third most frequent cause of cancer death [497].

#### 9.1.1 HeLa cancer cell line and culture preparation for in vitro studies

The HeLa cell line was derived from the cervical cancer cells of Henrietta Lacks, who died by cancer in 1951, and were propagated by George Otto Gey without her knowledge or permission [496]. The use of HeLa cells has contributed to the elucidation of important biological processes and more than 70,000 publications [498]. Cervical cancer is the fourth most common cancer in women, with an estimated 528,000 new cases in 2012 [15] and malignancies in the early stages are usually treated with radical hysterectomy or brachytherapy, whereas advanced-stage tumors are treated with radiation therapy and cisplatin-based chemotherapy combined with hycamtin (Topotecan<sup>®</sup>, a topoisomerase inhibitor) [499].

For our purposes, HeLa cells (American Type Culture Collection, ATCC) were cultured in 75 cm<sup>2</sup> cell culture flasks in Dulbecco's modified Eagle's medium (D-MEM), with addition of Fetal Bovine Serum (FBS) (10%), L-glutamine (5 mM), streptomycin (100 µg/mL), and penicillin (100 units/mL) (Sigma-Aldrich), and incubated at 37 °C in a 5% carbon dioxide controlled atmosphere.

For the cytotoxicity assay, the medium was removed from the flask, and the cells washed with 6 mL of PBS, and then shaken in presence of 1 mL of trypsin (Sigma-Aldrich), with 3 minutes-incubation. D-MEM was successively added, and the obtained cellular suspension seeded in 96-well microplates (5·10<sup>3</sup> cells/well) in the appropriate growth medium (200 µL), and incubated at 37 °C in a 5% CO<sub>2</sub> atmosphere for 24 h to allow cell adhesion, prior to drug testing.

### 9.1.2 HepG2 and HepG2/SB3 cancer cell lines, and cultures preparation for in vitro studies

HepG2 cells were derived from the liver tissue of a 15-year-old Caucasian American male with a well-differentiated hepatocellular carcinoma [497]. This human tumor cell line is widely used in cytotoxicity experiments since it displays many of the genotypic and phenotypic features of normal liver cells [500]. The hepatocellular carcinoma (HCC) is one of the most spread malignances worldwide, since in most cases it develops within an established background of liver diseases, such as the hepatitis B and C and chronic liver infections due to alcohol abuse. In the early stages, this cancer is treated by resection, ablation and liver transplantation [497]. On the other hand, progression into advanced stages is common, and no effective treatment is available to, except for the drug sorafenib (Nexavar®) [501]. This agent, which can be administered orally, is a tyrosine kinase inhibitor that acts in a targeted way as antiangiogenic to slow down the growth of the tumor. Unfortunately, although sorafenib was established as the standard cure for advanced hepatocellular carcinoma, the response rate is not particularly high (4%) and toxicity may be relevant, often associated with drug resistance [502], thus making HCC one of the most challenging cancers in clinical practice [503]. In this scenario, recent studies revealed that the serine-protease inhibitor SERPINB3 (SB3) plays a fundamental role in the development and resistance-to-apoptosis of HCC [504]. Indeed, SERPINB3, typically found over-expressed in cancer cells of epithelial origin and of the liver, significantly attenuates apoptosis triggered by anti-cancer drugs or TNF- $\alpha$ , thus allowing tumor growth [505]. Such inhibition of drug-induced apoptosis was shown indeed directly related to the level of expression of SB3 in cancer cells. It has been demonstrated that this protein locates in the inner mitochondrial compartments, where it binds to the respiratory *Complex I*, protecting cells from the cytotoxicity of chemotherapeutic agents endowed with a pro-oxidant action, such as doxorubicin and cisplatin [506].

These findings led us to test the action of the new metal-DTC derivatives synthesized during this PhD towards HCC cells transfected with the plasmid vector pCDNA3.1 carrying the SERPINB3 gene (hereinafter identified as HepG2/SB3 cells), in order to potentially identify new molecules that overcome the resistance to apoptosis induced by the SB3 protein. Moreover, we carried out parallel *in vitro* tests also towards the HepG2 cell line transfected with the empty vector (hereinafter identified as HepG2/CTR cells, where CTR stands for “control”) to better compare the final data.

Concerning the transfection procedure, commercial HepG2 cells (Provitro) were plated in a 6-well plate at a density of  $1 \cdot 10^6$  cells/well 24 hours before transfection, and then incubated with 1  $\mu$ g of plasmid DNA/well in the presence of Lipofectamin Reagent and Plus Reagent (Invitrogen). After 5-h incubation at 37 °C and 5% CO<sub>2</sub>, the plates were washed twice with OptiMEM (Invitrogen) and incubated with fresh RPMI medium (Sigma-Aldrich) supplemented with 10% FBS for further 48 hours [507].

For our purposes, HepG2/CTR and HepG2/SB3 cells were separately cultured in 75 cm<sup>2</sup> cell culture flasks in Minimum essential medium (MEM), with addition of FBS (10%), L-glutamine (2 mM), MEM non-essential

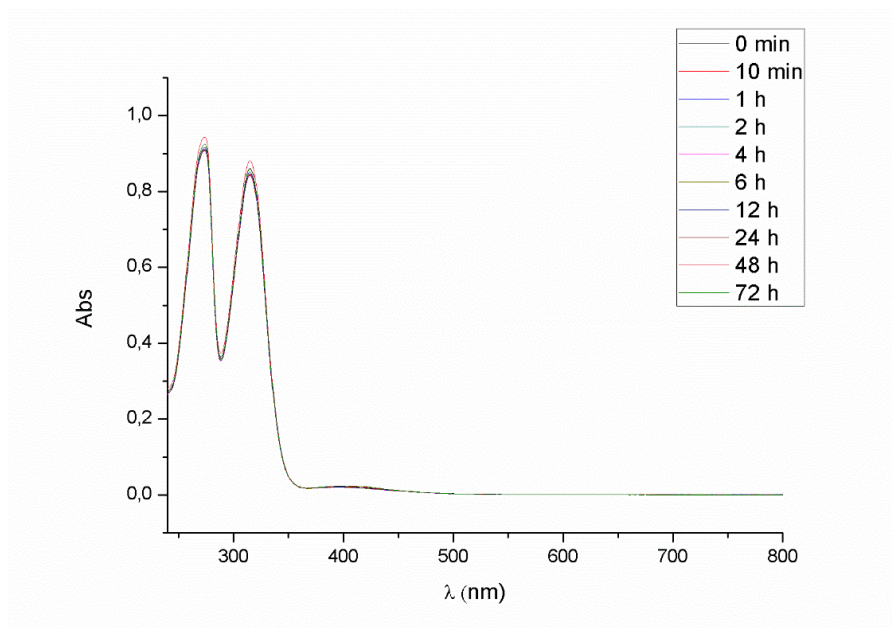


amino acid, streptomycin (100 µg/mL), and penicillin (100 units/mL) (Sigma-Aldrich), and incubated at 37 °C in a 5% carbon dioxide controlled atmosphere.

Before testing the antiproliferative activity of our metal-DTC derivatives and the PF127 formulations, the medium was removed from the flask, and the cells washed with 6 mL of PBS, and then shaken in presence of 1 mL of trypsin (Sigma-Aldrich), followed by 3-min incubation. MEM was successively added, and the obtained cell suspensions of HepG2/CTR and HepG2/SB3, were plated in 96-well microplates (5·10<sup>4</sup> cells/well) in the appropriate growth medium (200 µL) and incubated at 37 °C in a 5% CO<sub>2</sub> atmosphere for 24 h to allow cell adhesion, prior to drug testing.

## 9.2 Stability in aqueous media of the metal-dithiocarbamate complexes and sample preparation for in vitro studies

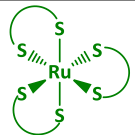
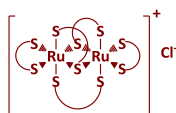
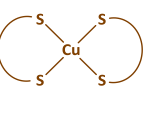
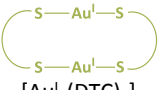


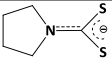
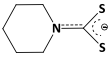
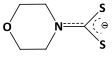
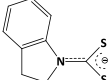
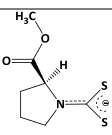
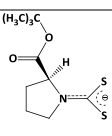
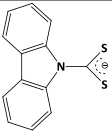
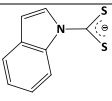
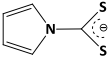
Due to a poor aqueous solubility, the synthesized metal compounds derived from cyclic dithiocarbamates were dissolved in DMSO (sterile-filtered, Sigma-Aldrich) just before the experiments. The only exceptions were the ionic complexes [Au<sup>III</sup>(PipeDTC)<sub>2</sub>]X (X= Cl, Br), which are water-soluble and hence were dissolved in saline solution (NaCl 0.9% w/v, Fresenius Kabi). All the metal-DTC complexes have been studied for their stability in dimethyl sulfoxide by means of UV-Vis spectrophotometry, except for 14 derivatives (**Table 9.1**). The studied Ru(III) compounds, both mono- and dinuclear, resulted stable in this solvent over 72 hours, as well as the Cu(II) derivatives. DMSO solutions of neutral Au(III)-DTC coordination compounds of the type [Au<sup>III</sup>X<sub>2</sub>(DTC)] (X= Cl, Br) have been prepared with a particular care in dark vials, since they undergo conversion into ionic [Au<sup>III</sup>(DTC)<sub>2</sub>]<sup>+</sup> species upon light irradiation (see **Section 7.4.5.1**). Concerning the saline solutions of the ionic [Au<sup>III</sup>(PipeDTC)<sub>2</sub>]X (X= Cl, Br), they displayed great stability over 72 hours at 37 °C (**Figure 9.1**), thus pointing out the stabilizing effect generated by the two PipeDTC ligands on the gold(III) ion.



**Figure 9.1** UV-Vis analysis over 72 hours of the ionic compound  $[\text{Au}^{\text{III}}(\text{PipeDTC})_2]\text{Cl}$  dissolved in saline solution (NaCl 0.9% w/v) at 37 °C.

The compounds were tested against the three abovementioned cancer cell lines at different micromolar concentrations to obtain dose-response plots. Briefly, the metal derivatives were dissolved in the appropriate solvent (DMSO or saline solution) at the concentration of 10 mM, 5 mM, 2 mM, 1 mM and 0.5 mM. Successively, one  $\mu\text{L}$  of each solution was dissolved in 999  $\mu\text{L}$  of cell culture medium, to yield the following final concentrations of metal complex: 10  $\mu\text{M}$ , 5  $\mu\text{M}$ , 2  $\mu\text{M}$ , 1  $\mu\text{M}$  and 0.5  $\mu\text{M}$ . This procedure allows a DMSO concentration of 0.1% v/v in the growth medium, which has no effect on cell viability [508].

The tested complexes are collected in **Table 9.1**. Among them, the Au(I)-DTC derivatives as well as some Ru(III) and Cu(II) aromatic-based compounds have not been studied for their antiproliferative activity *in vitro* due to their negligible solubility in dimethyl sulfoxide.

	 [Ru <sup>III</sup> (DTC) <sub>3</sub> ]	 β-[Ru <sup>III</sup> <sub>2</sub> (DTC) <sub>5</sub> ]Cl	 [Cu <sup>I</sup> (DTC) <sub>2</sub> ]	 [Au <sup>I</sup> <sub>2</sub> (DTC) <sub>2</sub> ]	 [Au <sup>III</sup> X <sub>2</sub> (DTC)] (X= Cl, Br)	 [Au <sup>III</sup> (DTC) <sub>2</sub> ]X <sup>+</sup> X <sup>-</sup> (X= Cl, Br, [Au <sup>III</sup> Cl <sub>4</sub> ], [Au <sup>I</sup> Br <sub>2</sub> ])
 PDT	✓	✓	✓ <sup>a</sup>	✗	✓	-
 PipeDTC	✓	✓	✓ <sup>a</sup>	✗	✓	✓ <sup>b</sup>
 MorphDTC	✓	✓	✓ <sup>a</sup>	✗	✓	-
 IndolineDTC	✓	✓	✗	✗	✓	-
 ProOMeDTC	✓	✓	✓	✗	✓	-
 ProOtBuDTC	✓	✓	✓	✗	✓	-
 CDT	✗	✗	✗	✗	✓ <sup>a</sup>	-
 IndDTC	-	-	✗	✗	✓ <sup>a</sup>	-
 PyrrDTC	-	-	✓ <sup>a</sup>	✗	✓	-

**Table 9.1** Schematic representation of the tested complexes and their ligands. Where ✓ is present, the related metal-DTC complex has been tested, whereas ✗ points out “complex not tested” due to limited solubility in DMSO or other organic solvents suitable for cell cultures. <sup>a</sup> the complex forms a suspension in DMSO, and its concentration is overestimated; <sup>b</sup> [Au<sup>III</sup>(PipeDTC)<sub>2</sub>]X (X= Cl and Br) have been dissolved in saline solution 0.9% w/v prior to dilution in cell culture medium.

### 9.3 Results of in vitro cytotoxicity studies on metal-dithiocarbamate samples

HeLa, HepG2/CTR and HepG2/SB3 cells were exposed to different concentrations of the metal-DTC complexes (*i.e.*, 10  $\mu\text{M}$ , 5  $\mu\text{M}$ , 2  $\mu\text{M}$ , 1  $\mu\text{M}$ , 0.5  $\mu\text{M}$  and in some cases lower) for 72 hours. Briefly, after the preparation of the 96-well plates (**Sections 9.1.1** and **9.1.2**), the medium was removed and replaced with a fresh one containing the compounds to be studied (previously dissolved in a suitable solvent, DMSO or saline solution, **Section 9.2**) at increasing concentrations. Triplicate conditions were established for each treatment and at least three independent experiments were carried out for each compound.

Cell viability was evaluated with two different methods, the resazurin assay for the HeLa cultures, and the MTT test for the HepG2/CTR and HepG2/SB3 cell lines. Concerning the first, resazurin (7-hydroxy-10-oxidophenoxazin-10-ium-3-one, Sigma-Aldrich) is a blue dye which is oxidized by mitochondrial enzymes and diaphorases of metabolic active cells to the pink resorufin (7-hydroxy-3H-phenoxazin-3-one) [509]. To perform the assay, the entire volume of incubation medium was removed after 72 hours from the treated wells, and 100  $\mu\text{L}$ /well of a 10% resazurin solution in D-MEM were added and incubated for 2 hours at 37  $^{\circ}\text{C}$ . According to this, cellular vitality was determined by absorbance measurements at 590 nm as follows:

$$\% \text{ vitality} = \frac{\frac{1}{\sum Abs_{treated\ cells}} - \frac{1}{\sum Abs_{resazurine\ blank}}}{\frac{1}{\sum Abs_{control\ cells}} - \frac{1}{\sum Abs_{resazurine\ blank}}} \cdot 100$$

Similarly, the MTT assay is a cell-viability evaluation method based on the mitochondrial-dependent reduction of MTT (3-(4,5-dimethylthiazol-2-yl)-2,5-diphenyltetrazolium bromide, Sigma-Aldrich -yellow) to formazan salts (purple) [510]. Experimentally, 10  $\mu\text{L}$  of a 5  $\text{mg mL}^{-1}$  MTT saline solution were added to the cultures, and incubated for 3 hours. After that, 100  $\mu\text{L}$  of Detergent Reagent (Sigma-Aldrich) were added to allow the spectrophotometric analysis of the microplates at 550 nm, measuring the cellular vitality according to the following equation:

$$\% \text{ vitality} = \frac{\sum Abs_{treated\ cells}}{\sum Abs_{control\ cells}} \cdot 100$$

For both methods, the control cells are those treated with cell culture medium containing the vehicle, DMSO or saline solution) in the percentage of 0.1% v/v. The obtained cell viabilities have been plotted against the compound concentration to determine the  $\text{IC}_{50}$  (concentration of the test agent inducing 50% reduction in cell number compared with control cell cultures). The final  $\text{IC}_{50}$  values and their standard deviations were evaluated from the data coming from at least three independent experiments. For comparison purposes, the cytotoxicity of cisplatin (dissolved in saline solution) was evaluated under the same experimental conditions. In this regard, it should be underlined that the experiments have been performed over a period of 72 hours since this is the time necessary to cisplatin to explicate its activity.

For clarity reasons, **Table 9.2** reports only the  $IC_{50}$  values lower than 10  $\mu$ M. In other words, the compounds generating  $IC_{50}$  numbers greater than 10  $\mu$ M are considered not cytotoxic enough for further pre-clinical development.

Compound	$IC_{50}$ ( $\mu$ M)		
	HeLa	HepG2/CTR	HepG2/SB3
$\beta$ -[Ru <sub>2</sub> (PDT) <sub>5</sub> ]Cl	0.45 ± 0.02	0.62 ± 0.08	0.59 ± 0.01
$\beta$ -[Ru <sub>2</sub> (PipeDTC) <sub>5</sub> ]Cl	0.46 ± 0.04	0.66 ± 0.01	0.75 ± 0.02
$\beta$ -[Ru <sub>2</sub> (ProOMeDTC) <sub>5</sub> ]Cl	3.95 ± 0.07	9.2 ± 0.2	> 10
$\beta$ -[Ru <sub>2</sub> (ProOtBuDTC) <sub>5</sub> ]Cl	0.27 ± 0.01	1.28 ± 0.05	0.90 ± 0.02
[Cu(PDT) <sub>2</sub> ]	0.32 ± 0.04	> 10	> 10
[Cu(PipeDTC) <sub>2</sub> ]	0.6 ± 0.3	> 10	> 10
[Cu(MorfDTC) <sub>2</sub> ]	6.7 ± 0.2	> 10	> 10
[Cu(ProOMeDTC) <sub>2</sub> ]	1.03 ± 0.03	2.97 ± 0.07	2.8 ± 0.1
[Cu(ProOtBuDTC) <sub>2</sub> ]	1.13 ± 0.07	5.0 ± 0.1	6.6 ± 0.1
[Cu(PyrroleDTC) <sub>2</sub> ]	1.99 ± 0.03	> 10	> 10
[AuCl <sub>2</sub> (PDT)]	6.4 ± 0.2	8.739 ± 0.003	> 10
[AuCl <sub>2</sub> (PipeDTC)]	1.73 ± 0.09	9.399 ± 0.007	> 10
[AuCl <sub>2</sub> (MorfDTC)]	4.641 ± 0.005	> 10	9.69 ± 0.08
[AuCl <sub>2</sub> (ProOMeDTC)]	7.5 ± 0.4	> 10	3.52 ± 0.04
[AuCl <sub>2</sub> (ProOtBuDTC)]	5.6 ± 0.2	> 10	5.6 ± 0.2
[AuBr <sub>2</sub> (PDT)]	3.9 ± 0.1	> 10	> 10
[AuBr <sub>2</sub> (PipeDTC)]	1.3 ± 0.3	9.05 ± 0.06	6.29 ± 0.03
[AuBr <sub>2</sub> (MorfDTC)]	3.7 ± 0.2	7.86 ± 0.06	> 10
[AuBr <sub>2</sub> (ProOMeDTC)]	7.84 ± 0.06	> 10	7.14 ± 0.06
[AuBr <sub>2</sub> (ProOtBuDTC)]	5.1 ± 0.1	> 10	5.5 ± 0.2
[Au(PipeDTC) <sub>2</sub> ]Cl	1.27 ± 0.04	> 10	> 10
[Au(PipeDTC) <sub>2</sub> ]Br	1.3 ± 0.2	> 10	> 10
[Au(PipeDTC) <sub>2</sub> ][AuCl <sub>4</sub> ]	1.51 ± 0.07	> 10	> 10
[Au(PipeDTC) <sub>2</sub> ][AuBr <sub>2</sub> ]	1.46 ± 0.09	> 10	> 10
Cisplatin	6.6 ± 0.3	> 10	> 10

**Table 9.2**  $IC_{50}$  values ( $\mu$ M) calculated after a 72-h treatment. Data represent the mean ± SD of at least three independent experiments (Vehicle: DMSO or saline solution).

Overall, 40 metal-dithiocarbamate compounds have been tested (**Table 9.1**, green tick), and 24 of them demonstrated remarkable cytotoxic activity ( $IC_{50}$  < 10  $\mu$ M) against HeLa cells, whereas 10 and 13 inhibited the proliferation of HepG2 and HepG2/SB3 cells, respectively. This first result highlights the resistance to chemotherapy of hepatocellular carcinoma (HCC) cells if compared to cervical cancer. Moreover, among the

most promising complexes, the dinuclear Ru(III)-DTC derivatives are the most active, with IC<sub>50</sub> values around 1 μM or sub-micromolar. On the contrary, mononuclear derivatives of the type [Ru(DTC)<sub>3</sub>] (not present in **Table 9.2**) did not show antiproliferative activity against the tested cultures. This behavior was already observed for other Ru(III)-DTC derivatives, thus supporting the hypothesis that the electronic interaction (anti-ferromagnetism) between two Ru(III) metal centers, mediated by the S atoms of bridged DTC ligands, may be the key element for the great activity of our dinuclear complexes (see **Section 5.2**) [140].

Our Cu(II)-dithiocarbamate complexes similarly showed a great activity against HeLa cells, but were less active against liver cancer cultures. However, it is worth mentioning that these copper derivatives suffer from low solubility in DMSO vehicle, and the activity could be underestimated. Indeed, the compounds involving proline ester as ligands are well soluble in DMSO thanks to the presence of the ester moiety and generate interesting IC<sub>50</sub> values. In particular, the complex [Cu(ProOMeDTC)<sub>2</sub>] demonstrated a slight selectivity towards the SB3-overexpressing cells HepG2/SB3. This behavior is more pronounced in the case of some neutral Au(III)-DTC complexes of the type [AuX<sub>2</sub>(DTC)] (X= Cl, Br), especially when DTC= proline ester dithiocarbamate (both methyl and *tert*-butyl esters). Indeed, in some cases these compounds result two-fold more cytotoxic towards HepG2/SB3 than HepG2/CTR cells, thus highlighting their capability to overcome the resistance to apoptosis induced by SERPINB3 (see **Section 9.1.2**). Moreover, the nature of the coordinated halogen in this kind of complexes seems not to affect the cytotoxic activity, except for the case of PDT derivatives as already observed in literature towards other cell lines [139]. In addition, according to the intriguing perspectives opened by Isab and coworkers [356], the [Au<sup>III</sup>(DTC)<sub>2</sub>]<sup>+</sup> cation is likely the biologically-relevant species accounting for the cytotoxicity of the Au(III)-DTC complexes. Indeed, for the compounds involving PipeDTC, the IC<sub>50</sub> values of the ionic Au(III)-DTC derivatives are almost the same observed for their neutral counterparts (**Table 9.2**). A possible explanation of this observation is the equilibrium wherein the [AuX<sub>2</sub>(DTC)] complexes undergo an interconversion into the cationic complexes in coordinating solvents, demonstrated in **Section 7.4.5.1**. Although the conversion is the most plausible explanation, further studies will be accomplished to verify the nature of the cytotoxic species.

Concerning the ligand nature, the most active compounds contain dithiocarbamates which prefer the thioureidic form of the ligand (see **Section 4.2, Figure 4.5 form III**), associated with a stronger C-N bond and, as a consequence, weaker metal-sulfur bond. Moreover, the obtained antiproliferative results point out also the lack of cytotoxic activity of the complexes containing aromatic moieties, except for the [Cu(PyrroleDTC)<sub>2</sub>] reporting an antitumor activity at about 2 μM. The aromatic derivatives correspond to ligands preferring the dithiocarbamic form (see **Section 4.2, Figure 4.5 form I,II**), with a strong M-S bond, but at the same time they have a pronounced hydrophobic character, which limits their solubility in the cell culture medium.

Remarkably, it is worth noting that none of the ligand salts resulted cytotoxic towards the tested cell cultures, thus confirming that the antiproliferative activity results from the whole complex.

Finally, it is possible to make some observations comparing the  $IC_{50}$  values obtained for our metal-DTC complexes with those of clinically established drugs generally used in the therapy of the studied cancers. Indeed, as presented at the bottom of the **Table 9.2**, most of the tested derivatives result more cytotoxic with respect to the reference drug cisplatin, which is used in standard regimens for the treatment of terminal-stage cervical cancer [511]. Moving to the HCC, as discussed in **Section 9.1.2**, sorafenib results the only chemotherapeutic agent able to reduce the spread of this cancer. The reported  $IC_{50}$  value for this drug is 8.99  $\mu$ M [512], about 20-fold higher than the values found for our dinuclear Ru(III)-DTC compounds. Taken together, these findings highlight the great potential of some of the synthesized metal-DTC derivatives.

#### 9.4 Selection of the Lead Compounds using the Lipophilic Efficiency (LipE) evaluation

The final aim of this PhD work is the selection of one or more Lead Compounds among the most active metal derivatives, synthesized from different metals and diverse cyclic *N,N*-disubstituted dithiocarbamates. In the previous section, the biological activity studies on the selected cancer cell lines have evidenced that all the metal centers present in the complexes exhibit cytotoxic properties. However, it is difficult to obtain a structure-activity relationship for the most active complexes since they present different coordination geometries and electronic features. On the basis of these considerations, in the process of drug discovery, other tools are useful to select the candidates for further development among a library of compounds [94]. In particular, the application of guidelines linked to the concept of “drug-likeness”, such as the “Lipinski rule of five”, has gained wide acceptance worldwide when developing new medicines. Remarkably, all these considerations are related to organic molecules and not directly transferable to potential metal-based drugs, and to date only a few of inorganic derivatives are approved in pharmacopeia.

The Lipinski's concept defines four simple physicochemical parameters ( $MW \leq 500$ ,  $\log P \leq 5$ , H-bond donors  $\leq 5$ , H-bond acceptors  $\leq 10$ ) associated with the 90% of orally active drugs that achieved phase II clinical status in 2001 [513, 514]. These values should define the “drug-like” properties associated with acceptable aqueous solubility and intestinal permeability [515]. However, a very common misunderstanding is that molecules fulfilling the Lipinski conditions are automatically “drug-like”. In fact, other key-parameters are important during the design of a new drug [516] and in the last years, a deeper understanding of the characteristics of clinically-established drugs led researchers to understand that lipophilicity plays a critical role in medicinal chemistry [517]. As an example, the number of hydrogen acceptors/donors can be relevant in the interaction with a specific target, but first of all the lipophilicity provides a more comprehensive framework to optimize the absorption, distribution, metabolism and excretion properties, toxicology profiles and ultimately pharmacological response [518-520]. The general parameter defining the lipophilicity of a molecule is the  $\log P$ , which is the decimal logarithm of the *n*-octanol/water partition coefficient *P* (the latter identifies the ratio between the concentration of an un-ionized drug in octanol and that in water at equilibrium at 25 °C). An analysis of the 592 oral drugs approved worldwide between 1983 and 2007

demonstrates that the mean  $\log P$  value ranges 2.3 to 2.6 [521]. This data points out that the careful control of lipophilicity is critical to success in drug discovery. Conversely, the other major determinant in achieving compounds active at low dosages is the potency against the target of interest. Thus, the concept of LipE (lipophilic efficiency) allows medicinal chemists to rationalize the observed potency with changes in lipophilicity [522]. The equation for calculating LipE is the following:

$$\text{Lipe} = -\log(\text{IC}_{50} \text{ (expressed in molar units)}) - \log P$$

The LipE equation mathematically describes the difference between potency and lipophilicity, and it can be used in both early- and late-stage drug-discovery programs. Indeed, potency is the partitioning to a well-defined target (usually a molecular entity such as an enzyme; in our case the cancer cell or cytoplasm), while  $\log P$  represents the partitioning to a lipophilic environment (such as the cell membrane) [517]. In general, optimal LipE values are comprised between 5 and 7, since they derive from ideal  $\log P \approx 2.5$  and  $\text{IC}_{50}$  in the nanomolar domain [523]. Overall, this parameter provides estimates of how to improve the physico-chemical properties of a compound in order to increase its affinity for a specific cell or molecular target.

Based on the previous discussion, the most active synthesized complexes have been evaluated for their  $\log P$  (**Section 9.4.1**) and successively for their LipE response (**Section 9.4.2**), taking into account the  $\text{IC}_{50}$  values presented in **Section 9.3**. The metal derivatives with the best LipE profiles (comprised in the ideal range 5-7) are  $\beta$ -[Ru<sub>2</sub>(PDT)<sub>5</sub>]Cl and [Cu(ProOMeDTC)<sub>2</sub>], therefore being selected as Lead Compounds for further antiproliferative *in vitro* evaluations, after encapsulation in cancer-targeting PF127 micelles (**Section 8.7.1**).

#### 9.4.1 LogP measurements

As previously mentioned, the lipophilicity of a molecule (represented as the logarithm of the *n*-octanol/water partition coefficient) often strongly correlates with its pharmacological activity and toxicity. In this regard, the bi-phasic solvent system *n*-octanol/water is commonly accepted in the scientific community since it well mimics the interface water/phospholipid membrane [524].

The  $\log P$  of the most active metal-DTC compounds was evaluated by means of UV-Vis spectrophotometry, identifying the concentration of the complex in the two distinct phases after equilibration [433, 525]. Briefly, a weighted amount of a selected metal-DTC complex (*ca.* 1 mg) was dissolved in 20 mL *n*-octanol (Sigma-Aldrich), previously pre-saturated with deionized water for 24 hours. The obtained solution was shaken for 2 hours in the presence of 20 mL of deionized water at 25 °C and, subsequently, the mixture was left to equilibrate for 30 minutes. The concentration of every metal-DTC derivative in the *n*-octanol phase before ( $C_0$ ) and after partitioning ( $C_1$ ) was measured by UV-Vis spectrophotometry, followed by the evaluation of the corresponding *n*-octanol/water partition coefficient as  $\log P = \log (C_1)/(C_0 - C_1)$ . The results, reported as mean  $\pm$  SD of at least three independent measurements, are presented in **Table 9.3**.



Compound	logP	Compound	logP
$\beta$ -[Ru <sub>2</sub> (PDT) <sub>5</sub> ]Cl	0.92 ± 0.04	[Au(PDT)Cl <sub>2</sub> ]	1.1 ± 0.1
$\beta$ -[Ru <sub>2</sub> (PipeDTC) <sub>5</sub> ]Cl	0.9 ± 0.2	[Au(PipeDTC)Cl <sub>2</sub> ]	1.08 ± 0.04
$\beta$ -[Ru <sub>2</sub> (ProOMeDTC) <sub>5</sub> ]Cl	0.78 ± 0.07	[Au(MorphDTC)Cl <sub>2</sub> ]	1.1 ± 0.3
$\beta$ -[Ru <sub>2</sub> (ProOtBuDTC) <sub>5</sub> ]Cl	1.4 ± 0.2	[Au(ProOMeDTC)Cl <sub>2</sub> ]	0.99 ± 0.04
[Cu(PDT) <sub>2</sub> ]	1.54 ± 0.04	[Au(ProOtBuDTC)Cl <sub>2</sub> ]	1.6 ± 0.2
[Cu(PipeDTC) <sub>2</sub> ]	1.5 ± 0.1	[Au(PDT)Br <sub>2</sub> ]	1.2 ± 0.1
[Cu(MorphDTC) <sub>2</sub> ]	1.37 ± 0.04	[Au(PipeDTC)Br <sub>2</sub> ]	1.1 ± 0.2
[Cu(ProOMeDTC) <sub>2</sub> ]	1.3 ± 0.2	[Au(MorphDTC)Br <sub>2</sub> ]	1.19 ± 0.06
[Cu(ProOtBuDTC) <sub>2</sub> ]	1.6 ± 0.3	[Au(ProOMeDTC)Br <sub>2</sub> ]	1.1 ± 0.1
[Cu(PyrrDTC) <sub>2</sub> ]	2.01 ± 0.04	[Au(ProOtBuDTC)Br <sub>2</sub> ]	1.69 ± 0.06
		[Au(PipeDTC) <sub>2</sub> ]Cl	- 1.05 ± 0.02
		[Au(PipeDTC) <sub>2</sub> ]Br	- 1.2 ± 0.2
		[Au(PipeDTC) <sub>2</sub> ][AuCl <sub>4</sub> ]	0.34 ± 0.06
		[Au(PipeDTC) <sub>2</sub> ][AuBr <sub>2</sub> ]	0.2 ± 0.1

**Table 9.3** LogP values of the most biologically-active metal-DTC derivatives, determined *via* UV-Vis analysis. Data represent the mean ± SD of at least three independent measurements.

On the whole, the synthesized derivatives are associated with positive values of logP, as expected due to the presence of hydrophobic ligands. Intriguingly, despite of the ionic nature of the dinuclear Ru(III) compounds, they showed higher affinity for the organic phase. Indeed, the hydrophobic surface made up of five dithiocarbamate ligands is predominant on the +1 charge of the complex, conferring a quite lipophilic character on the whole compound.

Concerning the copper(II) derivatives, the results well correlate with the neutral form of the complexes, as well as in the case of the Au(III) compounds of the type [AuX<sub>2</sub>(DTC)], with no significant difference between chloro- and bromo-derivatives. Finally, the ionic Au(III) coordination compounds present negative logP values when the counter ion is chlorine or bromine (indeed these two complexes results water-soluble). If the counterion is bigger and in particular a complex (such as [AuCl<sub>4</sub>]<sup>-</sup> or [AuBr<sub>2</sub>]<sup>-</sup>), the logP is positive. Despite these values are close to zero, the derivatives are not water soluble at all.

In conclusion, focusing on the nature of the ligand, if the metal center being equal, there are no great differences between compounds with distinct cyclic substituents, except for the proline derivatives. Indeed, the *tert*-butyl ester confers a higher lipophilicity on the compounds with respect to the methyl ester counterparts, even almost doubling the logP value on passing from the Ru(III)-proline methyl ester

dithiocarbamate complex to the *tert*-butyl ester one. Moreover, for the Cu(II) derivatives, the great hydrophobic character generated by the aromatic pyrrole results in the highest-recorded log*P* value.

#### 9.4.2 Lipophilic Efficiency (LipE) evaluation on most active compounds

As introduced before, the LipE parameter takes into account the IC<sub>50</sub> (expressed in molarity) and the log*P* values. **Table 9.4** summarizes the obtained LipE values for each compound, with reference to the different screened human cancer cell lines (see **Section 9.3**).

Compound	LipE		
	HeLa	HepG2/CTR	HepG2/SB3
β-[Ru <sub>2</sub> (PDT) <sub>5</sub> ]Cl	5.43	5.29	5.31
β-[Ru <sub>2</sub> (PipeDTC) <sub>5</sub> ]Cl	5.44	5.28	5.22
β-[Ru <sub>2</sub> (ProOMeDTC) <sub>5</sub> ]Cl	4.62	4.26	-
β-[Ru <sub>2</sub> (ProOtBuDTC) <sub>5</sub> ]Cl	5.17	4.49	4.65
-	-	-	-
[Cu(PDT) <sub>2</sub> ]	4.95	-	-
[Cu(PipeDTC) <sub>2</sub> ]	4.72	-	-
[Cu(MorfDTC) <sub>2</sub> ]	3.80	-	-
[Cu(ProOMeDTC) <sub>2</sub> ]	4.69	4.23	4.25
[Cu(ProOtBuDTC) <sub>2</sub> ]	4.35	3.70	3.58
[Cu(PyrroleDTC) <sub>2</sub> ]	3.69	-	-
-	-	-	-
[AuCl <sub>2</sub> (PDT)]	4.09	0.96	-
[AuCl <sub>2</sub> (PipeDTC)]	4.68	0.95	-
[AuCl <sub>2</sub> (MorfDTC)]	1.23	-	3.91
[AuCl <sub>2</sub> (ProOMeDTC)]	4.13	-	4.46
[AuCl <sub>2</sub> (ProOtBuDTC)]	3.65	-	3.65
-	-	-	-
[AuBr <sub>2</sub> (PDT)]	4.21	-	-
[AuBr <sub>2</sub> (PipeDTC)]	4.79	3.94	4.10
[AuBr <sub>2</sub> (MorfDTC)]	4.24	3.91	-
[AuBr <sub>2</sub> (ProOMeDTC)]	4.01	-	4.05
[AuBr <sub>2</sub> (ProOtBuDTC)]	3.60	-	3.57
-	-	-	-
[Au(PipeDTC) <sub>2</sub> ]Cl	6.95	-	-
[Au(PipeDTC) <sub>2</sub> ]Br	7.09	-	-
[Au(PipeDTC) <sub>2</sub> ][AuCl <sub>4</sub> ]	5.48	-	-
[Au(PipeDTC) <sub>2</sub> ][AuBr <sub>2</sub> ]	5.64	-	-

**Table 9.4** LipE values calculated for the most biologically-active metal-DTC derivatives.

In order to select the Lead Compounds, our attention was addressed to the complexes for which LipE data were calculable for all screened human cancer cell lines, *i.e.*  $\beta$ -[Ru<sub>2</sub>(PDT)<sub>5</sub>]Cl,  $\beta$ -[Ru<sub>2</sub>(PipeDTC)<sub>5</sub>]Cl,  $\beta$ -[Ru<sub>2</sub>(ProOtBuDTC)<sub>5</sub>]Cl, [Cu(ProOMeDTC)<sub>2</sub>], [Cu(ProOtBuDTC)<sub>2</sub>], and [AuBr<sub>2</sub>(PipeDTC)]. A comparative plot of the LipE profiles obtained for these derivatives is reported in **Figure 9.2**.

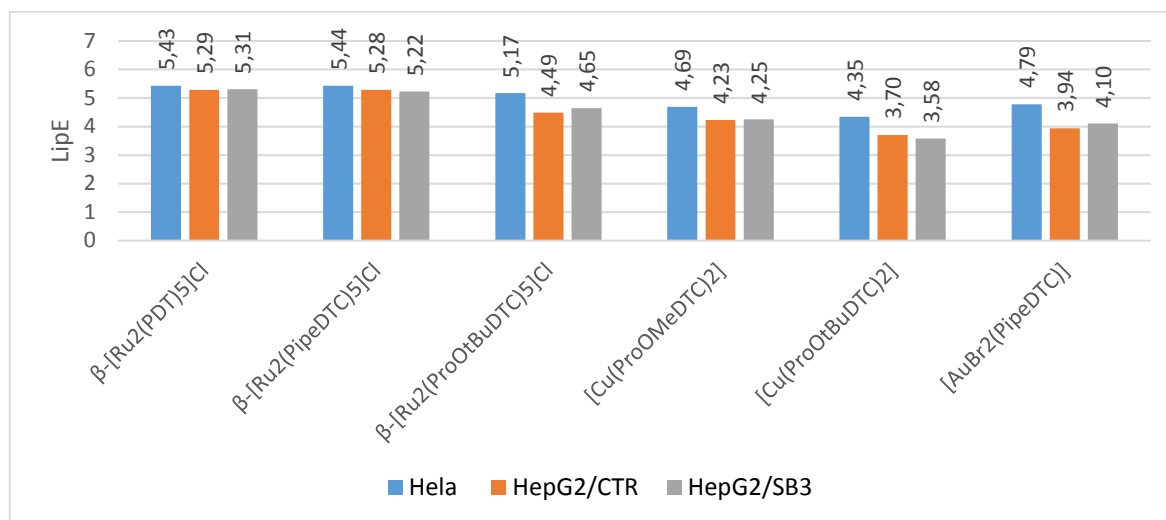


**Figure 9.2** Histogram representing a visual comparison of the LipE values obtained for those metal-DTC derivatives resulting cytotoxic against all the three screened human cancer cell lines.

As previously described, it is generally reported that a desirable drug is characterized by LipE values comprised between 5 and 7 [523]. Therefore, the candidates to be considered as Lead Compounds have been the ionic dinuclear Ru(III) derivatives of PDT and PipeDTC. The  $\beta$ -[Ru<sub>2</sub>(PDT)<sub>5</sub>]Cl was then selected since it is a widely studied complex in our research group [140]. On the other hand, in order to widen the spectrum of the most promising compounds, also one Cu(II) complex was considered, and the attention was focused on [Cu(ProOMeDTC)<sub>2</sub>].

The Au(III) candidate [AuBr<sub>2</sub>(PipeDTC)] has not been selected due to some stability issues observed during the first attempts of its encapsulation in PF127 micelles. It has been hypothesized that this behavior is correlated to the equilibrium previously presented in **Section 7.4.5.1**, since the ether groups of the polymer can act as a coordinating solvent.

Overall, the LipE evaluation allowed us to select the two complexes  $\beta$ -[Ru<sub>2</sub>(PDT)<sub>5</sub>]Cl and [Cu(ProOMeDTC)<sub>2</sub>] as Lead Compounds for further studies. First, they were encapsulated in micelles based on the copolymer Pluronic® F127, both pure and mixed cancer-targeting ones. The latter were prepared according the loading procedure presented in **Chapter 8**.

### 9.5 Results of *in vitro* cytotoxicity studies on Lead Compounds encapsulated in PF127 micelles

The preparation and characterization of the micellar systems carrying the two Lead Compounds  $\beta$ -[Ru<sub>2</sub>(PDT)<sub>5</sub>]Cl and [Cu(ProOMeDTC)<sub>2</sub>] have been presented in **Sections 8.7** and **8.8**, respectively. The *in vitro* studies have been carried out with the Hela, HepG2/CTR and HepG2/SB3 cell lines according to the experimental procedures described in the **Section 9.3**, with a modification. Indeed, the tested micelles have not been previously dissolved in dimethyl sulfoxide, but being water-soluble, the lyophilized nanosystems have been dissolved directly in the cell culture medium immediately before treatment, to realize a final concentration of 10  $\mu$ M, 5  $\mu$ M, 2  $\mu$ M, 1  $\mu$ M, or 0.5  $\mu$ M. This concentration is referred to the encapsulated complex, according to the loading measurements described in the **Section 8.8.1**.

The exploited procedure allows to achieve a maximum PF127 concentration (5 mg/mL) that triggers no effect on cell viability (tests on empty micelles as a control). Moreover, in order to investigate if the cancer-targeting moiety enhances or somehow affects the activity of the formulations, a parallel screening was carried out in the presence of the exofacial GLUT1 inhibitor 4,6-*O*-ethylidene-D-glucose, tested at 10 mM (**Figure 9.3 a**) [526]. Indeed, Lippard and coworkers demonstrated that this inhibitor selectively blocks the uptake of their Pt(II)-glucose conjugated complexes in A2780 cells (human ovarian carcinoma) [527]. In addition, it is worth underlining that GLUT1 transporters have been identified as major contributors to the glucose uptake in HepG2 and Hela cells [528, 529]. During the whole uptake process, a sugar binds GLUT1 first at its outside, then part of this membrane protein rearranges to a second stable configuration around the binding site, thus exposing the carbohydrate to the cytoplasm. However, while the binding of D-glucose or  $\beta$ -D-glucopyranosides to GLUT1 equilibrates keeping the inward-facing conformation, the binding of 4,6-*O*-ethylidene-D-glucose fixes the transporter in the outward-facing conformation, since the rearrangement for sugars with bulky groups in positions C4 and C6 is forbidden (**Figure 9.3 b**) [530]. According to this, the inhibitor present in our testing should compete with the micelle surface-linked carbohydrate, thus limiting the anticancer effects of the whole nanosystem. This test was designed to elucidate if the observed biological activity is mainly mediated by the GLUT1 transporters. In these studies, the inhibitor has been dissolved in the cell culture medium until a 10 mM concentration was reached (not toxic for cells). Then, this solution was used to prepare the treatments with the micellar carriers loaded with the Lead compounds. However, further studies are planned to better understand if the cell uptake is really mediated by GLUT. These investigations will be carried out *in vivo* and *in vitro* by gene silencing in collaboration.

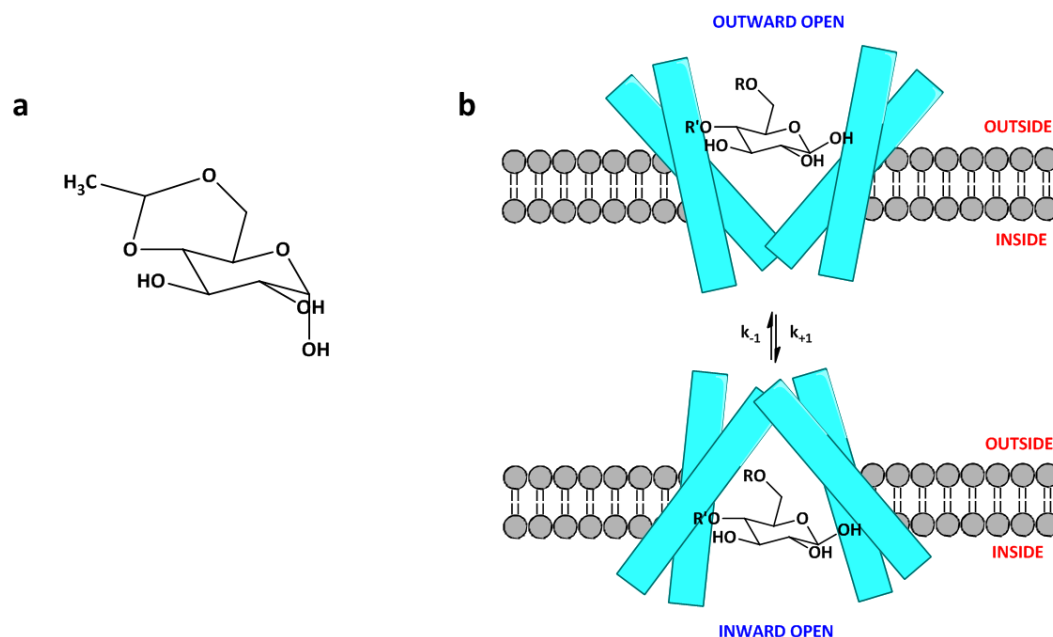


**Figure 9.3** Chemical drawing of the GLUT1 inhibitor 4,6-*O*-ethylidene-D-glucose **a**. The GLUT1 transporter is a uniporter membrane protein containing 12 membrane-spanning alpha helices **b**. Six of them bind together to create a polar channel through which glucose is transported inside the cell. In particular, if  $R = R' = H$ , both membrane conformations are possible and the transport occurs. On the other hand, if  $R = R' =$  a bulky group (as in the case of 4,6-*O*-ethylidene-D-glucose) the binding occurs only with the outward conformation, and transport is impossible.

The *in vitro* results collected for the two Lead Compounds encapsulated in the prepared nanosystems, also in presence of the GLUT1 inhibitor 4,6-*O*-ethylidene-D-glucose (10 mM), are reported in **Table 9.5**.

Formulation	$IC_{50}$			Formulation	$IC_{50}$		
	HeLa	HepG2/CTR	HepG2/SB3		HeLa	HepG2/CTR	HepG2/SB3
<b>RuA</b>	0.21 ± 0.6	1.72 ± 0.1	2.4 ± 0.3	/	/	/	/
<b>RuC</b>	0.12 ± 0.03	1.11 ± 0.09	1.4 ± 0.1	<b>RuC + inhibitor 10 mM</b>	0.19 ± 0.06	1.56 ± 0.08	1.8 ± 0.6
<b>RuE</b>	0.105 ± 0.009	0.89 ± 0.09	1.07 ± 0.09	<b>RuE + inhibitor 10 mM</b>	0.118 ± 0.006	0.97 ± 0.09	1.2 ± 0.3

<b>RuG</b>	0.12 ± 0.03	0.8 ± 0.1	1.3 ± 0.2	<b>RuG + inhibitor 10 mM</b>	0.122 ± 0.008	1.00 ± 0.05	1.4 ± 0.7
<b>RuI</b>	0.12 ± 0.06	0.56 ± 0.07	0.99 ± 0.07	<b>RuI+ inhibitor 10 mM</b>	0.12 ± 0.03	0.98 ± 0.08	1.3 ± 0.6
<b>CuA</b>	1.11 ± 0.04	2.6 ± 0.2	4.86 ± 0.04	/	/	/	/
<b>CuC</b>	0.54 ± 0.08	2.52 ± 0.06	7.4 ± 0.2	<b>CuC + inhibitor 10 mM</b>	0.55 ± 0.04	2.95 ± 0.1	7.5 ± 0.4
<b>CuE</b>	0.61 ± 0.07	2.91 ± 0.08	4.9 ± 0.3	<b>CuE + inhibitor 10 mM</b>	0.58 ± 0.02	3.65 ± 0.06	5.1 ± 0.4
<b>CuG</b>	0.58 ± 0.09	2.32 ± 0.07	4.8 ± 0.2	<b>CuG + inhibitor 10 mM</b>	0.62 ± 0.07	2.76 ± 0.09	4.9 ± 0.5
<b>CuI</b>	0.71 ± 0.07	2.4 ± 0.3	6.4 ± 0.5	<b>CuI + inhibitor 10 mM</b>	0.72 ± 0.08	2.8 ± 0.3	6.8 ± 0.3

**Table 9.5** IC<sub>50</sub> values (µM) evaluated after a 72-h treatment. Correlation between formulation name and micelle composition is reported in **Table 8.3**. Values are calculated based on the concentration of the encapsulated metal-DTC complex. Lyophilized micelles were dissolved in cell culture medium. The GLUT1 inhibitor = 4.6-*O*-ethylidene-D-glucose was dissolved in culture medium at 10 mM concentration. Data represent the mean ± SD of at least three independent experiments.

The comparison between the results presented in **Table 9.5** with those in **Table 9.2** highlights that the encapsulation of the metal complexes in PF127 micelles (both glucose-conjugated and not) generally modifies their cytotoxicity profiles. In particular, the Ru-based derivative is associated with a better IC<sub>50</sub> value towards the HeLa cells upon loading reaching values about 0.11 µM. In this context, the presence of the GLUT inhibitor does not affect the activity. The same compound tested against the hepatocellular carcinoma cells shows data passing from about 0.6 µM to higher values (3- and 4-fold higher for the

HepG2/CTR and HepG2/SB3 cells, respectively) when nanoformulated. However, the presence of carbohydrates on the hydrophilic surface of the micelle improves the recorded IC<sub>50</sub> values. In addition, a slight activity decrease is observed when treating cells in the presence of the GLUT inhibitor. This could account for a small involvement of the GLUT transporters in cell localization or uptake of our micelles.

With respect to the copper derivative, the activity against HeLa cells is maintained at 1 μM on passing from DMSO vehicle to the supramolecular aggregates. Remarkably, the cancer-targeting micelles improve the IC<sub>50</sub> value which is basically unchanged in the presence of the inhibitor.

Against the Hep/CTR cells, the copper complex keeps the anticancer activity at about 2.8 μM or, in some cases it increases its activity when encapsulated in functionalized micelles. Again, no sensible change in terms of IC<sub>50</sub> was detected in the presence of the inhibitor. Conversely, towards the Hep/SB3 cells the recorded IC<sub>50</sub> values become larger upon encapsulation.

To sum up, with respect to HeLa cells, β-[Ru<sub>2</sub>(PDT)<sub>5</sub>]Cl and [Cu(ProOMeDTC)<sub>2</sub>] result on average 3.75- and 2-fold more active when encapsulated in targeted PF127 micelles, respectively. As the IC<sub>50</sub> values are basically the same on passing from data obtained in the absence of the inhibitor to data achieved in its presence, the involvement of the GLUT1 transporter in the uptake or localization of the carbohydrate-modified micelles is limited or ruled out. Moreover, the nature of the sugar linked to the surface of the nanoparticle (β-glucose, glucosamine, β-maltose) seems not to influence the biological activity. On the other hand, when the micelles are tested against the hepatocellular carcinoma model, both HepG2/CTR and HepG2/SB3 cells, the cytotoxic activity of the metal-DTC compounds is in some cases slightly higher while lower in others.

The hepatocellular carcinoma cells overexpressing SerpinB3 are associated with an overall decrease of the activity of the metal-DTC compounds encapsulated in micelles, although the β-[Ru<sub>2</sub>(PDT)<sub>5</sub>]Cl compound maintains a promising IC<sub>50</sub> value near 1 micromolar when is loaded in carbohydrate-functionalized micelles. Taken together, the results obtained in the presence of the exofacial GLUT1 inhibitor 4,6-*O*-ethylidene-D-glucose (10 mM), are not homogenous. The inhibitor presence was planned to reduce the interaction of the GLUT1 transporters with the carbohydrate moiety conjugated to the surface of the micellar nanocarriers. According to this, when the antiproliferative activity is evaluated in the presence of the inhibitor, if there is an active participation of GLUT in the uptake of the encapsulated cytotoxic payload, the observed IC<sub>50</sub> value should decrease. The histograms displayed in **Figure 9.4** summarize the results reported in **Table 9.5**, thus facilitating the visualization of the differences in terms of IC<sub>50</sub> values associated with the inhibitor.

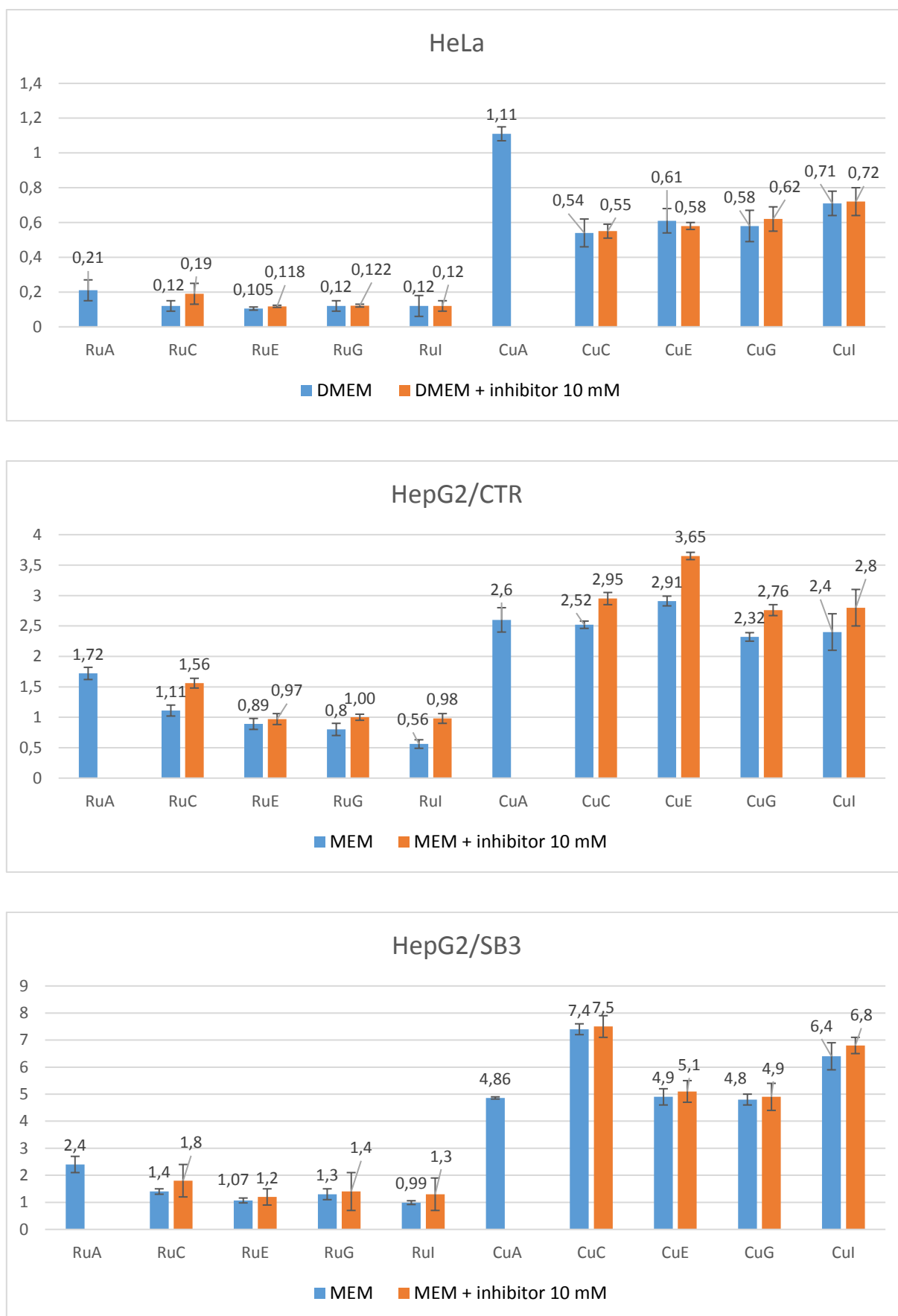


**Figure 9.4** Histograms representing the IC<sub>50</sub> values obtained in the presence (orange) or absence (blue) of the inhibitor 4,6-*O*-ethylidene-D-glucose (10 mM). Correlation between formulation name and micelle composition is reported in **Table 8.3**.



The presence or no of the inhibitor shows a well-defined trend only with the HepG2/CTR cancer cell line. In particular, 4,6-*O*-ethylidene-D-glucose generates an increment in the IC<sub>50</sub> values of on average 20%, with peaks of 40% and 75 % in the cases of RuC and RuI, respectively.

In conclusion, the PF127-based formulations represent a suitable method to increase the water solubility of the selected Lead Compounds  $\beta$ -[Ru<sub>2</sub>(PDT)<sub>5</sub>]Cl and [Cu(ProOMeDTC)<sub>2</sub>], and they will be used for *in vivo* studies so to avoid the organic solvent dimethyl sulfoxide, which is tolerated only at low concentrations. Moreover, the use of PF127 micelles conjugated with cancer-targeting moieties (*i.e.*,  $\beta$ -glucose, glucosamine and  $\beta$ -maltose) determined a general activity increase of the encapsulated metal-DTC derivatives.

Intriguingly, the designed active-targeting strategy was inhibited only in HepG2/CTR cells when the GLUT1 transporters were blocked by the exofacial inhibitor 4,6-*O*-ethylidene-D-glucose. At least in this case, we can state that the well-known Warburg effect (**Section 1.2.2**) could be involved in the biological activity of the new metal-based agents.

### 9.6 Confocal microscopy analysis on the HepG2/CTR and HepG2/SB3 cells treated with PF127-FITC micelles

The promising results obtained with the PF127 nanocarriers loaded with the two Lead Compounds, open intriguing perspectives for the use of these systems in preclinical studies. In the **Section 8.8.4** the complex-containing micelles were shown to be stable under different conditions, thus suggesting that the carriers could in principle reach the cancer tissue *in vivo* without undergoing some modification. Once in proximity of the cancer cell membrane, the cargo could be released, or the whole micelle endocytosed (in this case, it should release the metal-DTC compound inside the cell). To check this hypothesis, the PF127 block copolymer has been conjugated with fluorescein (see **Section 8.5.9**) to form micelles detectable *via* confocal laser scanning microscopy analysis (CLSM) [531, 532].

To perform the experiment, HepG2/CTR and HepG2/SB3 cells were incubated for two hours at 37 °C and 5% CO<sub>2</sub> with decreasing concentrations of PF127-FITC micelles (empty and with 45 % polymer functionalization), namely from 3 to 0.1 mg/mL. Successively, cells were fixed in 4% paraformaldehyde for 20 minutes, and washed twice with PBS. Cell nuclei were counterstained with DAPI (4'-6-diamidino-2-phenylindole). Then, slides were mounted with ELVANOL® (Sigma-Aldrich) and observed under a fluorescence microscope (Axiovert 200M) supported by Apotome.2, an optical sectioning system that increases the resolution of conventional fluorescence analysis (Carl Zeiss MicroImaging GmbH).

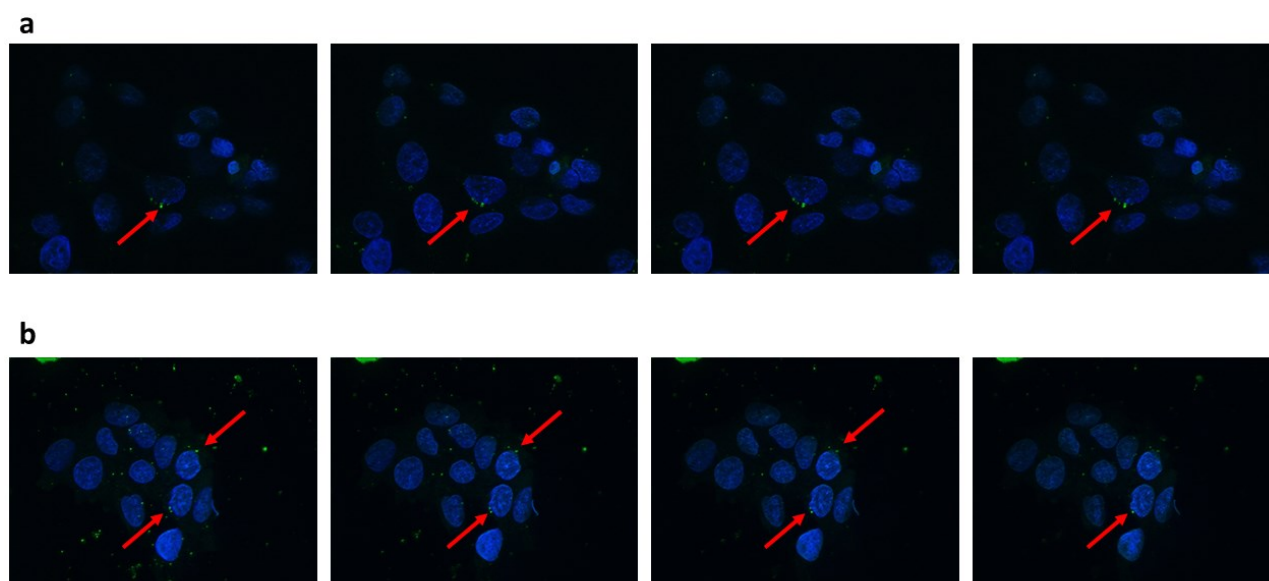


**Figure 9.5** Z-stack confocal microscopy images of HepG2/CTR **a** and HepG2/SB3 **b** cells treated with PF127-FITC micelles (3 mg/mL) for 2 hours. These micelles were empty, namely not encapsulating the Lead compounds. Green fluorescence arose from fluorescein in PF127-FITC nanosystems, whereas the blue color is the DAPI stain of the nuclei.

The results of the confocal microscopy analysis are presented in **Figure 9.5**. Although this experiment was carried out with empty PF127 micelles linked to fluorescein and without sugar-conjugation, the prepared system is a simplified model of the formulations tested for their cytotoxicity in section **Section 9.5**, since the dimension of the PF127-FITC micelles resembles those of the metal-DTC loaded counterparts (*ca.* 23 nm, **Section 8.8.2**).

The images show the intracellular matrix of adherent cells, with the nuclei being blue-colored with the fluorescent stain DAPI. From the Z-stack visualization of four different cell sections (reported in **Figure 9.5**, selected among five scanned Z-stacks for layout clearness), it is possible to state that the micellar carrier has entered the cytoplasm (green spots, highlighted by red arrows). Moreover, the cell uptake occurs to a larger extent in the control HepG2/CTR cells, with respect to the Serpin B3-overexpressing HepG2/SB3 cells.

The green fluorescence indicates that the PF127-FITC micelles were likely absorbed by the cells *via* endocytosis, similarly to other previously reported polymeric carriers [533, 534]. Although more detailed experiments will be performed in the next months (using different time-scansions and metal-DTC loaded micelles labeled with carbohydrates), this experiments points out the capability of our nanocarriers to penetrate the cell membrane of cancer cells. On the basis of these considerations and the findings reported in **Section 9.5**, it is possible to conceive that the nanoformulations investigated in this PhD work, are able to release the Lead Compounds  $\beta$ -[Ru<sub>2</sub>(PDT)<sub>5</sub>]Cl and [Cu(ProOMeDTC)<sub>2</sub>] once inside the cell.

## 9.7 xCELLigence measurements for real-time monitoring of HepG2/CTR and HepG2/SB3 cells viability after treatment with the selected Lead Compounds

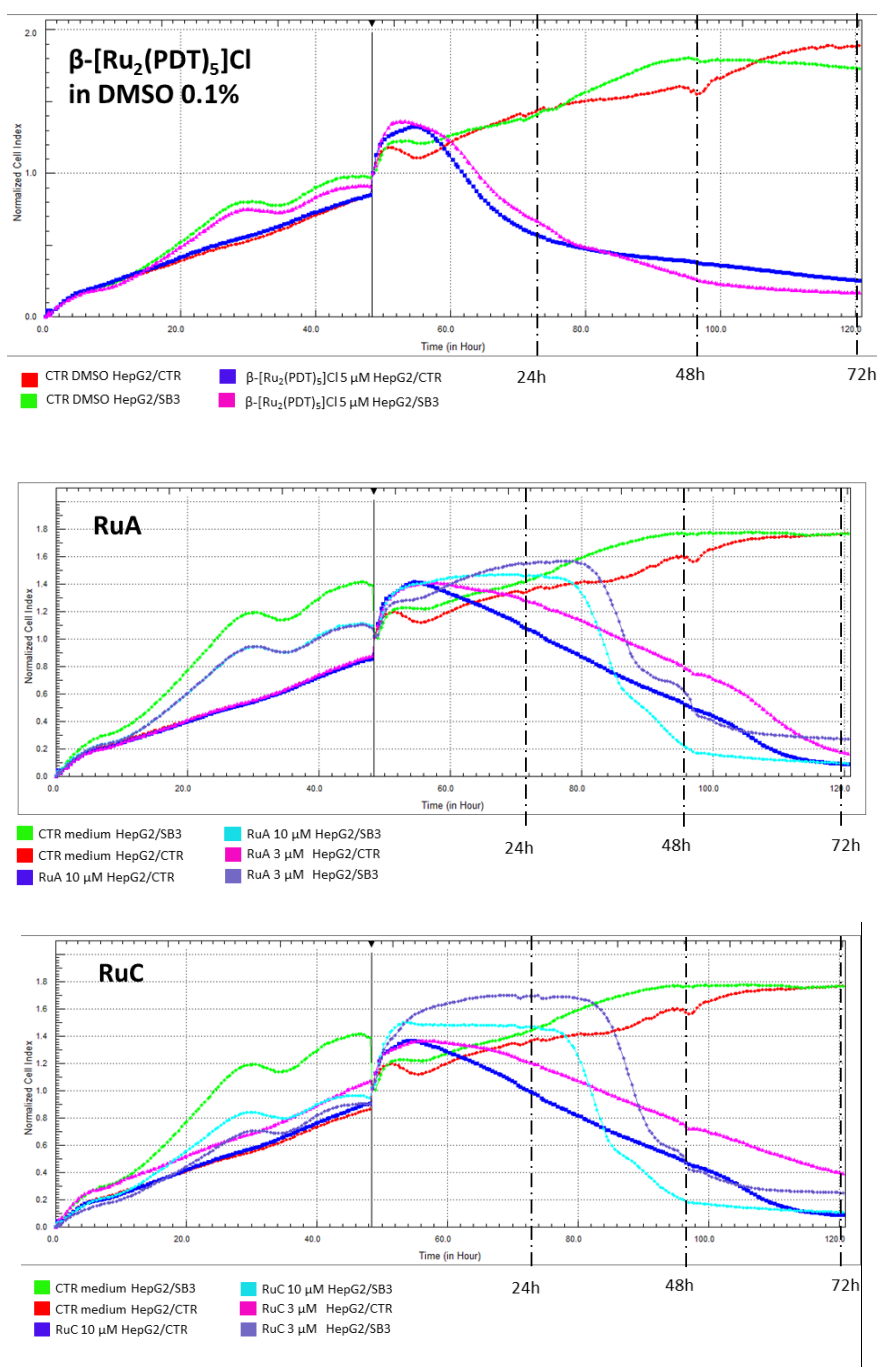
The IC<sub>50</sub> values recorded for the synthesized metal-DTC derivatives and their PF127-nanoformulations (**Table 9.2** with DMSO as a vehicle and **Table 9.5** with micelles as carriers) have been determined on the basis of dose-response curves, obtained by common viability assays, such as the MTT and resazurin tests (**Section 9.3** and **9.5**). The next step was the investigation of their mechanisms of action underlying the induction of cell death. Therefore, we first addressed our attention to the xCELLigence system which allows label-free and dynamic monitoring of the cellular phenotypic changes under real-time conditions [535]. The system measures the electrical impedance across interdigitated microelectrodes integrated on the bottom of the 16-well culture plates, the impedance value being detected using a pair of sensing (SE) and reference (RE) electrodes, submerged in cell culture medium. The latter acts also as an electrolyte, with charged particles carrying current between two electrodes in response to an applied AC voltage. The relative impedance value gradually increases as cells attach to the well bottom and then proliferate because cells act as insulating particles on the gold-surface area of the SE and restrict the current flow mediated by the culture medium. On the other hand, cell death leads to a release of cells from the SE surface, and it induces the decrease of the impedance measured across the electrodes [536]. The cell-sensor impedance, measured for each well, is expressed in arbitrary units called the “normalized cell index” (CI), defined as  $(R_n - R_b)/15$ , in which  $R_n$  is the cell-electrode impedance of the well when it contains cells and  $R_b$  is the background impedance of the well with only the medium (the system automatically averaged out the biological replicates).

Remarkably, the continuous monitoring of cellular response to biologically-active agents produces time-dependent cellular response profiles (TCRPs), that can be classified based on the mechanism of action [537]. To perform the experiments, HepG2/CTR and HepG2/SB3 cells have been cultured as reported in **Section 9.1.2**. Differently from the previously reported procedure, the cellular suspension was seeded in 16-well plates (E-plate, Roche Diagnostics GmbH,  $2.5 \cdot 10^3$  cells/well) in the appropriate growth medium (200  $\mu$ L). After allowing cell attachment for 30 min at room temperature, in accordance with the manufacturer’s guidelines, they were placed in the RTCA DP device in the incubator (37 °C in a 5% CO<sub>2</sub>) and the impedance value of each well was automatically monitored by the xCELLigence system (RTCA DP instrument, Roche Diagnostics, GmbH) and expressed as a “Normalized Cell Index” value (CI).

After 48 hours the cells were treated with either  $\beta$ -[Ru<sub>2</sub>(PDT)<sub>5</sub>]Cl and [Cu(ProOMeDTC)<sub>2</sub>] - dissolved in DMSO - or the nanoformulations of the Lead Compounds RuA, CuA, RuC, and CuC. In particular, for the metal-DTC complexes previously dissolved in DMSO, 5  $\mu$ M solutions in cell culture medium were prepared. The nanoformulations were instead screened at the concentrations of 3 and 10  $\mu$ M (related to the moles of the encapsulated complex). The choice of these three concentrations was based on the order of magnitude of the collected IC<sub>50</sub> values for the two lead compounds (around 1-2  $\mu$ M). Therefore, for both vehicles a slightly higher value (3 and 5  $\mu$ M) was used to better record distinguished TCRPs. Furthermore, for micelles, a 10-

fold higher concentration was taken into account, as future *in vitro/in vivo* studies will involve these supramolecular aggregates

Cell culture medium, alone or added of 0.1% v/v DMSO, was similarly tested in control wells. During the first hour, the plates were monitored every 2 minutes, then every 30 minutes up to 72 hours, end of the experiment. The time-dependent cellular response profiles for the two tested compounds are presented in **Figure 9.6**.



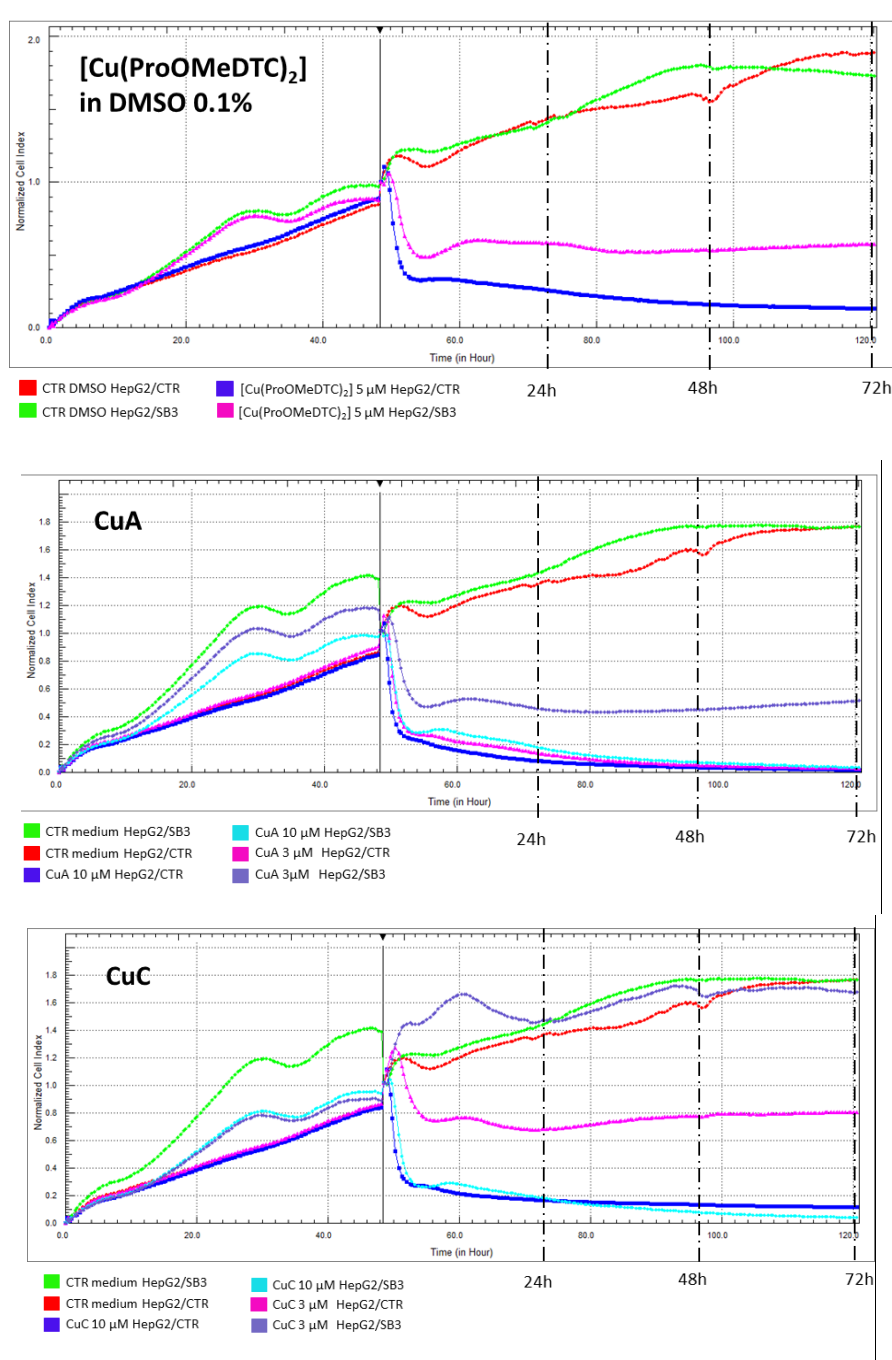


**Figure 9.6** The time-dependent (72 hours) cellular response profiles (TCRPs) for the tested compounds, obtained for the HepG2/CTR and HepG2/SB3 cell lines, in the order:  $\beta$ -[Ru<sub>2</sub>(PDT)<sub>5</sub>]Cl 5  $\mu$ M dissolved in DMSO (0.1% in cell culture medium), RuA 3 and 10  $\mu$ M, RuC 3 and 10  $\mu$ M,  $\beta$ -[Cu(ProOMeDTC)<sub>2</sub>] 5  $\mu$ M dissolved in DMSO (0.1% in cell culture medium), CuA 3 and 10  $\mu$ M, and CuC 3 and 10  $\mu$ M. The plots of every tested cytotoxic agent present also the CTR (control) which refers to not treated cells. Each concentration of every sample was tested in duplicate. Treatment starts at t= 48h from t= 0, in correspondence to the black arrow.

All the TCRPs present an initial impedance increment, which corresponds to the cell growth before the treatment with our compounds. After 48 hours from the seeding, the culture medium was removed and substituted with a new one containing the Lead Compounds, either dissolved in DMSO 0.1% v/v or as PF127 nanoformulations. In particular, for this experiment, we selected both the pure PF127 micelles (RuA and CuA) and the mixed micelles CuC and RuC, whose surface is functionalized with  $\beta$ -D-glucopyranoside (selected as

the most representative labeling). The concentrations of the tested agents was chosen to be higher than the previously calculated  $IC_{50}$ , in order to obtain a well-defined TCRP.

First of all, the two cell lines present different profiles before the treatment, since HepG2/SB3 cells are associated with a faster growth due to the overexpression of the SerpinB3 protein (besides a higher slope, this cell line is characterized by a double hump-shaped curve; the reasons of this phenomenon are not yet clarified). On the other hand, the treatment with each Lead Compound previously dissolved in DMSO leads to the same phenotypic behavior when comparing the two lines, with Ru(III) derivative being more active than the Cu(II) complex. In fact, the HepG2/SB3 cells, even after a fast response to copper-based treatment, seem to recover (in terms of CI).

Concerning the PF127 formulations, targeted and not, the profiles are usually quite different when comparing the two cell lines, the tested agent being equal (the CuC sample involves an anomalous behavior). In particular, SB3-associated cell cultures present some resistance to the treatment with the formulations, in particular those containing the copper compound. In this case, the PF127 micelles containing  $\beta$ -[Ru<sub>2</sub>(PDT)<sub>5</sub>]Cl induce a long-term cytotoxic activity, whereas those encapsulating [Cu(ProOMeDTC)<sub>2</sub>] trigger an antitumor activity already after 2 hours-treatment (cell index of 0.5). Interestingly, the profiles associated with RuA and RuC seem dosage-dependent, although the treatment with both formulations results in a drastic cell index diminution after 36-40 hours of treatment with respect to the most aggressive cell line. This slower profile is probably ascribable to the ligand exchange inertia associated with Ru(III) metal centers.

Moreover, the presence of a cancer-targeting agent ( $\beta$ -D-glucose) does not generate variations in the TCRPs of the formulations, with respect to the not targeted counterpart (RuA).

Notably, the nature of the solubilizing agent (*i.e.*, DMSO and PF127 micelles) slightly affects the time-dependent cellular response profiles of the Lead Compounds, with a small change of the shape of the observed curves, mainly for the Ru(III) complex.

The cytotoxicity profiles of [Cu(ProOMeDTC)<sub>2</sub>] well match in the three tested cases (except for the CuC sample-associated curve at 3  $\mu$ M for HepG2/SB3 cell line). If considering the results collected via MTT assay, confocal microscopy analysis (see **Section 9.6**) and these real time profiles, it is possible to state that the Cu(II) compound, both dissolved in DMSO and loaded in micelles, enters the cell (directly or it is released in the cytoplasm from the carrier), and here it can elicit its cytotoxic activity.

Focusing the attention on the shape of the cellular growth inhibition profiles recorded for the two compounds, it is evident that they are ascribable to distinct mechanisms of action. In particular, the Cu(II)-DTC complex is associated with a TCRP similar to those of the cytotoxic molecules Methiothepin and Amlodipine (two model drugs generally used in literature when studying mechanisms of action, **Figure 9.7** [537]). Overall, the curves related to the HepG2/CTR cell line show a profile close to that reported for the Methiothepin, acting as a dopamine and serotonin antagonist. Conversely, the HepG2/SB3 cell line is related to curves with a shape resembling that of Amlodipine, which interferes with Ca<sup>2+</sup> transporters. Intriguingly,

both drugs affect cellular growth/adhesion profiles very fast by binding specific receptors/transporters at the cell membrane level. This behavior is in contrast with the hypothesis that  $[\text{Cu}(\text{ProOMeDTC})_2]$  exerts its cytotoxic activity after entering the cell, and further investigations will be carried out in order to assess the nature of the cellular target(s) for this compound. On the contrary, the time-dependent cellular response profile of  $\beta\text{-}[\text{Ru}_2(\text{PDT})_5]\text{Cl}$  is similar to the model curves obtained with Etoposide, a Topoisomerase II inhibitor, and Methotrexate, well-known as competitive antagonist for the synthesis of tetrahydrofolate, the active derivative of folic acid (**Figure 9.7**) [537]. Both the effects are in agreement with a cytotoxic action of the dinuclear Ru(III) complex occurring inside the cell and, according to the model profiles,  $\beta\text{-}[\text{Ru}_2(\text{PDT})_5]\text{Cl}$  seems to interfere with the synthesis and the replication of DNA. Moreover, the TCRP showed by our Ru(III) complex resembles those of a series of Ru(II)-phenanthroline derivatives, which preferentially accumulate in the mitochondria of A549R cells (cisplatin-resistant human lung adenocarcinoma), and induce apoptosis through multiple pathways, involving the TrxR inhibition, high intracellular ROS levels, mitochondrial damage and cell cycle arrest [538].

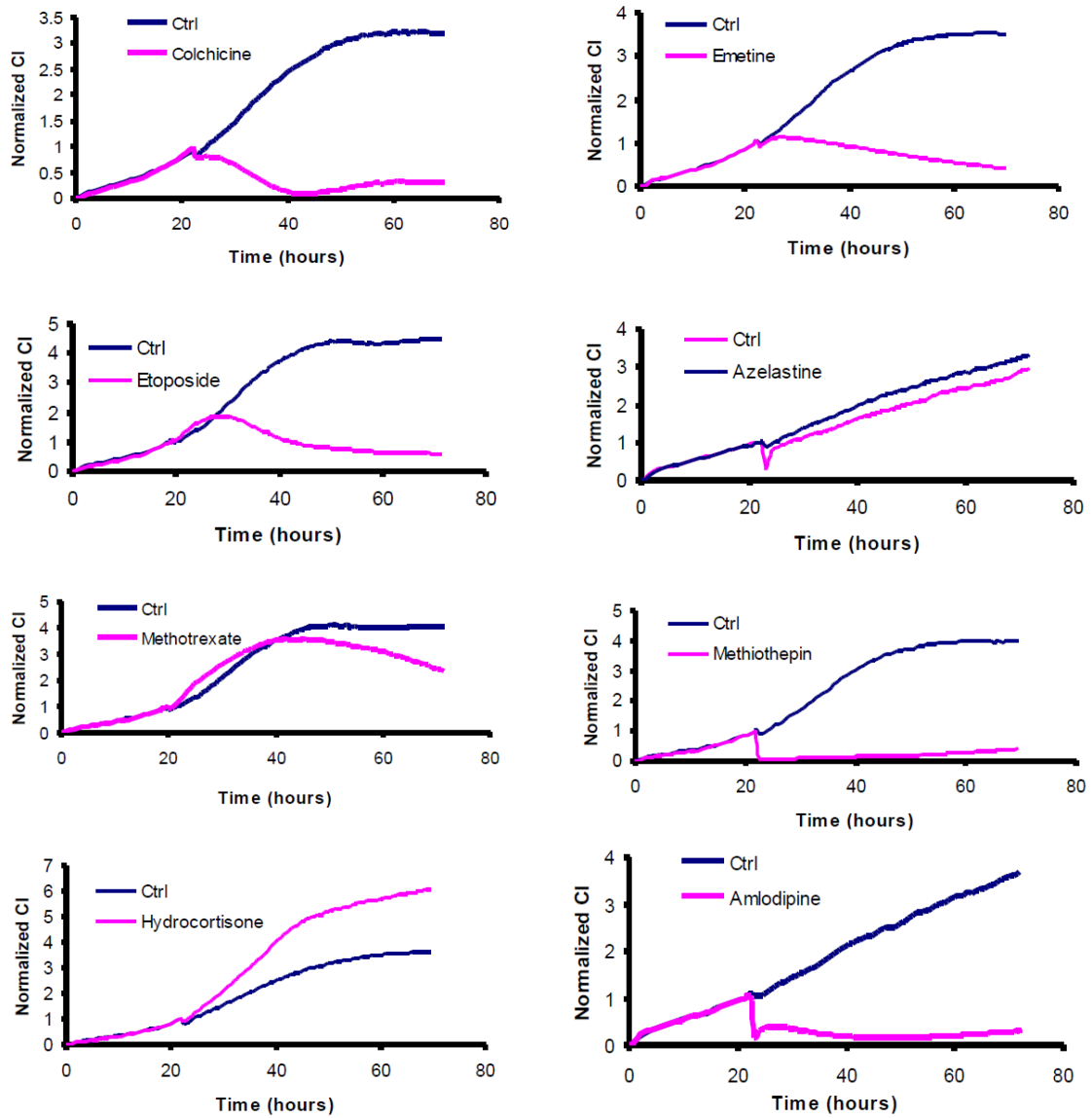


**Figure 9.7** Real time monitoring of apoptosis by using the xCELLigence system. HeLa cells were treated with different drugs for which different mechanism of action are recognized. Cell index values were monitored continuously for 72 h (reproduced from reference [539]).



## 10. FINAL REMARKS

During this 3-year PhD work, with the aim to obtain new complexes able to overcome the side-effects of cisplatin and endowed with higher therapeutic efficacy, we have synthesized and studied new coordination compounds wherein the metal ion coordinates cyclic *N,N*-disubstituted dithiocarbamate ligands. The selected biologically-active centers were Ru(III), Cu(II) and Au(III) due to their interesting chemical features, exploitable at the pharmaceutical level. Concerning the first, ruthenium-based complexes are widely studied in literature based on i) the rate of ligand exchange similar to that of Pt(II) complexes, ii) a wide range of oxidation states accessible under physiological conditions, and iii) the ability to mimic iron in binding to many biomolecules (*e.g.*, human serum albumin and transferrin). In addition, two Ru(III)-containing drugs (*i.e.*, NAMI-A and KP1019) reached clinical trials for the treatment of metastases and solid malignancies, respectively. Differently, copper is an essential micronutrient involved in fundamental life processes, and plays a role of paramount importance in angiogenesis, the physiological development of new blood vessels from pre-existing ones, being one of the key steps in the transition of tumors from a benign state to a malign one. Finally, gold has been known for centuries for its therapeutic properties (the so-called “chrysotherapy”) and its derivatives auranofin and sodium aurothiomalate have been used for a long time in the treatment of rheumatoid arthritis. This metal ion, in both its oxidation states +1 and +3, is associated with anti-inflammatory properties and several studies have demonstrated it is able to interfere with different cellular pathways, such as the TrxR system.

It is worth highlighting that the biological activity of a coordination compound depends not only on the nature of the metal center, but derives from a synergic effect of the metal-ligands system. According to this, during the first part of this PhD work, we combined the active metal centers Ru(III), Cu(II) and Au(III) with dithiocarbamate (DTC) chelating agents derived from cyclic amines, both aliphatic (*i.e.*, pyrrolidine, piperidine, morpholine, indoline, L-proline methyl- and *tert*-butyl ester) and aromatic (carbazole, indole, and pyrrole). Indeed, in light of our research group’s experience DTCs can confer great stability on the metal ion in terms of reactivity (both at the redox and coordination level), thus reducing side-interactions with sulfur-containing bio-molecules and enzymes in the biological environment.

The dithiocarbamate ligands and their complexes were synthesized using different strategies aimed at improving the reaction yields and the purity of the compounds, which were characterized by means of elemental analysis, X-ray crystallography, ESI-MS, <sup>1</sup>H-NMR spectroscopy, FT-IR and UV-Vis spectrophotometries.

The ruthenium(III) center has generated neutral [Ru<sup>III</sup>(DTC)<sub>3</sub>] and ionic β-[Ru<sup>III</sup><sub>2</sub>(DTC)<sub>5</sub>]Cl derivatives, while copper(II) is involved in neutral complexes of the type [Cu<sup>II</sup>(DTC)<sub>2</sub>]. Finally, the gold(III) ion is found in neutral complexes of the type [Au<sup>III</sup>X<sub>2</sub>(DTC)] (X= Cl, Br, obtained from oxidative addition of X<sub>2</sub> to the corresponding

gold(I) precursor  $[\text{Au}^{\text{I}}_2(\text{DTC})_2]$  and in the ionic counterparts  $[\text{Au}^{\text{III}}(\text{DTC})_2]\text{Y}$  ( $\text{Y} = \text{Cl}, \text{Br}, [\text{Au}^{\text{III}}\text{Cl}_4]$  and  $[\text{Au}^{\text{I}}\text{Br}_2]$  with  $\text{DTC} = \text{PipeDTC}$ ).

Concerning the structural and electronic properties of the synthesized metal-DTC derivatives, FT-IR spectroscopy as well as X-ray studies on crystal structures of some complexes, undoubtedly highlighted the difference between the dithiocarbamic and thioureidic forms of the coordinated ligands, on the basis of the cyclic amine nature. Indeed, the aromatic moiety of CDT, IndDTC, and PyrDTC (and usually IndolineDTC) leads to a C-N bond with a mainly single-bond character (dithiocarbamic form, **Figure 10.1 a**) due to a hampered nitrogen lone pair donation. In these molecules, chelating sulfur donor atoms have low-energy empty  $d$  orbitals which can accept  $\pi$ -retrodonation from metal  $d$  orbitals, thus strengthening the metal-ligand bond. On the contrary, PDT and PipeDTC possess positive inductive effects which determine the shift of the nitrogen lone pair to the -CSS moiety, giving rise to an almost C=N double bond (thioureidic form **Figure 10.1 b**) and to a limited metal-to-sulfur back donation. Finally, MorphDTC and L-Proline ester dithiocarbamate ligands displayed intermediate properties between the two limiting forms, with a preference for the thioureidic one.

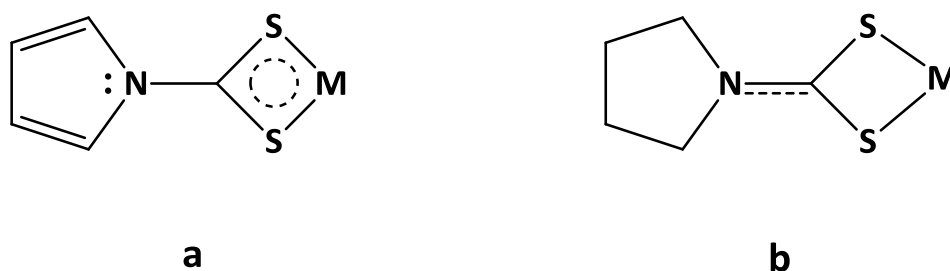


**Figure 10.1** Dithiocarbamate form **a** versus thioureidic form **b**.

The synthesized metal-DTC derivatives were also tested *in vitro* for their cytotoxicity against three human tumor cell lines (HeLa, HepG2/CTR and HepG2/SB3), in order to evaluate how the previously discussed nature of the ligand can influence the antiproliferative activity of the final complex. In general, complexes derived from aromatic DTCs suffered from low solubility in DMSO (reference solvent for *in vitro* studies), and did not show anticancer activity or the latter was not even estimable. Differently, the new compounds involving PDT, PipeDTC, ProOMeDTC and ProOtBuDTC generated promising results, also against the apoptosis-resistant cell line HepG2/SB3. This cell line was investigated based on the key role of the serine protease inhibitor SerpinB3 (SB3) in dictating hepatocellular carcinoma progression and invasion. In fact, high SerpinB3 levels were detected in patients with the most aggressive cancer subtypes. Based on these findings, the  $\text{IC}_{50}$  values of the most active compounds were combined with the corresponding lipophilic index ( $\log P$ ), thus achieving a LipE profile, being used to identify the best complexes in terms of drug-like properties. This evaluation led to the selection of two Lead Compounds, namely  $\beta\text{-}[\text{Ru}_2(\text{PDT})_5]\text{Cl}$  and  $[\text{Cu}(\text{ProOMeDTC})_2]$ , for future *in vivo* studies

and, in order to increase their water solubility and stability, the encapsulation in micellar systems of Pluronic® F127 (PF127) was planned and carried out in the second part of this work. This co-polymer is well-tolerated by living systems and it is modifiable to generate nanocarriers conjugated with cancer-targeting biomolecules. Thus, the second part of this PhD work was then focused on the loading of the Lead Compounds into carbohydrate-labeled micelles. First of all, we modified the terminal hydroxyl groups of PF127 with carbohydrates ( $\beta$ -D-glucose, glucosamine and  $\beta$ -maltose) to achieve an active targeting towards cancer cells exploiting their accelerated glucose metabolism (Warburg effect). After  $^1\text{H}$ - and  $^{13}\text{C}$ -NMR, and FT-IR characterizations of the conjugation products, the Lead Compounds were encapsulated in spherical micelles with an average 23-nm diameter (TEM and DLS analysis). These nanoformulations proved stable for at least 72 hours under physiological conditions, such as human serum and cell culture medium.

At the best of our knowledge, these are the first drug delivery systems containing Ru(III) and Cu(II) dithiocarbamate cytotoxic agents. All the nanosystems have been tested *in vitro* for their antiproliferative activity against the abovementioned human cancer cell lines. The cytotoxicity results, expressed as  $\text{IC}_{50}$  values, along with the xCELLigence analysis of the time-dependent cellular response profiles, showed that the activity of each complex encapsulated in PF127 micelles is similar to that of the free compound (pre-dissolved in DMSO). Moreover, the confocal microscopy analysis of the fluorescein-labelled PF127 empty carrier pointed out the cell internalization of the micelles and their localization in the perinuclear areas after 2 hours of treatment. On the other hand, the cancer-targeting sugar unit seems to increase the uptake of the loaded carrier in HepG2/CTR cells through the glucose transporter (data obtained using the GLUT1 inhibitor 4,6-*O*-ethylidene-D-glucose).

Taken together, the data collected for the encapsulated Lead Compounds pave the way to future *in vivo* studies, including those to investigate the effective active targeting mediated by the carbohydrates conjugated on the hydrophilic corona of the micelles. The results obtained with this PhD work have yielded ideal drug delivery systems, characterized by optimum dimensions and shape, and good stability in physiological environment (*i.e.*, human serum, and cell culture medium containing amino acids, phosphate and different salts). In addition, the *in vitro* studies on the formulations of the Lead Compounds have showed that their cytotoxic properties are maintained upon encapsulation, and the release (and consequent activity) of each complex takes place only after the nanocarrier endocytosis. This means that these systems may minimize side effects *in vivo*, driving the cytotoxic payload directly inside the cell.

The future development of this research is the *in vivo* investigation of the anticancer activity of the PF127-Lead Compound formulations in animal models, bearing solid tumors. In fact, these experiments will be crucial to determine if the passive targeting will be paralleled by the active one, elicited by the carbohydrate conjugation of the nanocarrier surface. Other studies have been already planned, and they will make use of radioactive tracers to follow the fate of the micelles *in vivo*. Inspired from the technology of the clinically-established PET diagnostic agent 2-deoxy-2- $(^{18}\text{F})$ fluoro-D-glucose (FDG), we aim to label cancer-targeting

Pluronic® mixed micelles with  $^{18}\text{F}$  (*via* tosylate substitution on the terminal hydroxyl group of PEO chain). In this manner, the foreseen accumulation of the micellar nanocarrier in cancer tissues should be detectable by PET experiments in tumor-bearing animals.

The data collected in this work along with other research results have led our research group to file two Italian Patent applications (filing date: December 2<sup>nd</sup>, 2016) titled “Composti di coordinazione, sintesi, nanoformulazione ed uso degli stessi in oncologia” (102016000122363; 102016000122406). On the basis of these achievements, at the end of the 3<sup>rd</sup> -PhD year, the bureaucratic procedures to found a new startup company have been started (approved by the Department of Chemical Sciences of the University of Padova, in date January 25<sup>th</sup>, 2017) to transfer the acquired knowledge into advanced preclinical testing and, if possible, clinics.

## 11. COLLABORATIONS

- X-ray analyses of the complexes [Cu(PipeDTC)<sub>2</sub>], [Cu(ProOMeDTC)<sub>2</sub>], [Cu(ProOtBuDTC)<sub>2</sub>], [AuCl<sub>2</sub>(PipeDTC)], [AuBr<sub>2</sub>(PipeDTC)], [Au(PipeDTC)<sub>2</sub>][AuCl<sub>4</sub>], and [Au(PipeDTC)<sub>2</sub>][AuBr<sub>2</sub>], as well as those of the by-products presented in **Figure 5.5**, were carried out by Prof. Luciano Marchiò at the Department of General and Inorganic Chemistry, Analytical Chemistry, Physical Chemistry of the University of Parma.
- Chemical modifications of Pluronic® F127 with oxime derivatives, namely PF127-β-D-glucopyranose and PF127-β-maltose were performed by the research group of Prof. Laura Cipolla at the Department of Biotechnology and Biosciences of the University of Milano-Bicocca.
- *In vitro* antiproliferative screening against HeLa cells were carried out in the laboratories of Prof. Andrea Trevisan, under the precious assistance of Dott. Alberto Gambalunga at the Department of Cardiac, Thoracic and Vascular Sciences of the University of Padova.
- *In vitro* cytotoxicity studies on HepG2 cells, confocal microscopy and xCELLigence analyses were conducted in the laboratories of Prof. Patrizia Pontisso, under the precious assistance of Dr. Santina Quarta at the Department of Medicine (DIMED) of the University of Padova.



## REFERENCES

- [1] K. H. Thompson, Medicinal Inorganic Chemistry: introduction, in *Encyclopedia of Inorganic Chemistry*, **2010**, John Wiley & Sons, New York (USA).
- [2] P. Chellan, P. J. Sadler, The elements of life and medicines, *Phil. Trans. R. Soc. A*, **2015**, 373(2037), 20140182.
- [3] W. Maret, The metals in the biological periodic system of the elements: concepts and conjectures, *Int. J. Mol. Sci.*, **2016**, 17(1), 1.
- [4] N. P. E. Barry, P. J. Salder, Exploration of the medical periodic table towards new targets, *Chem. Comm.*, **2013**, 49, 5106.
- [5] Different authors and different chapters, in *Metal ions in biological systems*, **2015**, A. Sigel, H. Sigel, R. K. Sigel eds., Royal Society of Chemistry, Cambridge (UK).
- [6] A. Krężel, W. Maret, The biological inorganic chemistry of zinc ions, *Arch. Biochem. Biophys.*, **2016**, doi:10.1016/j.abb.2016.04.010.
- [7] Y. Sheng, I. A. Abreu, D. E. Cabelli, M. J. Maroney, A.-F. Miller, M. Teixeira, J. S. Valentine, Superoxide dismutase and superoxide reductase, *Chem. Rev.*, **2014**, 114, 3854.
- [8] K. D. Mjos, C. Orvig, Metallo drugs in medicinal inorganic chemistry, *Chem. Rev.*, **2014**, 114, 4540.
- [9] N. P. E. Barry, P. J. Sadler, 100 years of metal coordination chemistry: from Alfred Werner to anticancer metallo drugs, *Pure Appl. Chem.*, **2014**, 86(12), 1897.
- [10] H. G. Raubenheimer, H. Schmidbaur, The late start and amazing upswing in gold chemistry, *J. Chem. Educ.*, **2014**, 91, 2024.
- [11] P. Ehrlich, A. Bertheim, Über das salzsaure 3.3'-diamino-4.4'-dioxy-arsenobenzol und seine nächsten verwandten, *Ber. Dtsch. Chem. Ges.*, **1912**, 45, 756.
- [12] B. Rosenberg, L. Van Camp, J. E. Trosko, V. H. Mansour, Platinum compounds: a new class of potent antitumor agents, *Nature*, **1969**, 222, 385.
- [13] Visiongain Report, *Leading anti-cancer drugs and associated market 2013-2023*, <http://www.visiongain.com/Report/1063/Leading-Anti-Cancer-Drugs-and-Associated-Market-2012-2013>, **2013** (accessed 09.06.2016).
- [14] *World Cancer Report 2014*, **2014**, B. W. Stewart, C. P. Wild eds., World Health Organization Press, Geneva (Switzerland).
- [15] J. Ferlay, I. Soerjomataram, R. Dikshit, S. Eser, C. Mathers, M. Rebelo, D. M. Parkin, D. Forman, F. Bray, Cancer incidence and mortality worldwide: sources, methods and major patterns in GLOBOCAN 2012, *Int. J. Cancer*, **2015**, 136, E359.
- [16] Analyze search result of the keyword "cancer" on Scopus, <http://www.scopus.com> (accessed 09.06.2016).
- [17] GBI Research, *Breast cancer therapeutics in major developed markets to 2021 - Growth driven by rapid uptake of premium priced biologics and rising incidence*, report code GBIHC379MR, <http://www.gbiresearch.com>, **2015** (accessed 10.06.2016).
- [18] G. M. Cooper GM, The Development and Causes of Cancer, in *The Cell: A Molecular Approach 2<sup>nd</sup> edition*, **2000**, Sinauer Associates, Sunderland (USA).
- [19] R. J. Gilbertson, Mapping cancer origins, *Cell*, **2011**, 145, 25.
- [20] S. M. Ametamey, M. Honer, P. A. Schubiger, Molecular imaging with PET, *Chem. Rev.*, **2008**, 108, 1501.
- [21] Z. Zhou, Z.-R. Lu, Gadolinium-based contrast agents for MR cancer imaging, *Wiley Interdiscip. Rev. Nanomed. Nanobiotechnol.*, **2013**, 5(1), 1.
- [22] F. R. Balkwill, M. Capasso, T. Hagemann, The tumor microenvironment at a glance, *J. Cell Sci.*, **2012**, 125, 5591.
- [23] S. J. Lunt, N. Chaudary, R. P. Hill., The tumor microenvironment and metastatic disease, *Clin. Exp. Metastasis*, **2009**, 26, 19.
- [24] L. M. F. Merlo, J. W. Pepper, B. J. Reid, C. C. Maley, Cancer as an evolutionary and ecological process, *Nat. Rev. Cancer*, **2006**, 6, 924.
- [25] P. C. Nowell, The clonal evolution of tumor cell populations, *Science*, **1976**, 194, 23.

- [26] J. E. Visvader, Cells of origin in cancer, *Nature*, **2011**, 469, 314.
- [27] A. P. Feinberg, R. Ohlsson, S. Henikoff, The epigenetic progenitor origin of human cancer, *Nat. Rev. Genet.*, **2006**, 7(1), 21.
- [28] M. Greaves, C. C. Maley, Clonal evolution in cancer, *Nature*, **2012**, 481, 306.
- [29] D. P. Tabassum, K Polyak, Tumorigenesis: it takes a village, *Nat. Rev. Cancer*, **2015**, 15, 473.
- [30] R. Axelrod, D. E. Axelrod, K. J. Pienta, Evolution of cooperation among tumor cells, *Proc. Natl. Acad. Sci. USA*, **2006**, 103, 13474.
- [31] A. Marusyk, D. P. Tabassum, P. M. Altrock, V. Almendro, F. Michor, K. Polyak, Non-cell-autonomous driving of tumor growth supports sub-clonal heterogeneity, *Nature*, **2014**, 514, 54.
- [32] D. Hanahan, R. A. Weinberg, The hallmarks of cancer, *Cell*, **2000**, 100(1), 57.
- [33] D. Hanahan, R. A. Weinberg, The hallmarks of cancer: the next generation, *Cell*, **2011**, 144(5), 646.
- [34] N. Bailon-Moscoco, J. C. Romero-Benavides, P. Ostrosky-Wegman, Development of anticancer drugs based on the hallmarks of tumor cells, *Tumor Biol.*, **2014**, 35(5), 3981.
- [35] B. Weinstein, A. K. Joe, Mechanism of disease: oncogene addiction – a rationale for molecular targeting in cancer therapy, *Nat. Clin. Pract. Oncol.*, **2006**, 3(8), 448.
- [36] S. Elmore, Apoptosis: a review of programmed cell death, *Toxicol. Pathol.*, **2007**, 35, 495.
- [37] D. Mendez, A. Inga, M. A. Resnick, The expanding universe of p53 targets, *Nat. Rev. Cancer*, **2009**, 9, 724.
- [38] J. W. Shay, W. E. Wright, Role of telomeres and telomerase in cancer, *Semin. Cancer Biol.*, **2011**, 21(6), 349.
- [39] F. Pezzella, A. L. Harris, M. Tavassoli, K. C. Gatter, Blood vessels and cancer much more than just angiogenesis, *Cell Death Discovery*, **2015**, 1, 15064.
- [40] N. S. Vasudev, A. R. Reynolds, Anti-angiogenic therapy for cancer: current progress, unresolved questions and future directions, *Angiogenesis*, **2014**, 17, 471.
- [41] R. A. Cairns, I. S. Harris, T. W. Mak, Regulation of cancer cell, *Nat. Rev. Cancer*, **2011**, 11, 85.
- [42] R. A. Gatenby, R. J. Gillies, Why do cancers have high aerobic glycolysis?, *Nat. Rev. Cancer*, **2004**, 4, 891.
- [43] R. J. Gillies, I. Robey, R. A. Gatenby, Causes and consequences of increased glucose metabolism of cancers, *J. Nucl. Med.*, **2008**, 49(suppl. 2), 245.
- [44] G. L. Semenza, Regulation of cancer cell metabolism by hypoxia-inducible factor 1, *Semin. Cancer Biol.*, **2009**, 19, 12.
- [45] L. Szablewski, Expression of glucose transporters in cancers, *Biochim. Biophys. Acta*, **2013**, 1835, 164.
- [46] R. J. De Berardinis, A. Mancuso, E. Daikhin, I. Nissim, M. Yudkoff, S. Wehrli, C. B. Thompson, Beyond aerobic glycolysis: transformed cell can engage in glutamine metabolism that exceeds the requirement for protein and nucleotide synthesis, *Proc. Natl. Acad. Sci. USA*, **2007**, 104(49), 19345.
- [47] S. Turajlic, C. Swanton, Metastasis as an evolutionary process, *Science*, **2016**, 352, 169.
- [48] K. W. Hunter, N. P. S Crawford, J. Alsarraj, Mechanism of metastasis, *Breast Cancer Res.*, **2008**, 10(suppl. 1), S2.
- [49] O. J. Finn, Immuno-oncology: understanding the function and dysfunction of the immune system in cancer, *Ann. Oncol.*, **2012**, 23(suppl. 8), vii6.
- [50] K. Bell, S. Ristovski-Slijepcevic, Cancer survivorship: why labels matter, *J. Clin. Oncol.*, **2013**, 31(4), 409.
- [51] M. M. Olszewski, Concepts of cancer from antiquity to the nineteenth century, *UTMJ*, **2010**, 87(3), 181.
- [52] S. Rockwell, I. T. Dobrucki, E. Y. Kim, S. Tucker Marrison, V. Thuc Vu, Hypoxia and radiation therapy: past history, ongoing research, and future promise, *Curr. Mol. Med.*, **2009**, 9(4), 442.
- [53] L. F. Povirk, D. E. Shuker, DNA damage and mutagenesis induced by nitrogen mustards, *Mutat. Res.*, **1994**, 318(3), 205.
- [54] M. Arruebo, N. Vilaboa, B. Saez-Gutierrez, J. Lambea, A. Tres, M. Valladares, A. Gonzalez-Fernandez, Assessment of the evolution of cancer treatment therapies, *Cancers*, **2011**, 3, 3279.
- [55] American Cancer Society, <http://www.cancer.org/treatment/> (accessed 07.09.2016).
- [56] J. D. Hoeschele, Dr. Barnett Rosenberg – a personal perspective, *Dalton Trans.*, **2016**, 45, 12966.



- [57] X. Lin, T. Okuda, A. Holzer, S. B. Howell, The copper transporter CTR1 regulates cisplatin uptake in *Saccharomyces cerevisiae*, *Mol. Pharmacol.*, **2002**, 62(5), 1154.
- [58] N. D. Eljack, H.-Y. M. Ma, J. Drucker, C. Shen, T. W. Hambley, E. J. New, T. Friedrich, R. J. Clarke, Mechanisms of cell uptake and toxicity of the anticancer drug cisplatin, *Metallomics*, **2014**, 6, 2126.
- [59] P. M. Takahara, C. A. Frederick, S. J. Lippard, Crystal structure of the anticancer drug cisplatin bound to duplex DNA, *J. Am. Chem. Soc.*, **1996**, 118(49), 12309.
- [60] M. P. M. Marques, D. Gianolio, G. Cibir, J. Tomkinson, S. F. Parker, R. Valero, R. Pedro Lopes, L. A. E. Batista de Carvalho, A molecular view of cisplatin's mode of action: interplay with DNA bases and acquired resistance, *Phys. Chem. Chem. Phys.*, **2015**, 17, 5155.
- [61] L. Kelland, The resurgence of platinum-based cancer chemotherapy, *Nat. Rev. Cancer*, **2007**, 7, 573.
- [62] R. P. Miller, R. K. Tadagavadi, G. Ramesh, W. B. Reeves, Mechanism of cisplatin nephrotoxicity, *Toxins*, **2010**, 2(11), 2490.
- [63] M. L. Hensley, K. L. Hagerty, T. Kewalramani, D. M. Green, N. J. Meropol, T. H. Wasserman, G. I. Cohen, B. Emami, W. J. Gradishar, R. B. Mitchell, *et al.*, American Society of Clinical Oncology 2008 practice guideline update: use of chemotherapy and radiation therapy protectants, *J. Clin. Oncol.*, **2009**, 27, 127.
- [64] A. J. Di Pasqua, J. Goodisman, J. C. Dabrowiak, Understanding how the platinum anticancer drug carboplatin works: from the bottle to the cell, *Inorg. Chim. Acta*, **2012**, 389, 29.
- [65] A. K. Holzer, S. B. Howell, The internalization and degradation of human copper transporter 1 following cisplatin exposure, *Cancer Res.*, **2006**, 66, 10944.
- [66] R. Safaei, A. K. Holzer, K. Katano, G. Saimi, S. B. Howell, The role of copper transporters in the development of resistance to Pt drugs, *J. Inorg. Chem.*, **2004**, 98, 1607.
- [67] R. G. Pearson, Hard and soft acids and bases, HSAB, part I, *J. Chem. Ed.*, **1968**, 45, 581.
- [68] P. Mistry, L. R. Kelland, G. Abel, S. Sidhar, K. R. Harrap, The relationships between glutathione, glutathione-S-transferase, and cytotoxicity of platinum drugs and melphalanin in eight human ovarian cancer cell lines, *Br. J. Cancer*, **1991**, 64, 215.
- [69] L. P. Rybak, C. A. Whitworth, D. Mukherjee, V. Ramkumar, Mechanisms of cisplatin-induced ototoxicity and prevention, *Hear. Res.*, **2007**, 226, 157.
- [70] O. Pinato, C. Musetti, C. Sissi, Pt-based drugs: the spotlight will be on proteins, *Metallomics*, **2014**, 6, 380.
- [71] L. P. Martin, T. C. Hamilton, R. J. Schilder, Platinum resistance: the role of DNA repair pathways, *Clin. Cancer Res.*, **2008**, 14(5), 1291.
- [72] E. Raymond, S. Faivre, S. Chaney, J. Woynarowski, E. Cvitkovic, Cellular and molecular pharmacology of oxaliplatin, *Mol. Cancer Ther.*, **2002**, 1, 227.
- [73] N. J. Wheate, S. Walker, G. E. Craig, R. Oun, The status of platinum anticancer drugs in the clinic and in clinical trials, *Dalton Trans.*, **2010**, 39, 8113.
- [74] B. A. Chabner, T. G. Roberts Jr, Chemotherapy and the war on cancer, *Nat. Rev. Cancer*, **2005**, 5, 65.
- [75] K. Strebhardt, A. Ullrich, Paul Ehrlich's magic bullet concept: 100 years of progress, *Nat. Rev. Cancer*, **2008**, 8, 473.
- [76] M. Deininger, E. Buchdunger, B. J. Druker, The development of Imatinib as a therapeutic agent for chronic myeloid leukemia, *Blood*, **2005**, 105, 2640.
- [77] S. Kumar Pal, R. A. Figlin, H. Yu, Deciphering the anticancer mechanism of sunitinib, *Cancer Biol. Ther.*, **2010**, 10(7), 712.
- [78] D. Chen, M. Frezza, S. Schmitt, J. Kanwar, Q. P. Dou, Bortezomib as the first proteasome inhibitor anticancer drug: current status and future perspectives, *Curr. Cancer Drug Targets*, **2011**, 11(3), 239.
- [79] I. Sanchez-Serrano, Translational research in the development of bortezomib: a core model, *Discov. Med.*, **2005**, 5(30), 527.
- [80] M. Vanneman, G. Dranoff, Combining immunotherapy and targeted therapies in cancer treatment, *Nat. Rev. Cancer*, **2012**, 12, 237.
- [81] A. M. Scott, J. D. Wolchik, L. J. Old, Antibody therapy of cancer, *Nat. Rev. Cancer*, **2012**, 12, 278.

- [82] G. J. Weiner, Building better monoclonal antibody-based therapeutics, *Nat. Rev. Cancer*, **2015**, 15, 361.
- [83] A. J. Grillo-Lopez, C. A. White, C. Varns, D. Shen, A. Wei, A. McLaure, B. K. Dallaire, Overview of the clinical development of rituximab: first monoclonal antibody approved for the treatment of lymphoma, *Semin. Oncol.*, **1999**, 26, 66.
- [84] Hematology/Oncology (Cancer) Approvals & Safety Notifications, <http://www.fda.gov/Drugs/InformationOnDrugs/ApprovedDRugs/ucm279174.htm> (accessed 08.09.2016).
- [85] A. Swaika, W. A. Hammond, R. W. Joseph, Current state of anti-PD-L1 and anti-PD-1 agents in cancer therapy, *Mol. Immunol.*, **2015**, 67,4.
- [86] T. T. Hansel, H. Kropshofer, T. Singer, J. A. Mitchell, A. J. T. George, The safety and side effects of monoclonal antibodies, *Nat. Rev. Drug Discov.*, **2010**, 9, 325.
- [87] i)H. Joensuu, J. Gligorov, Adjuvant treatments for triple-negative breast cancer, *Annal. Oncol.*, **2012**, 23(suppl. 6), vi40; ii) Personal communication with Dr. Giuseppe Curigliano, European Institute of Oncology, Milan (Italy).
- [88] S. Hoelder, P. A. Clarke, P. Workman, Discovery of small molecule cancer drugs: successes, challenges and opportunities, *Mol. Oncol.*, **2012**, 6, 155.
- [89] J. Frearson, P. Wyatt, Drug discovery in Academia – the third way?, *Expert Opin. Drug Discov.*, **2010**, 5(10), 909.
- [90] Pharmaceutical Research and Manufacturers of America (PhRMA), *Profile 2009*, **2009**, Washington, [www.phrma.org](http://www.phrma.org) (accessed 13.09.2016).
- [91] J. Eder, R. Sedrani, C. Wiesmann, The discovery of first-in-class drugs: origins and evolution, *Nat. Rev. Drug Discov.*, **2014**, 13, 577.
- [92] G. J. Kelloff, C. C. Sigman, Cancer biomarkers: selecting the right drug for the right patient, *Nat. Rev. Drug Discov.*, **2012**, 11, 202.
- [93] S. Neidle, D. E. Thurston, Chemical approach to the discovery and development of cancer therapies, *Nat. Rev. Cancer*, **2005**, 5, 287.
- [94] J. F. Pritchard, M. Jurima-Romet, M. L. J. Reimer, E. Mortimer, B. Rolfe, M. N. Cayen, Making better drugs: decision gates in non-clinical drug development, *Nat. Rev. Drug Discov.*, **2003**, 2, 542.
- [95] R. Perkins, H. Fang, W. Tong, W. J. Welsh, Quantitative structure-activity relationship methods: perspectives on drug discovery and toxicology, *Environ. Toxicol. Chem.*, **2003**, 22, 1666.
- [96] D. J. Adams, The Valley of Death in anticancer drug development: a reassessment, *Trends Pharmacol. Sci.*, **2012**, 33(4), 173.
- [97] C. Tailor Gilliland, D. Zuk, P. Kocis, M. Johnson, S. Hay, M. Hajduch, F. Bietrix, G. Aversa, C. P. Austin, E. Ussi, Putting translational science on to a global stage, *Nat. Rev. Drug Discov.*, **2016**, 15, 217.
- [98] FDA Content and Format of Investigational New Drug Applications (INDs) for Phase 1 studies of Drugs, including well-characterized, therapeutic, biotechnology-derived products, [www.fda.gov/downloads/Drugs/.../Guidances/ucm074908.pdf](http://www.fda.gov/downloads/Drugs/.../Guidances/ucm074908.pdf) (accessed 13.09.2016).
- [99] FDA Drug Development and Process – Step3: Clinical Research, [www.fda.gov/ForPatients/Approvals/Drug/ucm405622.htm](http://www.fda.gov/ForPatients/Approvals/Drug/ucm405622.htm) (accessed 13.09.2016).
- [100] M. Shea, L. Ostermann, R. Homan, S. Roberts, M. Kozak, R. Dull, J. Allen, E. Sigal, Regulatory watch: impact of breakthrough therapy designation on cancer drug development, *Nat. Rev. Drug Discov.*, **2016**, 15, 152.
- [101] B. Chabner, The traveling oncologist and the wages of sin, *Oncologist*, **2001**, 6, 1.
- [102] T. A. Yap, S. K. Sandhu, P. Workman, J. S. de Bono, Envisioning the future of early anticancer drug development, *Nat. Rev. Cancer*, **2010**, 10, 514.
- [103] P. J. Heard, Main group dithiocarbamate complexes, in *Progress in Inorganic Chemistry (Vol. 53)*, **2005**, K. D. Karlin ed., John Wiley & Sons, New York (USA).
- [104] G- Moad, D. Keddie, C. Guerrero-Sanchez, E. Rizzardo, S. H. Thang, Advances in switchable RAFT polymerization, *Macromol. Symp.*, **2015**, 350(1), 34.

- [105] J- R- Roede, D. P. Jones, Thiol-reactivity of the fungicide maneb, *Redox Biol.*, **2014**, 2(1), 651.
- [106] G. Vettorazzi, W. F. Almeida, G. J. Burin, R. B. Jaeger, F. R. Puga, A. F. Rahde, F. G. Reyes, S. Schwartsman, International safety assessment of pesticides: dithiocarbamate pesticides, ETU, and PTU – a review and update, *Teratog., Carcinog. Mutagen.*, **1995**, 15(6), 313.
- [107] V. Bala, G. Gupta, V. L. Sharma, Chemical and medicinal versatility of dithiocarbamates: an overview, *Mini-Rev. Med. Chem.*, **2014**, 14(12), 1021.
- [108] A. Imyim, P. Daorattanachai, F. Unob, Determination of cadmium, nickel, lead and zinc in fish tissue by flame and graphite furnace atomic absorption after extraction with pyrrolidine dithiocarbamate and activated carbon, *Anal. Lett.*, **2013**, 46, 2101.
- [109] G. Hogarth, Metal-dithiocarbamate complexes: chemistry and biological activity, *Mini-Rev. Med. Chem.*, **2012**, 12(12), 1202.
- [110] D. M. Miller, R. A. Latimer, The kinetic of decomposition and synthesis of some dithiocarbamates, *Can. J. Chem.*, **1962**, 40, 246.
- [111] E. Humeres, N. A. Debacher, M. M. de S. Sierra, J. D. Franco, A. Schutz, Mechanisms of acid decomposition of dithiocarbamates. 1. Alkyl dithiocarbamates, *J. Org. Chem.*, **1998**, 63, 1598.
- [112] E. Humeres, N. A. Debacher, M. M. de S. Sierra, Mechanisms of acid decomposition of dithiocarbamates. 2. Efficiency of the intramolecular general acid catalysis, *J. Org. Chem.*, **1999**, 64, 1807.
- [113] E. Humeres, N. A. Debacher, J. D. Franco, B. S. Lee, A. Martendal, Mechanisms of acid decomposition of dithiocarbamates. 3. Aryldithiocarbamates and the torsional effect, *J. Org. Chem.*, **2002**, 67, 3662.
- [114] D. J. Halls, The properties of dithiocarbamates, *Mikrochim. Acta*, **1969**, 62.
- [115] K. Ramadas, N. Srinivasan, Sodium chlorite – yet another oxidant for thiols and disulphides, *Synth. Commun.*, **1995**, 25(2), 227.
- [116] G. Hogarth, Transition metal dithiocarbamates: 1978-2003, in *Progress in Inorganic Chemistry (Vol. 53)*, **2005**, K. D. Karlin ed., John Wiley & Sons, New York (USA).
- [117] A. Domenicano, A. Vaciago, L. Zambonelli, P. L. Loader, L. M. Venanzi, The structure of nitrosylruthenium tris-(N,N-diethyldithiocarbamate): a complex with a monodentate dithiocarbamate group, *Chem. Commun. (London)*, **1966**, 14, 1966.
- [118] A. R. Hendrickson, J. M. Hope, R. L. Martin, Tris- and pentakis- dialkyldithiocarbamates of ruthenium,  $[\text{Ru}(\text{S}_2\text{CNR}_2)_3]^n$  and  $[\text{Ru}_2(\text{S}_2\text{CNR}_2)_5]^n$  (n = +1, 0, and -1): chemical and electrochemical interrelations, *J. Chem. Soc. Dalton Trans.*, **1976**, 20, 2032.
- [119] V. K. Sharma, J. S. Aulakh, A. K. Malik, Thiram: degradation, applications and analytical methods, *J. Environ. Monit.*, **2003**, 5(5), 717.
- [120] R. M. Swift, E. R. Aston, Pharmacotherapy for alcohol use disorder: current and emerging therapies, *Harv. Rev. Psychiatry*, **2015**, 23(2), 122.
- [121] N. Segovia, G. Crovetto, P. Lardelli, M. Espigares, In vitro toxicity of several dithiocarbamates and structure-activity relationships, *J. Appl. Toxicol.*, **2002**, 22, 353.
- [122] R. A. Goyer, M. G. Cherian, M. M. Jones, J. R. Reigart, Role of chelating agents for prevention, intervention, and treatment of exposures to toxic metals, *Environ. Health Perspect.*, **1995**, 103(11), 1048.
- [123] R. F. Borch, M. E. Pleasants, Inhibition of cis-platinum nephrotoxicity by diethyldithiocarbamate rescue in rat model, *Proc. Natl. Acad. Sci. USA*, **1979**, 76(12), 6611.
- [124] R. F. Borch, J. C. Katz, P. H. Lieder, M. E. Pleasants, Effect of diethyldithiocarbamate rescue on tumor response to cis-platinum in rat model, *Proc. Natl. Acad. Sci. USA*, **1980**, 77(9), 5441.
- [125] L. P. Rybak, R. Ravi, S. M. Somani, Mechanism of protection by diethyldithiocarbamate against cisplatin ototoxicity: antioxidant system, *Fund. Appl. Toxicol.*, **1995**, 26, 293.
- [126] P. K. Gessner, T. Gessner, *Disulfiram and its metabolite, diethyldithiocarbamate: pharmacology and status in the treatment of alcoholism, HIV infections, AIDS and heavy metal toxicity*, **1992**, Springer, New York (USA).

- [127] G. J. M. van der Kerk, H. L. Klöpping, Investigation on organic fungicides: VII. Further considerations regarding the relations between chemical structure and antifungal action of dithiocarbamate and bisdithiocarbamate derivatives, *Recl. Trav. Chim. Pays-Bas*, **1952**, 71, 1179.
- [128] G. J. M. van der Kerk, M. H. van Raalte, A. Kaars Sijpesteijn, A new type of plant growth-regulating substances, *Nature*, **1955**, 176, 308.
- [129] J. P. Cartier, C. Sandorfy, Inductive and mesomeric effects in substituted fulvene and pyridine derivatives, *Can. J. Chem.*, **1963**, 41, 2759.
- [130] R. R. Eley, R. R. Myers, N. V. Duffy, Electron spin crossover in iron(III) dithiocarbamates, *Inorg. Chem.*, **1972**, 11(5), 1128.
- [131] B. Leon, D. K. Straub, Magnetism of tris(dithiocarbamato)iron(III) complexes derived from cyclic amines, *Inorg. Chim. Acta*, **1989**, 156, 13.
- [132] K. Nakamoto, J. Fujita, R. A. Condrate, Y. Morimoto, Infrared spectra of metal chelate compounds. IX. A normal coordinate analysis of dithiocarbamate complexes, *J. Chem. Phys.*, **1963**, 39, 423.
- [133] F. A. Cotton, J. A. McCleverty, Dimethyl- and Diethyldithiocarbamate complexes of some metal carbonyl compounds, *Inorg. Chem.*, **1964**, 3(10), 1398.
- [134] E. J. Kupchik, P. J. Calabretta, Some phenyltin, -lead, and antimony dithiocarbamates, *Inorg. Chem.*, **1965**, 4(7), 973.
- [135] H. K. Hall Jr., Field and inductive effects on the base strengths of amines, *J. Am. Chem. Soc.*, **1955**, 78, 2570.
- [136] H. K. Hall Jr., Correlation of the base strengths of amines, *J. Am. Chem. Soc.*, **1957**, 79, 5441.
- [137] H. K. Hall Jr., Steric effects on the base strengths of cyclic amines, *J. Am. Chem. Soc.*, **1957**, 79, 5444.
- [138] M. N. Kouodom, G. Boscutti, M. Celegato, M. Crisma, S. Sitran, D. Aldinucci, F. Formaggio, L. Ronconi, D. Fregona, Rational design of gold(III)-dithiocarbamate peptidomimetics for the targeted anticancer chemotherapy, *J. Inorg. Biochem.*, **2012**, 117, 248.
- [139] C. Nardon, F. Chiara, L. Brustolin, A. Gambalunga, F. Ciscato, A. Rasola, A. Trevisan, D. Fregona, Gold(III)-pyrrolidinedithiocarbamate derivative as antineoplastic agents, *Open Chem.*, **2015**, 4(2), 183.
- [140] C. Nardon, L. Brustolin, D. Fregona, Is matching ruthenium dithiocarbamate ligands a potent chemotherapeutic weapon in oncology?, *Fut. Med. Chem.*, **2016**, 8(2), 211.
- [141] R. D. Bereman, D. Nalewajek, Preparation of dithiocarbamate ligands derived from indole, indoline, carbazole, and imidazole and representative transition-element complexes, *Inorg. Chem.*, **1978**, 17(4), 1085.
- [142] O. Esenturk, R. A. Walker, Indoline: a versatile probe of specific and non-specific solvation forces, *Phys. Chem. Chem. Phys.*, **2003**, 5, 2020.
- [143] M. A. Slifkin, S. M. Ali, Protonation rate constants of proline, *J. Mol. Liq.*, **1984**, 29, 75.
- [144] H. J. Chen, L. E. Hakka, R. L. Hinman, A. J. Kresge, E. B. Whipple, The basic strength of carbazole. An estimate of the nitrogen basicity of pyrrole and indole, *J. Am. Chem. Soc.*, **1971**, 93, 5102.
- [145] R. L. Hinman, J. Lang, The protonation of indoles. Basicity studies. The dependence of acidity functions on indicator structure, *J. Am. Chem. Soc.*, **1964**, 86, 3796.
- [146] Y. Chiang, E. B. Whipple, The protonation of pyrroles, *J. Am. Chem. Soc.*, **1963**, 85, 2763.
- [147] C. N. R. Rao, R. Venkataraghavan, The C=S stretching frequency and the “-N-C=S bands” in the infrared, *Spectrochim. Acta*, **1962**, 18, 541.
- [148] F. Bonati, R. Ugo, Organotin(IV) N, N-disubstituted dithiocarbamates, *J. Organometal. Chem.*, **1967**, 10, 257.
- [149] R. Kellner, G. S. Nikolov, Far IR spectra of dithiocarbamate complexes – correlations with structure parameters, *J. Inorg. Nucl. Chem.*, **1981**, 43, 1183.
- [150] F. A. Cotton, G. Wilkinson, *Advanced inorganic chemistry*, 3<sup>rd</sup> ed., **1972**, John Wiley & Sons, New York (USA).
- [151] J. Emsley, “Ruthenium”, *Nature’s building blocks: an A-Z guide to the Elements*, **2003**, Oxford University Press, Oxford (UK).

- [152] C. Rao, D. Trivedi, Chemical and electrochemical depositions of platinum group metals and their applications, *Coord. Chem. Rev.*, **2005**, 249, 613.
- [153] S. Kanbara, M. Kitano, Y. Inoue, T. Yokoyama, M. Hara, H. Hosono, Mechanism switching of ammonia synthesis over Ru-loaded electrified catalyst at metal-insulator transition, *J. Am. Chem. Soc.*, **2015**, 137(45), 14517.
- [154] J. Wang, W. Zhu, X. He, S. Yang, Catalytic wet air oxidation of acetic acid over different ruthenium catalysts, *Catal. Commun.*, **2008**, 9(13), 2163.
- [155] M. Yoshimura, S. Tanaka, M. Kitamura, Recent topics in catalytic asymmetric hydrogenation of ketones, *Tetrahedron Lett.*, **2014**, 55(27), 3635.
- [156] I. Kostova, Ruthenium complexes as anticancer agents, *Curr. Med. Chem.*, **2006**, 13(9), 1085.
- [157] F. P. Dwyer, E. C. Gyarfás, W. P. Rogers, J. H. Koch, Biological activity of complex ions, *Nature*, **1952**, 170, 190.
- [158] *Handbook of Chemistry and Physics (85<sup>th</sup> ed.)*, **2004**, D. R. Lide ed., CRC Press, London (UK).
- [159] M. J. Clarke, S. Bitler, D. Rennert, M. Buchbinder, A. D. Kelman, Reduction and subsequent binding of ruthenium ions catalyzed by subcellular components, *J. Inorg. Biochem.*, **1980**, 12, 79.
- [160] S. K. Parks, N. M. Mazure, L. Counillon, J. Pouysségur, Hypoxia promotes tumor cell survival in acid conditions by preserving ATP levels, *J. Cell. Physiol.*, **2013**, 228(9), 1854.
- [161] P. Schluga, C. G. Hartinger, A. Egger, E. Reisner, M. Galansky, M. A. Jakupec, B. K. Keppler, Redox behavior of tumor-inhibiting ruthenium(III) complexes and effects of physiological reductants on their binding to GMP, *Dalton Trans.*, **2006**, 14, 1796.
- [162] M. J. Clarke, Ruthenium metallopharmaceuticals, *Coord. Chem. Rev.*, **2003**, 236, 209.
- [163] J. M. Rademaker-Lakhai, D. van den Bongard, D. Pluim, J. H. Beijnen, J. H. M. Schellens, A Phase I and pharmacological study with imidazolium-trans-DMSO-imidazole-tetrachlororuthenate, a novel ruthenium anticancer agent, *Clin. Can. Res.*, **2004**, 10(11), 3717.
- [164] S. Leijen, S. A. Burgers, P. Baas, D. Pluim, M. Tibben, E. van Werkhoven, E. Alessio, G. Sava, J. H. Beijnen, J. H. M. Schellens, Phase I/II study with ruthenium compound NAMI-A and gemcitabine in patients with non small cell lung cancer after first line therapy, *Invest. New Drugs*, **2015**, 33, 201.
- [165] M. Cocchiello, S. Zorzet, A. Sorc, G. Sava, Primary tumor, lung, and kidney retention and antimetastatic effect of NAMI-A following different routes of administration, *Invest. New Drugs*, **2003**, 21, 55.
- [166] A. Bergamo, G. Sava, Ruthenium anticancer compounds: myths and realities of the emerging metal-based drugs, *Dalton Trans.*, **2011**, 40, 7817.
- [167] P. Som, Z. H. Oster, K. Matsui, G. Guglielmi, B. R. Persson, M. L. Pellettieri, S. C. Srivastava, P. Richards, H. L. Atkins, A. B. Brill, <sup>97</sup>Ru-transferrin uptake in tumor and abscess, *Eur. J. Nucl. Med.*, **1983**, 8, 491.
- [168] J. C. Pessoa, I. Tomaz, Transport of therapeutic vanadium and ruthenium complexes by blood plasma components, *Curr. Med. Chem.*, **2010**, 17(31), 3701.
- [169] W. Guo, W. Zheng, Q. Luo, X. Li, Y. Zhao, S. Xiong, F. Wang, Transferrin serves as mediator to deliver organometallic Ru(II) anticancer complexes into cells, *Inorg. Chem.*, **2013**, 52(9), 5328.
- [170] K. Spiewak, G. Stochel, M. Brindell, Influence of redox activation of NAMI-A on affinity to serum proteins: transferrin and albumin. *J. Coord. Chem.*, **2015**, 68, 3181.
- [171] V. Brabec, DNA modifications by antitumor platinum and ruthenium compounds: their recognition and repair, *Prog. Nucleic Acid Res. Mol. Bio.*, **2002**, 71, 1.
- [172] J. Reedijk, Metal-ligand exchange kinetics in platinum and ruthenium complexes. *Plat Met. Rev.*, **2008**, 45(2), 2.
- [173] V. Brabec, O. Novakova, DNA binding mode of ruthenium complexes and relationship to tumor cell toxicity, *Drug Resist. Updates*, **2006**, 9, 111.

- [174] J. Iida, E. T. Bell-Loncella, M. L. Purazo, Y. Lu, J. Dorchak, R. Clancy, J. Slavik, M. L. Cutler, C. D. Shriver, Inhibition of cancer cell growth by ruthenium complexes, *J. Transl. Med.*, **2016**, 14, 48.
- [175] S. Betanzos-Lara, O. Novakova, R. J. Deeth, A. M. Pizarro, G. J. Clarkson, B. Liskova, V. Brabec, P. J. Sadler, A. Habtemariam, Bipyrimidine ruthenium(II) arene complexes: structure, reactivity and cytotoxicity, *J. Biol. Inorg. Chem.*, **2012**, 17(7), 1033.
- [176] W. Han Ang, A. Casini, G. Sava, P. J. Dyson, Organometallic ruthenium-based antitumor compounds with novel mode of action, *J. Organomet. Chem.*, **2011**, 696(5), 989.
- [177] Z. Adhireskan, G. E. Davey, P. Campomanes, M. Groessler, C. M. Clavel, H. Yu, A. A. Nazarov, C. H. F. Yeo, W. Han Ang, *et al.*, Ligand substitution between ruthenium-cymene compounds can control protein versus DNA targeting and anticancer activity, *Nat. Commun.*, **2014**, 5, 1.
- [178] R. Trondl, P. Heffeter, C. R. Kovol, M. A. Jakupec, W. Berger, B. K. Keppler, NKP-1339, the first ruthenium-based anticancer drug on the edge to clinical application, *Chem. Sci.*, **2014**, 5, 2925.
- [179] C. G. Hartinger, M. A. Jakupec, M. Zorbas-Seifried, M. Groessler, A. Egger, W. Berger, H. Zorbas, P. J. Dyson, B. K. Keppler, KP1019, a new redox-active anticancer agent – preclinical development and results of a clinical phase I study in tumor patients, *Chem. Biodiv.*, **2008**, 5, 2140.
- [180] L. Malatesta, Sui ditiocarbammati di rutenio, rodio e palladio, *Gazz. Chim. Ital.*, **1938**, 68, 195.
- [181] A. R. Hendrickson, J. M. Hop, R. L. Martin, Tris- and pentakis-dialkyldithiocarbamates of ruthenium,  $[\text{Ru}(\text{S}_2\text{CNR}_2)_3]^n$  and  $[\text{Ru}_2(\text{S}_2\text{CNR}_2)_5]^n$  ( $n = +1, 0$ , and  $-1$ ): chemical and electrochemical interrelations. *J. Chem. Soc., Dalton Trans.*, **1976**, 20, 2032.
- [182] L. Pignolet, D. J. Duffy, L. Que, Stereochemically nonrigid ruthenium(III) and cobalt(III) tris-chelate complexes, *J. Amer. Chem. Soc.*, **1973**, 95(1), 295.
- [183] L. Pignolet, Dynamic stereochemistry of tris-chelate complexes. IV. Crystal structure of tris(N,N-diethyldithiocarbamato)ruthenium(III), *Inorg. Chem.*, **1974**, 13, 2051.
- [184] B. M. Mattson, J. R. Himan, L. Pignolet, Oxidation of tris(N,N-disubstituted-dithiocarbamato) complexes of ruthenium(III). X-ray structure determination of bis(N,N-diethyldithiocarbamato)- $\mu$ -tris(N,N-diethyldithiocarbamato)-diruthenium(III) tetrafluoroborate,  $[\text{Ru}_2(\text{Et}_2\text{dtc})_5]\text{BF}_4$ , *Inorg. Chem.*, **1976**, 15, 564.
- [185] L. Giovagnini, S. Sitran, I. Castigliuolo, P. Brun, M. Corsini, P. Zanello, A. Zoleo, A. Maniero, B. Biondi, D. Fregona, Ru(III)-based compounds with sulfur donor ligands: synthesis, characterization, electrochemical behavior and anticancer activity, *Dalton Trans.*, **2008**, 37, 6699.
- [186] E. M. Nagy, C. Nardon, L. Giovagnini, L. Marchiò, A. Trevisan, D. Fregona, Promising anticancer mono- and dinuclear ruthenium(III) dithiocarbamate complexes: systematic solution studies, *Dalton Trans.*, 2011, 40, 11885.
- [187] E. M. Nagy, A. Pettenuzzo, G. Boscutti, L. Marchiò, L. Dalla Via, D. Fregona, Ruthenium (II/III)-based compounds with encouraging antiproliferative activity against non-small-cell lung cancer, *Chem. Eur. J.*, **2012**, 12, 14464.
- [188] B. R. Cameron, M. C. Darkes, I. R. Baird, R. T. Skerlj, Z. L. Santucci, S. P. Fricker, Ruthenium(III) triazacyclononane dithiocarbamate, pyridinecarboxylate, or aminocarboxylate complexes as scavengers of nitric oxide, *Inorg. Chem.*, 2003, 42, 4102.
- [189] C. J. Marmion, B. R. Cameron, C. Mulcahy, S. P. Fricker, Ruthenium as an effective nitric oxide scavenger, *Curr. Top. Med. Chem.*, 2004, 4, 1585.
- [190] N. B. Janakiram, R. Chinthalapallay, Nitric oxide: immune modulation of tumor growth, in *Nitric oxide and cancer: pathogenesis and therapy*, **2015**, B. Bonavida ed., Springer, San Diego (USA).
- [191] L. Giovagnini, E. Mancinetti, L. Ronconi, S. Sitran, L. Marchiò, I. Castigliuolo, P. Brun, A. Trevisan, D. Fregona, Preliminary chemico-biological studies on Ru(III) compounds with S-methyl pyrrolidine/dimethyl dithiocarbamate, *J. Inorg. Biochem.*, **2009**, 103, 774.
- [192] C. Mari, V. Pierroz, S. Ferrari, G. Gasser, Combination of Ru(II) complexes and light: new frontiers in cancer therapy., *Chem. Sci.*, **2015**, 6, 2660.

- [193] C. Mari, G. Gasser, Lightening up ruthenium complexes to fight cancer?, *Chimia*, **2015**, 69(4), 176.
- [194] N. J. Wheate, J. G. Collins, Multi-nuclear platinum complexes as anticancer drugs, *Coord. Chem. Rev.*, **2003**, 241, 133.
- [195] C. G. Hartinger, A. D. Phillips, A. A. Nazarov, Polynuclear ruthenium, osmium and gold complexes. The quest for innovative anticancer chemotherapeutics, *Curr. Top. Med. Chem.*, **2011**, 11, 2688.
- [196] C. S. Allardyce, P. J. Dyson, Metal-based drugs that break the rules, *Dalton Trans.*, **2016**, 45, 3201.
- [197] X. Li, K. Heimann, X. T. Dinh, F. R. Keene, J. G. Collins, Biological processing of dinuclear ruthenium complexes in eukaryotic cells, *Mol. BioSyst.*, **2016**, 10, 3032.
- [198] K. T. Stanislaw, K. Kurzak, S. L. Randzio, Reactions of commercial ruthenium chlorides with O-donor ligands. Reaction with water: UV-Vis investigation of soluble products; analysis, thermogravimetry and IR study of precipitated solids, *Transition Met. Chem.*, **1995**, 20, 330.
- [199] A. R. Hendrickson, R. L. Martin, D. Taylor, A binuclear rhodium(III) dithiocarbamate complex,  $[\text{Rh}_2(\text{Me}_2\text{NCS}_2)_5]\text{BF}_4$ , *Aust. J. Chem.*, **1976**, 29, 269.
- [200] C. L. Raston, A. H. White, Structural studies in the ruthenium-dithiocarbamate system. Part I. Crystal structure of tris(morpholydithiocarbamato)ruthenium(III)-2.5 chloroform, *J. Chem. Soc. Dalton Trans.*, **1975**, 22, 2405.
- [201] C. Preti, G. Tosi, P. Zannini, Synthesis and characterization of ruthenium dithiocarbamate complexes, *J. Inorg. Nucl. Chem.*, **1979**, 41, 485.
- [202] F. Rastrelli, A. Bagno, Predicting the  $^1\text{H}$  and  $^{13}\text{C}$  NMR spectra of paramagnetic Ru(III) complexes by DFT, *Magn. Reson. Chem.*, **2010**, 48, S132.
- [203] M. C. Palazzotto, D. J. Duffy, B. L. Edgar, L. Que Jr., L. H. Pignolet, Dynamic stereochemistry of tris-chelate complexes. I. Tris(dithiocarbamato) complexes of iron, cobalt, and rhodium, *J. Am. Chem. Soc.*, **1973**, 95(14), 4537.
- [204] L. Que Jr., L. H. Pignolet, Dynamic stereochemistry of tris-chelate complexes. II. Tris(dithiocarbamato) complexes of manganese(III), vanadium(III), chromium(III), gallium(III), and indium(III), *Inorg. Chem.*, **1974**, 13(2), 351.
- [205] D. J. Duffy, L. H. Pignolet, Dynamic stereochemistry of tris-chelate complexes. III. Tris(dithiocarbamato) complexes of ruthenium(III), *Inorg. Chem.*, **1974**, 13(9), 2045.
- [206] L. H. Pignolet, Dynamic stereochemistry of tris-chelate complexes. IIII. Crystal structure of tris(N,N-diethyldithiocarbamato)ruthenium(III), *Inorg. Chem.*, **1974**, 13(9), 2051.
- [207] A. Rodger, B. F. G. Johnson, Which is more likely: the Ray-Dutt twist or the Bailar Twist?, *Inorg. Chem.*, **1988**, 27(18), 3061.
- [208] H. S. Rzepa, M. E. Cass, In search of the Bailar and Ray-Dutt twist mechanism that racemize chiral trischelates: a computational study of Sc(III), Ti(IV), Co(III), Zn(II), Ga(III), and Ge(IV) complexes of a ligand analogue of acetylacetonate, *Inorg. Chem.*, **2007**, 46(19), 8024.
- [209] D. A. Brown, W. K. Glass, M. A. Burke, The general use of IR spectral criteria in discussion of the bonding and structure of metal dithiocarbamates, *Spectrochim. Acta Mol. Biomol. Spectrosc.*, **1976**, 32, 137.
- [210] F. Forghieri, G. Graziosi, C. Preti, G. Tosi, Cyclic substituted dithiocarbamates as ligands. Vanadium(III) and oxovanadium(IV, V) complexes, *Transition Met. Chem.*, **1983**, 8, 372.
- [211] R. D. Bereman, M. R. Churchill, D. Nalewajek, Coordination chemistry of new sulfur-containing ligands. 16. Crystal and molecular structure of tris(pyrrole-N-carbodithioato)iron(III)-hemikis(dichloromethane),  $\text{Fe}(\text{S}_2\text{CNC}_4\text{H}_4)_3 \cdot 0.5\text{CH}_2\text{Cl}_2$ , a low spin dithiocarbamate complex of iron(III), *Inorg. Chem.*, **1979**, 18, 3112.
- [212] C. O'Connor, J. D. Gilbert, G. Wilkinson, Unidentate dithiocarbamate complexes of rhodium and iron: dithiocarbamate and dithiocarbonate complexes of ruthenium, *J. Chem. Soc. (A)*, **1969**, 0, 84.
- [213] L. Ronconi, L. Giovagnini, C. Marzano, F. Bettio, R. Graziani, G. Pilloni, D. Fregona, Gold dithiocarbamate derivative as potential antineoplastic agents: design, spectroscopic properties, and in vitro antitumor activity, *Inorg. Chem.*, **2005**, 44(6), 1867.

- [214] G. E. Manoussakis, C. A. Bolos, Synthesis and characterization of a series of new mixed ligand complexes of manganese(III), iron(III), nickel(II), copper(II) and zinc(II) with Schiff bases of N,N-diethylamino-dithiocarbamate as ligands, *Inorg. Chim. Acta*, **1985**, 108, 215.
- [215] C. K. Jorgensen, Absorption spectra of transition group complexes of Sulphur-containing ligands, *J. Inorg. Nucl. Chem.*, **1952**, 24, 1571.
- [216] J. F. Endicott, M. J. Uddin, Correlations of optical and thermal charge transfer, *Coord. Chem. Rev.*, **2001**, 219-221, 287.
- [217] S. F. A. Kettle, *Physical Inorganic Chemistry: a coordination chemistry approach*, **2004**, Spectrum Academic Publishers, Oxford (UK).
- [218] M. Jo, J. Seo, M. L. Seo, K. S. Choi, S. K. Cha, L. F. Lindoy, S. S. Lee, Donor-set-induced coordination sphere and oxidation-state switching in the copper complexes of O<sub>2</sub>S<sub>2</sub>X (X = S, O and NH) macrocycles, *Inorg. Chem.*, **2009**, 48(17), 8186.
- [219] M. C. Linder, Ceruloplasmin and other copper binding components of blood plasma and their functions: an update, *Metallomics*, **2016**, 8(9), 887.
- [220] M. Gerloch, The sense of Jahn-Teller distortions in octahedral Cu(II) and other transition-metal complexes, *Inorg. Chem.*, **1981**, 20(2), 638.
- [221] S. Kida, Y. Nishida, M. Sakamoto, Absorption band in the near-ultraviolet region observed for binuclear copper(II) complexes, *Bull. Chem. Soc. Jpn.*, **1973**, 46(8), 2428.
- [222] J. Gažo, I.B. Bersuker, J. Garaj, M. Kabešová, J. Kohout, H. Langfelderová, M. Melník, M. Serator, F. Valach, Plasticity of the coordination sphere of copper(II) complexes, its manifestation and causes, *Coord. Chem. Rev.*, **1976**, 19(3), 253.
- [223] A. K. Boal, A. C. Rosenzweig, Structural biology of copper trafficking, *Chem. Rev.*, **2009**, 109, 4760.
- [224] R. R. Crichton, J. L. Pierre, Old iron, young copper: from Mars to Venus, *BioMetals*, **2001**, 14, 99.
- [225] W. Kaim, J. Rall, Copper- A modern bioelement, *Angew. Chem. Int. Ed. Engl.*, **1996**, 35, 43.
- [226] S. Samantha, N. Lehnert, Metalloproteins: a switch for blue copper proteins?, *Nat. Chem.*, **2016**, 8, 639.
- [227] N. Kitajima, Y. Moro-oka, Copper-dioxigen complexes. Inorganic and bioinorganic perspectives, *Chem. Rev.*, **1994**, 94(3), 737.
- [228] G. A. Hamilton, P. K. Adolf, J. De Jersey, G. C. DuBois, G. R. Dyrkacz, R. D. Libby, Trivalent copper, superoxide, and galactose oxidase, *J. Am. Chem. Soc.*, **1978**, 100, 1899.
- [229] F. Himo, L. A. Eriksson, F. Maseras, P. E. M. Siegbahn, Catalytic mechanism of galactose oxidase: a theoretical study, *J. Am. Chem. Soc.*, **2000**, 122, 8031.
- [230] E. I. Solomon, D. E. Heppner, E. M. Johnston, J. W. Ginsbach, J. Cirera, M. Qayyum, M. T Kieber-Emmons, C. H. Kjaergaard, R. G. Hadt, L. Tian, Copper active sites in biology, *Chem. Rev.*, **2014**, 114, 3659.
- [231] S. Lutsenko, N. L. Barnes, M. Y. Bartee, O. Y. Dmitriev, Function and regulation of human copper-transporting ATPases, *Physiol. Rev.*, **2007**, 87(3), 1011.
- [232] M. Bost, S. Houdart, M. Oberli, E. Kalonji, J.-F. Huneau, I. Margaritis, Dietary copper and human health: current evidence and unresolved issues, *J. Trace Elem. Med. Biol.*, **2016**, 35, 107.
- [233] E. Gaggelli, H. Kozłowski, D. Valensin, G. Valensin, Copper Homeostasis and Neurodegenerative Disorders (Alzheimer's, Prion, and Parkinson's Diseases and Amyotrophic Lateral Sclerosis), *Chem. Rev.*, **2006**, 106, 1995.
- [234] J. F. B. Mercer, The molecular basis of Copper-Transport diseases, *Trends Mol. Med.*, **2001**, 7(2), 64.
- [235] H. Kim, X. Wu, J. Lee, SLC31 (CTR) family of copper transporters in health and disease, *Mol. Aspect. Med.*, **2013**, 34, 561.
- [236] L. Banci, I. Bertini, F. Cantini, S. C. Baffoni, Cellular copper distribution: a mechanistic system biology approach, *Cell. Mol. Life Sci.*, **2010**, 67, 2563.
- [237] C. J. De Feo, S. G. Aller, G. S. Siluvai, N. J. Blackburn, V. M. Unger, Three-dimensional structure of the human copper transporter hCTR1, *Proc. Natl. Acad. Sci. USA*, **2009**, 106, 4237.



- [238] J. F. Eisses, J. H. Kaplan, The mechanism of copper uptake mediated by human CTR1: a mutational analysis, *J. Biol. Chem.*, **2005**, 280, 37159.
- [239] X. Wu, D. Sinani, H. Kim, J. Lee, Copper transport activity of yeast Ctr1 is downregulated via its C terminus in response to excess copper, *J. Biol. Chem.*, **2009**, 284, 4112.
- [240] P. J. Schmidt, C. Kunst, V. C. Culotta, Copper activation of superoxide dismutase 1 (SOD1) *in vivo*, *J. Biol. Chem.*, **2000**, 275, 33771.
- [241] D. Horn, A. Barrientos, Mitochondrial copper metabolism and delivery to cytochrome *c* oxidase, *IUBMB Life*, **2008**, 60, 421.
- [242] G. Inesi, R. Pilankatta, F. Tadini-Buoninsegni, Biochemical characterization of P-type copper ATPases, *Biochem. J.*, **2014**, 463, 167.
- [243] B. Ruttakay-Nedecky, L. Nejdil, J. Gumulec, O. Zitka, M. Masarik, T. Eckschlagger, M. Stiborova, V. Adam, R. Kizek, The role of metallothionein in oxidative stress, *Int. J. Mol. Sci.*, **2013**, 14, 6044.
- [244] Z. Tumer, An overview and update of ATP7A leading to Menkes disease and occipital horn syndrome, *Hum. Mutat.*, **2013**, 34, 417.
- [245] L. T. Braiterman, A. Murthy, S. Jayakanthan, L. Nyasae, E. Tzeng, G. Gromadzka, T. B. Woolf, S. Lutsenko, A. L. Hubbard, Distinct phenotype of a Wilson disease mutation reveals a novel trafficking determinant in the copper transporter ATP7B, *Proc. Natl. Acad. Sci. USA*, **2014**, 111, E1364.
- [246] M. L. Turski, D. J. Thiele, New roles for copper metabolism in cell proliferation, signaling and disease, *J. Biol. Chem.*, **2009**, 284, 717.
- [247] M. R. Bleackley, R. T. A. MacGillivray, Transition metal homeostasis: from yeast to human disease, *BioMetals*, **2011**, 24(5), 785.
- [248] M. Zowczak, M. Iskra, L. Torlinski, S. Cofta, Analysis of serum copper and zinc concentrations in cancer patients, *Biol. Trace Elem. Res.*, **2001**, 82, 1.
- [249] M. Denoyer, S. Masaldan, S. La Fontaine, M. A. Carter, Targeting copper in cancer therapy: "Copper that cancer", *Metallomics*, **2015**, 7, 1459.
- [250] P. Carmeliet, Angiogenesis in life, disease and medicine, *Nature*, **2005**, 438, 932.
- [251] Y. Jiang, C. Reynolds, C. Xiao, W. Feng, Z. Zhou, W. Rodriguez, S. C. Tyagi, J. W. Eaton, J. T. Saari, Y. J. Kang, Dietary copper supplementation reverses hypertrophic cardiomyopathy induced by chronic pressure overload in mice, *J. Exp. Med.*, **2007**, 204(3), 657.
- [252] Q. Li, X. Ding, Y. J. Kang, Copper promotion of angiogenesis in isolated rat aortic ring: role of vascular endothelial growth factor, *J. Nut. Bio.*, **2014**, 25, 44.
- [253] D. C. Rigracciolo, A. Scarpelli, R. Lappano, A. Pisano, M. F. Santolla, P. De Marco, F. Cirillo, A. R. Cappello, V. Dolce, A. Belfiore, M. Maggiolini, E. M. De Francesco, Copper activates HIF-1 $\alpha$ /GPER/VEGF signaling in cancer cells, *Oncotarget*, **2015**, 6, 34158.
- [254] L. Finney, S. Mandava, L. Ursos, W. Zhang, D. Rodi, S. Vogt, D. Legnini, J. Maser, F. Ikpatt, O. I. Olopade, D. Glesne, X-ray fluorescence microscopy reveals large-scale relocalization and extracellular translocation of cellular copper during angiogenesis, *Proc. Natl. Acad. Sci. USA*, **2007**, 104, 2247.
- [255] S. Tardito, L. Marchiò, Copper compounds in anticancer strategies, *Curr. Med. Chem.*, **2009**, 16, 1325.
- [256] D. Krajčiová, M. Melníka, E. Havráneka, A. Forgáčsová, P. Mikušab, Copper compounds in nuclear medicine and oncology, *J. Coord. Chem.*, **2014**, 1.
- [257] S. K. Das, K. Ray, Wilson's disease: an update, *Nat. Clin. Pract. Neurol.*, **2006**, 2, 482.
- [258] J. Yoshii, H. Yoshiji, S. Kuriyama, Y. Ikenaka, R. Noguchi, H. Okuda, H. Tsujinoue, T. Nakatani, H. Kishida, D. Nakae, D. E. Gomez, M. S. De Lorenzo, A. M. Teira, H. Fukui, The copper-chelating agent, trientine, suppresses tumor development and angiogenesis in the murine hepatocellular carcinoma cells, *Int. J. Cancer*, **2001**, 94, 768.

- [259] Q. Pan, D. T. Rosenthal, L. Bao, C. G. Kleer, S. D. Merajver, Antiangiogenic tetrathiomolybdate protects against Her2/neu-induced breast carcinoma by hypoplastic remodeling of the mammary gland, *Clin. Cancer Res.*, **2009**, 15(23), 7441.
- [260] S. Brem, S. A. Grossman, K. A. Carson, P. New, S. Phuphanich, J. B. Alavi, T. Mikkelsen, J. D. Fisher, Phase 2 trial of copper depletion and penicilamine as antioangiogenesis therapy of glioblastoma, *Neuro-Oncol.*, **2005**, 7, 246.
- [261] C. Santini, M. Pellei, V. Gandin, M. Porchia, F. Tisato, C. Marzano, Advances in copper complexes as anticancer agents, *Chem. Rev.*, **2014**, 114, 815.
- [262] L. Tjioe, A. Meininger, T. Joshi, L. Spiccia, B. Graham, Efficient plasmid DNA cleavage by copper(II) complexes of 1,4,7-triazacyclononane ligands featuring xylyl-linked guanidinium groups, *Inorg. Chem.*, **2011**, 50(10), 4327.
- [263] H.-L. Seng, W.-S. Wang, S.-M. Kong, A. H.-K. Alan Ong, Y.-F. Win, R. N. Z. Raja Abd. Rahman, M. Chikira, W.-K. Leong, M. Ahmad, A. S.-B. Khoo, C.-H. Ng, Biological and cytoselective anticancer properties of copper(II)-polypyridil complexes modulated by auxiliary methylated glycine ligand, *BioMetals*, **2012**, 25, 1061.
- [264] B. M. Zeglis, V. Divilov, J. S. Lewis, Role of metalation in the Topoisomerase  $\alpha$  inhibition and antiproliferation activity of a series of  $\alpha$ -heterocyclic- $N^4$ -substituted thiosemicarbazones and their Cu(II) complexes, *J. Med. Chem.*, **2011**, 54, 2391.
- [265] V. Milacic, D. Chen, L. Giovagnini, A. Diez, D. Fregona, Q. P. Dou, Pyrrolidine dithiocarbamate-zinc(II) and copper(II) complexes induce apoptosis in tumor cells by inhibiting the proteasomal activity, *Toxicol. Appl. Pharmacol.*, **2008**, 231, 24.
- [266] P. T. Beurskens, J. A. Cras, J. J. Steggerda, Structures and properties of dibromo-N,N-di-n-buthyldithiocarbamate complexes of copper(III) and gold(III), *Inorg. Chem.*, **1968**, 7(4), 1968.
- [267] A. R. Hendrickson, R. L. Martin, N. M. Rhode, Dithiocarbamates of Cu(I), Cu(II) and Cu(III). An electrochemical study, *Inorg. Chem.*, **1976**, 15(9), 2116,
- [268] J. A. Cras, J. Willemsse, A. W. Gal, B. G. M. C. Hummelink-Peters, Preparation, structure and properties of compounds containing the dipositive tri-copper hexa (N,N-di-n-buthyldithiocarbamate) ion, compounds with copper in the oxidation states II and III, *Recl. Trav. Chim. Pays-Bas*, **1973**, 92, 641.
- [269] P. J. H. A. M van de Leemput, J. Willemsse, J. A. Cras, Preparation and properties of copper dithiocarbamate complexes with copper in the oxidation states I and III, *Recl. Trav. Chim. Pays-Bas*, **1976**, 95, 53.
- [270] C. S. I. Nobel, M. Kimland, B. Lind, S. Orrenius, A. F. G. Slater, Dithiocarbamates induce apoptosis in thymocytes by raising the intracellular level of redox-active copper, *J. Biol. Chem.*, **1995**, 270, 26202.
- [271] H. Schenk, M. Klein, W. Erdbrugger, W. Droge, K. Schulze-Osthoff, Distinct effects of thioredoxin and antioxidants on the activation of transcription factors NK-kappa B and AP-1, *Proc. Natl. Acad. Sci. USA*, **1994**, 91, 1972.
- [272] H.-H. Wu, J. A. Thomas, J. Momand, p53 protein oxidation in cultured cells in response to pyrrolidine dithiocarbamate: a novel method for relating the amount of p53 oxidation *in vivo* to the regulation of p53-responsive genes, *Biochem. J.*, **2000**, 351, 87.
- [273] S. Furuta, F. Ortiz, X. Zhu Sun, H.-H. Wu, A. Mason, J. Momand, Copper uptake is required for pyrrolidine dithiocarbamate-mediated oxidation and protein level increase of p53 in cells, *Biochem. J.*, **2002**, 365, 639.
- [274] W. Erl, C. Weber, G. K. Hansson, Pyrrolidine dithiocarbamate-induced apoptosis depends on cell type, density and the presence of  $\text{Cu}^{2+}$  and  $\text{Zn}^{2+}$ , *Am. J. Phys. Cell Phys.*, **2000**, 278, C1116.
- [275] D. Cen, D. Brayton, B. Shahandeh, F. L. Meyskens, P. J. Farmer, Disulfiram facilitates intracellular Cu uptake and induces apoptosis in human melanoma cells, *J. Med. Chem.*, **2004**, 47, 6914.
- [276] K. G. Daniel, D. Chen, S. Orlu, Q. C. Cui, F. R. Miller, Q. P. Dou, Clotrimazole and pyrrolidine dithiocarbamate complex with copper to form proteasome inhibitors and apoptosis inducers in human breast cancer cells, *Breast Cancer Res.*, **2005**, 7, R897.
- [277] L. Giovagnini, S. Sitran, M. Montopoli, L. Caparrotta, M. Corsini, C. Rosani, P. Zanello, Q. Ping Dou, D. Fregona, Chemical and biological profiles of novel copper(II) complexes containing S-donor ligands for the treatment of cancer, *Inorg. Chem.*, **2008**, 47(14), 6336.

- [278] B. Akella Radha, M. Seshasayee, G. Aravamudan, Structures of bis(piperidine-1-dithiocarbamato)nickel(II) and bis(8piperidine-1-dithiocarbamato)copper(II), *Acta. Cryst.*, **1988**, C44, 1378.
- [279] B. Elliott, K. Yang, A. M. Rao, H. D. Arman, W. T. Pennington, L. Echegoyen, A reassignment of the EPR spectra previously attributed to Cu@C<sub>60</sub>, *Chem. Comm.*, **2007**, 20, 2083.
- [280] D. F. Schoener, M. A. Olsen, P. G. Cummings, C. Basic, Electrospray ionization mass spectrometry: principles and clinical applications, *Clin. Biochem. Rev.*, **2003**, 24, 3.
- [281] N. N. Murthy, K. D. Karlin, I. Bertini, C. Luchinat, NMR and electronic relaxation in paramagnetic dicopper(II) compounds, *J. Am. Chem. Soc.*, **1997**, 119, 2156.
- [282] K. A. Hotzer, A. Klingert, T. Klumpp, E. Krissinel, D. Burssner, U. E. Steiner, Temperature-dependent spin relaxation: a major factor in electron backward transfer following the quenching of \*Ru(bpy)<sub>3</sub>2+ by methyl viologen, *J. Phys. Chem. A*, **2002**, 106, 2207.
- [283] I. Bertini, A. dei, A. Scozzafava, Proton magnetic resonance spectra of bis(N-alkylsalicylaldiminato)copper(II) complexes, *Inorg. Chem.*, **1975**, 14(7), 1526.
- [284] B. J. Corden, P. H. Rieger, Electron spin resonance study of the kinetics and equilibrium of adduct formation by copper(II) dibutylidithiocarbamate with nitrogen bases, *Inorg. Chem.*, **1971**, 10(2), 263.
- [285] B. I. Libutt, B. B. Wayland, A. F. Garito, Axial ligation of copper(II) bis(t-butylacetoacetate) by pyridine donors. Thermodynamics and solvent effect, *Inorg. Chem.*, **1969**, 8(7), 1510.
- [286] H. O. Desseyn, A. C. fabretti, F. Forghieri, C. Preti, Isotopic infrared study of some nickel(II) and copper(II) complexes containing heterocyclic dithiocarbamate ligands, *Spectrochim. Acta A*, **1985**, 41(9), 1105.
- [287] C. Furlani, G. Polzonetti, C. Preti, G. Tosi, XPS of coordination compounds: data on the electronic structure of a series of Cu(II) N,N'-cyclic substituted dithiocarbamates, *Inorg. Chim. Acta*, **1983**, 73, 105.
- [288] B. Morzyk-Ociepa, K. Dysz, I. Turowska-Tyrk, D. Michalska, New trans-dichloropalladium(II) complexes of 7-azaindole: crystal and molecular structures, FT-IR, FT-Raman and DFT studies, *J. Mol. Struct.*, **2016**, 1103, 202.
- [289] F. Takami, S. Wakahara, T. Maeda, The UV spectra and dissociation constants of some dithiocarbamates (1), *Tetrahedron Lett.*, 1971, 12(28), 2645.
- [290] D. Oktavec, J. stefanec, B. Siles, E. Beinrohr, V. Konecny, J. Garaj, The electronic spectra of the bis(8dithiocarbamate) chelates of Cu(II) and Zn(II), *Collect. Czech. Chem. Commun.*, 1982, 47, 2867.
- [291] M. V. Vedis, G. H. Schreiber, T. E. Gough, G. U. Palenik, Jahn-Teller distortions in octahedral copper(II) complexes, *J. Am. Chem. Soc.*, **1969**, 91(7), 1859.
- [292] S. Choi, E. R. Menzel, J. R. Wasson, Electronic spectra of copper(II) dithiocarbamates, *J. Inorg. Nucl. Chem.*, **1977**, 39, 417.
- [293] R. L. Carlin, Electronic spectra of transition metal complexes, *J. Chem. Ed.*, **1963**, 40(3), 135.
- [294] H. G. Raubenheimer, H. Schmidbaur, The late start and amazing upswing in gold chemistry, *J. Chem. Ed.*, **2014**, 91, 2014.
- [295] H. Schmidbaur, S. Cronje, B. Djordjevic, O. Schuster, Understanding gold chemistry through relativity, *Chem. Phys.*, **2005**, 311, 151.
- [296] K. S. Pitzer, Relativistic effects on chemical properties, *Acc. Chem. Res.*, **1979**, 12(8), 271.
- [297] P. Pyykko, J.-P. Desclaux, Relativity and the periodic system of elements, *Acc. Chem. Res.*, **1979**, 12(8), 276.
- [298] M. Seth, M. Dolg., P. Fulde, P. Schwerdtfeger, Lanthanide and actinide contractions: relativistic and shell structure effects, *J. Am. Chem. Soc.*, **1995**, 117(24), 6597.
- [299] E. van Lenthe, J. G. Snijders, E. J. Baerends, The zero-order regular approximation for relativistic effects: the effect of spin-orbit coupling in closed shell molecules, *J. Chem. Phys.*, **1996**, 105(15), 6505.
- [300] M. Jansen, Effect of relativistic motion of electrons on the chemistry of gold and platinum, *Solid State Sci.*, **2005**, 7, 1464.
- [301] P. Pyykko, Theoretical chemistry of gold, *Angew. Chem. In. Ed.*, **2004**, 43, 4412.

- [302] D. C. Calabro, B. A. Harrison, G. Todd Palmer, M. K. Moguel, R. L. Rebbert, J. L. Burmeister, Thiocyanation, selenocyanation, and halogenation reactions of dithiocarbamate complexes of gold(I) and silver(I). Generation of gold(II) and silver(II) complexes, *Inorg. Chem.*, **1981**, 20, 4311.
- [303] A. Laguna, M. Laguna, Coordination chemistry of gold(II) complexes, *Coord. Chem. Rev.*, **1999**, 193-195, 837.
- [304] Z. Huaizhi, N. Yuantao, China's ancient gold drugs, *Gold Bull.*, **2001**, 34(1), 24.
- [305] G. J. Higby, Gold in medicine. A review of its use in the west before 1900, *Gold Bull.*, **1982**, 15(4), 130.
- [306] T. G. Benedek, The history of gold therapy for tuberculosis, *J. Hist. Med. Allied. Sci.*, **2004**, 59, 50.
- [307] A. R. Sannella, a. Casini, C. Gabbiani, L. Messori, A. R. Bilia, F. F. Vincieri, G. Majori, C. Severini, New uses for old drug. Auranofin, a clinically established antiarthritic metallodrug, exhibits antimalarial effects in vitro: mechanistic and pharmacological implications, *FEBS Lett.*, **2008**, 582, 844.
- [308] A. Chircorian, A. M. Barrios, Inhibition of lysosomal cysteine by chrysotherapeutic compounds: a possible mechanism for the antiarthritic activity of Au(I), *Bioorg. Med. Chem. Lett.*, **2004**, 14, 5113.
- [309] E. Weidauer, Y. Yasuda, B. K. Biswal, M. Cherny, M. N. James, D. Bromme, Effect of disease modifying anti-rheumatic drugs (DMARDs) on the activities of rheumatoid arthritis-associated cathepsins K and S, *Biol. Chem.*, **2007**, 388, 331.
- [310] S. Gromer, L. D. Arscott, C. H. Williams Jr., R. H. Schirmer, K. Becker, Human placenta thioredoxin reductase. Isolation of the selenoenzyme, steady state kinetics, and inhibition by therapeutic gold compounds, *J. Biol. Chem.*, **1998**, 273, 20096.
- [311] K. Becker, S. Gromer, R. H. Schirmer, S. Muller, Thioredoxin reductase as a pathophysiological factor and drug target, *Eur. J. Biochem.*, **2000**, 267(20), 6118.
- [312] A. Bindoli, M. P. Rigobello, G. Scutari, C. Gabbiani, A. Casini, L. Messori, Thioredoxin reductase: a target for gold compounds acting as potential anticancer drugs, *Coord. Chem. Rev.*, **2009**, 253, 11-12, 1692.
- [313] I. Ott, On the medicinal chemistry of gold complexes as anticancer agents, *Coord. Chem. Rev.*, **2009**, 253, 1670.
- [314] T. Zou, C. T. Lum, C.-N. Lok, J.-J. Zhang, C.-M. Che, Chemical biology of anticancer gold(III) and gold(I) complexes, *Chem. Soc. Rev.*, **2015**, 44, 8786.
- [315] C. Nardon, N. Pettenuzzo, D. Fregona, Gold complexes for therapeutic purpose: an updated patent review (2010-2015), *Curr. Med. Chem.*, **2016**, 23(29), 3374.
- [316] M. Stallings-Mann, L. Jamieson, R. P. Regala, C. Weems, N. R. Murray, A. P. Fields, A novel small-molecule inhibitor of protein kinase C<sub>γ</sub> blocks transformed growth of non-small-cell lung cancer cells, *Cancer Res.*, **2006**, 66, 1767.
- [317] A. F. Oryschak, F. N. Ghadially, Aurosome formation in articular tissues after parental administration of gold, *J. Pathol.*, **1976**, 119, 183.
- [318] F. N. Ghadially, The aurosome, *J. Rheumatol. Suppl.*, **1979**, 5, 45.
- [319] S. J. Berners-Price, A. Filipovska, Gold compounds as therapeutic agents for human disease, *Metallomics*, **2011**, 3, 863.
- [320] B. Bertrand, A. Casini, A golden future in medicinal inorganic chemistry: the promise of anticancer gold organometallic compounds, *Dalton Trans.*, **2014**, 43, 4209.
- [321] J. Henry-Mowatt, C. Dive, J.-C. Martinou, D. James, Role of mitochondrial membrane permeabilization in apoptosis and cancer, *Oncogene*, **2004**, 23, 2850.
- [322] V. Andemark, K. Goke, M. Kokoschka, M. A. Abu el Maaty, C. T. Lum, T. Zou, R. Wai-Tin Sun, E. Aguilo, L. Oehninger, L. Rodriguez, H. Bunjes, S. Wolfi, C.-M. Che, I. Ott, Alkynyl gold(I) phosphane complexes: evaluation of structure-activity-relationship for the phosphane ligands, effects on key signaling proteins and preliminary in-vivo studies with a nanoformulated complex, *J. Inorg. Biochem.*, **2016**, 160, 140.
- [323] K. Yan, C.-N. Lok, K. Bierla, C.-M. Che, Gold(I) complexes of N,N'-disubstituted cyclic thiourea with in vitro and in vivo anticancer properties – potent tight-binding inhibition of thioredoxin reductase, *Chem. Commun.*, **2010**, 46, 7691.
- [324] P. I. da Silva Maia, V. M. Deflon, U. Abram, Gold(III) complexes in medicinal chemistry, *Fut. Med. Chem.*, **2014**, 6(13), 1515.

- [325] A. de Almeida, L. Oliveira, J. Correia, G. Soveral, A. Casini, Emerging protein targets for metal-based pharmaceutical agents: an update, *Coord. Chem. Rev.*, **2013**, 257, 2689.
- [326] G. Marcon, S. Carotti, M. Coronello, L. Messori, E. Mini, P. Orioli, T. Mazzei, M. A. Cinellu, G. Minghetti, Gold(III) complexes with pipyridil ligands: solution chemistry, cytotoxicity, and DNA binding properties, *J. Med. Chem.*, **2002**, 45, 1672.
- [327] C. T. Lum, A. S. Wong, M. C. Lin, C.-M. Che, R. W. Sun, A gold(III) porphyrin complex as an anti-cancer candidate to inhibit growth of cancer-stem cells, *Chem. Commun.*, **2013**, 49(39), 4364.
- [328] R. Sun, C.-N. Lok, T. Fong, C. Li, Z. Fan Yang, T. Zou, A. Siu, C.-M. Che, A dinuclear cyclometalated gold(III)-phosphine complex targeting thioredoxin reductase inhibits hepatocellular carcinoma in vivo, *Chem. Sci.*, **2013**, 4, 1979.
- [329] R. G. Buckley, A. M. Elsome, S. P. Fricker, G. R. Henderson, B. R. C. Theobald, R. V. Parish, B. P. Howe, L. R. Kelland, Antitumor properties of some 2-[(dimethylamino)methyl]phenylgold(III) complexes, *J. Med. Chem.*, **1996**, 39, 5208.
- [330] T. Zou, C. T. Lum, S. Chui, C.-M. Che, Gold(III) complexes containing N-heterocyclic carbene ligands: thiol "switch-on" fluorescent probes and anticancer agents, *Angew. Chem. Int. Ed.*, **2013**, 52, 2930.
- [331] C. Nardon, G. Boscutti, D. Fregona, Beyond platinum: gold complexes as anticancer agents, *Anticancer Res.*, **2014**, 34(1), 487.
- [332] C. Nardon, S. M. Schmitt, H. Yang, J. Zuo, D. Fregona, Q. P. Dou, Gold(III)-dithiocarbamate peptidomimetics in the forefront of the targeted anticancer therapy: preclinical studies against human breast neoplasia, *Plos ONE*, **2014**, 9, e84248.
- [333] L. Ronconi, D. Aldinucci, Q. P. Dou, D. Fregona, Latest insight into the reactivity of gold(III)-dithiocarbamate complexes, *Anticancer Agents Med. Chem.*, **2010**, 10, 283.
- [334] M. Delepine, Thiosulfocarbamates métalliques: preparation des sulfocarbimides de la série grasse, *Compt. Rend.*, **1907**, 144, 1125.
- [335] A. Burawoy, C. S. Gibson, The organic compounds of gold. Part IV. N-propyl compounds, *J. Chem. Soc.*, **1935**, 219.
- [336] H. J. A. Blaauw, R. J. F. Nivard, G. J. M. van der Kerk, Syntheses and properties of dihalogold(III) N,N-dialkyldithiocarbamates and dialkylgold(III) N,N-dialkyldithiocarbamates, *J. Organomet. Chem.*, **1964**, 2, 236.
- [337] P. T. Beurskens, H. J. A. Blauw, J. A. Cras, J. J. Steggerda, Preparation, structure and properties of bis(N,N-di-n-buthyldithiocarbamato)gold(III) dihaloaurate(I), *Inorg. Chem.*, **1968**, 7(4), 805.
- [338] P. T. Beurskens, J. A. Cras, J. J. Steggerda, Structure and properties of dibromo-N,N-di-n-buthyldithiocarbamato complexes of copper(III) and gold(III), *Inorg. Chem.*, **1968**, 7(4), 810.
- [339] P. T. Beurskens, J. A. Cras, J. G. M. van der Linden, Preparation, structure, and properties of bis(N,N-di-n-buthyldithiocarbamato)gold(III) bromide and bis(N,N-di-n-buthyldithiocarbamato)gold(III) tetrabromoaurate(III), *Inorg. Chem.*, **1970**, 9(3), 475.
- [340] F. Forghieri, C. Preti, L. Tassi, G. Tosi, Preparation, properties and reactivity of gold complexes with some heterocyclic dithiocarbamates as ligands, *Polyhedron*, **1988**, 7(14), 1231.
- [341] V. Milacic, D. Fregona, Q. P. Dou, Gold complexes as prospective metal-based anticancer drugs, *Histol. Histopathol.*, **2008**, 23(1), 101.
- [342] D. Fregona, L. Ronconi, The Midas touch in cancer chemotherapy: from platinum- to gold-dithiocarbamate complexes, **2009**, *Dalton Trans.*, 48, 10670.
- [343] A. A. Mohamed, A. E. Bruce, M. R. M. Bruce, The electrochemistry of gold and silver complexes, in *Patai's chemistry of functional groups*, **2009**, John Wiley & Sons.
- [344] L. Cattaruzza, D. Fregona, M. Mongiat, L. Ronconi, A. Fassina, A. Colombatti, D. Aldinucci, Antitumor activity of gold(III)-dithiocarbamate derivatives on prostate cancer cells and xenografts, *Int. J. Cancer*, **2011**, 128, 206.
- [345] C. Marzano, L. Ronconi, F. Chiara, M. C. Giron, I. Faustini, P. Cristofori, A. Trevisan, D. Fregona, Gold(III)-dithiocarbamate anticancer agents: activity, toxicological and histopathological studies in rodents, *Int. J. Cancer*, **2011**, 129, 487.

- [346] C. Nardon, D. Fregona, Gold(III) complexes in the oncological preclinical arena: from aminoderivatives to peptidomimetics, *Curr. Top. Med. Chem.*, **2016**, 16, 360.
- [347] C. U. Nielsen, B. Brodin, F. S. Jorgensen, S. Frokjaer, B. Steffansen, Human peptide transporters: therapeutic applications, *Expert Opin. Ther. Patents*, **2002**, 12, 1329.
- [348] M. Celegato, D. Fregona, M. Mongiat, L. Ronconi, C. Borgese, V. Canzonieri, N. Casagrande, C. Nardon, A. Colombatti, D. Aldinucci, Preclinical activity of multiple-targeted gold(III)-dithiocarbamate peptidomimetics in prostate cancer cells and xenografts, *Fut. Med. Chem.*, 2014, 6, 1249.
- [349] V. Milacic, D. Chen, L. Ronconi, K. R. Landis-Piwowar, D. Fregona, Q. P. Dou, A novel anticancer gold(III) dithiocarbamate compound inhibits the activity of a purified 20S proteasome and 26S proteasome in human breast cancer cell cultures and xenografts, *Cancer Res.*, **2006**, 66, 10478.
- [350] D. Saggiaro, M. P. Rigobello, L. Paloschi, A. Folda, S. A. Moggach, S. Parsons, L. Ronconi, D. Fregona, A. Bindoli, Gold(III)-dithiocarbamate complexes induce cancer cell death triggered by thioredoxin redox system inhibition and activation of ERK pathway, *Chem. Biol.*, **2007**, 14, 1128.
- [351] L. Cattalini, G. Chessa, G. Michelon, B. Pitteri, M. L. Tobe, A. Zanardo, Ligand substitution kinetics and equilibria in the systems formed by tetrabromoaurate(III) anion and heterocyclic nitrogen donors, *Inorg. Chem.*, **1985**, 24(21), 3409.
- [352] H. W. Chen, C. Paparizos, J. P. Fackler Jr., Dimethylgold(III) complexes. Synthesis of several compounds with  $Au_2S_2$  coordination. The crystal and molecular structure of  $[(CH_3)_2AuSC_2H_5]_2$ , *Inorg. Chim. Acta*, **1985**, 96, 137.
- [353] F. Basolo, Substitution reactions of square planar complexes, in *Mechanism of Inorganic Reactions*, **1965**, *Advances in Chemistry* 49(4), 81, J. Kleinberg, R. K. Murmann, R. T. M. Fraser, J. Bauman eds.
- [354] J. Cordon, G. Jimenez-Oses, J. M. Lopez de Luzuaga, M. Monge, M. E. Olmos, D. Pascual, Experimental and theoretical study of gold(III)-catalyzed hydration of alkynes, *Organometallics*, **2014**, 33, 3823.
- [355] D. D. Heinrich, J.-C. Wang, J. P. Fackler Jr., Structure of  $Au_2[S_2CN(C_2H_5)_2]_2$  bis(diethyldithiocarbamate)digold(I), *Acta Cryst.*, **1990**, C46, 1444.
- [356] M. Altaf, A. A. Isab, J. Vanco, Z. Dvorak, Z. Travnicek, H. Stoeckli-Evans, Synthesis, characterization and in vitro cytotoxicity of gold(III) dialkyl/diaryldithiocarbamate complexes, *RSC Adv.*, **2015**, 5(99), 81599.
- [357] F. A. Allen, O. Kennard, D. G. Watson, L. Brammer, A. Guy Orpen, R. Taylor, Tables of bond lengths determined by X-ray and neutron diffraction. Part 1. Bond lengths in organic compounds, *J. Chem. Soc., Perkin Trans. 2*, **1987**, S1.
- [358] H. Schmidbaur, The aurophilicity phenomenon: a decade of experimental findings, theoretical concepts and emerging application, *Gold Bull.*, **2000**, 33(1), 3.
- [359] L. Ronconi, C. Maccato, D. Barreca, R. Saini, M. Zancato, D. Fregona, Gold(III) dithiocarbamate derivatives of N-methylglycine: an experimental and theoretical investigation, *Polyhedron*, **2005**, 24, 521.
- [360] F. K. Keter, I. A. Guzei, M. Nell, W. E. van Zyl, J. Darkwa, Phosphinogold(I) dithiocarbamate complexes: effect of the nature of phosphine ligand on anticancer properties, *Inorg. Chem.*, **2014**, 53, 2058.
- [361] R. Hesse, P. Jennische, The crystal and molecular structure of the gold(I) dipropyldithiocarbamate dimer, *Acta Chem. Scand.*, **1972**, 26, 3855.
- [362] H. O. Desseyn, A. C. Fabretti, F. Forghieri, C. Preti, Isotopic infrared study of some nickel(II) and copper(II) complexes containing heterocyclic dithiocarbamate ligands, *Spectrochim. Acta A*, **1985**, 41, 1105.
- [363] A. Lapinski, R. Swietlik, L. A. Kushch, Infrared spectra of  $[Ni(dddtd)_2]_3(AuBr_2)_2$  and  $[Pd(dddtd)_2]_2X$  ( $X = TeCl_6, SbF_6, AuBr_2$ ) crystals, *Adv. Funct. Mat.*, **1996**, 6, 321.
- [364] A. Sabatini, L. Sacconi, V. Schettino, Far-infrared spectra and vibrational force constants of the ions  $AuCl_4^-$ ,  $AuBr_4^-$  and  $PtCl_4^{2-}$ , *Inorg. Chem.*, **1964**, 3(12), 1775.
- [365] H. B. Gray, C. J. Ballhausen, A molecular orbital theory for square planar metal complexes, *Inorg. Chem.*, **1963**, 85(5), 260.

- [366] W. R. Mason III, H. B. Gray, Electronic structures and spectra of square-planar gold(III) complexes, *Inorg. Chem.*, **1968**, 7(1), 55.
- [367] D.H. Brown, G. C. McKinlay, W.E. Smith, The electronic spectra of some gold(III) complexes, *Inorg. Chim. Acta*, **1979**, 32, 117.
- [368] C. C. Hadjikostas, G. A. Katsoulos, S. K. Shakatreh, Synthesis and spectral studies of some new palladium(II) and platinum(II) dithiocarbamate complexes. Reactions of bases with the corresponding N-alkyldithiocarbamates, *Inorg. Chim. Acta*, **1987**, 133, 129.
- [369] A. K. Gangopadhyay, A. Chakravorty, Charge transfer spectra of some gold(III) complexes, *J. Chem. Phys.*, **1961**, 35, 2206.
- [370] R. Narayanaswamy, M. A. Young, E. Parkhurst, M. Ouellette, M. E. Kerr, M. H. Douglas, R. C. Elder, A. E. Bruce, M. R. M. Bruce, Synthesis, structure, and electronic spectroscopy of neutral, dinuclear gold(I) complexes. Gold(I)-gold(I) interactions in solution and in the solid state, *Inorg. Chem.*, **1993**, 32, 2506.
- [371] H.-R. Jaw, M. M. Savas, W. R. Mason, Electronic absorption and MCD spectra for the binuclear three-coordinate gold(I) complex  $Au_2(dmpm)_3^{2+}$  (dmpm = bis(dimethylphosphino)methane), *Inorg. Chem.*, **1989**, 28, 4366.
- [372] A. Vogler, H. Kunkely, Absorption and emission spectra of tetrameric gold(I) complexes, *Chem. Phys. Lett.*, **1988**, 150, 135.
- [373] H. Jatzkewitz, Incorporation of physiologically-active substances into a colloidal blood plasma substitute. I. Incorporation of mescaline peptide into polyvinylpyrrolidone. *Hoppe-Seylers Z. Physiol. Chem.*, **1954**, 297, 149.
- [374] M. E. Davis, Z. Chen, D. M. Shin, Nanoparticle therapeutics: an emerging treatment modality for cancer, *Nature Rev. Drug Discov.*, **2008**, 7, 771.
- [375] O. C. Farokhzad, R. Langer, Impact of nanotechnology on drug delivery, *ACS Nano*, **2009**, 3, 16.
- [376] D. Peer, J. M. Karp, S. Hong, O. C. Farokhzad, R. Margalit, R. Langer, Nanocarriers as an emerging platform for cancer therapy, *Nat. Nanotech.*, **2007**, 2, 751.
- [377] *Biomedical Nanomaterials*, Y. Zhao, Y. Shen eds., **2016**, Wiley-VCH.
- [378] L. Bregoli, D. Movia, J. D. Gavigan-Imedio, J. Lysaght, J. Reynolds, A. Prina-Mello, Nanomedicine applied to translational oncology: a future perspective on cancer treatment, *Nanomed. Nanotech. Biol. Med.*, **2016**, 12, 81.
- [379] M. Antonietti, S. Forster, Vesicles and liposomes: a self-assembly principle beyond lipids, *Adv. Mat.*, **2003**, 15(16), 1323.
- [380] P.P. Deshpande, S. Biswas, V. P. Torchilin, Current trends in the use of liposomes for tumor targeting, *Nanomedicine*, **2013**, 8(9), 1509.
- [381] Y. Barenholz, Doxil® - the first FDA-approved nano-drug: lesson learned, *J. Control. Release*, **2012**, 160, 117.
- [382] S. Phuphanich, B. Maria, R. Braeckman, M. Chamberlain, A pharmacokinetic study of intra-CSF administered encapsulated cytarabine (DepoCyt) for the treatment of neoplastic meningitis in patients with leukemia, lymphoma, or solid tumors as part of a phase III study. *J. Neurooncol.*, **2007**, 81(2), 201.
- [383] J. A. Silverman, S. R. Deitcher, Marqibo® (vincristine sulfate liposome injection) improves the pharmacokinetics and pharmacodynamics of vincristine, *Cancer Chemother. Pharmacol.*, **2013**, 71(3), 555.
- [384] H.-I. Chang, M.-K. Yeh, Clinical development of liposome-based drugs: formulation, characterization, and therapeutic efficacy, *Int. J. Nanomedicine*, **2012**, 7, 49.
- [385] R. B. Greenwald, PEG drugs: an overview, *J. Control. Release*, **2001**, 74, 159.
- [386] P. A. Dinndorf, J. Gootenberg, M. H. Cohen, P. Keegan, R. pazdur, FDA drug approval summary: pegaspargase (Oncospar) for the first-line treatment of children with acute lymphoblastic leukemia (ALL), *Oncologist*, **2007**, 12, 991.
- [387] J. M. Harris, R. B. Chess, Effect of pegylation on pharmaceuticals, *Nat. Rev. Drug Disc.*, **2003**, 2, 214.
- [388] N. J. Butcher, G. M. Mortimer, R. F. Minchin, Unravelling the stealth effect, *Nat. Nanotech.*, **2016**, 11, 310.
- [389] G. S. Kwon, K. Kataoka, Block copolymer micelles as long-circulating drug vehicles, *Adv. Drug. Deliv. Rev.*, **1995**, 16, 295.
- [390] K. Kataoka, A. Harada, Y. Nagasaki, Block copolymer micelles for drug delivery: design, characterization and biological significance, *Adv. Drug. Deliv. Rev.*, **2001**, 47, 113.

- [391] E. V. Batrakova, S. Li, A. M. Brynskikh, A. K. Sharma, Y. Li, M. Boska, N. Gong, R. L. Mosley, V. Y. Alakhov, H. E. Gendelman, A. V. Kabanov, Effects of pluronic and doxorubicin on drug uptake, cellular metabolism, apoptosis and tumor inhibition in animal models of MDR cancers, *J. Control. Release*, **2010**, 143, 290.
- [392] J. Kim, S. Shin, Cost-effectiveness of genexol-PM for treating metastatic breast cancer, *J. Breast Cancer*, **2010**, 13, 104.
- [393] F. Danhier, O. Feron, V. Préat, To exploit the tumor microenvironment: passive and active tumor targeting of nanocarriers for anti-cancer drug delivery, *J. Control. Release*, **2010**, 148, 135.
- [394] K. Hida, N. Ohga, T. Kurosu, Y. Totsuka, M. Shindoh, Crosstalk between blood vessels and tumor microenvironment, *Oral Sci. International*, **2010**, 7, 1.
- [395] P. Baluk, H. Hashizume, D. M. McDonald, Cellular abnormalities of blood vessels as targets in cancer, *Curr. Opin. Genet. Dev.*, **2005**, 15, 102.
- [396] V. P. Torchilin, Drug targeting, *Eur. J. Pharm. Sci.*, **2000**, 11, S81.
- [397] H. Maeda, G. Y. Bharate, J. Daruwalla, Polymeric drugs for efficient tumor-targeted drug delivery based on EPR-effect, *Eur. J. Pharm. Biopharm.*, **2009**, 71, 409.
- [398] A. K. Iyer, G. Khaled, J. Fang, H. Maeda, Exploiting the enhanced permeability and retention effect for tumor targeting, *Drug. Discov. Today*, **2006**, 11, 812.
- [399] S. V. Vinogradov, T. K. Bronich, A. V. Kabanov, Nanosized cationic hydrogels for drug delivery: preparation, properties and interactions with cells, *Adv. Drug Deliv. Rev.*, **2002**, 54, 135.
- [400] L. Ilium, S. S. Davis, C. G. Wilson, N. W. Thomas, M. Frier, J. G. Hardy, Blood clearance and organ deposition of intravenously administered colloidal particles. The effect of particle size, nature and shape, *Int. J. Pharm.*, **1982**, 12, 135.
- [401] C. H. Heldin, K. Rubin, K. Pietras, A. Ostman, High interstitial fluid pressure – an obstacle in cancer therapy, *Nat. Rev. Cancer*, **2004**, 4, 806.
- [402] L. Tang, X. Yang, Q. Yin, K. Cai, H. Wang, *et al.*, Investigating the optimal size of anticancer nanomedicine, *Proc. Natl. Acad. Sci. USA*, **2014**, 111(43), 15344.
- [403] N. Bertrand, J. Wu, X. Xu, N. Kamaly, O. C. Farokhzad, Cancer nanotechnology: the impact of passive and active targeting in the era of modern cancer biology, *Adv. Drug. Deliv. Rev.*, **2014**, 66, 2.
- [404] O. Lieleg, R. M. Baumgartel, A. R. Bausch, Selective filtering of particles by the extracellular matrix: an electrostatic bandpass, *Biophys. J.*, **2009**, 97, 1569.
- [405] C. he, Y. Hu, L. Yin, C. Tang, C. Yin, Effects of particle size and surface charge on cellular uptake and biodistribution of polymeric nanoparticles, *Biomaterials*, **2010**, 31, 3657.
- [406] J. M. Lohr, S. L. Haas, W.-O. Bechstein, G. Bodoky, K. cwiertka, W. Fischbach, U. R. Folsch, D. Jager, D. Osinsky, J. Prausova, W. E. Schmidt, M. P. Lutz, Cationic liposomal paclitaxel plus gemcitabine or gemcitabine alone in patients with advanced pancreatic cancer: a randomized controlled phase II trial, *Ann. Oncol.*, **2012**, 23, 1214.
- [407] R. Toy, M. P. Peiris, K. B Ghaghada, E. Karathanasis, Shaping cancer nanomedicine: the effect of particle shape on the in vivo journey of nanoparticles, *Nanomedicine*, **2014**, 9, 121.
- [408] R. A. Petros, J. M. DeSimone, Strategies in the design of nanoparticles for therapeutic applications, *Nat. Rev. Drug. Disc.*, **2010**, 9, 615.
- [409] T. M. Fahmya, P. M. Fonga, A. Goyalb, W. M. Saltzmana, Targeted for drug delivery, *Mater. Today*, **2005**, 8(8), 18.
- [410] M. Huang, A. Shen, J. Ding, M. Geng, Molecularly targeted cancer therapy: some lessons from the past decade, *Trends Pharmacol. Sci.*, **2014**, 35, 1.
- [411] K. F. Pirolo, E. H. Chang, Does targeting ligand influence nanoparticle tumor localization or uptake?, *Trends Biotechnol.*, **2008**, 26, 552.
- [412] E. Garanger, D. Boturyn, P. Dumy, Tumor targeting with RGD peptide ligands-design of new molecular conjugates for imaging and therapy of cancers, *Anticancer Agents Med. Chem.*, **2007**, 7(5), 552.



- [413] K. de Bruin, N. Ruthardt, K. von Gersdorff, R. Bausinger, E. Wagner, M. Ogris, C. Bräuchle, Cellular dynamics of EGF receptor-targeted synthetic viruses, *Mol. Ther.*, **2007**, 15, 1297.
- [414] G. L. Zwicke, G. A. Mansoori, C. J. Jeffery, Utilizing the folate receptor for active targeting of cancer nanotherapeutics, *Nano Rev.*, **2012**, 3, 18496.
- [415] C. H. J. Choi, C. A. Alabi, P. Webster, M. E. Davis, Mechanism of active targeting in solid tumors with transferrin-containing gold nanoparticles, *Proc. Natl. Acad. Sci. USA*, **2010**, 107, 1235.
- [416] A. M. Scott, J. D. Wolchok, L. J. Old, Antibody therapy of cancer, *Nat. Rev. Cancer*, **2012**, 12, 278.
- [417] B. Yu, H. C. Tai, W. Xue, L. J. Lee, R. J. Lee, Receptor-targeted nanocarriers for therapeutic delivery to cancer, *Mol. Membr. Biol.*, **2010**, 27(7), 286.
- [418] B. Alberts, A. Johnson, J. Lewis, *et al.*, Transport into the Cell from the Plasma Membrane: Endocytosis, in *Molecular Biology of the Cell - 4th edition*, **2002**, Garland Science, New York (USA).
- [419] G. Sahay, D. Y. Alakhova, A. V. Kabanov, Endocytosis of Nanomedicines, *J. Control. Release*, **2010**, 145, 182.
- [420] G. J. Doherty, H. T. McMahon, Mechanisms of endocytosis, *Annu. Rev. Biochem.*, **2009**, 78, 857.
- [421] H. T. McMahon, E. Boucrot, Molecular mechanism and physiological functions of clathrin-mediated endocytosis, *Nat. Rev. Mol. Cell Biol.*, **2011**, 12, 517.
- [422] P. Oh, P. Borgstrom, H. Witkiewicz, Y. Li, B. J. Borgstrom, A. Chrastina, K. Iwata, K.R. Zinn, R. Baldwin, J. E. Testa, J. E. Schnitzer, Live dynamic imaging of caveolae pumping targeted antibody rapidly and specifically across endothelium in the lung, *Nat. Biotech.*, **2007**, 25, 327.
- [423] H. Uchino, Y. Matsumura, T. Negishi, F. Koizumi, T. Hayashi, T. Honda, N. Nishiyama, K. Kataoka, S. Naito, T. Kakizoe, Cisplatin-incorporating polymeric micelles (NC-6004) can reduce nephrotoxicity and neurotoxicity of cisplatin in rats, *Br. J. Cancer*, **2005**, 93, 678.
- [424] T. Ueno, K. Endo, K. Hori, N. Ozaki, A. Tsuji, S. Kondo, N. Wakisaka, S. Muro, K. Kataoka, Y. Kato, T. Yoshishizaki, Assessment of antitumor activity and acute peripheral neuropathy of 1,2-diaminocyclohexane platinum(II)-incorporating micelles (NC-4016), *Int. J. Nanomedicine*, **2014**, 9, 3005.
- [425] R. Plummer, R.H. Wilson, H. Clavert, A. V. Boddy, M. Griffin, J. Sludden, M. J. Tilby, M. Eatock, D. G. Pearson, C. J. Ottley, Y. Matsumura, K. Kataoka, T. Nishiya, A Phase I clinical study of cisplatin-incorporated polymeric micelles (NC-6004) in patients with solid tumors, *Br. J. Cancer*, **2011**, 104, 593.
- [426] X. Kang, H.-H. Xiao, H.-Q. Song, X.-B. Jing, L.-S. Yan, R.-G. Qi, Advances in drug delivery system for platinum agents based combination therapy, *Cancer Biol. Med.*, **2015**, 12, 362.
- [427] G. P. Stathopoulos, T. Boulikas, A. Kourvetaris, J. Stathopoulos, Liposomal oxaliplatin in the treatment of advanced cancer: a phase I study, *Anticancer Res.*, **2006**, 26, 1489.
- [428] K. K. Sankhala, A. C. Mita, R. Adinin, L. Wood, M. Beeram, S. Bullock, N. Yamagata, K. Matsuno, T. Fujisawa, A. Phan, A phase I pharmacokinetic (PK) study of MBP-246, a novel liposome encapsulated oxaliplatin, *J. Clin. Oncol.*, **2009**, 27, 155.
- [429] N. P. E. Barry, P. J. Sadler, Challenges for metals in medicine: how nanotechnology may help to shape the future, *ACS Nano*, **2013**, 7(7), 5654.
- [430] B. M. Blunden, M. H. Stenzel, Incorporating ruthenium into advanced drug delivery carriers – an innovative generation of chemotherapeutics, *J. Chem. Tech. Biotech.*, **2015**, 90, 1177.
- [431] G. Mangiapia, G. D'Errico, L. Simeone, C. Irace, A. radulescu, A. Di Pascale, A. Colonna, D. Montesarchio, L. Paduano, Ruthenium-based complex nanocarriers for cancer therapy, *Biomaterials*, **2012**, 33, 3770.
- [432] C. Nardon, G. Boscutti, L. Dalla Via, P. Ringhieri, V. Di Noto, G. Morelli, A. Accardo, D. Fregona, CCK8 peptide-labelled Pluronic® F127 micelles as a targeted vehicle of gold based anticancer chemotherapeutics, *Med. Chem. Comm.*, **2015**, 6, 155.

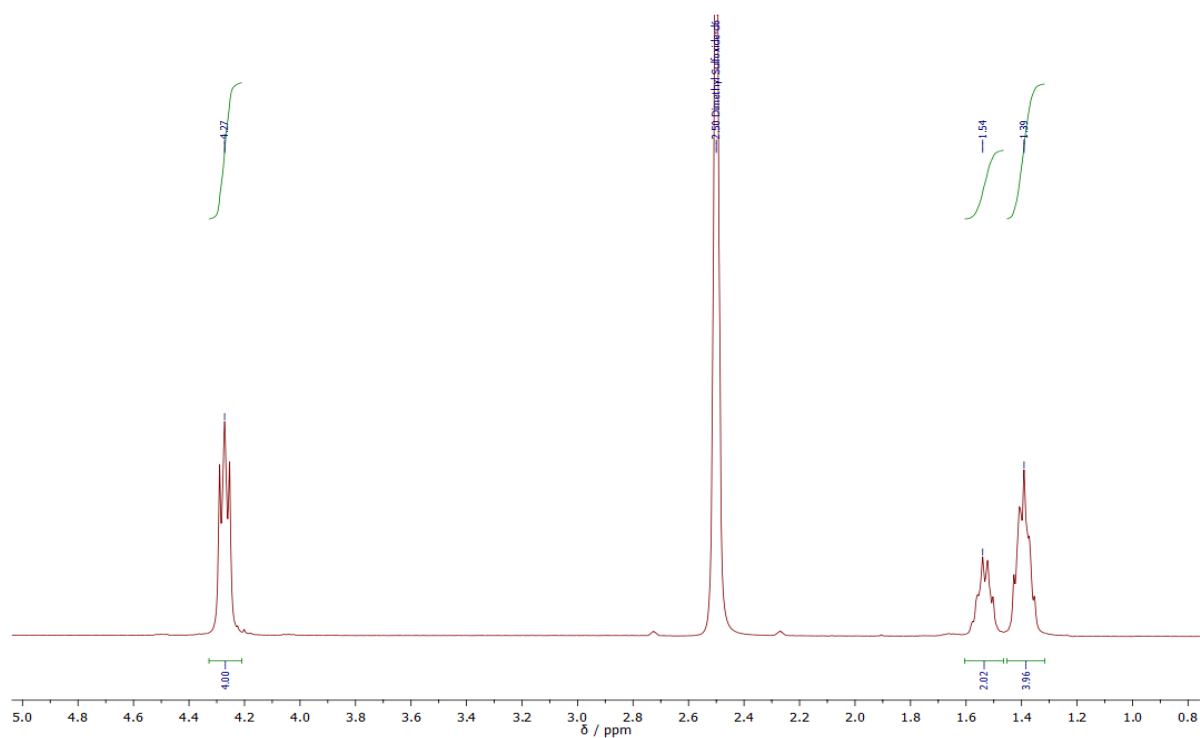
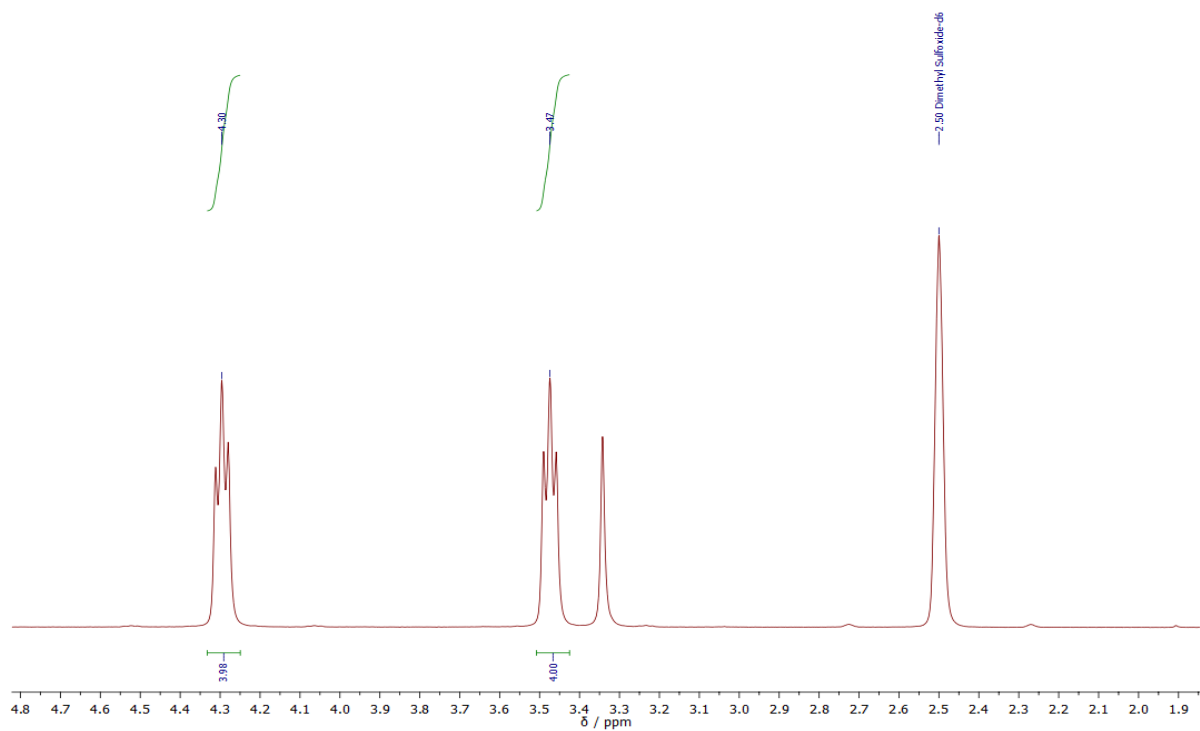
- [433] L. Brustolin, S. Scintilla, A. Gambalunga, F. Chiara, A. Trevisan, C. Nardon, D. Fregona, Ru(III) anticancer agents with aromatic and non-aromatic dithiocarbamates as ligands: loading into pF127 micelles and preliminary biological studies, *J. Inorg. Biochem.*, **2016**, 166, 76.
- [434] G. Dumortier, J. L. Grossiord, F. Agnely, J. C. Chaumeil, A review of Polaxamer 407 pharmaceutical and pharmacological characteristics, *Pharm. Res.*, **2006**, 23, 2709.
- [435] Z. Takats, K. Vekey, I. Hegedus, Qualitative and quantitative determination of polaxamer surfactants by mass spectrometry, *Rapid Commun. Mass Spectrom.*, **2001**, 15, 805.
- [436] R. W. Egan, Hydrophile-lipophile balance and critical micelle concentration as key factors influencing surfactant disruption of mitochondrial membranes, *J. Biol. Chem.*, **1976**, 251, 4442.
- [437] A. V. Kabanov, E. V. Batrakova, V. Y. Alakhov, Pluronic® block copolymers as novel polymer therapeutics for drug and gene delivery, *J. Control. Release*, **2002**, 82, 189.
- [438] M. Y. Kozlov, N. S. Melik-Nubarov, E. V. Batrakova, A. V. Kabanov, Relationship between Pluronic block copolymer structure, critical micellization concentration and partitioning coefficients of low molecular mass solutes, *Macromolecules*, **2000**, 33, 3305.
- [439] R. Rowe, P. Sheskey, S. Owen, *Pharmaceutical Handbook of Pharmaceutical Excipients*, 5<sup>th</sup> ed., **2005**, Pharmaceutical London (UK) and American Pharmaceutical Association, Washington (USA).
- [440] S. Danson, D. Ferry, V. Alakhov, J. Margison, D. Kerr, D. Jowle, M. Brampton, G. Halbert, M. Ranson, Phase I dose escalation and pharmacokinetic study of pluronic polymer-bound doxorubicin (SP1049C) in patients with advanced cancer, *Br. J. Cancer*, **2004**, 90, 2085.
- [441] E. V. Batrakova, A. V. Kabanov, Pluronic block copolymers: evolution of drug delivery concept from inert nanocarrier to biological response modifier, *J. Control. Release*, **2008**, 130, 98.
- [442] U. Adhikari, A. Goliaei, L. Tsereteli, M. L. Berkowitz, Properties of polaxamer molecules and polaxamer micelles dissolved in water next to lipid bilayers: result from computer simulations, *J. Chem. Phys. B*, **2016**, 120, 5823.
- [443] D. Y. Alakhova, N. Y. Rapoport, E. V. Batrakova, A. A. Timoshin, S. Li, D. Nicholls, V. Y. Alakhov, A. V. Kabanov, Differential metabolic response to Pluronic in MDR and non-MDR cells: a novel pathway for chemosensitization of drug resistant cancers, *J. Control. Release*, **2010**, 142, 89.
- [444] A. V. Kabanov, E. V. Batrakova, V. Y. Alakhov, An essential relationship between ATP depletion and chemosensitizing activity of Pluronic block copolymers, *J. Control. Release*, **2003**, 91, 75.
- [445] M. Werle, Natural and synthetic polymers as inhibitors of drug efflux pumps, *Pharm. Res.*, **2008**, 25, 500.
- [446] S. Sriadibhatla, Z. Yang, C. Gebhart, V. Y. Alakhov, A. V. Kabanov, Transcriptional activation of gene expression by pluronic block copolymers in stably and transiently transfected cells, *Mol. Ther.*, **2006**, 13, 804.
- [447] D. Y. Alakhova, A. V. Kabanov, Pluronic and MDR reversal: an update, *Mol. Pharm.*, **2014**, 11, 2566.
- [448] N. S. Melik-Nubarov, O. O. Pomaz, T. Y. Dorodnych, G. A. Badun, A.L. Ksenofontov, O. B. Schemchukova, S. A. Arzhakov, Interaction of tumor and normal blood cells with ethylene oxide and propylene oxide block copolymers, *FEBS Lett.*, **1999**, 446, 194.
- [449] A. Pitto-Barry, N. P. E. Barry, Pluronic® block-copolymers in medicine: from chemical and biological versatility to rationalization and clinical advances, *Polym. Chem.*, **2014**, 5, 3291.
- [450] G. Sahay, E. V. Batrakova, A. V. Kabanov, Different internalization pathways of polymeric micelles and unimers and their effects on vesicular transport, *Bioconjugate Chem.*, **2008**, 19, 2023.
- [451] S. J. Huang, T. P. Wang, S. I. Lue, L. F. Wang, Pentablock copolymers of pluronic F127 and modified poly(2-dimethyl amino) ethyl methacrylate for internalization mechanism and gene transfection studies, *Int. J. Nanomedicine*, **2013**, 8, 2011.
- [452] M. G. Vander Heiden, Targeting cancer metabolism: a therapeutic window opens, *Nat. Rev. Drug. Disc.*, **2011**, 10, 671.
- [453] E. M. Rohren, T. G. Turkington, R. E. Coleman, Clinical application of PET in oncology, *Radiology*, **2004**, 231, 306.

- [454] C. C. Martin, B. T. Christian, M. R. Satter, L. H. Nickerson, R. J. Nickles, Quantitative PET with positron emitters that emit prompt gamma rays, *IEEE Trans. Med. Imaging*, **1995**, 14, 681.
- [455] N. Avril, GLUT1 expression in tissue and <sup>18</sup>F-FDG uptake, *J. Nucl. Med.*, **2004**, 45, 930.
- [456] I. S. Wood, P. Trayhurn, Glucose transporters (GLUT and SGLT): expanded families of sugar transport proteins, *Br. J. Nutr.*, **2003**, 89, 3.
- [457] R. A. Medina, G. I. Owen, Glucose transporters: expression, regulation and cancer, *Biol. Res.*, **2002**, 35, 9.
- [458] M. L. Macheda, S. Rogers, J. D. Best, Molecular and cellular regulation of glucose transporter (GLUT) proteins in cancer, *J. Cell. Physiol.*, **2005**, 202, 654.
- [459] D. Deng, C. Xu, P. Sun, J. Wu, C. Yan, M. Hu, N. Yan, Crystal structure of the human glucose transporter GLUT1, *Nature*, **2014**, 510, 121.
- [460] E. C. Calvaresi, P. J. Hergenrother, Glucose conjugation for the specific targeting and treatment of cancer, *Chem. Sci.*, **2013**, 4, 2319.
- [461] M. Srinivasarao, C. V. Galliford, P. S. Low, Principles in the design of ligand-targeted cancer therapeutics and imaging agents, *Nat. Rev. Drug. Disc.*, **2015**, 14, 203.
- [462] D. Lacombe, Glufosfamide: can we improve the process of anticancer agent development?, *Expert Opin. Investig. Drugs*, **2012**, 21, 749.
- [463] L. Venturelli, S. Nappini, M. Bulfoni, G. Gianfrancesch, S. Dal Zilio, G. Coceano, F. Dal Ben, M. Turetta, G. Scoles, L. Vaccari, D. Cesselli, D. Cojoc, Glucose is a key driver for GLUT1-mediated nanoparticles internalization in breast cancer cells, *Sci. Rep.*, **2016**, 2, 1.
- [464] J. Niu, A. Wang, Z. Ke, Z. Zheng, Glucose transporter and folic acid receptor-mediated Pluronic P105 polymeric micelles loaded with doxorubicin for brain tumor treating, *J. Drug. Target*, **2014**, 22, 712.
- [465] J. R. Parikh, W. von E. Doering, Sulfur trioxide in the oxidation of alcohols by dimethyl sulfoxide, *J. Am. Chem. Soc.*, **1967**, 89, 5505.
- [466] V. N. R. Pillai, M. Mutter, E. Bayer, I. Gatfield, New, easily removable poly(ethylene glycole) supports for the liquid-phase method of peptide synthesis, *J. Org. Chem.*, **1980**, 45, 5364.
- [467] O. Stoutland, L. Helgen, C. L. Agre, Reactions of diamines with isocyanates and isothiocyanates, *J. Org. Chem.*, **1959**, 24, 818.
- [468] B. Mukhopadhyay, K. P. R. Kartha, D. A. Russell, R. A. Field, Streamlined synthesis of per-O-acetylated sugars, glycosyl iodides, or thioglycosides from unprotected reducing sugars, *J. Org. Chem.*, **2004**, 69, 7758.
- [469] B. Ren, M. Wang, J. Liu, J. Ge, X. Zhang, H. Dong, Zemplén transesterification: a name reaction that has misled us for 90 years, *Green Chem.*, **2015**, 17, 1390.
- [470] G. Magnusson, G. Noori, J. Dahmén, T. Frejd, T. Lave, BF<sub>3</sub> – etherate induced formation of 2,2,2-trichloroethyl glycopyranosides. Selective visualization of carbohydrate derivatives on TLC plates, *Acta. Chem. Scand. B*, **1981**, 35, 213.
- [471] D. M. Whitfield, S. P. Douglas, Glycosilation reactions – present status future directions, *Glycoconj. J.*, **1996**, 13, 5.
- [472] D. Crich, Mechanism of a chemical glycosylation reaction, *Acc. Chem. Res.*, **2010**, 43, 1144.
- [473] P. Cunningham, I. Afzal-Ahmed, R. J. Naftalin, Docking studies show that D-glucose and quercetin slide through the transporter GLUT1, *J. Biol. Chem.*, **2005**, 281, 5797.
- [474] J. M. Harris, E. C. Struck, M. G. Case, M. S. Paley, M. Yalpani, J. M. van Alstine, D. E. Brooks, Synthesis and characterization of poly(ethylene glycol) derivatives, *J. Polym. Sci. A Polym. Chem.*, **1984**, 22, 341.
- [475] B. Liberek, A. Melcer, A. Osuch, R. Wakicec, S. Milewski, A. Wisniewski, N-alkyl derivatives of 2-amino-2-deoxy-D-glucose, *Carb. Res.*, **2005**, 340, 1876.
- [476] F. Chen, X.-M. Liu, K. C. Rice, X. Li, F. Yu, R. A. Reinhardt, K. W. Bayles, D. Wang, Tooth-binding micelles for dental caries prevention, *Antimicrob. Agents Chemother.*, **2009**, 53, 4898.

- [477] M. Bahta, F. Liu, S.-E. Kim, A. G. Stephen, R. J. Fisher, T.R. Burke Jr, Oxime-based linker libraries as a general approach for the rapid generation and screening of multidentate inhibitors. *Nat. Protoc.*, **2012**, 7(4), 686.
- [478] C. Yanic, M. W. Bredenkamp, E. P. Jacobs, H. S. C. Spies, P. Swart, NMR spectroscopy as basis for characterization of Pluronic® 108 and its derivatives, *J. Appl. Polym. Sci.*, **2000**, 78, 109.
- [479] R. Sardzik, G. T. Noble, M. J. Weissenborn, A. Martin, S. J. Webb, S. L. Flitsch, Preparation of aminoethyl glycosides for glycoconjugation, *Beilstein. J. Org. Chem.*, **2010**, 6, 699.
- [480] M. A. K. L. Dissanayake, R. Frech, Infrared spectroscopic study of the phases and phase transitions in poly(ethylene oxide) and poly(ethylene oxide)-lithium trifluoromethanesulfonate complexes, *Macromolecules*, **1995**, 28, 5312.
- [481] N. Kimura, J. Umemura, S. Hayashi, Polarized FT-IR spectra of water in the middle phase of Triton X100-water system, *J. Colloid. Interface Sci.*, **1996**, 182, 356.
- [482] Y.-L. Su, J. Wang, H.-Z. Liu, FTIR Spectroscopic investigation of effects of temperature and concentration on PEO-PPO-PEO block copolymer properties in aqueous solutions, *Macromolecules*, **2002**, 35, 6426.
- [483] J. Zhu, Y. Zhang, D. Lu, R. N. Zare, J. Ge, Z Liu, Temperature-responsive enzyme-polymer nanoconjugates with enhanced catalytic activities in organic media, *Chem. Comm.*, **2013**, 49, 6090.
- [484] J. C. Yang, M. J. Jablonsky, J. W. Mays, NMR and FT-IR studies of sulfonated styrene-based homopolymers and copolymers, *Polymer*, **2002**, 43, 5125.
- [485] N. T. Huynh, E. Roger, N. Lautram, J. P. Benoit JP, C. Passirani, The rise and rise of stealth nanocarriers for cancer therapy: passive versus active targeting, *Nanomedicine*, **2010**, 5, 1415.
- [486] D. R. Elias, A. Poloukhine, V. Popik, A. Tsourkas, Effect of ligand density, receptor density, and nanoparticle size on cell targeting, *Nanomed. Nanotech. Biol. Med.*, **2013**, 9, 194.
- [487] V. Sanna, N. Pala, M. Sechi, Targeted therapy using nanotechnology: focus on cancer, *Int. J. Nanomedicine*, **2014**, 9, 467.
- [488] L. Chen, X. Sha, X. Jiang, Y. Chen, Q. Ren, X. Fang, Pluronic P105/F127 mixed micelles for the delivery of docetaxel against taxol-resistant non-small cell lung cancer: optimization and in vitro, in vivo evaluation, *Int. J. Nanomedicine*, **2013**, 8, 73.
- [489] M. Ding, L. Zhou, X. Fu, H. Tan, J. Lia, Q. Fu, Biodegradable gemini multiblock poly( $\epsilon$ -caprolactone urethane)s toward controllable micellization, *Soft Matter*, **2010**, 6, 2087.
- [490] S. L. Nolan, R. J. Phillips, P. M. Cotts, S. R. Dungan, Light scattering study on the effect of polymer composition on the structural properties of PEO-PPO-PEO micelles, *J. Colloid Interface Sci.*, **1997**, 191, 291.
- [491] J. Lin, S. P. Yeap, H. X. Che, S. C. Low, Characterization of magnetic nanoparticle by dynamic light scattering, *Nanoscale Res. Lett.*, **2013**, 8, 831.
- [492] R. Basak, R. Bandyopadhyay, Encapsulation of hydrophobic drugs in pluronic F127 micelles: effects of drug hydrophobicity, solution temperature, and pH, *Langmuir*, **2013**, 29, 4350.
- [493] Z. Zeng, Z. Peng, L. Chen, Y. Chen, Facile fabrication of thermally responsive Pluronic F127-based nanocapsules for controlled release of doxorubicin hydrochloride, *Colloid Polym. Sci.*, **2014**, 292, 1521.
- [494] C. J. Lovitt, T. B. Shelper, V. M. Avery, Advanced cell culture techniques for cancer drug discovery, *Biology*, **2014**, 3, 345.
- [495] L. Jia, X. Liu, The conduct of drug metabolism studies considered good practice (II): in vitro experiments, *Curr. Drug. Metab.*, **2007**, 8, 822.
- [496] J. R. Master, HeLa cells 50 years on: the good, the bad and the ugly, *Nat. Rev. Cancer*, **2002**, 2, 315.
- [497] A. Forner, J. M. Llovet, J. Bruix, Hepatocellular carcinoma, *Lancet*, **2012**, 379, 1245.
- [498] J. J. M. Landry, P. T. Pyl, T. Rausch, T. Zichner, M. M. Tekkedil, A. M. Stutz, A. Jauch, R. S. Aiyar, G. Pau, N. Delhomme, J. Gagneur, J. O. Korb, W. Huber, L. M. Steinmetz, The genomic and transcriptomic landscape of a HeLa cell line, *G3*, **2013**, 3, 1213.
- [499] K. S. Pfaendler, K. S. Tewari, Changing paradigms in the systematic treatment of advanced cervical cancer, *Am. J. Obstet. Gynecol.*, **2016**, 214, 22.

- [500] H. H. J. Gerets, K. Tilmant, B. Gerin, H. Chanteux, B. O. Depelchin, S. Dhalluin, F. A. Atienzar, Characterization of primary human hepatocytes, HepG2 cells, and HepaRG cells at the mRNA level and CYP activity in response to inducers and their predictivity for the detection of human hepatoxins, *Cell. Biol. Toxicol.*, **2012**, 28, 69.
- [501] G. M. Keating, A. Santoro, Sorafenib: a review of its use in advanced hepatocellular carcinoma, *Drugs*, **2009**, 69, 223.
- [502] R. Mazzanti, U. Arena, R. Tassi, Hepatocellular carcinoma: where are we?, *World J. Exp. Med.*, **2016**, 6, 21.
- [503] J. M. Lovet, A. Villanueva, A. Lachenmayer, R. S. Finn, Advances in targeted therapies for hepatocellular carcinoma in the genomic era, *Nat. Rev. Clin. Oncol.*, **2015**, 12, 436.
- [504] L. Vidalino, A. Doria, S. Quarta, M. Zen, A. Gatta, P. Pontisso, SERPINB3, apoptosis and autoimmunity, *Autoimmun. Rev.*, **2009**, 9, 108.
- [505] P. Pontisso, Role of SERPINB3 in hepatocellular carcinoma, *Ann. Hepatol.*, **2014**, 13, 722.
- [506] F. Piscato, M. Sciacovelli, G. Villano, C. Turato, P. Bernardi, A. Rasola, P. Pontisso, SERPINB3 protects from oxidative damage by chemotherapeutics through inhibition of mitochondrial respiratory complex I, *Oncotarget*, **2014**, 5, 2418.
- [507] C. Turato, F. Calabrese, A. Biasiolo, S. Quarta, M. Ruvoletto, N. Tono, D. Pacagnella, G. Fassina, C. Merkel, T. J. Harrison, A. Gatta, P. Pontisso, SERPINB3 modulates TGF- $\beta$  expression in chronic liver disease, *Lab. Invest.*, **2010**, 90, 1016.
- [508] Evaluation of the cytotoxicity effect of dimethyl sulfoxide (DMSO) on Caco2/TC7 colon tumor cell cultures, *Biol. Pharm. Bull.*, **2002**, 25(12), 1600.
- [509] J. O'Brien, I. Wilson, T. Orton, F. Pognan, Investigation of the Alamar Blue (resazurin) fluorescent dye for the assessment of mammalian cell cytotoxicity, *Eur. J. Biochem.*, **2000**, 267, 5421.
- [510] D. Gerlier, N. Thomasset, Use of MTT colorimetric assay to measure cell activation, *J. Immunol. Methods*, **1986**, 94, 57.
- [511] American Cancer Society, *Treatment options for cervical cancer, by stage*, <http://www.cancer.org/cancer/cervicalcancer> (accessed 03.11.2016).
- [512] F. Pascale, L. Bedouet, M. Baylatry, J. Namur, A. Laurent, Comparative chemosensitivity of VX2 and HCC cell lines to drugs used in TACE, *Anticancer Res.*, **2015**, 35, 6497.
- [513] C. A. Lipinski, Drug-like properties and the causes of poor solubility and poor permeability, *J. Pharmacol. Toxicol. Methods*, **2000**, 44, 235.
- [514] C. A. Lipinski, F. Lombardo, B. W. Dominy, P. J. Feeney, Experimental and computational approaches to estimate solubility and permeability in drug discovery and development settings, *Adv. Drug. Deliv. Rev.*, **2001**, 46, 3.
- [515] C. A. Lipinski, Lead- and drug-like compounds: the rule-of-five revolution, *Drug. Disc. Today. Technol.*, **2004**, 1, 337.
- [516] H. Kubinyi, Drug research: myths, hype and reality, *Nat. Rev. Drug Disc.*, **2003**, 2, 665.
- [517] K. D. Freeman-Cook, R. L. Hoffman, T. W. Johnson, Lipophilic efficiency: the most important efficiency metric in medicinal chemistry, *Fut. Med. Chem.*, **2013**, 5, 113.
- [518] M. J. Waring, Lipophilicity in drug discovery, *Expert Opin. Drug Disc.*, **2010**, 5, 235.
- [519] J. A. Arnott, S. L. Planey, The influence of lipophilicity in drug discovery and design, *Expert Opin. Drug Disc.*, **2012**, 7, 863.
- [520] C. A. S. Bergstrom, M. Yazdaniyan, Lipophilicity in drug development: too much or not enough?, *AAPS J.*, **2016**, 18, 1095.
- [521] P. D. Leeson, B. Springthorpe, The influence of drug-like concepts on decision-making in medicinal chemistry, *Nat. Rev. Drug Disc.*, **2007**, 6, 881.
- [522] M. P. Edwards, D. A. Price, Role of physicochemical properties and ligand lipophilicity efficiency in addressing drug safety risk, *Ann. Reports Med. Chem.*, **2010**, 45, 381.
- [523] A. L. Hopkins, G. M. Keseru, P. D. Leeson, D. C. Rees, C. H. Reynolds, The role of ligand efficiency metrics in drug discovery, *Nat. Rev. Drug Disc.*, **2014**, 13, 105.
- [524] G. Klopman, H. Zhu, Recent methodologies for the estimation of n-octanol/water partition coefficients and their use in the prediction of membrane transport properties of drugs, *Mini-Rev. Med. Chem.*, **2005**, 5, 127.

- [525] A. V. Rudnev, L. S. Foteeva, C. Kowol, R. Berger, M. A. Jakupec, V. B. Arion, A. R. Timerbaev, B. K. Keppler, Preclinical characterization of anticancer gallium(III) complexes: solubility, stability, lipophilicity and binding to serum proteins, *J. Inorg. Biochem.*, **2006**, 100, 1819.
- [526] J. Barnett, G. D. Holman, R. A. Chalkley, K. A. Munday, Evidence for two asymmetric conformational states in the human erythrocyte sugar-transport system, *Biochem. J.*, **1975**, 145(3), 417.
- [527] M. Patra, T. C. Johnstone, K. Suntharalingam, S. J. Lippard, A potent glucose–platinum conjugate exploits glucose transporters and preferentially accumulates in cancer cells, *Angew. Chem.*, **2016**, 128, 2596.
- [528] H. Takanao, B. Chaudhuri, W. B. Frommer, GLUT1 and GLUT9 as major contributors to glucose influx in HepG2 cells identified by a high sensitivity intramolecular FRET glucose sensor, *Biochim. Biophys. Acta*, **2008**, 1778, 1091.
- [529] S. Rodríguez-Enríquez, A. Marín-Hernández, J. C. Gallardo-Pérez, R. Moreno-Sánchez, Kinetics of transport and phosphorylation of glucose in cancer cells, *J. Cell. Physiol.*, **2009**, 221, 552.
- [530] J. E. G. Barnett, G. D. Holman, K. A. Munday, An explanation of the asymmetric binding of sugars to the human erythrocyte sugar-transport system, *Biochem. J.*, **1973**, 135, 539.
- [531] D. S. Miller, D. M. Barnes, J. B. Pritchard, Confocal microscopic analysis of fluorescein compartmentation within crab urinary bladder cells, *Am. J. Physiol.*, **1994**, 267, R16.
- [532] E. V. Batrakova, S. Li, Sergey V. Vinogradov, V. Y. Alakhov, D. W. Miller, A. V. Kabanov, Mechanism of pluronic effect on p-glycoprotein efflux system in blood-brain barrier: contributions of energy depletion and membrane fluidization, *J. Pharmacol. Exp. Ther.*, **2001**, 299, 483.
- [533] A. Gigout, M. D. Buschmann, M. Jolicoeur, The fate of Pluronic F-68 in chondrocytes and CHO cells, *Biotechnol. Bioeng.*, **2008**, 5, 975.
- [534] D. Zhang, L. Tao, H. Zhao, H. Yuan, M. Lan, A functional drug delivery platform for targeting and imaging cancer cells based on Pluronic F127, *J. Biomater. Sci. Polym. Ed.*, **2015**, 26, 468.
- [535] N. Ke, X. Wang, X. Xu, Y. A. Abassi, The xCELLigence system for real-time and label-free monitoring of cell viability in *Mammalian Cell Viability: Methods and Protocols*, **2011**, M. J. Stoddart ed., Methods in molecular biology (740), Humana Press.
- [536] S. Y. Park, J. B. Choi, S. Kim, Measurement of cell-substrate impedance and characterization of cancer cell growth kinetics with mathematical model, *Int. J. Precis. Eng. Man.*, **2015**, 16, 1859.
- [537] Y. A. Abassi, W. Zhang, P. Ye, S. L. Kirstein, M. R. Gaylord, S. C. Feinstein, X. Wang, X. Xu, Kinetic cell-based morphological screening: prediction of mechanism of compound action and off-target effects, *Chem. Biol.*, **2009**, 16, 712.
- [538] L. Zeng, Y. Chen, J. Liu, H. Huang, R. Guan, L. Ji, H. Chao, Ruthenium(II) complexes with 2-phenylimidazo[4,5-f][1,10]phenanthroline derivatives that strongly combat cisplatin-resistant tumor cells, *Sci. Rep.*, **2016**, 6, 19449.
- [539] C. Nardon, G. Boscutti, C. Gabbiani, L. massai, N. Pettenuzzo, A. Fassina, L. Messori, D. Fregona, Cell and cell-free mechanistic studies on two gold(III) complexes with proven antitumor properties, *Eur. J. Inorg. Chem.*, **2017**, DOI: 10.1002/ejic.201601215.

SUPPORTING INFORMATION A -  $^1\text{H-NMR}$  spectra of the synthesized dithiocarbamate ligands**Figure A1.**  $^1\text{H-NMR}$  (DMSO- $d_6$ , 298 K, 300.13 MHz) spectrum of piperidine dithiocarbamate potassium salt (K PipeDTC).**Figure A2.**  $^1\text{H-NMR}$  (DMSO- $d_6$ , 298 K, 300.13 MHz) spectrum of morpholine dithiocarbamate potassium salt (K MorphDTC).

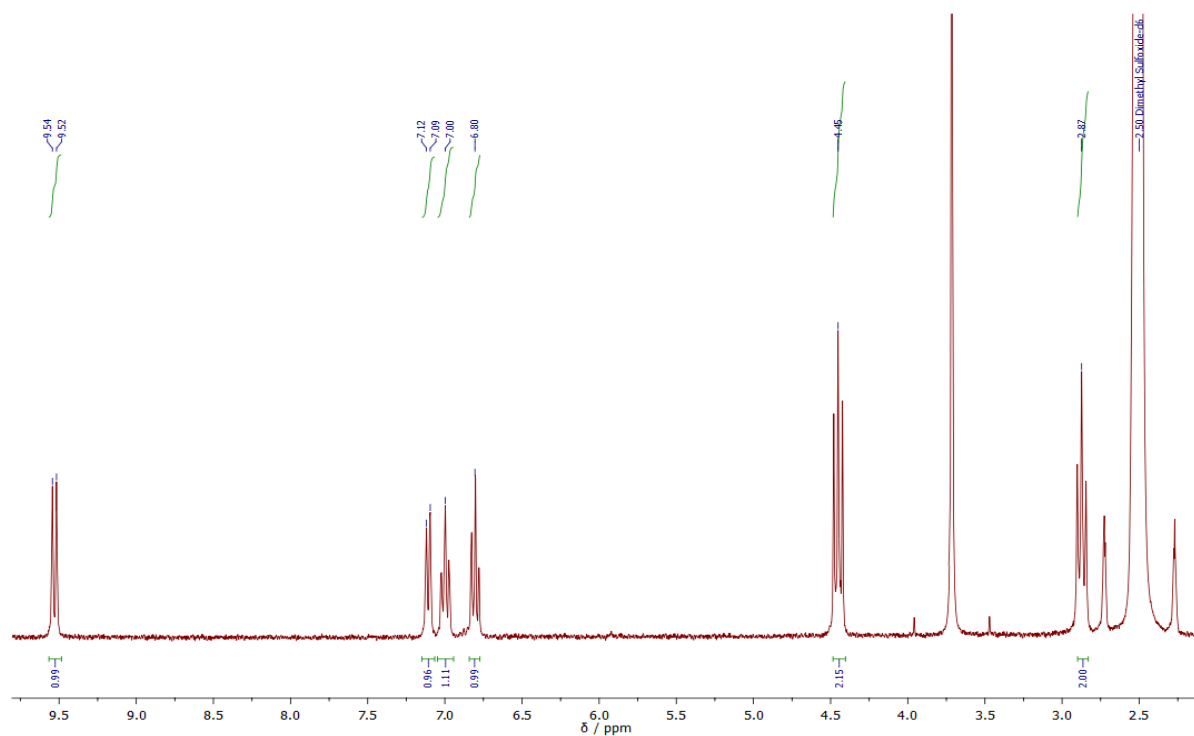


**Figure A3.** <sup>1</sup>H-NMR (DMSO-d<sub>6</sub>, 298 K, 300.13 MHz) spectrum of indoline dithiocarbamate potassium salt (K IndolineDTC).

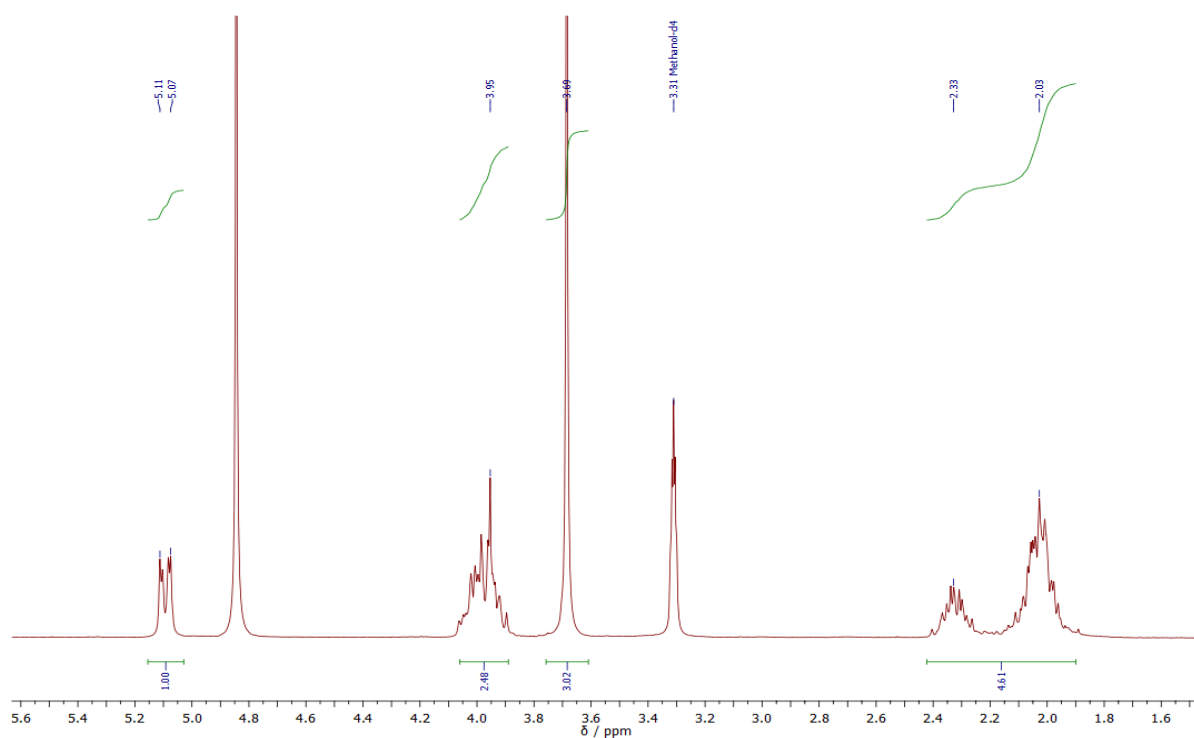


**Figure A4.** <sup>1</sup>H-NMR (CD<sub>3</sub>OD, 298 K, 300.13 MHz) spectrum of L-proline methyl ester dithiocarbamate sodium salt (Na ProOMeDTC).



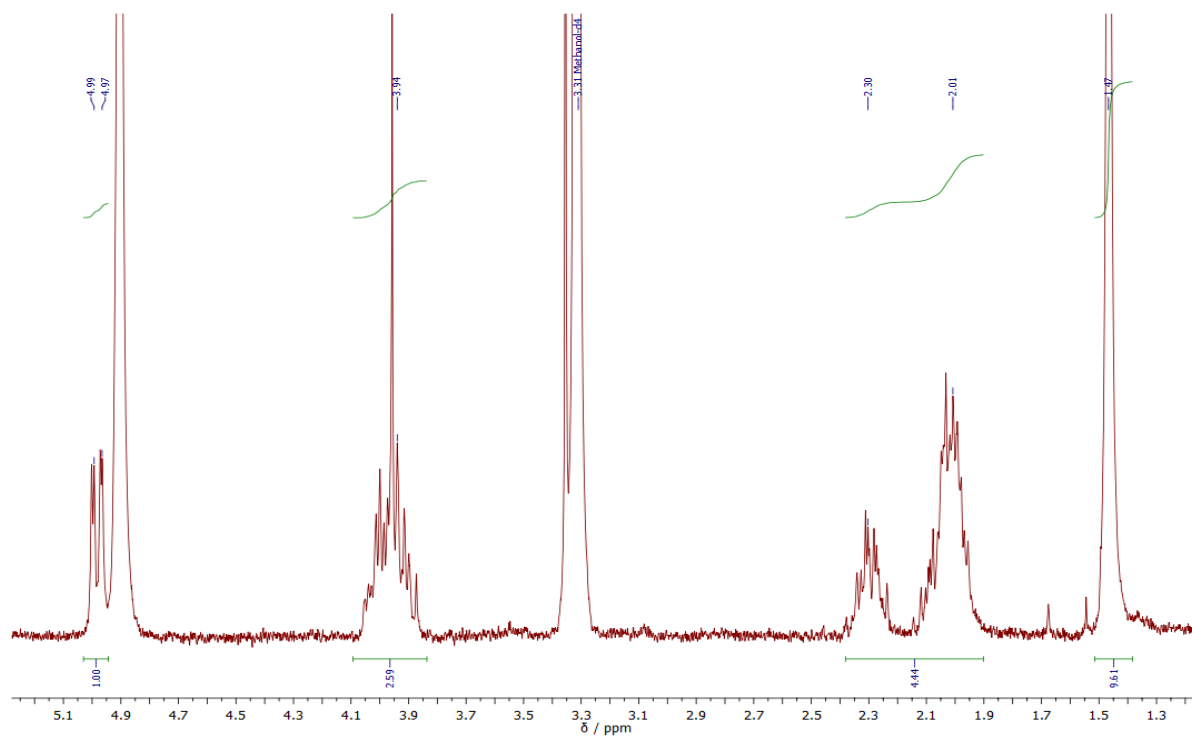


**Figure A5.**  $^1\text{H-NMR}$  ( $\text{CD}_3\text{OD}$ , 298 K, 300.13 MHz) spectrum of L-proline *tert*-butyl ester dithiocarbamate sodium salt (Na ProOtBuDTC).

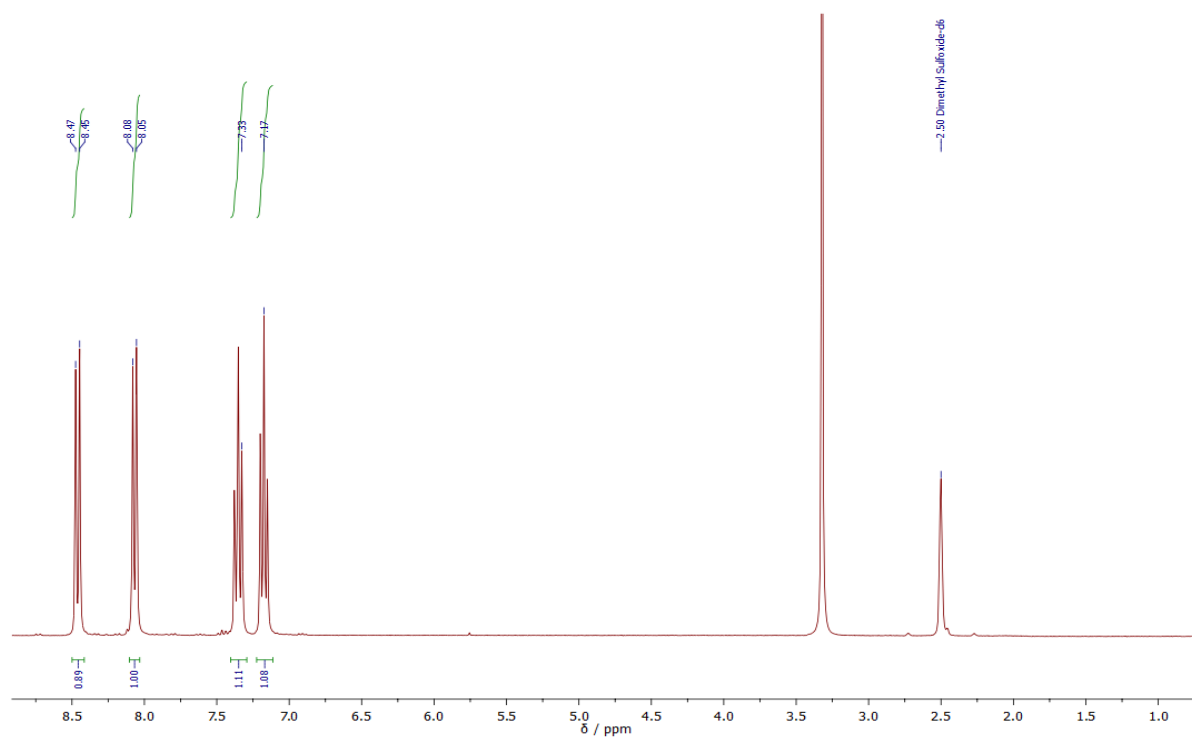


**Figure A6.**  $^1\text{H-NMR}$  ( $\text{DMSO-d}_6$ , 298 K, 300.13 MHz) spectrum of carbazole dithiocarbamate sodium salt (Na CDT).

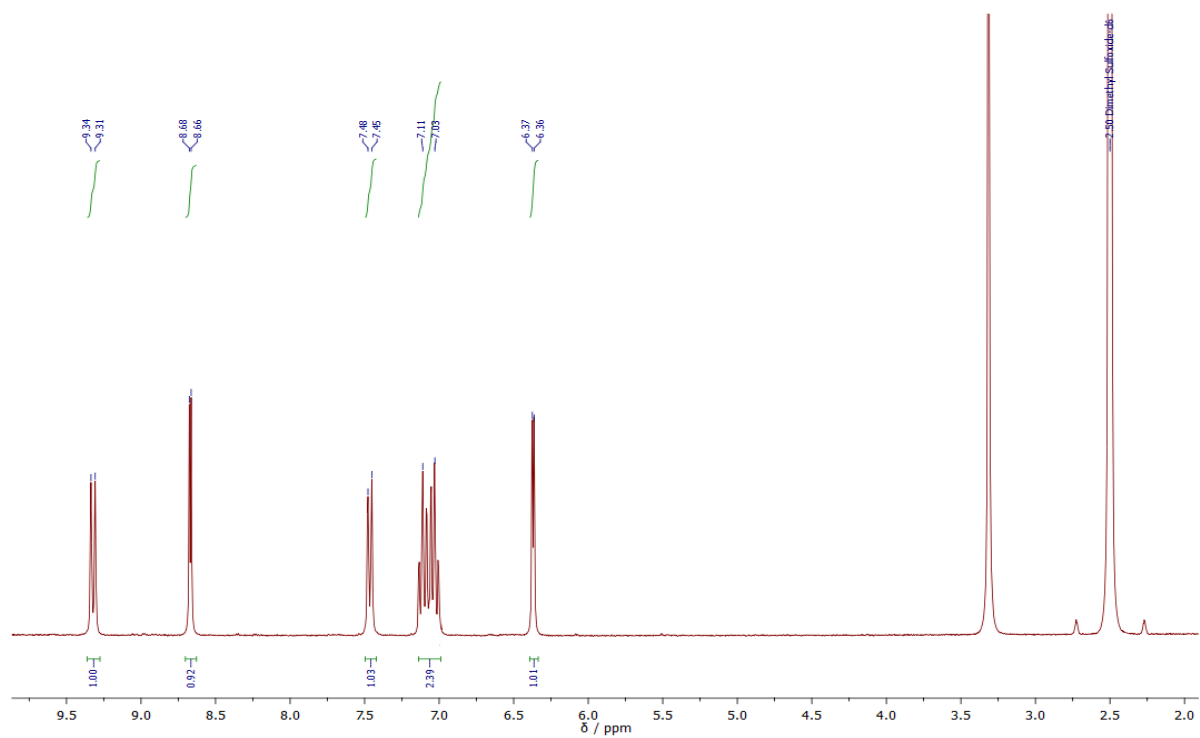


Figure A7.  $^1\text{H-NMR}$  ( $\text{DMSO-d}_6$ , 298 K, 300.13 MHz) spectrum of indole dithiocarbamate sodium salt (Na IndDTC).

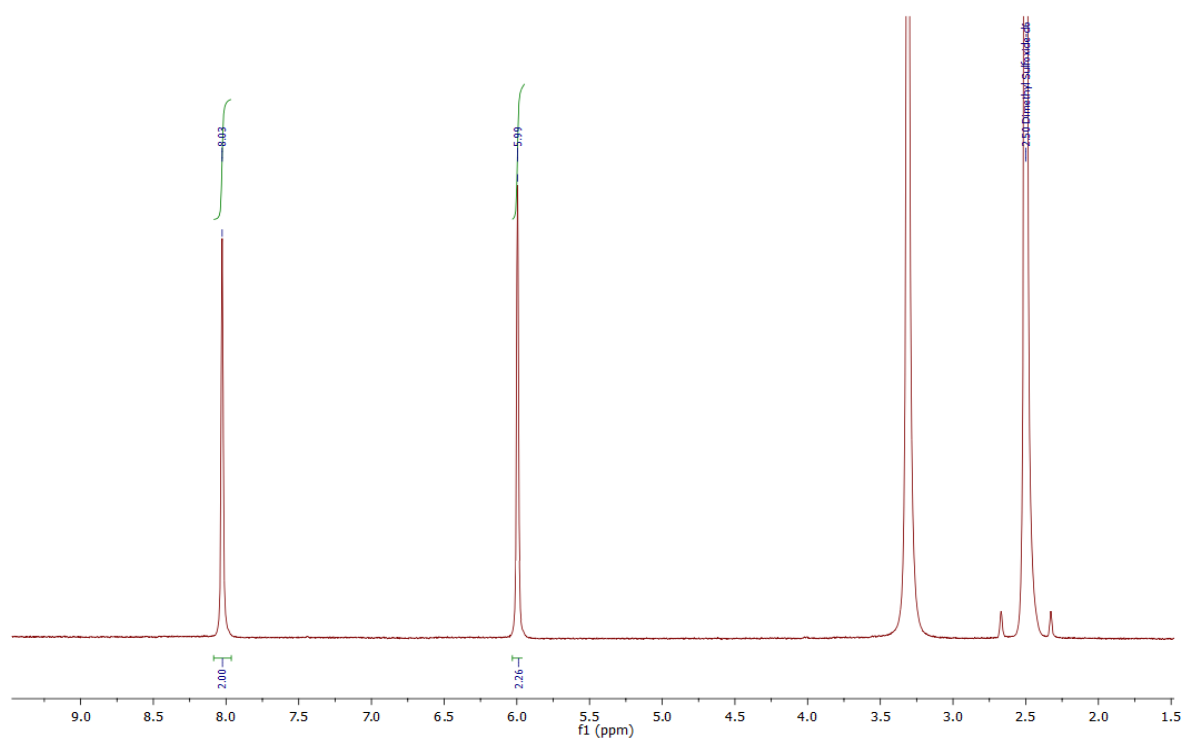
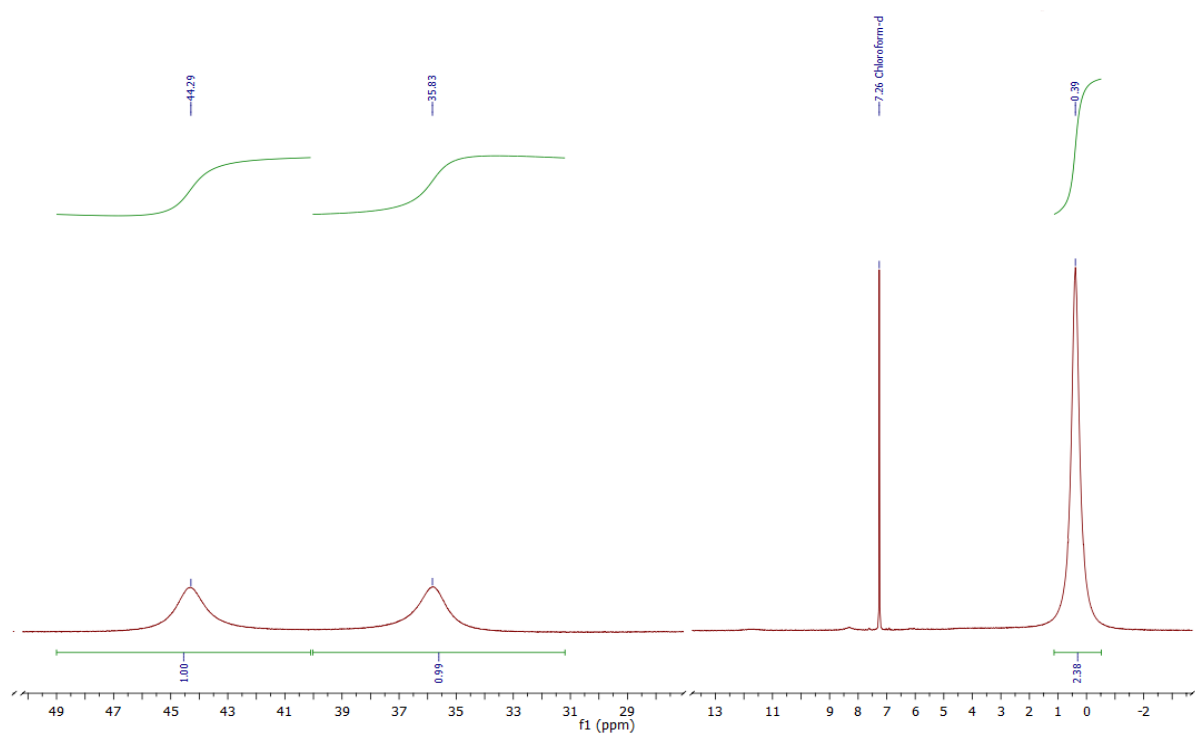
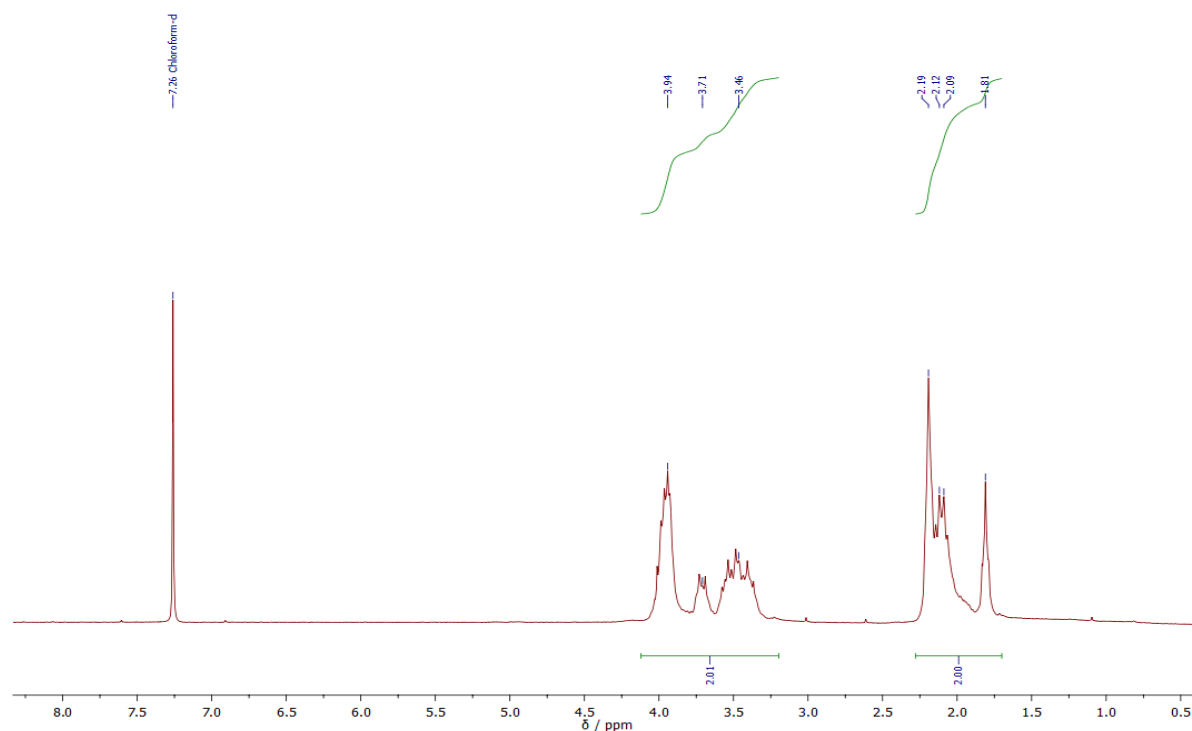
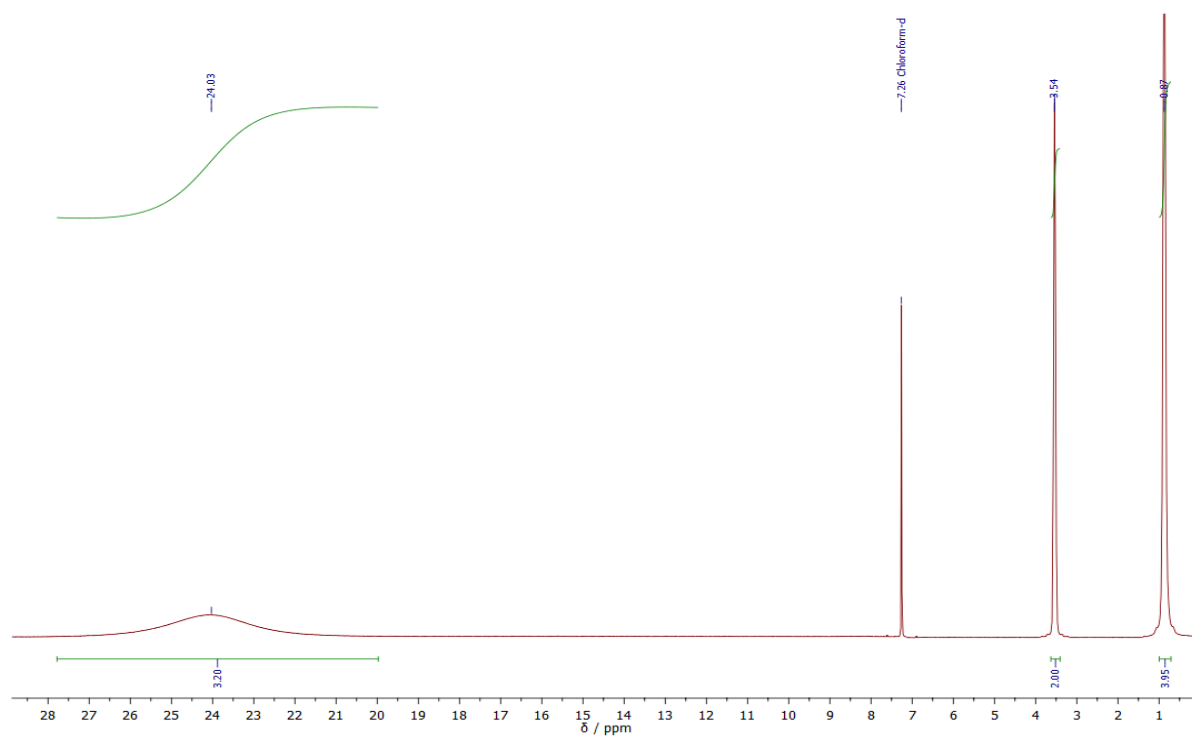
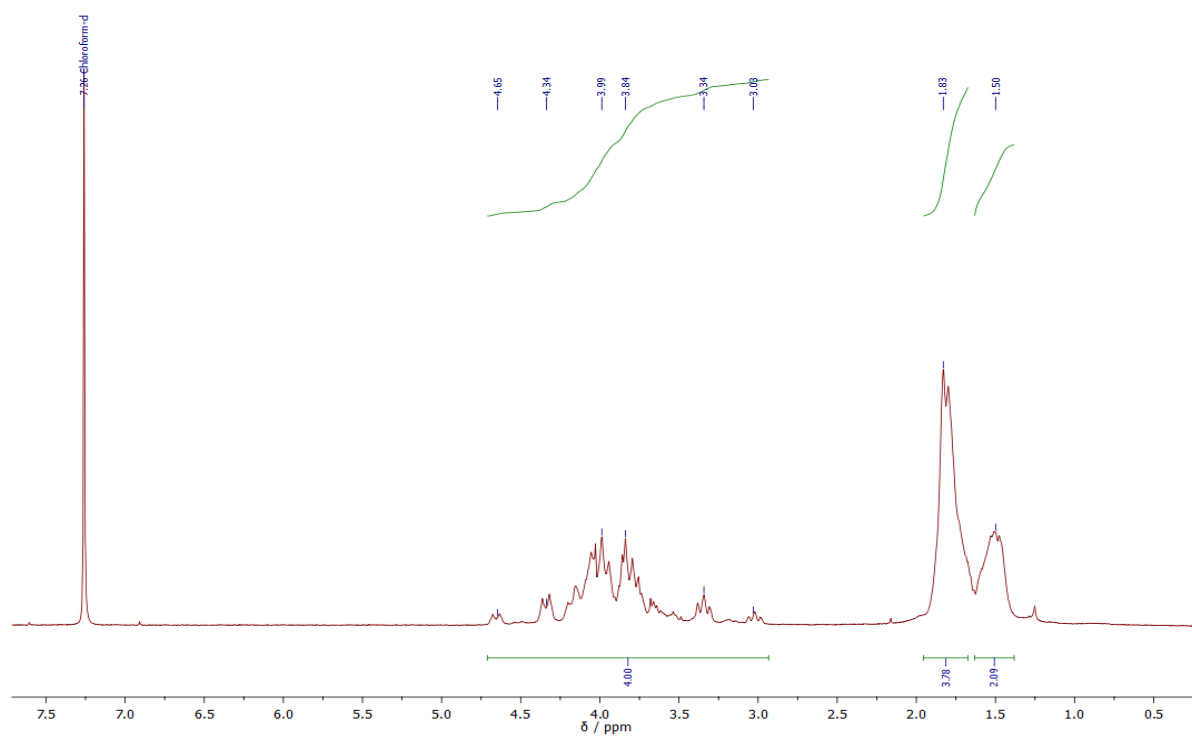


Figure A7.  $^1\text{H-NMR}$  ( $\text{DMSO-d}_6$ , 298 K, 300.13 MHz) spectrum of pyrrole dithiocarbamate sodium salt (Na PyrDTC).

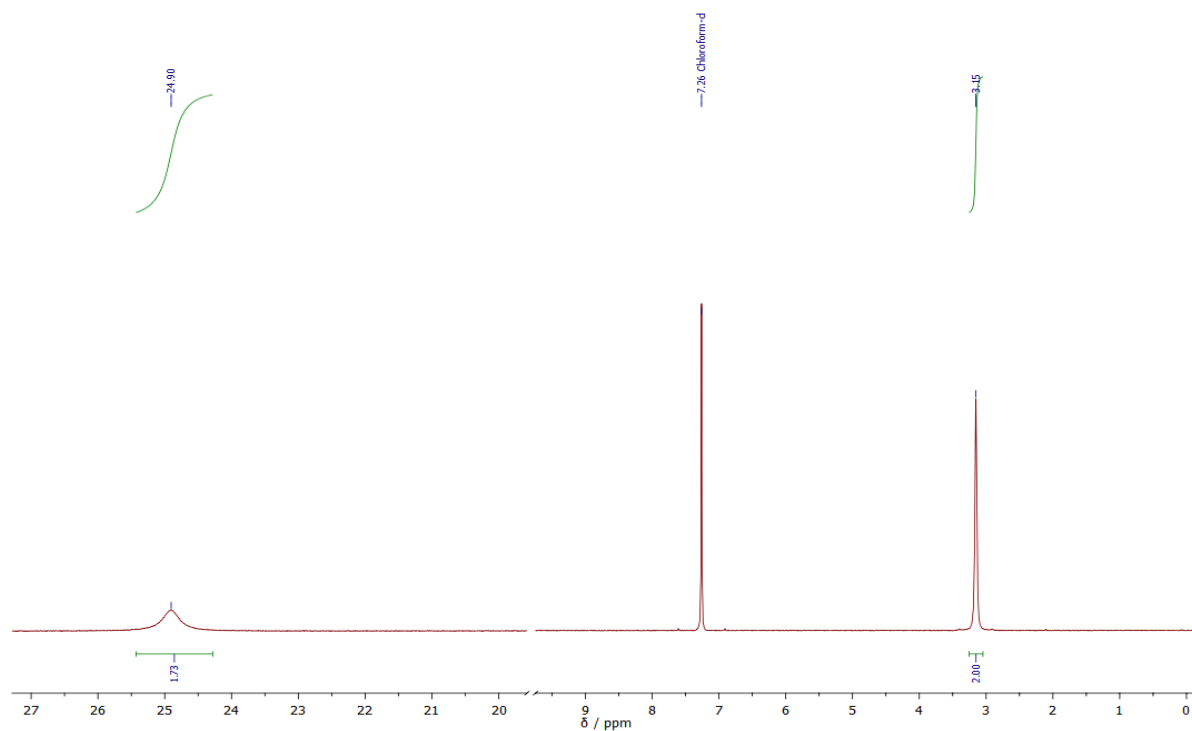
SUPPORTING INFORMATION B -  $^1\text{H-NMR}$  spectra of the synthesized Ru(III) dithiocarbamate complexes**Figure B1.**  $^1\text{H-NMR}$  ( $\text{CDCl}_3$ , 298 K, 300.13 MHz) spectrum of tris(pyrrolidine dithiocarbamate)ruthenium(III),  $[\text{Ru}(\text{PDT})_3]$ .**Figure B2.**  $^1\text{H-NMR}$  ( $\text{CDCl}_3$ , 298 K, 300.13 MHz) spectrum of  $\beta$ -pentakis(pyrrolidine dithiocarbamate)diruthenium(III) chloride,  $\beta\text{-}[\text{Ru}_2(\text{PDT})_5]\text{Cl}$ .



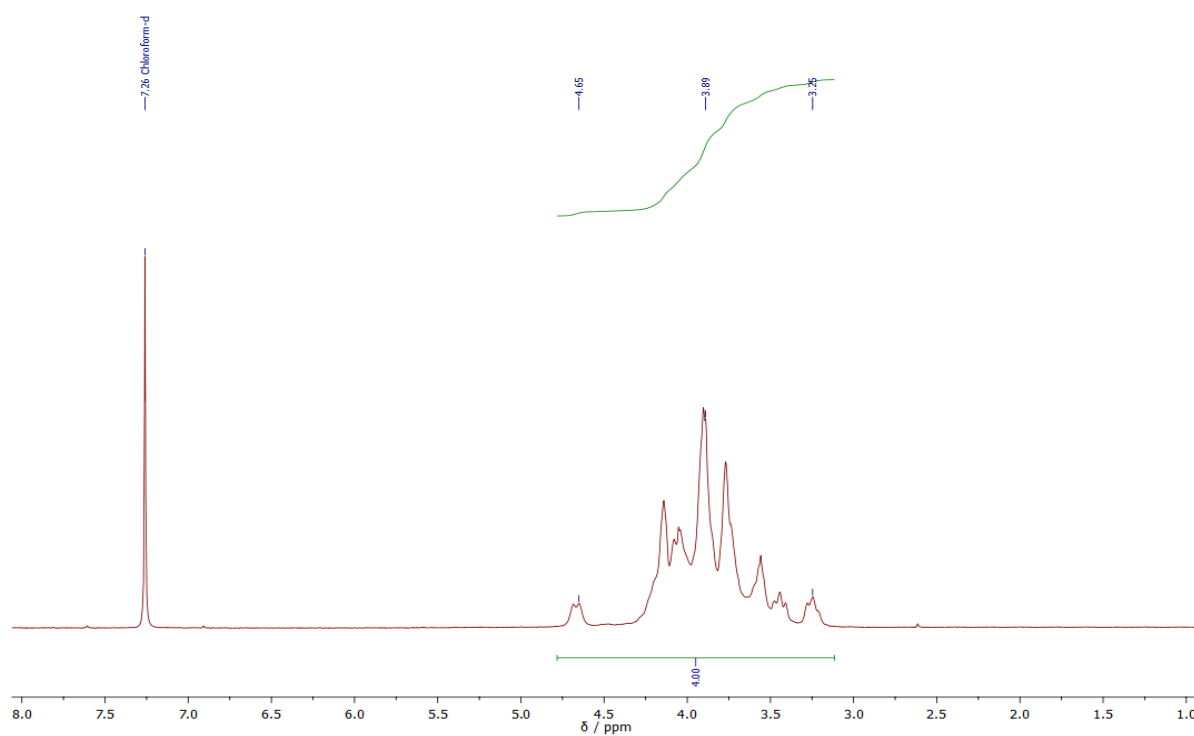
**Figure B3.**  $^1\text{H-NMR}$  ( $\text{CDCl}_3$ , 298 K, 300.13 MHz) spectrum of tris(piperidine dithiocarbamate)ruthenium(III),  $[\text{Ru}(\text{PipeDTC})_3]$ .



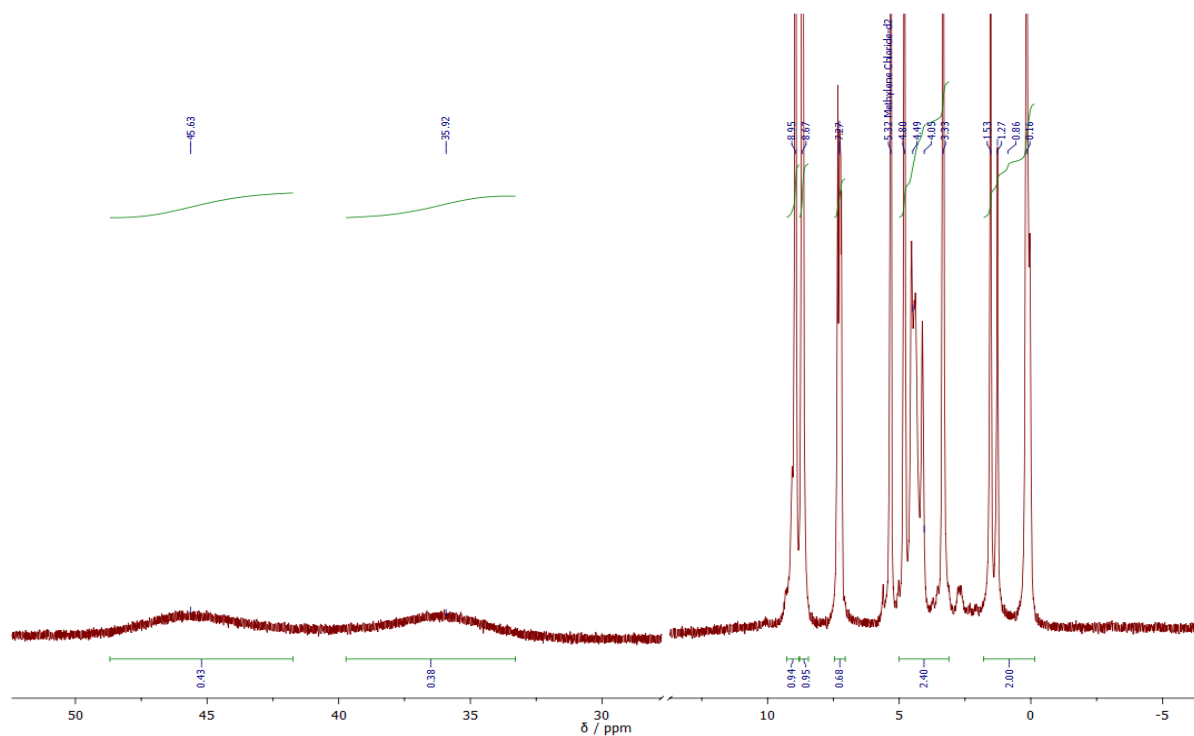
**Figure B4.**  $^1\text{H-NMR}$  ( $\text{CDCl}_3$ , 298 K, 300.13 MHz) spectrum of  $\beta$ -pentakis(piperidine dithiocarbamate)diruthenium(III) chloride,  $\beta\text{-}[\text{Ru}_2(\text{PipeDTC})_5]\text{Cl}$ .



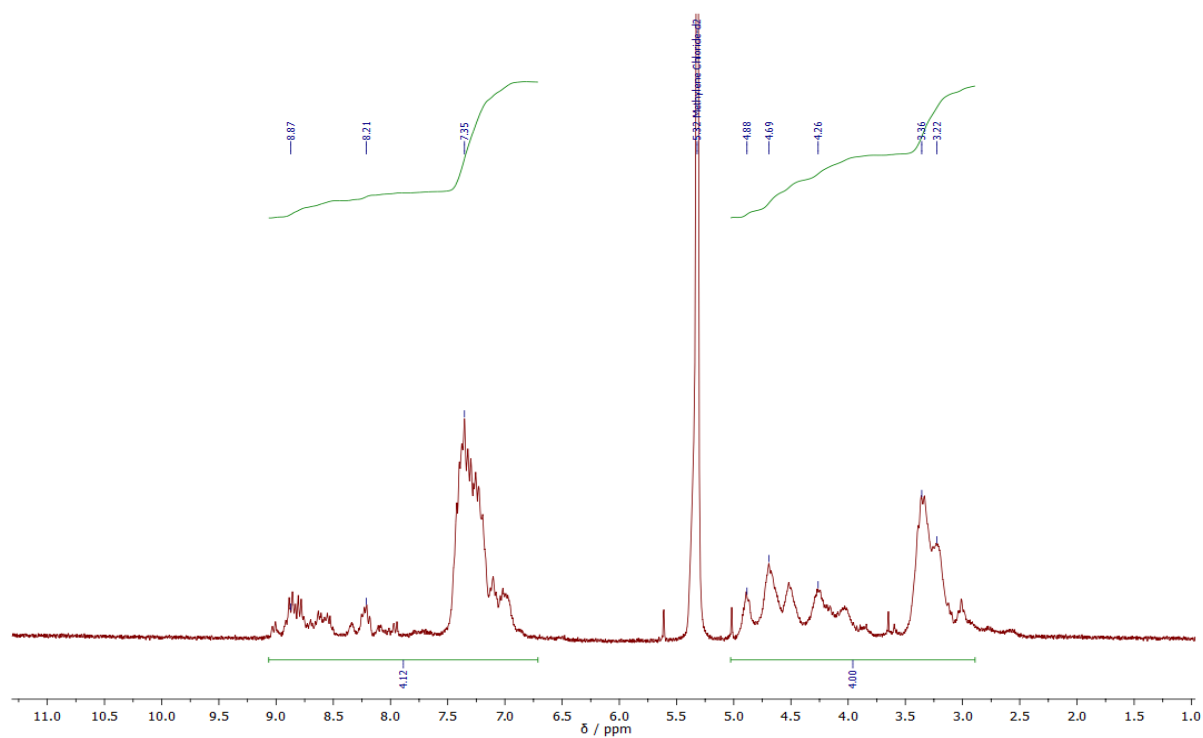
**Figure B5.**  $^1\text{H-NMR}$  ( $\text{CDCl}_3$ , 298 K, 300.13 MHz) spectrum of tris(morpholine dithiocarbamate)ruthenium(III),  $[\text{Ru}(\text{MorphDTC})_3]$ .



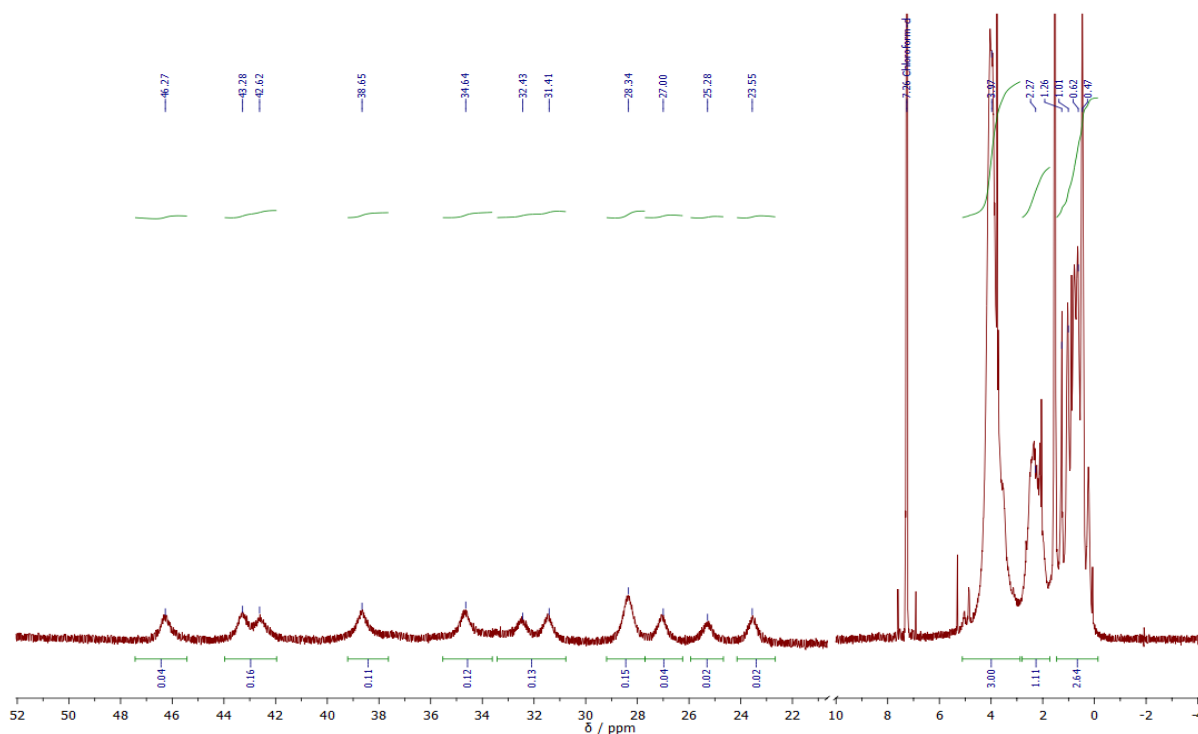
**Figure B6.**  $^1\text{H-NMR}$  ( $\text{CDCl}_3$ , 298 K, 300.13 MHz) spectrum of  $\beta$ -pentakis(morpholine dithiocarbamate)diruthenium(III) chloride,  $\beta$ - $[\text{Ru}_2(\text{MorphDTC})_5]\text{Cl}$ .



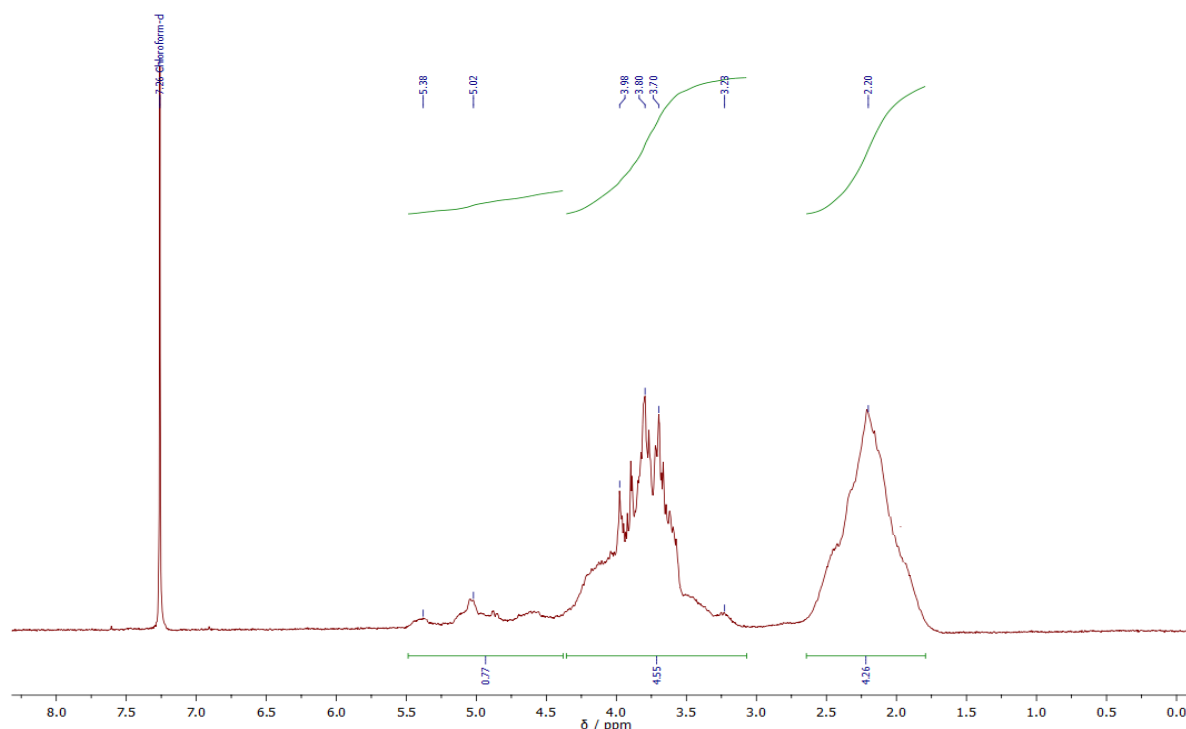
**Figure B7.** <sup>1</sup>H-NMR (CD<sub>2</sub>Cl<sub>2</sub>, 298 K, 300.13 MHz) spectrum of tris(indoline dithiocarbamate)ruthenium(III), [Ru(IndolineDTC)<sub>3</sub>].



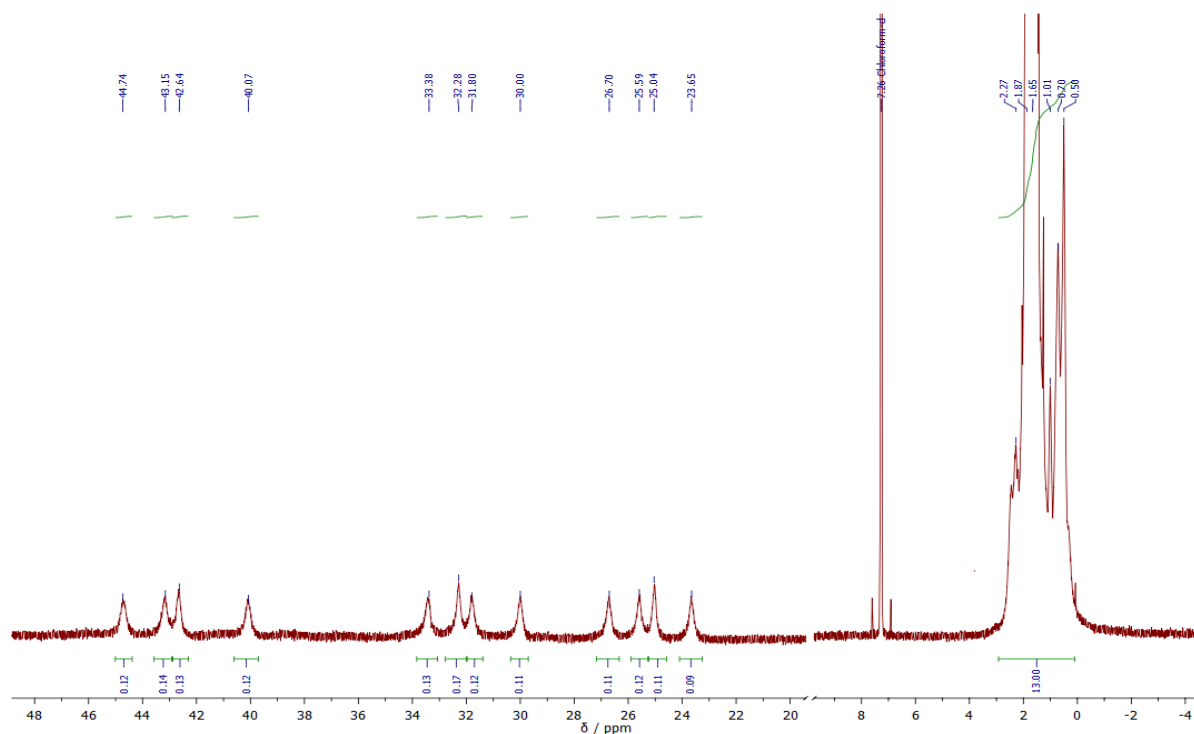
**Figure B8.** <sup>1</sup>H-NMR (CD<sub>2</sub>Cl<sub>2</sub>, 298 K, 300.13 MHz) spectrum of β-pentakis(indoline dithiocarbamate)diruthenium(III) chloride, β-[Ru<sub>2</sub>(IndolineDTC)<sub>5</sub>]Cl.



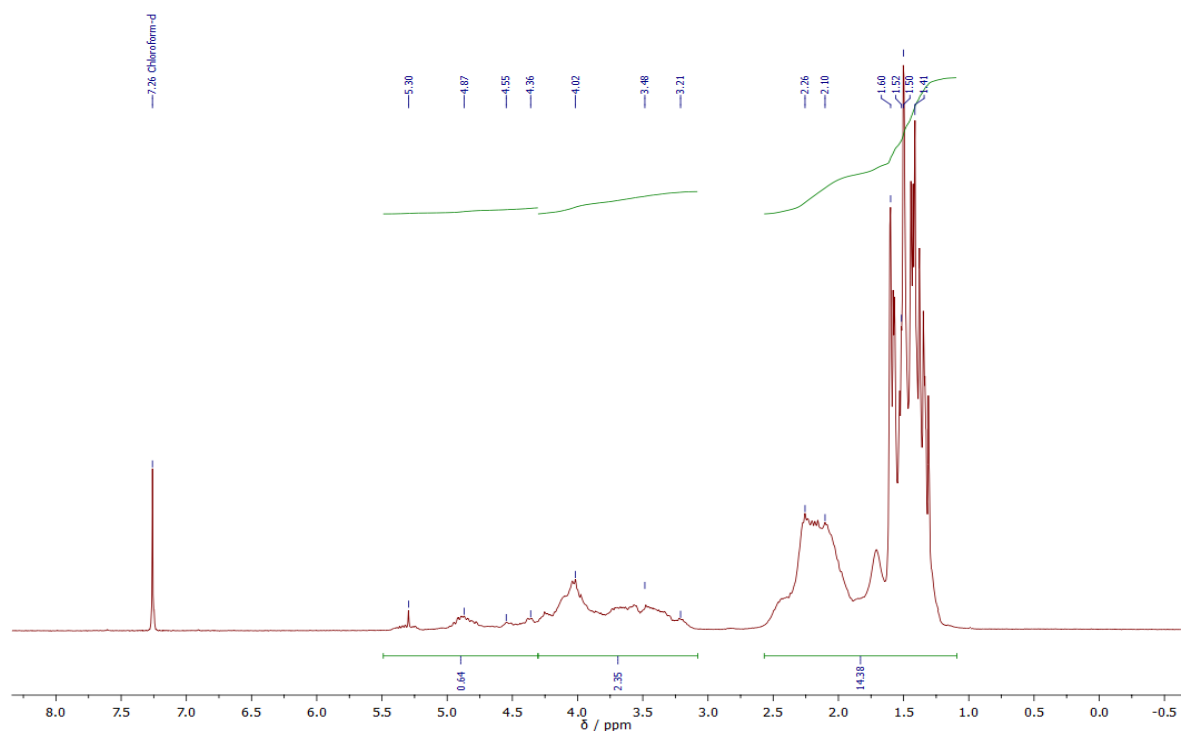
**Figure B9.**  $^1\text{H-NMR}$  ( $\text{CDCl}_3$ , 298 K, 300.13 MHz) spectrum of tris(L-proline methyl ester dithiocarbamate)ruthenium(III),  $[\text{Ru}(\text{ProOMeDTC})_3]$ .



**Figure B10.**  $^1\text{H-NMR}$  ( $\text{CDCl}_3$ , 298 K, 300.13 MHz) spectrum of  $\beta$ -pentakis(L-proline methyl ester dithiocarbamate)diruthenium(III) chloride,  $\beta$ - $[\text{Ru}_2(\text{ProOMeDTC})_5]\text{Cl}$ .

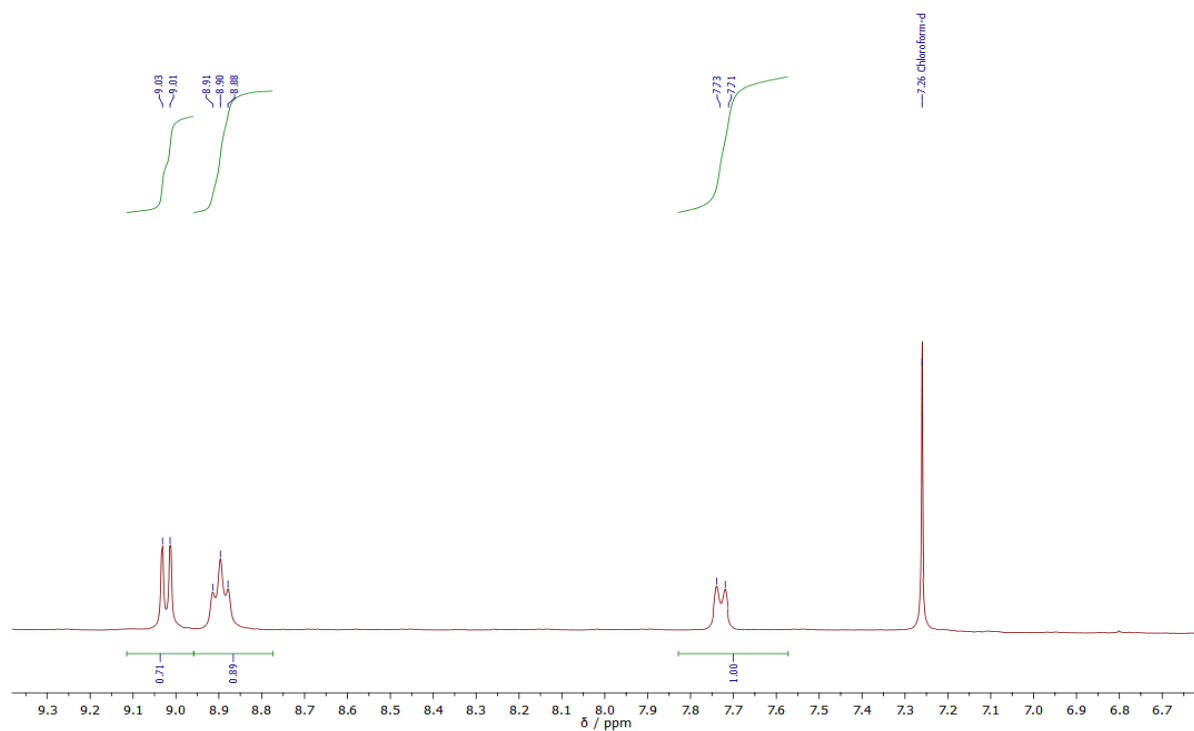


**Figure B11.** <sup>1</sup>H-NMR (CDCl<sub>3</sub>, 298 K, 300.13 MHz) spectrum of tris(L-proline *tert*-butyl ester dithiocarbamate)ruthenium(III), [Ru(ProOtBuDTC)<sub>3</sub>].

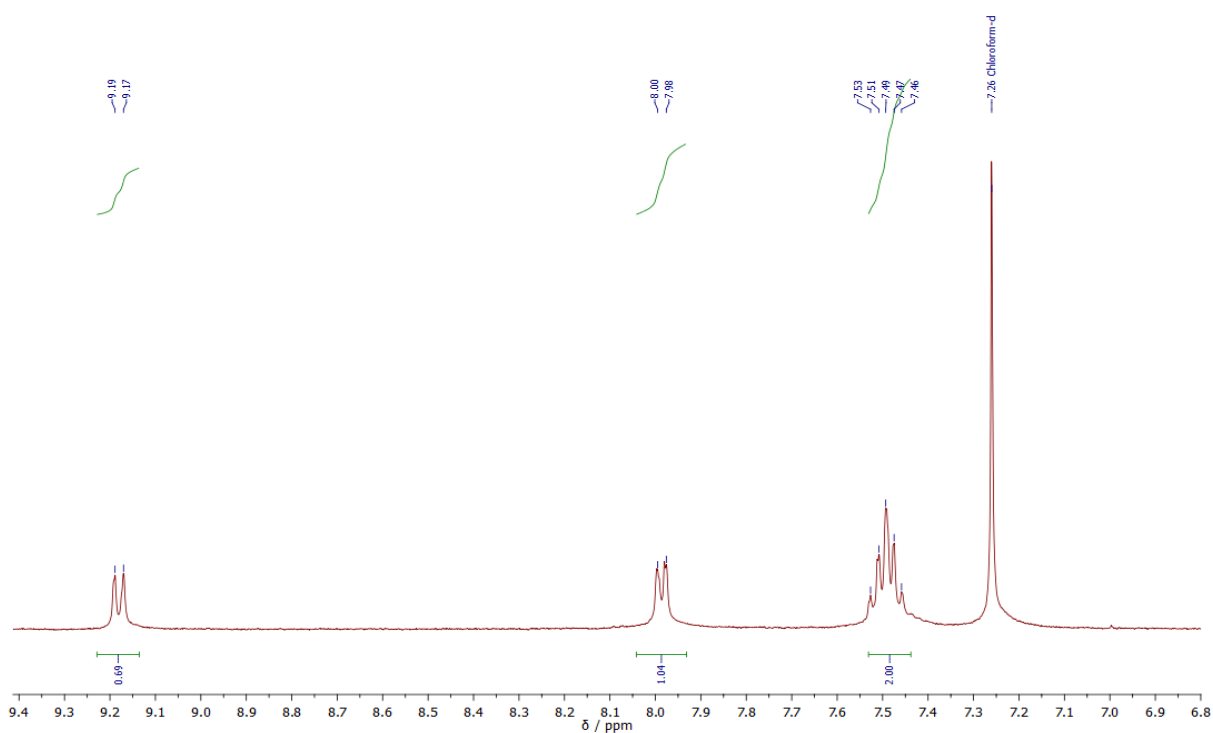


**Figure B12.** <sup>1</sup>H-NMR (CDCl<sub>3</sub>, 298 K, 300.13 MHz) spectrum of β-pentakis(L-proline *tert*-butyl ester dithiocarbamate)diruthenium(III) chloride, β-[Ru<sub>2</sub>(ProOtBuDTC)<sub>5</sub>]Cl.



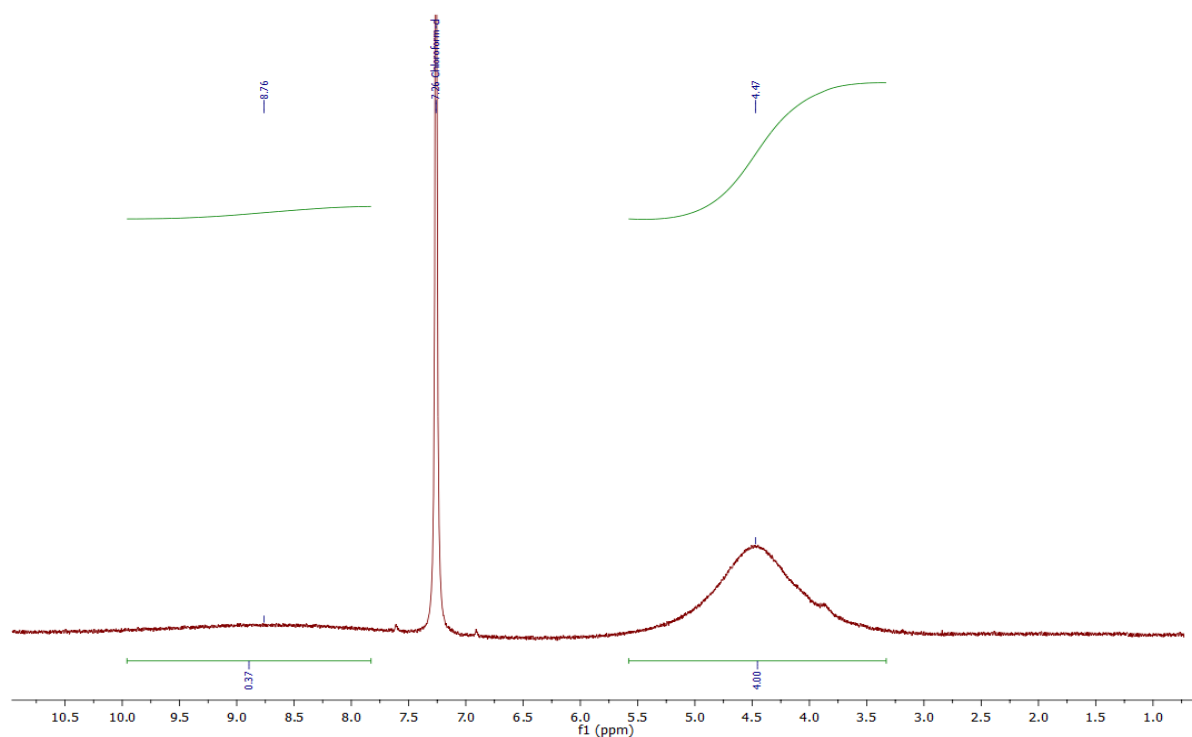
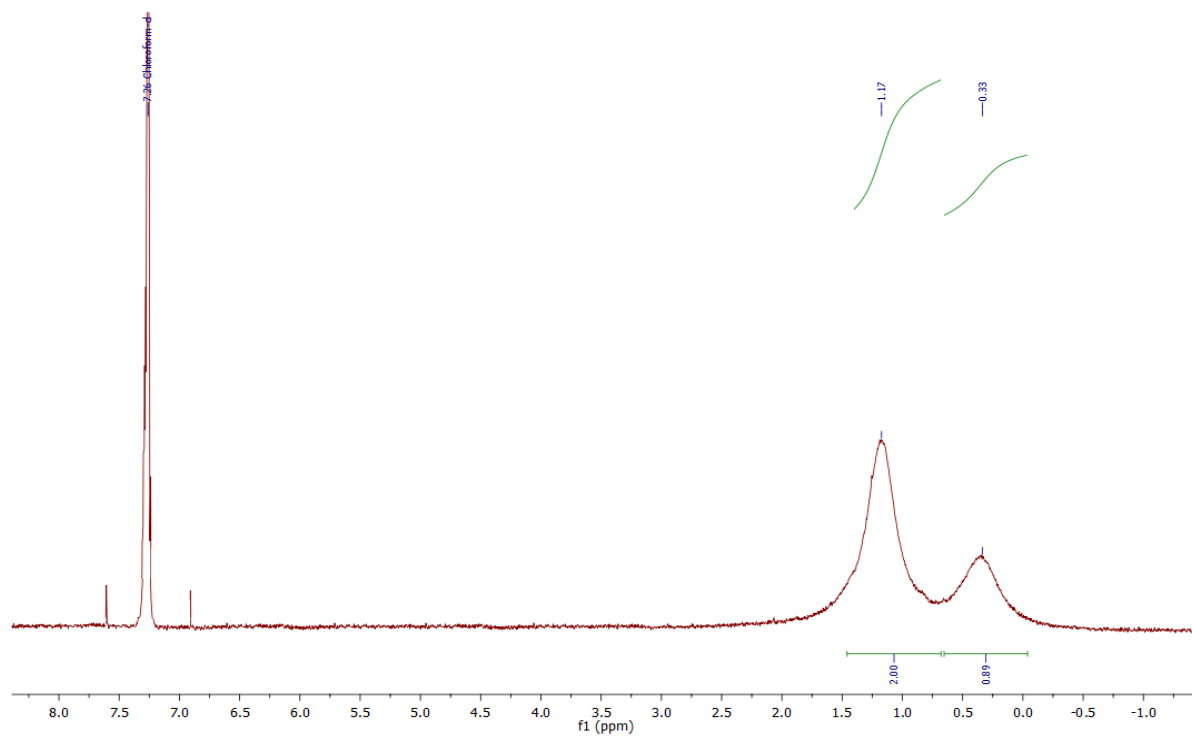


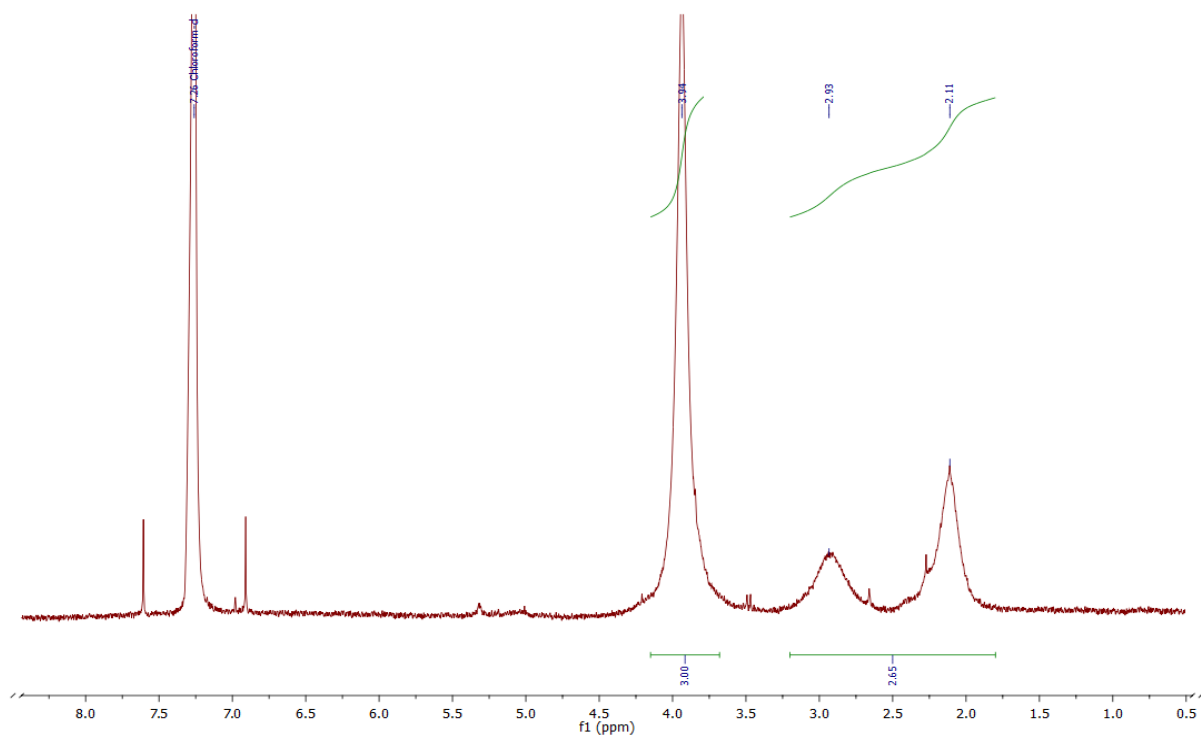
**Figure B13.**  $^1\text{H-NMR}$  ( $\text{CDCl}_3$ , 298 K, 300.13 MHz) spectrum of tris(carbazole dithiocarbamate)ruthenium(III),  $[\text{Ru}(\text{CDT})_3]$ .



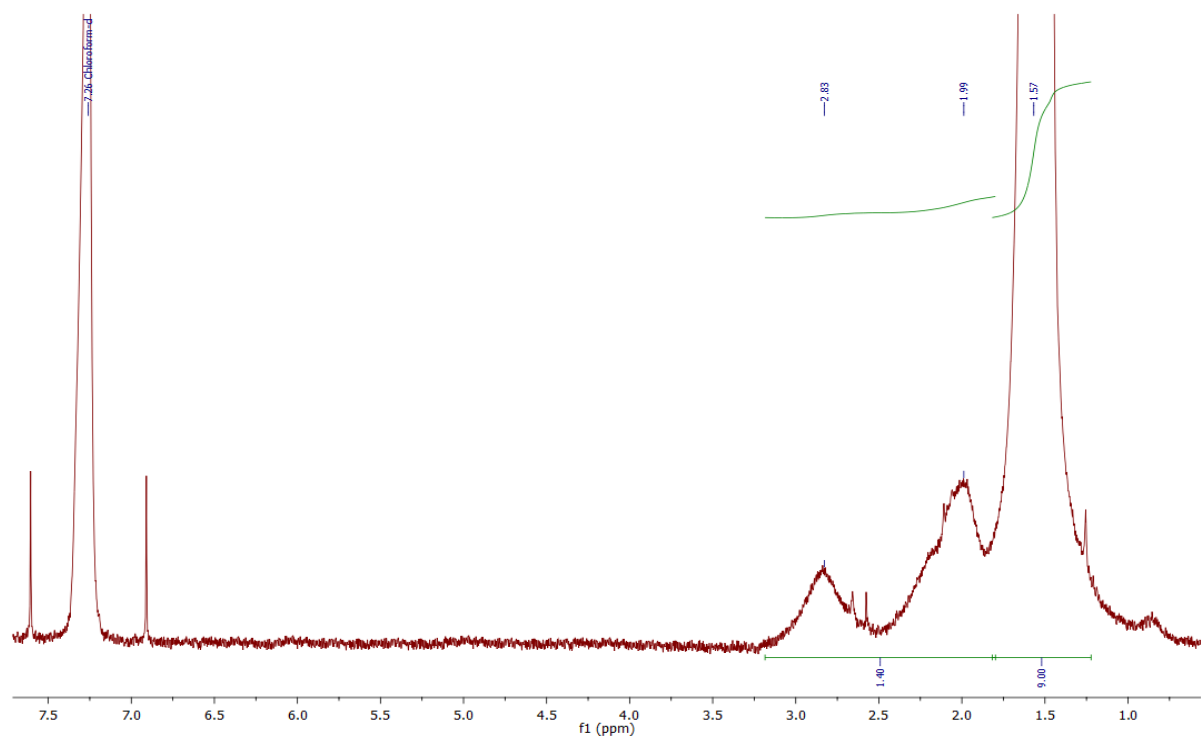
**Figure B14.**  $^1\text{H-NMR}$  ( $\text{CDCl}_3$ , 298 K, 300.13 MHz) spectrum of  $\beta$ -pentakis(carbazole dithiocarbamate)diruthenium(III) chloride,  $\beta$ - $[\text{Ru}_2(\text{CDT})_5]\text{Cl}$ .



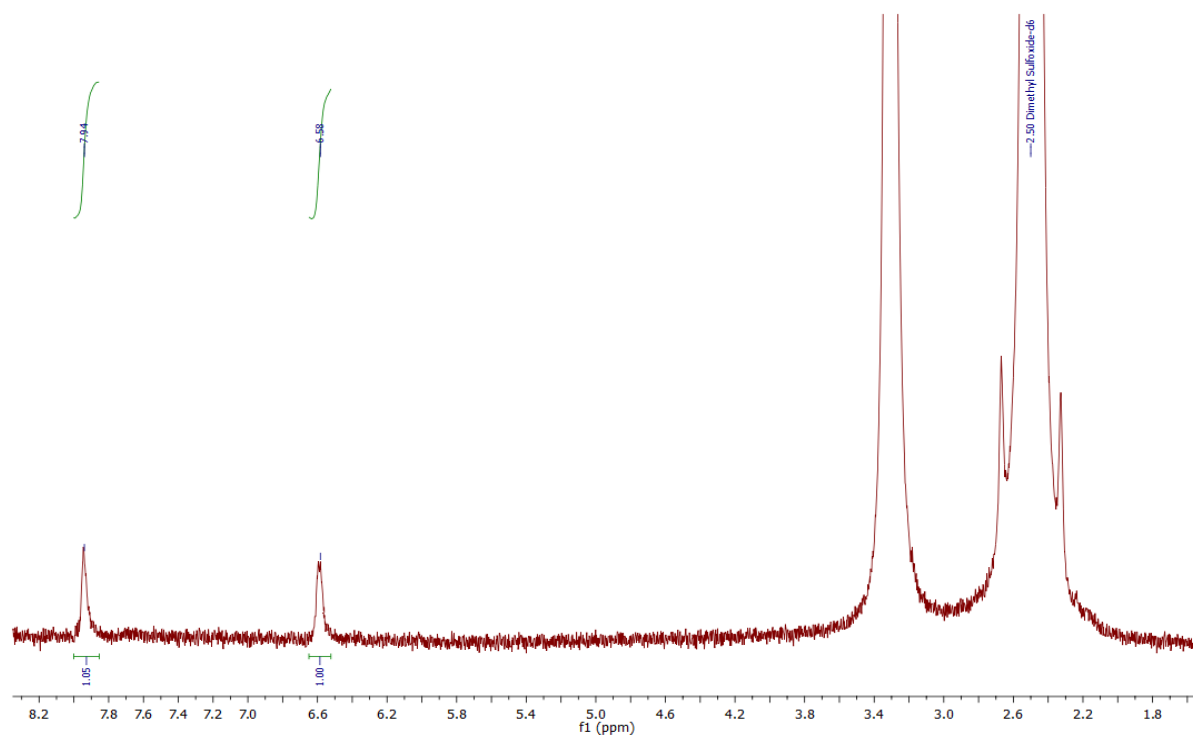
SUPPORTING INFORMATION C -  $^1\text{H-NMR}$  spectra of the synthesized Cu(II) dithiocarbamato complexes**Figure C1.**  $^1\text{H-NMR}$  ( $\text{CDCl}_3$ , 298 K, 300.13 MHz) spectrum of bis(pyrrolidine dithiocarbamate)copper (II),  $[\text{Cu}(\text{PDT})_2]$ .**Figure C2.**  $^1\text{H-NMR}$  ( $\text{CDCl}_3$ , 298 K, 300.13 MHz) spectrum of bis(piperidine dithiocarbamate)copper(II),  $[\text{Cu}(\text{PipeDTC})_2]$ .



**Figure C3.** <sup>1</sup>H-NMR (CDCl<sub>3</sub>, 298 K, 300.13 MHz) spectrum of bis(L-proline methyl ester dithiocarbamate)copper(II), [Cu(ProOMeDTC)<sub>2</sub>].



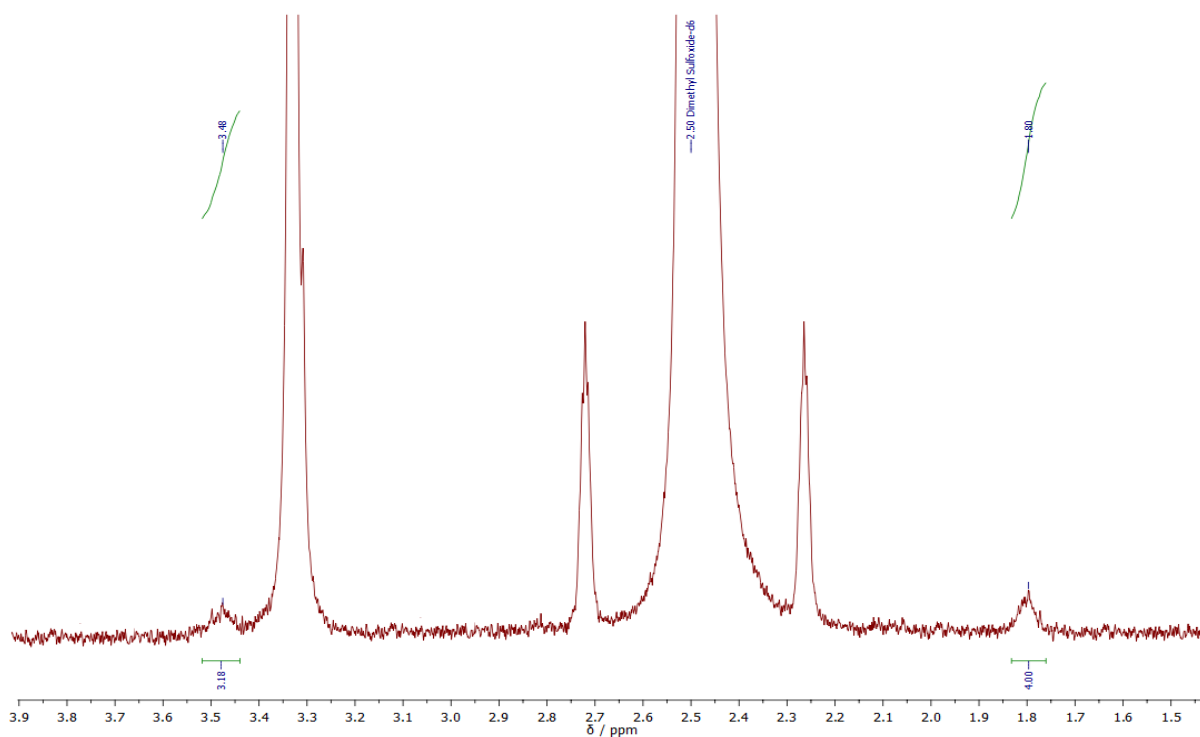
**Figure C4.** <sup>1</sup>H-NMR (CDCl<sub>3</sub>, 298 K, 300.13 MHz) spectrum of bis(L-proline *tert*-butyl ester dithiocarbamate)copper(II), [Cu(ProOtBuDTC)<sub>2</sub>].



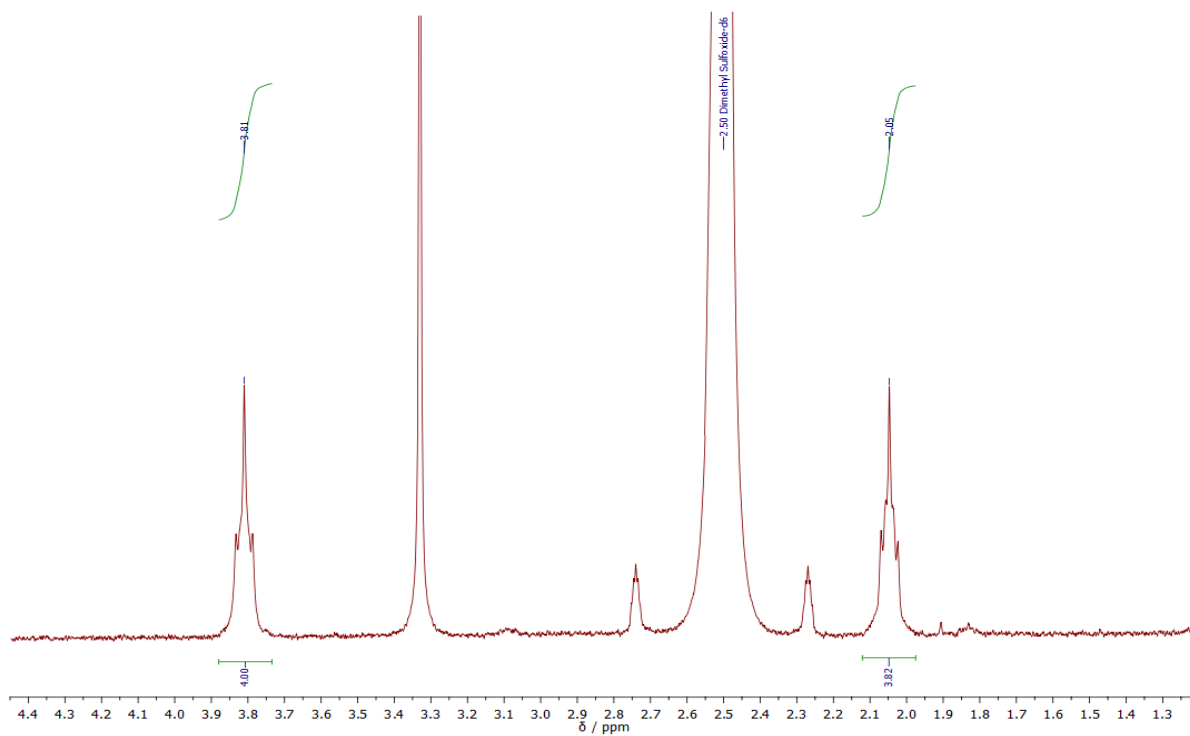
**Figure C5.** <sup>1</sup>H-NMR (DMSO-d<sub>6</sub>, 298 K, 300.13 MHz) spectrum of bis(pyrrole dithiocarbamate)copper(II), [Cu(PyrroleDTC)<sub>2</sub>].



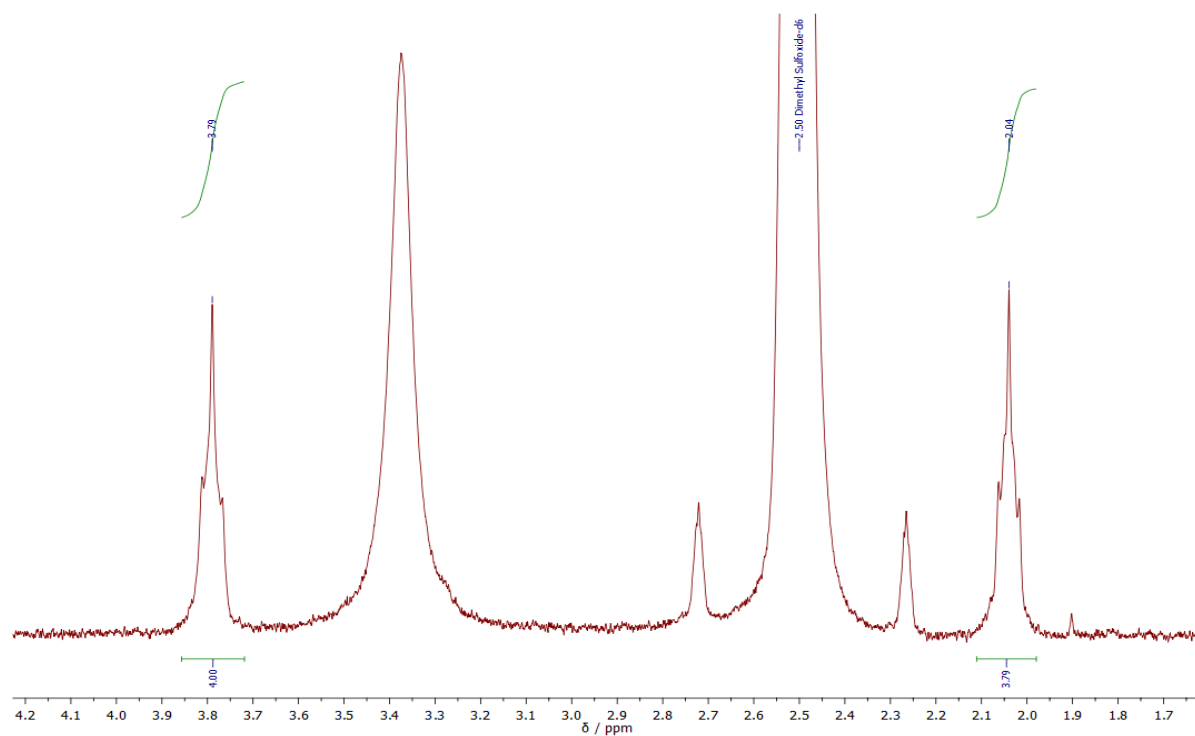
SUPPORTING INFORMATION D -  $^1\text{H-NMR}$  spectra of the synthesized Au(I)/(III) dithiocarbamate complexes



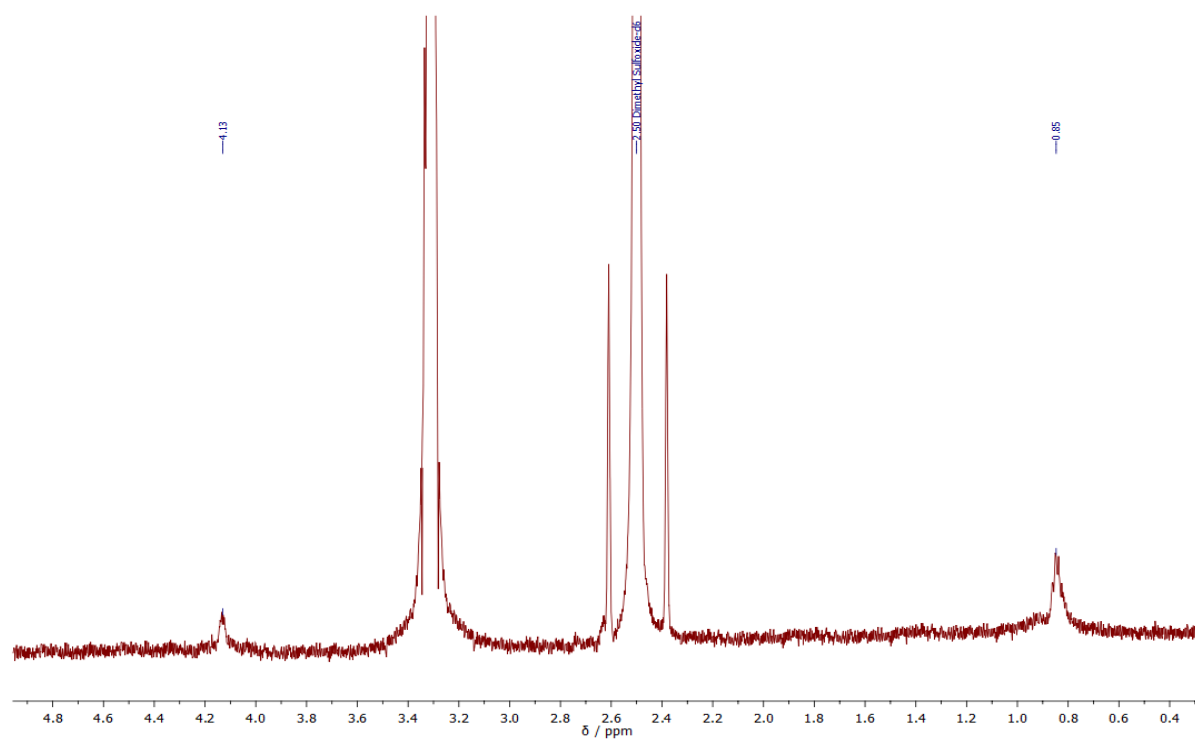
**Figure D1.**  $^1\text{H-NMR}$  (DMSO- $d_6$ , 298 K, 300.13 MHz) spectrum of bis(pyrrolidine dithiocarbamate)digold(I),  $[\text{Au}_2(\text{PDT})_2]$ .



**Figure D2.**  $^1\text{H-NMR}$  (DMSO- $d_6$ , 298 K, 300.13 MHz) spectrum of dichloro(pyrrolidine dithiocarbamate)gold(III),  $[\text{AuCl}_2(\text{PDT})]$ .

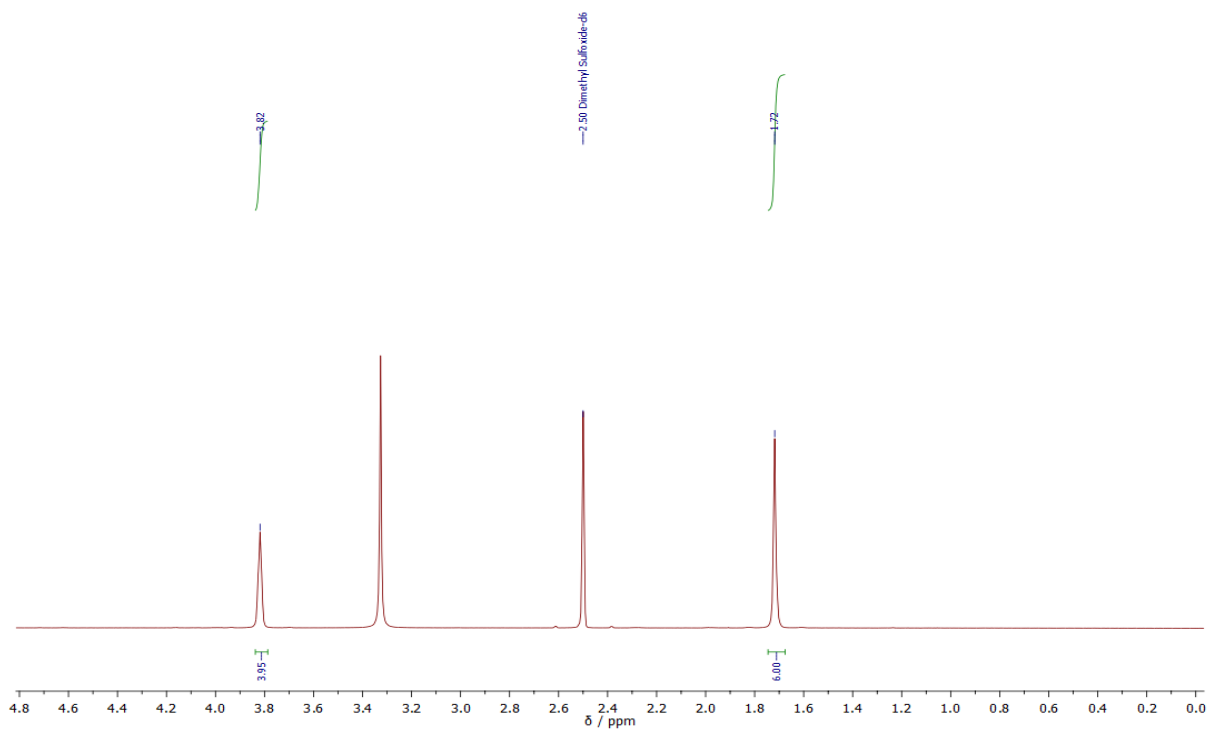


**Figure D3.** <sup>1</sup>H-NMR (DMSO-d<sub>6</sub>, 298 K, 300.13 MHz) spectrum of dibromo(pyrrolidine dithiocarbamate)gold(III), [AuBr<sub>2</sub>(PDT)].

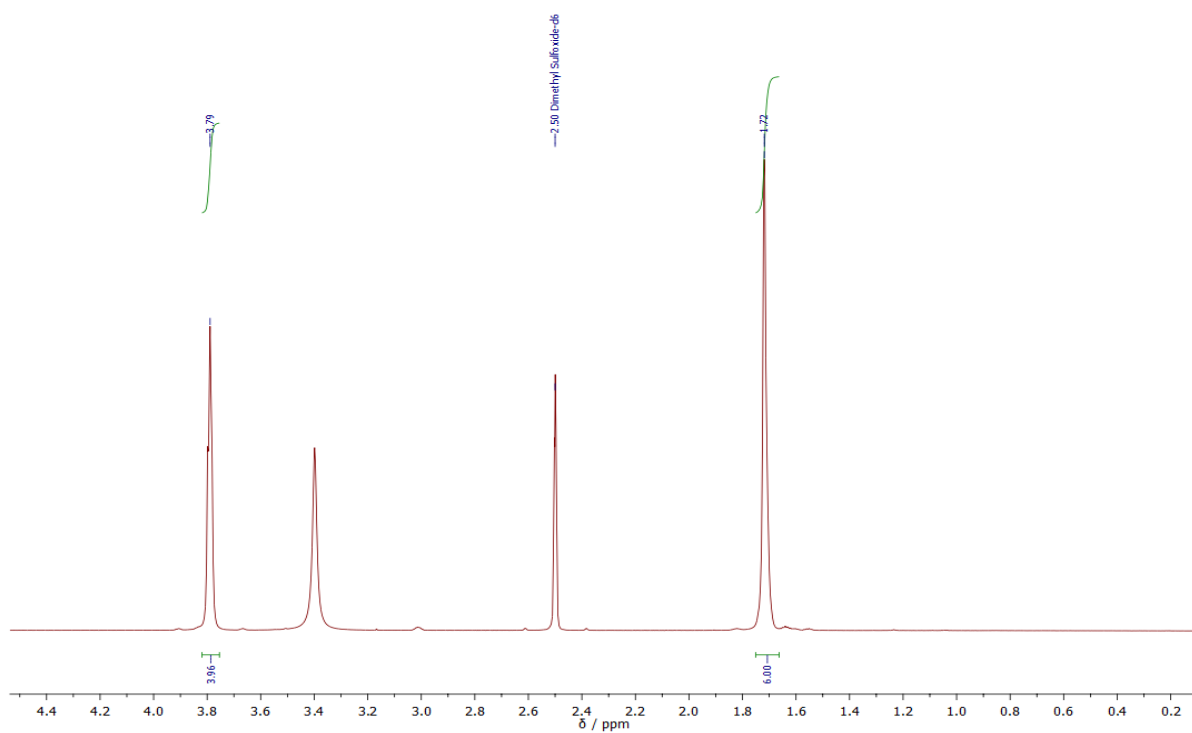


**Figure D4.** <sup>1</sup>H-NMR (DMSO-d<sub>6</sub>, 298 K, 300.13 MHz) spectrum of bis(piperidine dithiocarbamate)digold(I), [Au<sub>2</sub>(PipeDTC)<sub>2</sub>].

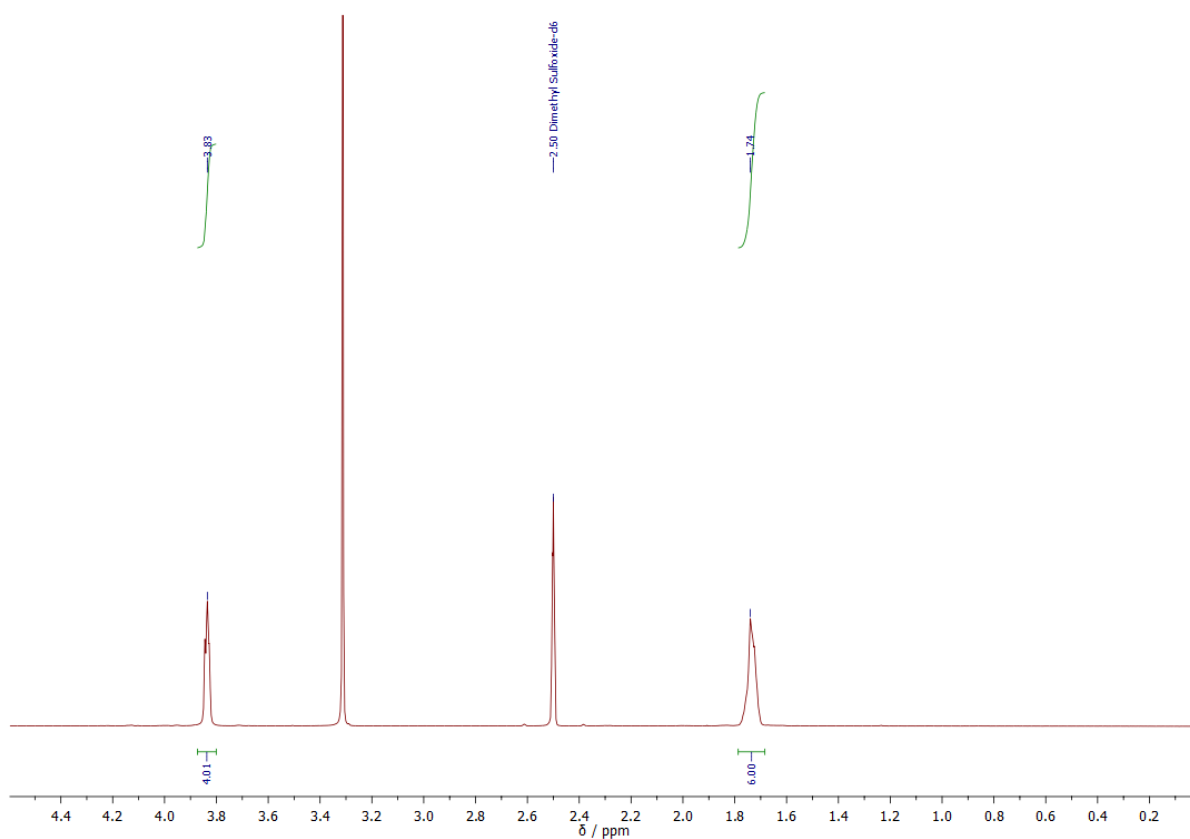




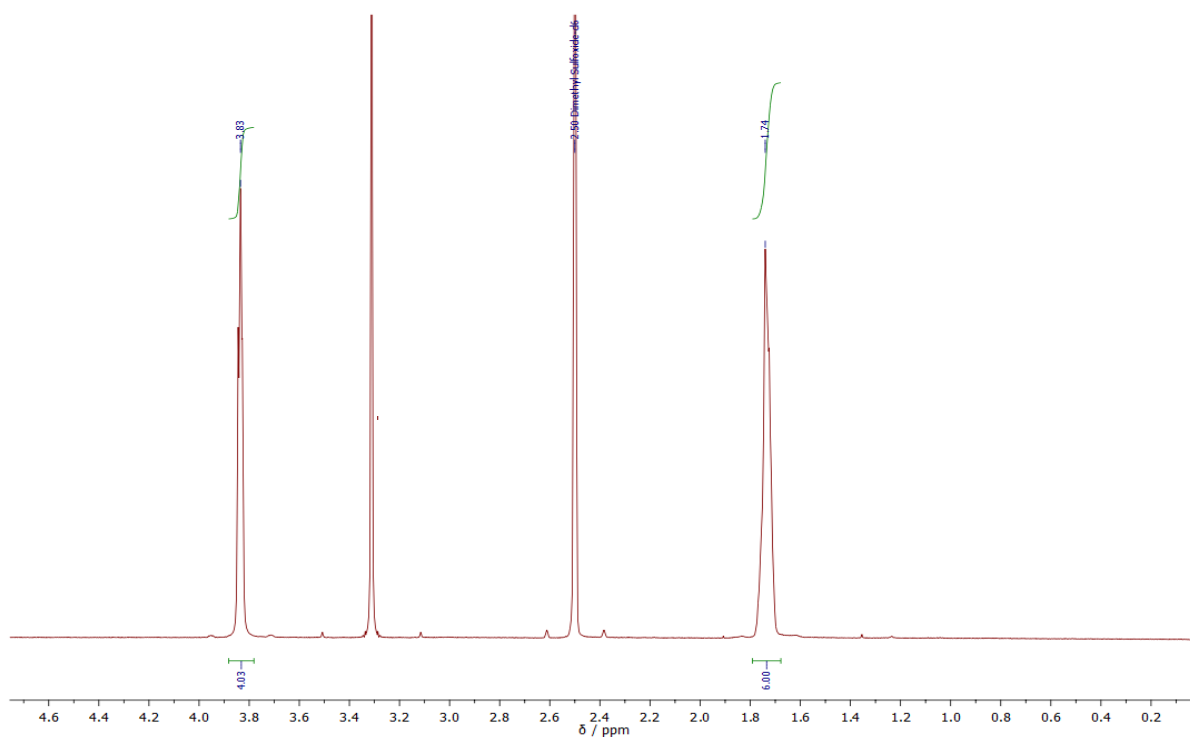
**Figure D5.** <sup>1</sup>H-NMR (DMSO-d<sub>6</sub>, 600 MHz) spectrum of dichloro(piperidine dithiocarbamate)gold(III), [AuCl<sub>2</sub>(PipeDTC)].



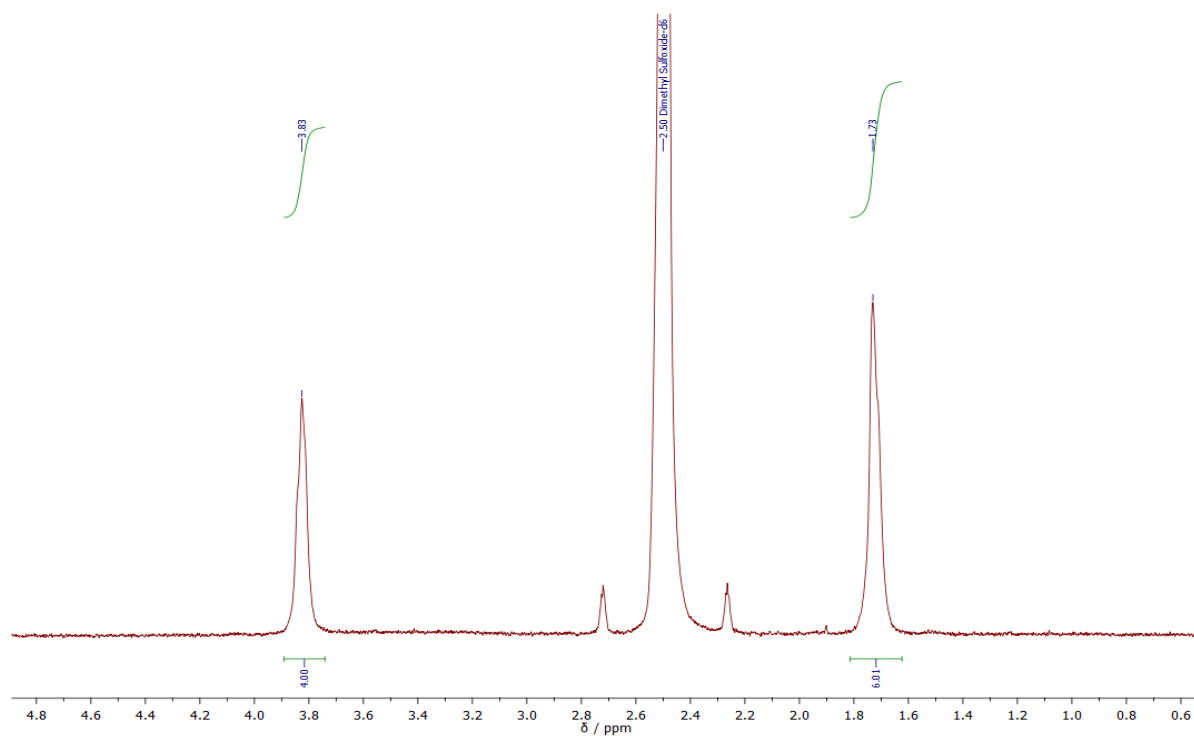
**Figure D6.** <sup>1</sup>H-NMR (DMSO-d<sub>6</sub>, 600 MHz) spectrum of dibromo(piperidine dithiocarbamate)gold(III), [AuBr<sub>2</sub>(PipeDTC)].



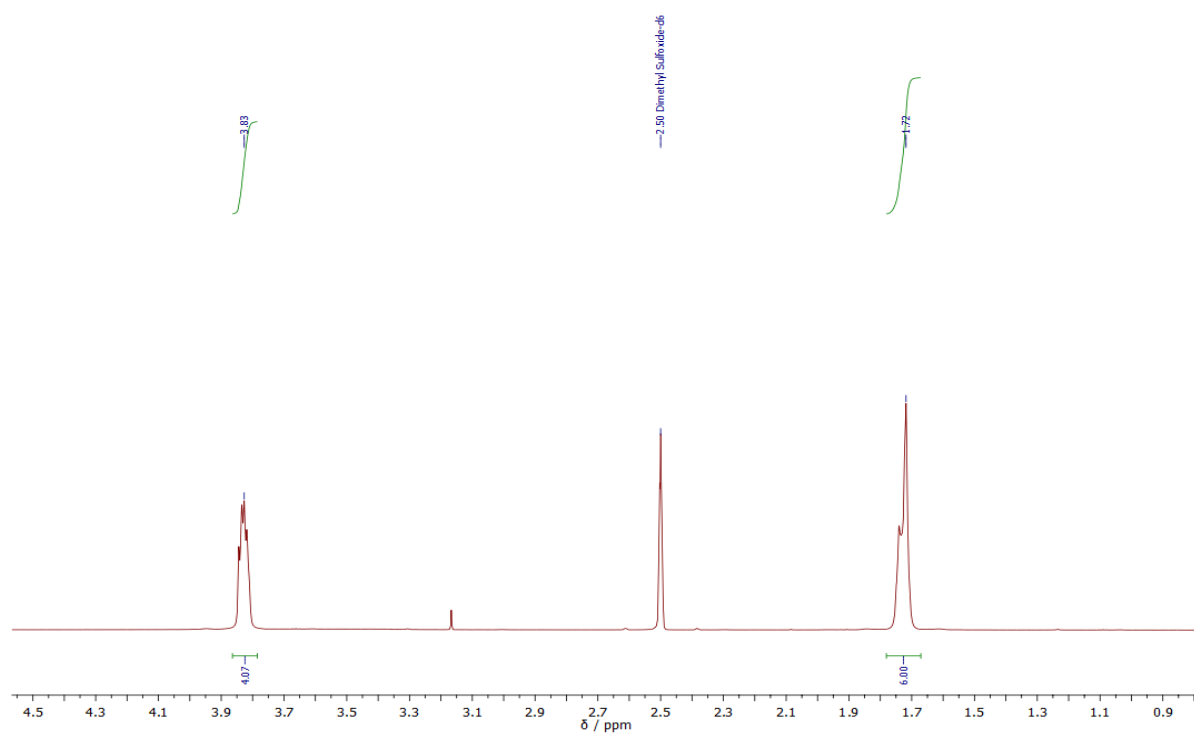
**Figure D7.** <sup>1</sup>H-NMR (DMSO-d<sub>6</sub>, 600 MHz) spectrum of bis(piperidine dithiocarbamate)gold(III) chloride, [Au(PipeDTC)<sub>2</sub>]Cl.



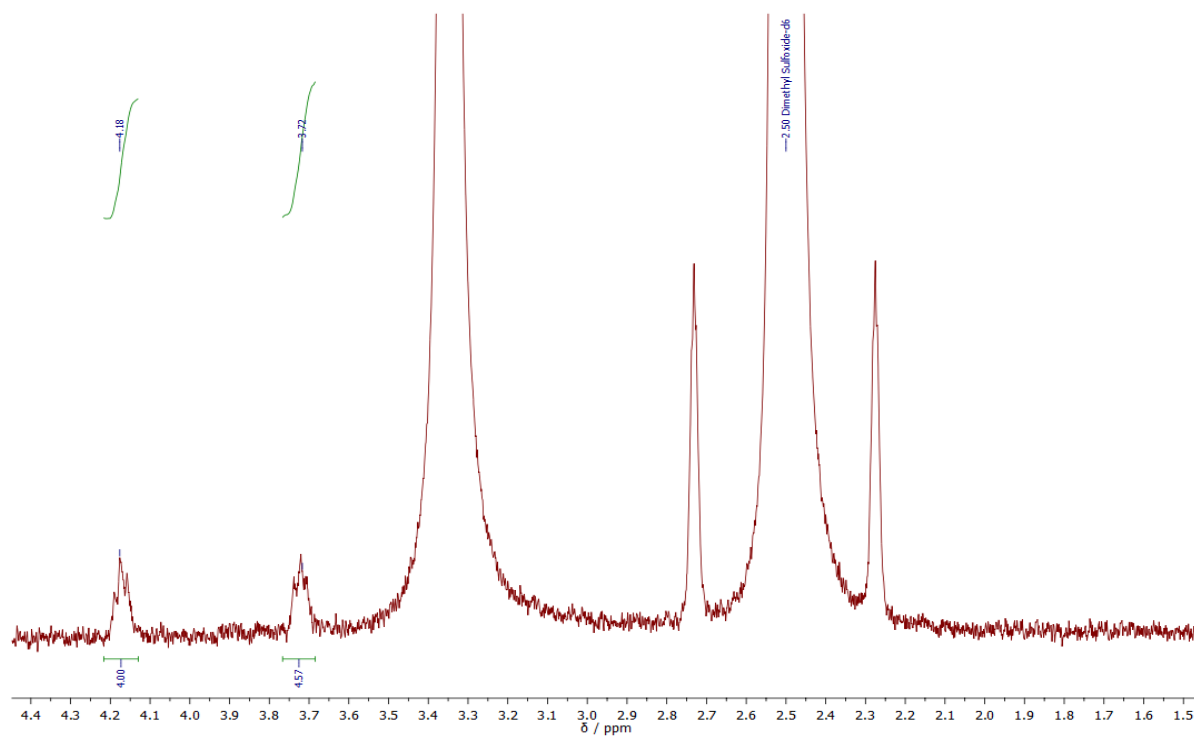
**Figure D8.** <sup>1</sup>H-NMR (DMSO-d<sub>6</sub>, 600 MHz) spectrum of bis(piperidine dithiocarbamate)gold(III) bromide, [Au(PipeDTC)<sub>2</sub>]Br.



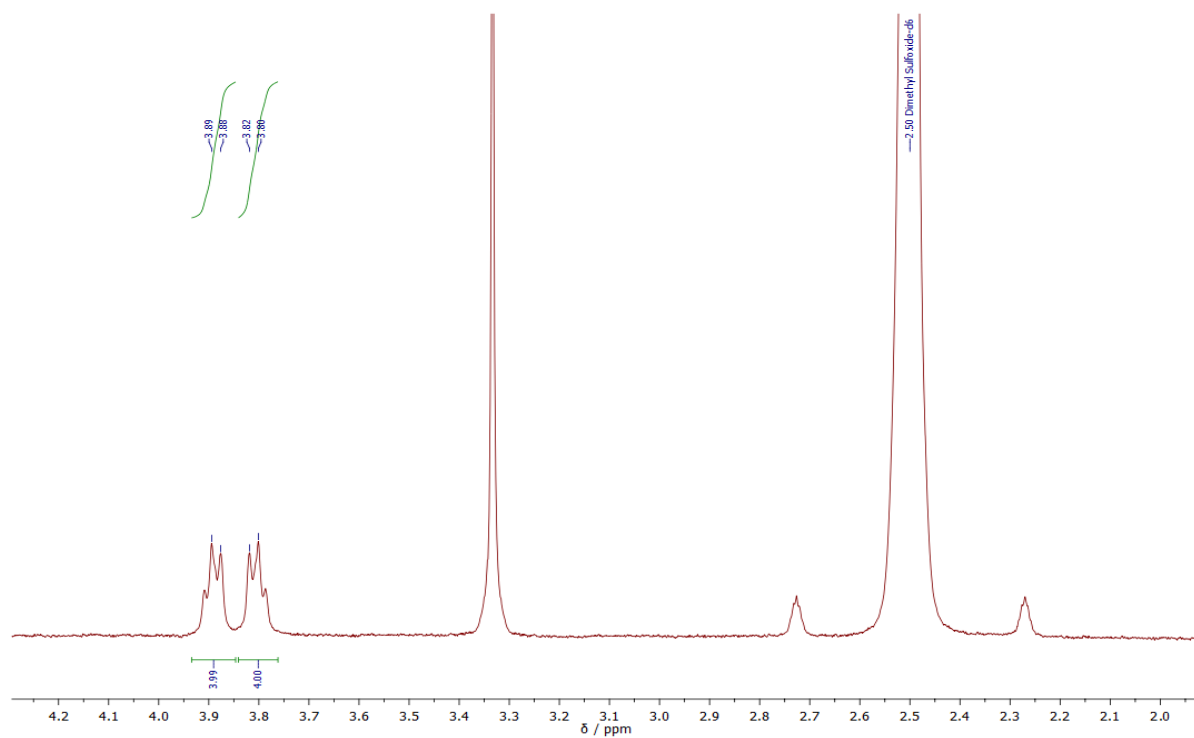
**Figure D9.**  $^1\text{H-NMR}$  (DMSO- $d_6$ , 600 MHz) spectrum of bis(piperidine dithiocarbamate)gold(III) tetrachlorogold(III),  $[\text{Au}(\text{PipeDTC})_2][\text{AuCl}_4]$ .



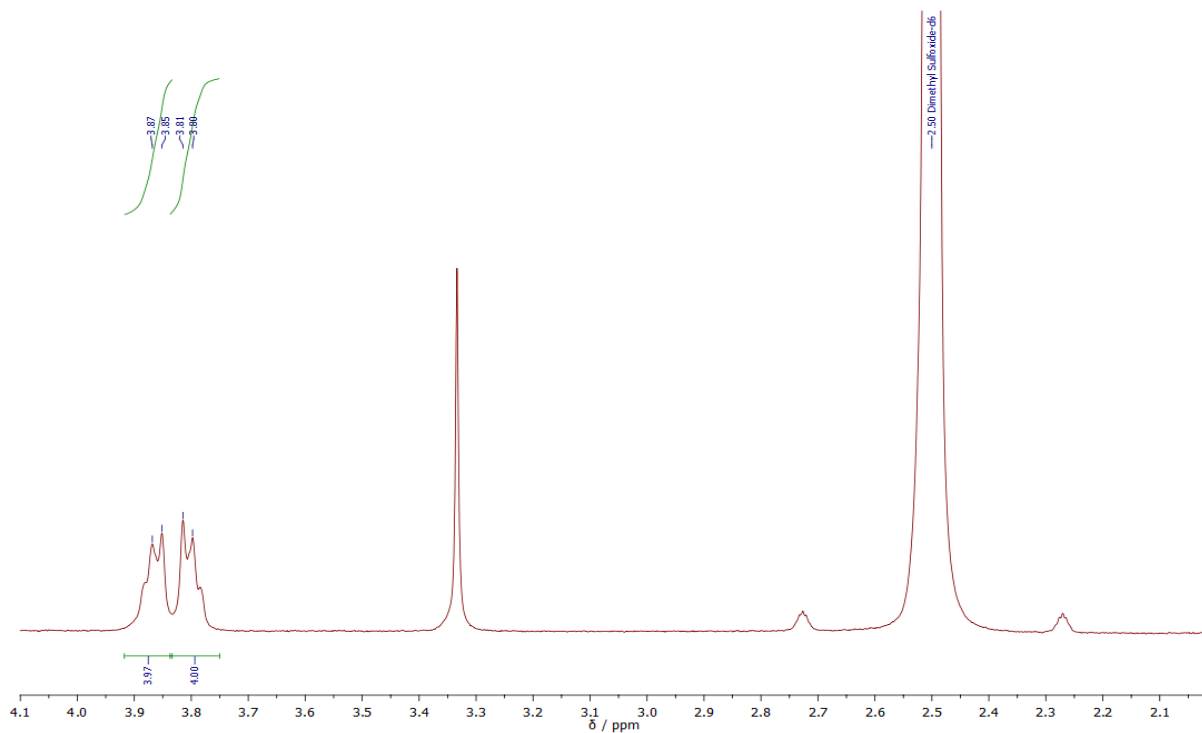
**Figure D10.**  $^1\text{H-NMR}$  (DMSO- $d_6$ , 600 MHz) spectrum of bis(piperidine dithiocarbamate)gold(III) dibromogold(I),  $[\text{Au}(\text{PipeDTC})_2][\text{AuBr}_2]$ .



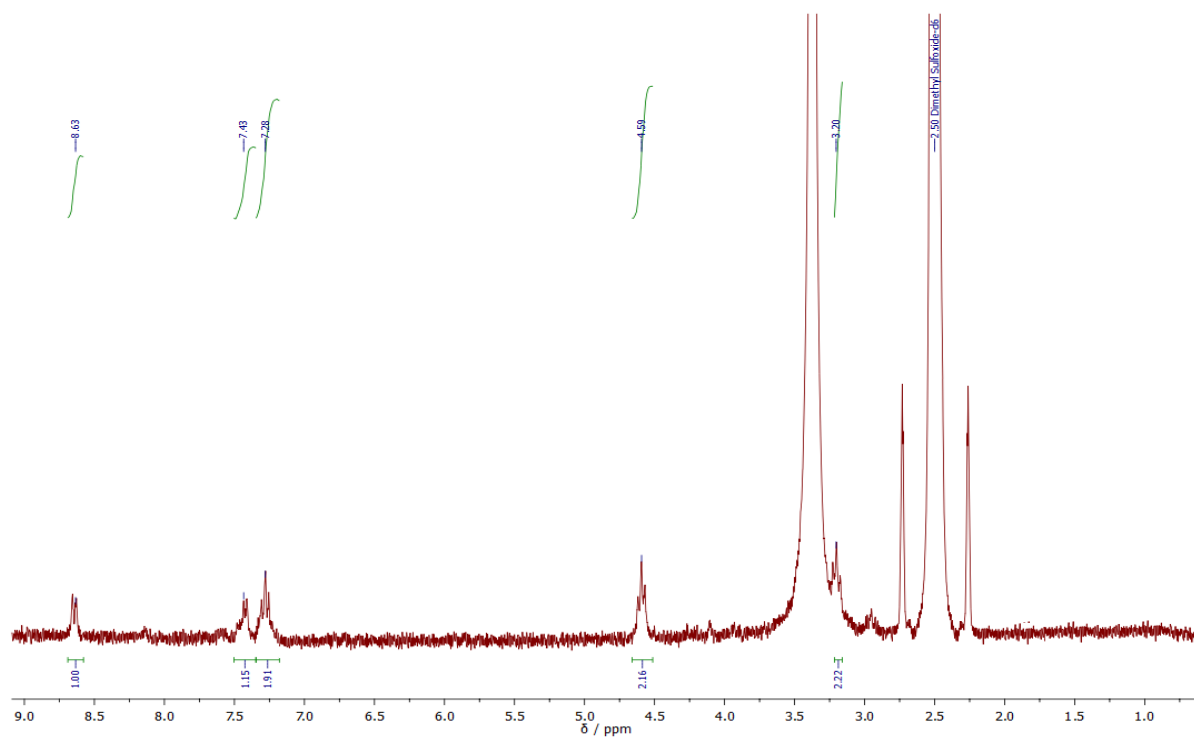
**Figure D11.** <sup>1</sup>H-NMR (DMSO-d<sub>6</sub>, 298 K, 300.13 MHz) spectrum of bis(morpholine dithiocarbamate)digold(I), [Au<sub>2</sub>(MorphDTC)<sub>2</sub>].



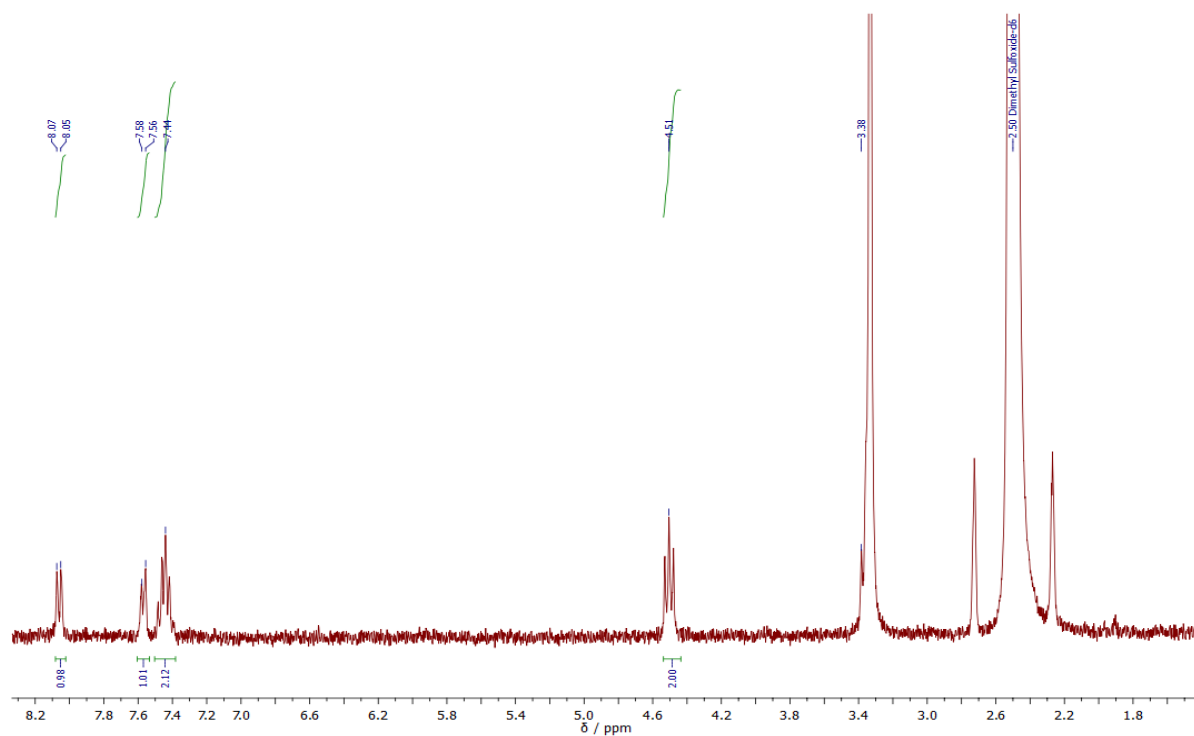
**Figure D12.** <sup>1</sup>H-NMR (DMSO-d<sub>6</sub>, 298 K, 300.13 MHz) spectrum of dichloro(morpholine dithiocarbamate)gold(III), [AuCl<sub>2</sub>(MorphDTC)].



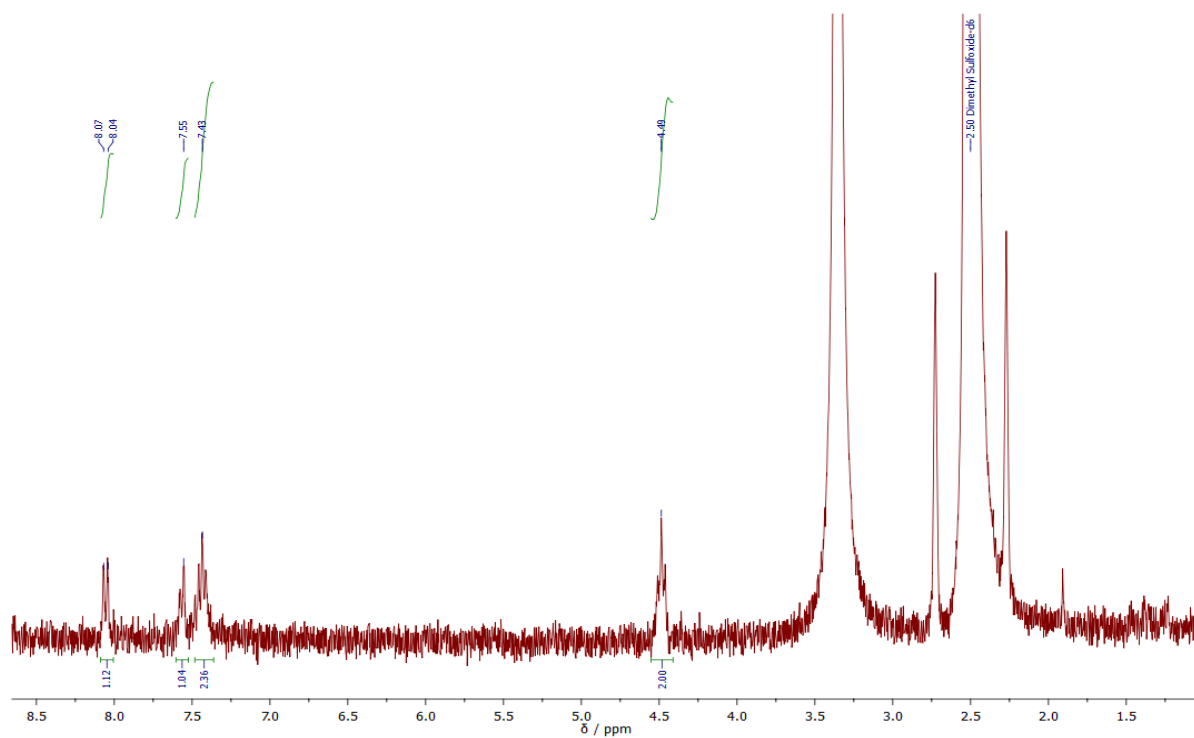
**Figure D13.** <sup>1</sup>H-NMR (DMSO-d<sub>6</sub>, 298 K, 300.13 MHz) spectrum of dibromo(morpholine dithiocarbamate)gold(III), [AuBr<sub>2</sub>(MorphDTC)].



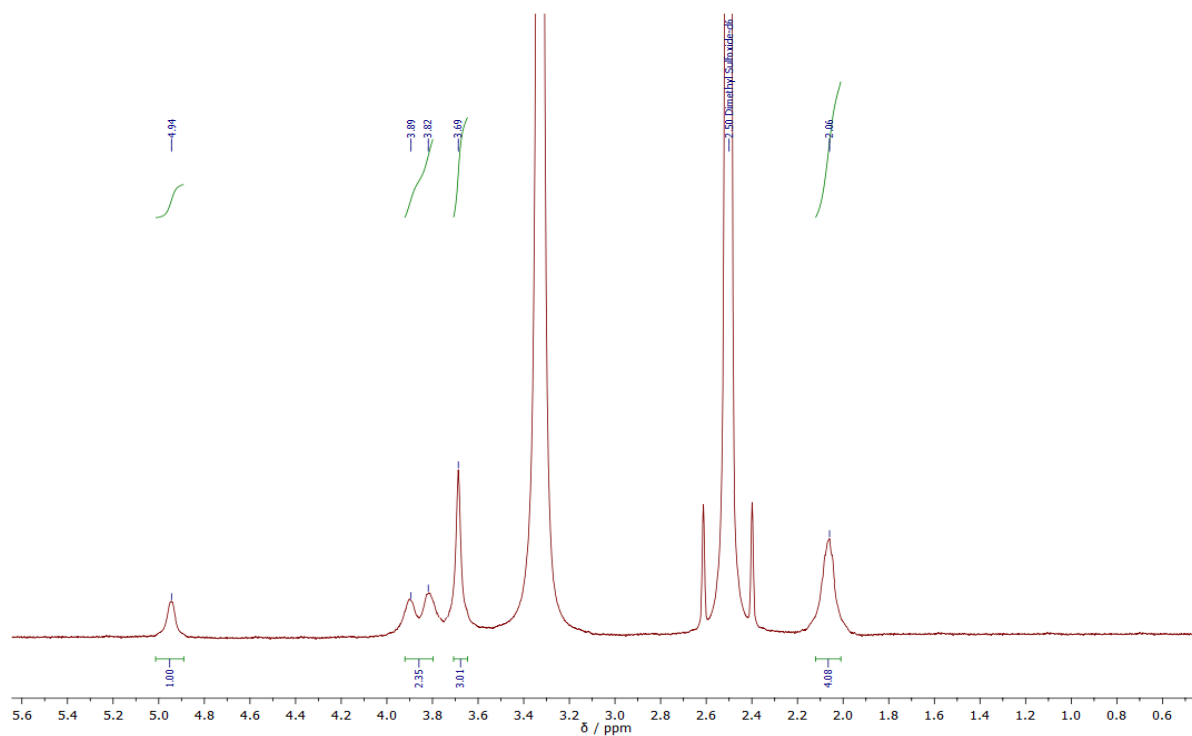
**Figure D14.** <sup>1</sup>H-NMR (DMSO-d<sub>6</sub>, 298 K, 300.13 MHz) spectrum of bis(indoline dithiocarbamate)digold(I), [Au<sub>2</sub>(IndolineDTC)<sub>2</sub>].



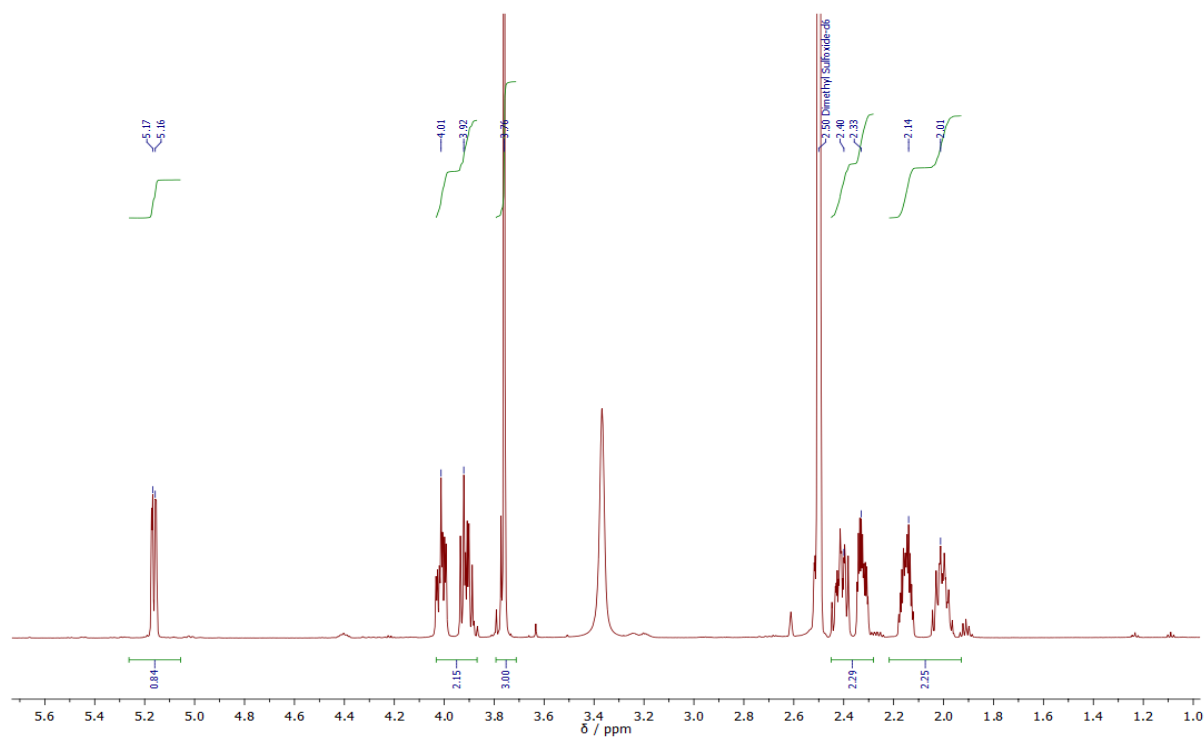
**Figure D15.** <sup>1</sup>H-NMR (DMSO-d<sub>6</sub>, 298 K, 300.13 MHz) spectrum of dichloro(indoline dithiocarbamate)gold(III), [AuCl<sub>2</sub>(IndolineDTC)].



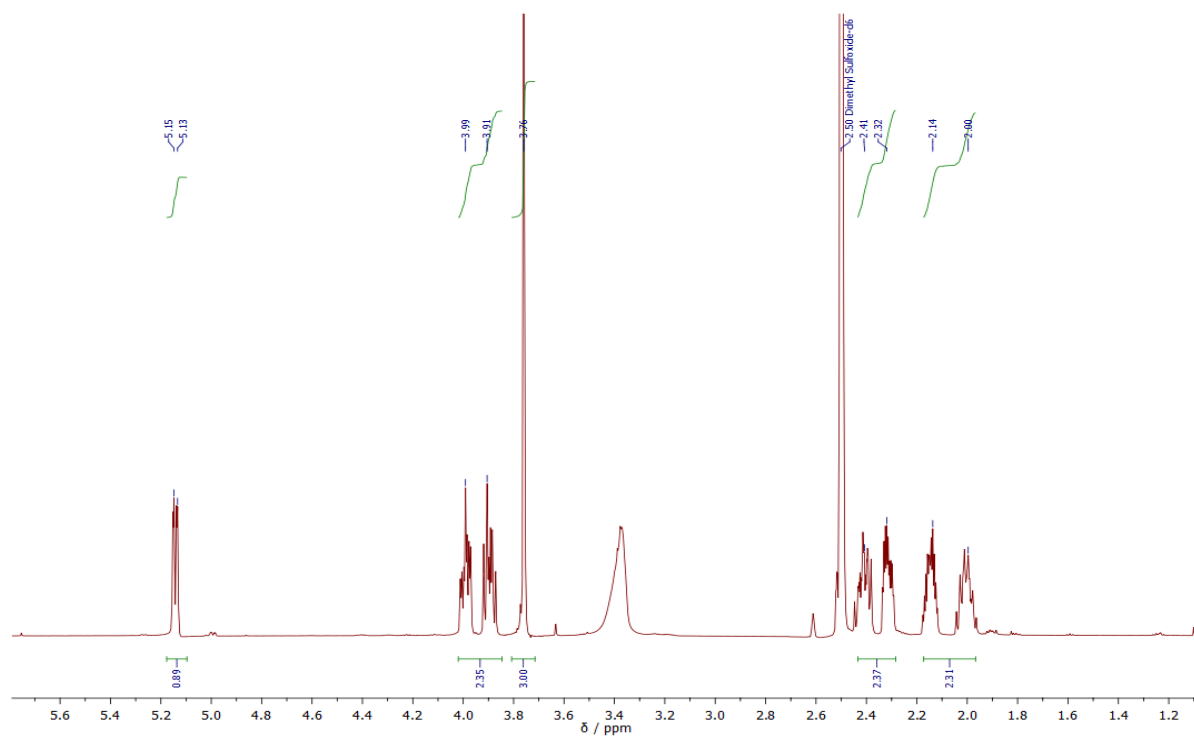
**Figure D16.** <sup>1</sup>H-NMR (DMSO-d<sub>6</sub>, 298 K, 300.13 MHz) spectrum of dibromo(indoline dithiocarbamate)gold(III), [AuBr<sub>2</sub>(IndolineDTC)].



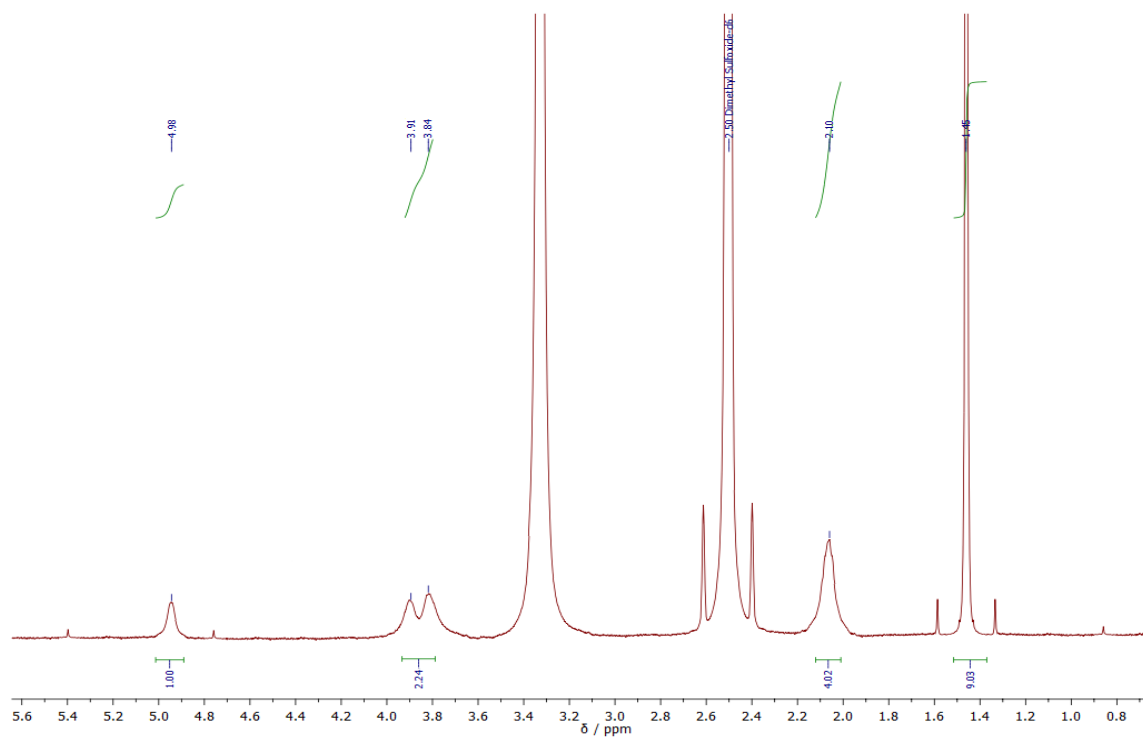
**Figure D17.**  $^1\text{H-NMR}$  ( $\text{DMSO-d}_6$ , 298 K, 300.13 MHz) spectrum of bis(L-proline methyl ester dithiocarbamate)digold(I),  $[\text{Au}_2(\text{ProOMeDTC})_2]$ .



**Figure D18.**  $^1\text{H-NMR}$  ( $\text{DMSO-d}_6$ , 298 K, 300.13 MHz) spectrum of dichloro(L-proline methyl ester dithiocarbamate)gold(III),  $[\text{AuCl}_2(\text{ProOMeDTC})]$ .

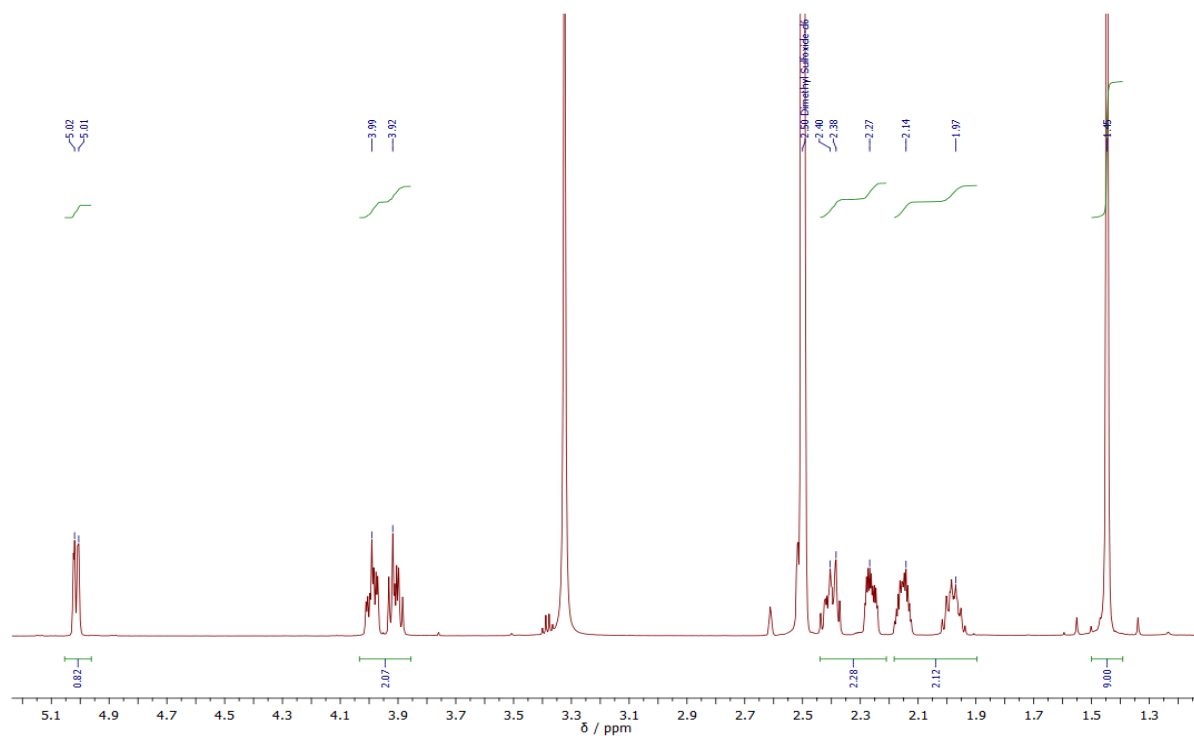


**Figure D19.**  $^1\text{H-NMR}$  (DMSO- $d_6$ , 298 K, 300.13 MHz) spectrum of dibromo(L-proline methyl ester dithiocarbamate)gold(III),  $[\text{AuBr}_2(\text{ProOMeDTC})]$ .

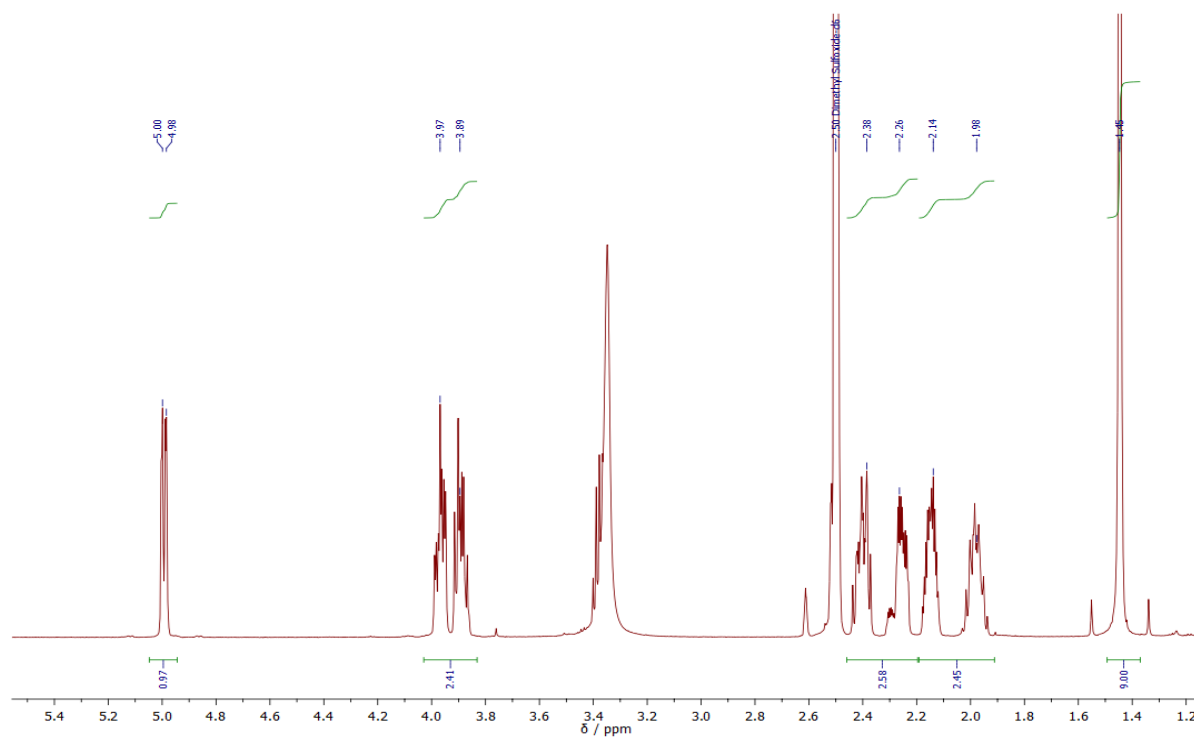


**Figure D20.**  $^1\text{H-NMR}$  (DMSO- $d_6$ , 298 K, 300.13 MHz) spectrum of bis(L-proline *tert*-butyl ester dithiocarbamate)digold(I),  $[\text{Au}_2(\text{ProOtBuDTC})_2]$ .

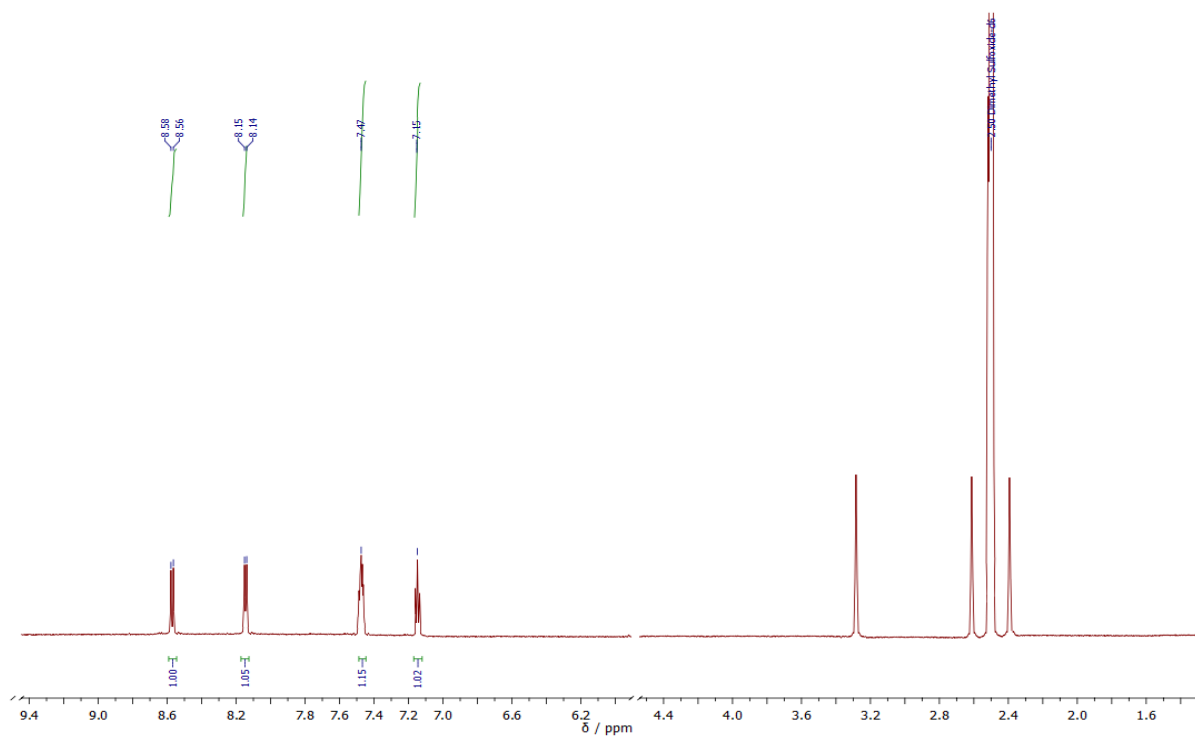
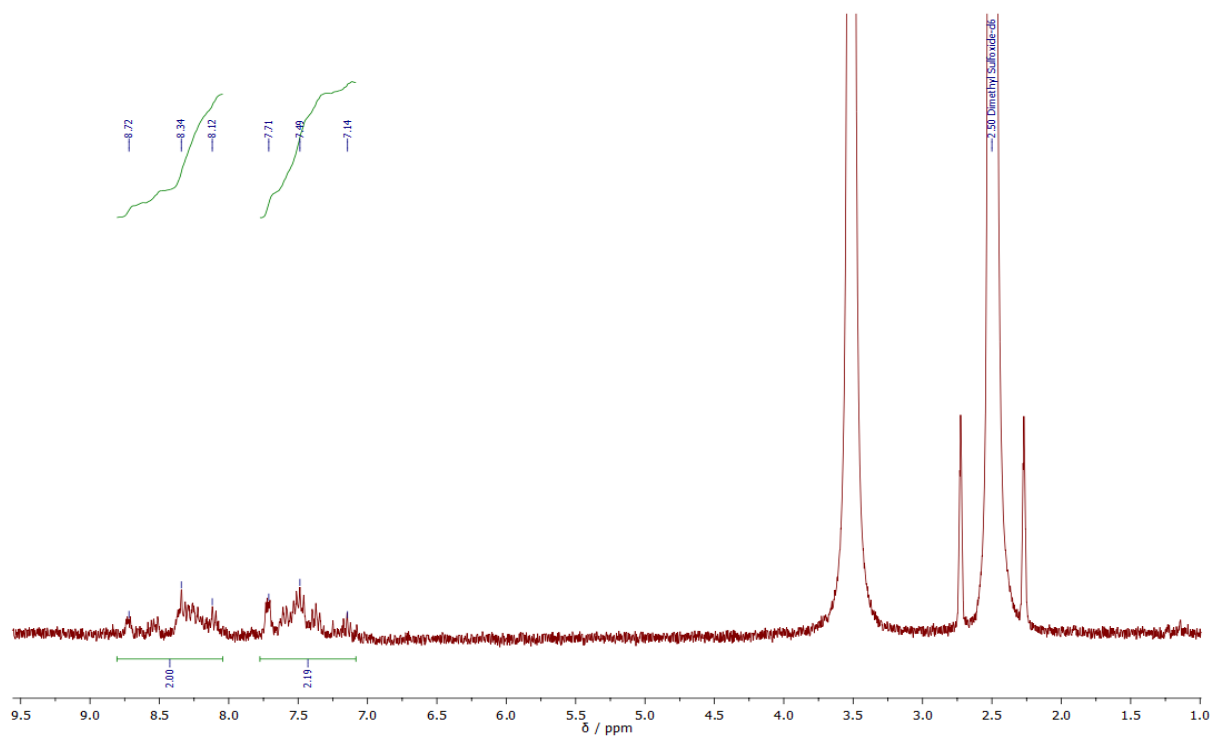


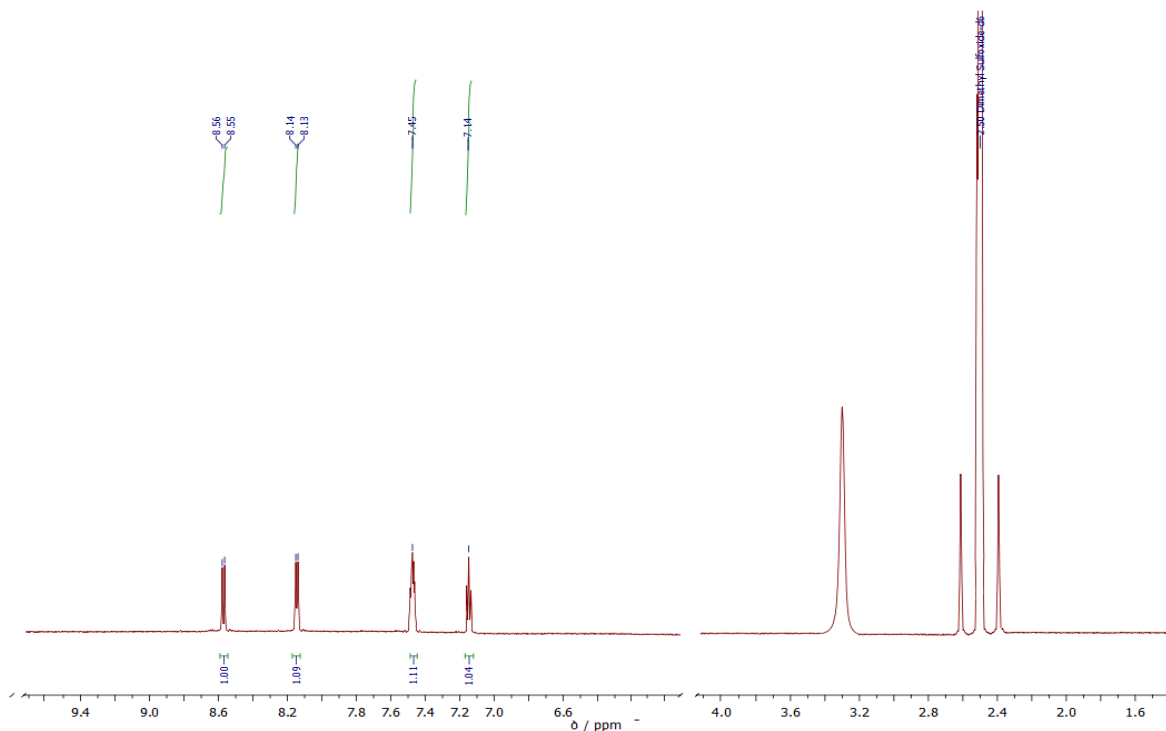


**Figure D21.** <sup>1</sup>H-NMR (DMSO-d<sub>6</sub>, 298 K, 300.13 MHz) spectrum of dichloro(L-proline *tert*-butyl ester dithiocarbamate)gold(III), [AuCl<sub>2</sub>(ProOtBuDTC)].

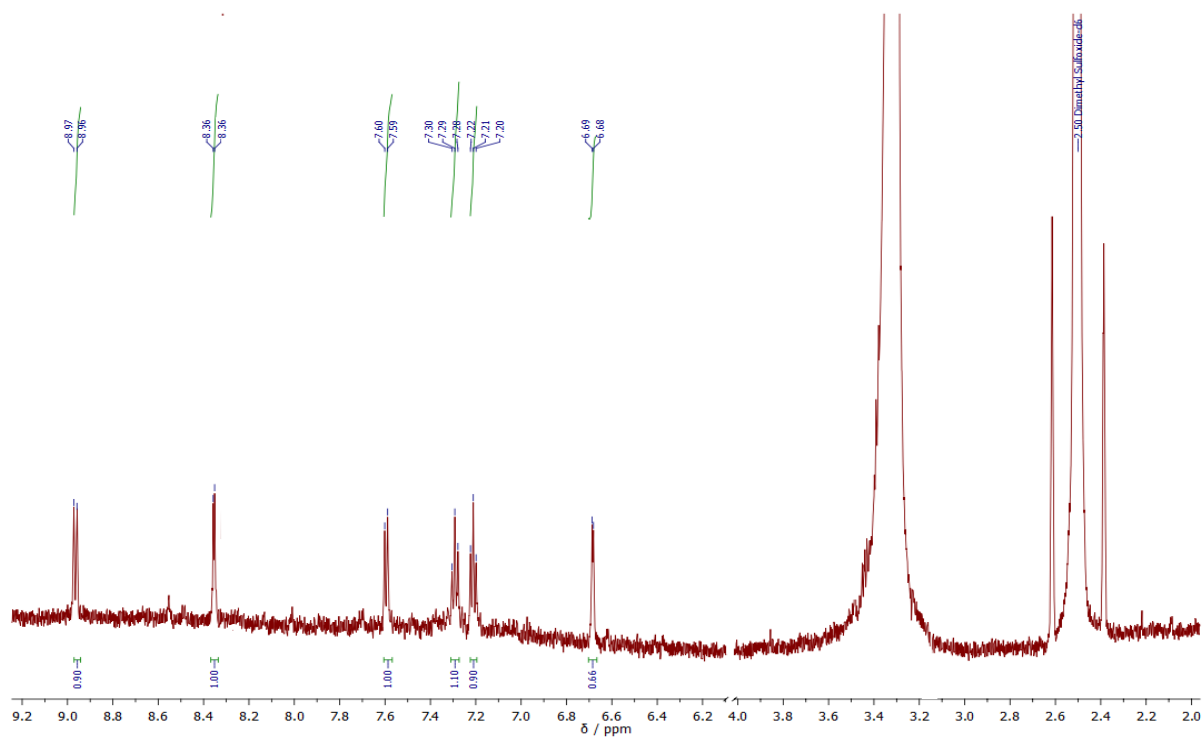


**Figure D22.** <sup>1</sup>H-NMR (DMSO-d<sub>6</sub>, 298 K, 300.13 MHz) spectrum of dibromo(L-proline *tert*-butyl ester dithiocarbamate)gold(III), [AuBr<sub>2</sub>(ProOtBuDTC)].

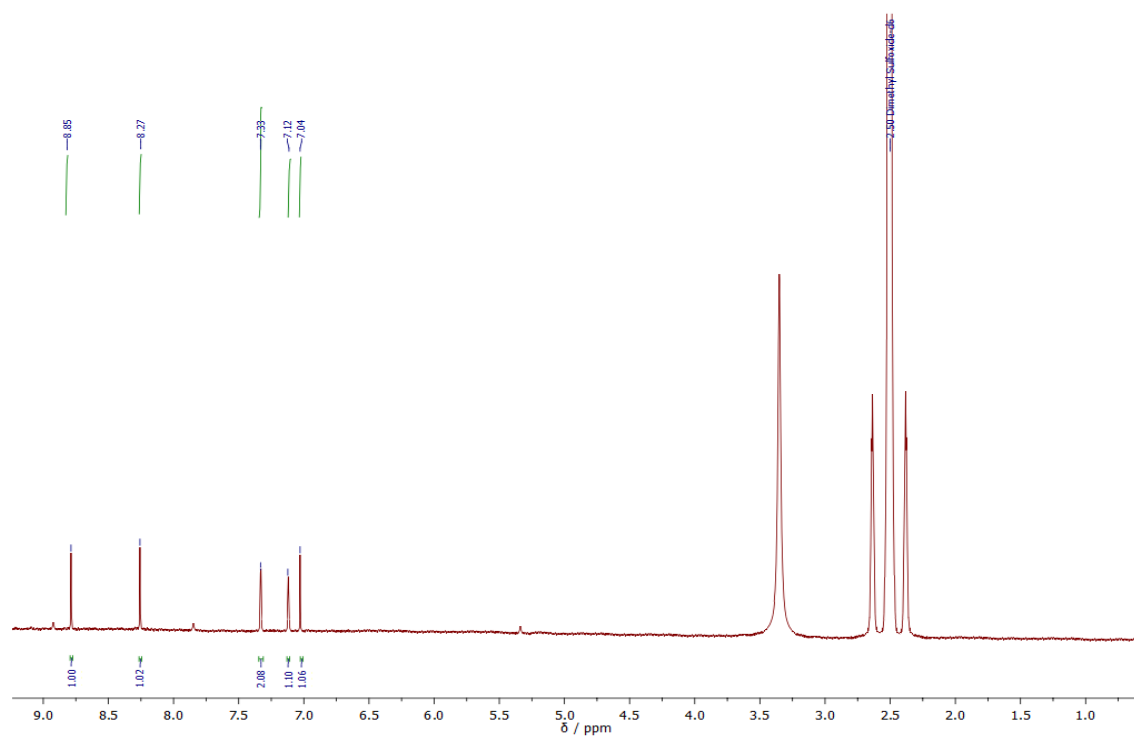




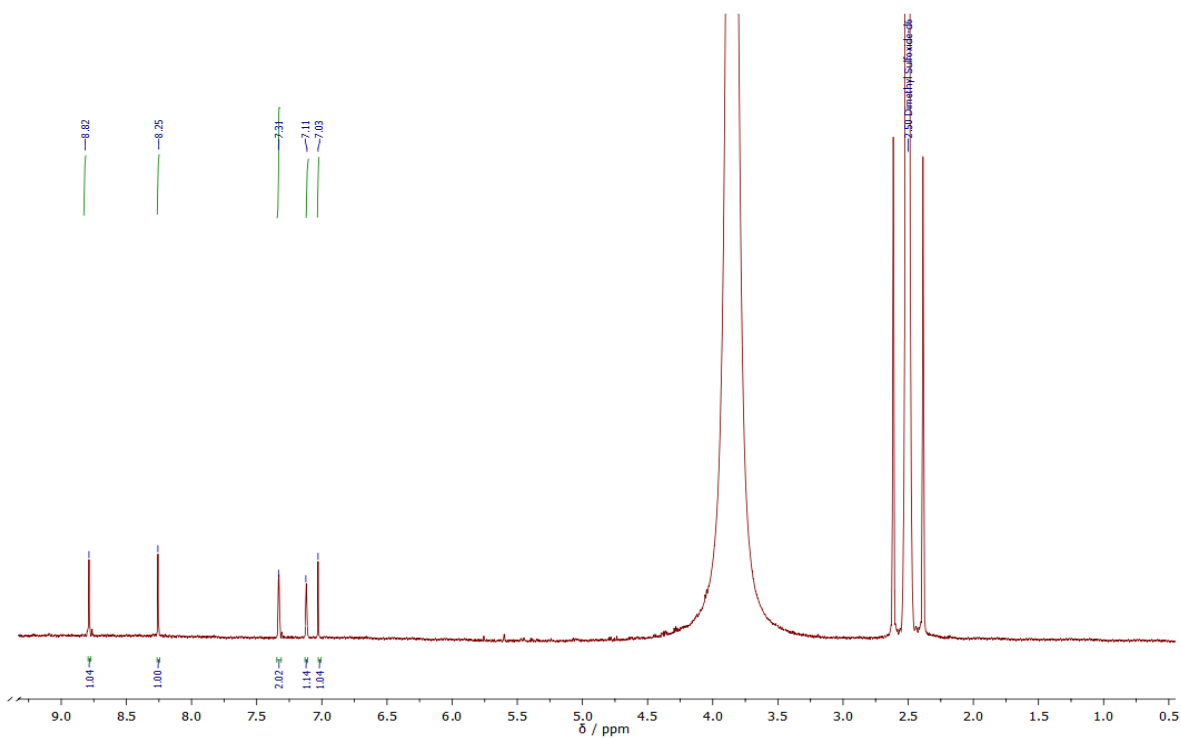
**Figure D25.** <sup>1</sup>H-NMR (DMSO-d<sub>6</sub>, 298 K, 300.13 MHz) spectrum of dibromo(carbazole dithiocarbamate)gold(III), [AuBr<sub>2</sub>(CDT)].



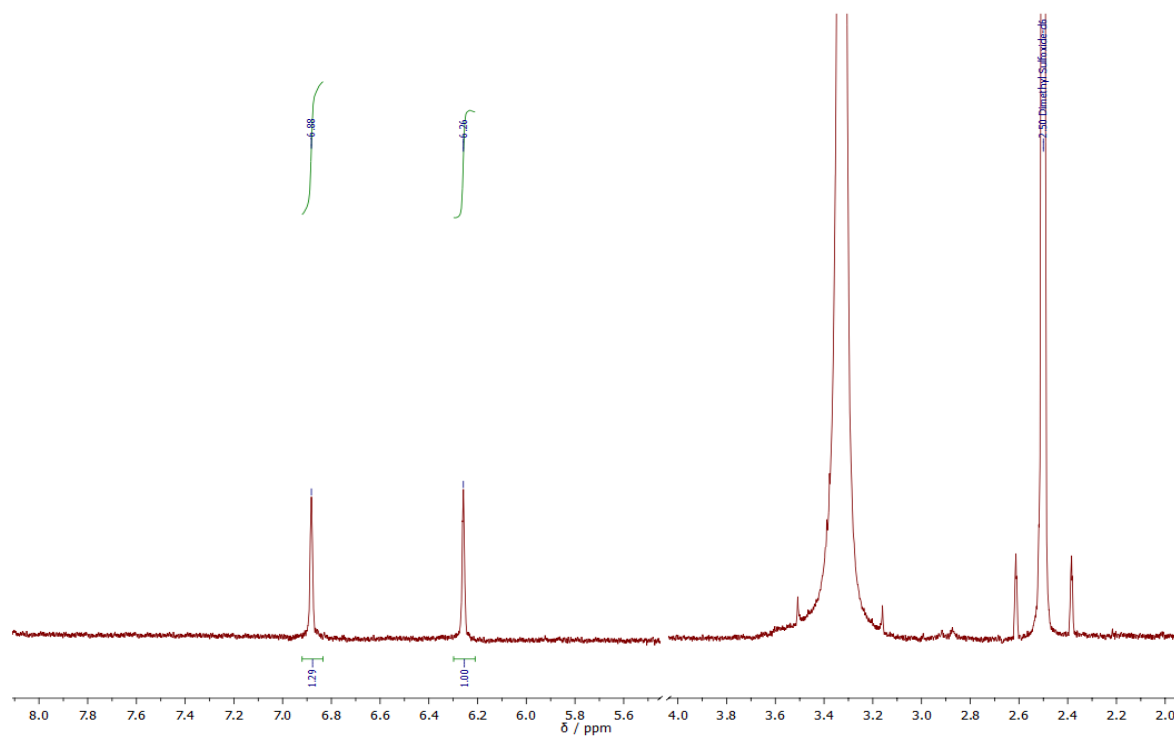
**Figure D26.** <sup>1</sup>H-NMR (DMSO-d<sub>6</sub>, 298 K, 300.13 MHz) spectrum of bis(indole dithiocarbamate)digold(I), [Au<sub>2</sub>(IndDTC)<sub>2</sub>].



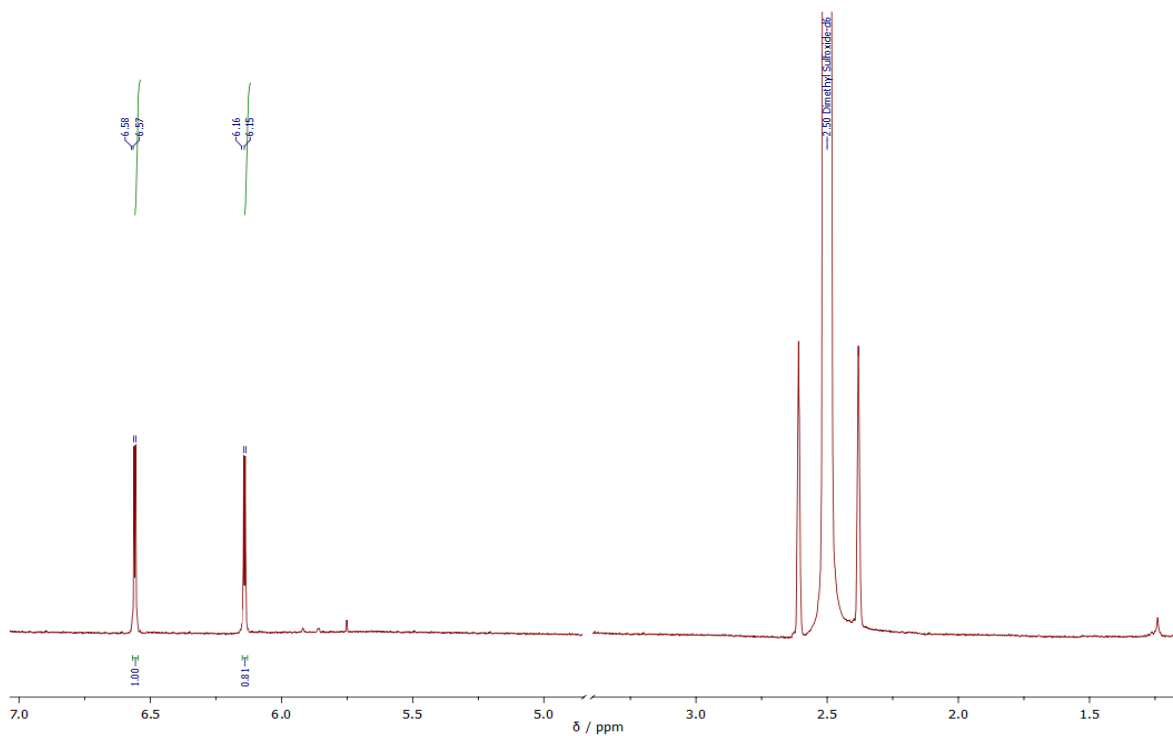
**Figure D27.** <sup>1</sup>H-NMR (DMSO-d<sub>6</sub>, 298 K, 300.13 MHz) spectrum of dichloro(indole dithiocarbamate)gold(III), [AuCl<sub>2</sub>(IndDTC)].



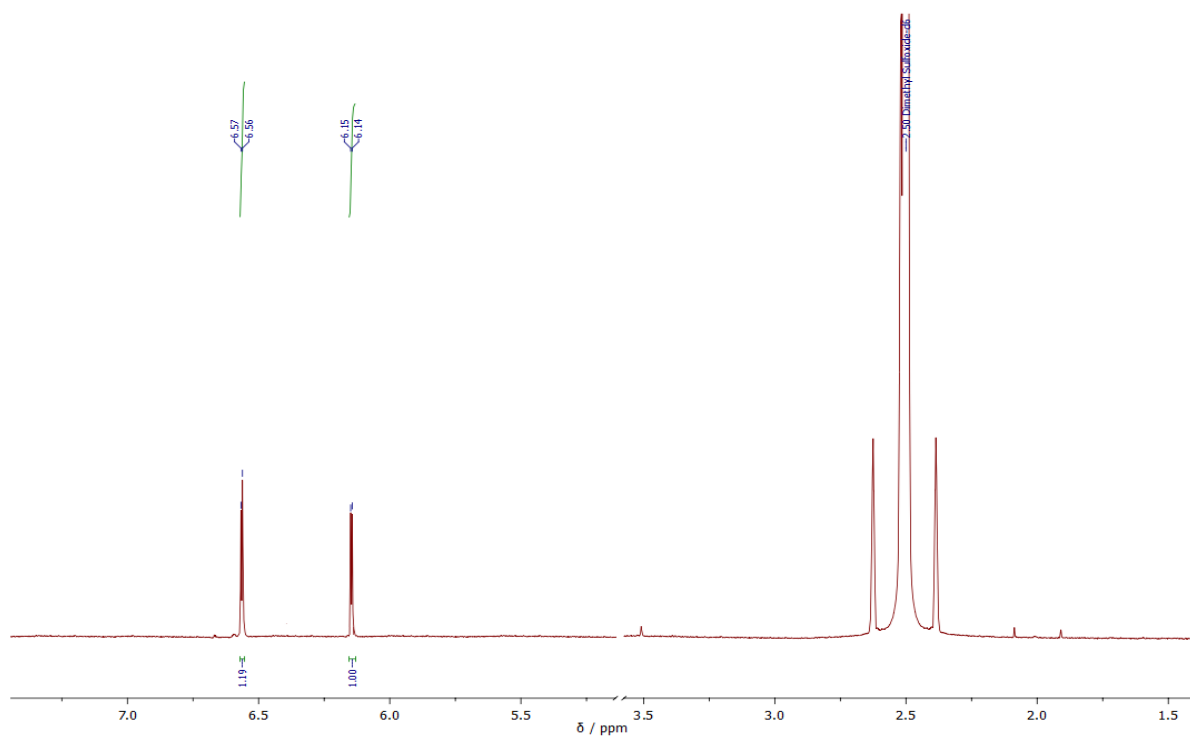
**Figure D28.** <sup>1</sup>H-NMR (DMSO-d<sub>6</sub>, 298 K, 300.13 MHz) spectrum of dibromo(indole dithiocarbamate)gold(III), [AuBr<sub>2</sub>(IndDTC)].



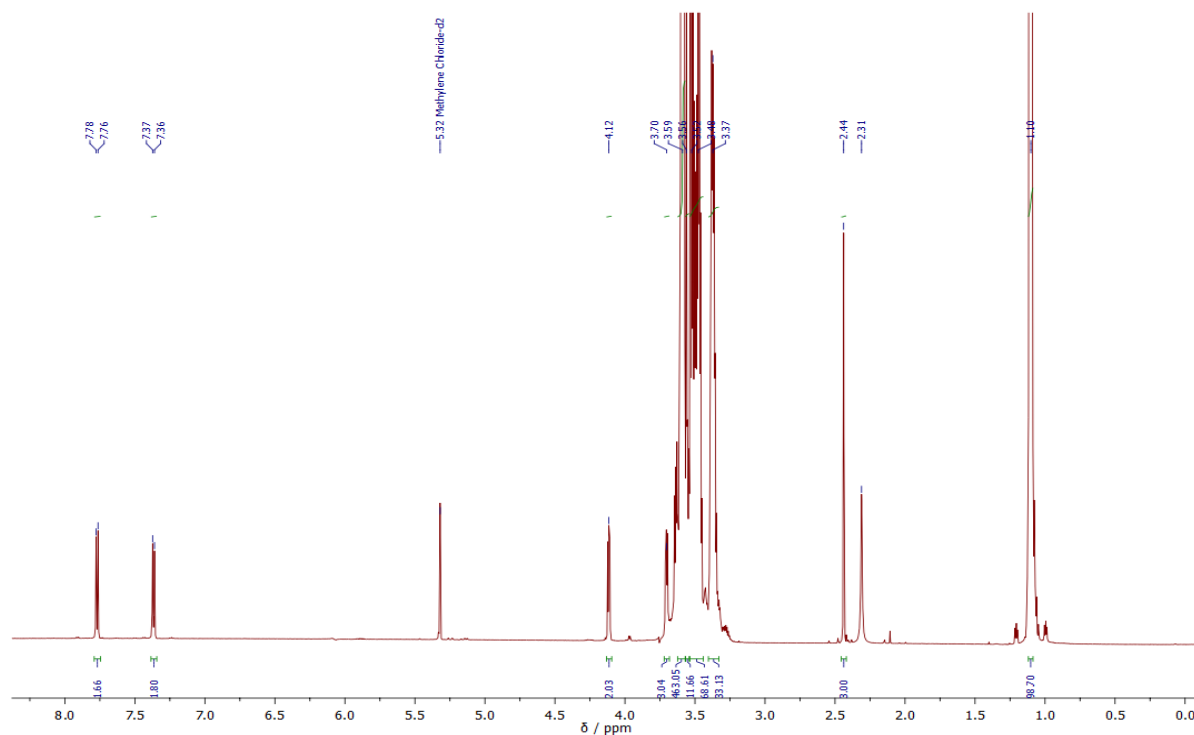
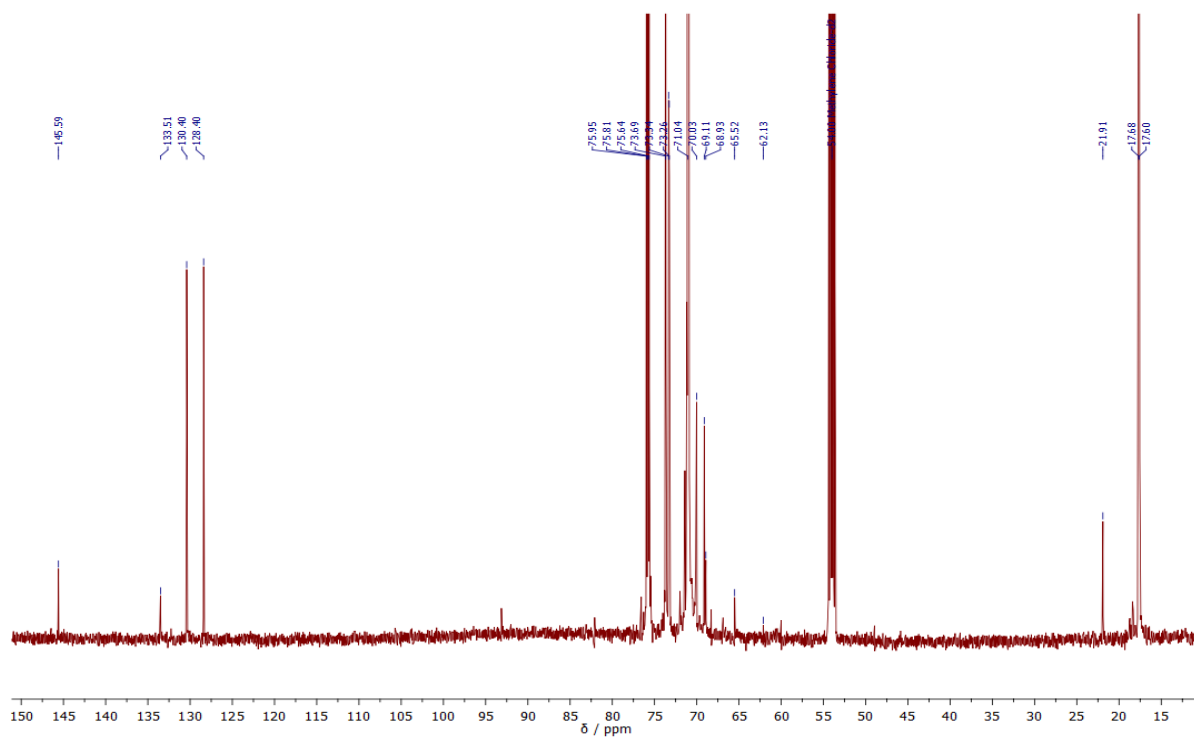
**Figure D29.** <sup>1</sup>H-NMR (DMSO-d<sub>6</sub>, 298 K, 300.13 MHz) spectrum of bis(pyrrole dithiocarbamate)digold(I), [Au<sub>2</sub>(PyrroleDTC)<sub>2</sub>].



**Figure D30.** <sup>1</sup>H-NMR (DMSO-d<sub>6</sub>, 298 K, 300.13 MHz) spectrum of dichloro(pyrrole dithiocarbamate)gold(III), [AuCl<sub>2</sub>(PyrroleDTC)].



**Figure D31.** <sup>1</sup>H-NMR (DMSO-d<sub>6</sub>, 298 K, 300.13 MHz) spectrum of dibromo(pyrrrole dithiocarbamate)gold(III), [AuBr<sub>2</sub>(PyrrroleDTC)].

SUPPORTING INFORMATION E -  $^1\text{H}$ -NMR and  $^{13}\text{C}$ -NMR spectra of the synthesized Pluronic<sup>®</sup> F127 derivatives**Figure E1.**  $^1\text{H}$ -NMR ( $\text{CD}_2\text{Cl}_2$ , 298 K, 599.90 MHz) spectrum of Pluronic<sup>®</sup> F127 tosylate, PF127-Ts.**Figure E2.**  $^{13}\text{C}$ -NMR ( $\text{CD}_2\text{Cl}_2$ , 298 K, 150.84 MHz) spectrum of Pluronic<sup>®</sup> F127 tosylate, PF127-Ts.

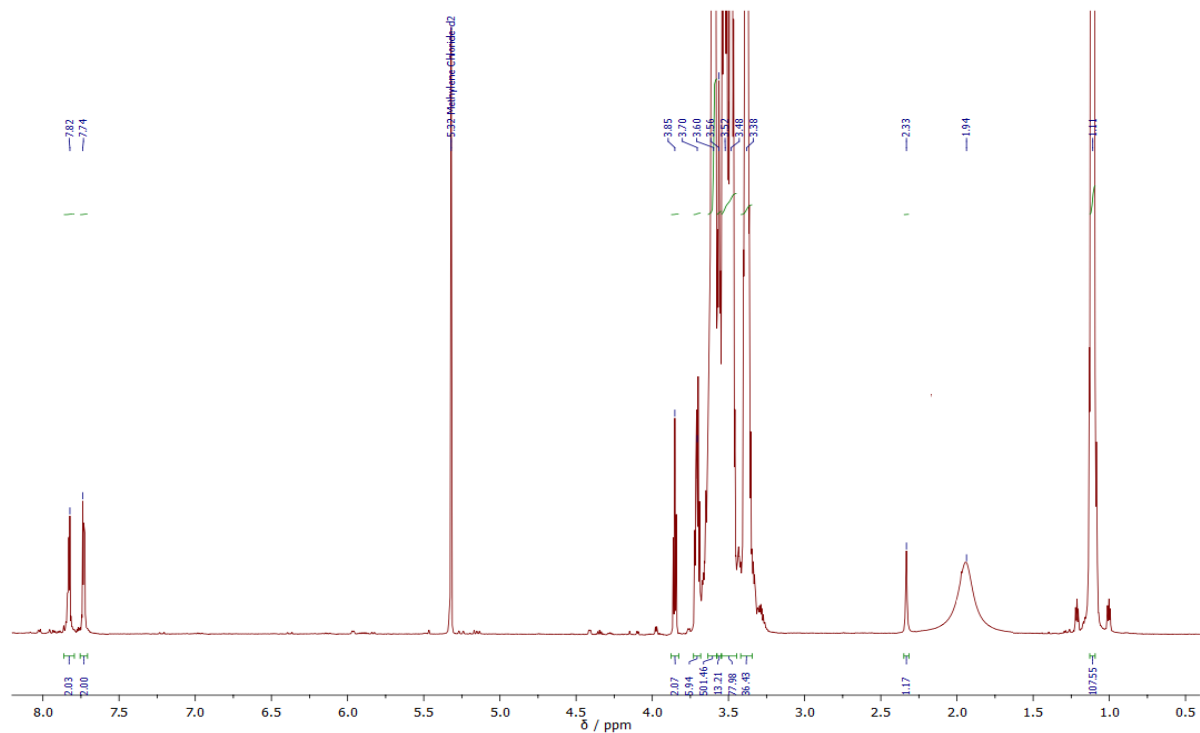


Figure E3.  $^1\text{H-NMR}$  ( $\text{CD}_2\text{Cl}_2$ , 298 K, 599.90 MHz) spectrum of Pluronic<sup>®</sup> F127 phthalimide, PF127-Phtha.

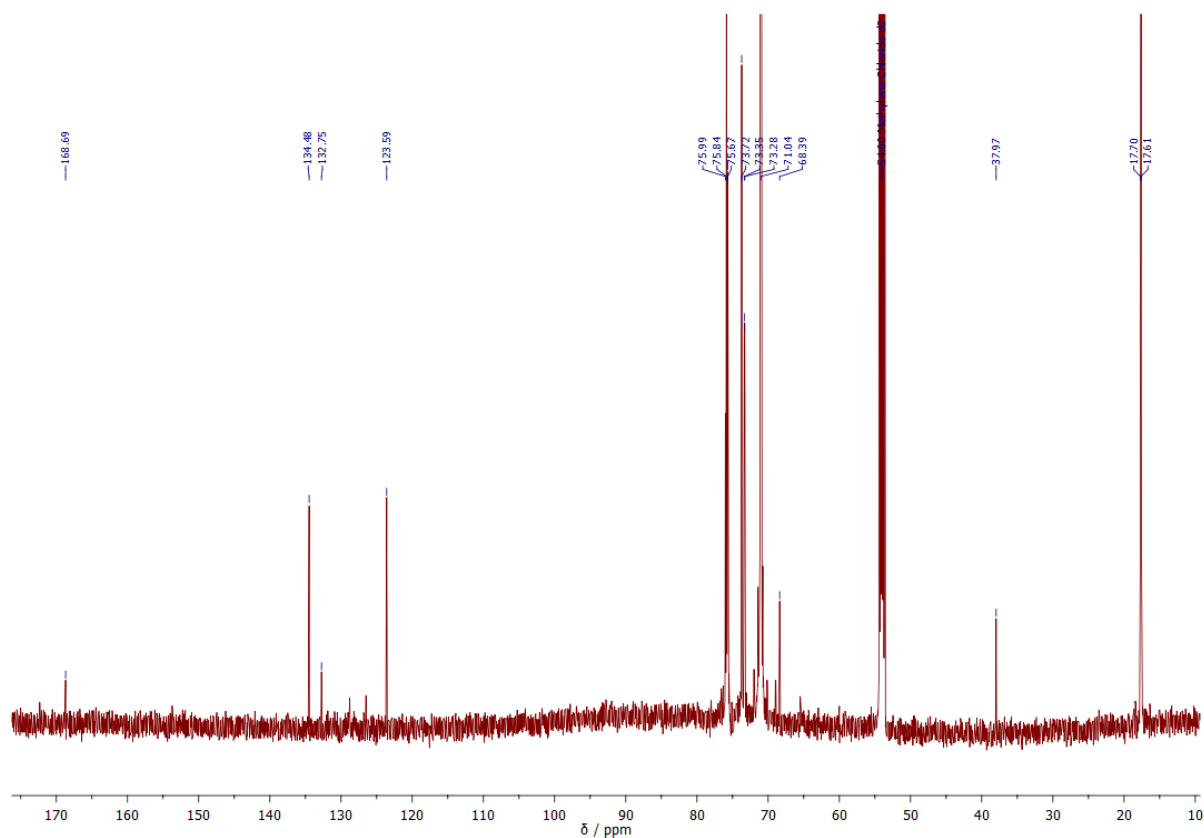


Figure E4.  $^{13}\text{C-NMR}$  ( $\text{CD}_2\text{Cl}_2$ , 298 K, 150.84 MHz) spectrum of Pluronic<sup>®</sup> F127 phthalimide, PF127-Phtha.



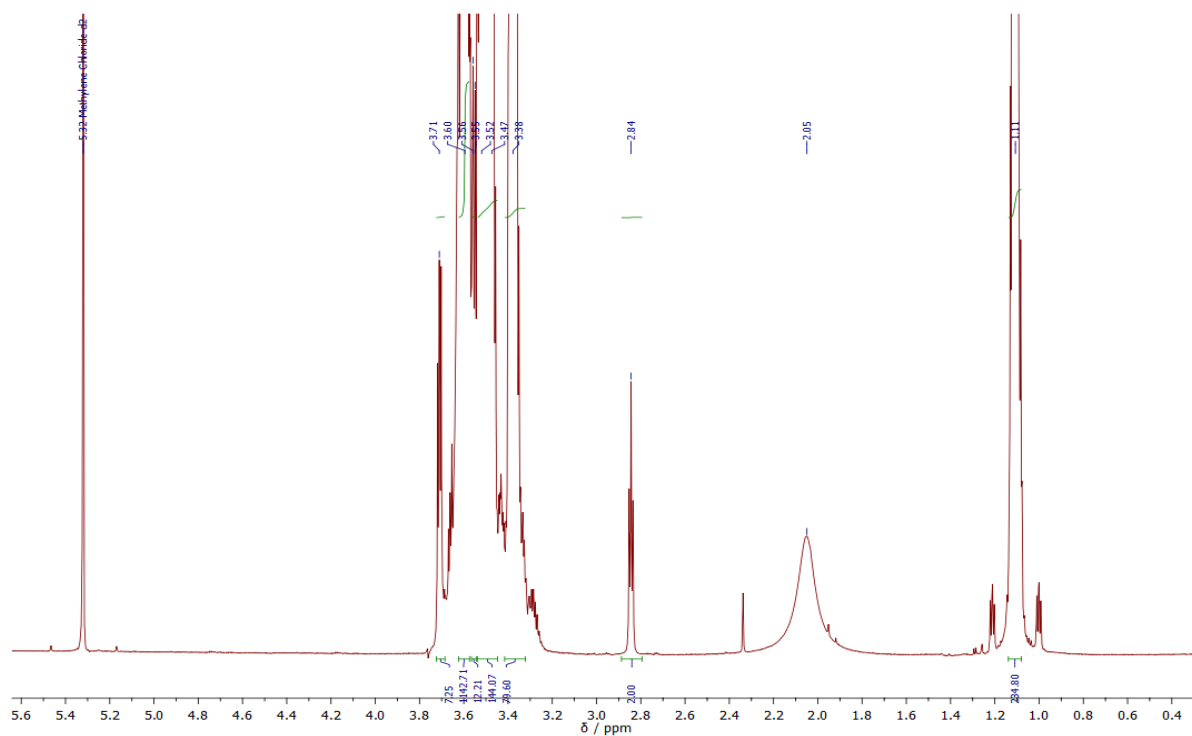


Figure E5.  $^1\text{H-NMR}$  ( $\text{CD}_2\text{Cl}_2$ , 298 K, 599.90 MHz) spectrum of Pluronic<sup>®</sup> F127 amine, PF127-NH<sub>2</sub>.

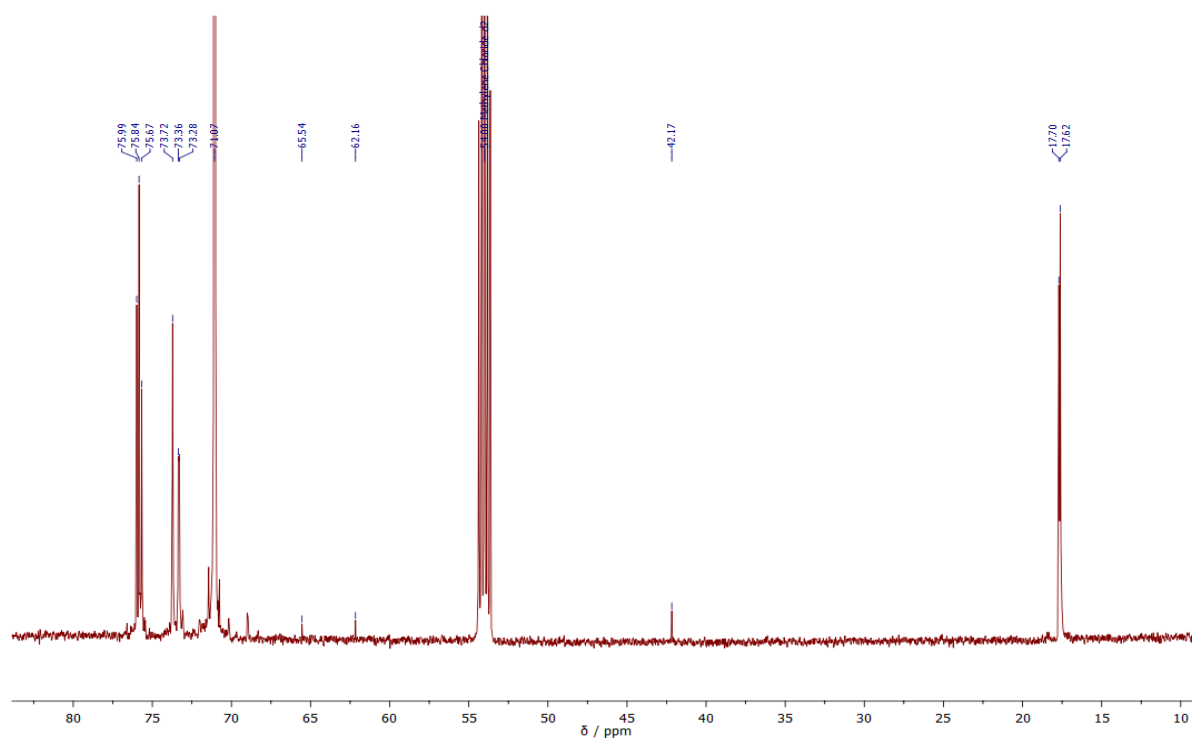
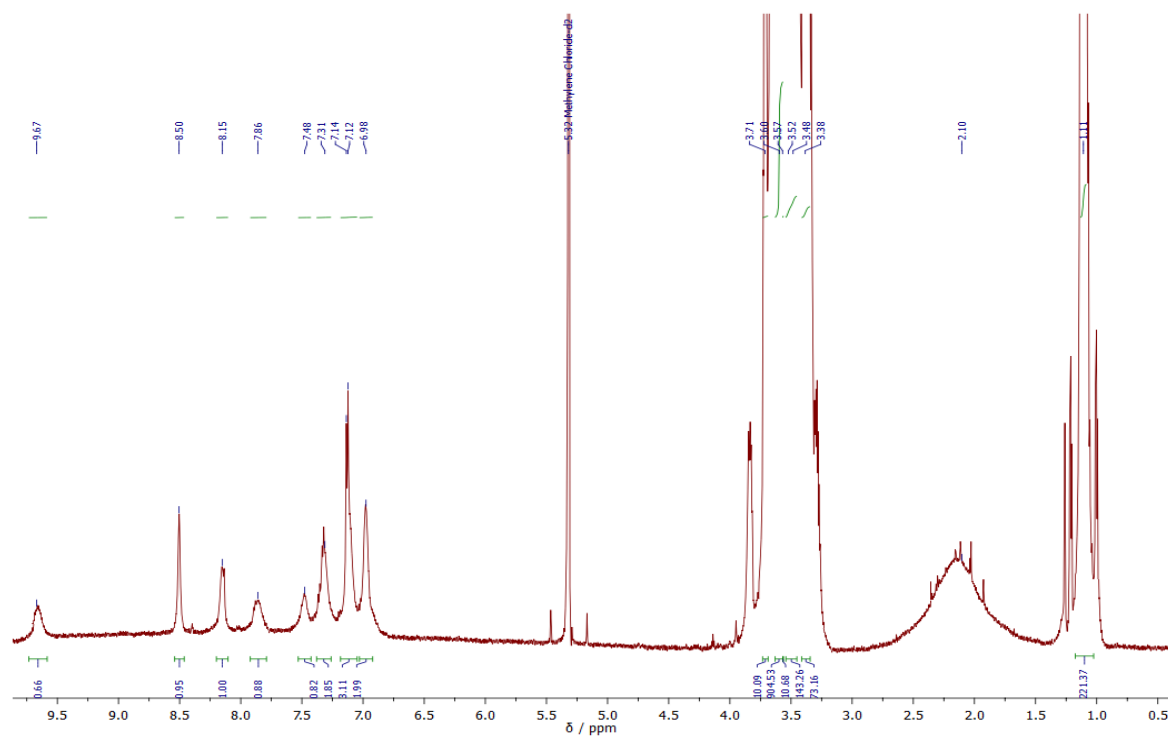
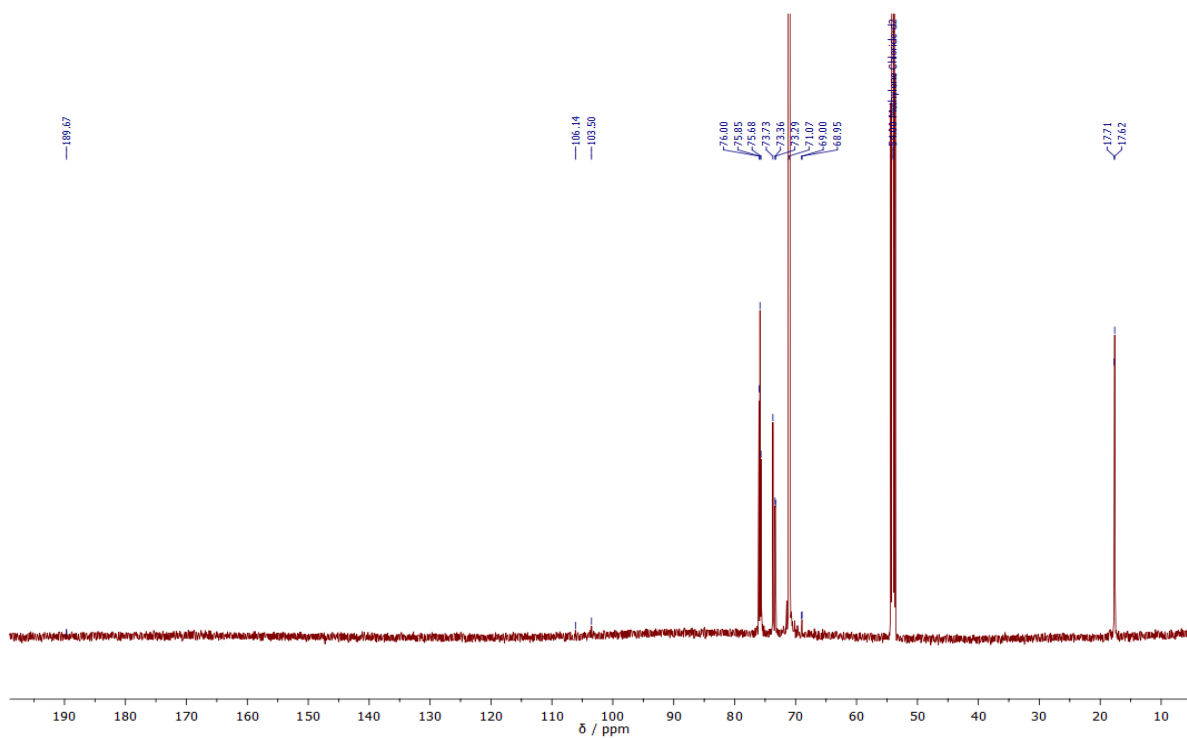


Figure E6.  $^{13}\text{C-NMR}$  ( $\text{CD}_2\text{Cl}_2$ , 298 K, 150.84 MHz) spectrum of Pluronic<sup>®</sup> F127 amine, PF127-NH<sub>2</sub>.



**Figure E7.**  $^1\text{H-NMR}$  ( $\text{CD}_2\text{Cl}_2$ , 298 K, 599.90 MHz) spectrum of Pluronic<sup>®</sup> F127 conjugated to fluorescein *via* thiourea, PF127-FITC.



**Figure E8.**  $^{13}\text{C-NMR}$  ( $\text{CD}_2\text{Cl}_2$ , 298 K, 150.84 MHz) spectrum of Pluronic<sup>®</sup> F127 conjugated to fluorescein *via* thiourea, PF127-FITC.

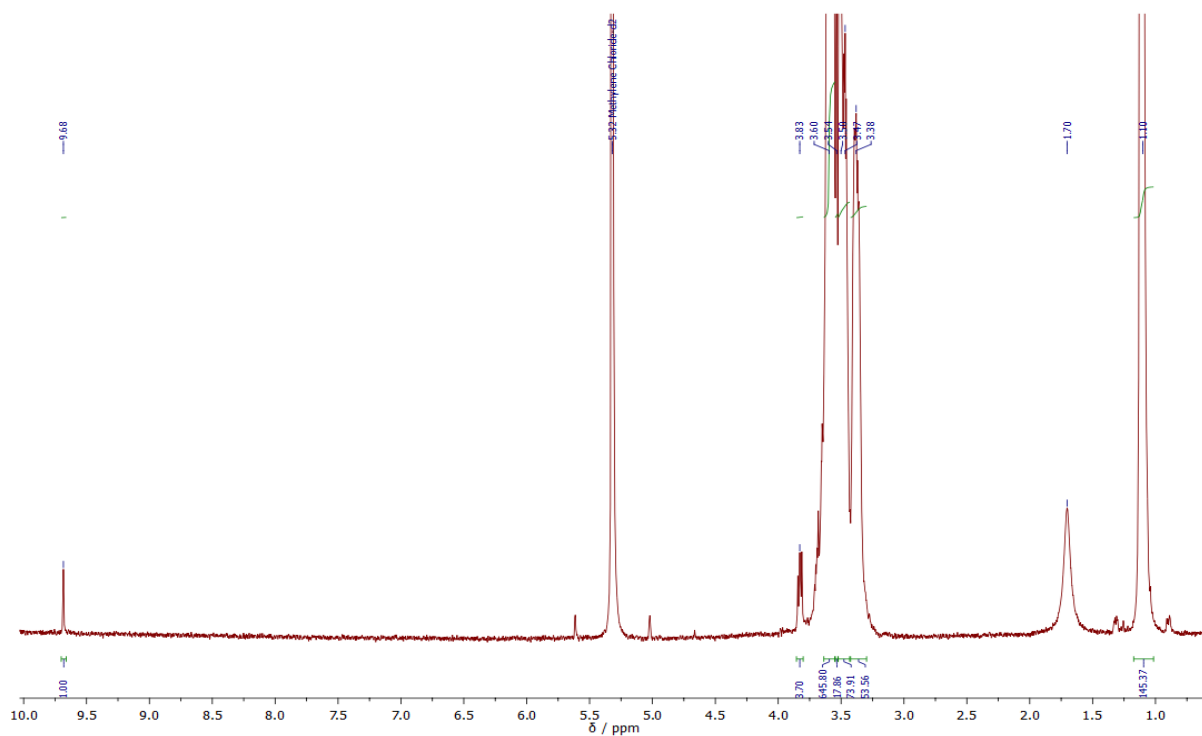


Figure E9.  $^1\text{H-NMR}$  ( $\text{CD}_2\text{Cl}_2$ , 298 K, 599.90 MHz) spectrum of Pluronic<sup>®</sup> F127 aldehyde, PF127-CHO.

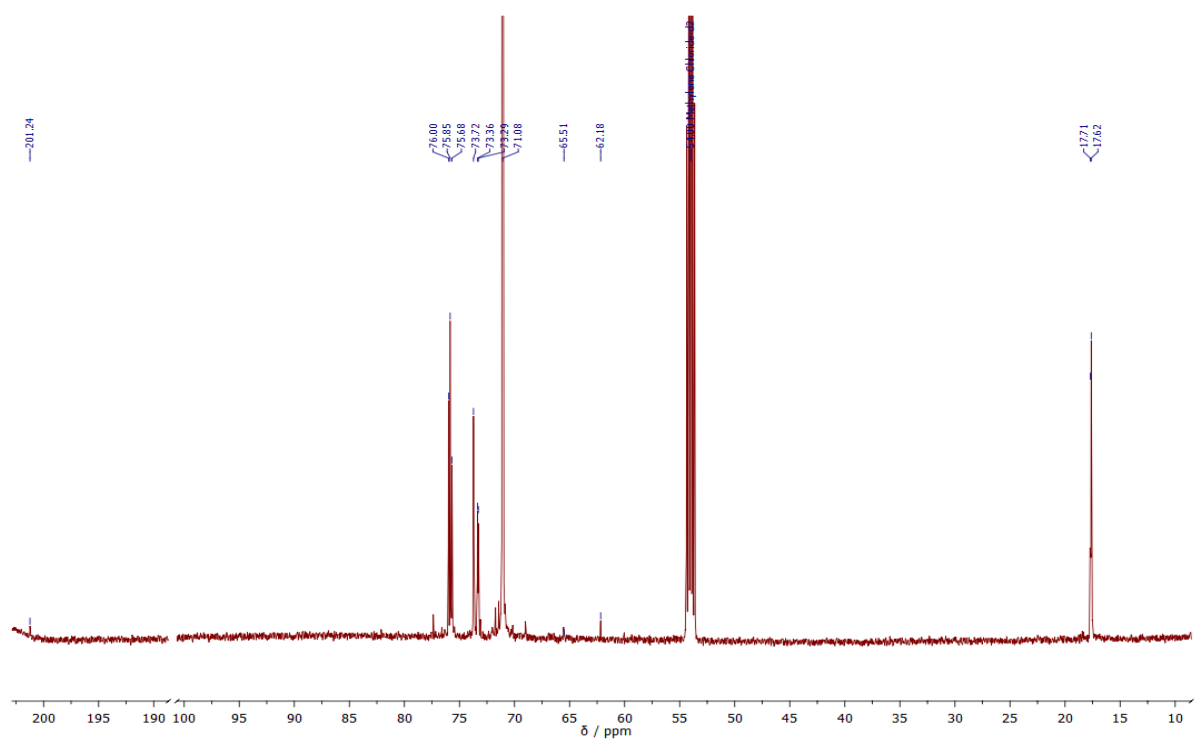
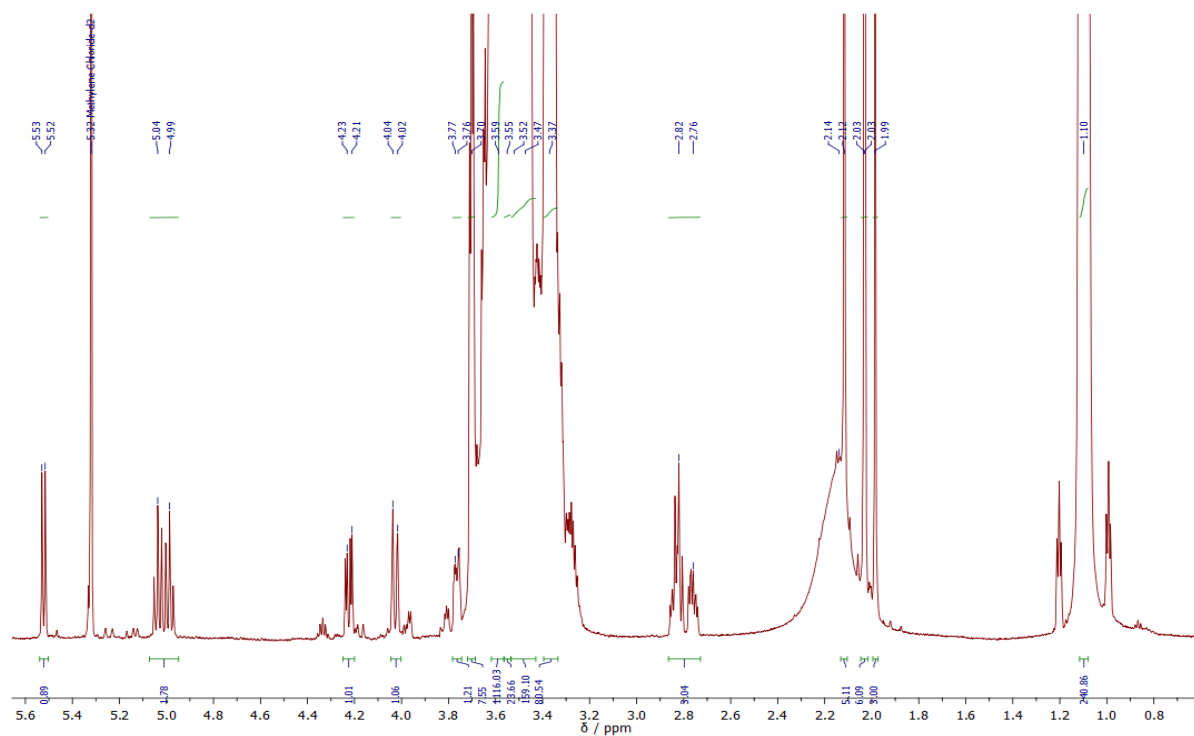
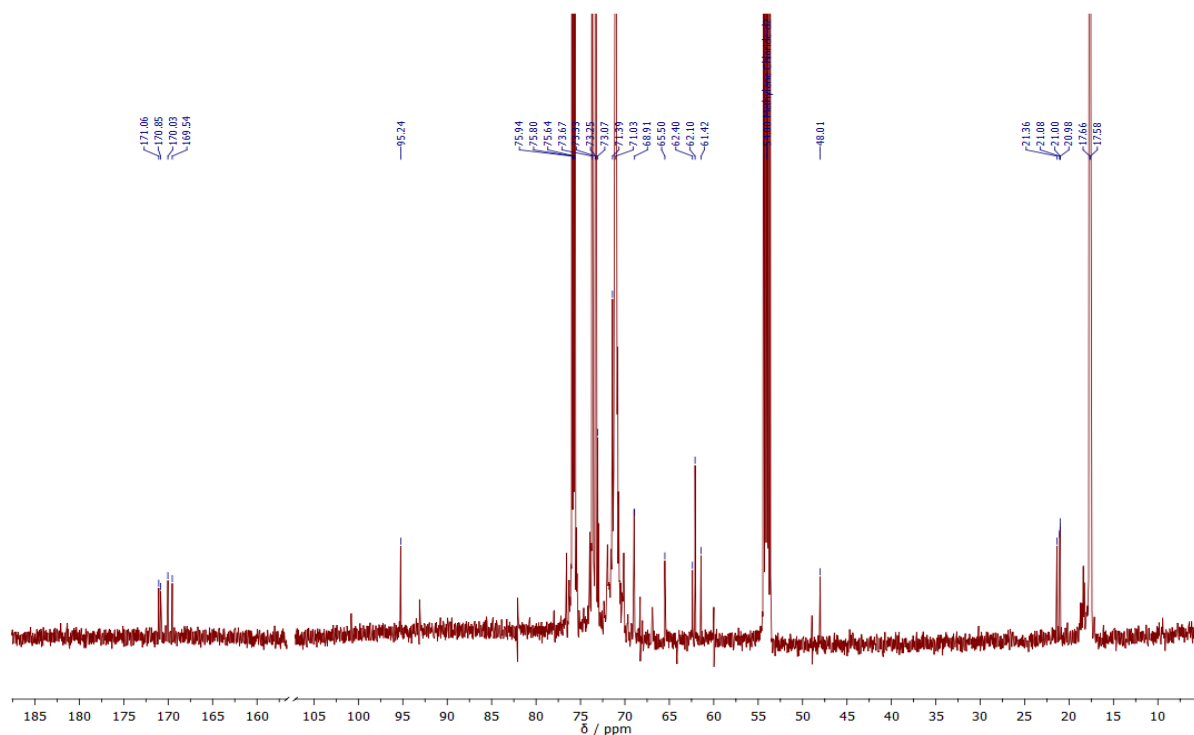


Figure E10.  $^{13}\text{C-NMR}$  ( $\text{CD}_2\text{Cl}_2$ , 298 K, 150.84 MHz) spectrum of Pluronic<sup>®</sup> F127 aldehyde, PF127-CHO.



**Figure E11.**  $^1\text{H}$ -NMR ( $\text{CD}_2\text{Cl}_2$ , 298 K, 599.90 MHz) spectrum of Pluronic<sup>®</sup> F127 conjugated to 1,3,4,6-tetra-*O*-acetyl-2-amino-2-deoxy- $\beta$ -D-glucopyranose *via* reductive amination, PF127-GlnOAc.



**Figure E12.**  $^{13}\text{C}$ -NMR ( $\text{CD}_2\text{Cl}_2$ , 298 K, 150.84 MHz) spectrum of Pluronic<sup>®</sup> F127 conjugated to 1,3,4,6-tetra-*O*-acetyl-2-amino-2-deoxy- $\beta$ -D-glucopyranose *via* reductive amination, PF127-GlnOAc.

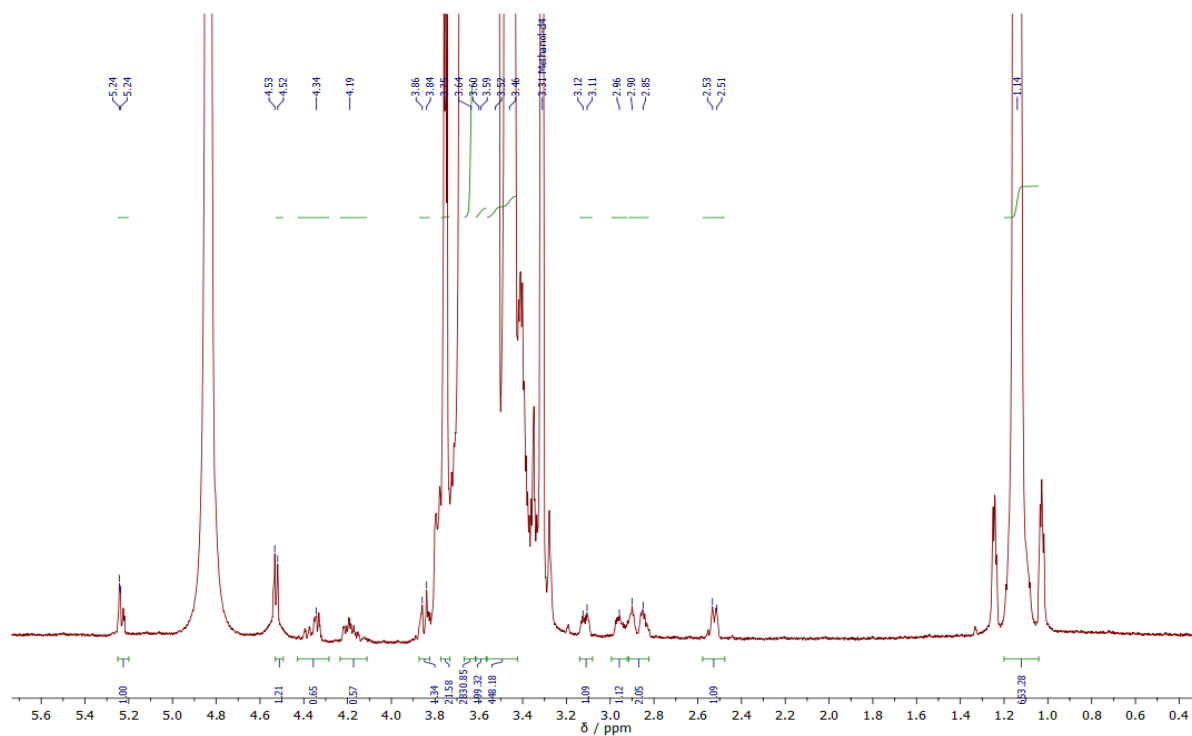


**Figure E13.**  $^1\text{H-NMR}$  ( $\text{CD}_3\text{OD}$ , 298 K, 599.90 MHz) spectrum of Pluronic<sup>®</sup> F127 conjugated to 2-amino-2-deoxy-D-glucose, PF127-GlnOH.

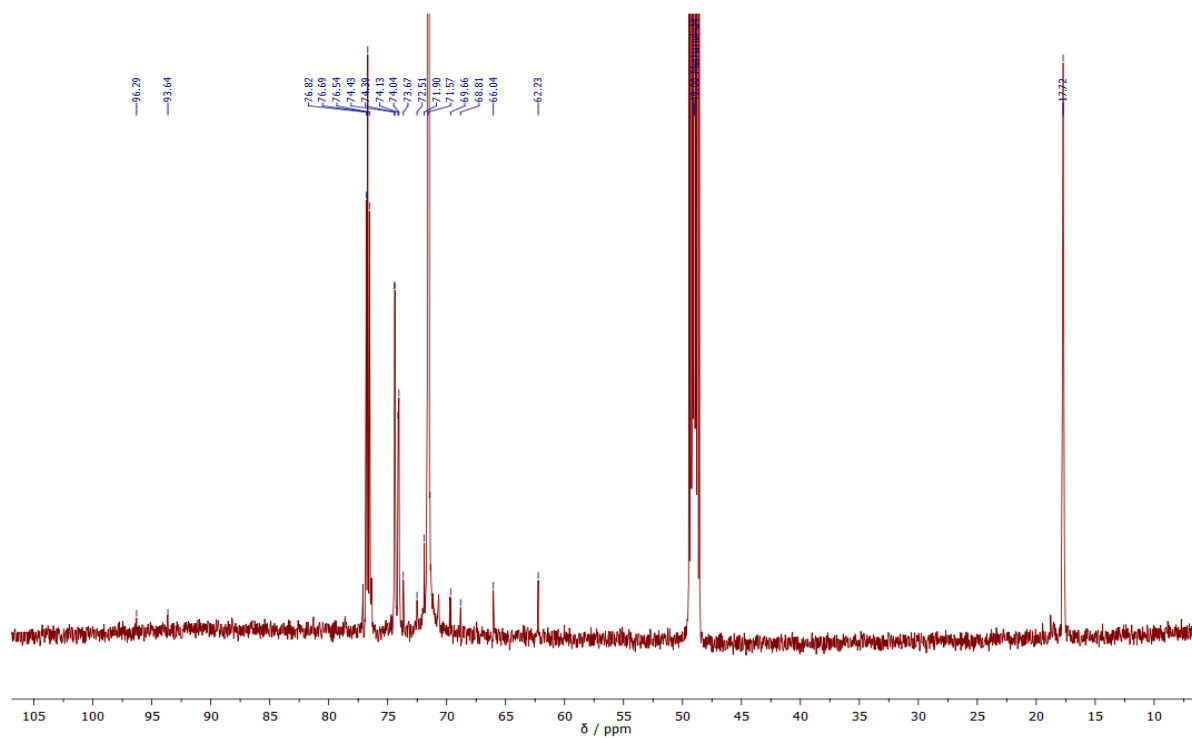


**Figure E14.**  $^{13}\text{C-NMR}$  ( $\text{CD}_3\text{OD}$ , 298 K, 150.84 MHz) spectrum of Pluronic<sup>®</sup> F127 conjugated to 2-amino-2-deoxy-D-glucose, PF127-GlnOH.

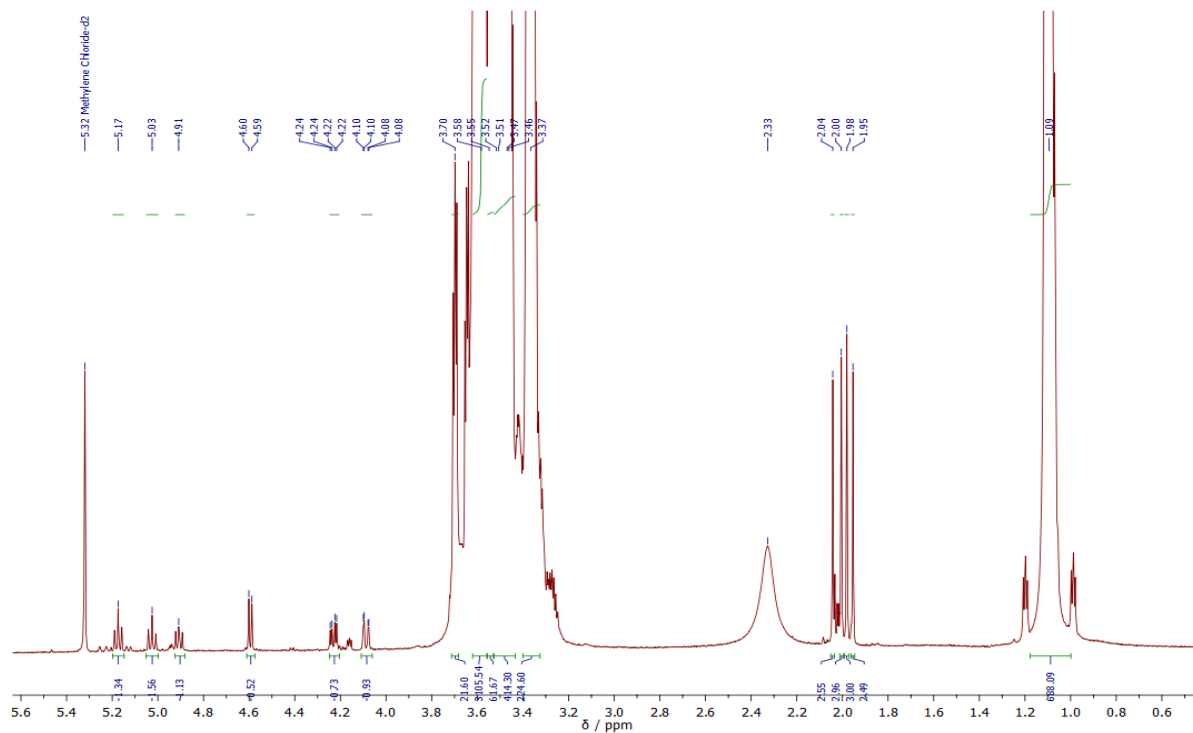


**Figure E15.** <sup>1</sup>H-NMR (CD<sub>2</sub>Cl<sub>2</sub>, 298 K, 599.90 MHz) spectrum of Pluronic® F127 conjugated to 2,3,4,6-tetra-*O*-acetyl-β-D-glucopyranose *via* glycosylation, PF127-GluOAc.

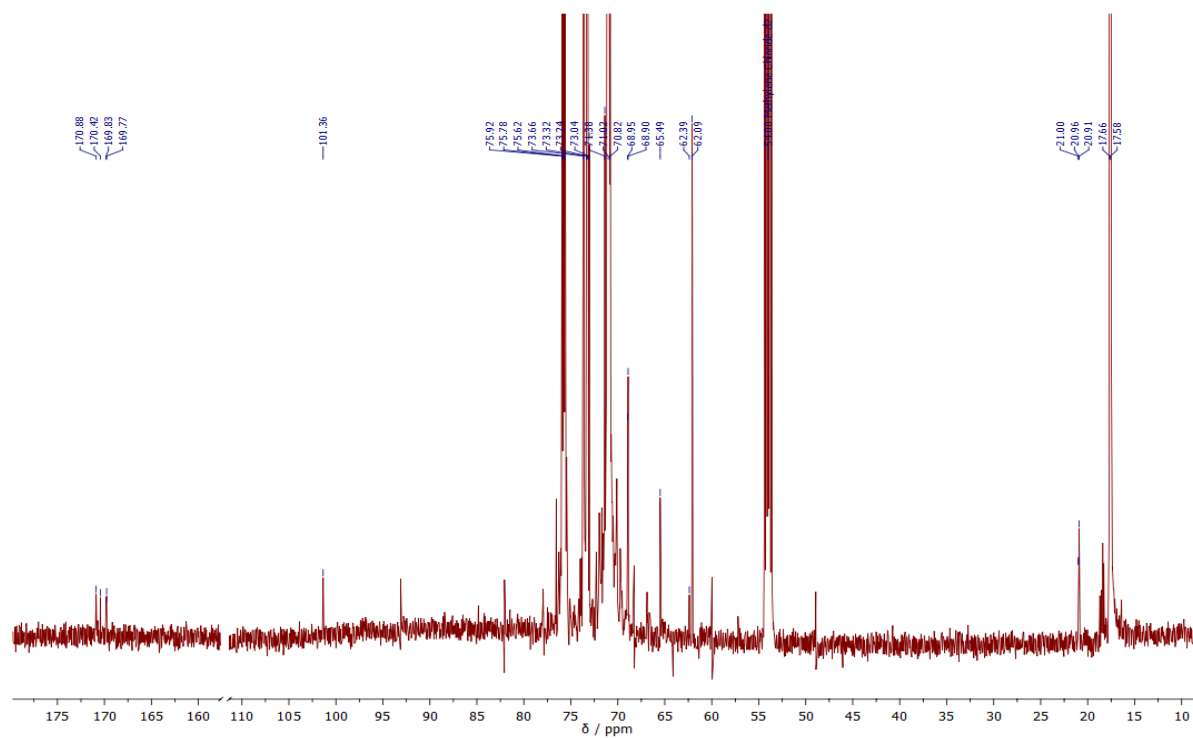


**Figure E16.** <sup>13</sup>C-NMR (CD<sub>2</sub>Cl<sub>2</sub>, 298 K, 150.84 MHz) spectrum of Pluronic® F127 conjugated to 2,3,4,6-tetra-*O*-acetyl-β-D-glucopyranose *via* glycosylation, PF127-GluOAc.

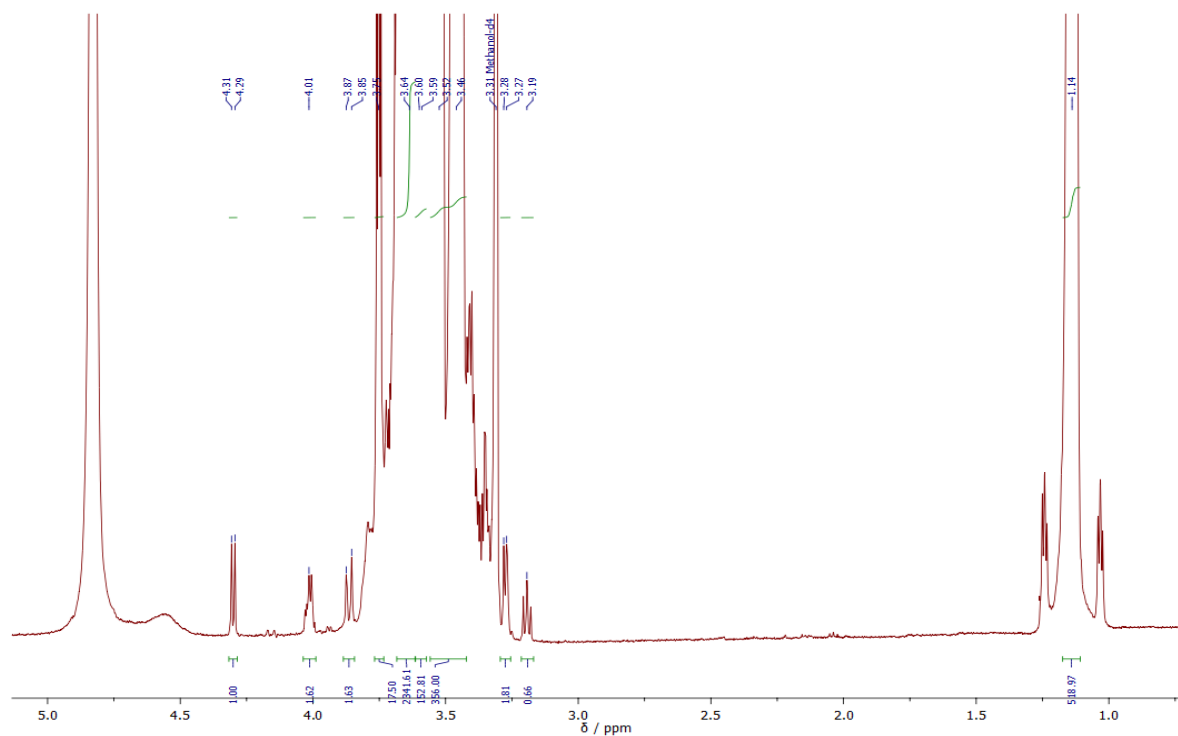


**Figure E17.**  $^1\text{H-NMR}$  ( $\text{CD}_3\text{OD}$ , 298 K, 599.90 MHz) spectrum of Pluronic<sup>®</sup> F127 conjugated to  $\beta$ -D-glucopyranose, PF127-GluOH.

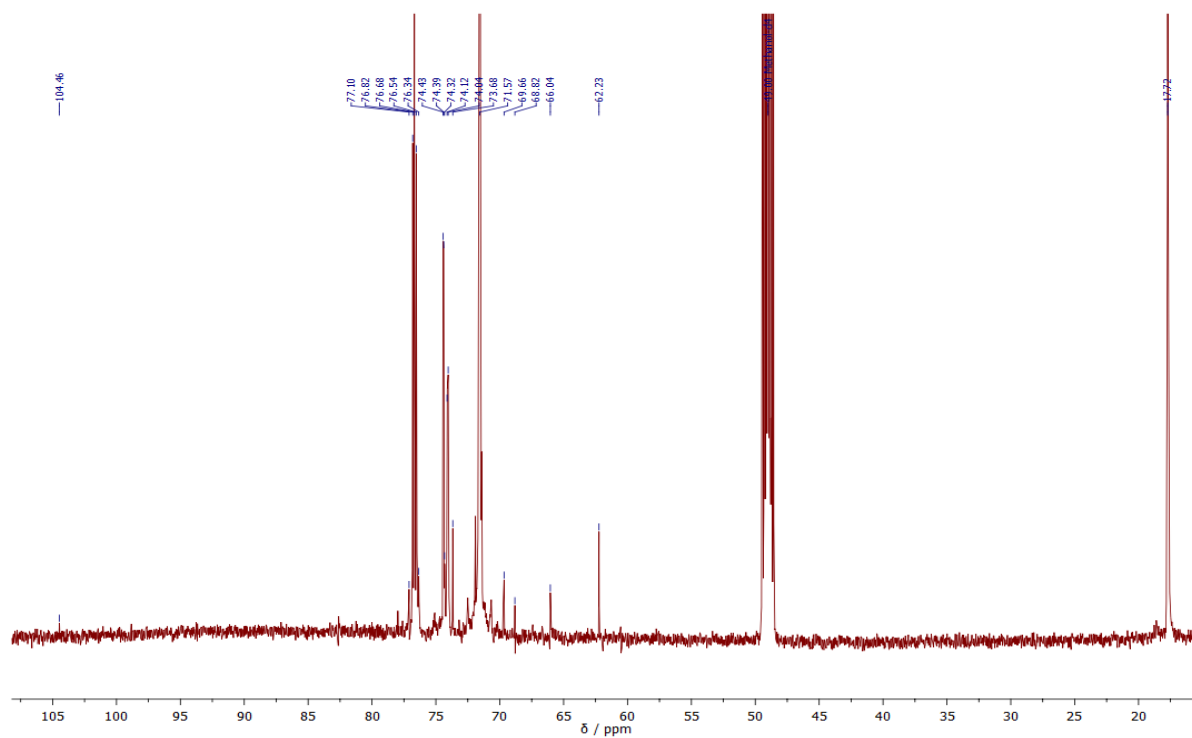


**Figure E18.**  $^{13}\text{C-NMR}$  ( $\text{CD}_3\text{OD}$ , 298 K, 150.84 MHz) spectrum of Pluronic<sup>®</sup> F127 conjugated to  $\beta$ -D-glucopyranose, PF127-GluOH.





## SUPPORTING INFORMATION F - FT-IR spectra of the synthesized dithiocarbamate ligands

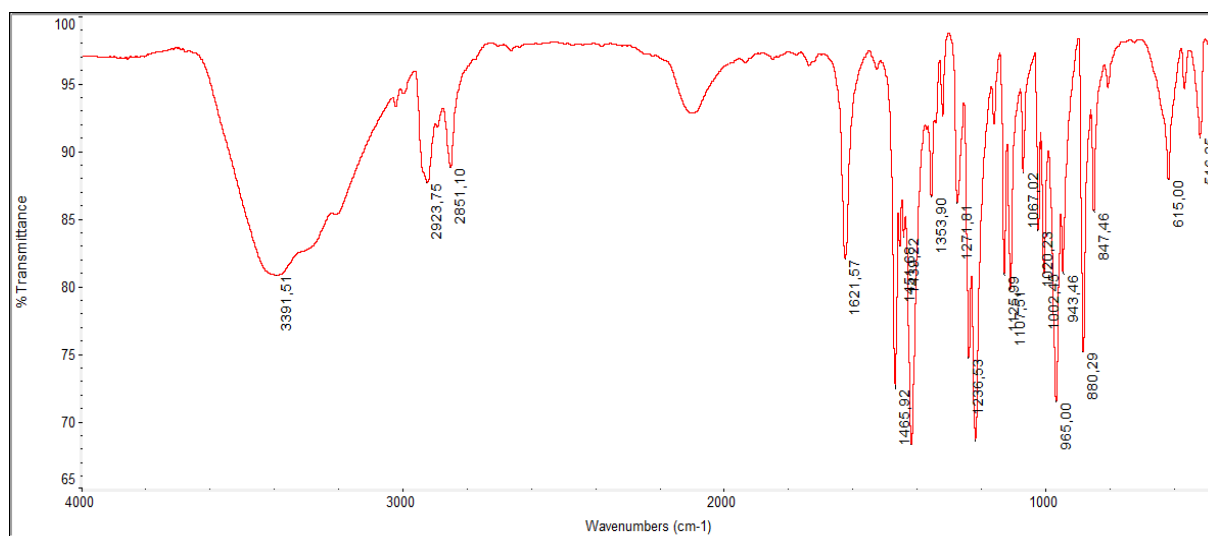


Figure F1. Medium FT-IR (4000-500 cm<sup>-1</sup>, KBr) spectrum of piperidine dithiocarbamate potassium salt (Na PipeDTC).

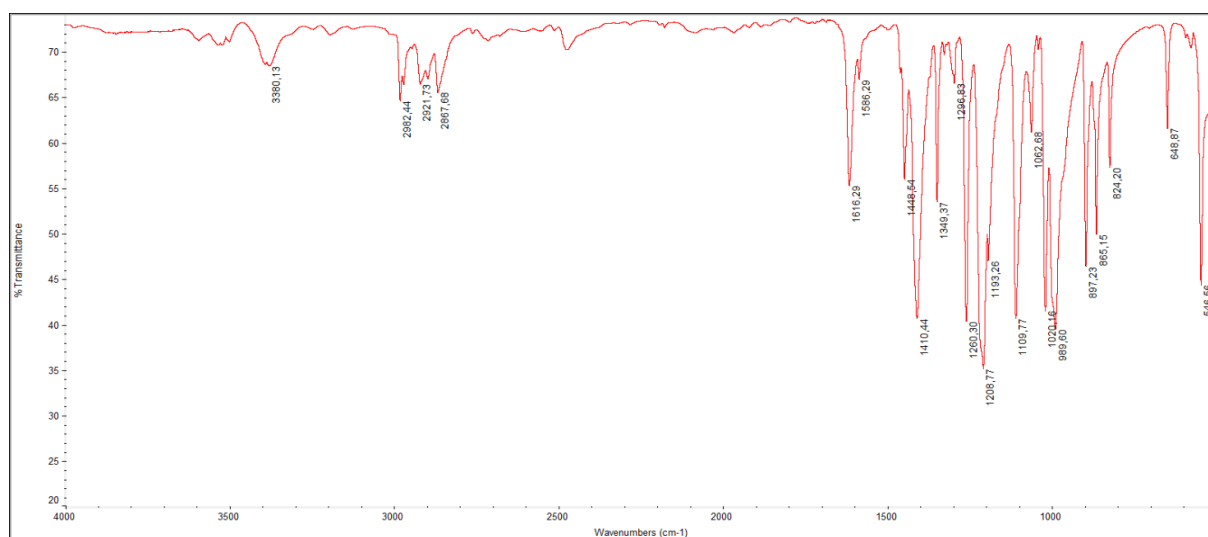


Figure F2. Medium FT-IR (4000-500 cm<sup>-1</sup>, KBr) spectrum of morpholine dithiocarbamate potassium salt (Na MorphDTC).

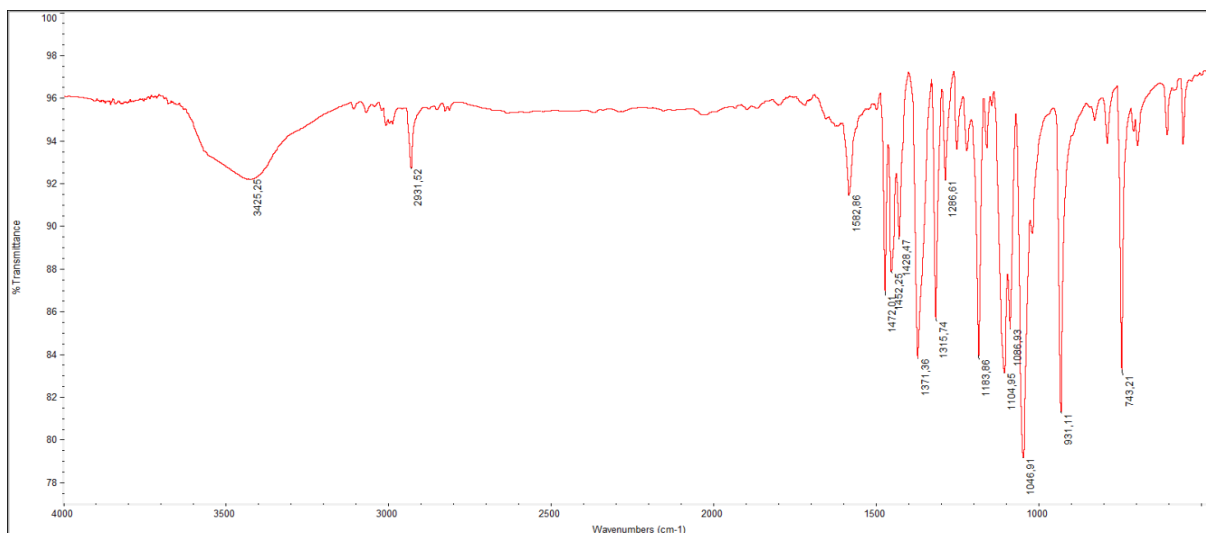


Figure F3. Medium FT-IR (4000-500 cm<sup>-1</sup>, KBr) spectrum of indoline dithiocarbamate potassium salt (K IndolineDTC).

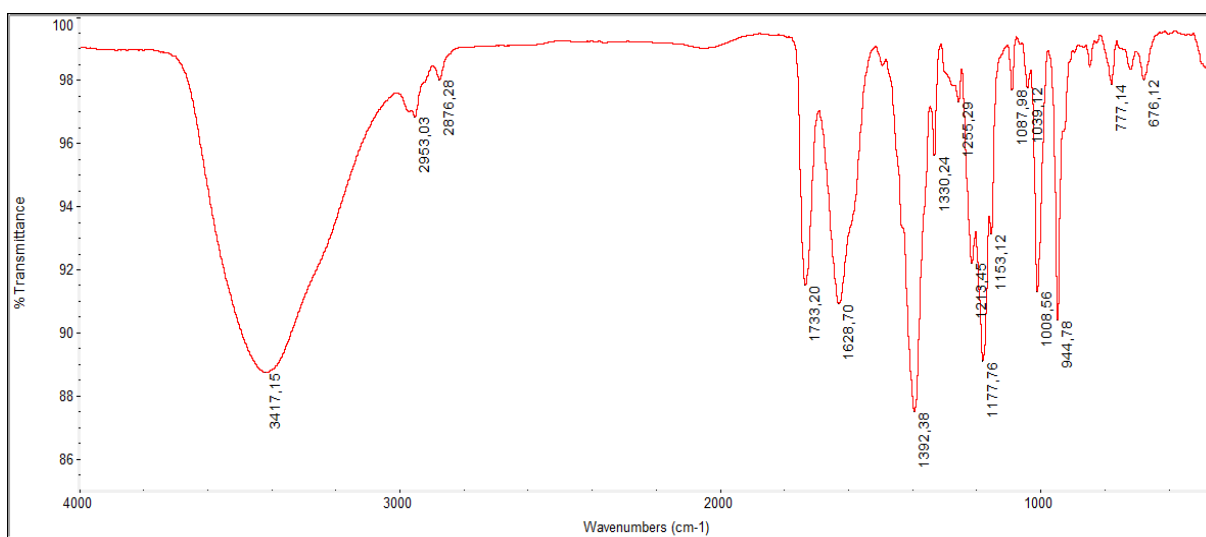


Figure F4. Medium FT-IR (4000-500 cm<sup>-1</sup>, KBr) spectrum of L-proline methyl ester dithiocarbamate sodium salt (Na ProOMeDTC).

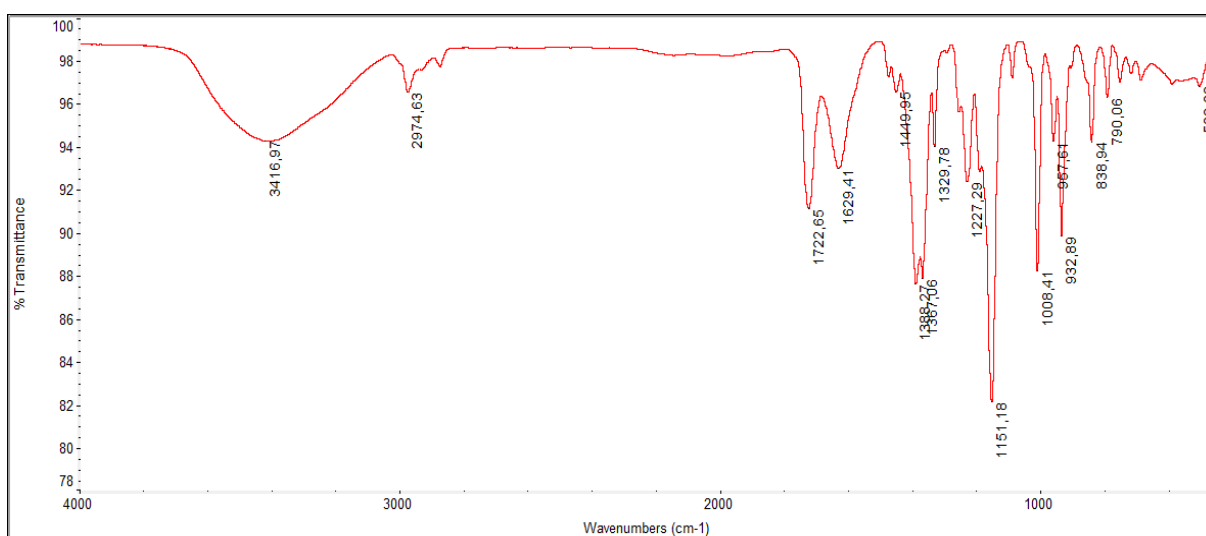


Figure F5. Medium FT-IR (4000-500 cm<sup>-1</sup>, KBr) spectrum of L-proline *tert*-butyl ester dithiocarbamate sodium salt (Na ProOtBuDTC).

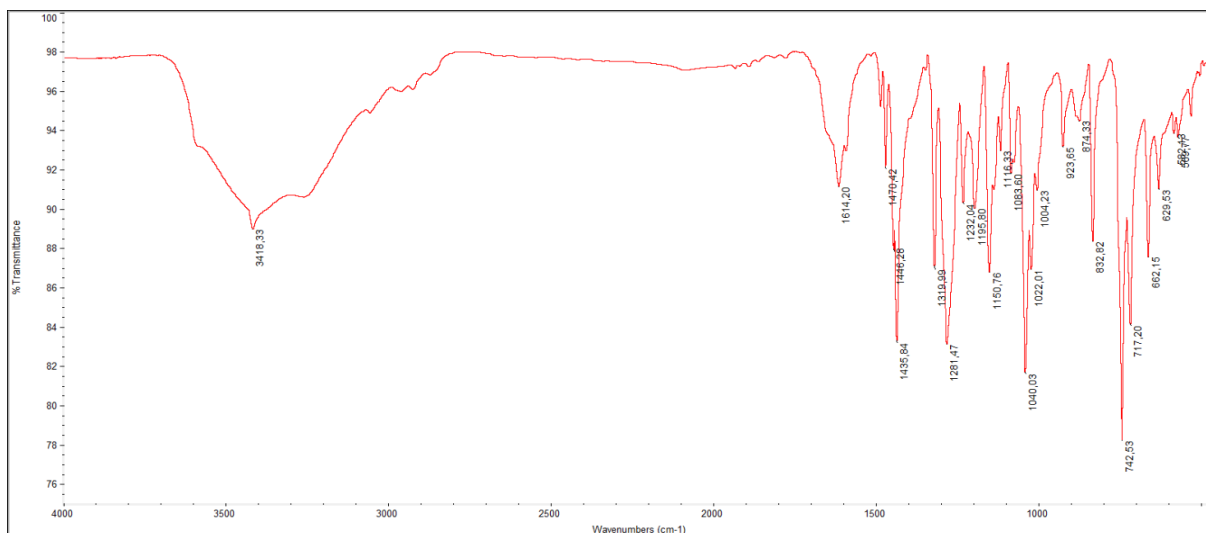


Figure F6. Medium FT-IR (4000-500 cm<sup>-1</sup>, KBr) spectrum of carbazole dithiocarbamate sodium salt (Na CDT).

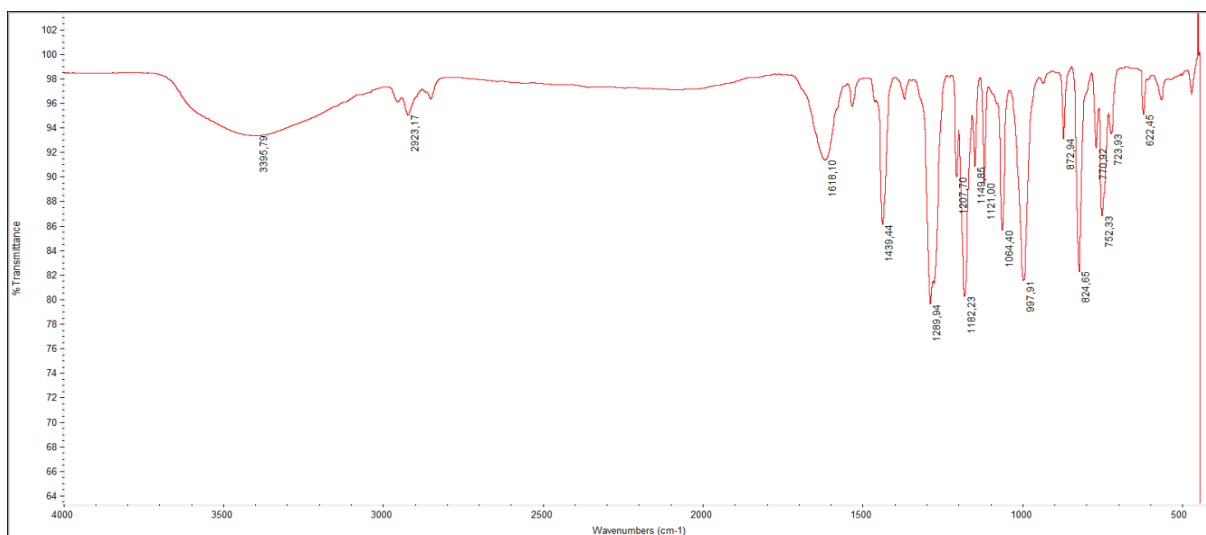


Figure F7. Medium FT-IR (4000-500 cm<sup>-1</sup>, KBr) spectrum of indole dithiocarbamate sodium salt (Na IndDTC).

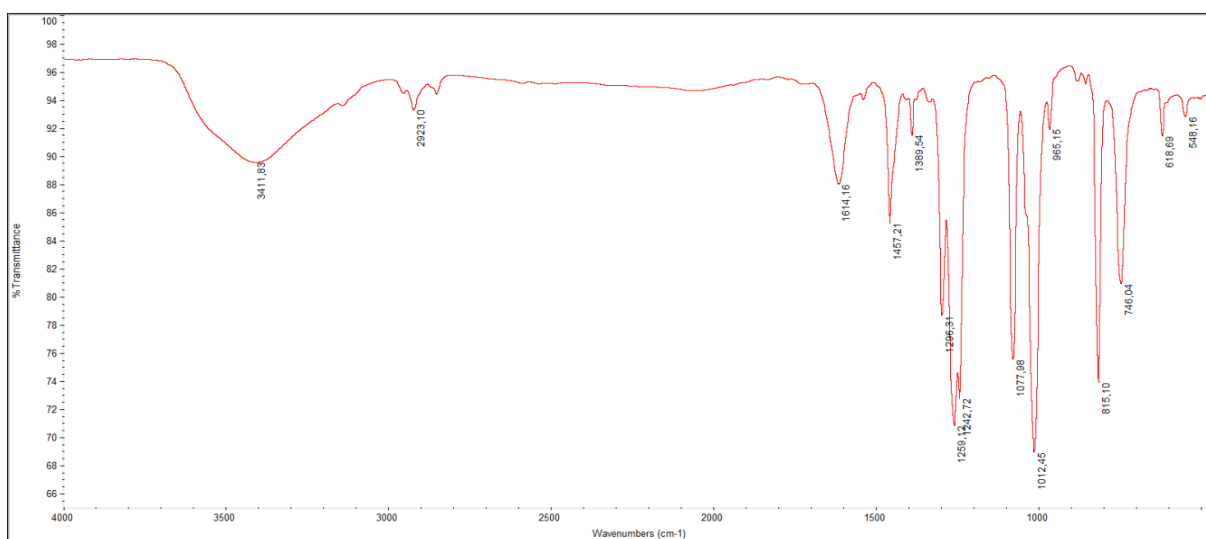
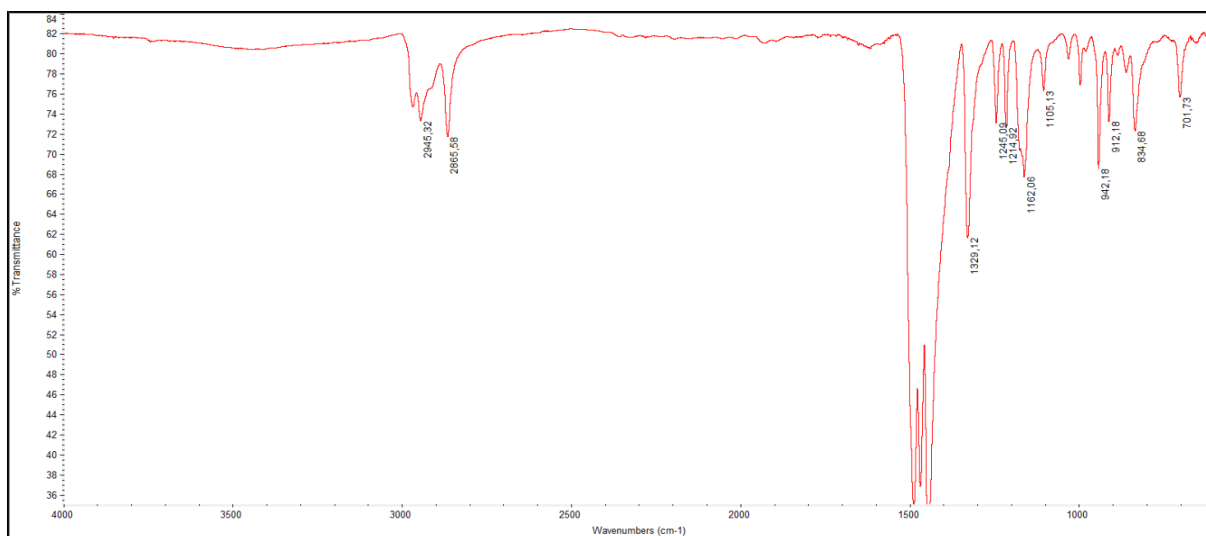


Figure F8. Medium FT-IR (4000-500 cm<sup>-1</sup>, KBr) spectrum of pyrrole dithiocarbamate



## SUPPORTING INFORMATION G - FT-IR spectra of the synthesized Ru(III) dithiocarbamate complexes



**Figure G1.** Medium FT-IR (4000-600 cm<sup>-1</sup>, KBr) spectrum of tris(pyrrolidine dithiocarbamate)ruthenium(III), [Ru(PDT)<sub>3</sub>].

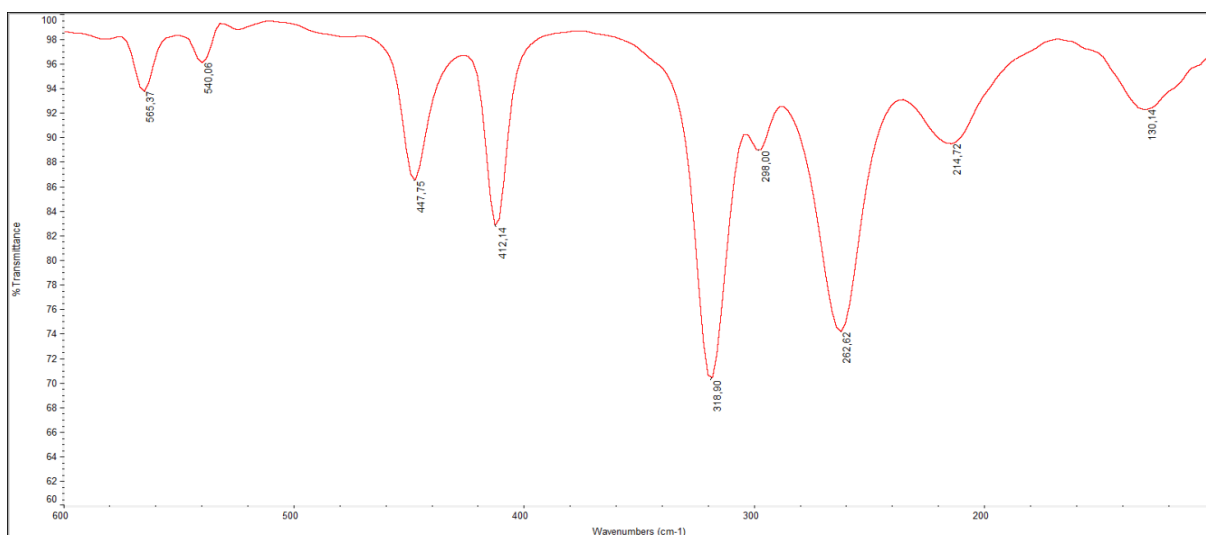


**Figure G2.** Far FT-IR (600-100 cm<sup>-1</sup>, nujol) spectrum of tris(pyrrolidine dithiocarbamate)ruthenium(III), [Ru(PDT)<sub>3</sub>].

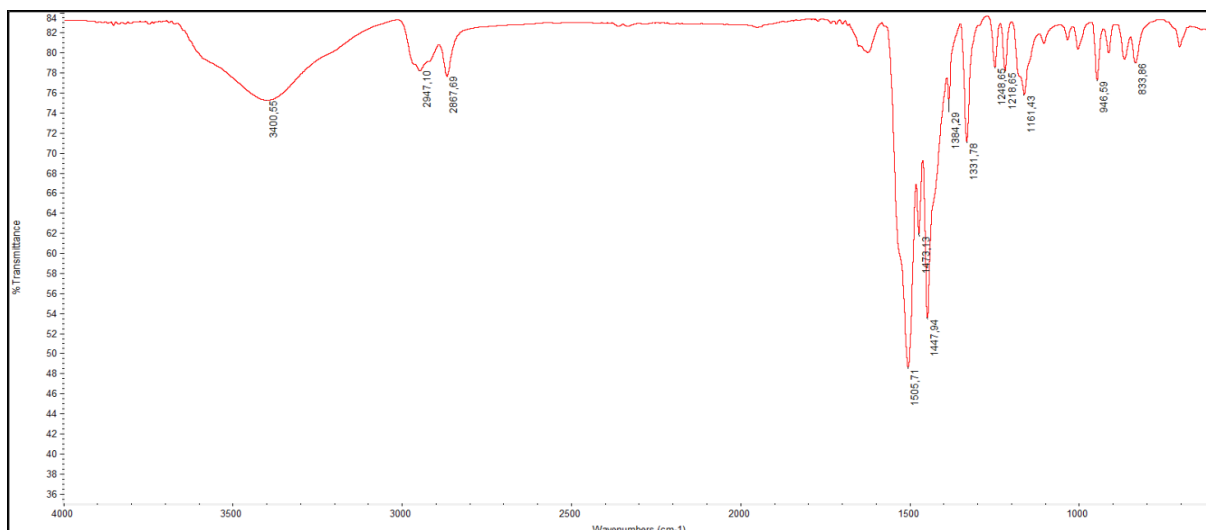


**Figure G3.** Medium FT-IR (4000-600 cm<sup>-1</sup>, KBr) spectrum of  $\beta$ -pentakis(pyrrolidine dithiocarbamate)diruthenium(III) chloride,  $\beta$ -[Ru<sub>2</sub>(PDT)<sub>5</sub>]Cl.

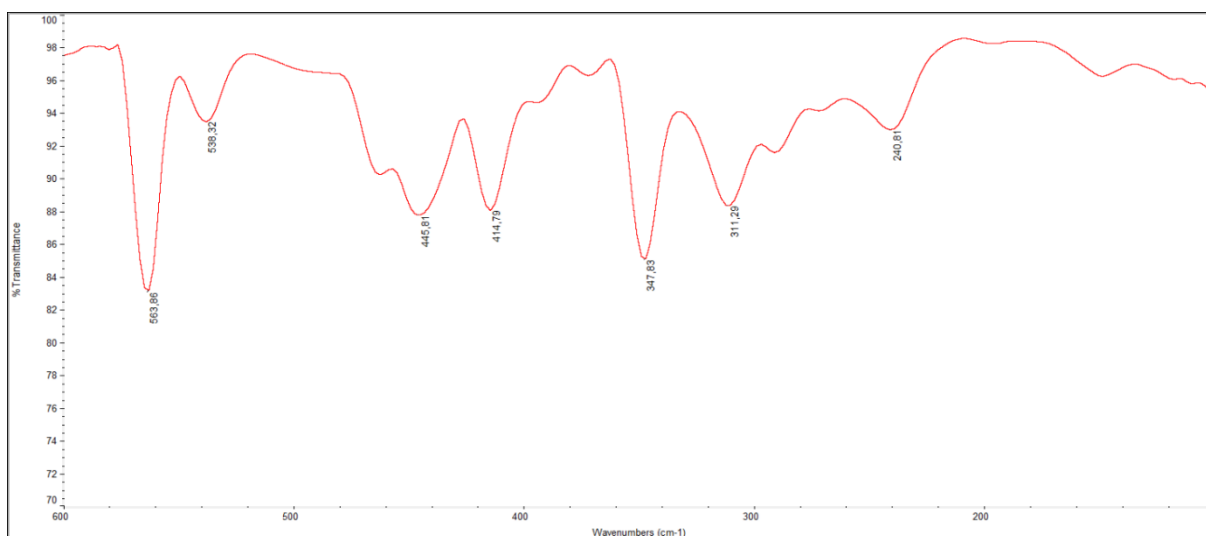


**Figure G4.** Far FT-IR (600-100 cm<sup>-1</sup>, nujol) spectrum of  $\beta$ -pentakis(pyrrolidine dithiocarbamate)diruthenium(III) chloride,  $\beta$ -[Ru<sub>2</sub>(PDT)<sub>5</sub>]Cl.

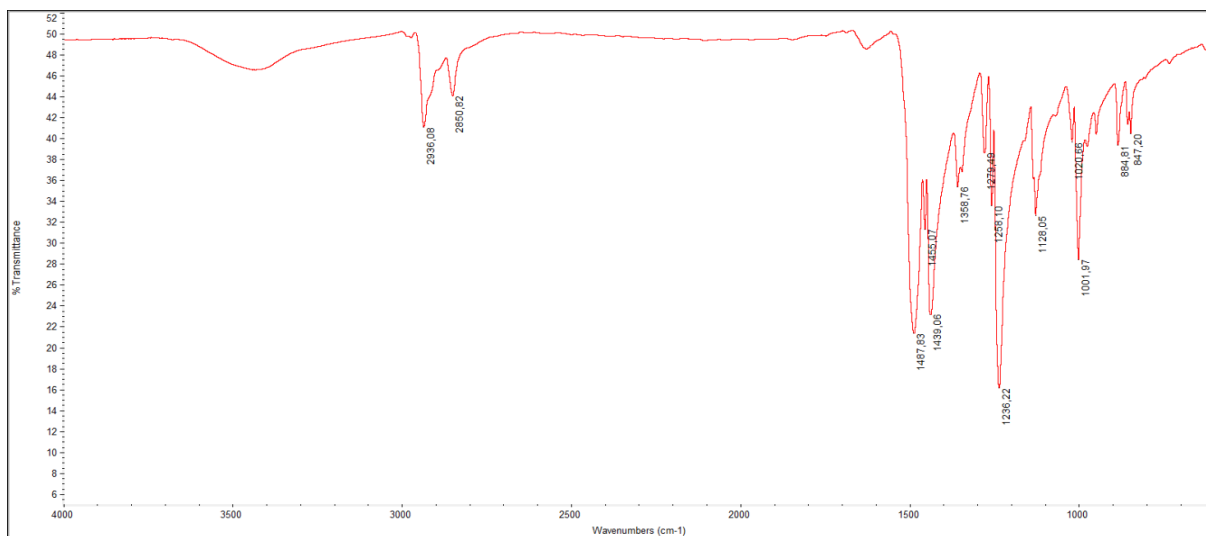


**Figure G5.** Medium FT-IR (4000-600 cm<sup>-1</sup>, KBr) spectrum of tris(piperidine dithiocarbamate)ruthenium(III), [Ru(PipeDTC)<sub>3</sub>].

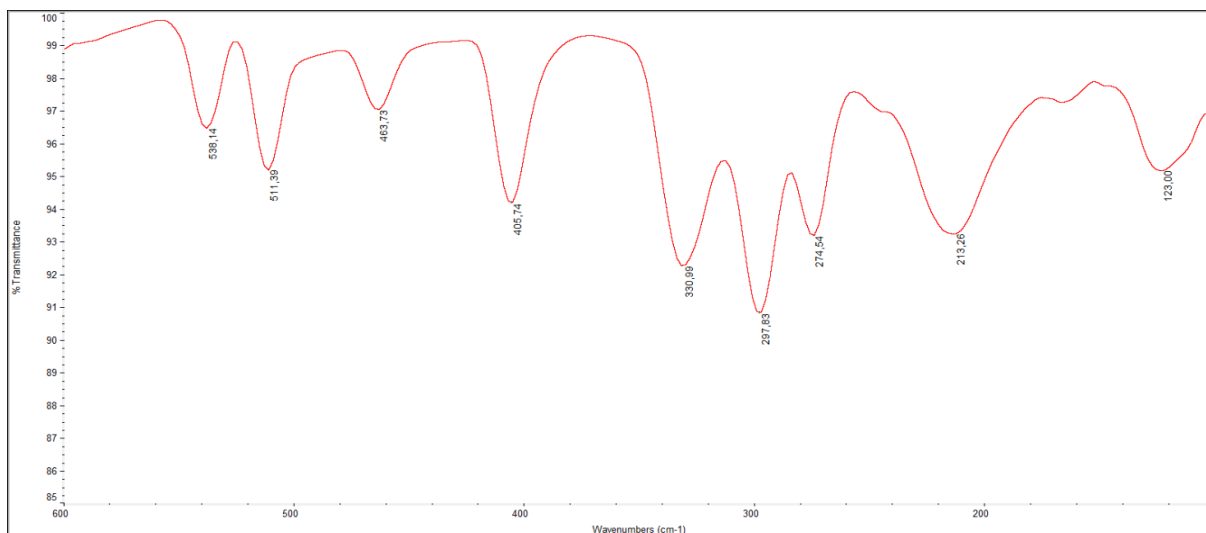


**Figure G6.** Far FT-IR ( $600\text{-}100\text{ cm}^{-1}$ , nujol) spectrum of tris(piperidine dithiocarbamate)ruthenium(III),  $[\text{Ru}(\text{PipeDTC})_3]$ .

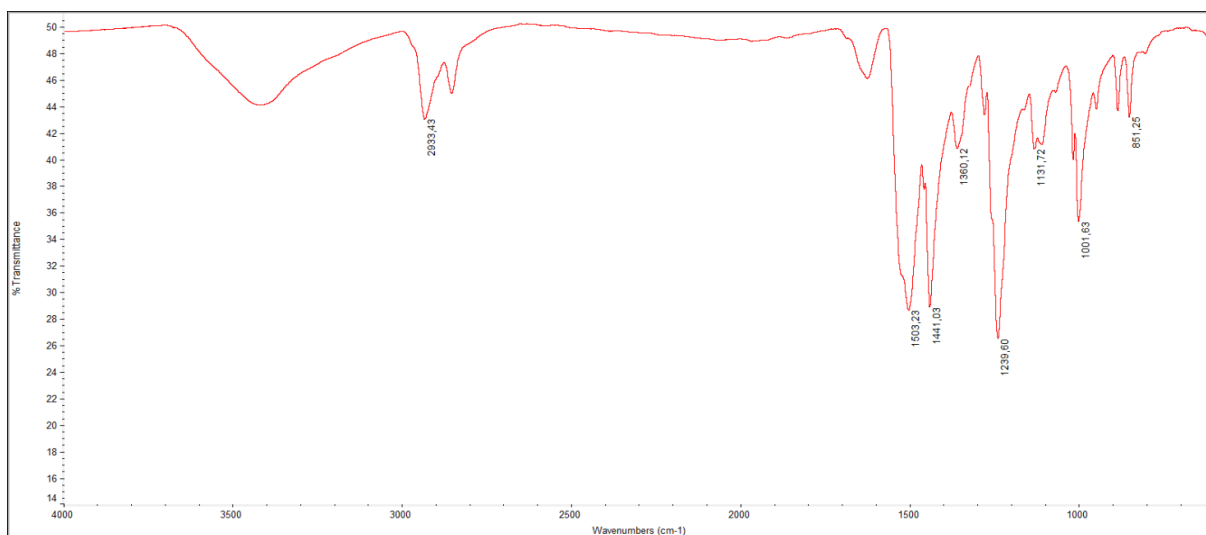


**Figure G7.** Medium FT-IR ( $4000\text{-}600\text{ cm}^{-1}$ , KBr) spectrum of  $\beta$ -pentakis(piperidine dithiocarbamate)diruthenium(III) chloride,  $\beta\text{-}[\text{Ru}_2(\text{PipeDTC})_5]\text{Cl}$ .

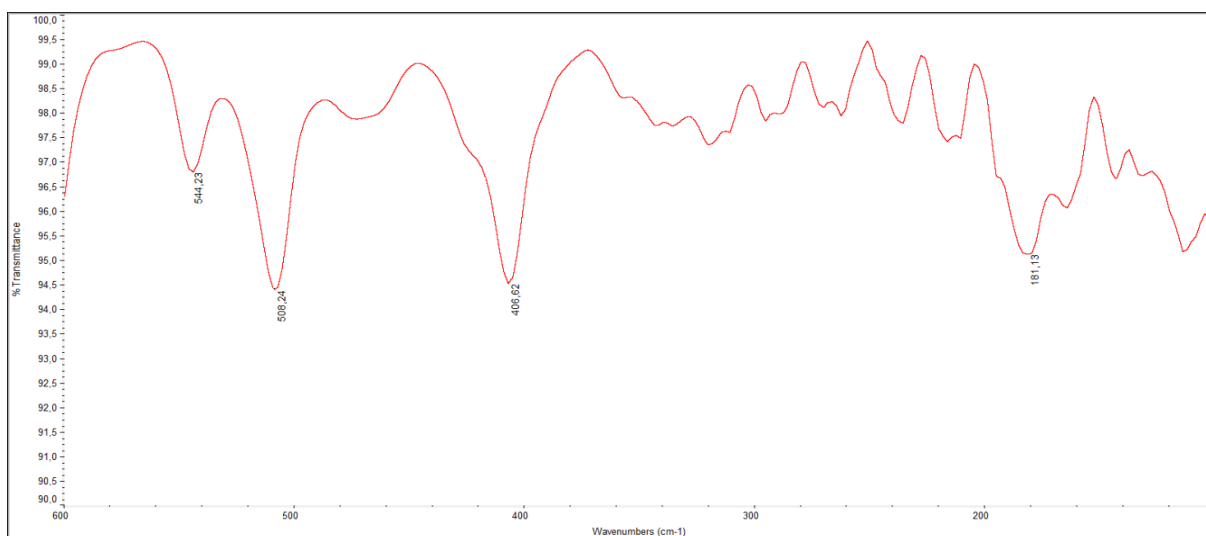


**Figure G8.** Far FT-IR ( $600\text{-}100\text{ cm}^{-1}$ , nujol) spectrum of  $\beta$ -pentakis(piperidine dithiocarbamate)diruthenium(III) chloride,  $\beta\text{-}[\text{Ru}_2(\text{PipeDTC})_5]\text{Cl}$ .

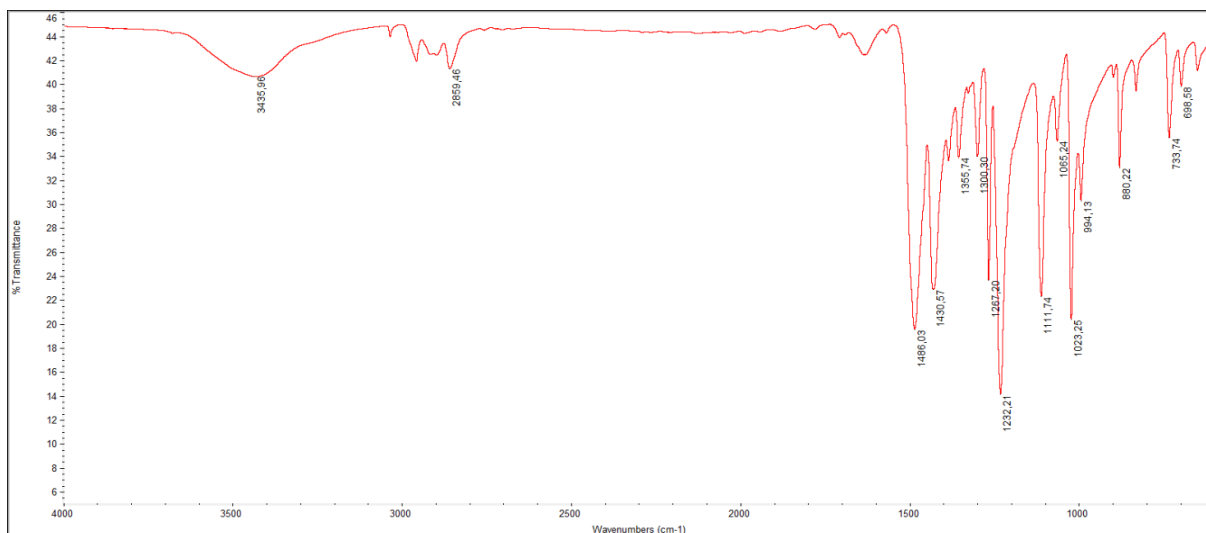


**Figure G9.** Medium FT-IR (4000-600 cm<sup>-1</sup>, KBr) spectrum of tris(morpholine dithiocarbamate)ruthenium(III), [Ru(MorphDTC)<sub>3</sub>].

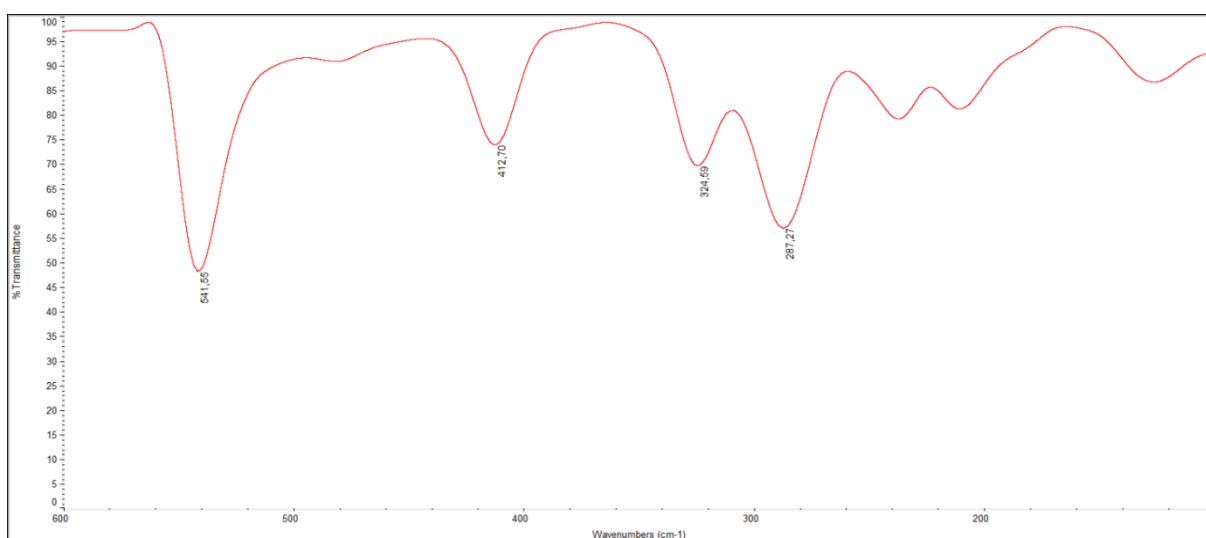


**Figure G10.** Far FT-IR (600-100 cm<sup>-1</sup>, nujol) spectrum of tris(morpholine dithiocarbamate)ruthenium(III), [Ru(MorphDTC)<sub>3</sub>].

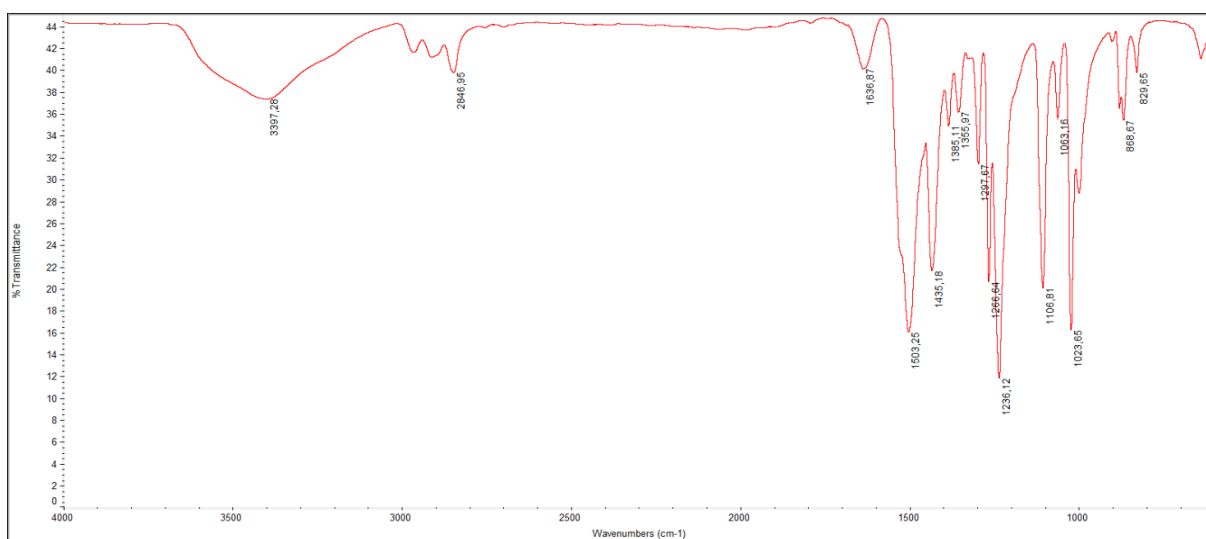


**Figure G11.** Medium FT-IR (4000-600 cm<sup>-1</sup>, KBr) spectrum of  $\beta$ -pentakis(morpholine dithiocarbamate)diruthenium(III) chloride,  $\beta$ -[Ru<sub>2</sub>(MorphDTC)<sub>5</sub>]Cl.



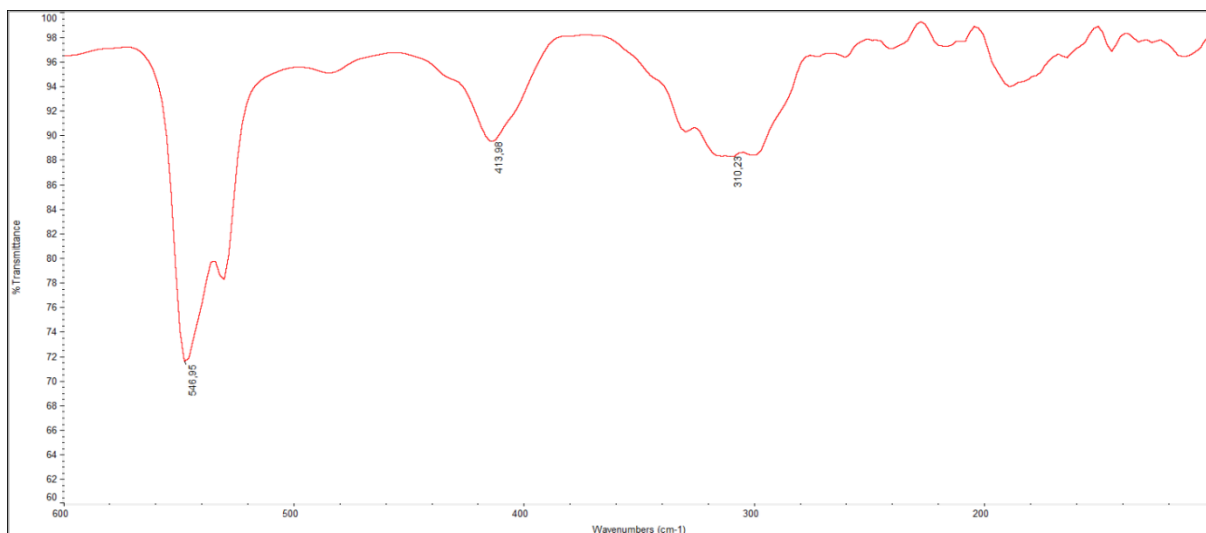


**Figure G12.** Far FT-IR (600-100  $\text{cm}^{-1}$ , nujol) spectrum of  $\beta$ -pentakis(morpholine dithiocarbamate)diruthenium(III) chloride,  $\beta$ - $[\text{Ru}_2(\text{MorphDTC})_5]\text{Cl}$ .

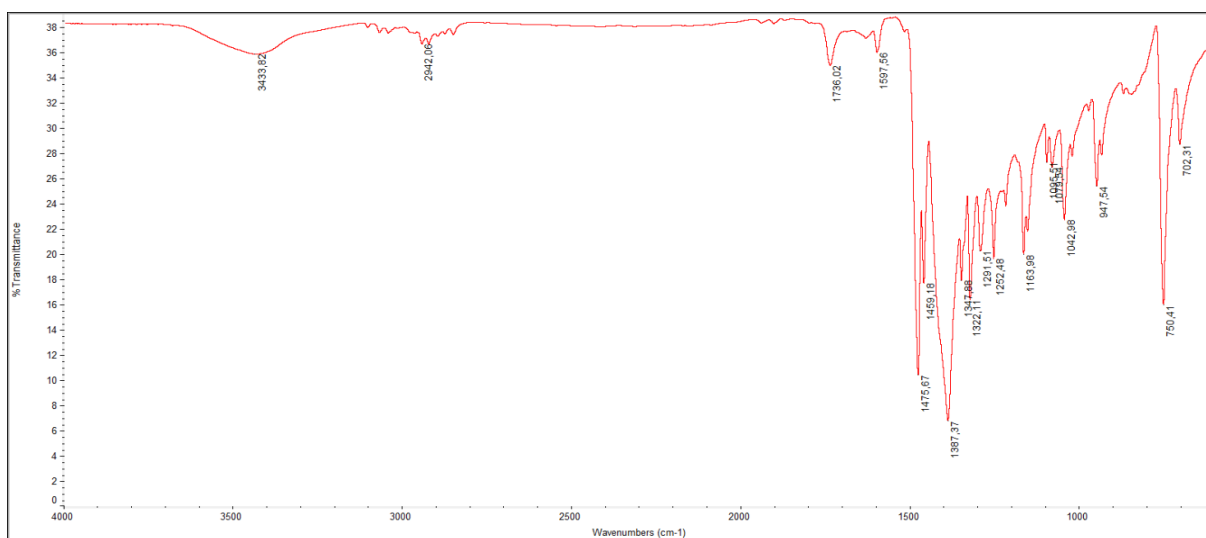


**Figure G13.** Medium FT-IR (4000-600  $\text{cm}^{-1}$ , KBr) spectrum of tris(indoline dithiocarbamate)ruthenium(III),  $[\text{Ru}(\text{IndolineDTC})_3]$ .

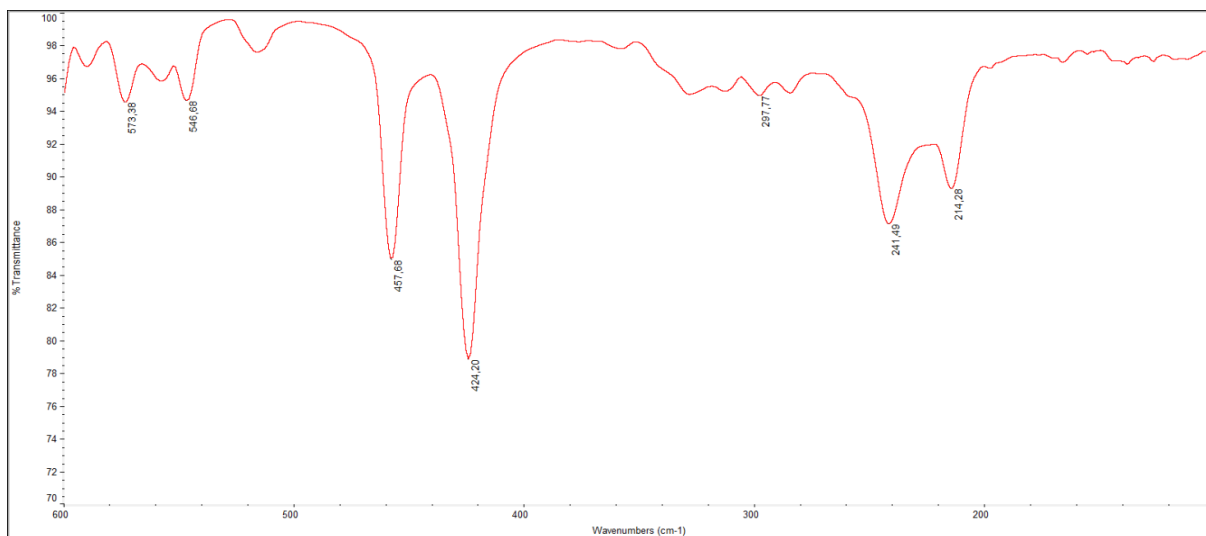


**Figure G14.** Far FT-IR (600-100  $\text{cm}^{-1}$ , nujol) spectrum of tris(indoline dithiocarbamate)ruthenium(III),  $[\text{Ru}(\text{IndolineDTC})_3]$ .

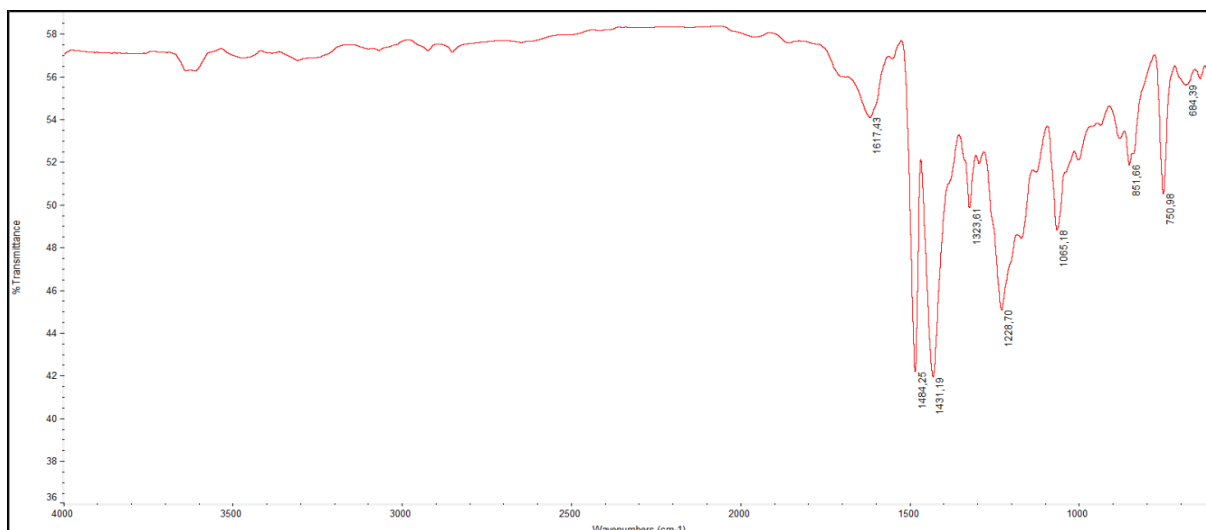


**Figure G15.** Medium FT-IR ( $4000\text{-}600\text{ cm}^{-1}$ , KBr) spectrum of  $\beta$ -pentakis(indoline dithiocarbamate)diruthenium(III) chloride,  $\beta\text{-}[\text{Ru}_2(\text{IndolineDTC})_5]\text{Cl}$ .

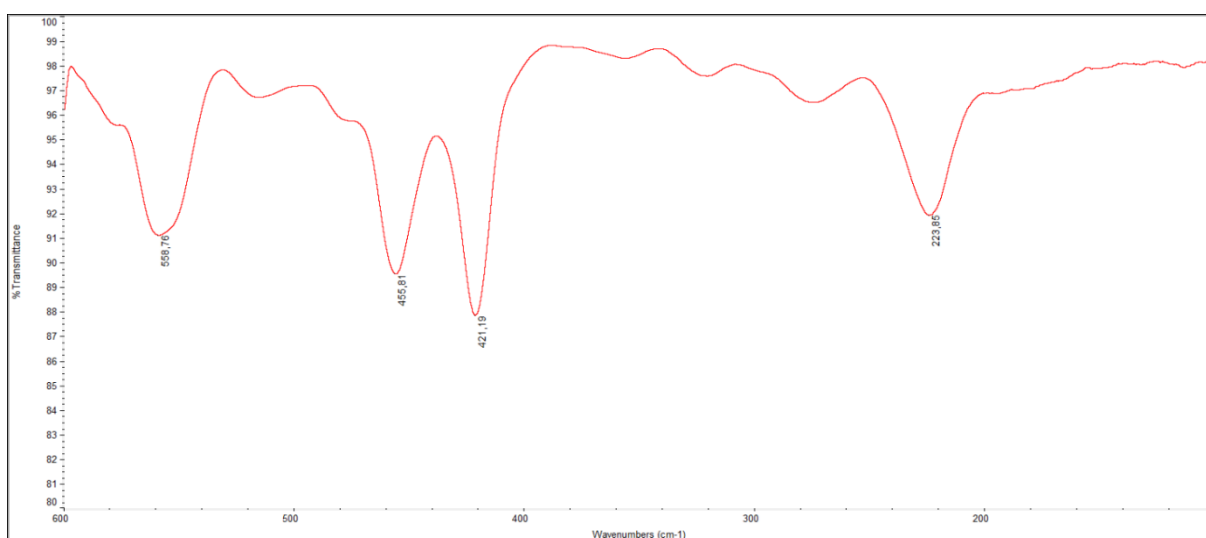


**Figure G16.** Far FT-IR ( $600\text{-}100\text{ cm}^{-1}$ , nujol) spectrum of  $\beta$ -pentakis(indoline dithiocarbamate)diruthenium(III) chloride,  $\beta\text{-}[\text{Ru}_2(\text{IndolineDTC})_5]\text{Cl}$ .

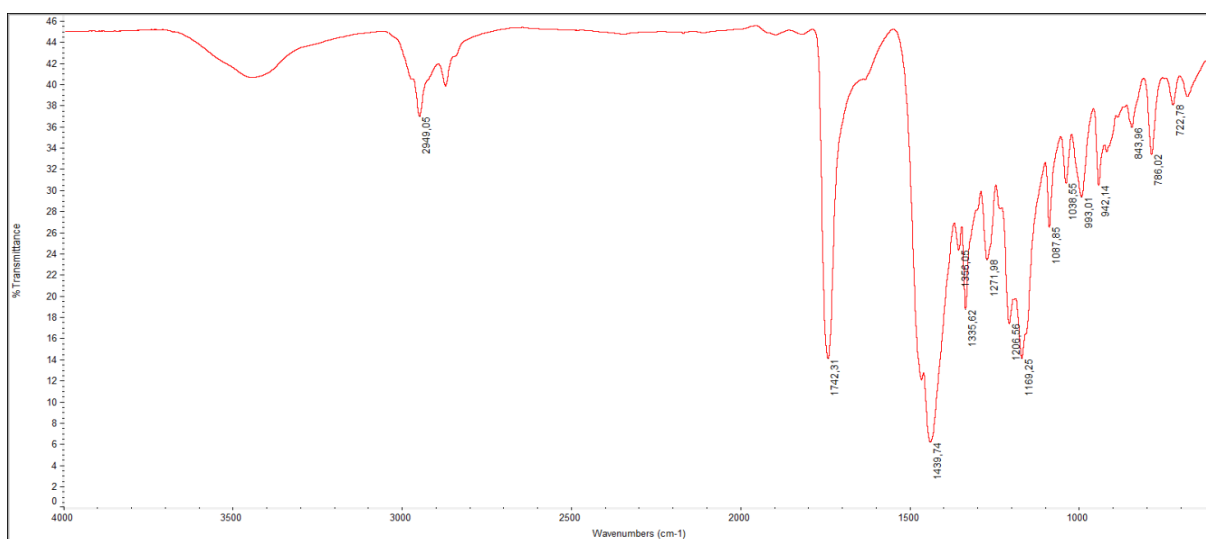


**Figure G17.** Medium FT-IR ( $4000\text{-}600\text{ cm}^{-1}$ , KBr) spectrum of tris(L-proline methyl ester dithiocarbamate)ruthenium(III),  $[\text{Ru}(\text{ProOMeDTC})_3]$ .

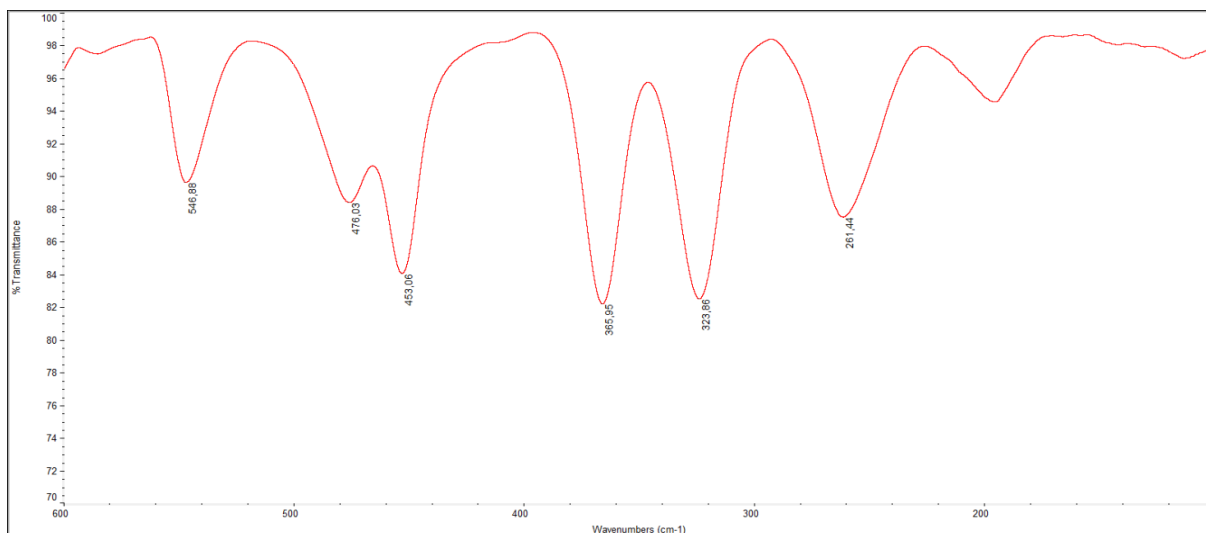


**Figure G18.** Far FT-IR ( $600\text{-}100\text{ cm}^{-1}$ , nujol) spectrum of tris(L-proline methyl ester dithiocarbamate)ruthenium(III),  $[\text{Ru}(\text{ProOMeDTC})_3]$ .

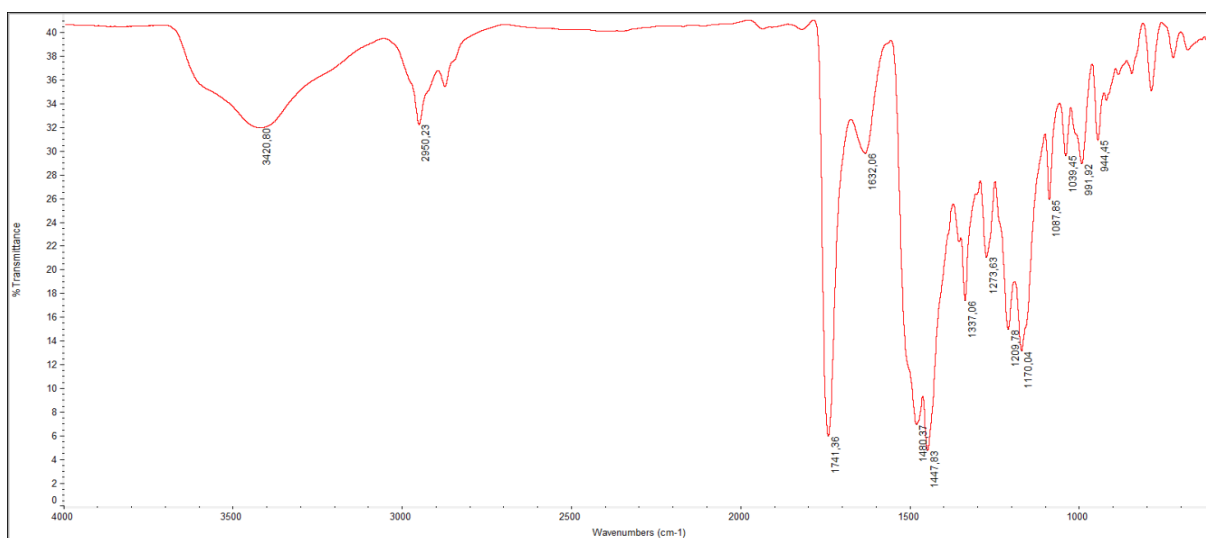


**Figure G19.** Medium FT-IR ( $4000\text{-}600\text{ cm}^{-1}$ , KBr) spectrum of  $\beta$ -pentakis(L-proline methyl ester dithiocarbamate)diruthenium(III) chloride,  $\beta\text{-}[\text{Ru}_2(\text{ProOMeDTC})_5]\text{Cl}$ .

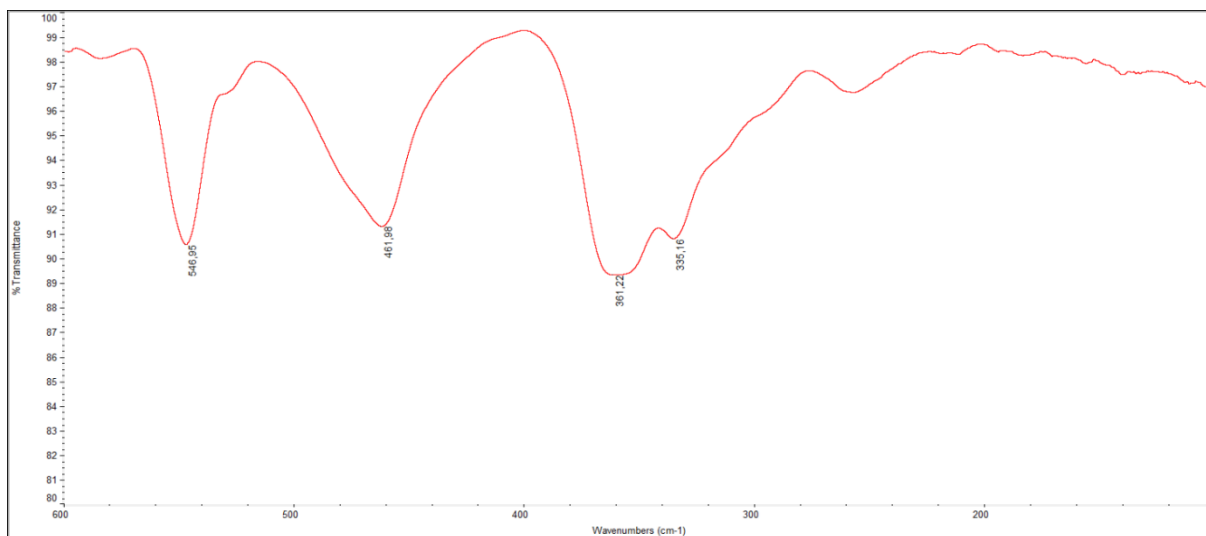


**Figure G20.** Far FT-IR ( $600\text{-}100\text{ cm}^{-1}$ , nujol) spectrum of  $\beta$ -pentakis(L-proline methyl ester dithiocarbamate)diruthenium(III) chloride,  $\beta\text{-}[\text{Ru}_2(\text{ProOMeDTC})_5]\text{Cl}$ .

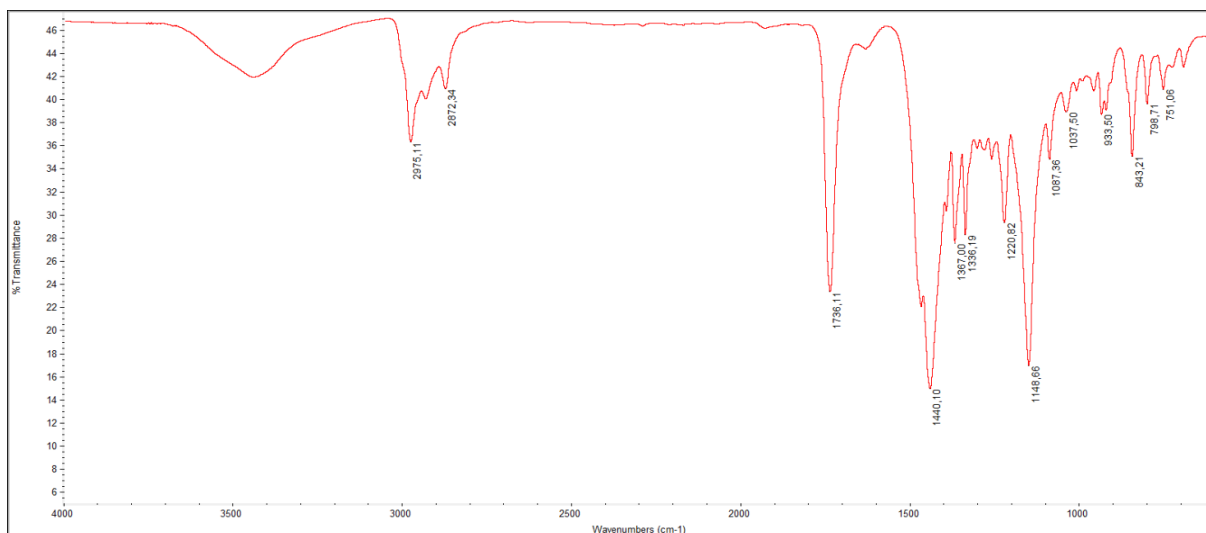


**Figure G21.** Medium FT-IR (4000-600 cm<sup>-1</sup>, KBr) spectrum of tris(L-proline *tert*-butyl ester dithiocarbamate)ruthenium(III), [Ru(ProOtBuDTC)<sub>3</sub>].

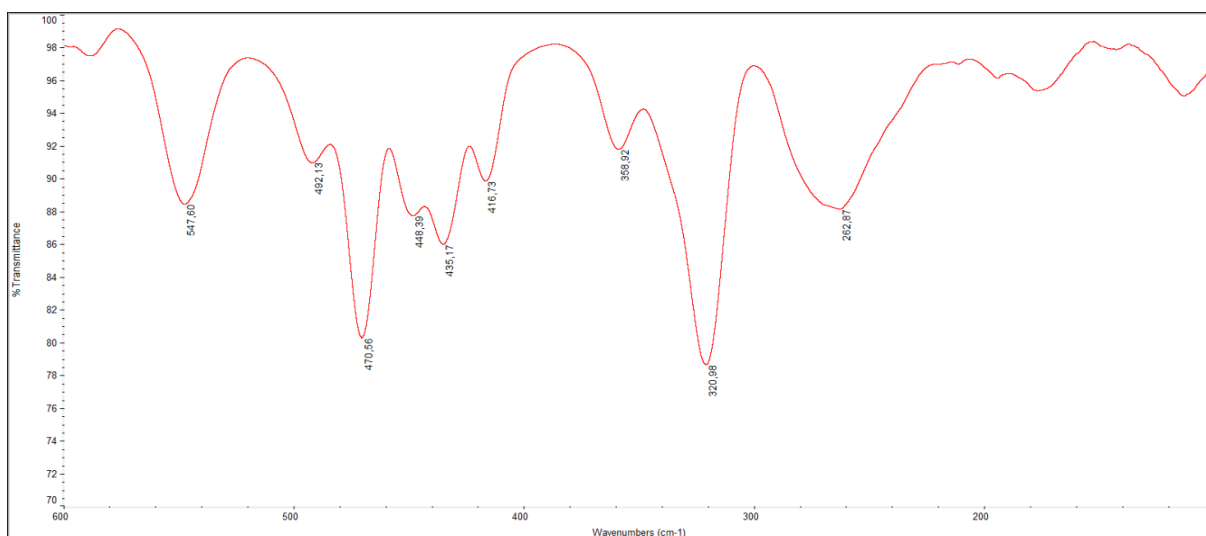


**Figure G22.** Far FT-IR (600-100 cm<sup>-1</sup>, nujol) spectrum of tris(L-proline *tert*-butyl ester dithiocarbamate)ruthenium(III), [Ru(ProOtBuDTC)<sub>3</sub>].

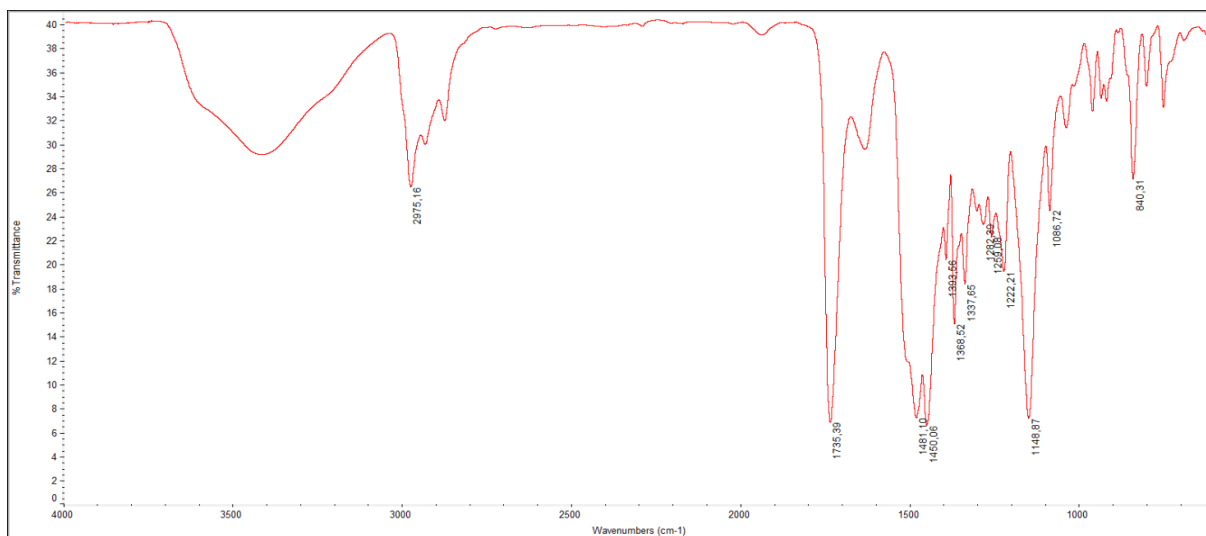


**Figure G23.** Medium FT-IR (4000-600 cm<sup>-1</sup>, KBr) spectrum of  $\beta$ -pentakis(L-proline *tert*-butyl ester dithiocarbamate)diruthenium(III) chloride,  $\beta$ -[Ru<sub>2</sub>(ProOtBuDTC)<sub>5</sub>]Cl.

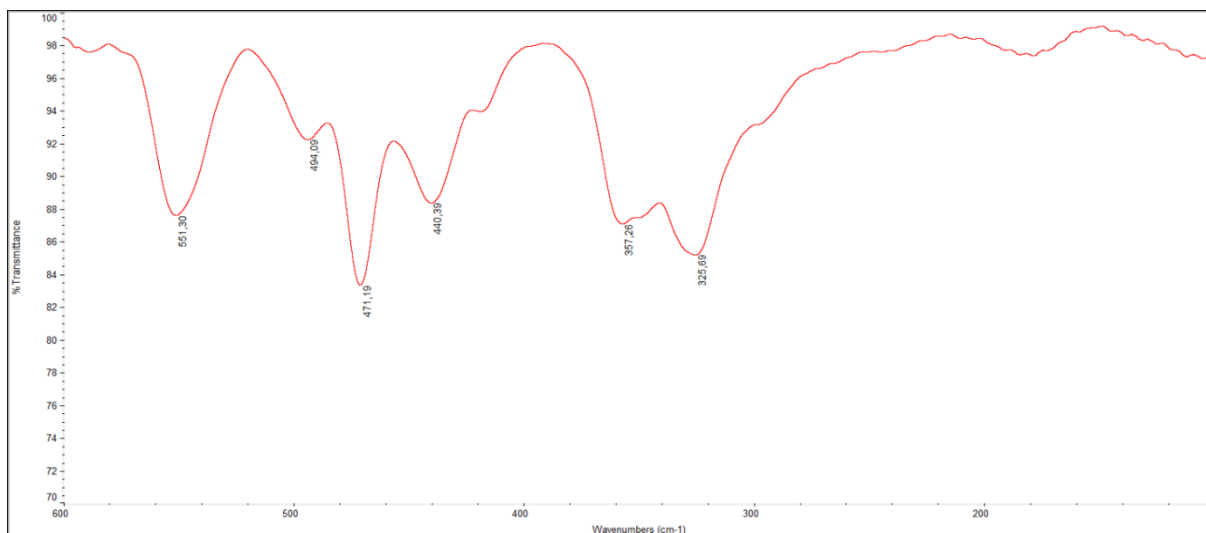


**Figure G24.** Far FT-IR (600-100  $\text{cm}^{-1}$ , nujol) spectrum of  $\beta$ -pentakis(L-proline *tert*-butyl ester dithiocarbamate)diruthenium(III) chloride,  $\beta$ - $[\text{Ru}_2(\text{ProOtBuDTC})_5]\text{Cl}$ .

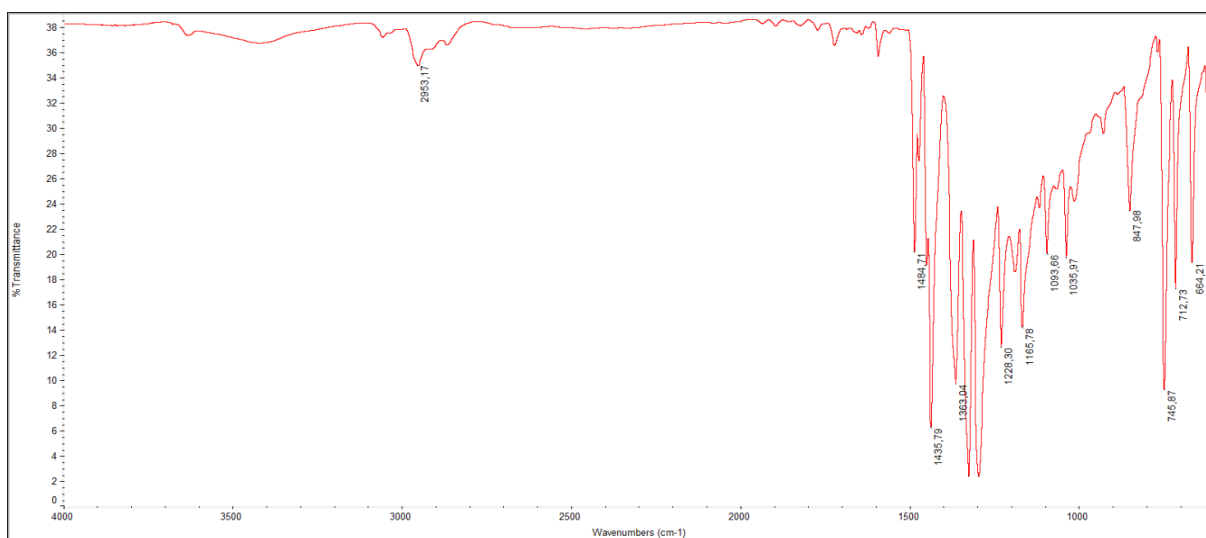


**Figure G25.** Medium FT-IR (4000-600  $\text{cm}^{-1}$ , KBr) spectrum of tris(carbazole dithiocarbamate)ruthenium(III),  $[\text{Ru}(\text{CDT})_3]$ .

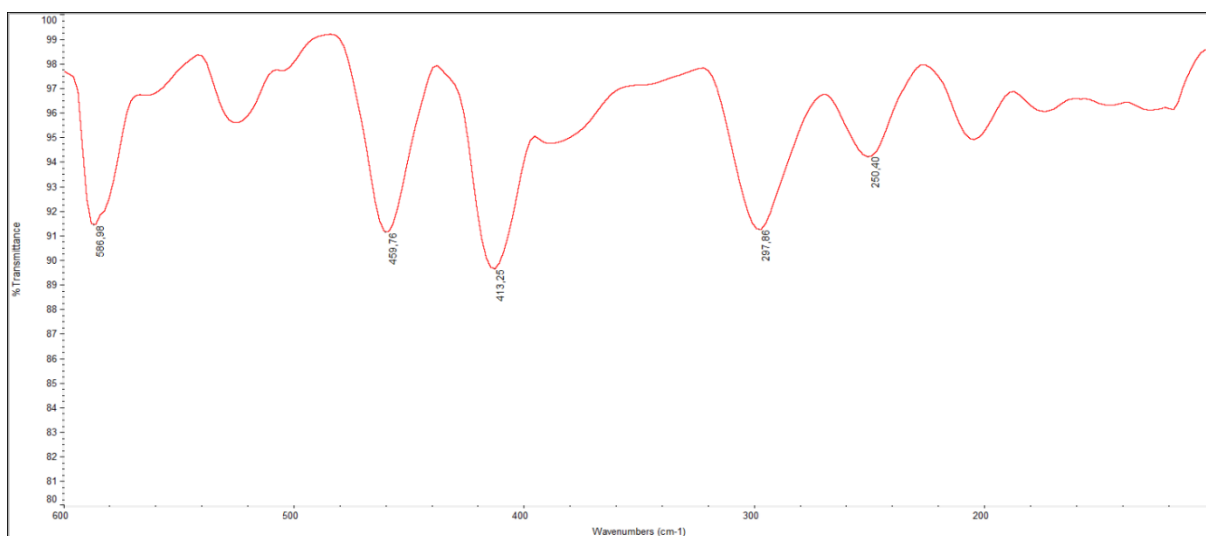


**Figure G26.** Far FT-IR (600-100  $\text{cm}^{-1}$ , nujol) spectrum of tris(carbazole dithiocarbamate)ruthenium(III),  $[\text{Ru}(\text{CDT})_3]$ .

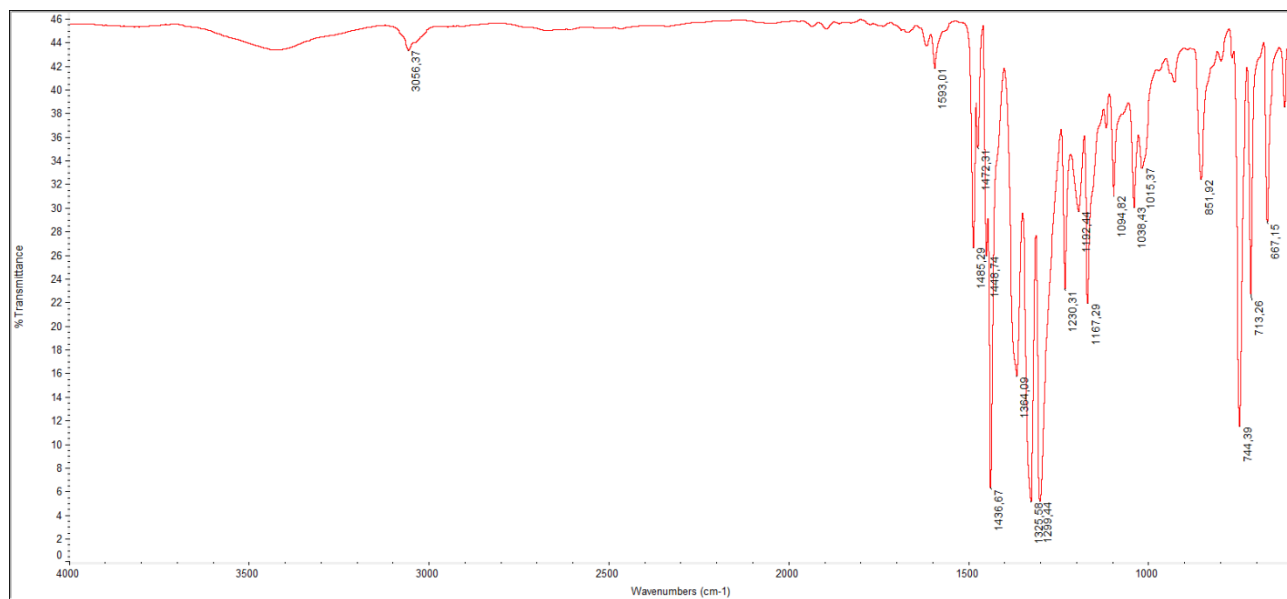


**Figure G27.** Medium FT-IR (4000-600 cm<sup>-1</sup>, KBr) spectrum of  $\beta$ -pentakis(carbazole dithiocarbamate)diruthenium(III) chloride,  $\beta$ -[Ru<sub>2</sub>(CDT)<sub>5</sub>]Cl.

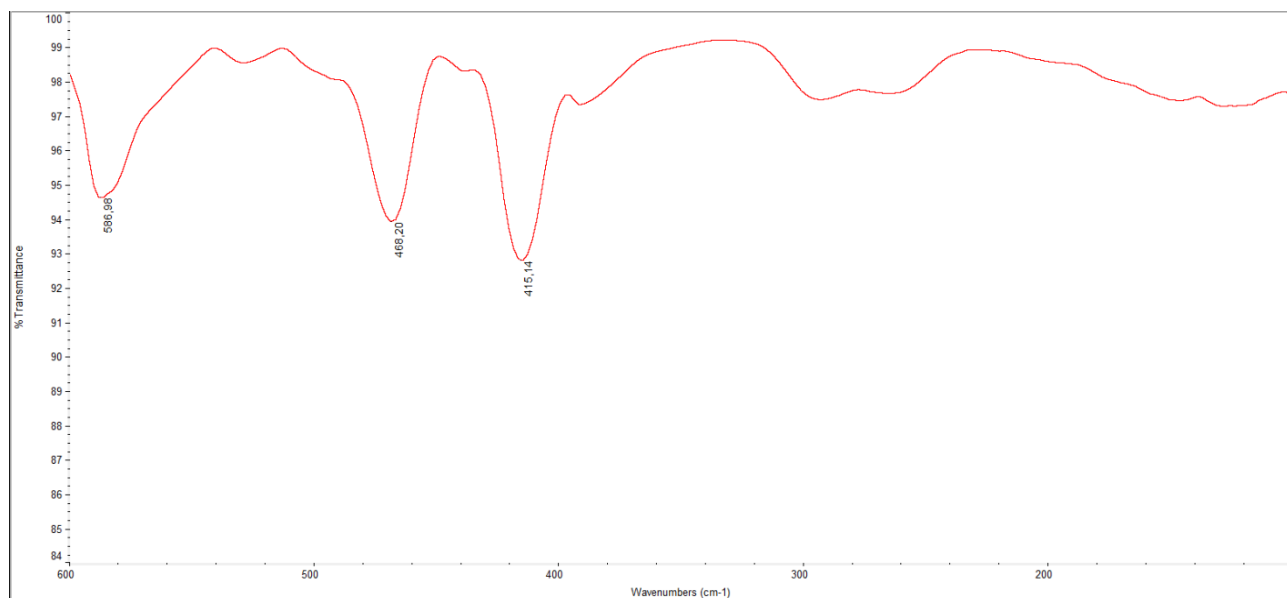


**Figure G28.** Far FT-IR (600-100 cm<sup>-1</sup>, nujol) spectrum of  $\beta$ -pentakis(carbazole dithiocarbamate)diruthenium(III) chloride,  $\beta$ -[Ru<sub>2</sub>(CDT)<sub>5</sub>]Cl.

## SUPPORTING INFORMATION H - FT-IR spectra of the synthesized Cu(II) dithiocarbamate complexes

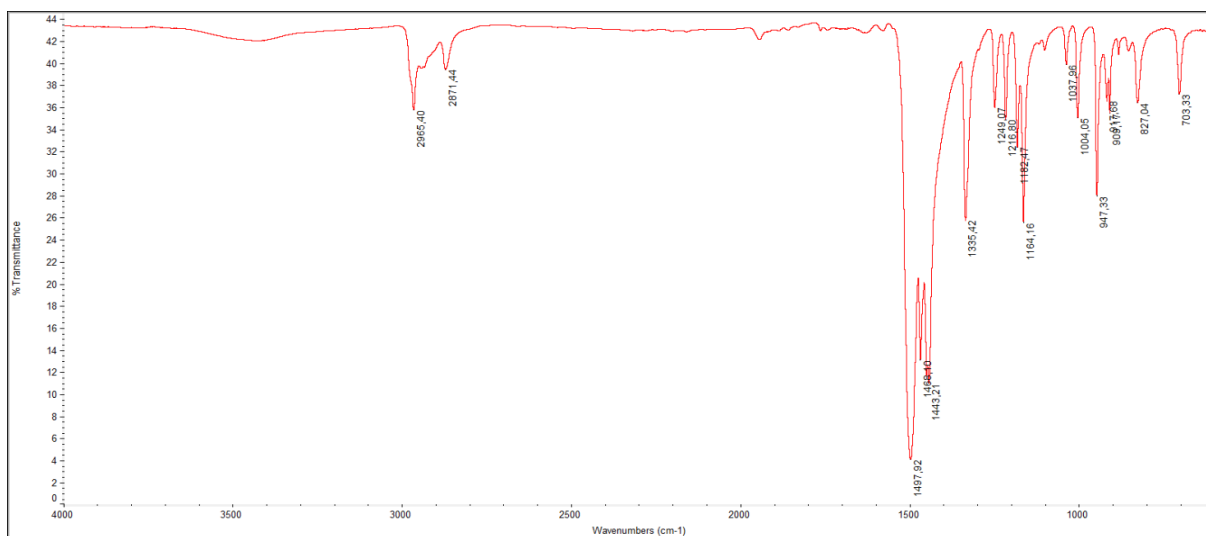


Figure H1. Medium FT-IR (4000-600 cm<sup>-1</sup>, KBr) spectrum of bis(pyrrolidine dithiocarbamate)copper(II), [Cu(PDT)<sub>2</sub>].

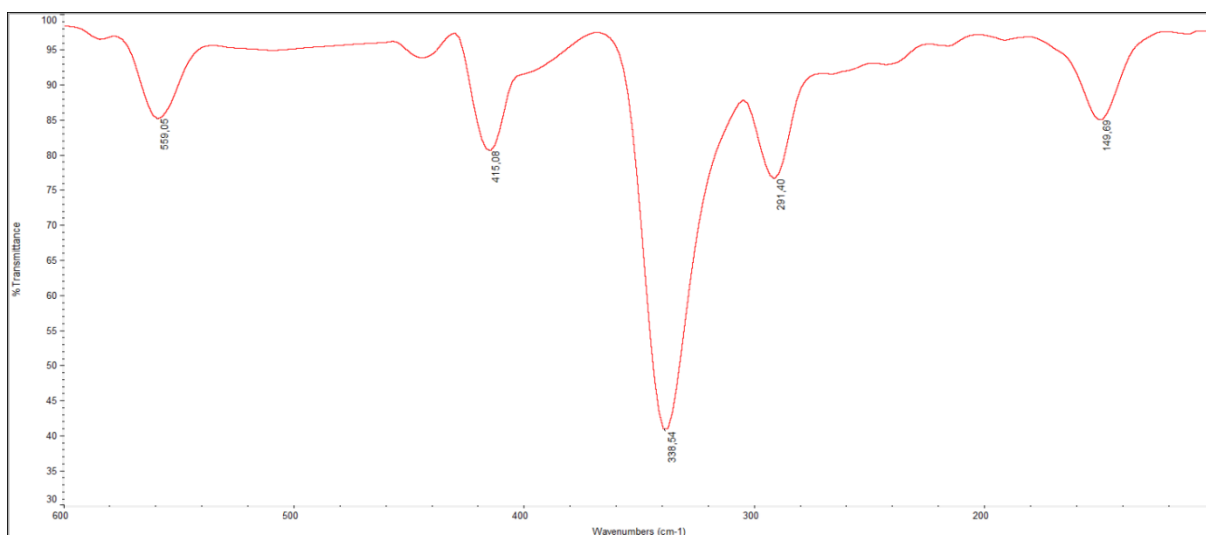


Figure H2. Far FT-IR (600-100 cm<sup>-1</sup>, nujol) spectrum of bis(pyrrolidine dithiocarbamate)copper(II), [Cu(PDT)<sub>2</sub>].

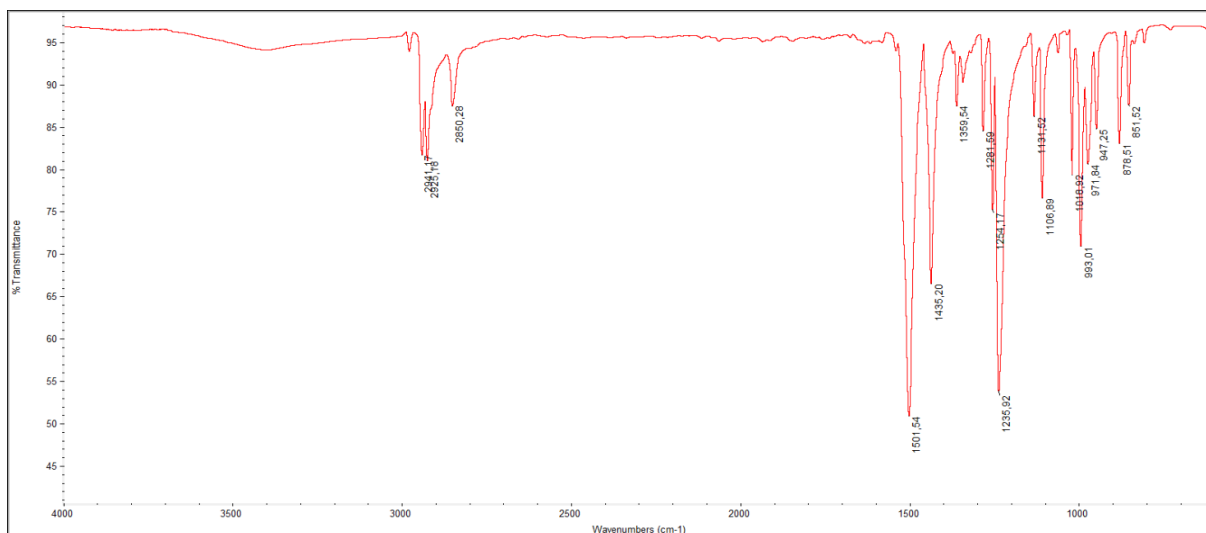


Figure H3. Medium FT-IR (4000-600 cm<sup>-1</sup>, KBr) spectrum of bis(piperidine dithiocarbamate)copper(II), [Cu(PipeDTC)<sub>2</sub>].

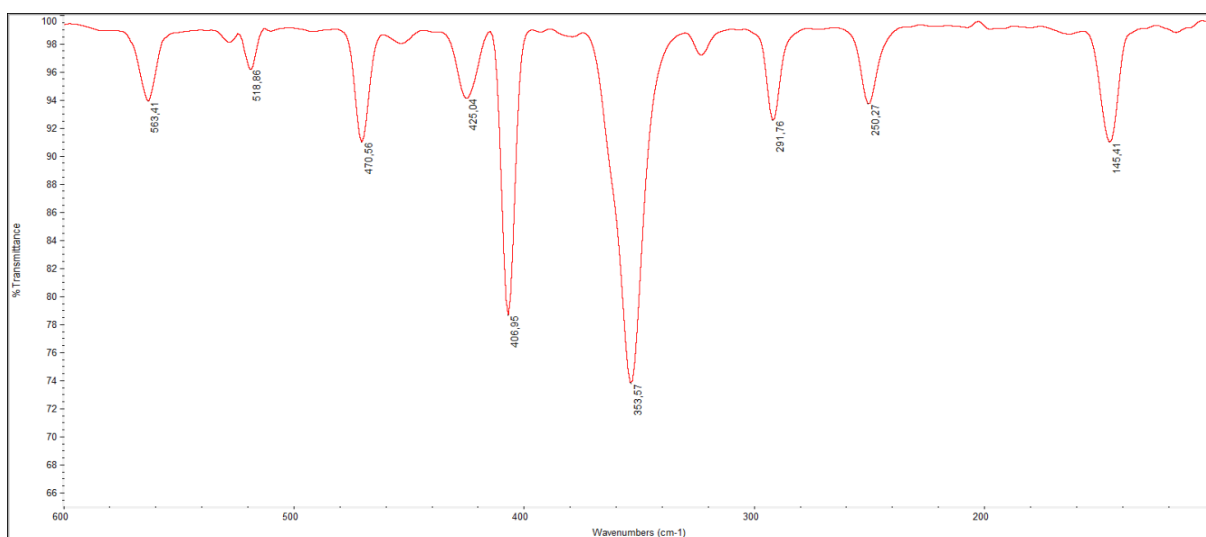


Figure H4. Far FT-IR (600-100 cm<sup>-1</sup>, nujol) spectrum of bis(piperidine dithiocarbamate)copper(II), [Cu(PipeDTC)<sub>2</sub>].

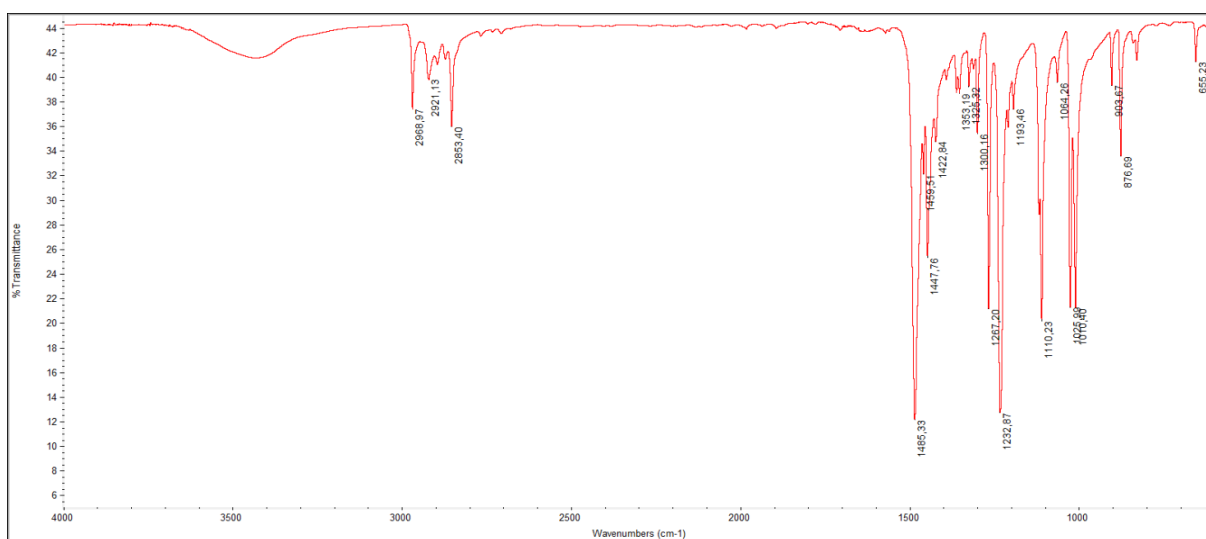


Figure H5. Medium FT-IR (4000-600 cm<sup>-1</sup>, KBr) spectrum of bis(morpholine dithiocarbamate)copper(II), [Cu(MorphDTC)<sub>2</sub>].



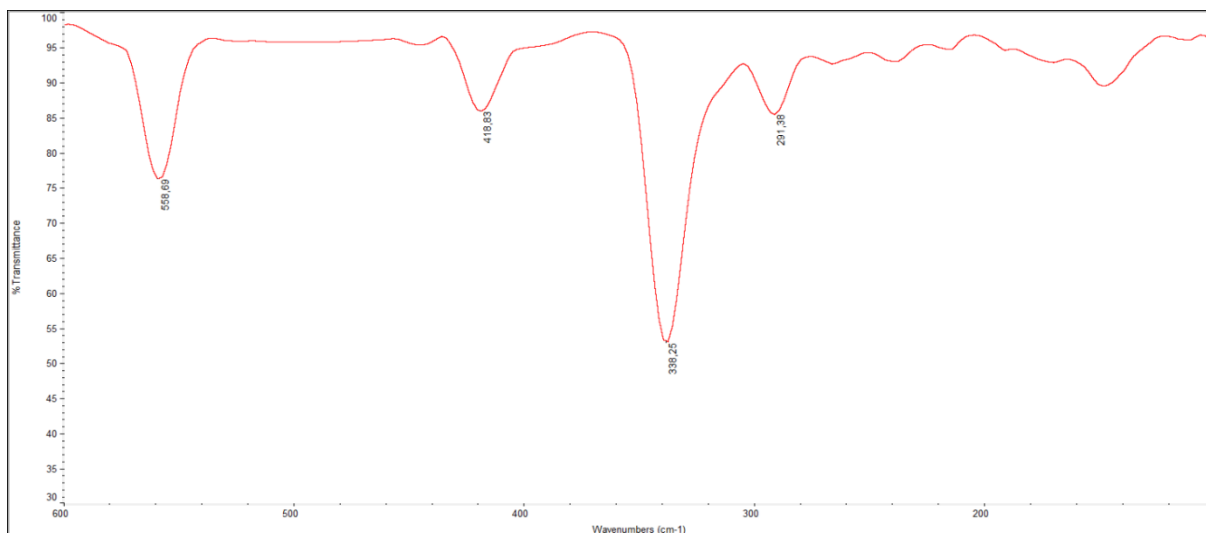


Figure H6. Far FT-IR (600-100 cm<sup>-1</sup>, nujol) spectrum of bis(morpholine dithiocarbamate)copper(II), [Cu(MorphDTC)<sub>2</sub>].

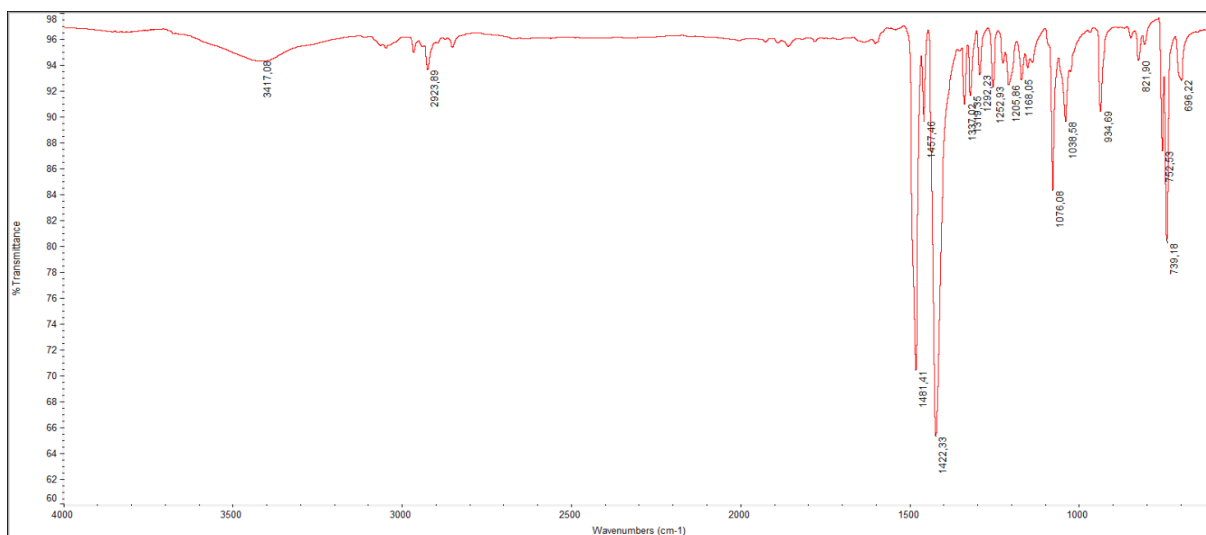


Figure H7. Medium FT-IR (4000-600 cm<sup>-1</sup>, KBr) spectrum of bis(indoline dithiocarbamate)copper(II), [Cu(IndolineDTC)<sub>2</sub>].

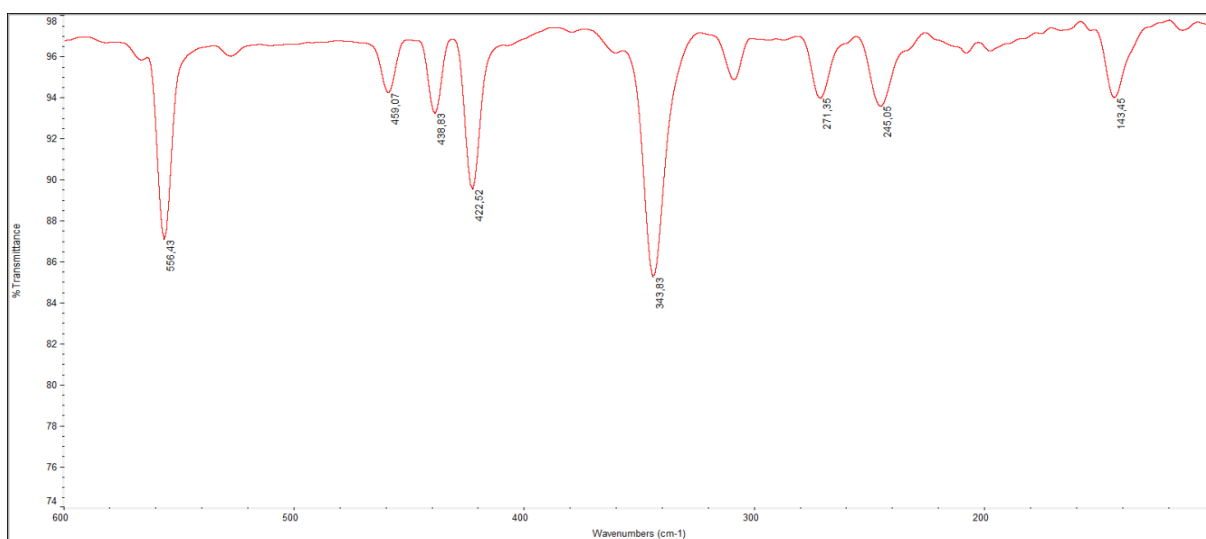
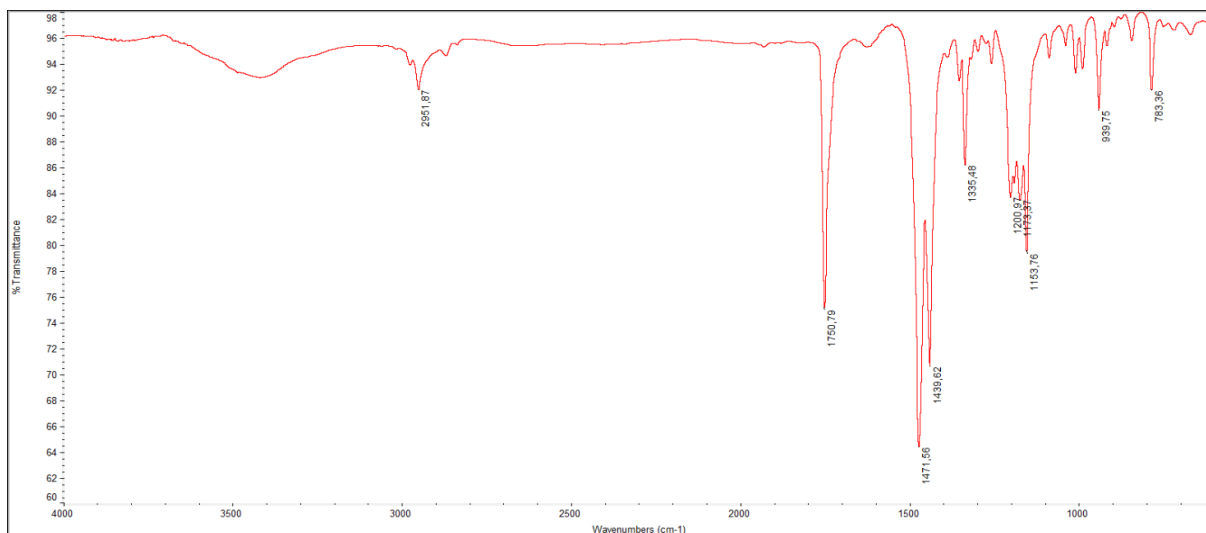
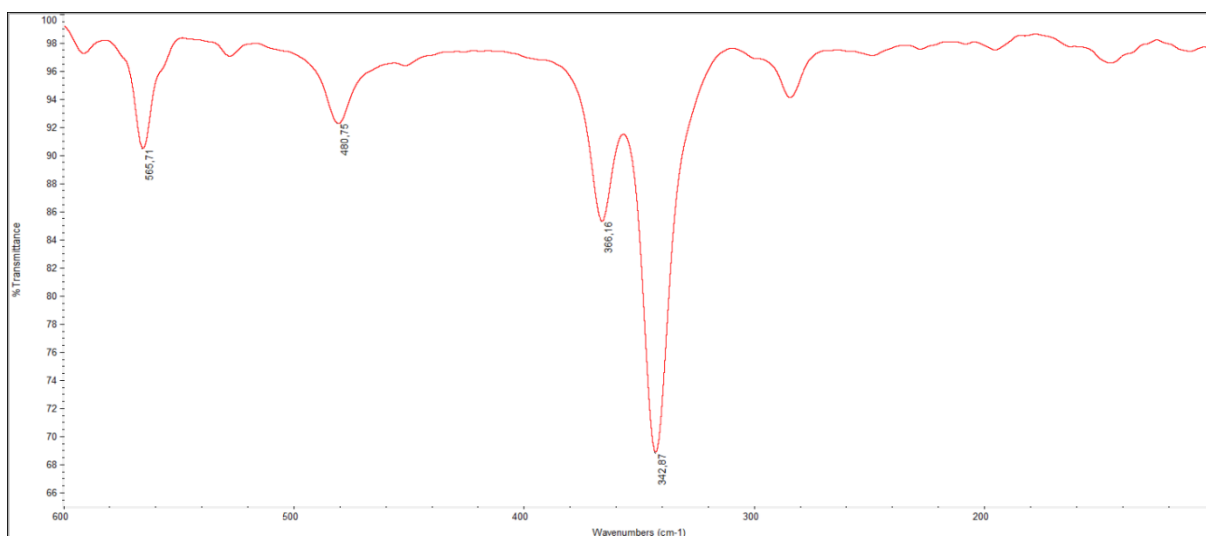


Figure H8. Far FT-IR (600-100 cm<sup>-1</sup>, nujol) spectrum of bis(indoline dithiocarbamate)copper(II), [Cu(IndolineDTC)<sub>2</sub>].



**Figure H9.** Medium FT-IR (4000-600 cm<sup>-1</sup>, KBr) spectrum of bis(L-proline methyl ester dithiocarbamate)copper(II), [Cu(ProOMeDTC)<sub>2</sub>].



**Figure H10.** Far FT-IR (600-100 cm<sup>-1</sup>, nujol) spectrum of bis(L-proline methyl ester dithiocarbamate)copper(II), [Cu(ProOMeDTC)<sub>2</sub>].

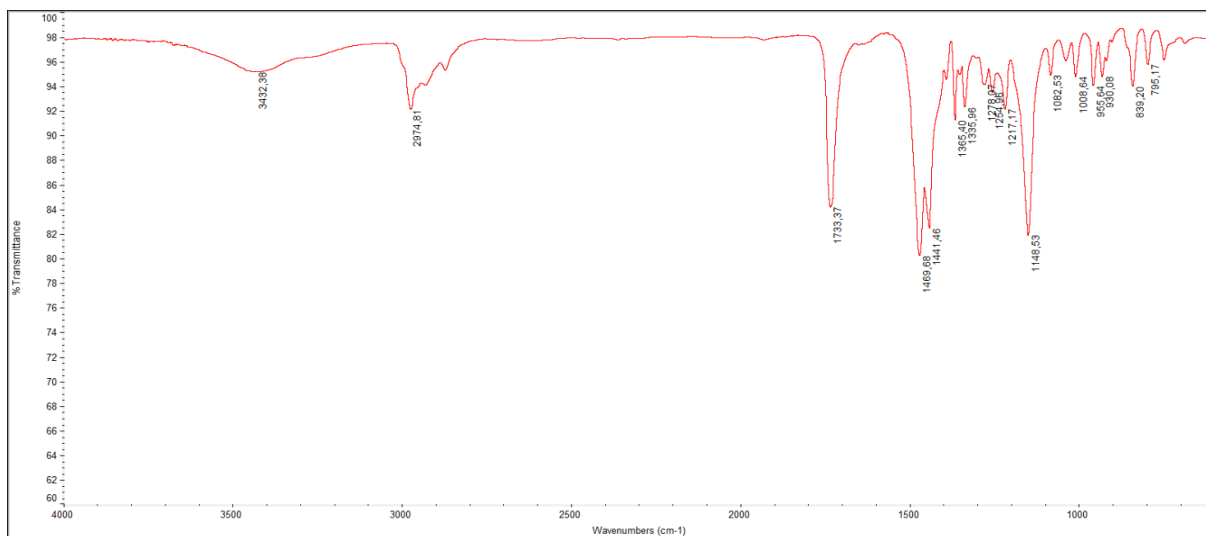


**Figure H11.** Medium FT-IR (4000-600 cm<sup>-1</sup>, KBr) spectrum of bis(L-proline *tert*-butyl ester dithiocarbamate)copper(II), [Cu(ProOtBuDTC)<sub>2</sub>].

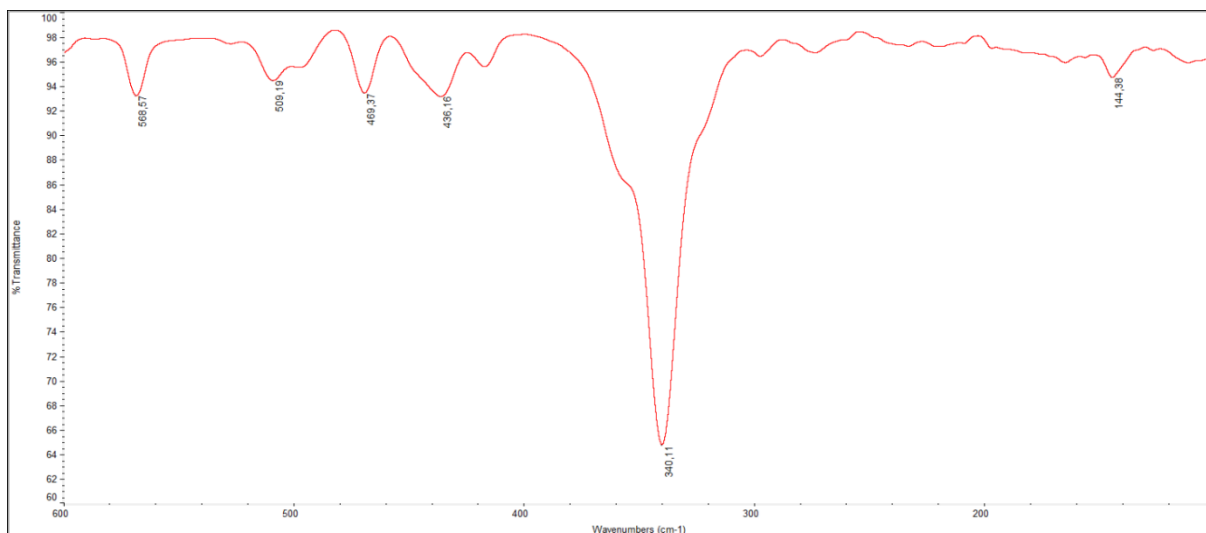


**Figure H12.** Far FT-IR (600-100 cm<sup>-1</sup>, nujol) spectrum of bis(L-proline *tert*-butyl ester dithiocarbamate)copper(II), [Cu(ProOtBuDTC)<sub>2</sub>].

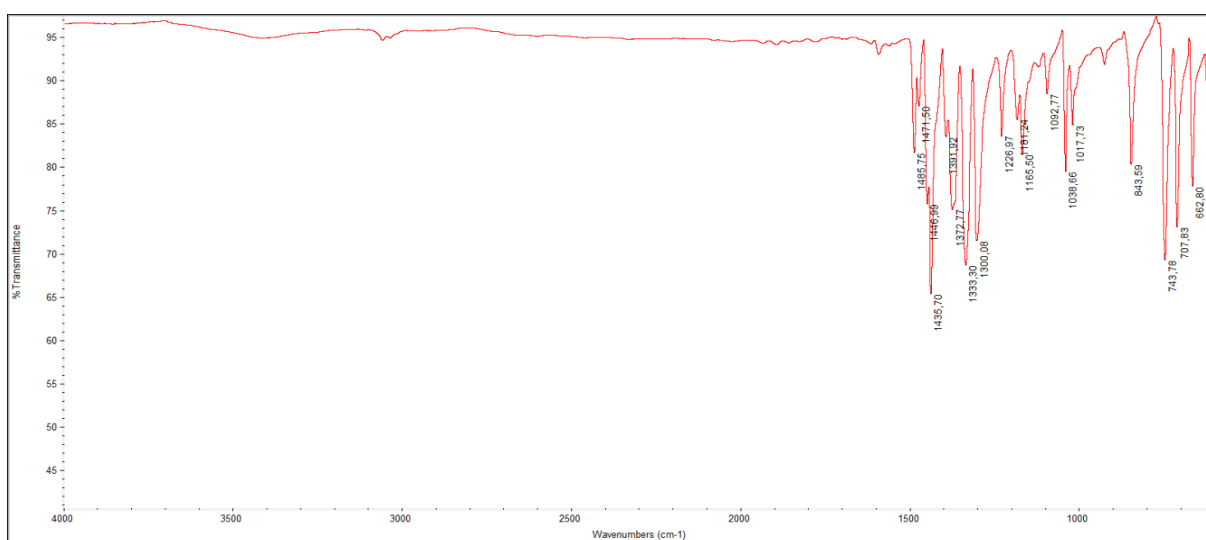


**Figure H13.** Medium FT-IR (4000-600 cm<sup>-1</sup>, KBr) spectrum of bis(carbazole dithiocarbamate)copper(II), [Cu(CDT)<sub>2</sub>].

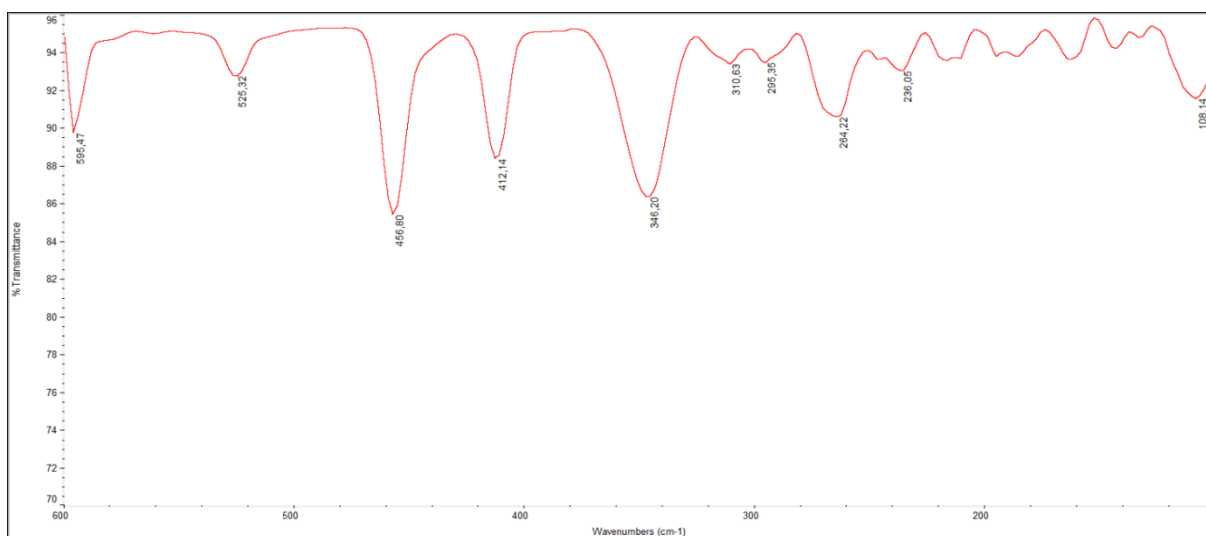


**Figure H14.** Far FT-IR (600-100 cm<sup>-1</sup>, nujol) spectrum of bis(carbazole dithiocarbamate)copper(II), [Cu(CDT)<sub>2</sub>].

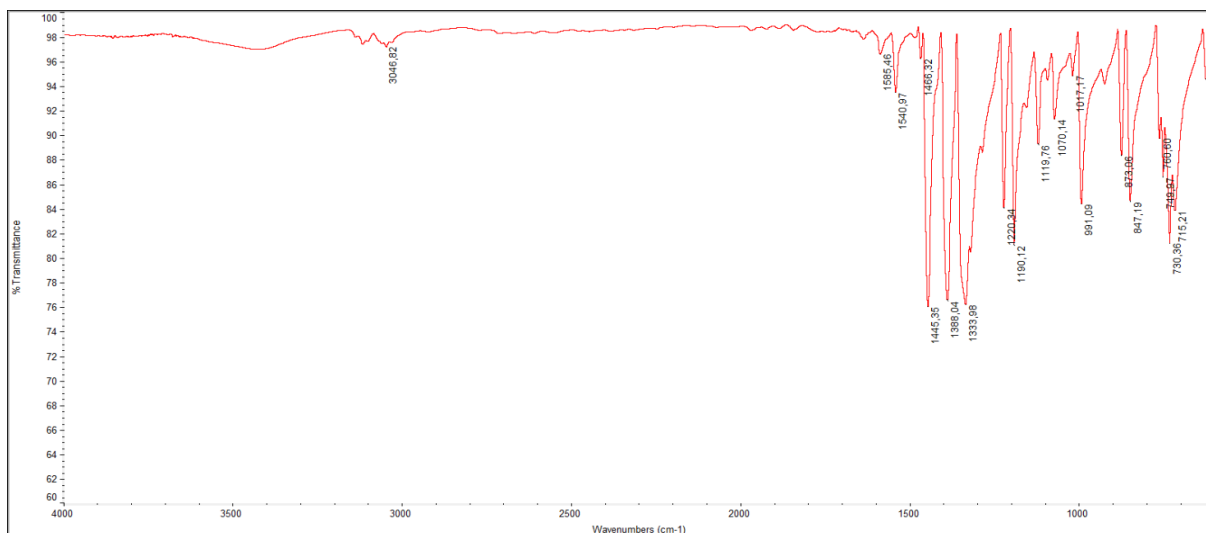


Figure H15. Medium FT-IR (4000-600 cm<sup>-1</sup>, KBr) spectrum of bis(indole dithiocarbamate)copper(II), [Cu(IndDTC)<sub>2</sub>].

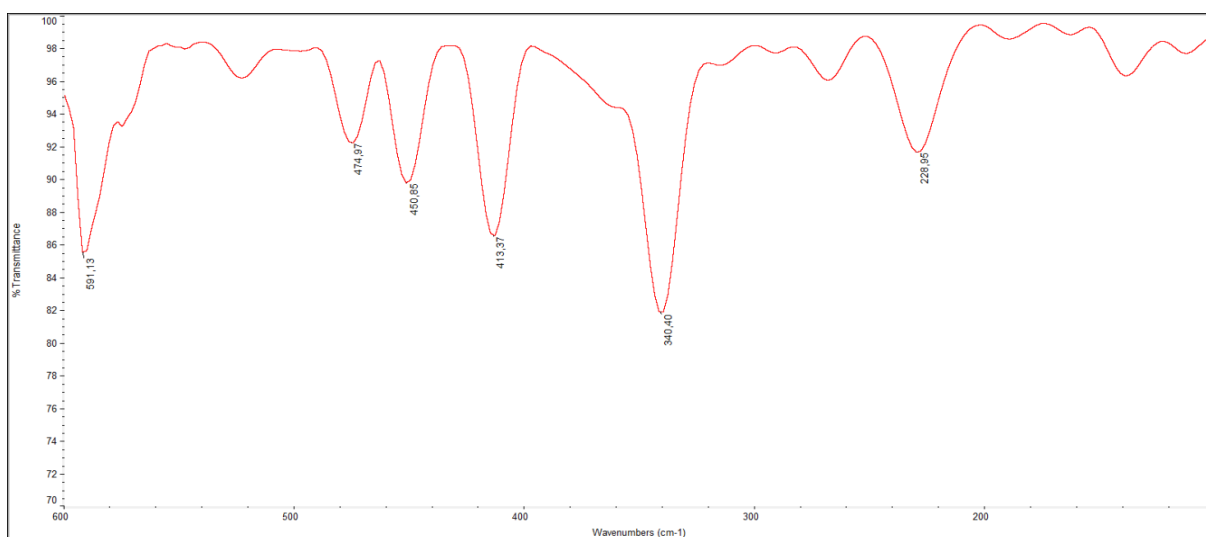


Figure H16. Far FT-IR (600-100 cm<sup>-1</sup>, nujol) spectrum of bis(indole dithiocarbamate)copper(II), [Cu(IndDTC)<sub>2</sub>].

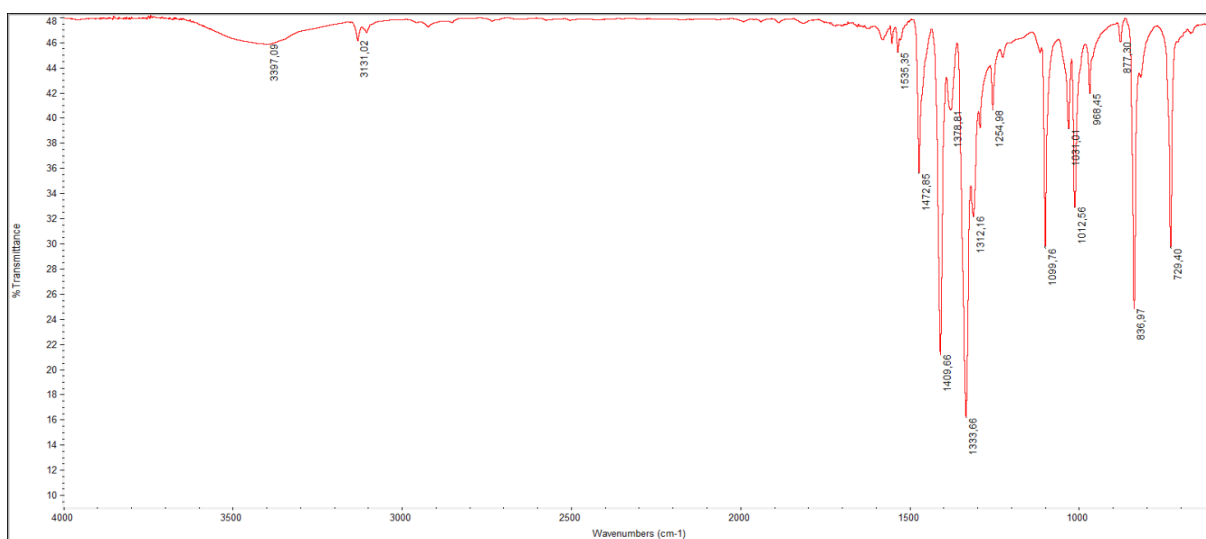
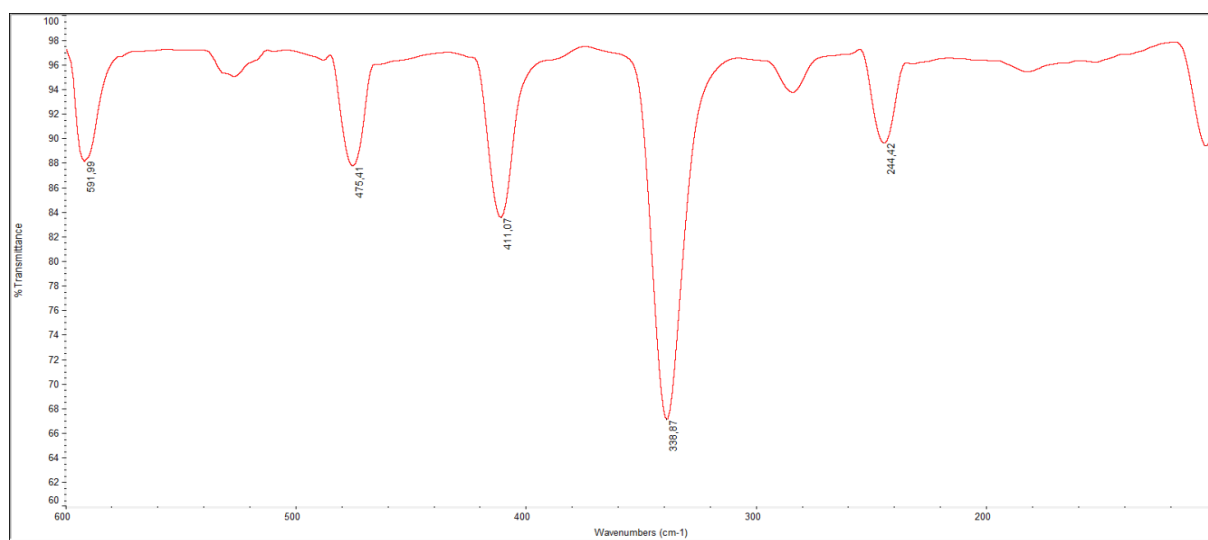


Figure H17. Medium FT-IR (4000-600 cm<sup>-1</sup>, KBr) spectrum of bis(pyrrrole dithiocarbamate)copper(II), [Cu(PyrrDTC)<sub>2</sub>].



**Figure H18.** Far FT-IR (600-100 cm<sup>-1</sup>, nujol) spectrum of bis(pyrrole dithiocarbamate)copper(II), [Cu(PyrroleDTC)<sub>2</sub>].



## SUPPORTING INFORMATION I - FT-IR spectra of the synthesized Au(I)/(III) dithiocarbamate complexes

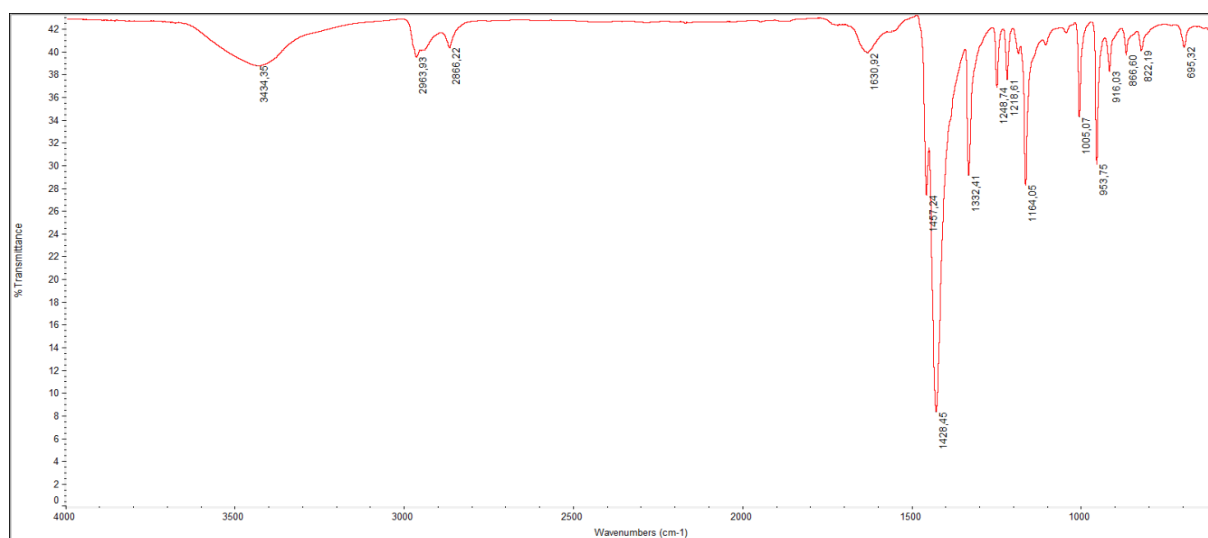


**Figure I1.** Medium FT-IR ( $4000\text{-}600\text{ cm}^{-1}$ , KBr) spectrum of bis(pyrrolidine dithiocarbamate)digold(I),  $[\text{Au}_2(\text{PDT})_2]$ .

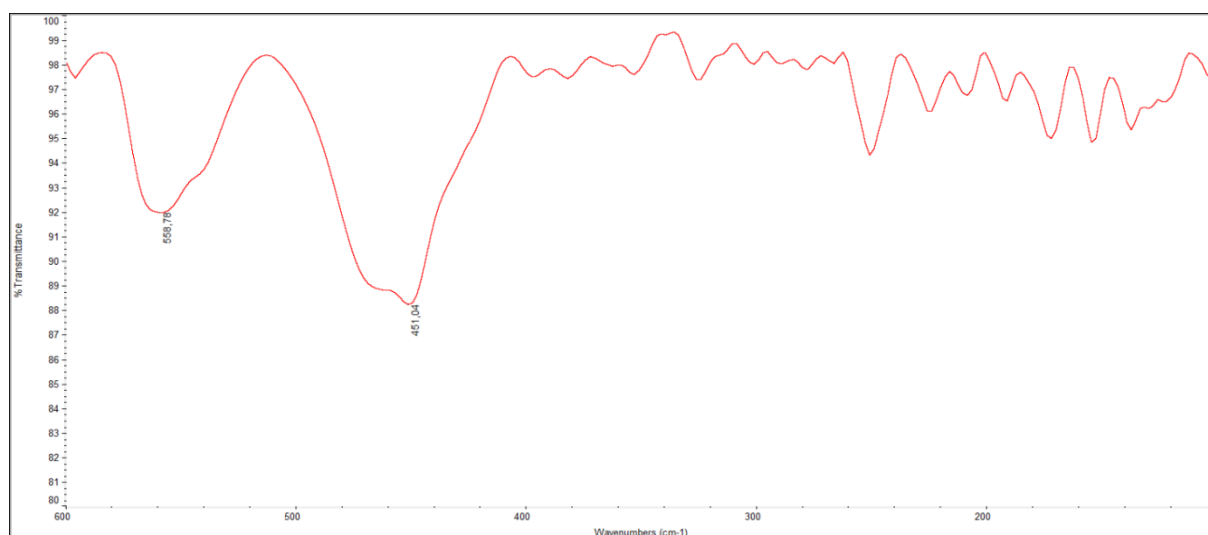


**Figure I2.** Far FT-IR ( $600\text{-}100\text{ cm}^{-1}$ , nujol) spectrum of bis(pyrrolidine dithiocarbamate)digold(I),  $[\text{Au}_2(\text{PDT})_2]$ .

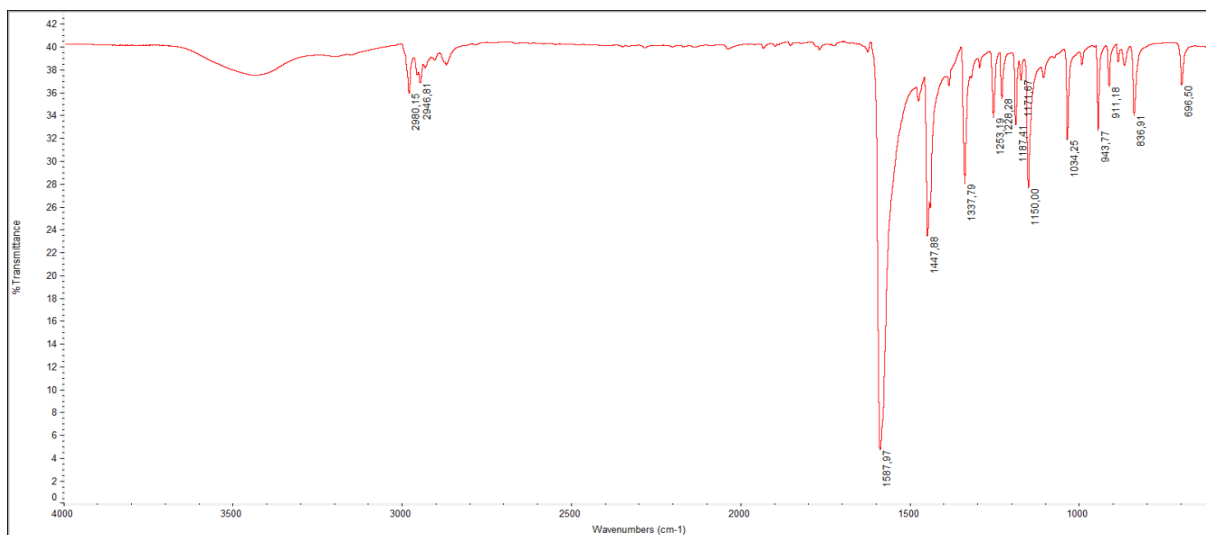


Figure I3 Medium FT-IR (4000-600 cm<sup>-1</sup>, KBr) spectrum of dichloro(pyrrolidine dithiocarbamate)gold(III), [AuCl<sub>2</sub>(PDT)].

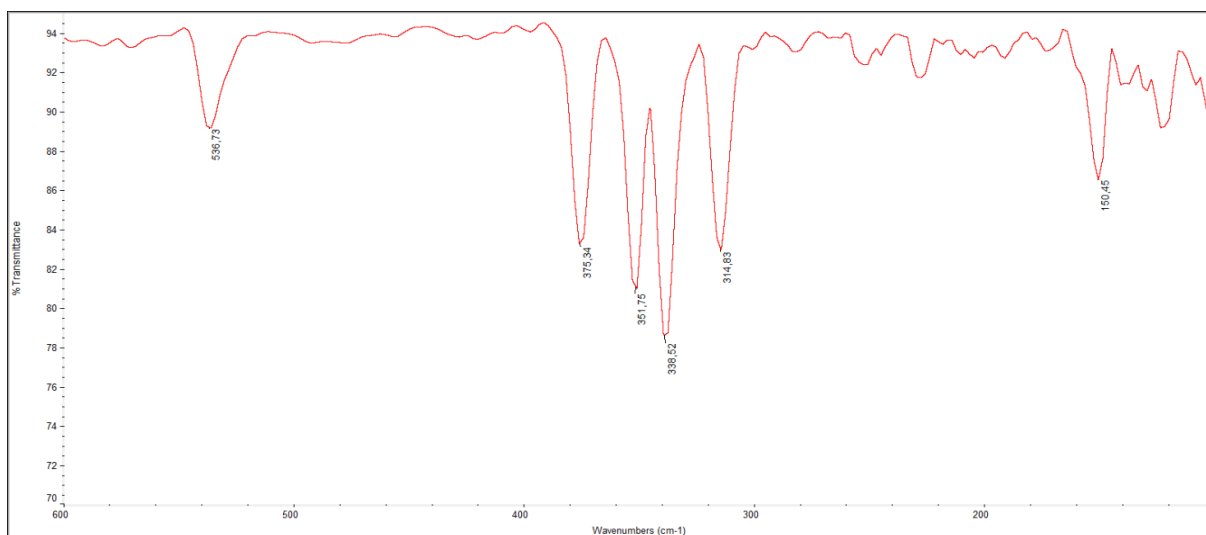


Figure I4. Far FT-IR (600-100 cm<sup>-1</sup>, nujol) spectrum of dichloro(pyrrolidine dithiocarbamate)gold(III), [AuCl<sub>2</sub>(PDT)].

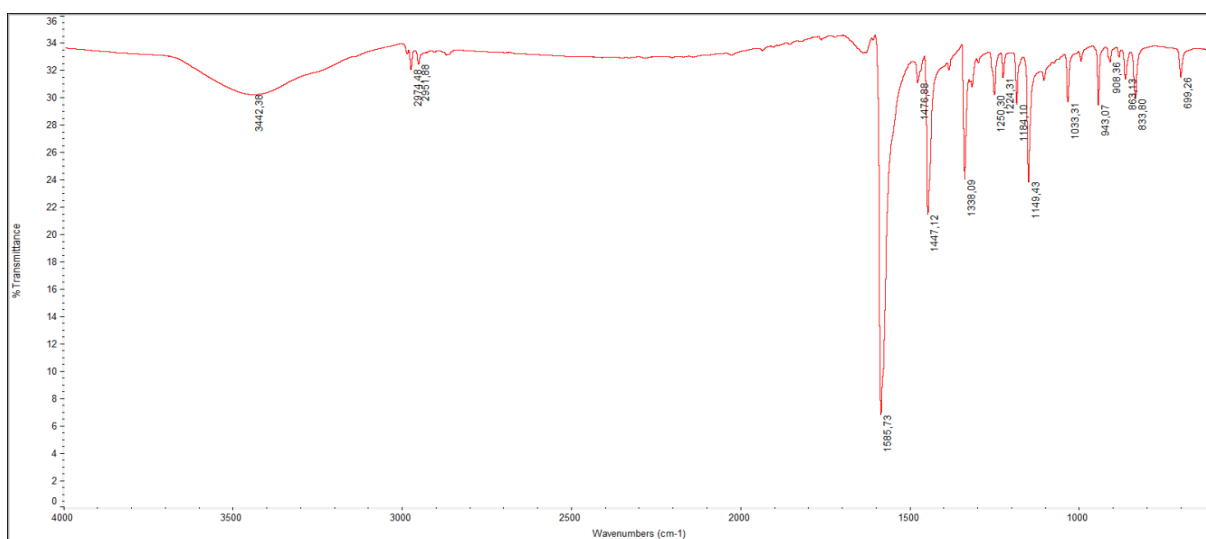


Figure I5. Medium FT-IR (4000-600 cm<sup>-1</sup>, KBr) spectrum of dibromo(pyrrolidine dithiocarbamate)gold(III), [AuBr<sub>2</sub>(PDT)].



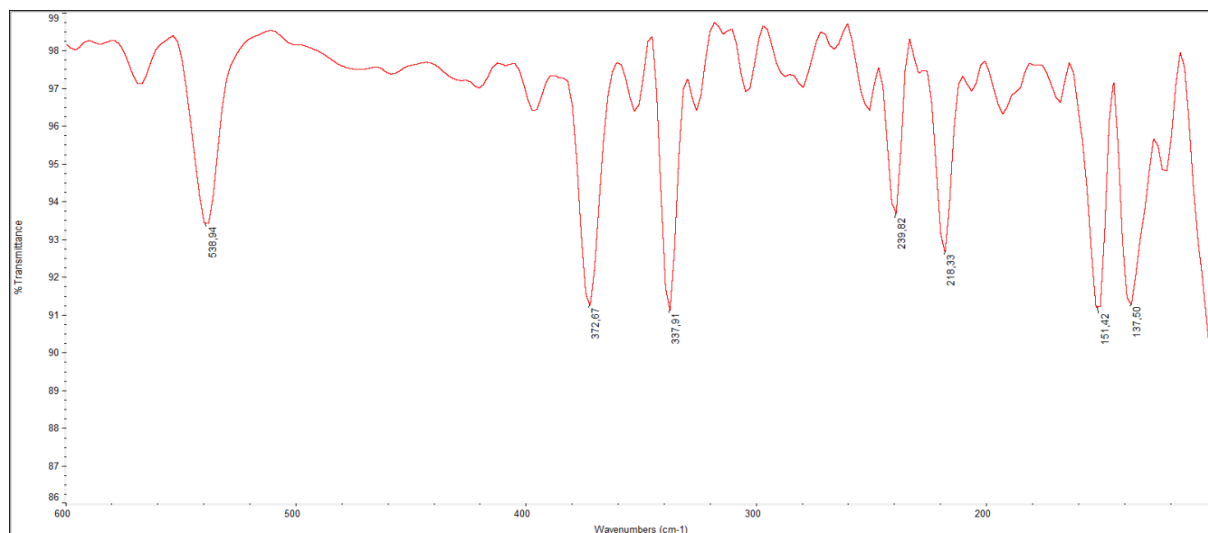


Figure I6. Far FT-IR (600-100  $\text{cm}^{-1}$ , nujol) spectrum of dibromo(pyrrolidine dithiocarbamate)gold(III),  $[\text{AuBr}_2(\text{PDT})]$ .

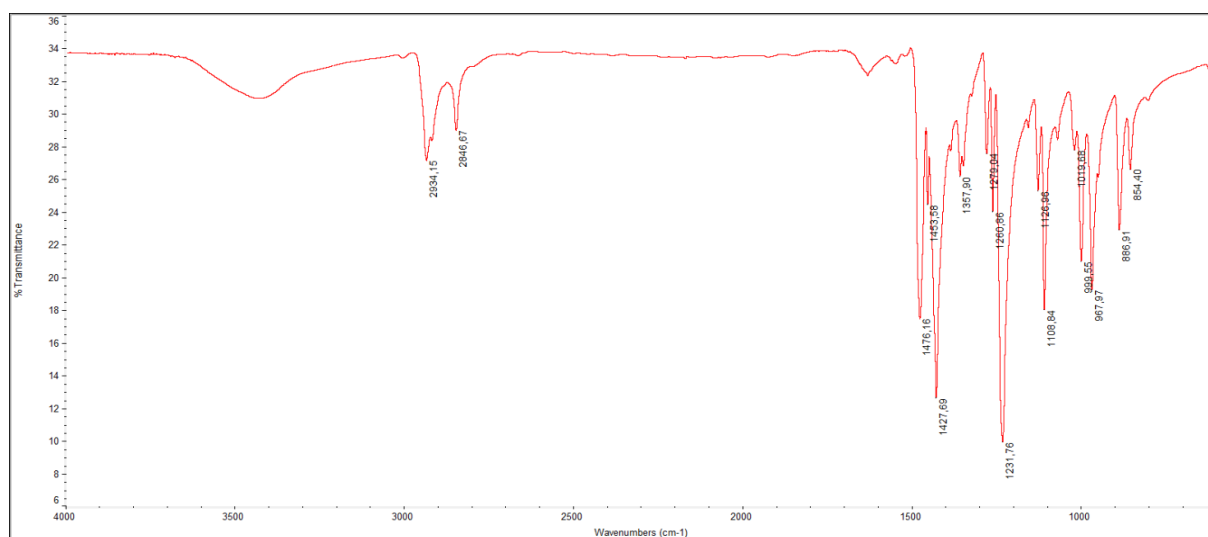


Figure I7. Medium FT-IR (4000-600  $\text{cm}^{-1}$ , KBr) spectrum of bis(piperidine dithiocarbamate)digold(I),  $[\text{Au}_2(\text{PipeDTC})_2]$ .

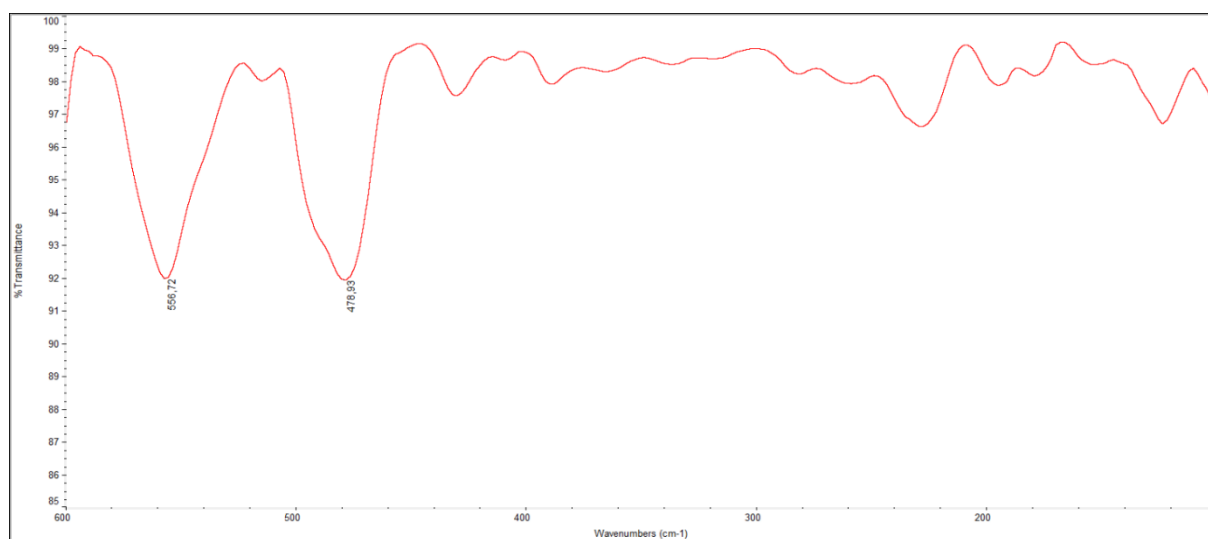
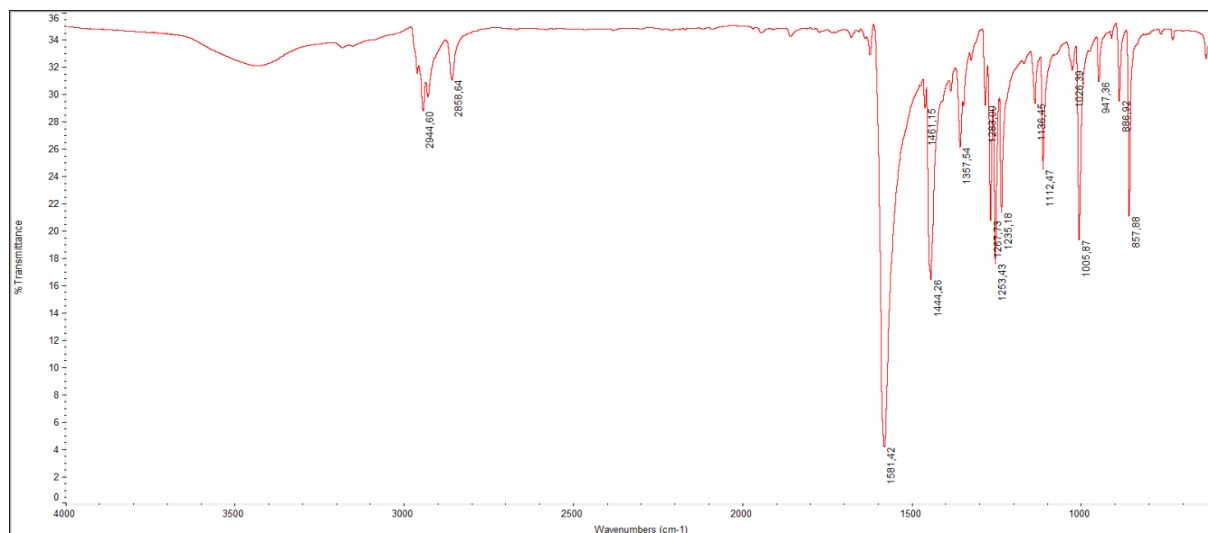
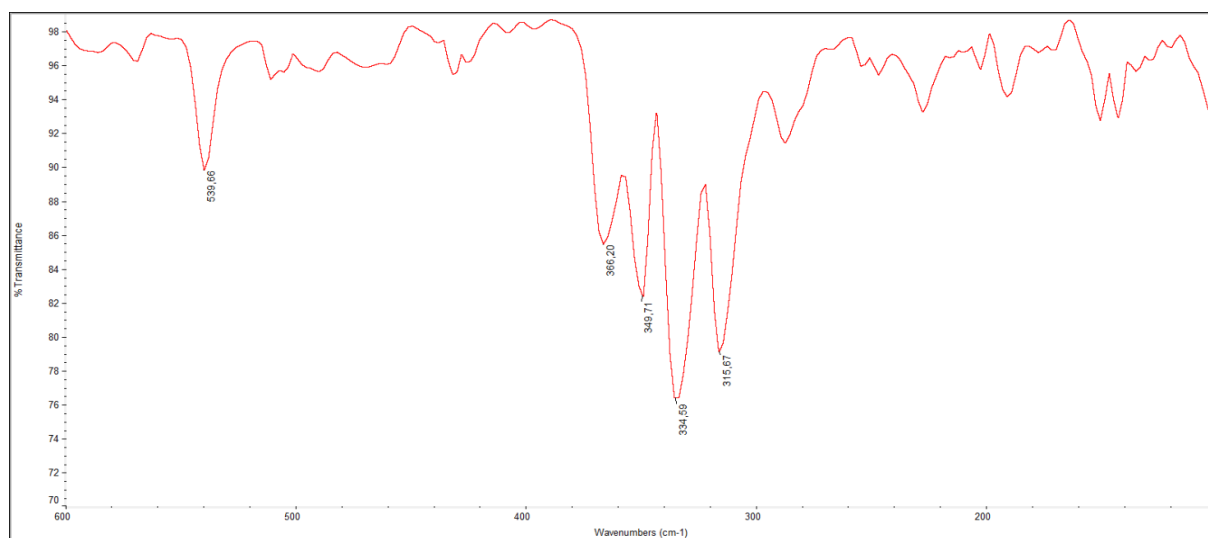


Figure I8. Far FT-IR (600-100  $\text{cm}^{-1}$ , nujol) spectrum of bis(piperidine dithiocarbamate)digold(I),  $[\text{Au}_2(\text{PipeDTC})_2]$ .



**Figure 19.** Medium FT-IR (4000-600 cm<sup>-1</sup>, KBr) spectrum of dichloro(piperidine dithiocarbamate)gold(III), [AuCl<sub>2</sub>(PipeDTC)].



**Figure 10.** Far FT-IR (600-100 cm<sup>-1</sup>, nujol) spectrum of dichloro(piperidine dithiocarbamate)gold(III), [AuCl<sub>2</sub>(PipeDTC)].

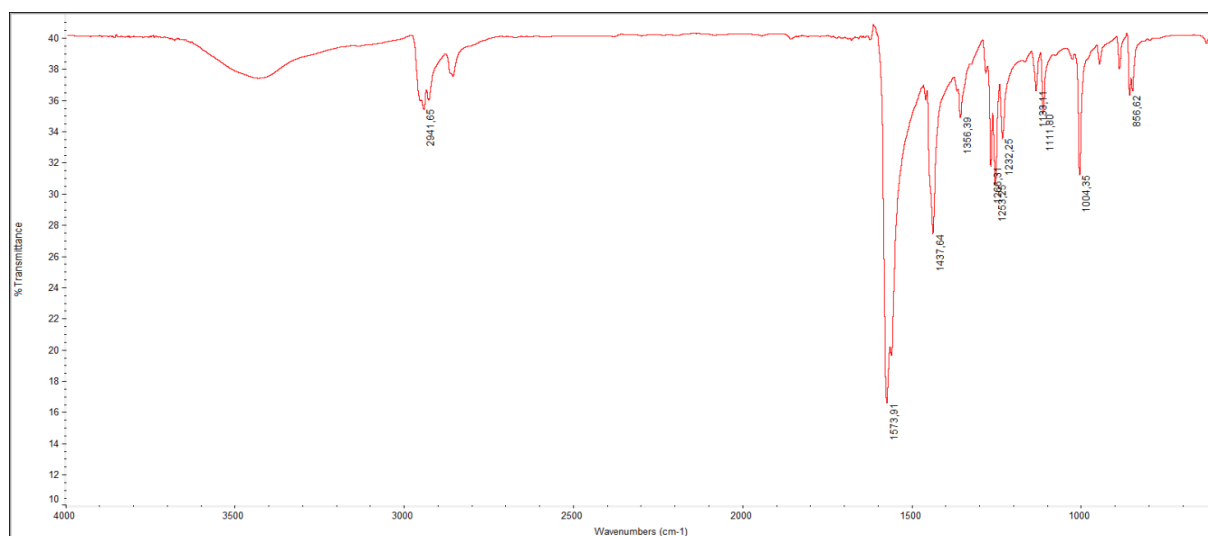


**Figure 11.** Medium FT-IR (4000-600 cm<sup>-1</sup>, KBr) spectrum of dibromo(piperidine dithiocarbamate)gold(III), [AuBr<sub>2</sub>(PipeDTC)].

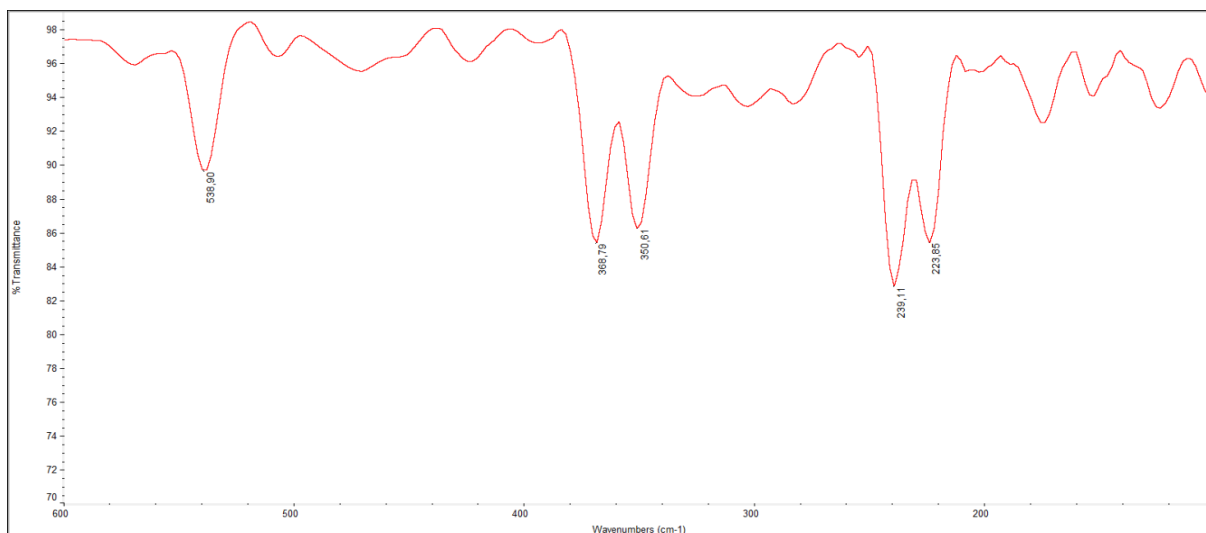


**Figure I12.** Far FT-IR (600-100 cm<sup>-1</sup>, nujol) spectrum of dibromo(piperidine dithiocarbamate)gold(III), [AuBr<sub>2</sub>(PipeDTC)].

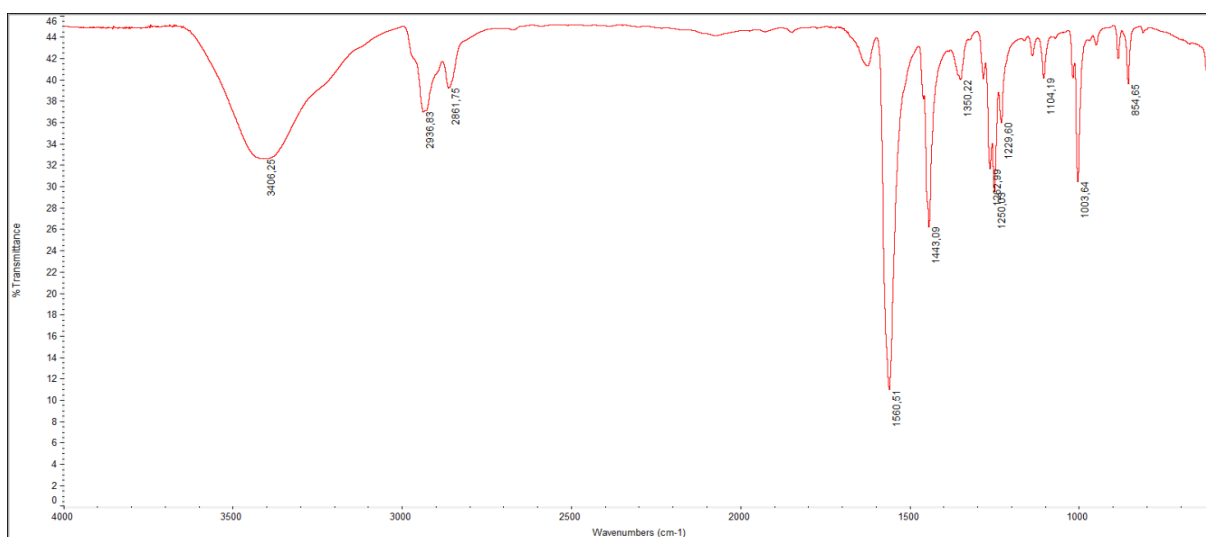


**Figure I13.** Medium FT-IR (4000-600 cm<sup>-1</sup>, KBr) spectrum of bis(piperidine dithiocarbamate)gold(III) chloride, [Au(PipeDTC)<sub>2</sub>]Cl.

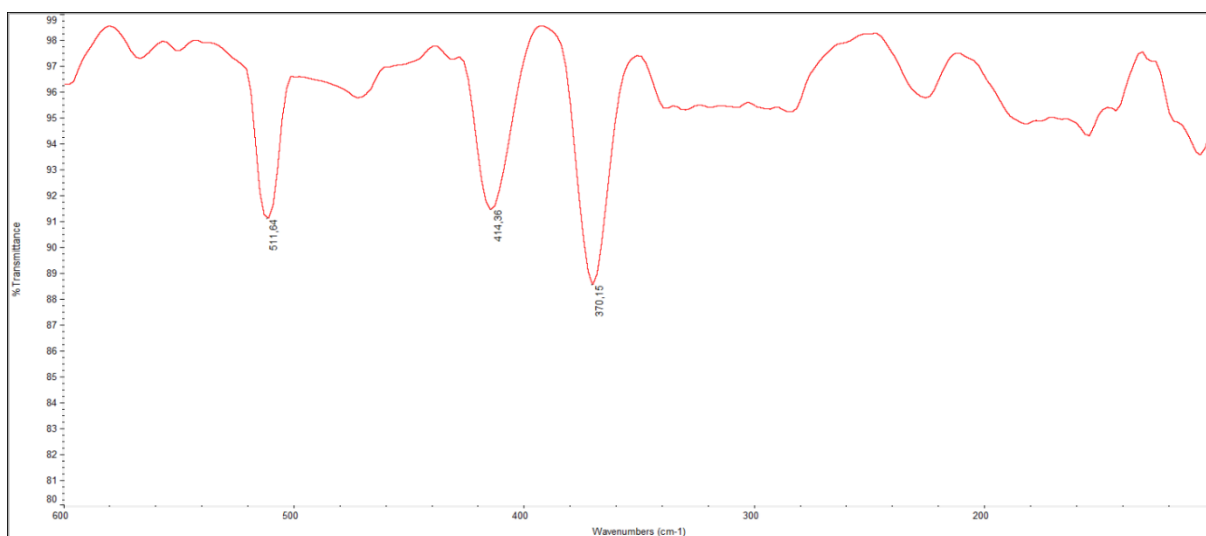


**Figure I14.** Far FT-IR (600-100 cm<sup>-1</sup>, nujol) spectrum of bis(piperidine dithiocarbamate)gold(III) chloride, [Au(PipeDTC)<sub>2</sub>]Cl.

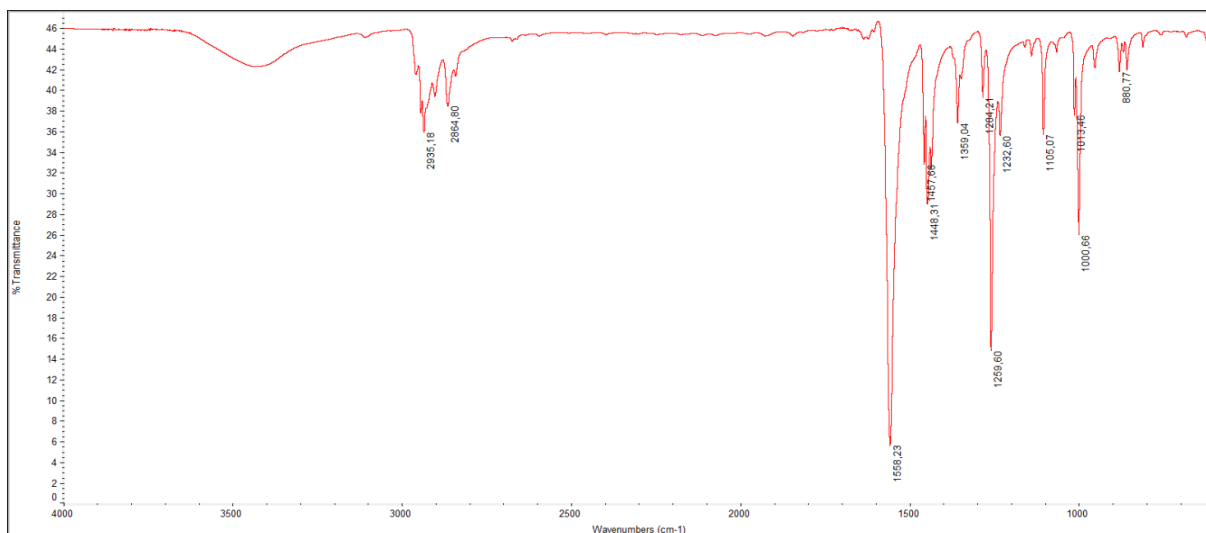


**Figure 115.** Medium FT-IR (4000-600 cm<sup>-1</sup>, KBr) spectrum of bis(piperidine dithiocarbamate)gold(III) bromide, [Au(PipeDTC)<sub>2</sub>]Br.

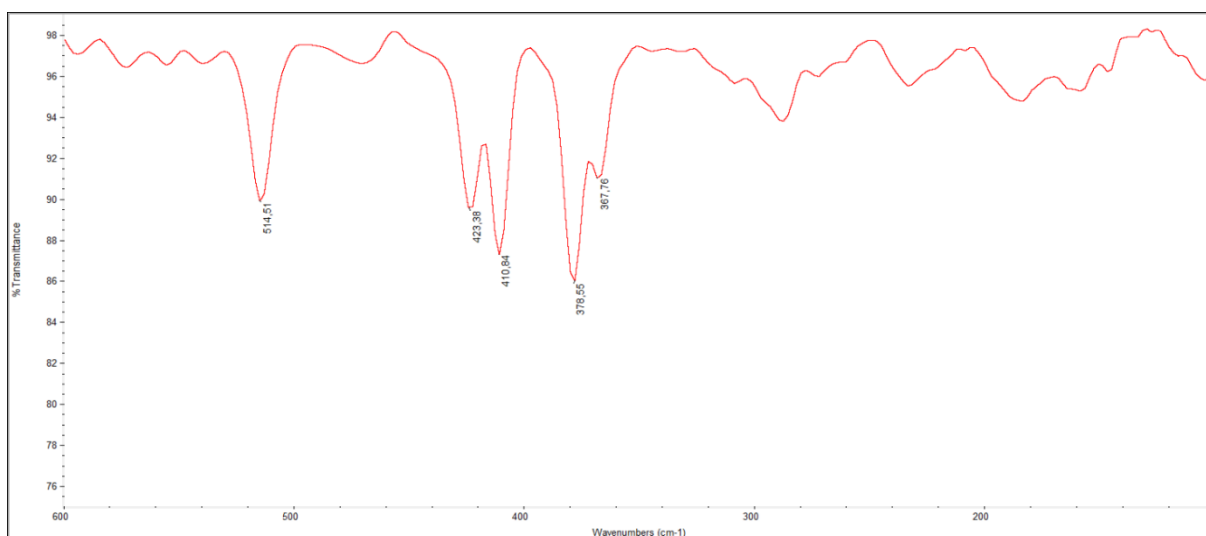


**Figure 116.** Far FT-IR (600-100 cm<sup>-1</sup>, nujol) spectrum of bis(piperidine dithiocarbamate)gold(III) bromide, [Au(PipeDTC)<sub>2</sub>]Br.

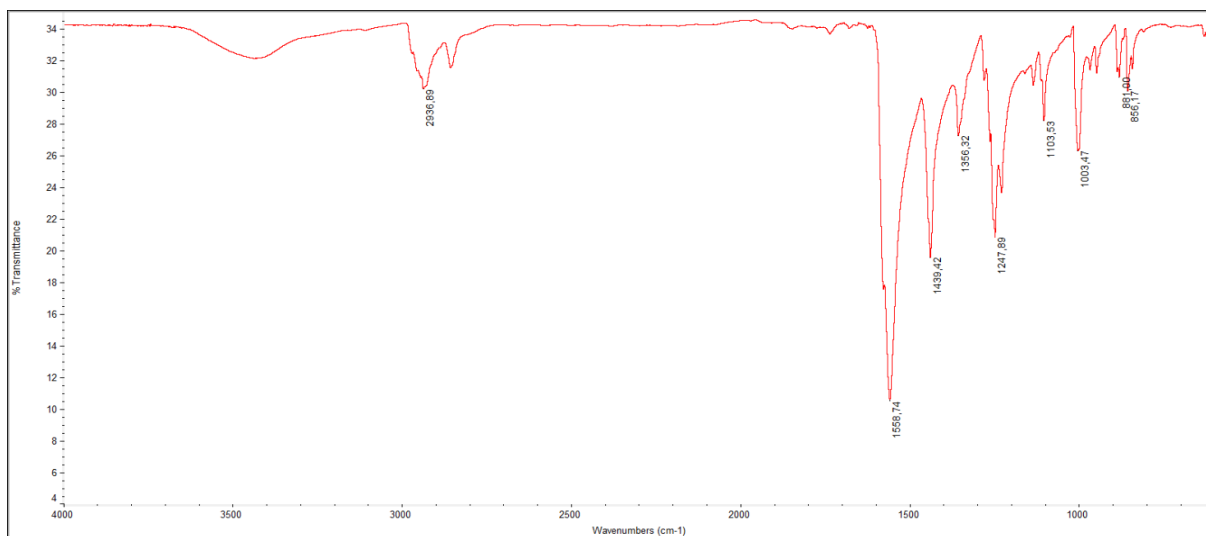


**Figure 117.** Medium FT-IR (4000-600 cm<sup>-1</sup>, KBr) spectrum of bis(piperidine dithiocarbamate)gold(III) tetrachlorogold(III), [Au(PipeDTC)<sub>2</sub>][AuCl<sub>4</sub>].

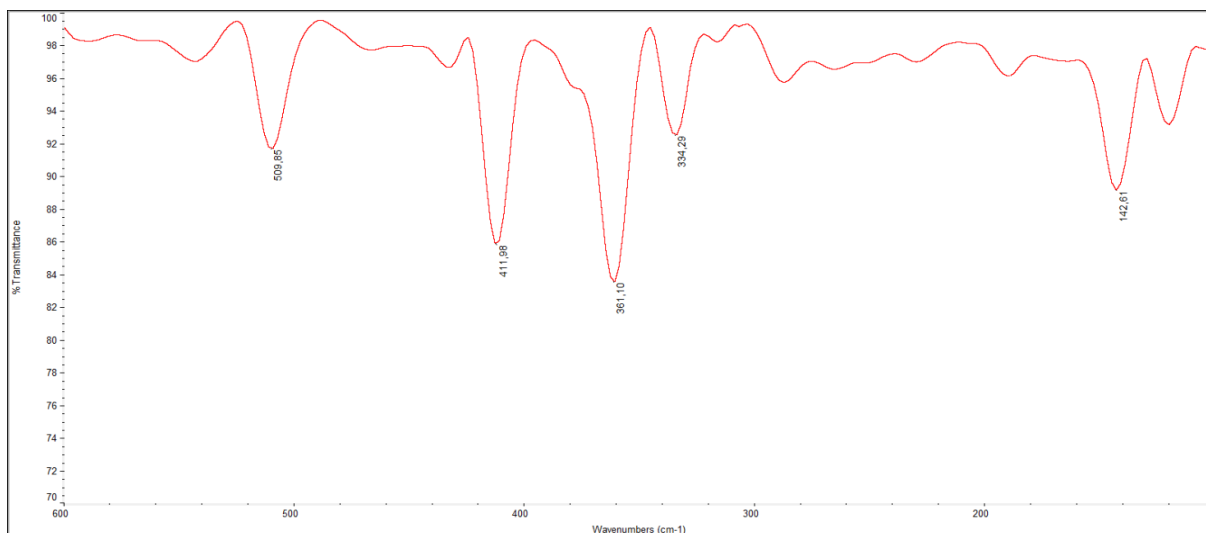


**Figure I18.** Far FT-IR (600-100  $\text{cm}^{-1}$ , nujol) spectrum of bis(piperidine dithiocarbamate)gold(III) tetrachlorogold(III),  $[\text{Au}(\text{PipeDTC})_2][\text{AuCl}_4]$ .

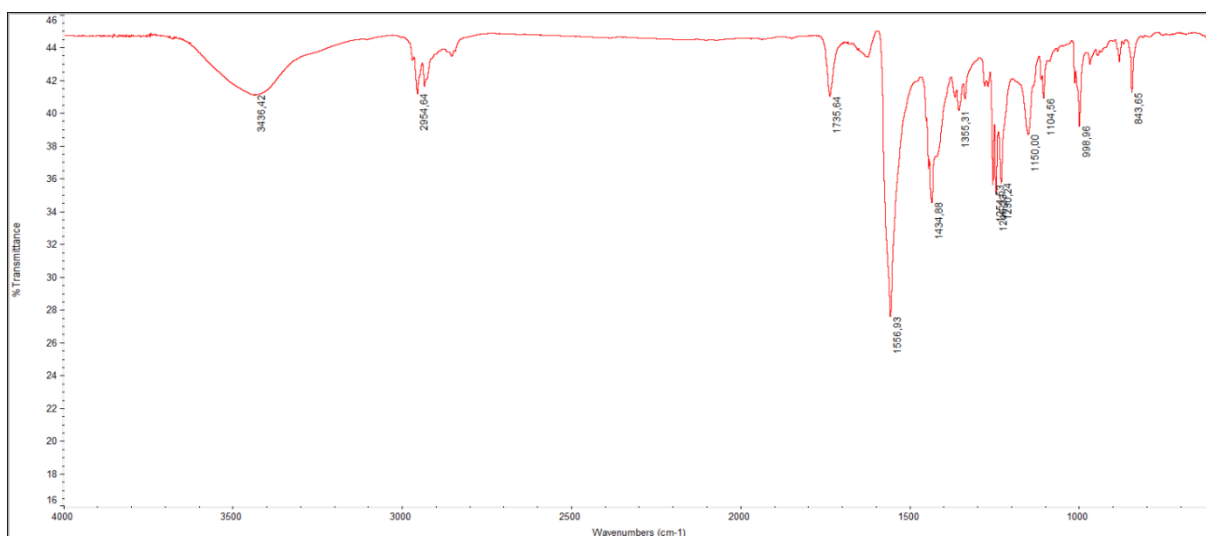


**Figure I19.** Medium FT-IR (4000-600  $\text{cm}^{-1}$ , KBr) spectrum of bis(piperidine dithiocarbamate)gold(III) dibromogold(I),  $[\text{Au}(\text{PipeDTC})_2][\text{AuBr}_2]$ .

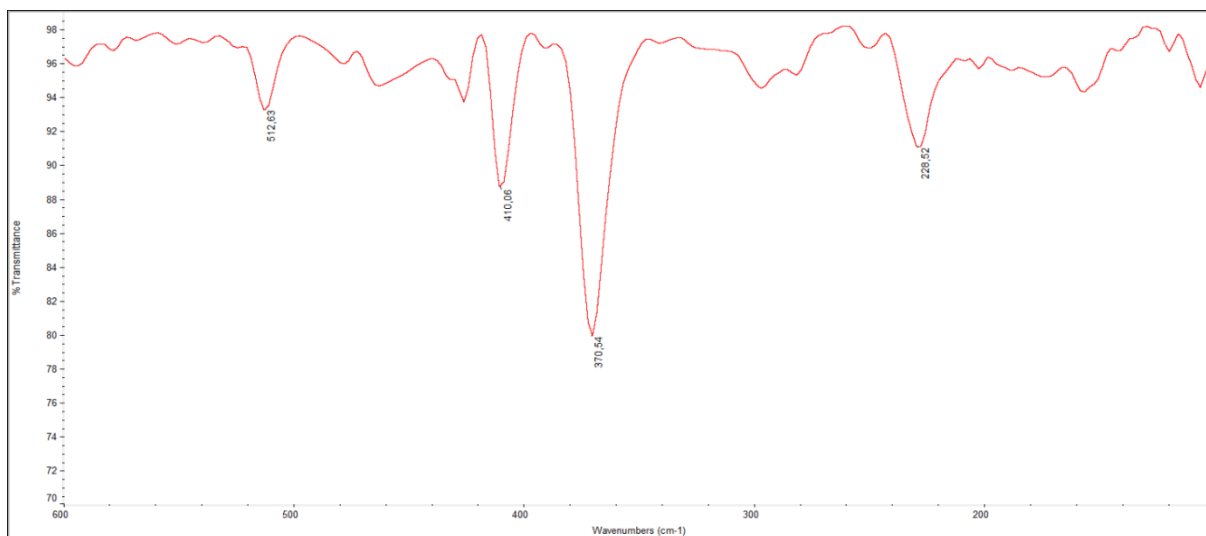


**Figure I20.** Far FT-IR (600-100  $\text{cm}^{-1}$ , nujol) spectrum of bis(piperidine dithiocarbamate)gold(III) dibromogold(I),  $[\text{Au}(\text{PipeDTC})_2][\text{AuBr}_2]$ .

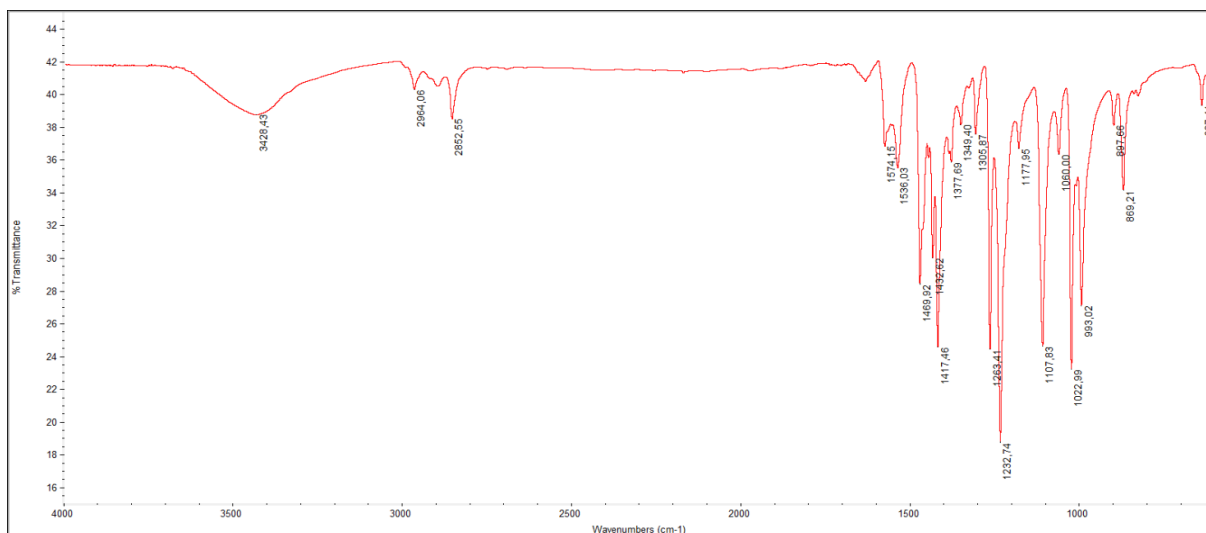


**Figure I21** Medium FT-IR ( $4000\text{-}600\text{ cm}^{-1}$ , KBr) spectrum of bis(morpholine dithiocarbamate)digold(I),  $[\text{Au}_2(\text{MorphDTC})_2]$ .

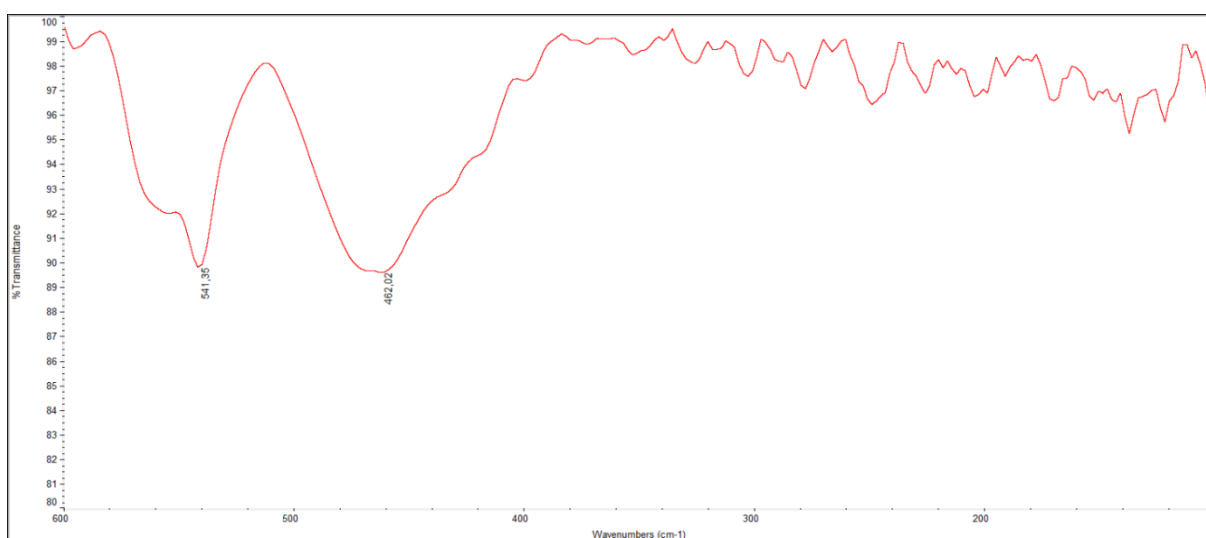


**Figure I22.** Far FT-IR ( $600\text{-}100\text{ cm}^{-1}$ , nujol) spectrum of bis(morpholine dithiocarbamate)digold(I),  $[\text{Au}_2(\text{MorphDTC})_2]$ .

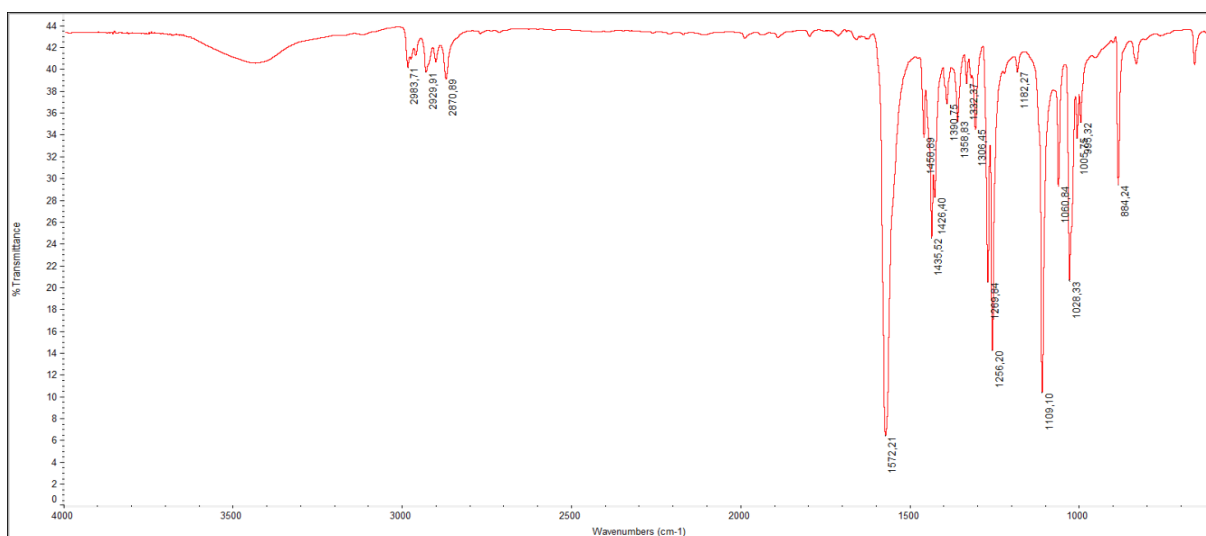


**Figure I23.** Medium FT-IR ( $4000\text{-}600\text{ cm}^{-1}$ , KBr) spectrum of dichloro(morpholine dithiocarbamate)gold(III),  $[\text{AuCl}_2(\text{MorphDTC})]$ .

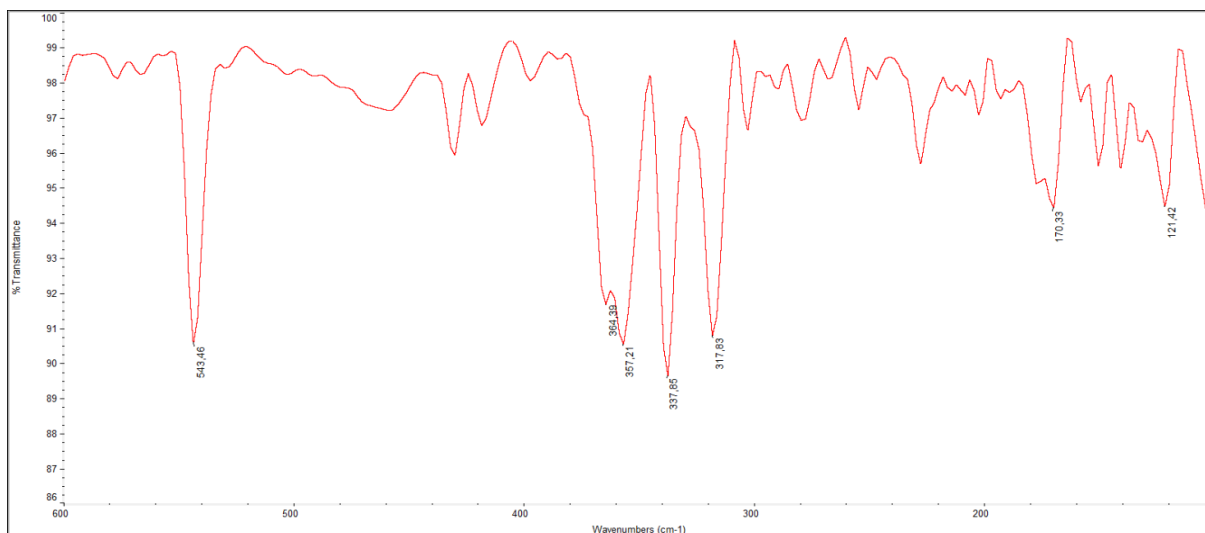


**Figure I24.** Far FT-IR (600-100  $\text{cm}^{-1}$ , nujol) spectrum of dichloro(morpholine dithiocarbamate)gold(III),  $[\text{AuCl}_2(\text{MorphDTC})]$ .

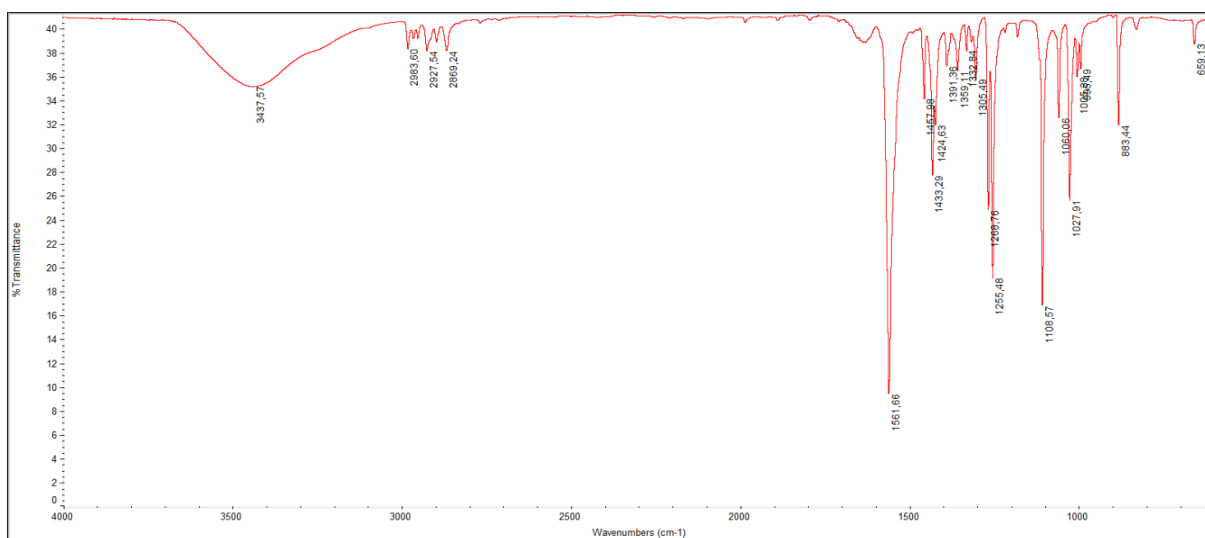


**Figure I25.** Medium FT-IR (4000-600  $\text{cm}^{-1}$ , KBr) spectrum of dibromo(morpholine dithiocarbamate)gold(III),  $[\text{AuBr}_2(\text{MorphDTC})]$ .

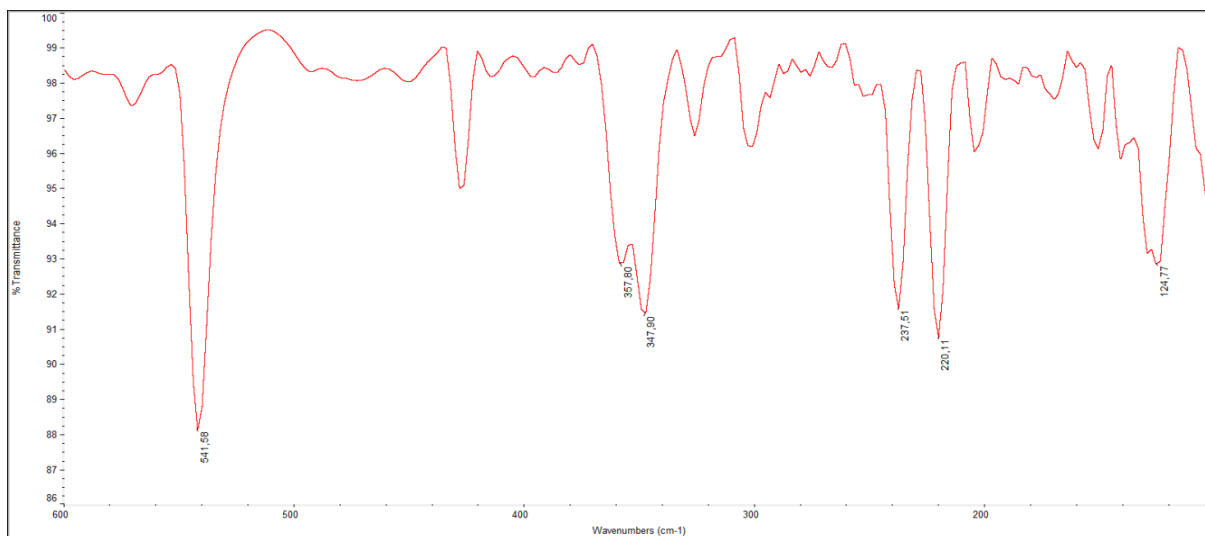


**Figure I26.** Far FT-IR (600-100  $\text{cm}^{-1}$ , nujol) spectrum of dibromo(morpholine dithiocarbamate)gold(III),  $[\text{AuBr}_2(\text{MorphDTC})]$ .

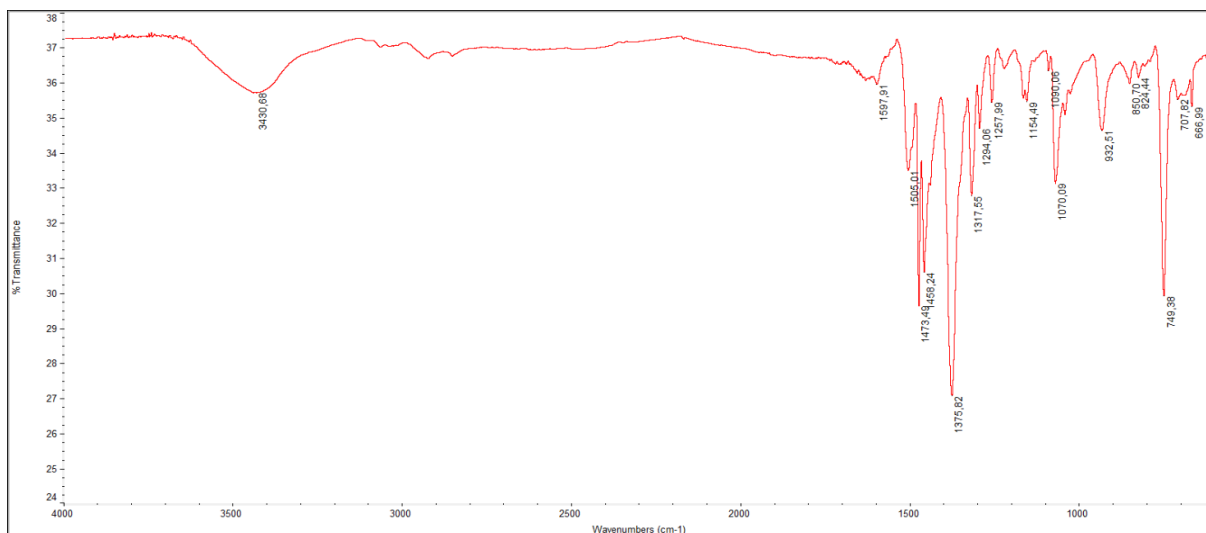


Figure I27. Medium FT-IR (4000-600 cm<sup>-1</sup>, KBr) spectrum of bis(indoline dithiocarbamate)digold(I),  $[\text{Au}_2(\text{IndolineDTC})_2]$ .

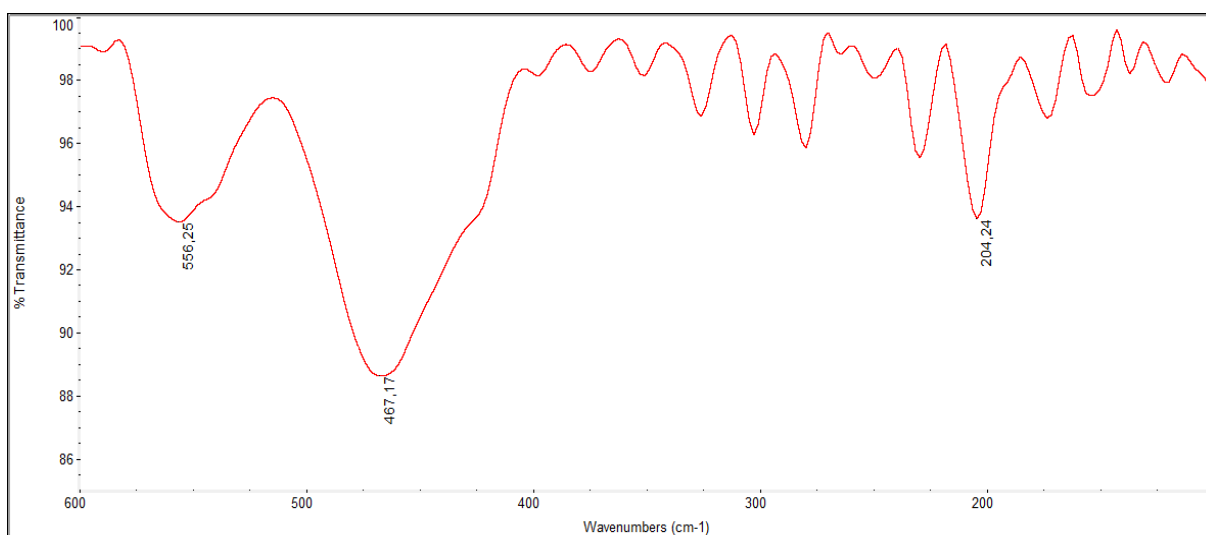


Figure I28. Far FT-IR (600-100 cm<sup>-1</sup>, nujol) spectrum of bis(indoline dithiocarbamate)digold(I),  $[\text{Au}_2(\text{IndolineDTC})_2]$ .

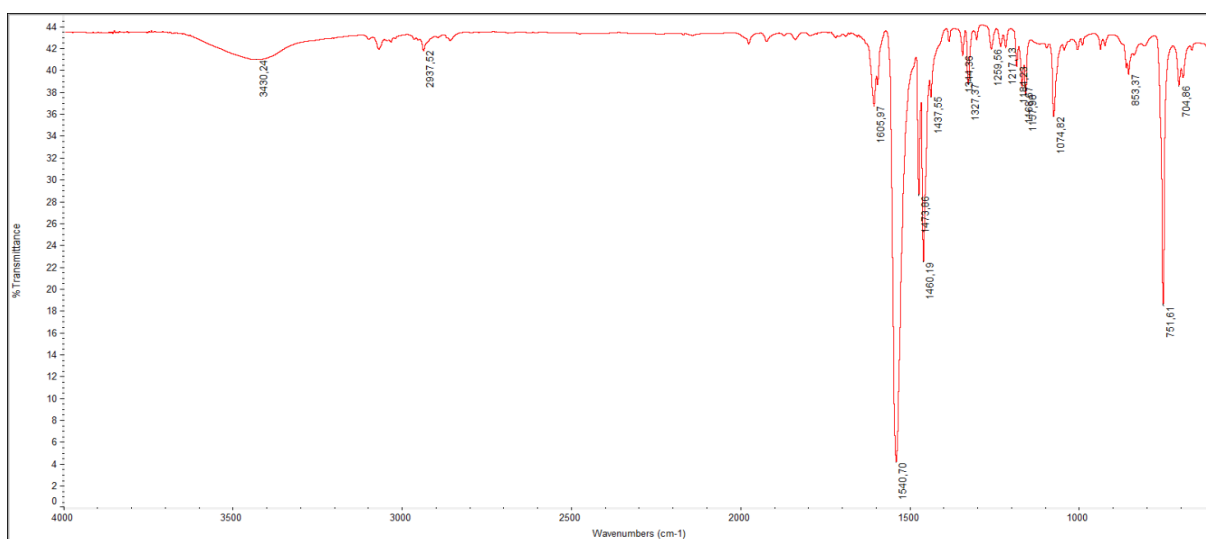
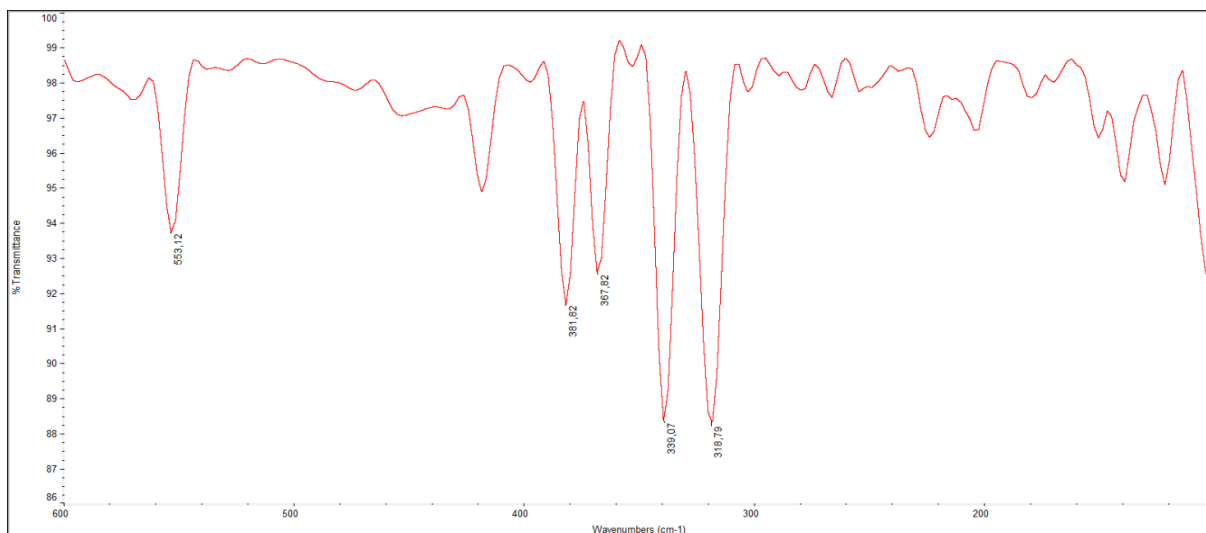
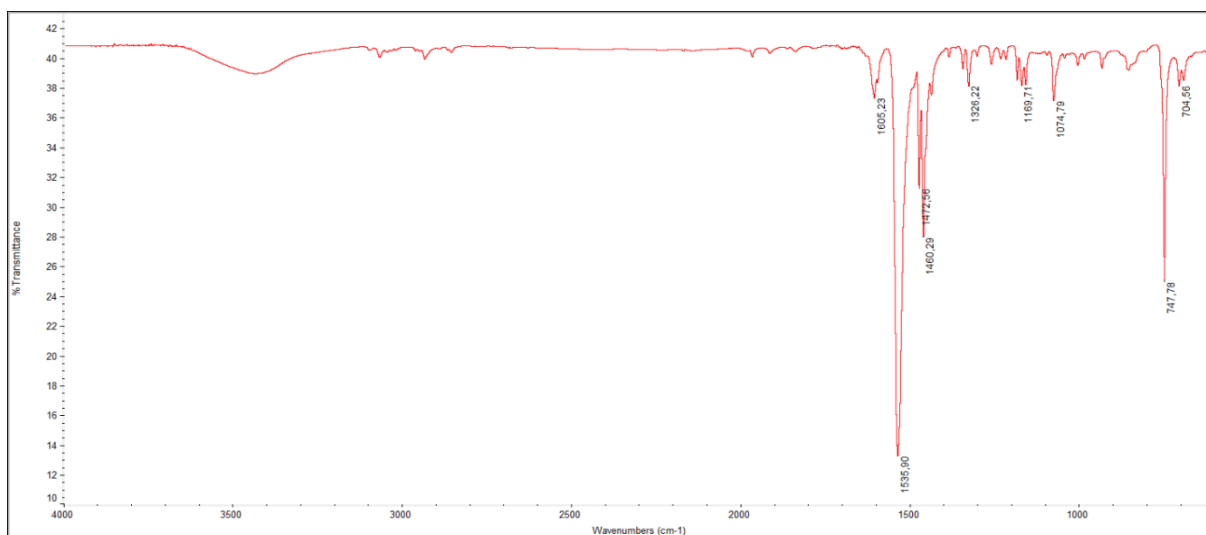


Figure I29. Medium FT-IR (4000-600 cm<sup>-1</sup>, KBr) spectrum of dichloro(indoline dithiocarbamate)gold(III),  $[\text{AuCl}_2(\text{IndolineDTC})]$ .





**Figure I30.** Far FT-IR (600-100  $\text{cm}^{-1}$ , nujol) spectrum of dichloro(indoline dithiocarbamate)gold(III),  $[\text{AuCl}_2(\text{IndolineDTC})]$ .



**Figure I31.** Medium FT-IR (4000-600  $\text{cm}^{-1}$ , KBr) spectrum of dibromo(indoline dithiocarbamate)gold(III),  $[\text{AuBr}_2(\text{IndolineDTC})]$ .

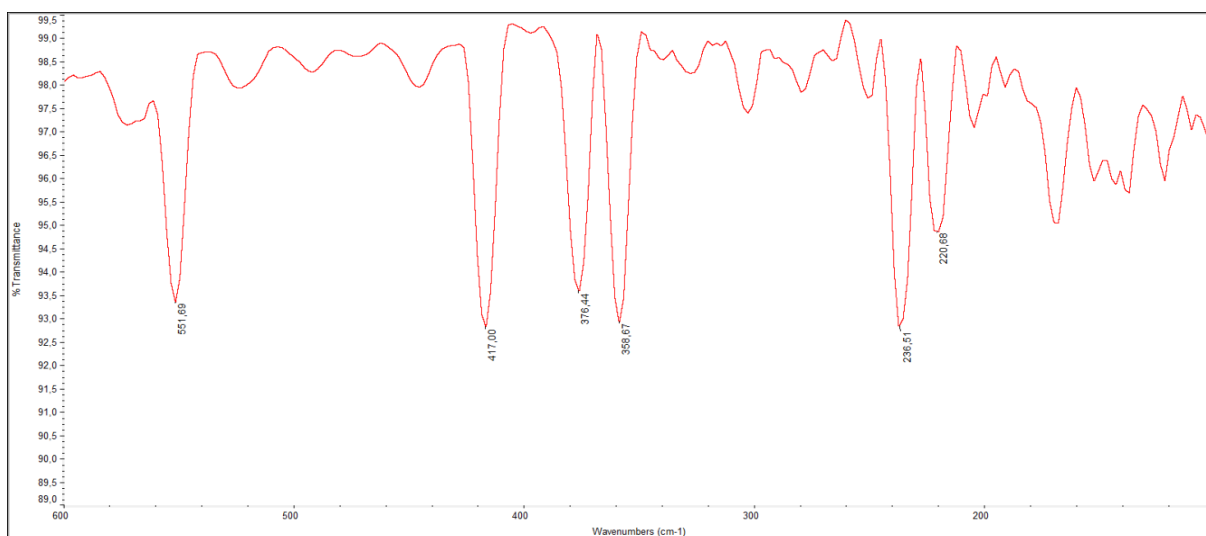


**Figure I32.** Far FT-IR (600-100  $\text{cm}^{-1}$ , nujol) spectrum of dibromo(indoline dithiocarbamate)gold(III),  $[\text{AuBr}_2(\text{IndolineDTC})]$ .

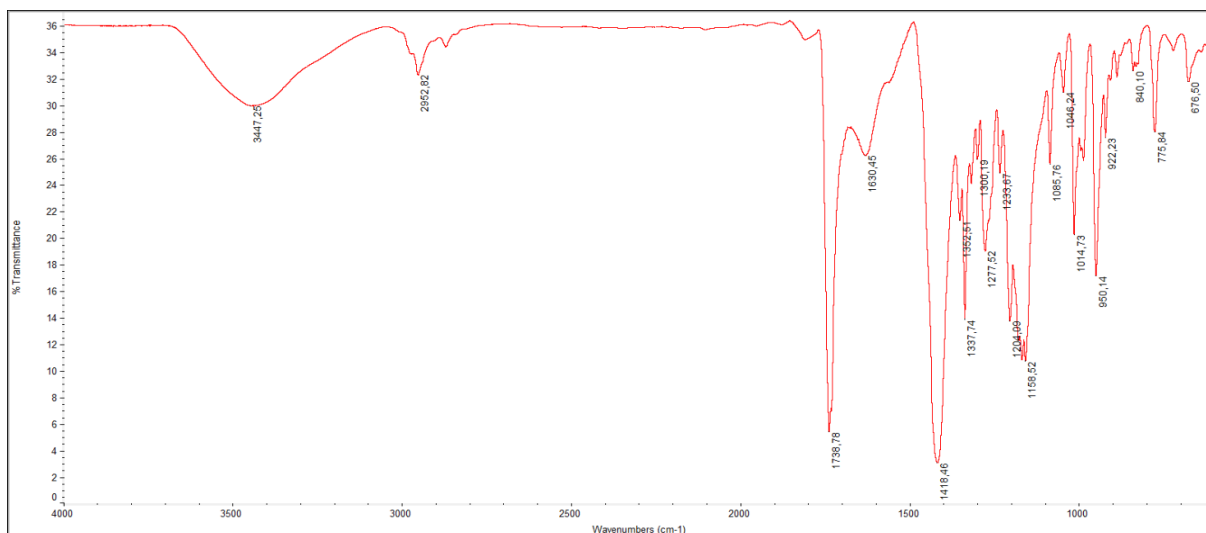


**Figure 133.** Medium FT-IR (4000-600 cm<sup>-1</sup>, KBr) spectrum of bis(L-proline methyl ester dithiocarbamate)digold(I), [Au<sub>2</sub>(ProOMeDTC)<sub>2</sub>].

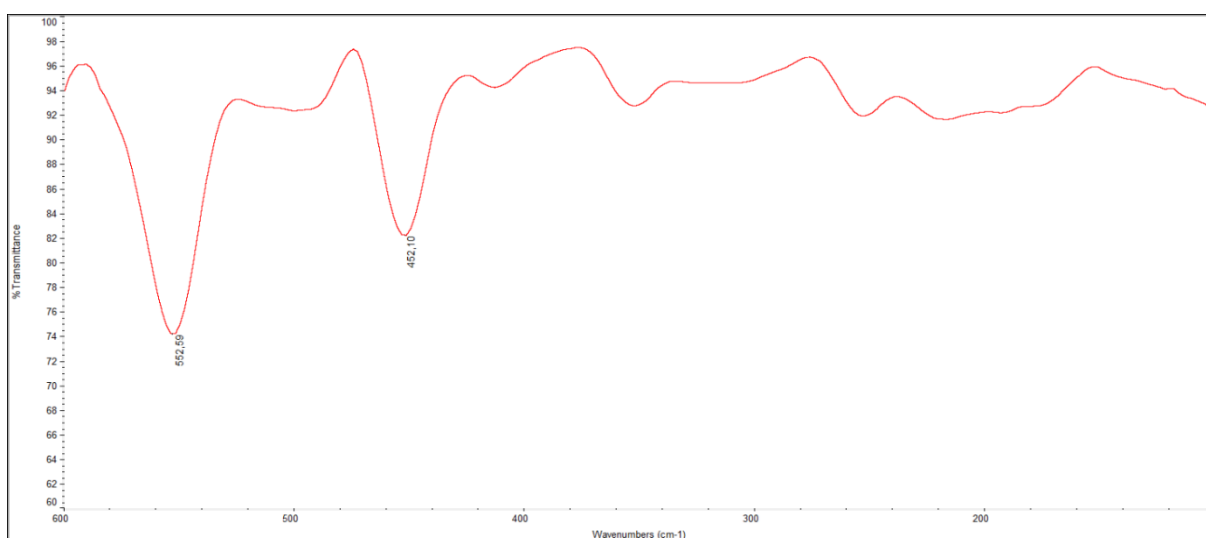


**Figure 134.** Far FT-IR (600-100 cm<sup>-1</sup>, nujol) spectrum of bis(L-proline methyl ester dithiocarbamate)digold(I), [Au<sub>2</sub>(ProOMeDTC)<sub>2</sub>].

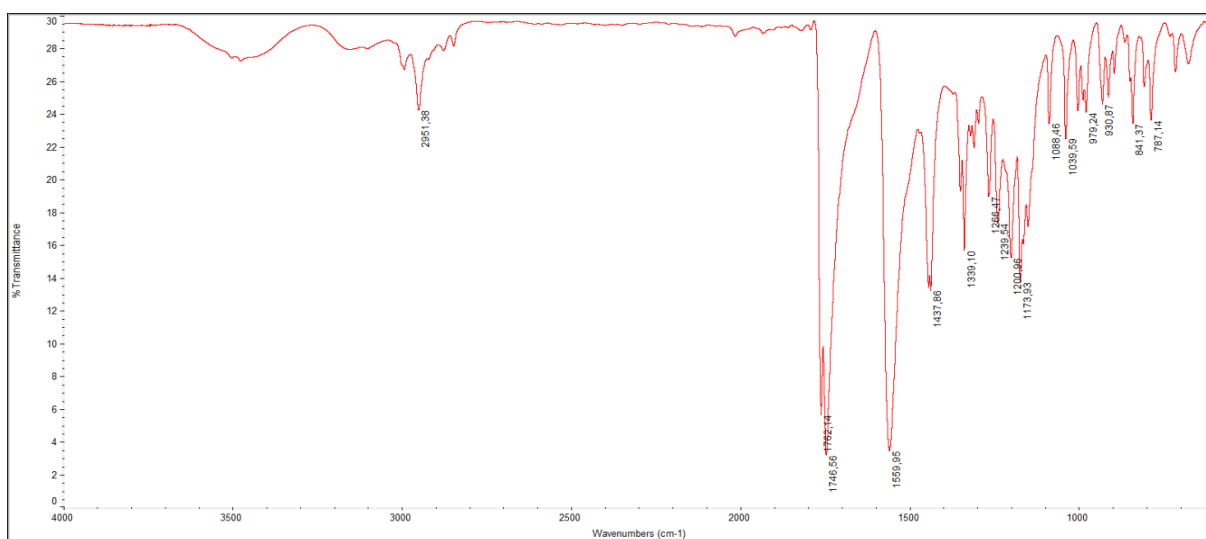


**Figure 135.** Medium FT-IR (4000-600 cm<sup>-1</sup>, KBr) spectrum of dichloro(L-proline methyl ester dithiocarbamate)gold(III), [AuCl<sub>2</sub>(ProOMeDTC)].

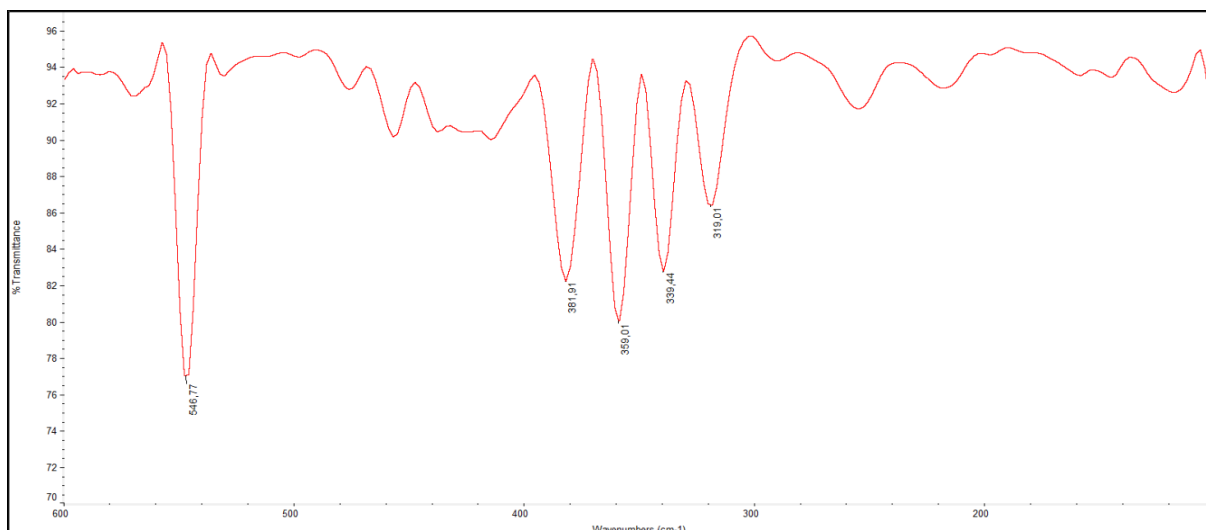


**Figure I36.** Far FT-IR (600-100  $\text{cm}^{-1}$ , nujol) spectrum of dichloro(L-proline methyl ester dithiocarbamate)gold(III),  $[\text{AuCl}_2(\text{ProOMeDTC})]$ .

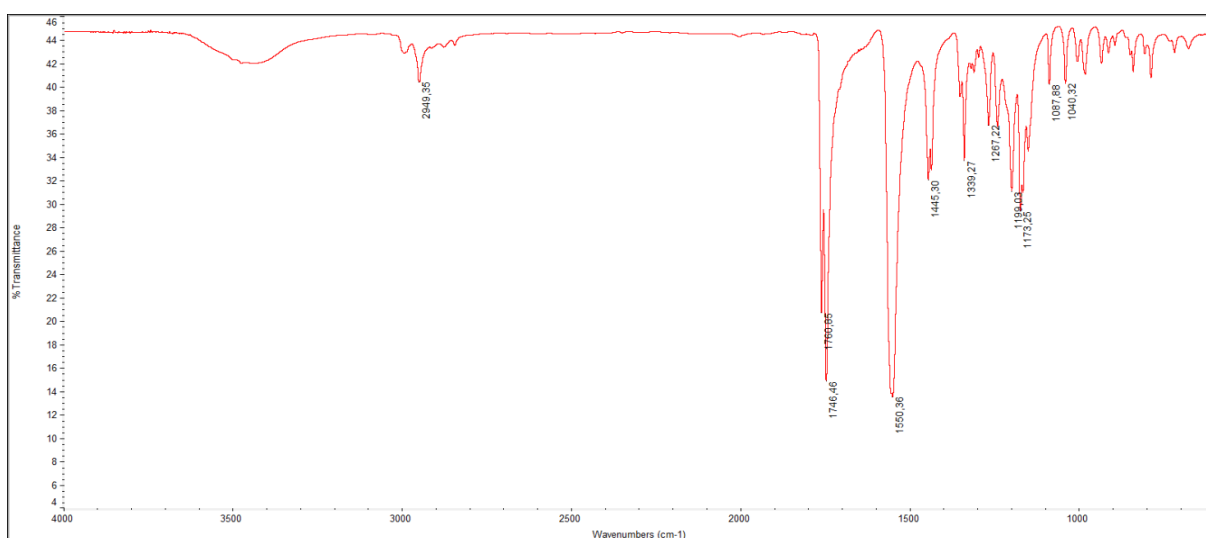


**Figure I37.** Medium FT-IR (4000-600  $\text{cm}^{-1}$ , KBr) spectrum of dibromo(L-proline methyl ester dithiocarbamate)gold(III),  $[\text{AuBr}_2(\text{ProOMeDTC})]$ .

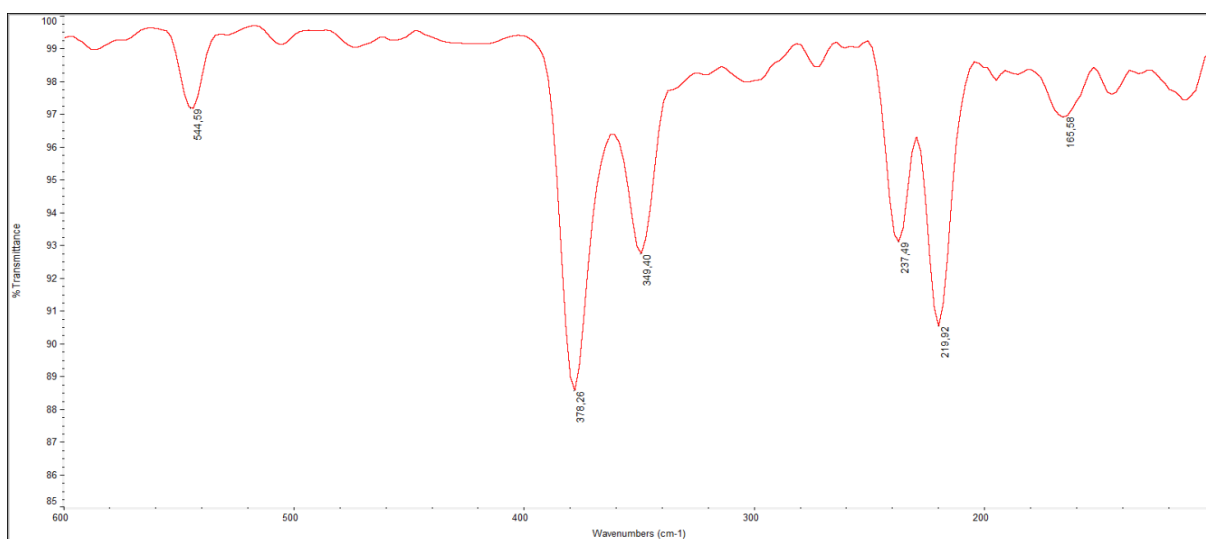


**Figure I38.** Far FT-IR (600-100  $\text{cm}^{-1}$ , nujol) spectrum of dibromo(L-proline methyl ester dithiocarbamate)gold(III),  $[\text{AuBr}_2(\text{ProOMeDTC})]$ .

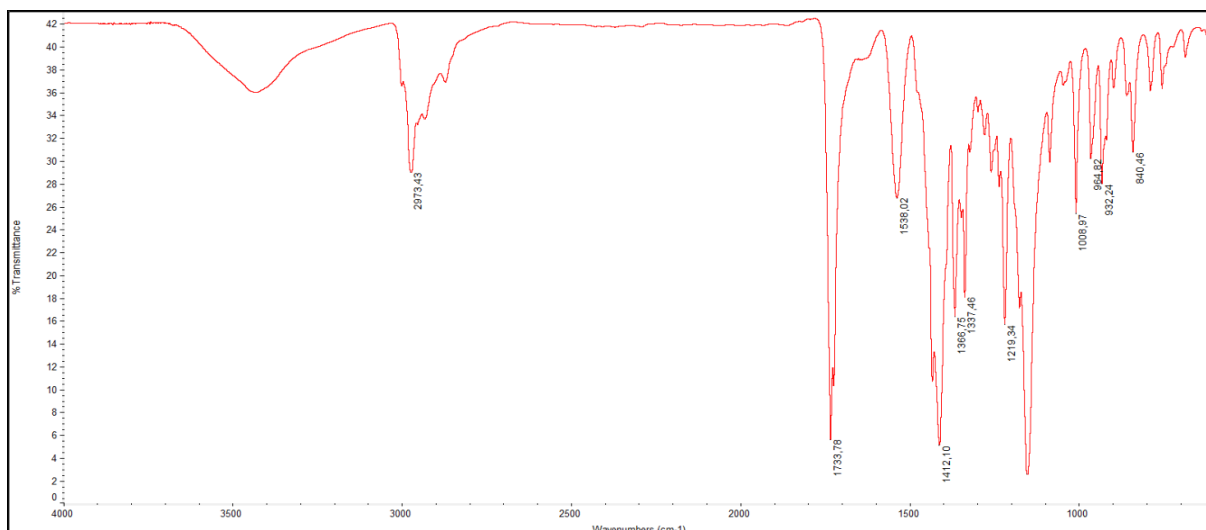


**Figure 139.** Medium FT-IR (4000-600 cm<sup>-1</sup>, KBr) spectrum of bis(L-proline *tert*-butyl ester dithiocarbamate)digold(I), [Au<sub>2</sub>(ProOtBuDTC)<sub>2</sub>].

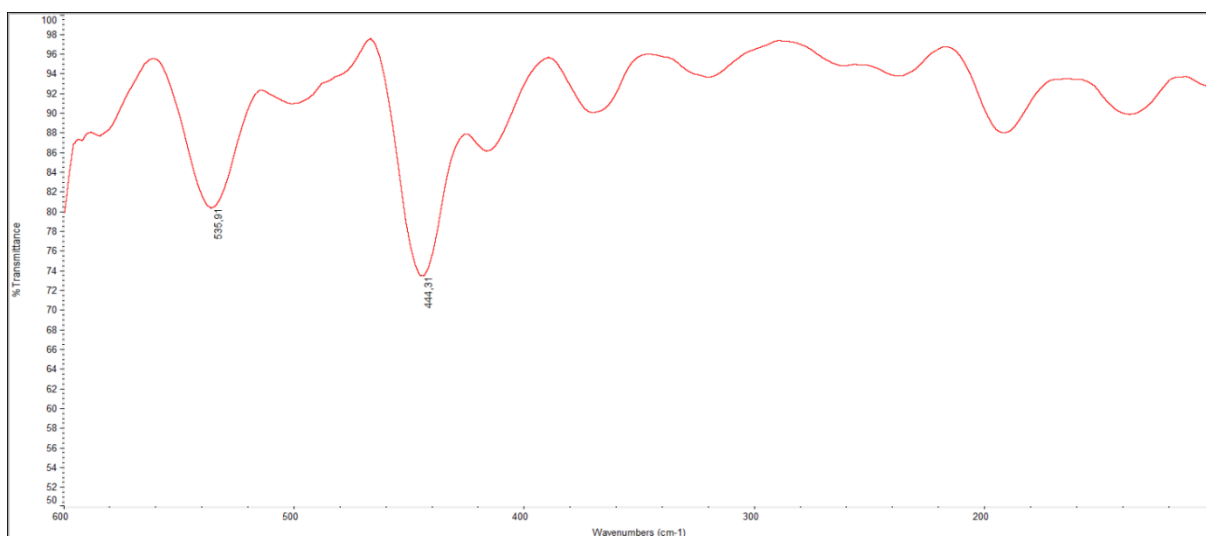


**Figure 140.** Far FT-IR (600-100 cm<sup>-1</sup>, nujol) spectrum of bis(L-proline *tert*-butyl ester dithiocarbamate)digold(I), [Au<sub>2</sub>(ProOtBuDTC)<sub>2</sub>].

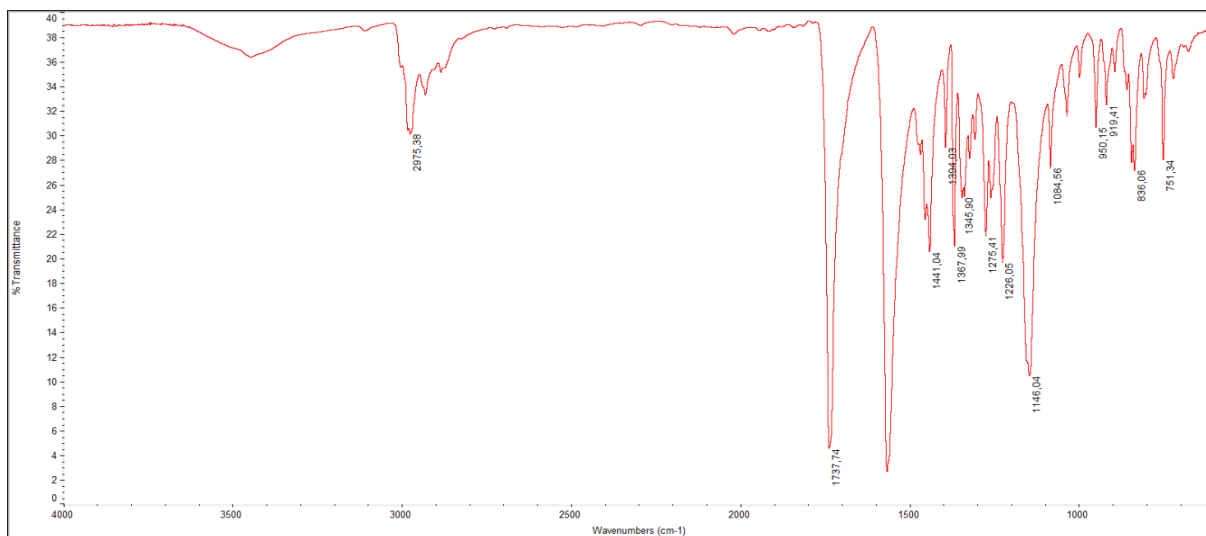


**Figure 141.** Medium FT-IR (4000-600 cm<sup>-1</sup>, KBr) spectrum of dichloro(L-proline *tert*-butyl ester dithiocarbamate)gold(III), [AuCl<sub>2</sub>(ProOtBuDTC)].

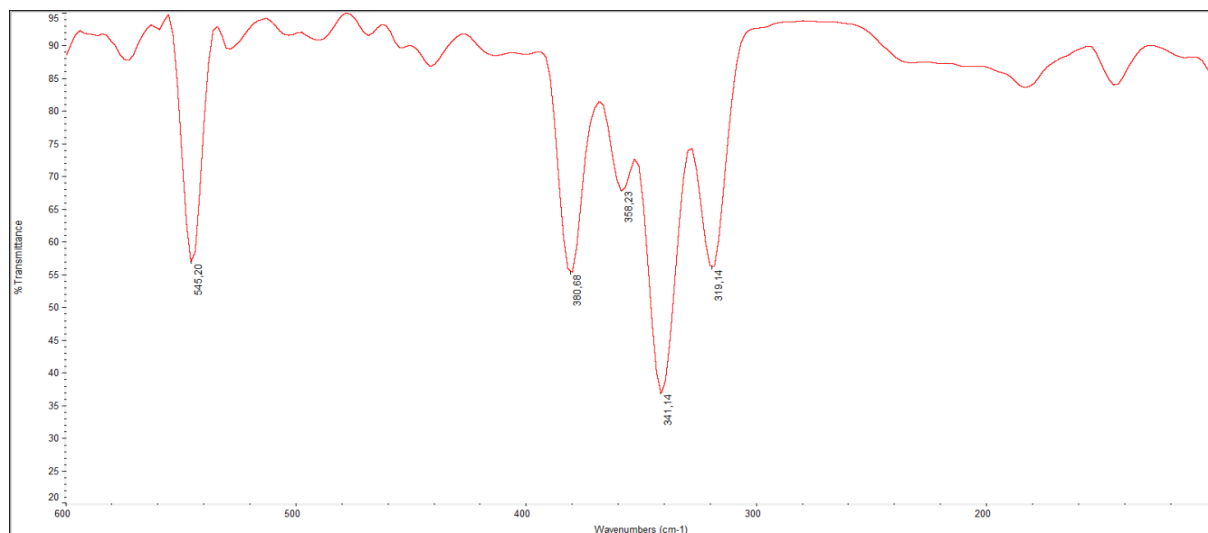


**Figure I42.** Far FT-IR (600-100  $\text{cm}^{-1}$ , nujol) spectrum of dichloro(L-proline *tert*-butyl ester dithiocarbamate)gold(III),  $[\text{AuCl}_2(\text{ProOtBuDTC})]$ .

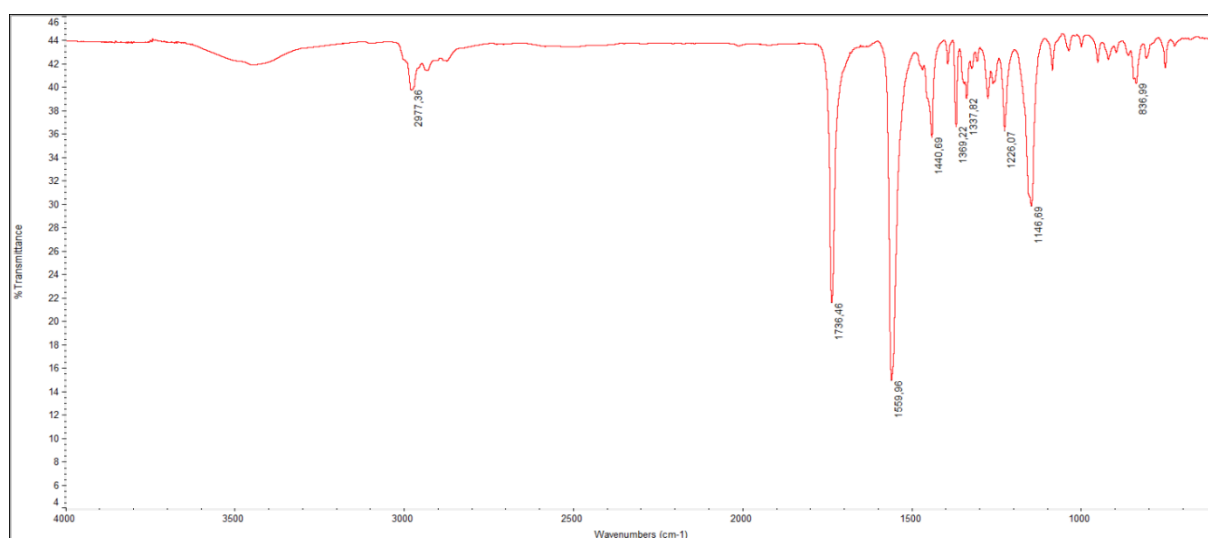


**Figure I43.** Medium FT-IR (4000-600  $\text{cm}^{-1}$ , KBr) spectrum of dibromo(L-proline *tert*-butyl ester dithiocarbamate)gold(III),  $[\text{AuBr}_2(\text{ProOtBuDTC})]$ .

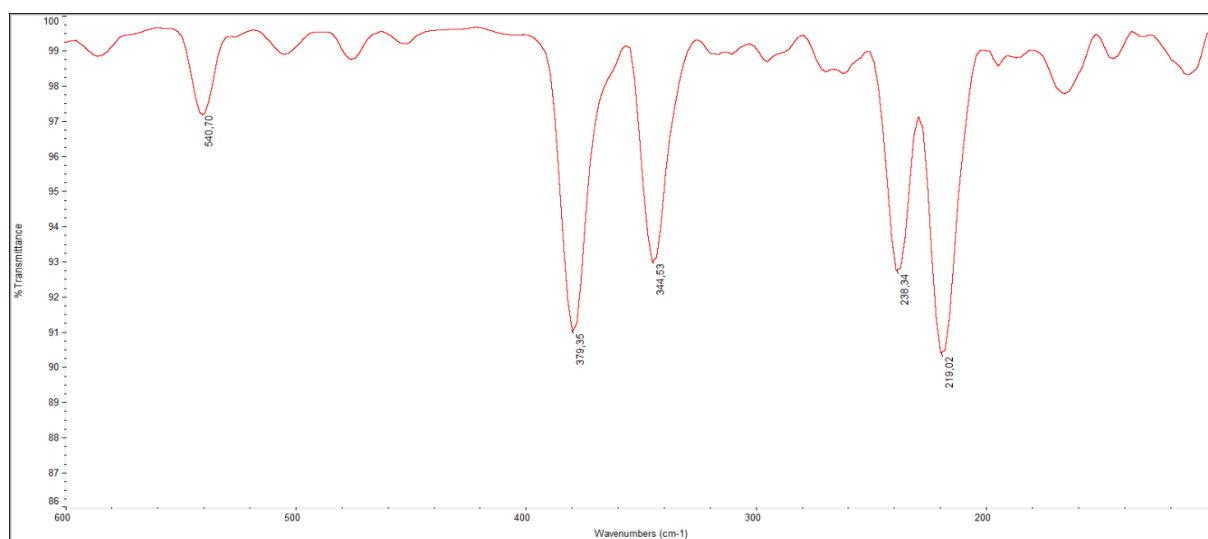


**Figure I44.** Far FT-IR (600-100  $\text{cm}^{-1}$ , nujol) spectrum of dibromo(L-proline *tert*-butyl ester dithiocarbamate)gold(III),  $[\text{AuBr}_2(\text{ProOtBuDTC})]$ .

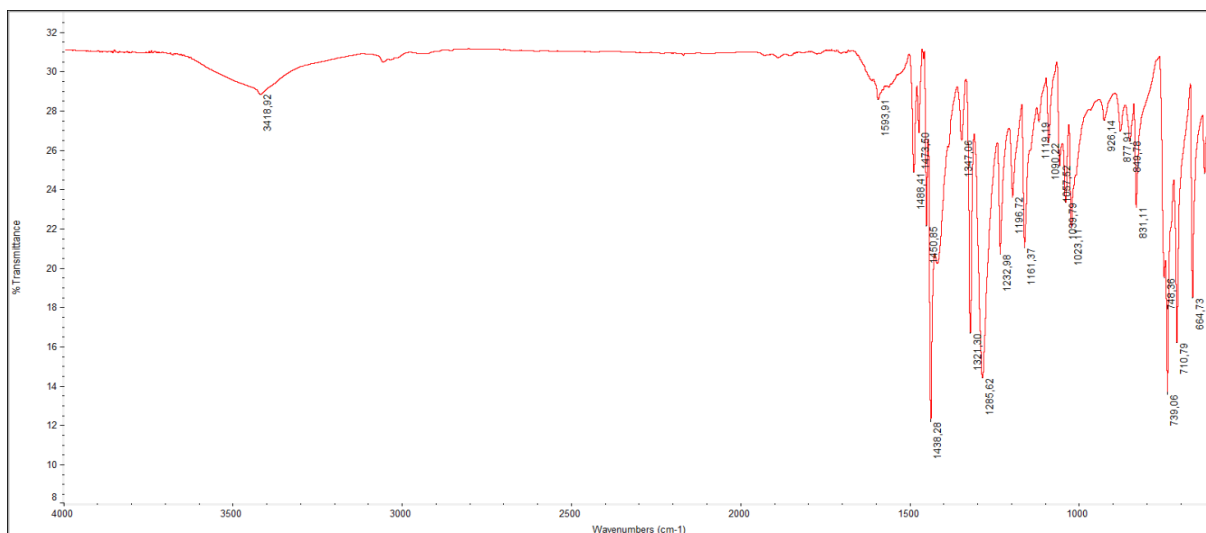


Figure I45. Medium FT-IR (4000-600 cm<sup>-1</sup>, KBr) spectrum of bis(carbazole dithiocarbamate)digold(I), [Au<sub>2</sub>(CDT)<sub>2</sub>].

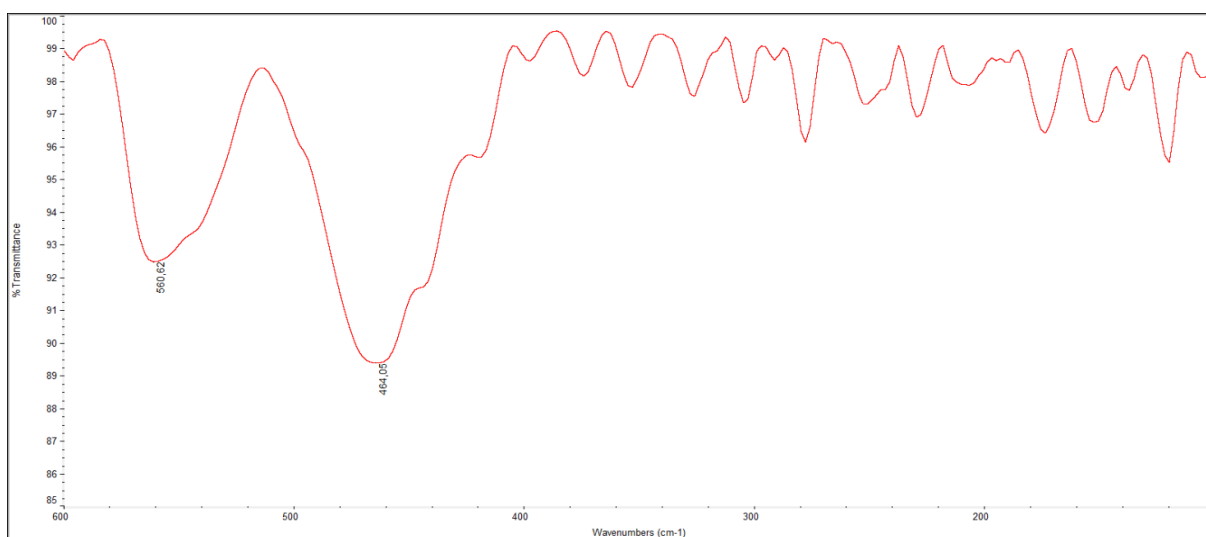


Figure I46. Far FT-IR (600-100 cm<sup>-1</sup>, nujol) spectrum of bis(carbazole dithiocarbamate)digold(I), [Au<sub>2</sub>(CDT)<sub>2</sub>].

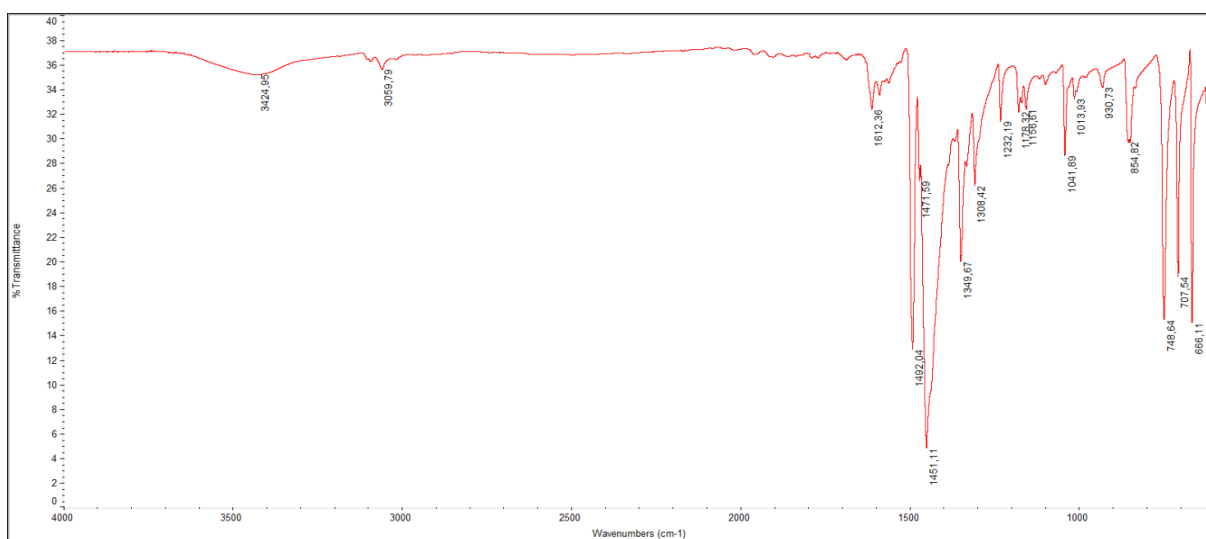


Figure I47. Medium FT-IR (4000-600 cm<sup>-1</sup>, KBr) spectrum of dichloro(carbazole dithiocarbamate)gold(III), [AuCl<sub>2</sub>(CDT)].

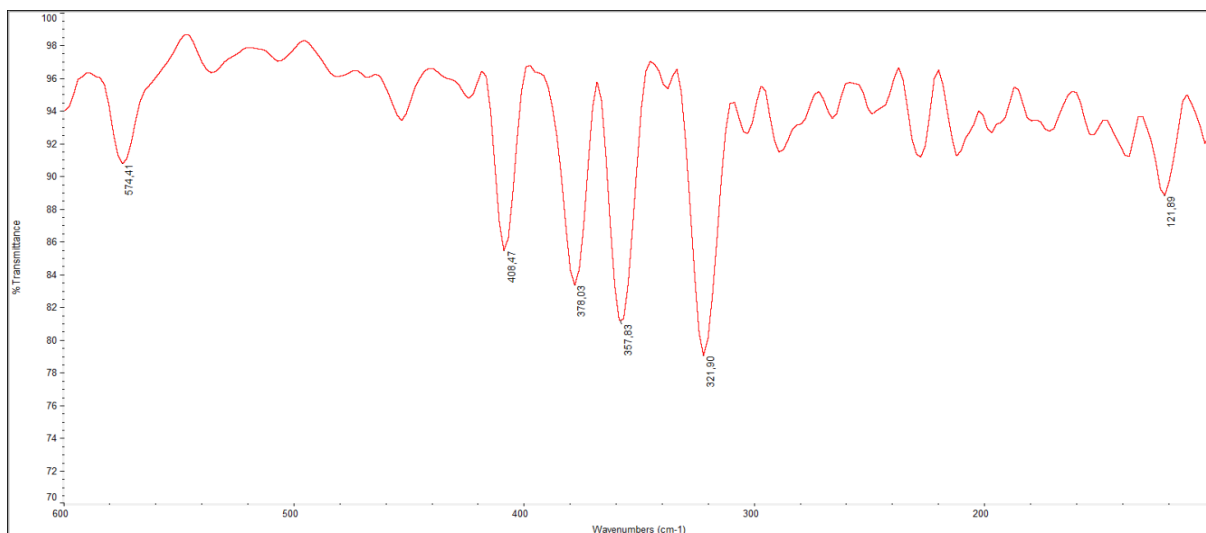


Figure I48. Far FT-IR (600-100 cm<sup>-1</sup>, nujol) spectrum of dichloro(carbazole dithiocarbamate)gold(III), [AuCl<sub>2</sub>(CDT)].

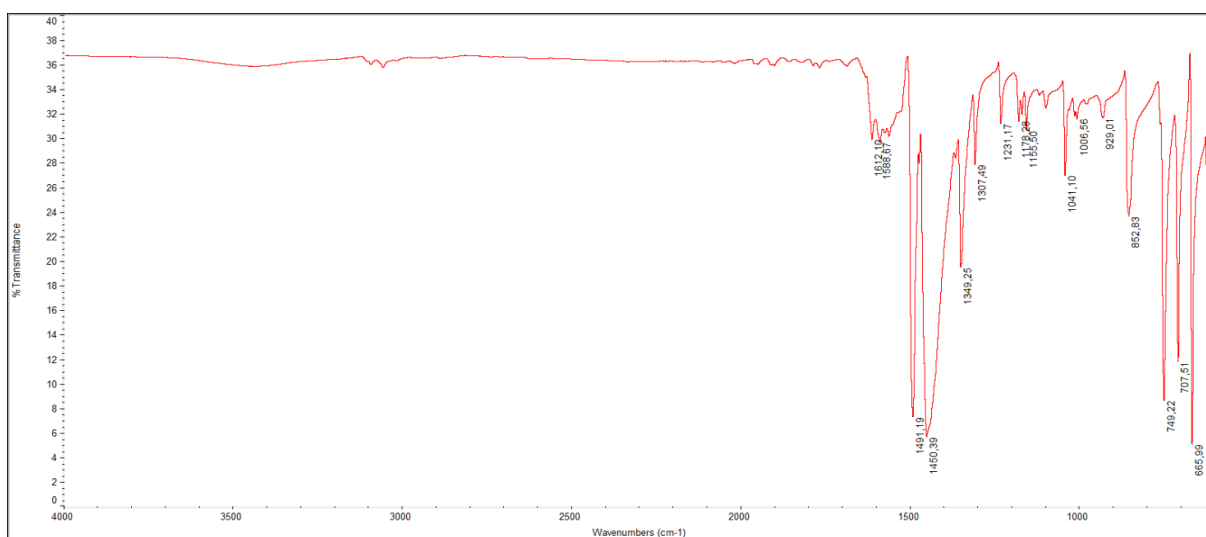


Figure I49. Medium FT-IR (4000-600 cm<sup>-1</sup>, KBr) spectrum of dibromo(carbazole dithiocarbamate)gold(III), [AuBr<sub>2</sub>(CDT)].

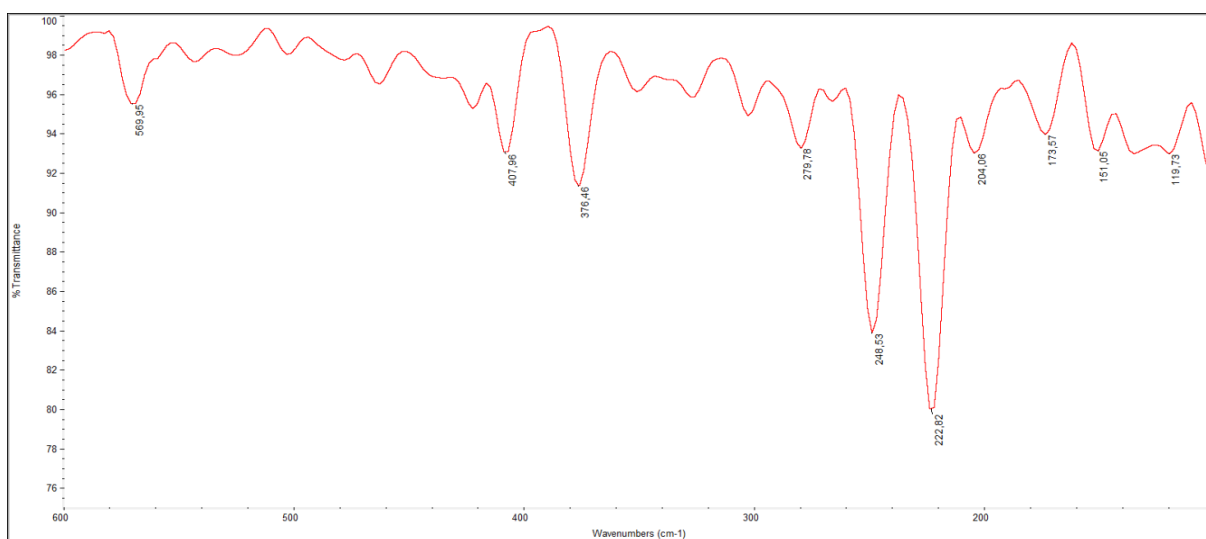


Figure I50. Far FT-IR (600-100 cm<sup>-1</sup>, nujol) spectrum of dibromo(carbazole dithiocarbamate)gold(III), [AuBr<sub>2</sub>(CDT)].

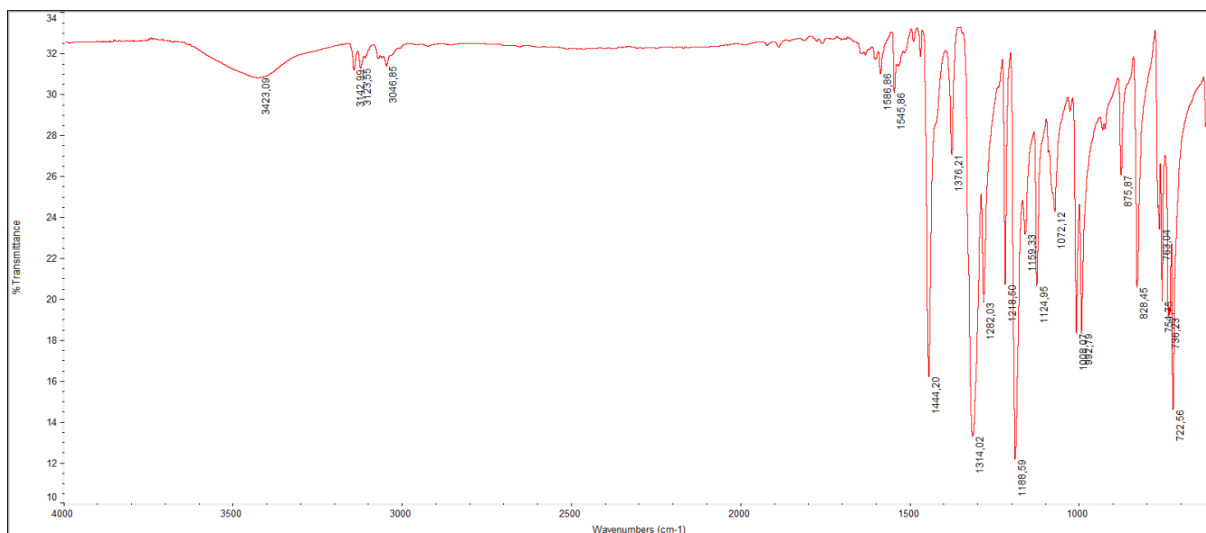


Figure I51. Medium FT-IR (4000-600 cm<sup>-1</sup>, KBr) spectrum of bis(indole dithiocarbamate)digold(I), [Au<sub>2</sub>(IndDTC)<sub>2</sub>].

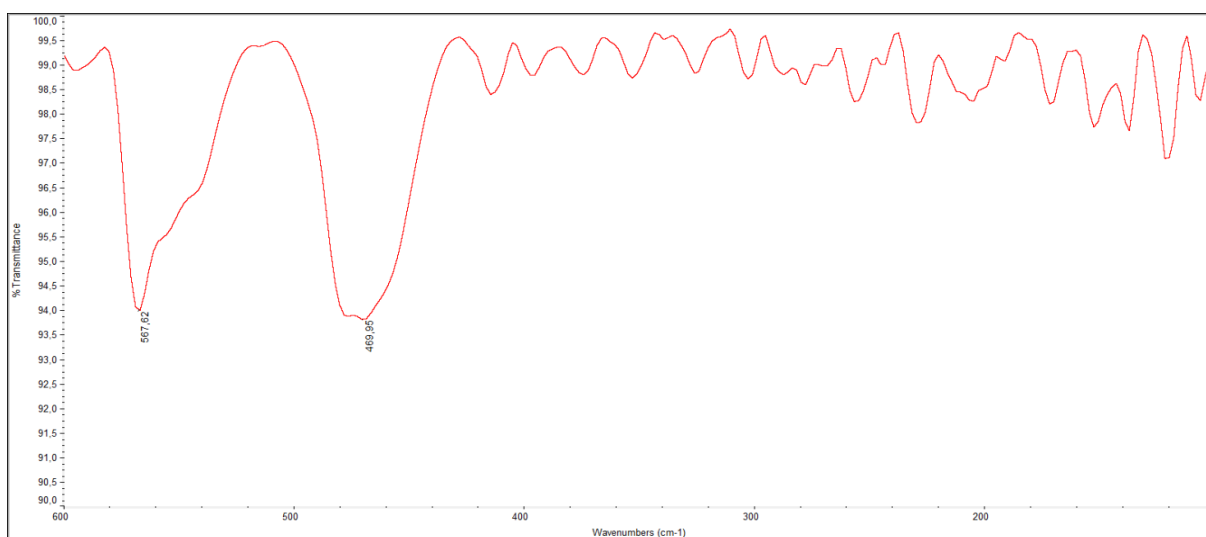


Figure I52. Far FT-IR (600-100 cm<sup>-1</sup>, nujol) spectrum of bis(indole dithiocarbamate)digold(I), [Au<sub>2</sub>(IndDTC)<sub>2</sub>].

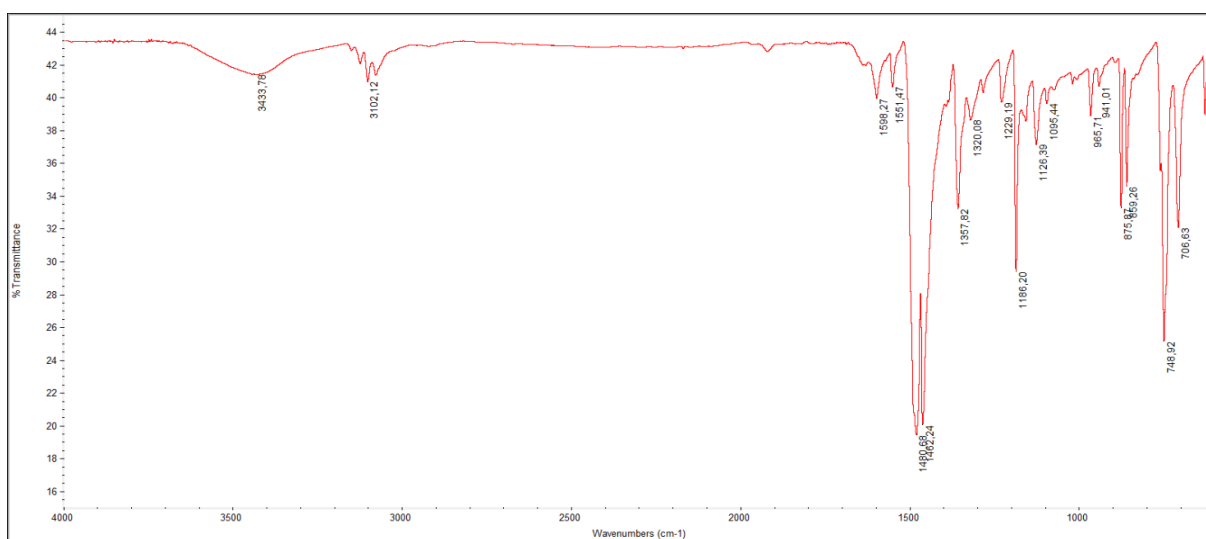


Figure I53. Medium FT-IR (4000-600 cm<sup>-1</sup>, KBr) spectrum of dichloro(indole dithiocarbamate)gold(III), [AuCl<sub>2</sub>(IndDTC)].



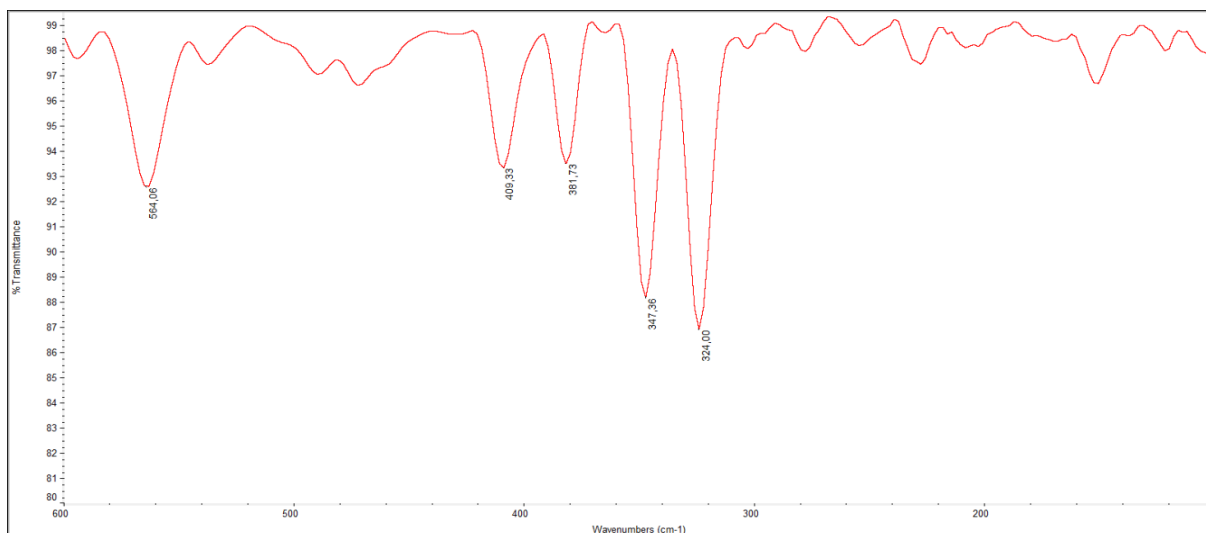


Figure I54. Far FT-IR (600-100  $\text{cm}^{-1}$ , nujol) spectrum of dichloro(indole dithiocarbamate)gold(III),  $[\text{AuCl}_2(\text{IndDTC})]$ .

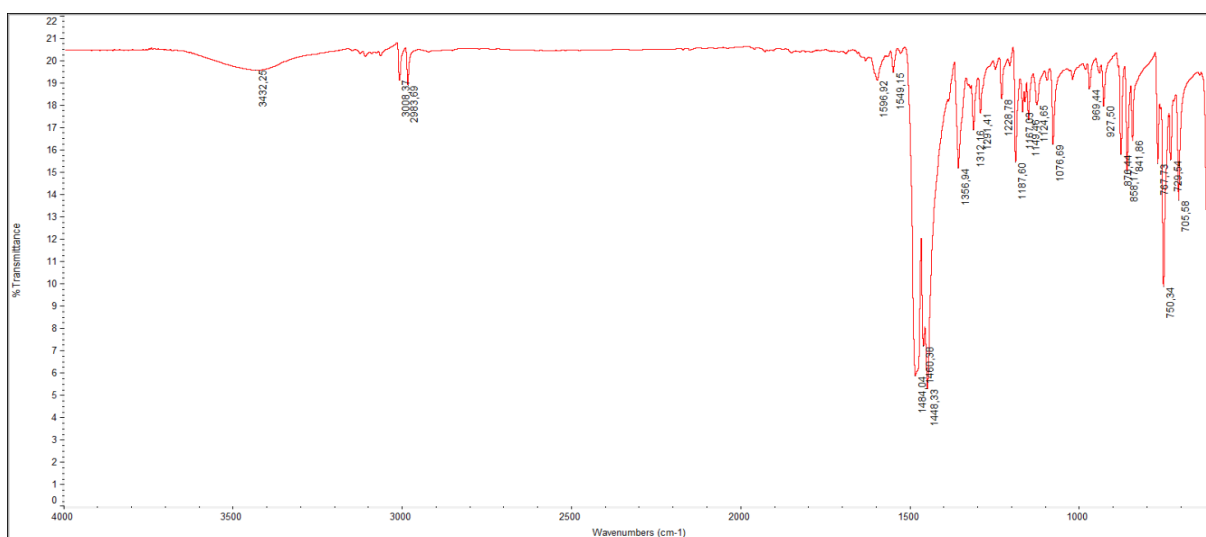


Figure I55. Medium FT-IR (4000-600  $\text{cm}^{-1}$ , KBr) spectrum of dibromo(indole dithiocarbamate)gold(III),  $[\text{AuBr}_2(\text{IndDTC})]$ .

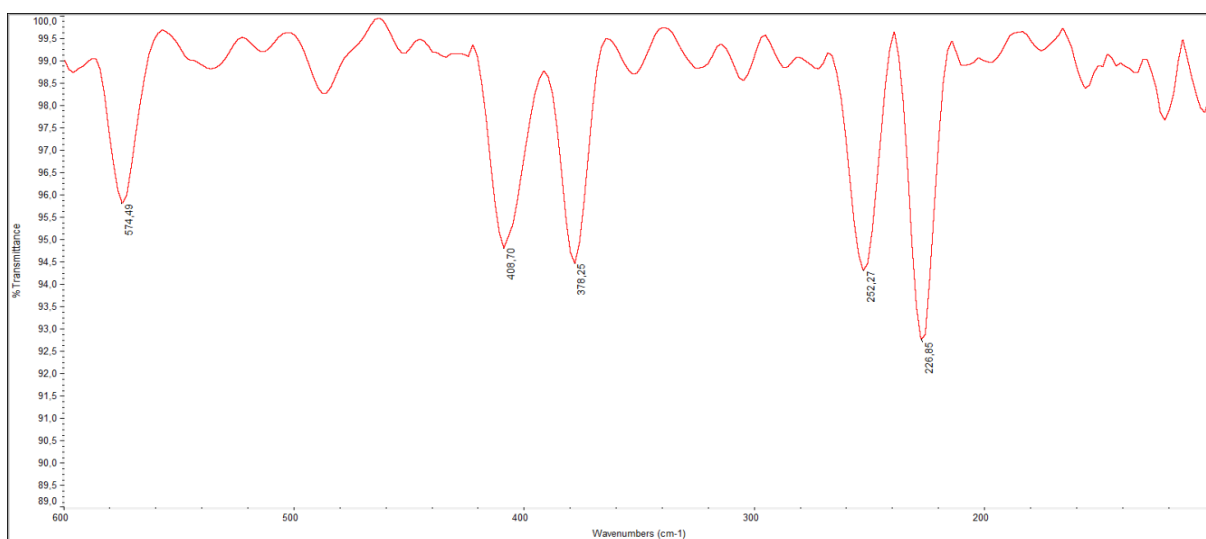


Figure I56. Far FT-IR (600-100  $\text{cm}^{-1}$ , nujol) spectrum of dibromo(indole dithiocarbamate)gold(III),  $[\text{AuBr}_2(\text{IndDTC})]$ .

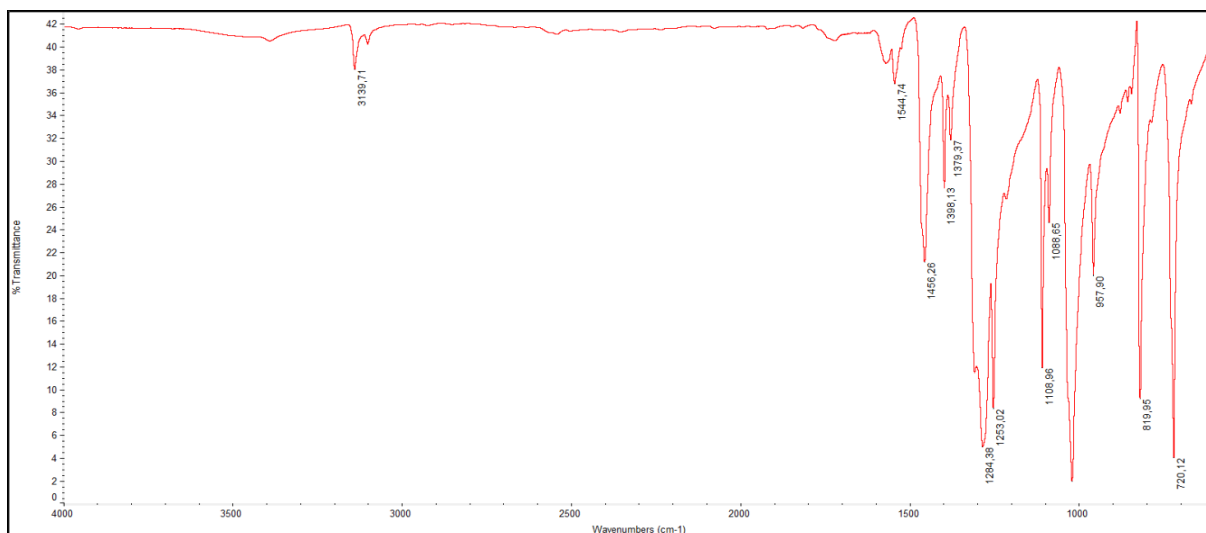


Figure I57. Medium FT-IR (4000-600 cm<sup>-1</sup>, KBr) spectrum of bis(pyrrole dithiocarbamate)digold(I), [Au<sub>2</sub>(PyrroleDTC)<sub>2</sub>].

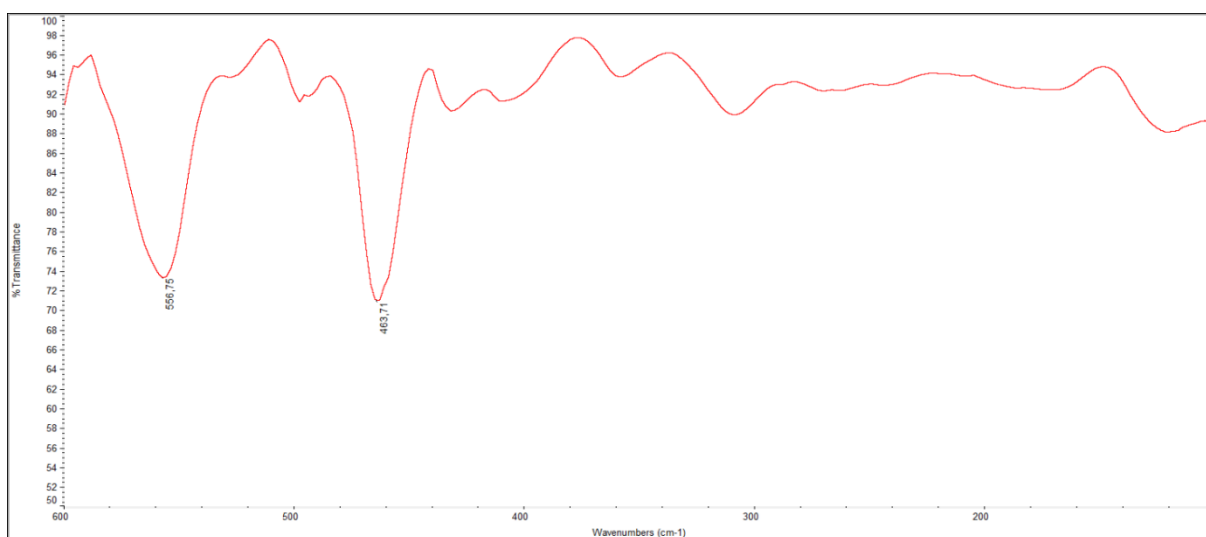


Figure I58. Far FT-IR (600-100 cm<sup>-1</sup>, nujol) spectrum of bis(pyrrole dithiocarbamate)digold(I), [Au<sub>2</sub>(PyrroleDTC)<sub>2</sub>].

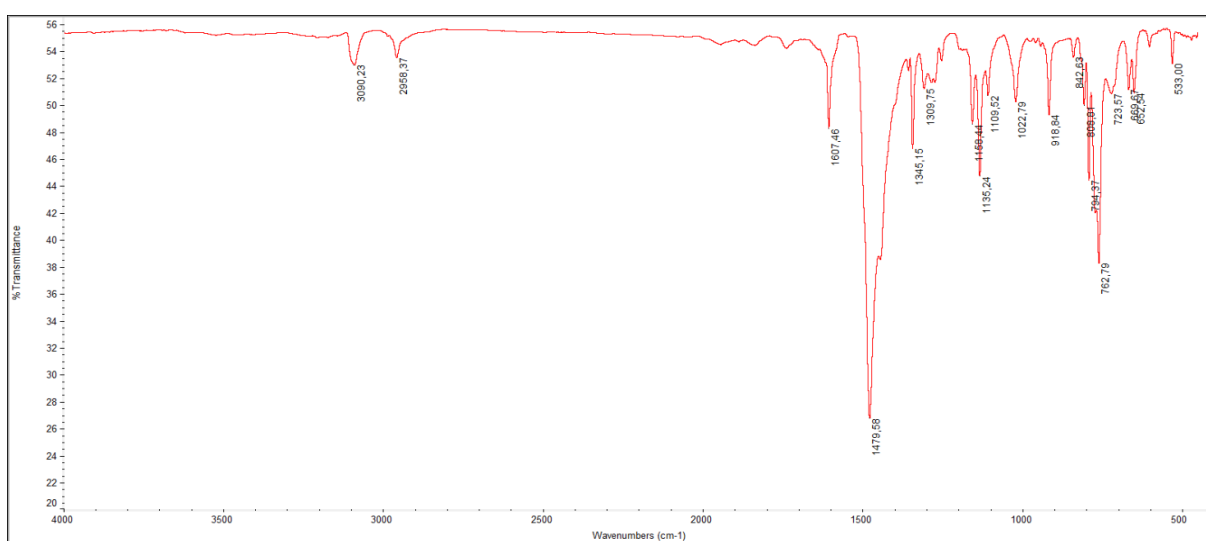
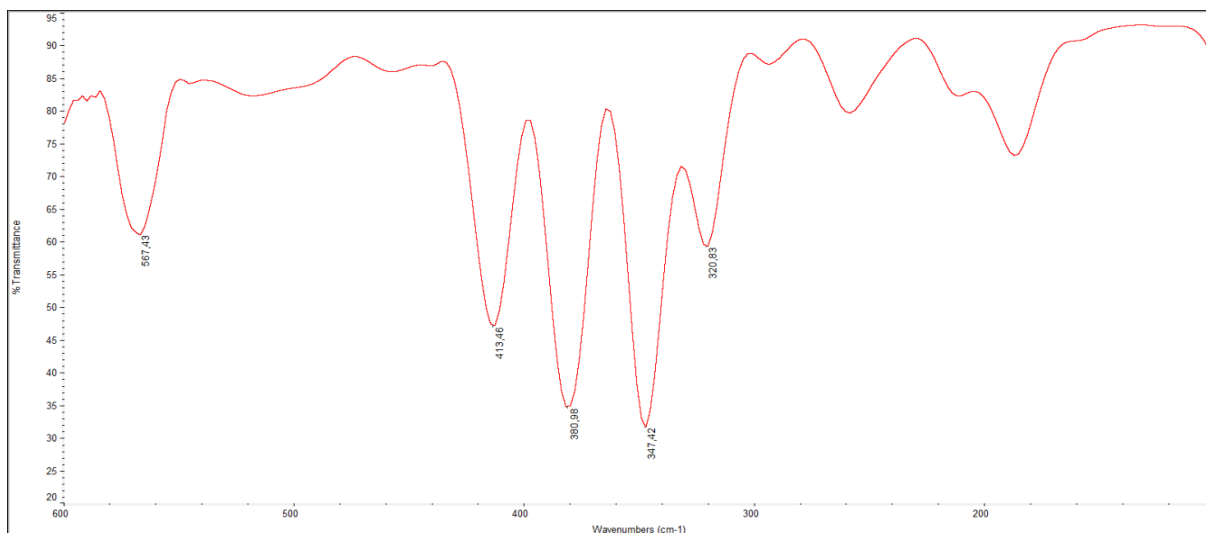
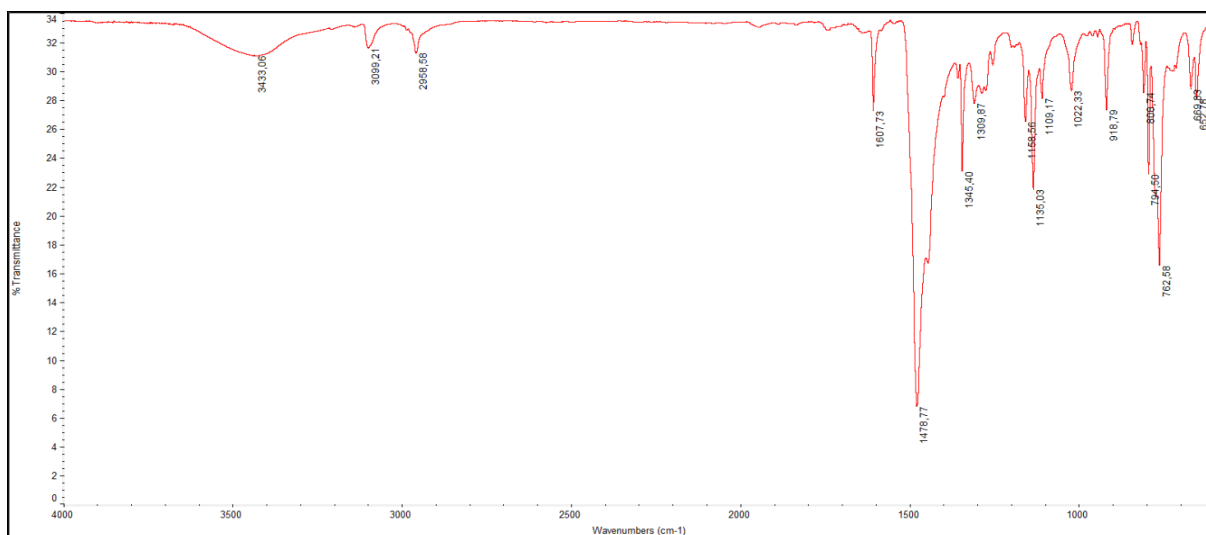


Figure I59. Medium FT-IR (4000-600 cm<sup>-1</sup>, KBr) spectrum of dichloro(pyrrole dithiocarbamate)gold(III), [AuCl<sub>2</sub>(PyrroleDTC)].



**Figure I60.** Far FT-IR (600-100 cm<sup>-1</sup>, nujol) spectrum of dichloro(pyrrrole dithiocarbamate)gold(III), [AuCl<sub>2</sub>(PyrrroleDTC)].



**Figure I61.** Medium FT-IR (4000-600 cm<sup>-1</sup>, KBr) spectrum of dibromo(pyrrrole dithiocarbamate)gold(III), [AuBr<sub>2</sub>(PyrrroleDTC)].

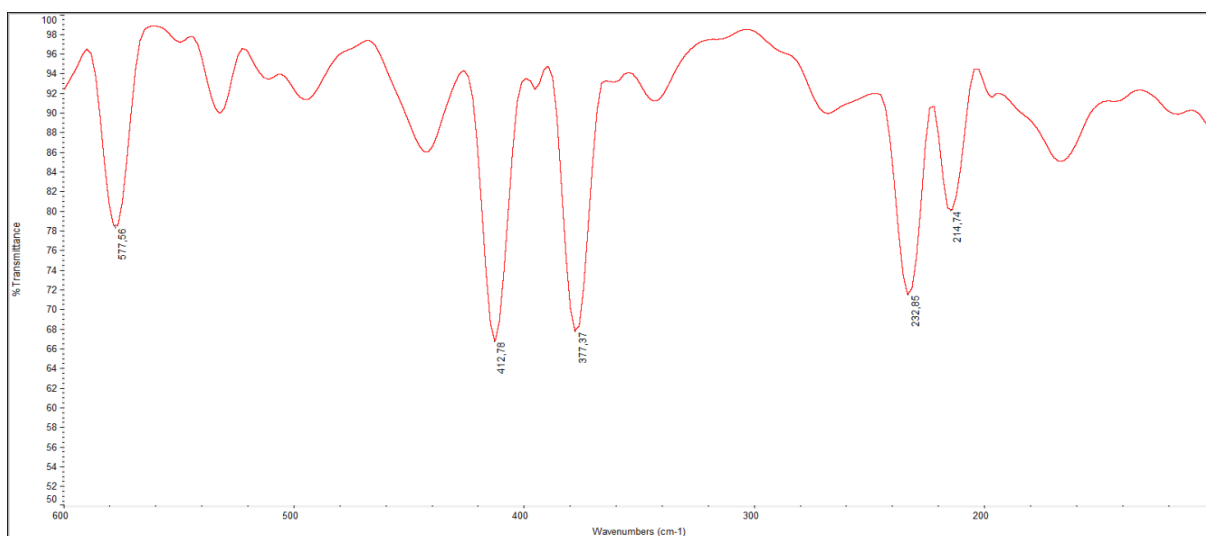


**Figure I62.** Far FT-IR (600-100 cm<sup>-1</sup>, nujol) spectrum of dibromo(pyrrrole dithiocarbamate)gold(III), [AuBr<sub>2</sub>(PyrrroleDTC)].



## SUPPORTING INFORMATION J - FT-IR spectra of the synthesized Pluronic® F127 derivatives

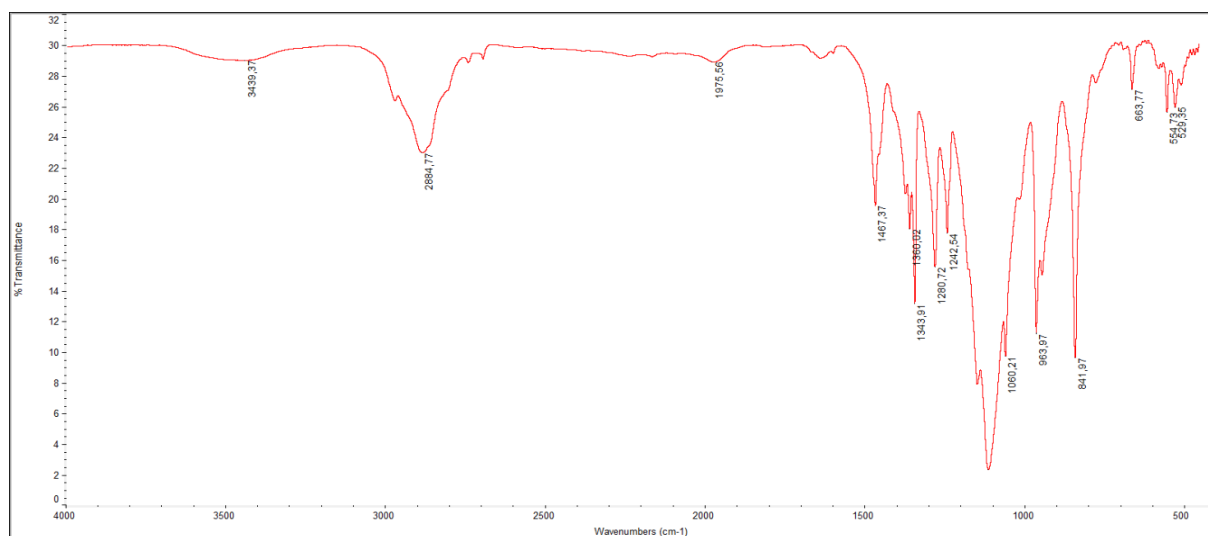


Figure J1. Medium FT-IR (4000-500 cm<sup>-1</sup>, KBr) spectrum of Pluronic® F127 tosylate, PF127-Ts.

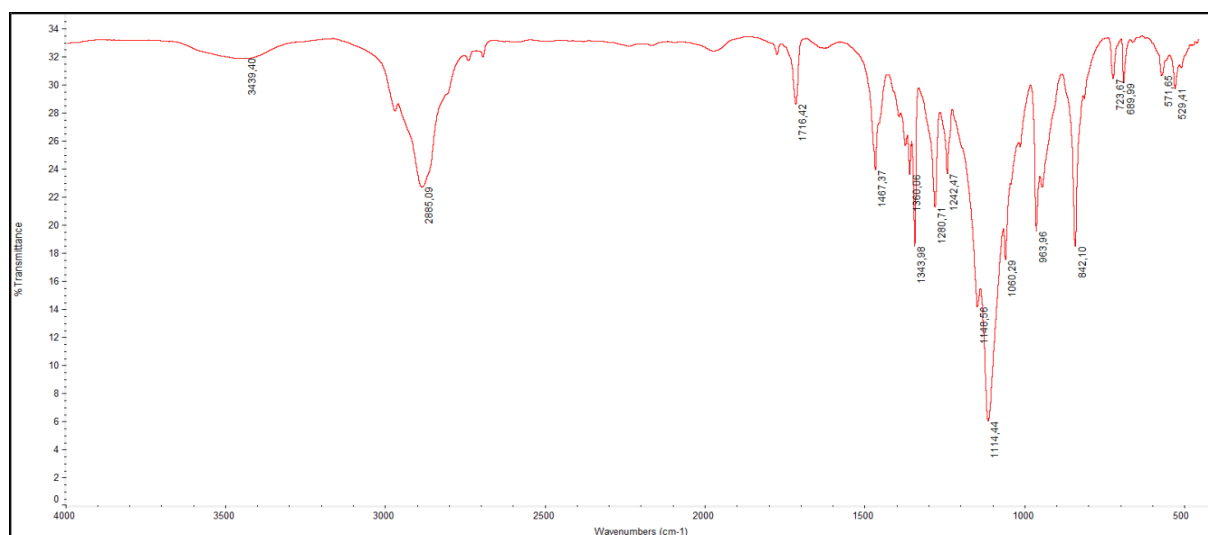


Figure J2. Medium FT-IR (4000-500 cm<sup>-1</sup>, KBr) spectrum of Pluronic® F127 phthalimide, PF127-Phtha.

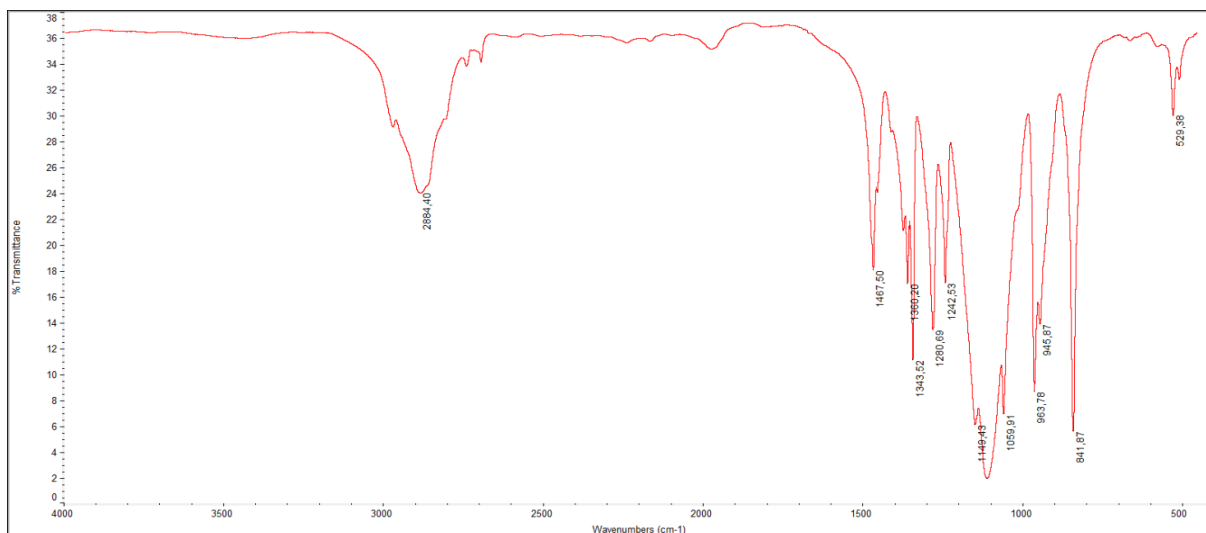


Figure J3. Medium FT-IR (4000-500  $\text{cm}^{-1}$ , KBr) spectrum of Pluronic® F127 amine, PF127-NH<sub>2</sub>.

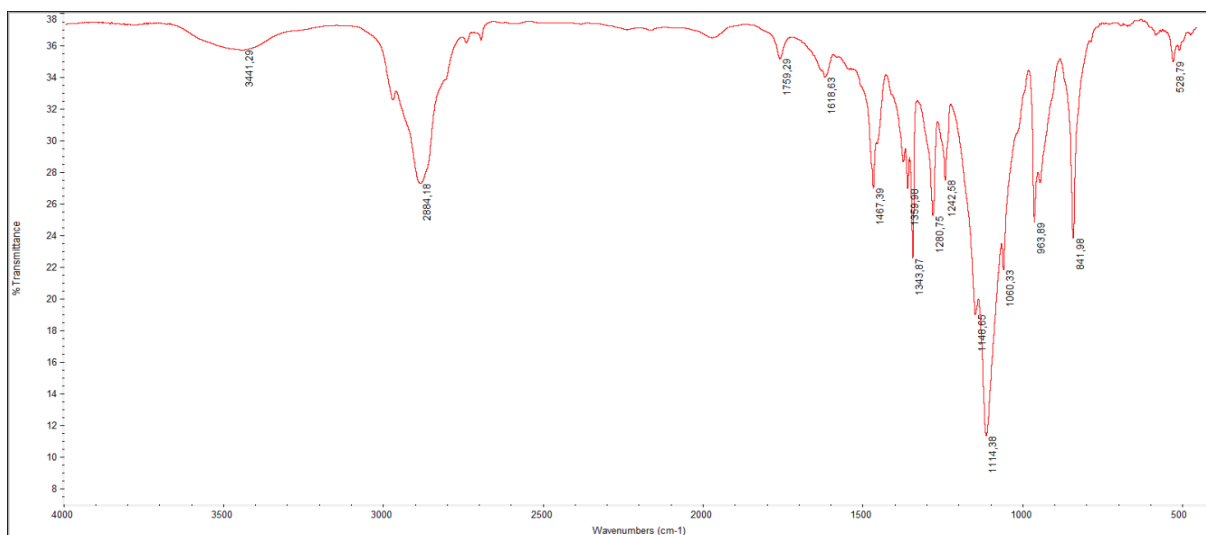


Figure J4. Medium FT-IR (4000-500  $\text{cm}^{-1}$ , KBr) spectrum of Pluronic® F127 conjugated to fluorescein *via* thiourea, PF127-FITC.

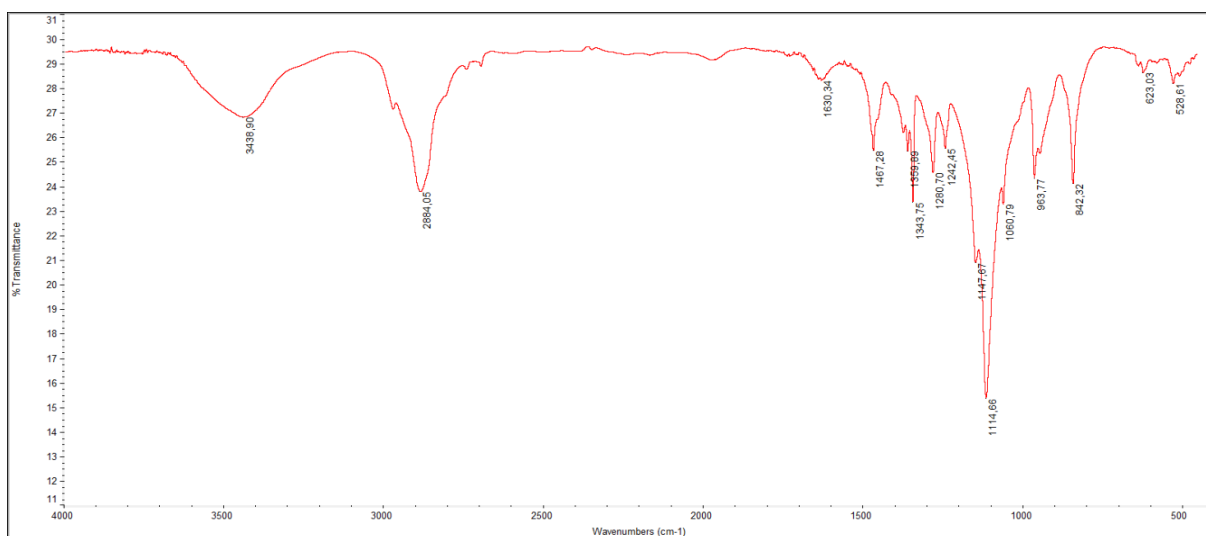
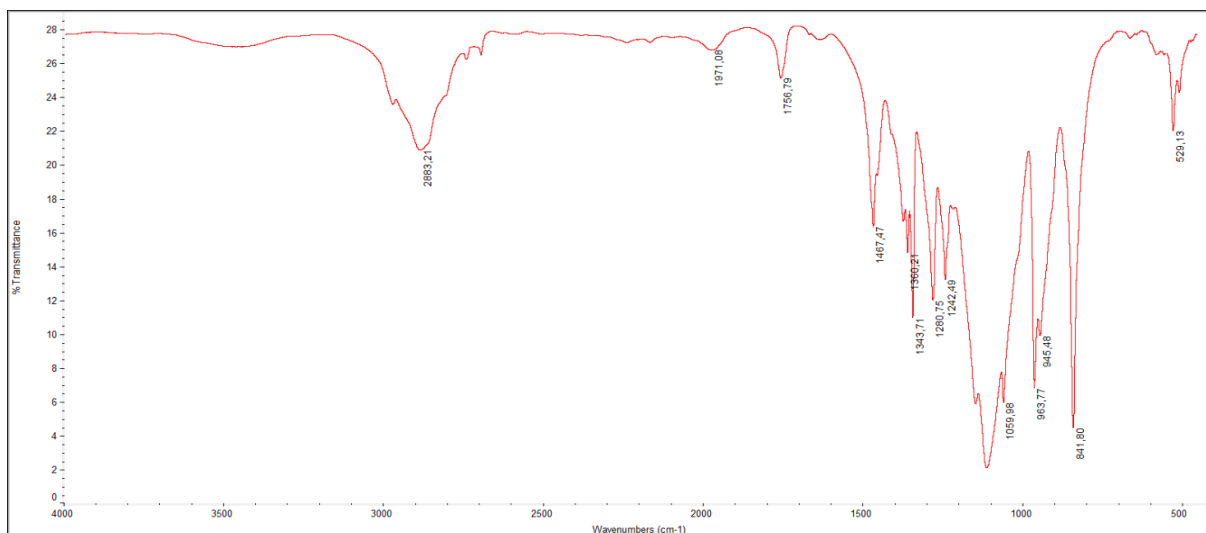
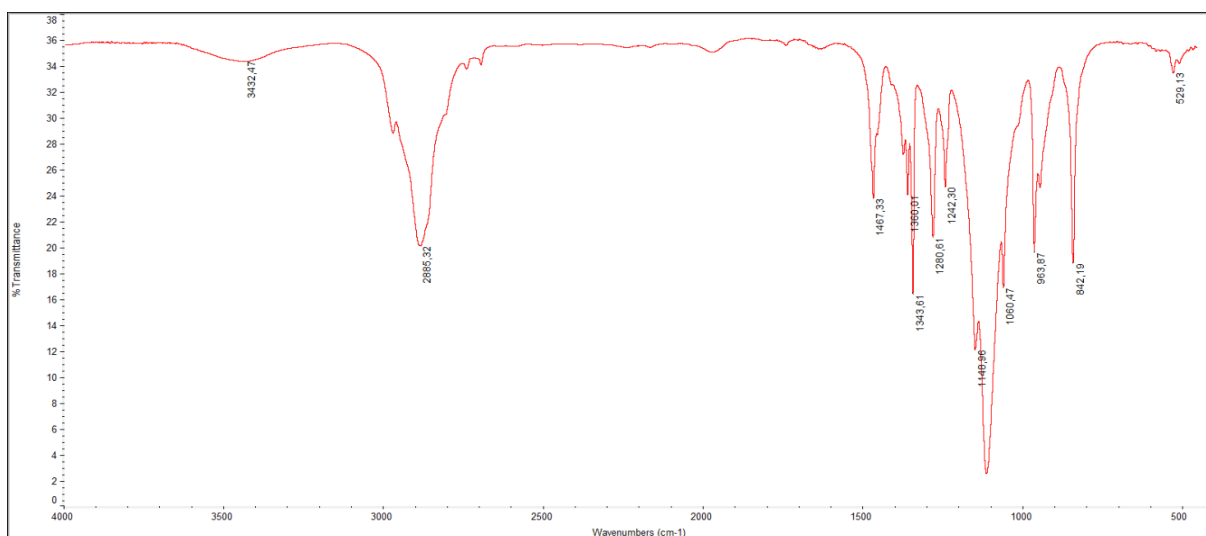


Figure J5. Medium FT-IR (4000-500  $\text{cm}^{-1}$ , KBr) spectrum of Pluronic® F127 aldehyde, PF127-CHO.



**Figure J6.** Medium FT-IR (4000-500  $\text{cm}^{-1}$ , KBr) spectrum of Pluronic® F127 conjugated to 1,3,4,6-tetra-*O*-acetyl-2-amino-2-deoxy- $\beta$ -D-glucopyranose *via* reductive amination, PF127-GlnOAc.



**Figure J7.** Medium FT-IR (4000-500  $\text{cm}^{-1}$ , KBr) spectrum of Pluronic® F127 conjugated to 2-amino-2-deoxy-D-glucose, PF127-GlnOH.

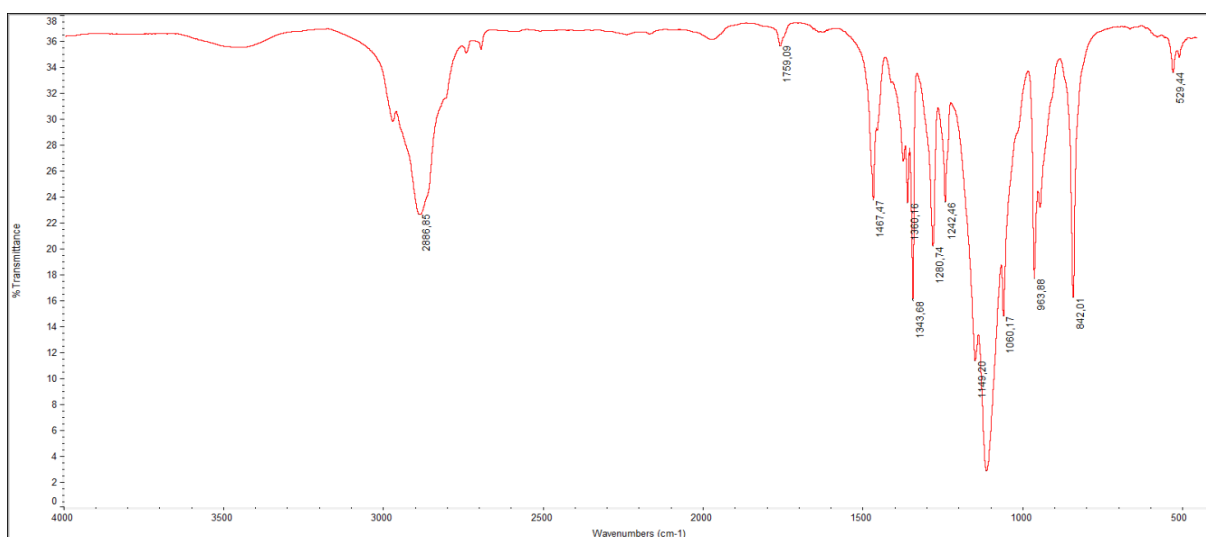


**Figure J8.** Medium FT-IR (4000-500  $\text{cm}^{-1}$ , KBr) spectrum of Pluronic® F127 conjugated to 2,3,4,6-tetra-*O*-acetyl- $\beta$ -D-glucopyranose *via* glycosylation, PF127-GluOAc.

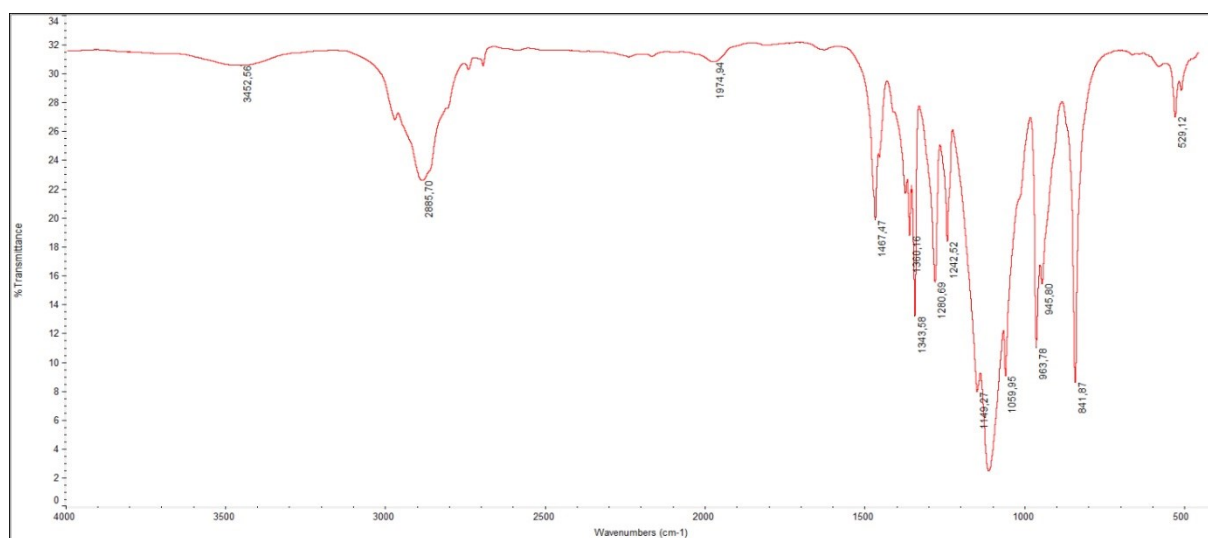


**Figure J9.** Medium FT-IR (4000-500 cm<sup>-1</sup>, KBr) spectrum of Pluronic<sup>®</sup> F127 conjugated to  $\beta$ -D-glucopyranose, PF127-GluOH.



## CONGRESS PARTICIPATIONS, COMMUNICATIONS AND PUBLICATIONS DURING THE PhD STUDIES

### Congress participations

- *14<sup>th</sup> School-Congress on the Chemistry of Carbohydrates–XIV CSCC 2014*. Certosa di Pontignano (Italy), 22-25 June 2014.
- *6<sup>th</sup> European Conference on Chemistry in Life Sciences (6<sup>th</sup> ECCLS)*. Lisbon (Portugal), 10-12 June 2015.
- *OneStart (World's largest healthcare accelerator) European Business Bootcamp: member of the research team ranked among the 40 Semifinalists starting from 750 teams*. London (UK), 5-6 February, 2016.
- *OneStart Final Phase (World's largest healthcare accelerator): member of the research team ranked among the 10 Finalists starting from 750 teams. From February to May 2016 constantly supervised by two Pharma mentors by conference calls followed by exams and drawing up of a Business Plan. The Top-10 exam and the Final Gala held in London (UK) on 12<sup>th</sup> May, 2016.*
- *3<sup>rd</sup> Liver Gymnasium - pre-meeting*. Padova (Italy), 22 September 2016.

### Conference proceedings

- C. Nardon, **L. Brustolin**, M. Coluccia, D. Fregona, "A preclinical overview on gold(III)compounds in the forefront of the target anticancer therapy", *4<sup>th</sup> World Congress on Cell Science & Stem Cells Research, June 24-26, 2014, Valencia*. doi: dx.doi.org/10.4172/2157-7013.S1.028 (oral)
- **L. Brustolin**, C. Nardon, D. Fregona, "From passive to active targeting of metal-dithiocarbamate complexes in anticancer chemotherapy: carbohydrates as good candidates", *14<sup>th</sup> School-Congress on the Chemistry of Carbohydrates –XIV CSCC 2014, Certosa di Pontignano (Italy), 22-25 June 2014*. (poster)
- **L. Brustolin**, N. Fantoni, L. Marchiò, A. Citta, A. Folda, M. P. Rigobello, D. Fregona, "Proline derivatives of different metals: from design and synthesis to preliminary biological studies", *6<sup>th</sup> European Conference on Chemistry in Life Sciences (6<sup>th</sup> ECCLS), Lisbon (Portugal), 10-12 June 2015*. (poster + short oral communication)
- R. Luisetto, C. Nardon, F. Lette de Oliveira, N. Bassi, **L. Brustolin**, N. Pettenuzzo, D. Fregona, L. Punzi, A. Doria, "Studio pilota sull'efficacia di una formulazione micellare contenente un complesso di Au(III) nel trattamento dell'artrite sperimentale da collagene nel topo", *Congresso Nazionale SIR (Società Italiana Reumatologia), Rimini (Italy), 25-28 November 2015*. (oral)
- M. Beggio, R. Luisetto, C. Nardon, F. Lette de Oliveira, N. Bassi, **L. Brustolin**, N. Pettenuzzo, A. Ghirardello, D. Fregona, A. Doria, "Efficacy of a micellar formulation of Au(III) complex in collagen

induced arthritis”, *10<sup>th</sup> International Congress on Autoimmunity, Leipzig (Germany), 6-10 April 2015*. (poster)

- **N. Pettenuzzo, L. Brustolin, C. Nardon, D. Fregona**, “An excellence in medicinal inorganic chemistry: a portrait of the gold(I/III) complexes patented for therapeutic purposes from 2010 to 2015”, *Proc. 1<sup>st</sup> International Symposium on “Clinical and experimental metallodrugs in medicine: cancer chemotherapy”, Honolulu (HI), USA, 12-15 December 2015*. (poster)
- **C. Nardon, L. Brustolin, N. Pettenuzzo, D. Fregona**, “Exploring new strategies to overcome the drug death valley in oncology”, *2<sup>nd</sup> International Conference on “Clinical Sciences and Drug Discovery”, 27-29 July 2016, Dundee (Scotland)*. (oral)
- **C. Nardon, N. Pettenuzzo, L. Brustolin, D. Fregona**, “The current horizon of gold-based therapeutics: from chemical features to benefits”, *XLVI Congresso Nazionale della Divisione di Chimica Inorganica della Società Chimica Italiana, Padova (Italy), 13-17 September 2016*. (oral)
- **C. Nardon, L. Brustolin, N. Pettenuzzo, S. Scintilla, A. Accardo, G. Morelli, S. Salmaso, P. Caliceti, D. Fregona**, “Natural and synthetic macromolecules as carriers for metal-based anticancer chemotherapeutics: an in vitro and in vivo survey”, *Convegno Nazionale della Divisione di Chimica dei Sistemi Biologici della Società Chimica Italiana – Verona (Italy), 21-23 September 2016*. (oral)
- **L. Brustolin, C. Nardon, N. Pettenuzzo, S. Quarta, P. Pontisso, D. Fregona**, “Groundbreaking metal-based anticancer agents in the treatment of hepatocellular carcinoma”, *3<sup>rd</sup> Liver Gymnasium - pre-meeting, Padova (Italy), 22 September 2016*. (oral)

### Peer-reviewed papers

- “Gold(III)-pyrrolidinedithiocarbamate derivative as antineoplastic agents”, **C. Nardon, F. Chiara, L. Brustolin, A. Gambalunga, F. Ciscato, A. Rasola, A. Trevisan, D. Fregona**, *Open Chem.*, **2015**, 4, 183.
- “Is matching ruthenium with dithiocarbamate ligands a potent chemotherapeutic weapon in oncology?”, **C. Nardon, L. Brustolin, D. Fregona**, *Fut. Med. Chem.*, **2016**, 8(2), 211.
- “Ru(III) anticancer agents with aromatic and non-aromatic dithiocarbamates as ligands: loading into PF127 micelles and preliminary biological studies”, **L. Brustolin, S. Scintilla, A. Gambalunga, F. Chiara, A. Trevisan, C. Nardon, D. Fregona**, *J. Inorg. Biochem.*, **2016**, 166, 76.

### Patents

- Italian patent n. 102016000122363 (Title: COMPOSTI DI COORDINAZIONE, SINTESI, NANOFORMULAZIONE ED USO DEGLI STESSI IN ONCOLOGIA); Inventors: **D. Fregona, C. Nardon, L. Brustolin, N. Pettenuzzo**; Filing: December 2, 2016.

- Italian patent n. 102016000122406 (Title: COMPOSTI DI COORDINAZIONE, SINTESI, NANOFORMULAZIONE ED USO DEGLI STESSI IN ONCOLOGIA); Inventors: D. Fregona, C. Nardon, **L. Brustolin**, N. Pettenuzzo; Filing: December 2, 2016.



